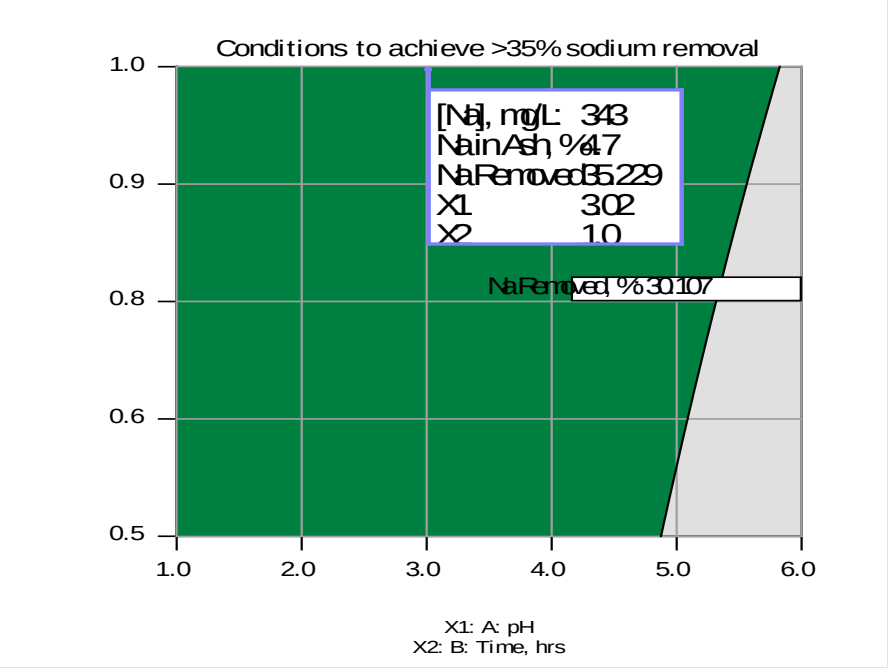

Figure ES-2. Optimization of conditions for leaching Coal B with hydrochloric acid solutions (The selection of time/pH conditions in the dark green region should result in the removal of >30% of the sodium. Note also that a flag has been added to show the amount of sodium in the leach solution, 35% sodium removal, and the sodium content in the product ash).

Coal D

Coal D showed significantly greater sodium removal than Coal B for similar treatment conditions. The treatability of Coal B is demonstrated in Figures ES3 to ES5.

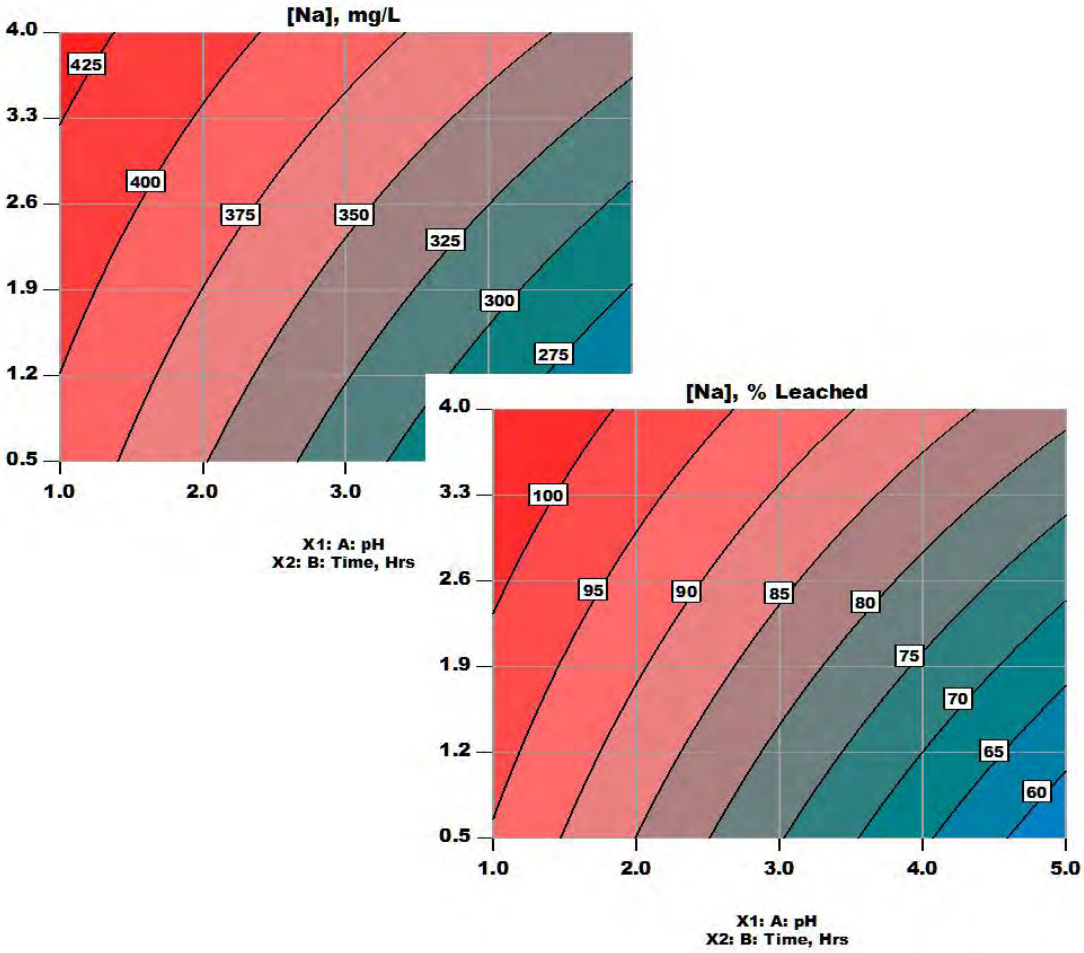

Figure ES3. Coal D leach results for hydrochloric acid solutions (Greater than 75% of the sodium was removed using pH 3 acidic solutions at a 1-hour treatment time. The initial sodium, reported as sodium oxide in the ash, was 6.16 %. The removal of over one-half of the sodium can be achieved using conditions of pH 5, 0.5 hours).

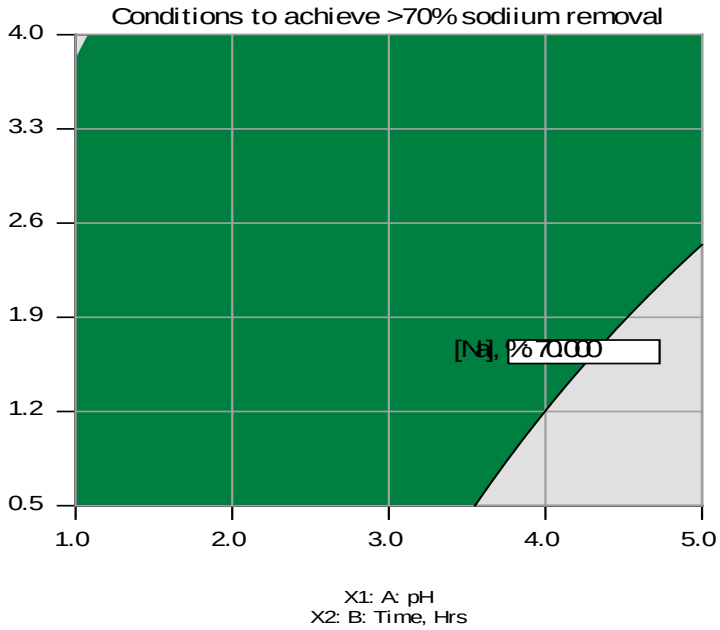

Figure ES-4. Optimization of conditions for leaching Coal D with hydrochloric acid solutions (The selection of time/pH conditions in the dark green region should result in the removal of >70% of the sodium. Coal D is much more amenable to acidic leaching than was Coal B.

Recommended Future Studies

It is recommended that future studies include, but not be limited to:

- Investigation to determine if multiple leach solution contacts with new coal will allow recycle of the leach solution without detrimentally affecting the leachability of the coals and to produce a concentrated sodium bearing solution in order to limit the amount of leach solution that would have to be treated prior to water recycle or disposal.
- Water cleanup will be required because of the relatively high sodium and chloride or sulfate content.
- Evaluation of where and how the leachate could be introduced into the coal preparation treatment system.
- Evaluation of the possible impact of pretreatment on the subsequent shipping and combustion processes.
- The anticipated cost of the sodium cleansing treatment and subsequent water treatments.

FINAL REPORT
TABLE OF CONTENTS

INTRODUCTION

Background

The US Department of Energy (DOE) Center for Advanced Separation Technologies (CAST), Great Northern Properties (GN), and the Montana Board Research and Commercialization Technology (MBRCT) are funding this project. The project is being administered and the research directed and conducted at CAMP. The intent of the project is to identify, and validate selected currently used (or previously studied) removal and sodium recovery treatment alternative(s) using laboratory bench-scale tests on four Montana coal samples. If the coals cannot be effectively treated by known techniques, alternative treatments will be developed. The evaluation of selected sodium removal technologies are presently underway and the following four stages are being and will be followed in future work: the successful removal of sodium from the coal so that the ash will content less than three percent, the rate at which the sodium ions are removed, characterization of the waste produced by sodium removal processing, and the overall economics of viable processes. Not part of the initial Project, but a necessary follow-up, will be the scale-up of the most appropriate sodium removal technology(s) in applications with companies using Clean Coal Technology to demonstrate sodium removal process or processes on a pilot scale.

Objective and Approach

The overall objectives of the project are to develop and implement viable sodium removal and sodium recovery treatment alternatives for the Low-Rank Coal Industry.

Project Tasks

To properly develop and evaluate viable sodium removal and sodium recovery treatment alternatives for the Montana Coal Industry, the following tasks have been completed. The Project is separated into ten (10) Tasks (listed below and presented in Table 1). Following the completion of Task 6, GN and other participating coal companies and CAMP reviewed the literature review and preliminary test work to select the technologies to be bench-scale tested and evaluated. Tasks 6 through 10 was then performed using the chosen technology to validate their applicability. However, Task 9 was not completed and will be discussed later. The technology selection was based on the technical viability of the sodium removal and sodium recovery technology(s)/treatment approach(s) selected in Task 5.

The Project Tasks are specified below:

1. Literature Search
2. Identification of Primary Coal Producers/Users Needs
3. Characterization
4. Physical and Chemical Property Evaluation
5. Selection of Treatment Approach(s)
6. First Interim Report
7. Test Plan Development
8. Bench-Scale Testing and Evaluations
9. Economic Evaluation of Promising Treatment Approach(s)
10. Project Report

The performance benchmarks and target dates for each task are provided in Table 1.

Table 1. Task Number, Performance Benchmarks, and Target Dates (Start Date 01/01/09)		
Task No.	**Task Description**	**Target Date**
1	Literature Search	10/30/09 (completed)
2	Identification of Primary Coal Producers/Users Needs	04/30/09 (completed)
3	Characterization of Coals	09/30/09 (completed)
4	Physical and Chemical Property Evaluations	11/31/09 (completed)
5	Selection of Treatment Approach(s)	12/30/09 (Completed)
6	First Interim Report	01/31/10 (Completed)
7	Test Plan Development	03/31/10 (Completed)
8	Bench-Scale Testing and Evaluations	03/31/12
9	Economic Evaluation of Promising Treatment Approach(s)	Not Performed
10	Project Final Report	4/30/12

Task 1-Literature Search and Review

The literature search has been completed and the results are attached as Appendix A.

Summary of Literature Review-A detailed literature review (over 220 publications) has been conducted summarizing usual treatment approaches for the removal of sodium (and in some cases potassium) from low-rank coal. The reviewed publications are summarized in this report and are presented in detail in the attached Appendix A report: LITERATURE REVIEW: SODIUM REMOVAL FROM LOW-RANK COALS [Twidwell and Dudley 2010).

Background- Lignite and sub-bituminous coal reserves (low-rank coals) are plentiful in the high plains of Montana, North and South Dakota, and Wyoming, see Figure 1 (*American Coal Foundation, 2007*). In general, low-rank coals contain more ash, sodium, potassium, and, in some cases, calcium, magnesium, iron, and aluminum than do the hard coals (anthracites and bituminous). The emphasis of this review was focused on sodium, potassium removal from low-rank coals.

Multiple mines and power plants exist in the Western states region, e.g. Montana Major Coal mines 6 (5 sub-bituminous, 1 lignite) (*Montana Coal Council, 2009*), coal-fired generating plants 5 (1 major) (*Electric Power Monthly, 2009*); North Dakota Major Lignite mines 4, Lignite coal-fired generating facilities 5 (*Lignite Energy Council, 2009*); Wyoming Major Bituminous and sub-bituminous mines 14 (4 major), Bituminous coal-fired generating facilities 23 (4 major) (*SourceWatch, 2009*).

For interested users of this report The National Coal Council's "Coal: America's Energy Future, Volume II" (NCC, 2006) is recommended as a general review and description of present day coal usage technologies (discussed further in the General Review section). General characterization data are presented for Western and Texas low-rank coals (Figure 2) and a comparison of world coal reserves is presented in Figures 3 (*Stiegel, 2008*) and 4 (*Thielemann, et al, 2007*). The outlook for possible future US coal production, based on demonstrated reserve base, is presented in Figure 5 (Hook and Aleklett, 2009).

Figure 1. Estimated Coal Reserves in 2005 (American Coal Foundation, 2006)

Properties of U.S. Low-Rank Coals

	Wyoming Subbituminous *Spring Creek*	Montana Subbituminous *Decker*	N. Dakota Lignite *Freedom*	Texas Lignite *S. Hallsville*
Heating Value, kcal/kg (as received)	5,107	5,301	3,940	3,934
Proximate, wt%:				
Moisture	24.1	23.4	33.3	37.7
Volatile matter, dry	43.1	40.8	43.6	45.2
Fixed carbon, dry	51.2	54.0	45.3	44.4
Ash, dry	5.7	5.2	11.1	10.4
Ultimate, wt% moisture free:				
Carbon	70.3	72.0	63.3	66.3
Hydrogen	5.0	5.0	4.5	4.9
Nitrogen	0.96	0.95	1.0	1.0
Sulfur	0.35	0.44	1.1	1.2
Ash	5.7	5.2	11.1	10.4
Oxygen	17.69	16.41	19.0	16.2

Figure 2. General Properties of U.S. Low-Rank Coals (Power point Presentation by Stiegel, US DOE 2008)

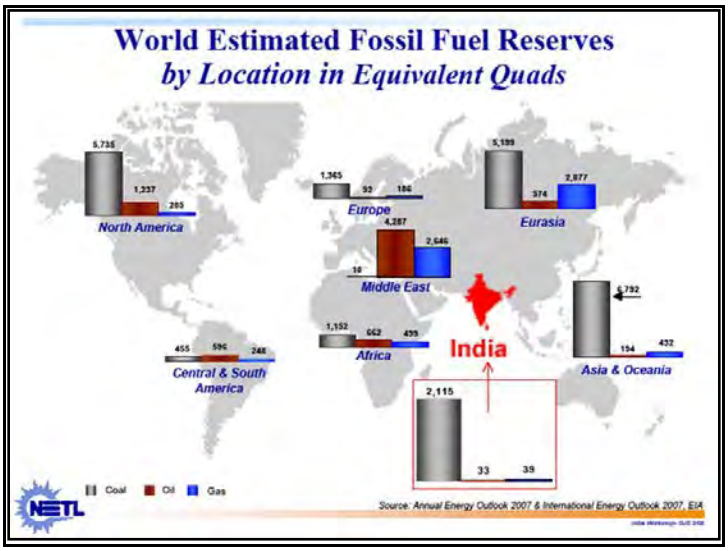

Figure 3. Estimated World Fossil Fuel Reserves in 2005 (Power point Presentation by Stiegel, US DOE 2008)

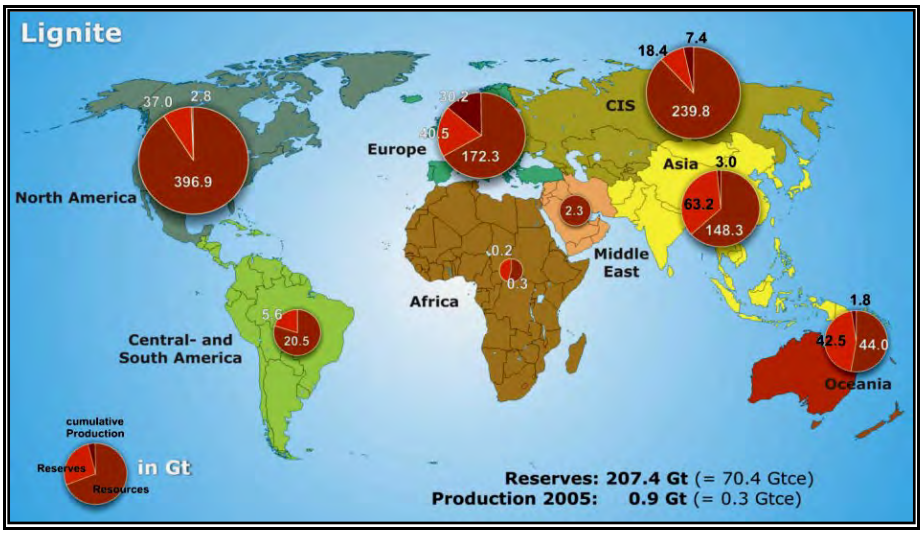

Figure 4. Estimated World Lignite Reserves in 2005 (Thielemann, et al (2007)

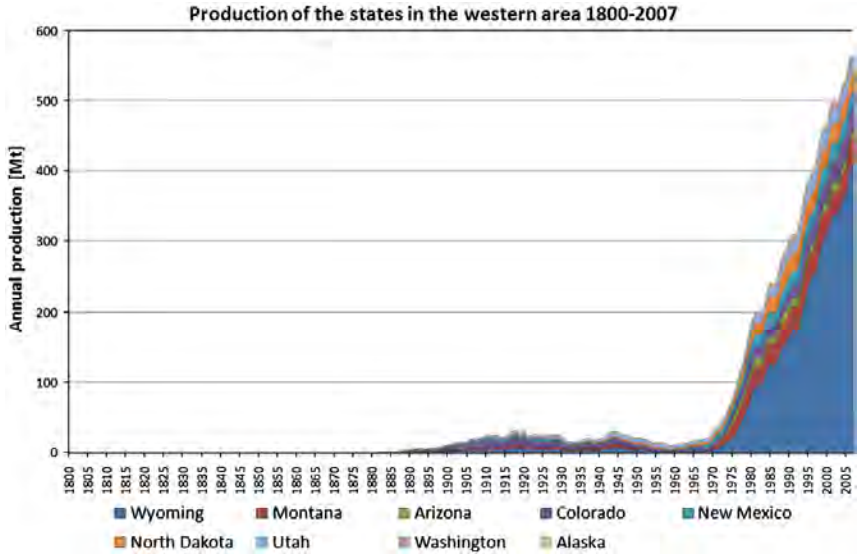

Figure 5. Coal Production in the western United States (Hook and Aleklett, 2009)

Occurrence of Inorganic Constituents in Low-Rank Coals- Coals may be considered to be made-up of two general types of matter, i.e. organic components, i.e. macerals, and inorganic compounds, i.e. minerals. The type of matter, and the relative concentration of maceral and mineral content, is very important with respect to how a coal acts during combustion. The maceral content is, to a large extent, responsible for determining the coals energy output during combustion. Both the maceral fraction and mineral fraction contain inorganic constituents. These inorganic constituents determine the characteristics of the ash produced during combustion and whether the ash products are present as solids or molten liquids. In general, it is the inorganic constituents that cause problems during coal combustion. Inorganic elements can be present as a variety of species in low-rank coals. Primarily they are present as species associated with organic matter, bonded within the carbon structure, dissolved in pore moisture, crystalline salts, and as constituents in mineral phases. The associations in the maceral fraction are cations bound as carboxylate groups, and inorganic complexes coordinated with carboxyl and phenolic groups. The content of inorganic elements, including sodium, potassium, calcium, magnesium, and iron, in low-rank coals is usually

concentrated in the maceral matter. Lesser amounts of inorganic elements can be associated with the carbon structure as oxy-hydroxyl polymeric complexes. Low-rank coals that contain appreciable chloride or sulfur contents (like low-rank coals in Australia but not the coals in the Western United States) often contain appreciable amounts of the crystalline salts, sodium chloride or sodium sulfate. Also, sodium can be present in the moisture component of the coal. Inorganic elements are also associated with mineral phases dispersed throughout the coal matrix.

The organic matter in low-rank coals have been extensively studied by many investigators and it has been demonstrated that a significant portion of the inorganic elements reside there . The reported results by *Zhongsheng, et al (2009 and 2007)* are an example. Their results, of course are specific for the low-rank coals they studied, but do demonstrate that a significant concentration of the inorganic elements are present in the maceral matter, e.g. Ca (up to 15000 mg/kg of maceral content), Al (up to 5000 mg/kg), Fe (up to 7000 mg/kg). The knowledge that significant sodium and potassium reside in the organic fraction is important because these elements tend to volatilize as atomic species during combustion and these species are very reactive and readily promote the formation of low-melting slags and other fouling species (*Falcone and Schobert, 1986*). Examples of other publications that have describe the containment of inorganic elements in macerals are *Ward, et al (2005, 2003*) and *Chen, et al (2004*).

The mineral content is usually greater in low-rank coals than in higher rank coals. A significant fraction of the mineral content in low-rank coals may be "intimately" present as a part of the maceral content and it is often difficult to separate the mineral components from the organic components by normal physical separation processes, therefore, removal of the mineral fraction by normal mineral processing technologies may not be effective. Sodium and potassium bearing minerals present in the Montana coals have been identified: apatite:albite ($Ca_5(PO_4)_3OH$:$NaAlSi_3O_8$); sodium amphibole ($Na_2(Mg,Fe)_3Al_2Si_8O_{22}(OH)_2$); and potassium feldspar ($KAlSi_3O_8$). Other minerals identified in the Montana coals relevant to the present study are presented in Table 13.

The Problem with Sodium and Potassium-The detrimental effects of ash forming constituents in low-rank coals during combustion are well documented. Alkali constituents and high moisture content are characteristics of low-rank coals. During combustion the alkaline constituents form gaseous and liquid species that readily form molten and semi-molten silicates. These molten products (slags) have an adverse effect on boiler and gasification combustors. A long list of detrimental consequences caused by alkaline constituents, especially sodium and potassium, can be quoted, e.g. fireside fouling, inhibition of heat transfer, obstruction of gas flow, excessive corrosion of boiler surfaces, formation of sticky chars that promote particle agglomeration, and formation of fly ash that is readily soluble in outdoor storage ponds.

Technologies- The present literature review has shown that two major technological approaches have been investigated to mitigate the sodium problem during combustion; e.g., Solution leaching of sodium using reagents to remove sodium salts, and/or organically bound species that are a part of the coal maceral matter or are present as sodium bearing mineral phases; and Addition of metal compounds or mineral phases to react with the sodium and sodium compounds during the combustion process to form compounds that remain solid and/or less-corrosive at combustion temperatures.

Solution Leaching Technologies-There have been only a limited number of investigations to demonstrate partial removal of sodium from low-rank coals by mild solution phase (leaching) treatments on a laboratory scale. **We could not find publications where this technique has advanced to industrial use**. A relatively large number of recent investigations have focused on

treating low-rank coals to remove essentially all of the ash forming elements so that ash does not form during combustion. The emphases of these papers are based on the desire to utilize low-rank coals to produce a clean feedstock for gasification processes (aggressive treatments to remove ash formation species, i.e. to produce a "clean" coal).

Solution Leaching-The literature review, modeling, and preliminary test work results suggest that coal leaching in pH adjusted water containing an ion exchange reagent (acids, calcium chloride or ammonium acetate) may be appropriate for the removal of approximately forty to eighty percent of the total sodium present, e.g. sodium salts and maceral phase organically bound sodium. The sodium and potassium mineral phases are likely not dissolved in water, mild acids, or ion exchange reagent bearing water. The removal of greater amount of sodium require that a portion of the mineral compounds be dissolved and for this to occur the treatment conditions must be aggressive. Aggressive reagent leaches would be relatively expensive, therefore, they may be limited to coals that require very low ash "Clean" coals as fuels for gasification or liquefaction processes. Clean Coal Technology Pty (*Domazetis, et al, 2009*) is an example of a company that is aggressive developing a commercial technology that would upgrade low-rank coals for use in power generation that would have low level greenhouse gas emissions.

General low-rank coal upgrading leaching pretreatment techniques are presented in Table 2.

Table 2. General Low-Rank Coal Upgrading Techniques

Treatment	Removal	Reagent	Comments (See accompanying Literature Review)
Physical techniques/washability	Mineral fines, dissolved sodium salts	Water	Physical separations can be effective including float/sink, froth flotation, and centrifugal washing. In some cases low-rank Western coals respond well to washability techniques for removal of all elements analyzed in the ash except for calcium and magnesium.
Hydrothermal	Moisture	Water at 320^{o}C	Many studies have been reported for treatment of low-rank coals, some showed 70% sodium removal at pHs of 5-6.5. Treatment waters contain 3-6 g/L dissolved organics and high sodium levels so leach waters have to be cleaned.
Leaching Techniques			
Water	Sodium	Water	Can be effective for coals containing crystallized salts in the coal matrix and dissolved in pore water. Not very effective for coals not containing salts. Not effective for dissolving mineral phases.
Acidic	Na, K, Al, Ca, Mg	Inorganic acids, formic, acetic, pHs 2 to 6	Primarily removes organically bound elements, crystalline salts, dissolved sodium compounds; only a minor amount of minerals removed.
Acidic/Ion Exchange Reagent	Na, K, Al, Ca, Mg	Inorganic acids, ammonium acetate,	Primarily removes organically bound elements, crystalline salts, dissolved

Table 2. General Low-Rank Coal Upgrading Techniques			
Treatment	**Removal**	**Reagent**	**Comments (See accompanying Literature Review)**
		calcium chloride, sodium acetate, aluminum lactate	sodium compounds. The treatment can be effective for dissolving a minor amount of mineral phases.
Aggressive	All ash elements	Low pH leaching (<1-2) using hydrochloric, nitric, hydrofluoric, combination of acids, caustic, and elevated temperatures	Technique to lower the coal ash solids so that the amount of ash formed during combustion is very low. Applied to produce a "Clean" coal for gasification processes.

Addition of Mineral Compounds or Mineral Phases-The literature review and modeling results suggest that addition of reagent compounds or minerals to change the characteristics of the ash formed during combustion is an appropriate technology. This technique has been demonstrated in numerous laboratory and several demonstration studies (see the accompanying Literature Review). The technique has been used for years to control sulfur removal by injection (or premixing with the coal) of calcium or magnesium hydroxide. In fact, several companies market such technologies. As an example Fuel Tech *(Davis and Schulz, 2008)* markets their Targeted In-Furnace Injection (TIFI) technology that is based on injecting chemical reagents (designed for the specific application but not specified for sodium control) at critical points in the combustor. The claim is that by using specific injection points the amount of reagent is much less than mixing the reagent with the coal prior to combustion.

The use of this treatment technology would require its implementation at power plant sites, i.e. it would not be a technology appropriate for use at the mine sites.

Task 2-Identification of Primary Coal Producers/Users Needs

Four Montana coal mining companies were identified, contacted and they agreed to support this project. Coal samples were collected from each of the participating Montana coal companies. The coal companies have requested that they not be presently identified and all data and discussions are, therefore, referred to in this report as Company A through D.

Task 3-Characterization of Coal Samples (Presentation of Historical and Experimental Data)

General characterization data for typical Montana coals are presented in Table 3 (*Montana Means Business, 2009*). Characterization data for specific Montana coals used in this study are presented in Tables 4 to 6, e.g. Sample Identification, Sodium Content in Coal Fines, and Ash (Table 4); Proximate Analysis (Table 5); and, Ultimate Analysis, Heating Value, and Softening Temperature (Table 6). Additional characterization data are presented in the following Task 4 discussion.

Table 3. Montana Coal General Proximate Characterization for Ash, Sodium, and Sulfur Contents (Montana Means Business, 2009)				
Area	**Ash %**	**Sodium, %**	**Sulfur, %**	**Moisture, %**
1 (Sub-Bituminous)	12.0	0.27	1.0	16.9
2 (Sub-Bituminous	9, 8.2, 9	0.5, 0.3, 1.2	0.7, 0.7, 0.9	25.5, 25.6, 25.7
3 (Sub-Bituminous)	4.1, 4.6,3.6	6.8, 6.4, 8.0	0.38, 0.45,0,32	24.3, 24.2, 25.0
4 (Lignite)	18.5	0.3	0.35	30

Table 3. Montana Coal General Proximate Characterization for Ash, Sodium, and Sulfur Contents (Montana Means Business, 2009)				
Area	**Ash %**	**Sodium, %**	**Sulfur, %**	**Moisture, %**
5 (Lignite)	7.5	5	-	35
6 (Sub-Bituminous)	5	7	0.17	28

Source: Montana Means Business (2009) at website: business mt.gov/docs/coal.pdf

Table 4. Sample List, Sample Description, and Alkali Content in Montana Coals and Ashes						
Sample No.	**Sample ID**	**Sample Description**	**Sodium and Potassium Content, mg/kg**			
			Coal		**Ash**	
			Na	**K**	**Na**	**K**
1	A1	Coarse Split			390	12
2	A2	Fine Split	341.4± 13.8	42.6± 14.5	370	25
3	A3	Waste Fine			816	37091
4	B1	Coarse Split			12277	94
5	B2	Fine Split	2510± 160	64.9± 25.3	9750	126
6	B3	Waste Coarse			2523	34021
7	B4	Waste Fine			2597	34436
8	C1	Coarse			735	221
9	C2	Fine	1332.6± 182.1	82.5± 26.3	582	270
10	C3	Waste Coarse			6010	32943
11	C4	Fine			5787	32611
12	C5	Waste (Burnout) Coarse			4526	23732
13	C6	Waste (Burnout) Fine			4971	34811
14	D1	Coal Fines	3132.0± 437.3	27.8± 19.0	9795	48
15	D2	As-received, January 2012	3460±400	-	45700	9049

The collected as-received coal samples were crushed, roll sized, then pulverized. The Coarse and Fine sample designations are for the sample splits -5/+3 and -1.7/+0.038 mm, respectively. Sodium contents in the coal are for as-received samples. Coal D2 was received late in the project. Coals B2 and D2 were extensively investigated by experimental design studies for potential sodium removal by acidic leaching.

Table 5. Proximate Analysis of As-Received Montana Coal Fines (wt. %)				
Coal Company-Sample	**Moisture**	**Ash**	**Volatiles**	**Fixed Carbon**
A2	20.6	10.2	32.2	37.0
B2	20.7	4.6	32.4	42.2
C2	22.4	13.2	31.3	31.4
D1	29.3	4.1	33.1	35.2
D2	5.38	8.9	37.7	48.0

Wyoming Analytical Laboratory, Inc (Wallaramie@wal-lab.com,2009and 2012)

Table 6. Ultimate Analysis (wt %), Heating Value (BTU/lb), and Softening Temperature (°C) of As-Received Montana Coal Fines							
Coal Company-Sample	**Hydrogen**	**Carbon**	**Nitrogen**	**Sulfur**	**Oxygen**	**Heating Value**	**Softening Temp**
A2	2.5	52.9	0.9	0.6	12.3	9,013	1300
B2	3.0	56.8	1.0	0.6	13.2	9,950	1093
C2	2.4	49.8	1.0	0.5	13.8	8,383	1381
D1	2.7	49.9	0.8	0.1	13.9	8,508	1170
D2	3.6	65.56	1.0	0.21	15.32	10858	1288

Wyoming Analytical Laboratory, Inc (Wallaramie@wal-lab.com,2009and2012)

Task 4-Physical and Chemical Property Evaluation

Coals *(presentation of data)*-Sieve analyses for all the "fine" Montana coal fractions are presented in Appendix B; Coals B2 and D2 results are presented in Tables 7 and 7a, respectively, as examples of the data. The sodium concentrations in the coal fine composite samples were presented previously in Table 4; the sodium concentrations in the analyzed coal samples varied widely between coal companies, e.g. 341 mg/kg (coal A2) to 3460 mg/kg (Coal D2). These results are in general agreement with historical low-rank coal sodium content data, except for coal A2, for the Western United States coals, e.g. USGS COALQUAL and the Montana Bureau of Mines and Geology (MBMG) databases, Table 8.

The sodium concentration as a function of particle size for each Montana coal is presented in Table 9, and for other associated elements in Appendix B; Coal B2 and D2 results are presented in Table 10 as examples of the data. The data presented in Table 11 are important because the presence of associated inorganic elements, along with sodium and potassium, influences the temperature at which molten liquids form. The formation of molten liquids may create problems during combustion. The data presented in Appendix B for all elements are in general agreement for the present Montana coals with historical low-rank QUALCOAL coal data for the Western United States, Table 12. The concentration of associated elements in coals in the Montana and other Western States vary greatly, as would be expected because of the varied mineralogical make-up of the coals.

Knowledge of the mineral phases present in the low-rank coals is very important with respect to what reactions occur during combustion. The mineralogical make-up of the presently studied coals is presented in Table 13. The percent of each phase present in the mineral matter present in each coal is presented in Appendix B; Coal B2 mineral content is presented in Table 14 as an example of the data.

Table 7. Sieve Analysis for Fine Fraction of Montana Coal B2				
Size (Tyler Mesh)	**Size (mm)**	**Mass (g)**	**% Retained**	**% Passing**
+7	2.8	2.6	0%	0%
-7/+12	1.7	14	1%	2%
-12/+20	0.85	75.8	7%	9%
-20/50	0.3	291.5	27%	36%
+140	0.106	346.3	33%	69%
-140/+200	0.075	89.1	8%	77%

-200/+325	0.045	100	9%	86%
9-325/+400	0.038	46.6	4%	91%
-400	<.038	97.7	9%	100%
Total		1063.6		

Table 7a. Sieve Analysis for Montana Coal D2				
Size (Tyler Mesh)	**Size (mm)**	**Mass (g)**	**% Retained**	**% Passing**
+6	3.36	140.1	23%	77%
-6/+12	1.41	225.0	36%	41%
-12/+20	0.841	105.6	17%	24%
-20/+48	0.297	93.5	15%	9%
-48/+150	0.105	32.1	5%	3%
-150/+250	0.063	7.7	1%	2%
-250/+325	0.044	3.2	1%	2%
-325/+400	0.037	1.4	0%	1%
-400	-0.037	8.7	1%	0%
Total		617.3		

Size analyses were determined for this coal on October 2011 and March 2012. The results were similar.

Table 8. Historical Data for Sodium and Potassium Concentration in As-Received Western States Coals and Ash Temperatures (COALQUAL Database)				
State	**Raw Coal, mg/kg, (number of samples)**		**Ash Temperature °C , (number of samples)**	
	Na	**K**	**Initial Deformation**	**Liquid**
Montana	3069±1928 (274); MBMG 2590±2173 (365)	818±1319 (274); MBMG 797±1380 (365)	1159±61 (280)	1253±66 (280)
N. Dakota	3823±2635 (173)	654±867 (173)	1156±63 (169)	1241±65 (169)
Wyoming	1324±851 (411)	708±1087 (411)	1212±95 (453)	1298±91 (453)

Notes: ± standard deviation; Geochemistry characterization of coals has been summarized for over 13,000 samples and the results are available in the United States Geological Society's (USGS) COALQUAL database (Bragg et al, 1998). The COALQUAL data was searched for the sodium and potassium content of as-received coal samples from all counties in Montana, Wyoming, and North Dakota.

Table 9. Sodium Concentration as a Function of Particle Size in Montana Coal Fines (mg/kg)							
Company	**Particle Size (mm)**						
	-1.7+0.85	**-0.85+0.30**	**-0.30+0.106**	**-0.106+0.075**	**-0.075+0.045**	**-0.045+0.038**	**-0.038**
A2	410	445	327	341	364	340	335
B2	2450	2670	2740	2570	2370	2350	2520
C2	1366	1500	1460	1420	1510	1150	1123

Table 9. Sodium Concentration as a Function of Particle Size in Montana Coal Fines (mg/kg)							
Company	**Particle Size (mm)**						
	-1.7+0.85	**-0.85+0.30**	**-0.30+0.106**	**-0.106+0.075**	**-0.075+0.045**	**-0.045+0.038**	**-0.038**
D1	-	3700	2780	2760	3030	3270	3820
D2	**+6**	**-6+12**	**-12+20**	**-20+48**			
	3260	3470	3460	3660			

All samples analyzed by Wyoming Analytical Laboratory, Inc (Wallaramie@wal-lab.com, 2009) except Coal D2 which was analyzed by Proton Emission X-ray Emission. The concentration of associated elements in Coal D2 are presented in Appendix B.

Table 10. Element Concentration as a Function of Particle Size in Montana Coal B2 (Labeled Sample 5)

REPORT OF ANALYSIS

Lab Number	M0410	M0409	M0408	M0407	M0406
Sample ID	**Sample 5 +140**	**Sample 5 -140+200**	**Sample 5 -200+325**	**Sample 5 -325+400**	**Sample 5 -400**
Arsenic, mg/kg	1.66	2.7	3.78	5.16	6.48
Lead, mg/kg	9.97	7.34	17.7	29.8	61.9
Aluminum, mg/kg	1,935	2,020	2,078	2,064	2,290
Silica, mg/kg	225	263	296	313	403
Phosphorus, mg/kg	400	393	403	425	518
Calcium, mg/kg	4,400	4,180	3,980	4,280	4,880
Iron, mg/kg	1,790	1,790	984	1,230	2,460
Magnesium, mg/kg	505	526	519	584	640
Sodium, mg/kg	2,740	2,570	2,370	2,350	2,520
Potassium, mg/kg	48.7	45.1	37.6	55.1	67.8
Chloride, mg/kg	0.001	0.002	0.002	0.002	0.002
Sulfur, As determined wt.%	0.64	0.72	0.78	0.78	0.76

Wyoming Analytical Laboratory, Inc (Wallaramie@wal-lab.com, 2009)

Table 11. Historical Data for Element Concentration in As-Received Western States Coals (COALQUAL Database)						
State	**Concentration in Raw Coal, mg/kg (no. samples)**					
	Al	**Ca**	**Fe**	**Mg**	**S**	**Si**
Montana (274)	8387± 7074	9614± 4235	818± 1319	2654± 1460	4898± 3587	16515± 15212
N. Dakota (173)	6384± 4346	12174± 3163	8000± 5799	3682± 970	8638± 4704	16206± 16660
Wyoming (411)	8970± 7165	9730± 5348	5898± 6396	2054± 987	5234± 3629	18499± 16686

± standard deviation; The presence of inorganic elements also may have a significant effect on the formation of liquids at combustion and gasification temperatures. The major inorganic mineral species present in low-rank Western coals are presented in Table 12.

Table 12. Mineralization in Fine Fraction of Montana Coals by Mineral Liberation Analyses (MLA)		
Company	**Major**	**Minor**
A2	$KAlSi_3O_8$, SiO_2	$(Mg,Fe)_3Al2Si_8O_{22}(OH)_2$, $Na_2(Mg,Fe)_3Al2Si_8O_{22}(OH)_2$, FeS_2
B2	SiO_2, $Ca_5(PO_4)_3OH$, $NaAlSi_3O_8$, Al_2OSiO_4	FeS_2, $Na_2(Mg,Fe)_3Al_2Si_8O_{22}(OH)_2$, $KAlSi_3O_8$, $BaSO_4$, $(Mg,Fe)_3Al_2Si_8O_{22}(OH)_2$
C2	$KAlSi_3O_8$, SiO_2,	FeS_2

	$Na_2(Mg,Fe)_3Al2Si_8O_{22}(OH)_2$, Al_2OSiO_4, $CaCO_3$	
D1	SiO_2, $Ca_5(PO_4)_3OH$: $NaAlSi_3O_8$, Al_2OSiO_4, $(Mg,Fe)_3Al_2Si_8O_{22}(OH)_2$	FeS_2, $KAlSi_3O_8$, $BaSO_4$

Miranda (Mineral Liberation Analyses, pmiranda@mtech.edu).

Table 13. Mineral Content in Montana Coal B2 Fines

Mineral/Phase	Compound	Content (wt.%)
Quartz	SiO_2	51.90
Apatite	$Ca_5(PO_4)_3OH$	26.71
Apatite-Albite	$Ca_5(PO_4)_3OH$ $NaAlSi_3O_8$	8.47
Kyanite	Al_2OSiO_4	5.69
Pyrite	FeS_2	2.74
Na-Amphibole	$Na_2(Mg,Fe)_3Al_2Si_8O_{22}(OH)_2$	1.50
K-Feldspar	$KAlSi_3O_8$	1.48
Barite	$BaSO_4$	1.37
Amphibole	$(Mg,Fe)_3Al_2Si_8O_{22}(OH)_2$	0.11
Ilmenite	$FeTiO_3$	0.02
Calcite	$CaCO_3$	0.01

The content is based on the specific mineral fraction evaluated (Miranda ,Mineral Liberation Analyses, pmiranda@mtech.edu 2009)

Ash- The elemental content (reported as oxides) for each coal ash is presented in Appendix D along with other characteristics of the ash. The elemental content of each coal ash is presented in Table 15. The elemental content and other characteristics for coal B2 are presented in Table 16 as an example of the data.

Table 14. Element Concentration in Ash from Montana Coal Fines (wt.%)

Coal	Al	Ca	Mg	Fe	K	Na	O	P	S	Si
A2	8.0	12.7	1.8	3.6	0.1	0.5	45.5	0.2	4.1	21.1
B2	8.32	10.16	1.73	4.61	0.67	5.68	43.90	1.08	7.16	13.74
C2	7.63	10.26	1.28	2.15	1.17	1.17	46.39	0.07	2.54	25.67
D1	10.70	16.72	2.96	3.02	0.24	7.95	40.25	0.34	2.58	12.18
D2	8.35	10.28	2.21	2.92	0.90	4.57	40.19	0.08	1.77	22.51

Wyoming Analytical Laboratory, Inc (Wallaramie@wal-lab.com, 2009, 2012)

Table 15. ASH Properties for Montana Coal B2 (Labeled Sample 5)

REPORT OF ANALYSIS

Proximate Analysis ASTM D-5142	As Received Wt%	Moisture Free wt%	MAF Basis wt%
Moisture	20.74	******	******
Ash	4.62	5.83	******
Volatile Matter	32.42	40.90	43.43
Fixed Carbon	42.22	53.27	56.57
Total	100.00	100.00	100.00

Ultimate Analysis/ Method: ASTM D5142/5373			
Moisture	20.74	******	******
Hydrogen	3.01	3.80	4.04
Carbon	56.83	71.70	76.14
Nitrogen	0.96	1.21	1.28
Sulfur	0.61	0.77	0.82
Oxygen	13.23	16.69	17.72
Ash	4.62	5.83	******
Total	100.00	100.00	100.00

Heating Value, Btu/lb Method: ASTM D-5865	9,950	12,554	13,331

Coal Ash Analysis, wt% Ignited Basis	
Silicon Dioxide, % as SiO2	29.39
Aluminum Oxide, % as Al2O3	15.72
Iron Oxide, % as Fe2O3	6.59
Calcium Oxide, % as CaO	14.21
Magnesium Oxide, % as MgO	2.87
Sodium Oxide, % as Na2O	7.66
Potassium Oxide, % as K2O	0.81
Titanium Dioxide, % as TiO2	0.77
Manganese Dioxide, % as MnO2	0.04
Phosphorus Pentoxide, % as P2O5	1.91
Strontium Oxide, % as SrO	0.88
Barium Oxide, % as BaO	1.27
Sulfur Trioxide, % as SO3	17.88

Alkalies as Na20	8.19
Base to Acid Ratio	0.7
Silica Ratio	0.55
T250, °F	2000

Trace Element, mg/kg Method: D6357	As Rec. Basis	Dry Basis
Beryllium	0.181	0.228
Vanadium	4.52	5.703
Chromium	2.73	3.444
Manganese	7.85	9.904
Cobalt	0.609	0.768
Nickel	1.42	1.792
Zinc	4.11	5.185
Arsenic	1.11	1.400
Molybdenum	0.215	0.271
Cadmium	0.061	0.077
Lead	3.70	4.668
Sodium	9750	12329
Uranium	0.167	0.211
Potassium	126	159

Wyoming Analytical Laboratory, Inc (Wallaramie@wal-lab.com, 2009)

Table 15a. ASH Properties for Montana Coal D2

REPORT OF ANALYSIS

Proximate Analysis ASTM D-5142	As Received Wt%	Moisture Free wt%	MAF Basis wt%
Moisture	5.38	******	******
Ash	8.93	9.44	******
Volatile Matter	37.73	39.87	44.03
Fixed Carbon	47.96	50.69	55.97
Total	100.00	100.00	100.00

Ultimate Analysis/ Method: ASTM D5142/5373			
Moisture	5.38	******	******
Hydrogen	3.60	3.80	4.20
Carbon	65.56	69.29	76.51
Nitrogen	1.00	1.06	1.17
Sulfur	0.21	0.22	0.25
Oxygen	15.32	16.19	17.87
Ash	8.93	9.44	******
Total	100.00	100.00	100.00

Heating Value, Btu/lb Method: ASTM D-5865	10,858	11,475	12,671

Coal Ash Analysis, wt% Ignited Basis	
Silicon Dioxide, % as SiO2	48.15
Aluminum Oxide, % as Al2O3	15.78
Iron Oxide, % as Fe2O3	4.18
Calcium Oxide, % as CaO	14.39
Magnesium Oxide, % as MgO	3.66
Sodium Oxide, % as Na2O	6.16
Potassium Oxide, % as K2O	1.09
Titanium Dioxide, % as TiO2	0.76
Manganese Dioxide, % as MnO2	0.08
Phosphorus Pentoxide, % as P2O5	0.18
Strontium Oxide, % as SrO	0.47
Barium Oxide, % as BaO	0.69
Sulfur Trioxide, % as SO3	4.41

Alkalies as Na20	6.88
Base to Acid Ratio	0.46
Silica Ratio	0.68
T250	2350

Trace Element, mg/kg	Method: D6357)
Beryllium	0.442
Vanadium	3.88
Chromium	19
Manganese	43.2
Cobalt	1.36
Nickel	5.79
Copper	12
Zinc	11.8
Arsenic	1.03
Molybdenum	0.504
Cadmium	0.11
Antimony	0.11

Forms of Sulfur (Method: ASTM D-2492)

Sulfate Sulfur	Pyretic Sulfur	Organic Sulfur
0.01%	0.04%	0.23%

Note: The coal supplied for analyses was made up of the same fraction sizes as used in the leach tests. The coal was pre-dried to the moisture content reported above and then sized.

Task 4a- Chemical Property Evaluation

Modeling Results for Montana Coal Using Hydrochloric Acid-Preliminary modeling studies were conducted to evaluate what reagents may be effective in lowering the sodium and potassium concentrations to the project goal level of less than approximately three percent sodium oxide in the final ash solids. Therefore, the influence of incremental reagent additions on the stability of coal ash solids was modeled using the speciation/titration equilibrium calculation program developed by H.H. Huang (STABCAL, 2010). Six standard free energies of formation databases are available to the user of the STABCAL program. We used the National Bureau of Standards (NBS) and Twidwell Personal databases. The reagents modeled included hydrochloric acid, sulfuric acid, sulfurous acid, carbonic acid, acetic acid, sodium hydroxide, and ammonium acetate. Example figures are presented here to illustrate the results of the modeling effort applied to Coal B2 treated with hydrochloric acid. The results for other acids, caustic, and ammonium acetate are presented in detail in Appendix C. The conclusions for the modeling task are summarized and presented in Table 16. Please refer to Appendix C for information on what mineral and aqueous species present were used in this study. However, be aware that the modeling results are based on equilibrium considerations and does not reflect the possibility of slow kinetic reaction rates nor do the results show the potential response of the coals to removal of organically bonded sodium. Therefore, the modeling results are to be viewed as very conservative estimates of sodium removal and, of course, experimental test work must be conducted.

In general the modeling results support acidic and caustic leaching as a viable treatment approach for removing sodium bearing mineral phases.

Example Modeling Results for Montana Coal B2 Using Hydrochloric Acid-The influence of HCl titration is presented in Figures 6-8 to define the solubility of the sodium and potassium bearing compounds i.e. albite, $NaAlSi_3O_8$ (major); sodium amphiboles $Na_2Mg_3Al_2Si_8O_{22}(OH)_2$ (glacuophane); $Na_2Fe_3Al_2Si_8O_{22}(OH)_2$ (ferroglacuophane); and potassium feldspar, $KAlSi_3O_8$. All titration results are based on beginning the titration at a solution pH of six. Annotation notes are added the figure captions to illustrate features of the results shown by each figure. Only two sodium bearing phases are present in this coal, sodium albite and sodium amphibole. Figure 6 illustrates that albite will be completed dissolved in acid solutions containing 30 g/L (the pH would be about 4-4.5), and for these same conditions amphibole would be completely dissolved. As noted on the figure caption an acid solution containing 30 g/L hydrochloric will solubilize enough sodium so that the final ash would contain less than three percent sodium oxide. Of course, the chloride and sodium content in the leach water would be increased and treatment of the wash water would have to be addressed.

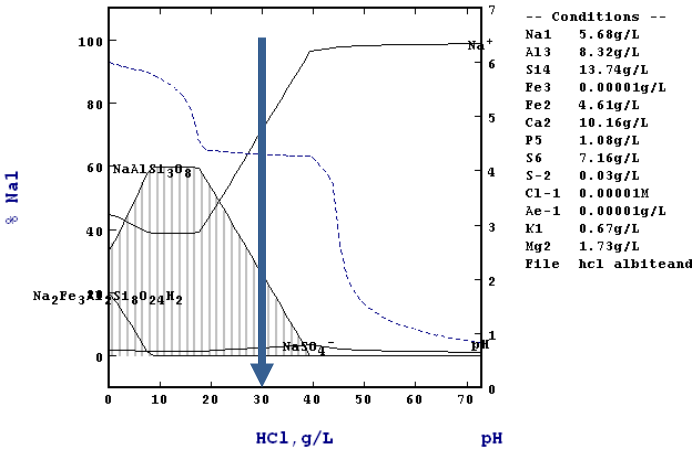

Figure 6. An illustration of the influence of titrating hydrochloric acid on the distribution of sodium solid and aqueous species. Note that a significant amount of acid is required to completely dissolve the albite. However, it is not necessary to remove all the sodium to attain the project goal concentration in the ash solids.

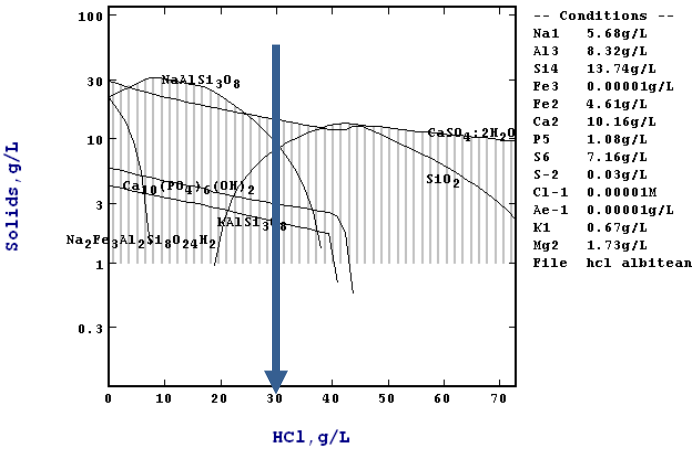

Figure 7. An illustration of the influence of titrating hydrochloric acid on the presence of solids. The conditions to achieve a combination of sodium and potassium that is less than three percent in the final ash solids is marked on the diagram (30.6 g/L HCl).

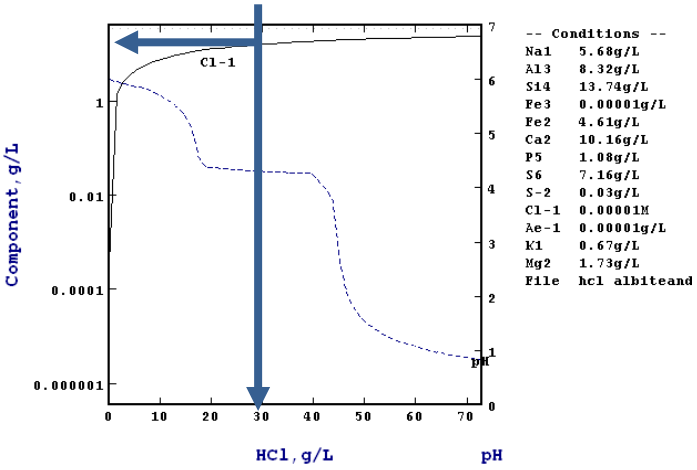

Figure 8. An illustration of the influence of titrating hydrochloric acid on the increase in chloride content in the final leach solution. The chloride content (at three percent sodium plus potassium in the final ash solids) is marked on the diagram (16.2 g/L Cl^-).

Table 16. Summary Conclusion Results for STABCAL Speciation/Titration Modeling

Company	Anticipated Na and K Response		Comments
	HCl	H_2SO_4	
A	Ash from as-received coal already below project goal	Ash from as-received coal already below project goal	Modeling not performed
B	Requires acid to reduce the pH to ~ 4 to achieve an ash with <3%	Requires acid to reduce the pH to ~ 4 to achieve an ash with <3% sodium oxide	Leach water would have to be treated. Laboratory verification was conducted in this study.
C	Good response at low acid additions	Good response at low acid additions	Ash from as-received coal already below project goal but near enough that modeling performed.
D	Good response at low acid additions	Good response at low acid additions	Laboratory verification was conducted in this study.

Combustion Modeling Prior to Preliminary Test Work-A second modeling effort was conducted to understand what reactions may happen during the combustion of Montana Coals, especially with respect to sodium speciation at elevated temperatures. Each coal was modeled using the software available from Outokumpu (Roine, 2006), HSC Chemistry 6.0. This software uses an algorithm that minimizes the free energy of reactions and, thereby, determines what phases may be present and how much of each phase would be thermodynamically stable under the selected exposure conditions.

The results for modeling coal B2 is presented in Appendix D. Please refer to that appendix for the assumptions and specification of the solid, liquid and gaseous specie chosen to be used in the calculation. The importance of this type modeling is that, for a specific coal mineralogy, "what if" type questions can be posed , e.g. what are the expected species formed at ashing temperatures or at combustion temperatures; would appreciable sodium be present in the gas phase during combustion, what molten liquids may be present; what is the effect of the presence of mineral species that may react with the sodium; what is the effect of adding mineral species that are known to react with sodium, thereby stabilizing the sodium in a form that would not form a liquid phase at combustion temperatures. Thermodynamic modeling results cannot be used to predict actual phase relationships because the program calculates the phase distribution at equilibrium which may or may not be attained because of kinetic restrictions and also the thermodynamic activities in molten liquid slags are unknown. The calculations should be used to investigate trends rather than predicting the specific amounts of species that may be present.

HSC modeling of Coal B2- The influence of temperature on the thermodynamically stable solids formed and the distribution of sodium and potassium species at ashing and combustion temperatures are shown in Figures 9 and 10, respectively. The predicted distribution of other species in the system are presented in Appendix D.

Ashing Coal B2-The solid species as reported by Miranda are verified by the HSC modeling to be thermodynamically stable (Figure 9) , i.e. kyanite, albite, quartz, potassium feldspar, and apatite can thermodynamically coexist at the ashing temperature. Note that a significant amount of sodium is likely lost from the system during ashing as Na_2SO_4(g). The loss would be greater if chloride is present in the feed coal.

Combustion Coal B2- At combustion temperatures the sodium and potassium will be present as solid albite, potassium feldspar, a liquid slag phase, and a gas phase. A greater amount of the sodium and potassium will be present within the solids and liquid slag phases at elevated temperatures than in the gas phase; although a smaller but significant amount will be evolved as Na_2SO_4(g), NaOH(g),Na(g), and KOH(g) (Figure 10).

Addition of Kaolinite to React With Sodium-the addition of kaolinite to coal B2 is presented in Figures 11 and 12 to illustrate that the corrosive molten liquid sodium silicate specie can be decreased significantly by forming solid albite at 1150°C. The addition of approximately three percent kaolinite to the coal converts essentially all of the sodium silicate liquid to a solid phase.

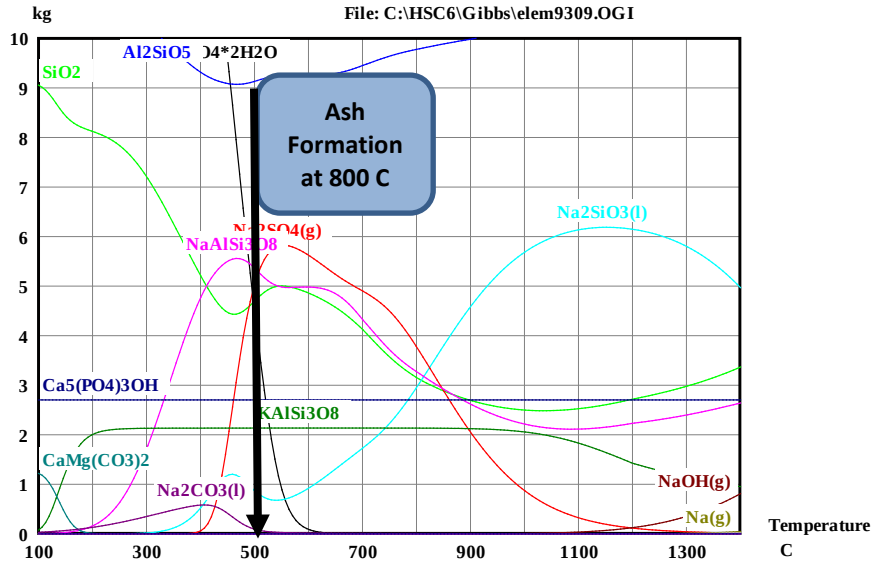

Figure 9. The influence of temperature on the formation of thermodynamically stable phases using 1.3 times the stoichiometric amount of air required for the combustion of carbon (1000 kg). Anticipated species when coal is ashed at 800°C are: Al_2SiO_5 (kyanite), Na_2CO_3(g), $NaAlSi_3O_8$ (albite), SiO_2 (quartz), $KAlSi_3O_8$ (feldspar), $Ca_5(PO_4)_3(OH)$ (apatite), Na_2SiO_3(liquid) begins to form at about 780°C. Note that a significant amount of the sodium is expected to be lost to the gas phase as Na_2SO_4(g) at ashing temperature.

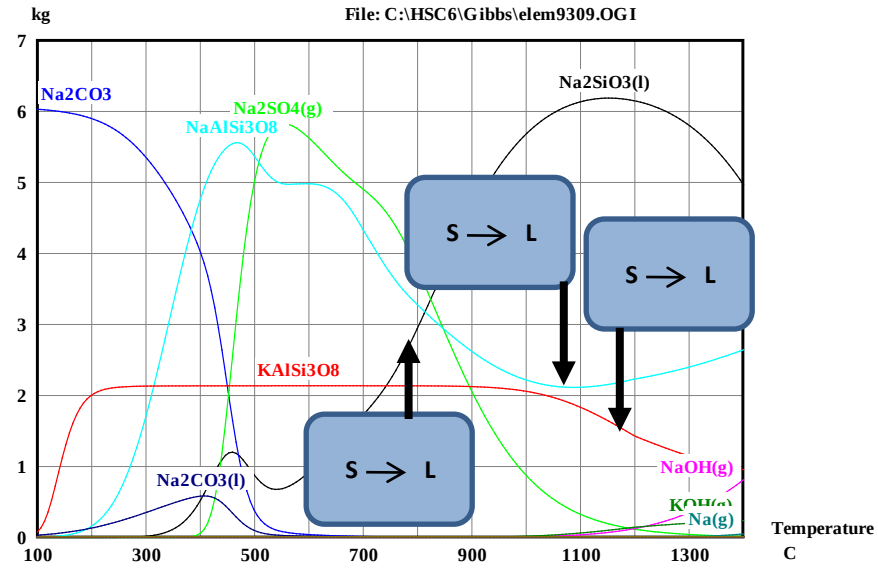

Figure 10. The influence of temperature on the formation of thermodynamically stable sodium and potassium species using 1.3 times the stoichiometric amount of air required for the combustion of carbon (1000 kg). Anticipated sodium and potassium species are shown when coal is combusted at temperatures of 1150°C and above. Al_2SiO_5 (kyanite) and $Ca_5(PO_4)_3OH$ remain stable as solids, A sodium (and potassium) rich liquid (molten slag) forms and gaseous NaOH(g) and KOH(g) species form at combustion temperatures.

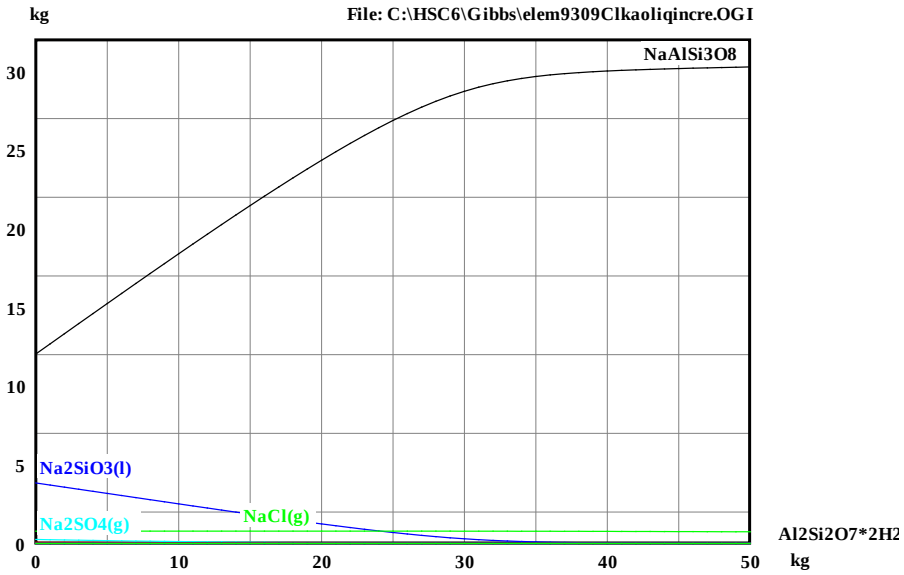

Figure 11. The influence of adding kaolinite to coal and combusting at 1150°C on the formation of thermodynamically stable phases using 1.3 times the stoichiometric amount of air required for the combustion of carbon (1000 kg). Na_2SiO_3(liquid) begins to form at about 780°C. Note that most of the liquid sodium silicate is converted to solid albite.

Task 4b. Preliminary Leach Test Work

Leach test work has been conducted to pre-test feasible approaches and to establish boundary conditions to be used in subsequent experimental design studies. The preliminary test work conducted were based on successful literature reported approaches and includes: pH adjusted water leaching using the following reagents: tap water, hydrochloric acid, sulfuric acid, acetic acid, and calcium chloride

doped acidic solutions. The results are in general agreement with published studies on other low-rank coals, e.g. preliminary results for treating 100 g/L of Coal B2 for 2 hours using-tap water removed <10% of the sodium, acidic solutions removed approximately 10-20%, acidic solutions containing an ion exchange reagent like calcium chloride removed approximately 30-50% of the sodium.

Influence of Particle Size-Each coal was subjected to a screen analysis and each coal fraction was leached using the following conditions: 100 g/L sized coal was placed in an agitation reactor, the pH was maintained at three with hydrochloric acid and 25 g/L of calcium chloride was added, the exposure time was 2 hrs and 24 hrs. The solution phase was analyzed (ICP) for sodium. The results for coal A2, B2, C2, and D1 are presented in Tables 17 to 20. Coal A2 showed no leachability for any of the size fractions. Coal B2 showed appreciable sodium removal for two hour leaching, e.g. from 40 to 48% for the major size fractions. This result suggests that the sodium oxide content in the ash would be reduced from 7.7% to 1.3% (which meets the desired goal of less than 3% in the ash). Coal C2 showed approximately 40% sodium removal for the larger size fractions but the removal decreased as the particle size fractions decreased; likely because of readsorption onto the finer particulate surfaces. Coal D1 showed approximately 50% sodium removal for the size fraction -0.85mm/+0.106 mm. However, because there was insufficient sample, larger size fractions were not evaluated. Late in the test program coal D2 was subjected to intensive study. The results are summarized later in this report.

The sodium content in the various size fractions is relatively independent of particle size in each of the coals. The susceptibility of the various size fractions to sodium leaching is relatively constant for Coal B2 and D2. The Coal B2 data suggest that the concept of sizing coal into fractions and subsequently only leaching selected fractions (therefore, only treating a portion of the coal) would not be more effective than treating the whole coal fines. The susceptibility of the various size fractions to sodium leaching is variable for Coal C2, with the finer fractions showing less sodium removal.

Table 17. Size Distribution, Sodium Content, and Amount of Sodium Removed by Leaching Coal A2

Coal A2 Fines		Mass, g	Initial Na, mg/kg	Na Removed, %	
Mesh	mm			2 hrs	24 hrs
+7	+2.8	0	-	-	-
-7/+12	-2.8/+1.7	1.7	410	0.0	0.0
-12/+20	-1.7/+0.85	20	445	0.0	0.0
-20/+50	-0.85/+0.3	225.7	428	0.0	0.0
-50/+140	-0.3/+0.106	233.80	327	0.0	0.0
-140/+200	-0.106/+0.075	233.80	341	0.0	0.0
-200/+325	-0.075/+0.045	76.40	364	0.0	0.0
-325/+400	-0.045/+0.038	87.60	340	0.0	0.0
-400	-0.038	60.60	335	0.0	0.0
Initial Grade, %		0.017			
Final Grade after 2 hrs, %		-			
Final Grade after 24 hrs, %		-			

Conditions of leach-hydrochloric acid, pH 3 maintained during exposure, 10 g coal/100 mL; 25 g/L $CaCl_2$, 25^{o}C

Table 18. Size Distribution, Sodium Content, and Amount of Sodium Removed by Leaching Coal B2					
Coal B2 Fines		Mass, g	Initial Na, mg/kg	Na Removed, %	
Mesh	mm			2 hrs	24 hrs
+7	+2.8	0.0	-	-	-
-7/+12	-2.8/+1.7	4.4	2510	22.2	-
-12/+20	-1.7/+0.85	69.1	2450	22.2	38.1
-20/+50	-0.85/+0.3	307.2	2670	40.8	54.9
-50/+140	-0.3/+0.106	218	2740	48.2	53.1
-140/+200	-0.106/+0.075	63.5	2570	33.2	42.0
-200/+325	-0.075/+0.045	76.4	2370	35.0	43.0
-325/+400	-0.045/+0.038	41.4	2350	46.2	47.4
-400	-0.038	40.4	2520	45.7	50.9
Initial Grade, %		0.26			
Final Grade after 2 hrs, %		0.17			
Final Grade after 24 hrs, %		-			

Conditions of leach-hydrochloric acid, pH 3 maintained during exposure, 10 g coal/100 mL; 25 g/L $CaCl_2$, 25^{o}C

Table 19. Size Distribution, Sodium Content, and Amount of Sodium Removed by Leaching Coal C2					
Coal C2 Fines		Mass, g	Initial Na, mg/kg	Na Removed, %	
Mesh	mm			2 hrs	24 hrs
+7	+2.8	0.0	-	-	-
-7/+12	-2.8/+1.7	14	1330	-	-
-12/+20	-1.7/+0.85	75.8	1370	42.6	-
-20/+50	-0.85/+0.3	291.5	1500	34.9	38.8
-50/+140	-0.3/+0.106	346.30	1460	24.8	49.0
-140/+200	-0.106/+0.075	89.10	1420	15.2	-
-200/+325	-0.075/+0.045	100.00	1510	12.1	-
-325/+400	-0.045/+0.038	46.60	1150	3.9	-
-400	-0.038	97.70	1120	8.3	-
Initial Grade, %		0.200			
Final Grade after 2 hrs, %		0.151			

Conditions of leach-hydrochloric acid, pH 3 maintained during exposure, 10 g coal/100 mL; 25 g/L $CaCl_2$, 25^{o}C

Table 20. Size Distribution, Sodium Content, and Amount of Sodium Removed by Leaching Coal D1, Coal D2 Results are Summarized Later					
Coal D1 Fines		Mass, g	Initial Na, mg/kg	Na Removed, %	
Mesh	mm			2 hrs	24 hrs
+7	+2.8	0	-	-	-
-7/+12	-2.8/+1.7	2.1		-	-
-12/+20	-1.7/+0.85	10.5		-	-
-20/+50	-0.85/+0.3	61.8	3700	50.8	-

Table 20. Size Distribution, Sodium Content, and Amount of Sodium Removed by Leaching Coal D1, Coal D2 Results are Summarized Later					
Coal D1 Fines		Mass, g	Initial Na, mg/kg	Na Removed, %	
Mesh	mm			2 hrs	24 hrs
-50/+140	-0.3/+0.106	97.70	2780	58.9	58.0
-140/+200	-0.106/+0.075	41.10	2760	0.0	-
-200/+325	-0.075/+0.045	39.40	3030	0.0	-
-325/+400	-0.045/+0.038	13.10	3270	0.0	-
-400	-0.038	5.0	3820	0.0	-
Initial Grade, %		0.21			
Final Grade after 2 hrs, %		-			

Conditions of leach-hydrochloric acid, pH 3 maintained during exposure, 10 g coal/100 mL; 25 g/L $CaCl_2$, 25°C

Task 5-Selection of Treatment Approaches

Based on the literature review, STABCAL modeling effort, preliminary test work, and recommendations from the stakeholder meeting in June 2010 it was decided to further investigate the leachability of Montana coals. Coal B2 and D1 have the highest concentration of sodium. It was decided to concentrate our efforts on Coal B2 because there was only a small amount of Coal D1 available (and a sufficient amount would not be available until the Spring of 2011). The desire was to answer a number of questions, e.g. what would be the best leachate reagent (hydrochloric or sulfuric acid), their concentration (pH), is the presence of ion exchange species required, and what is the appropriate leaching time. A sufficient amount of Coal D2 was made available in January 2012 and the coal was subjected to a complete evaluation of its leachability. These results are summarized later in this report.

Task 6-First Interim Report

The First Interim Report was submitted January, 2010. This is the Project Final Report.

Task 7-Test Plan Development

An experimental statistically designed test plan was developed to investigate the influence of five variables concurrently on the leachability of Coal B. Design Expert software (Version 8.0, 2010) marketed by STATEASE (2010) was used to formulate a the two-level Experimental Design Matrix. The specific software program used in this study is referred to by STATEASE as Resolution V. The value of using the Resolution V matrix is that it is statistically formulated so that the main and binary factors (variables) can be identified. None of the main factors or binary factors are aliased, i.e., the main factors and binary interaction factors are not influenced by other factors. This allows the study responses to be optimized, maximized, minimized, etc. Coal D2 was also evaluated using the experimental design approach. The software model utilized was two-level factorial.

Task 8-Bench Scale Testing and Evaluations

Coals B2 and D2 were subjected to detailed leaching and optimization tests.

Coal B2

Based on the STABCAL modeling effort and the preliminary test work a Two-Level Experimental Design Study was formulated for Coal B2. The Coal B design study was formulated to evaluate the influence of five variables on the removal of sodium from the coal e.g. pH, time, type of ion exchange reagent, concentration of the ion exchange reagent, and type of acid.

The specific experimental conditions are presented in Table 21. The range of conditions studied included: pH 0.4 to 5, time 0.5 to 4 hrs, ion exchange reagents for either ammonium acetate or calcium chloride 0 20 g/L, and type acid either hydrochloric or sulfuric. Each experiment was replicated once to satisfy our quality control requirement of reproducibility.

Experimental Procedure

The experimental procedure used for conducting the experiments that were presented in Table 21 follows:

- Place 10.0 gm coal 5 fines in a 200 mL plastic bottle (equivalent to 100 gm/Liter), add 100 mL of DI water
- Place on the shaker table for 30 minutes, measure and record pH
- Collect sample, filter 20 gm of the solution phase through 0.45 um filter disk into a 20 mL scintillation vial, add 1.0 g High Purity Concentrated Nitric acid, cap for analysis.
- Be sure to label the sample correctly both in your lab book and on the scintillation vial.
- The above should be your standard procedure for each of the 14 tests
- After the wash test do the following to each solution in each bottle
- Adjust the pH to the desired value with the specific acid
- Record the amount of acid used for each test in your lab book
- If specified by the design matrix add the ion reagent (CaCl2 or Ammonium Acetate), readjust and maintain pH for the specified time.
- All samples will be ICP analyzed for Na, K, Ca, Fe, Mg, Al
- Some solutions will be sampled at 30 minutes, then again at 4 hours. For those to be sampled at 4 hrs, readjust pH every 15 minutes over the 4 hour period.
- Collect sample, filter 20 gm of the solution phase through 0.45 um filter disk into a scintillation vial, add 1.0 g High Purity Concentrated Nitric acid, cap for analysis.

Philosophy of Statistical Evaluation

Statistical analyses of the data were conducted using the software Design-Expert Version 8.0 (Stat Ease 2010). The procedure was as follows:

- The data was input into the statistically designed experimental matrix.
- A transformation model was selected from seven available options, including none, natural log, base ten log, square root, inverse square root, inverse, power, and logit.
- The factors considered significant was selected using either a half-normal versus percent probability plot or Pareto chart.
- An Analysis of Variance (ANOVA) evaluation was performed and a P-Test was used to evaluate whether the model and factors were significant or not.
    - The model was deemed appropriate if the p-value test was <0.05; if the value was not less than this value then the selection process was started over and a new transformation model was selected. If the p-value test was <0.05 then the evaluation process was continued.
    - The individual factors were deemed appropriate if the p-value test was <0.10
- The Analysis of Variance (ANOVA) evaluation was continued to ascertain that the selected model and factors could be used to “navigate the design space”. This was accomplished by evaluating several statistically calculated parameters:
    - R-squared (should be as high as possible and near 1.0 as possible)

- Adjusted R-squared (as near R-squared as possible)
- Predicted R-squared (within 0.2 of the Adjusted R-squared value and >0.6)
- Adequate Precision (as large as possible but at least >4).

- If the evaluation was not satisfactory then the process of model selection, effects selection, ANOVA recalculation was repeated until the above p-test and R-squared evaluation was satisfactory. If the evaluation did not find a satisfactory solution this result was noted. If the ANOVA evaluation was satisfactory then further diagnostic evaluations were performed (example plots are presented for each DOE study), including:
  - Normal probability versus Internally Studentized Residuals
  - Externally Studentized Residuals versus Standardized Run Number
  - Leverage
  - Cook' Distance.

Discussion of Experimental Results for Coal B2

The specific experimental results for sodium removal are presented in Table 22.

Table 21. Two-Level Factorial Design Resolution V Matrix for Leaching Coal B2

Standard Run Number	Factors				
	A:pH	B:Time, hrs	C:Ion Reagent	D:Ion Exchange, g/L	E:Acid
1	0.42	0.5	Am Ac	20	HCl
2	2.18	4.0	CaCl2	0	HCl
3	0.41	0.5	CaCl2	0	H2SO4
4	4.99	4.0	Am Ac	20	HCl
5	0.43	4.0	CaCl2	20	HCl
6	3.62	4.0	Am Ac	0	HCl
7	4.44	0.5	CaCl2	20	HCl
8	0.38	4.0	CaCl2	20	H2SO4
9	5.03	0.5	Am Ac	0	HCl
10	5.23	0.5	Am Ac	20	H2SO4
11	4.66	0.5	CaCl2	20	H2SO4
12	4.83	4.0	CaCl2	20	H2SO4
13	0.40	4.0	CaCl2	0	H2SO4
14	4.94	4.0	Am Ac	0	HCl
15	0.43	0.5	Am Ac	20	H2SO4
16	5.80	0.5	CaCl2	0	H2SO4
17	0.50	4.0	Am Ac	0	HCl
18	0.60	0.5	CaCl2	0	HCl
19	0.60	0.5	CaCl2	20	HCl
20	0.28	4.0	Am Ac	20	H2SO4
21	5.02	4.0	Am Ac	0	H2SO4
22	0.42	0.5	Am Ac	20	HCl
23	2.18	0.5	CaCl2	0	HCl
24	5.06	0.5	Am Ac	20	HCl

Table 21. Two-Level Factorial Design Resolution V Matrix for Leaching Coal B2					
Standard Run Number	Factors				
	A:pH	B:Time, hrs	C:Ion Reagent	D:Ion Exchange, g/L	E:Acid
25	4.61	4.0	CaCl2	20	HCl
26	0.39	0.5	CaCl2	20	H2SO4
27	5.06	4.0	Am Ac	20	H2SO4
28	4.94	9.5	Am Ac	0	HCl
29	0.42	0.5	Am Ac	20	HCl
30	0.41	0.5	Am Ac	0	H2SO4

Notes: actual pH values were used in the Design Expert evaluation. The experimental procedure is described in Appendix E. As part of the test procedure all samples were leached for 30 minutes in deionized water.

Table 22. Two-Level Factorial Design Resolution V Matrix-Results			
Standard Run Number	Responses		
	[Na], mg/L	[Na], %	[Na] in Ash, %
1	257	26.3	5.4
2	606	62.1	2.8
3	278	28.6	5.2
4	267	27.4	5.3
5	365	37.5	4.6
6	274	28.1	5.2
7	325	33.3	4.9
8	398	40.8	4.3
9	249	25.6	5.4
10	243	24.9	5.5
11	146	14.9	6.2
12	294	30.2	5.1
13	238	24.4	5.5
14	396	40.6	4.3
15	329	33.7	4.8
16	156	16.0	6.1
17	285	29.2	5.2
18	372	38.2	4.5
19	328	33.7	4.8
20	265	27.1	5.3
21	283	29.1	5.2
22	332	30.5	4.8
23	473	48.5	3.8
24	338	34.7	4.8
25	294	30.1	5.1
26	289	29.7	5.1

Table 22. Two-Level Factorial Design Resolution V Matrix-Results			
Standard Run Number	Responses		
	[Na], mg/L	[Na], %	[Na] in Ash, %
27	292	30.0	5.1
28	479	49.1	3.7
29	276	28.3	5.2
30	297	31.3	5.1

Notes: Initial sodium in coal 9750 mg/kg. The sodium in ash was calculated from the amount of sodium leached and Wyoming data on unleached coal composition, proximate analyses, and sodium in ash. This set of data needs to be verified by analysis of the ash content remaining in the leached coal ash.

Models have been developed for three responses, e.g. concentration of sodium in the leach solution (mg/L); percent sodium removal by the leach process; and anticipated sodium content in the ash after leaching. A summary of the design space equations that describe the response results are presented in Appendix E.

Leach Solution Sodium Concentration, Percent Extraction, Percent in Ash-Several figures are presented to illustrate the influence of the studied factors on the amount of sodium extracted. Annotation notes are added to the figure captions to illustrate features of the results shown by each figure. A reference set of conditions are superimposed on each appropriate figure so that the reader can easily compare results, i.e. pH 3, 1 hr.

Influence of Time, pH, Ion Exchange Reagent Concentration, and Type Acid (Cubic Visualization)

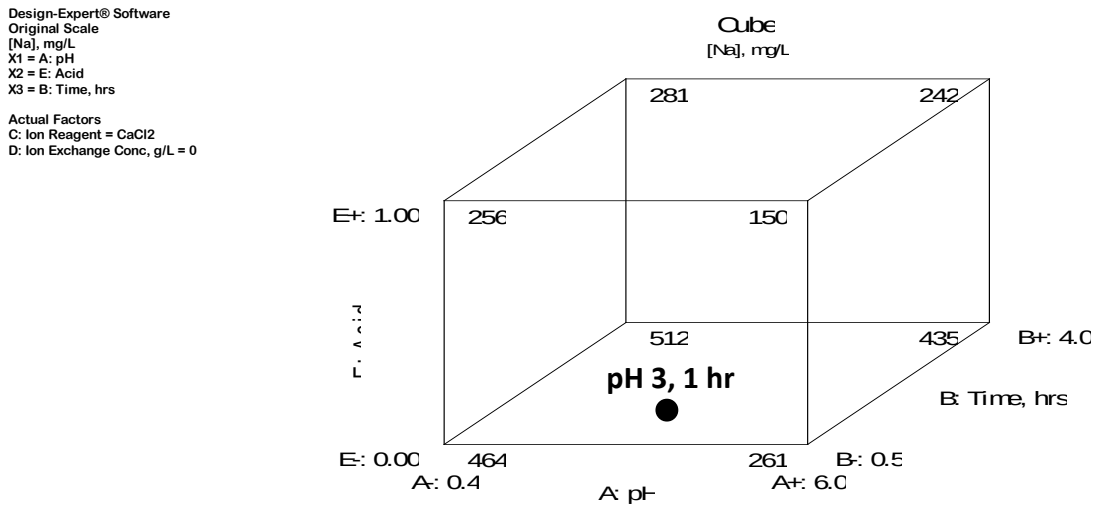

Figure 12. Cubic illustration of the influence of time, pH, and type of acid on **sodium content in the leach solution** without the presence of an ion exchange reagent. Note that the most effective leaching of sodium occurs under two conditions, i.e. at low pH using HCl acid for a short or long exposure time and at high pH using HCl acid for a long exposure time. Compare this figure with Figure 13 to visualize the difference when CaCl2 is added at its high value.

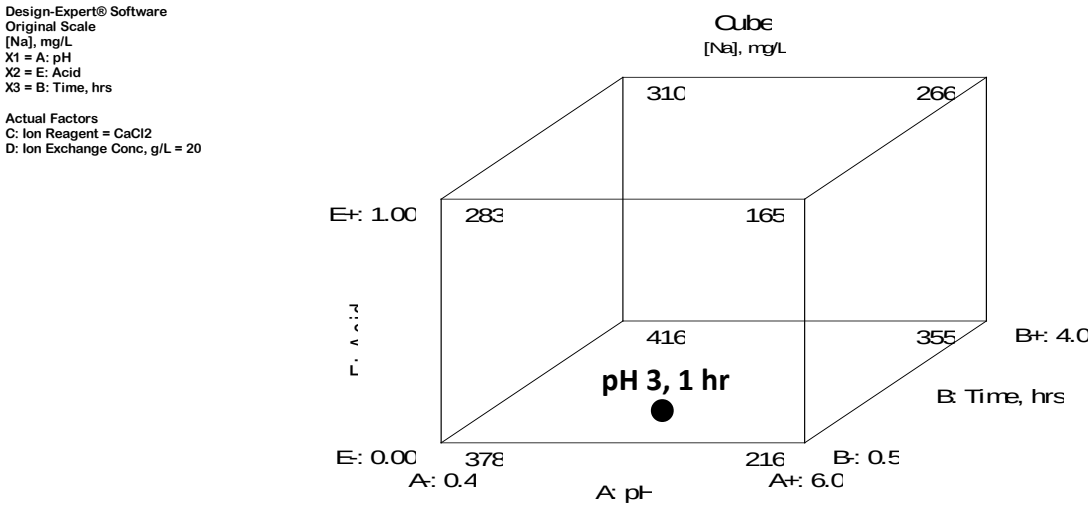

Figure 13. Cubic illustration of the influence of time, pH, and type of acid on **sodium content in the leach solution** in the presence of CaCl2. Compare this figure with Figure 12. The trends are similar but the presence of CaCl2 is detrimental.

Influence of Time and pH Without Ion Exchange Reagent Using HCl Acid (3-D Visualization)

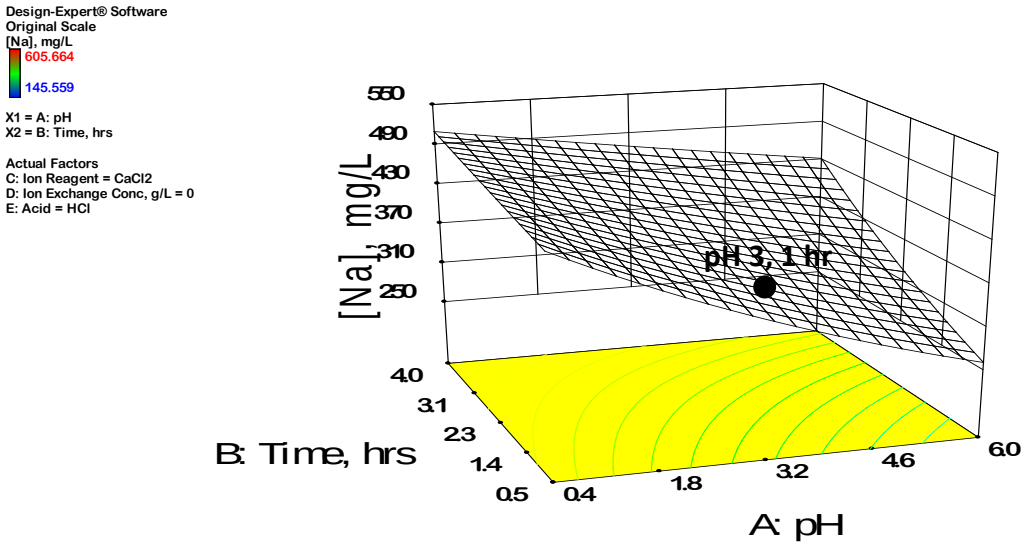

Figure 14. 3-D illustration of the influence of time and pH on **sodium content in the leach solution.** Note that the acid **reagent is HCl and that there is no CaCl2 present. At relatively low pH levels the sodium leached is independent of time but** at higher pH values the concentration is a strong function of leach time. This same effect can be seen in the following contour plot (Figure 15). The percent sodium leached, of course, follows the same trend (Figure 14a).

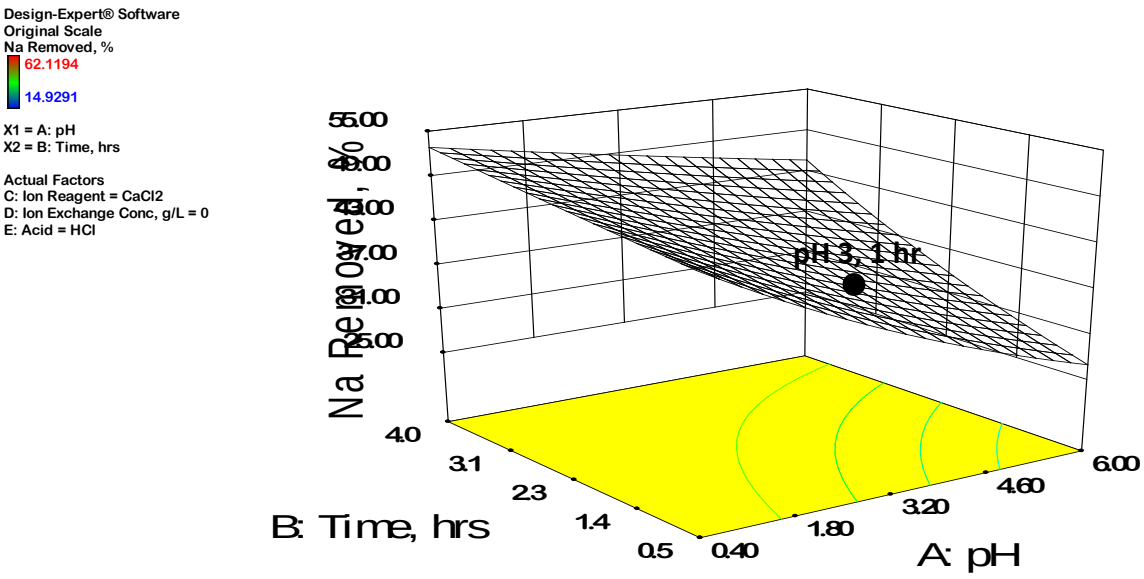

Figure 14a. 3-D illustration of the influence of time and pH on **percent sodium removed** from the coal. This plot is for the same conditions used to generate Figure 14.

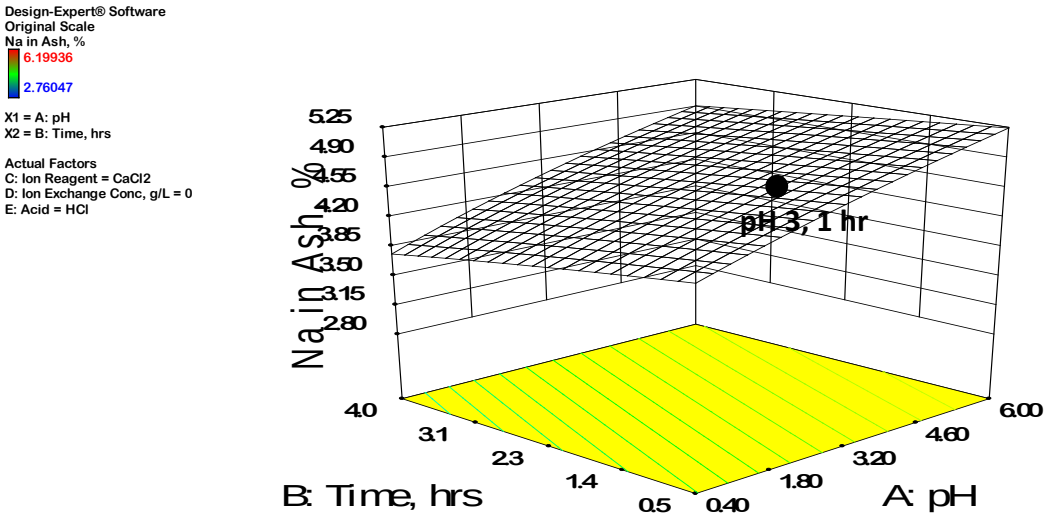

Figure 14b. 3-D illustration of the influence of time and pH on **percent sodium in the ash** from the leached coal (calculated). This plot is for the same conditions used to generate Figure 14.

Influence of Time and pH Without Ion Exchange Reagent Using HCl Acid (Contour Visualization)

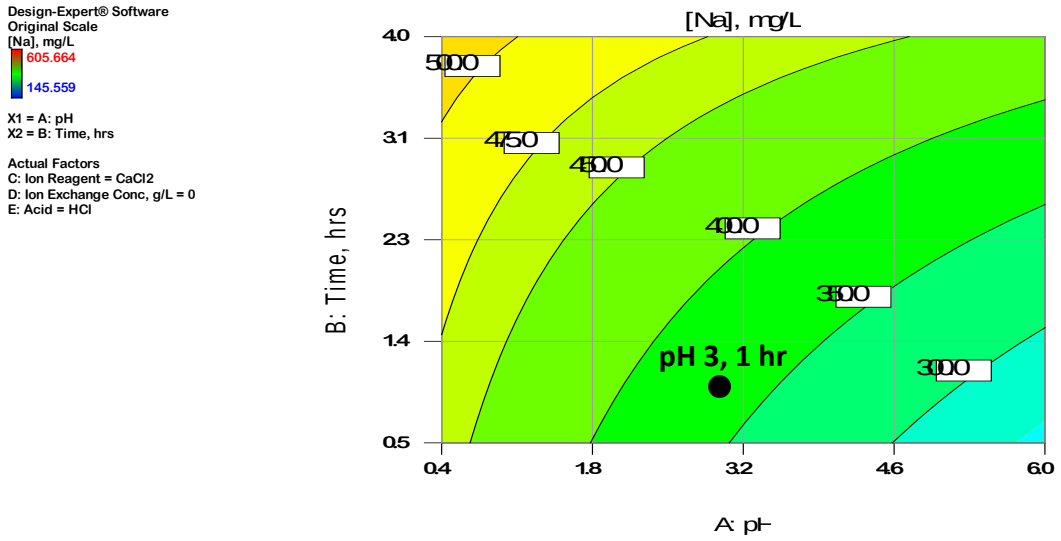

Figure 15. Contour illustration of the influence of time and pH on **sodium content in the leach solution**. Note that the acid reagent is HCl and that there is no CaCl2 present. At relatively low pH levels the sodium leached is independent of time but at higher pH values the concentration is a strong function of leach time.

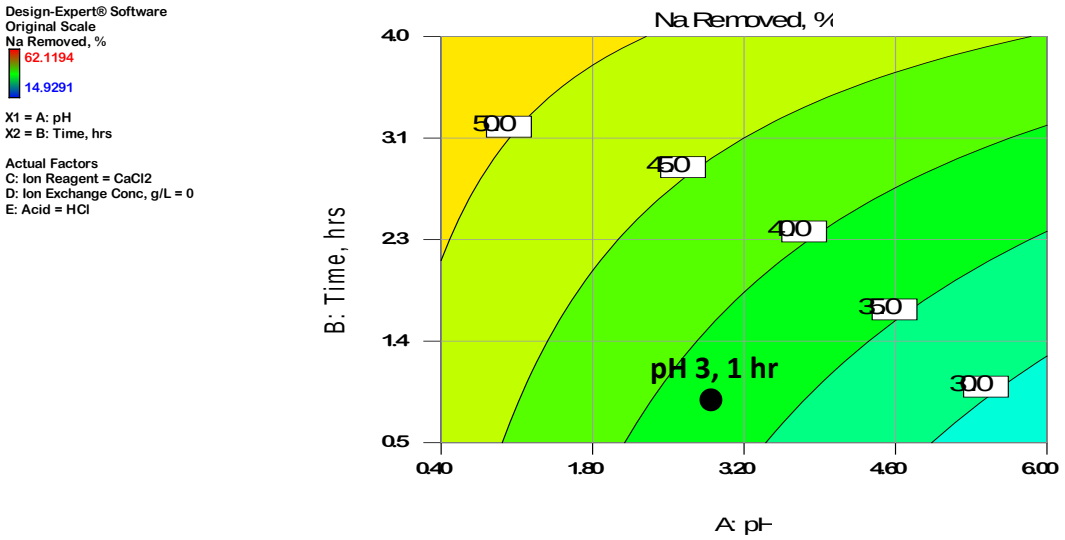

Figure 15a. Contour illustration of the influence of time and pH on **percent sodium removed** from the coal. This plot is for the same conditions used to generate Figure 15.

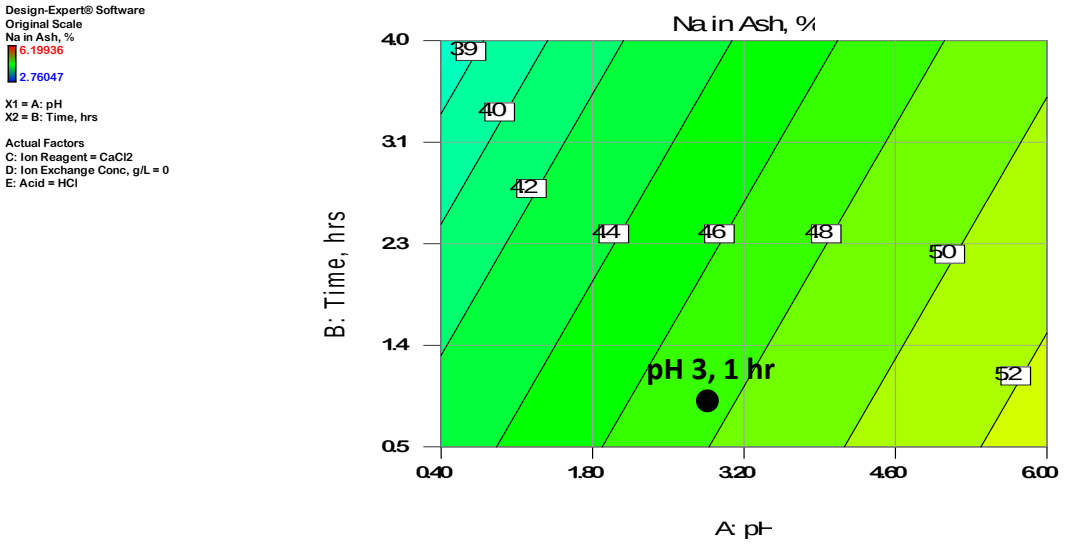

Figure 15b. Contour illustration of the influence of time and pH on **percent sodium in the ash** from the leached coal (calculated). This plot is for the same conditions used to generate Figure 15.

Influence of Time and pH With Ion Exchange Reagent Using H2SO4 Acid (3-D Visualization)

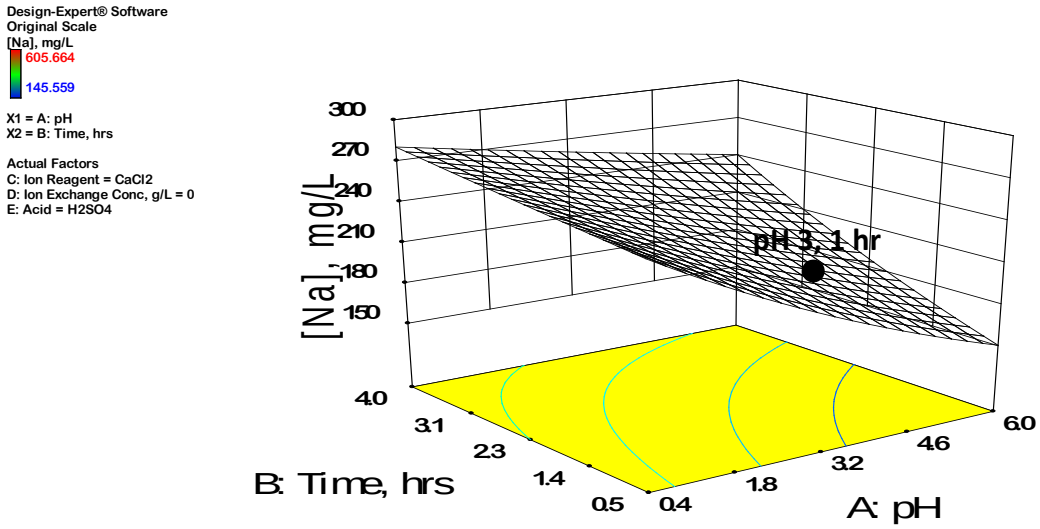

Figure 16. 3-D illustration of the influence of time and pH on **sodium content in the leach solution**. Note that the acid reagent is H2SO4 and that there is no CaCl2 present. Sulfuric acid is not as effective as HCl in extracting sodium from the coal (compare to Figure 14).

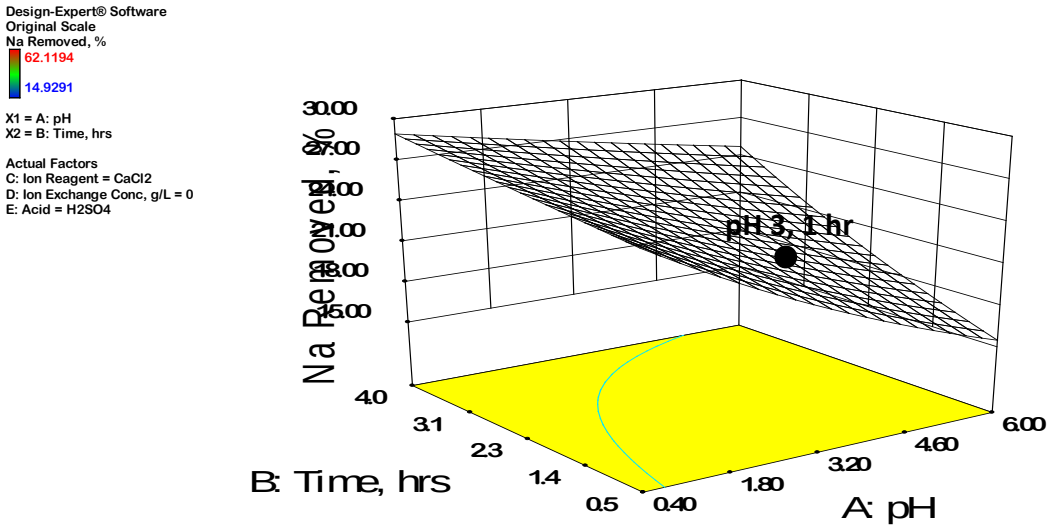

Figure 16a. 3-D illustration of the influence of time and pH on **percent sodium removed**. This plot is for the same conditions used to generate Figure 16.

Influence of Time and pH With Ion Exchange Reagent Using H2SO4 Acid (Contour Visualization)

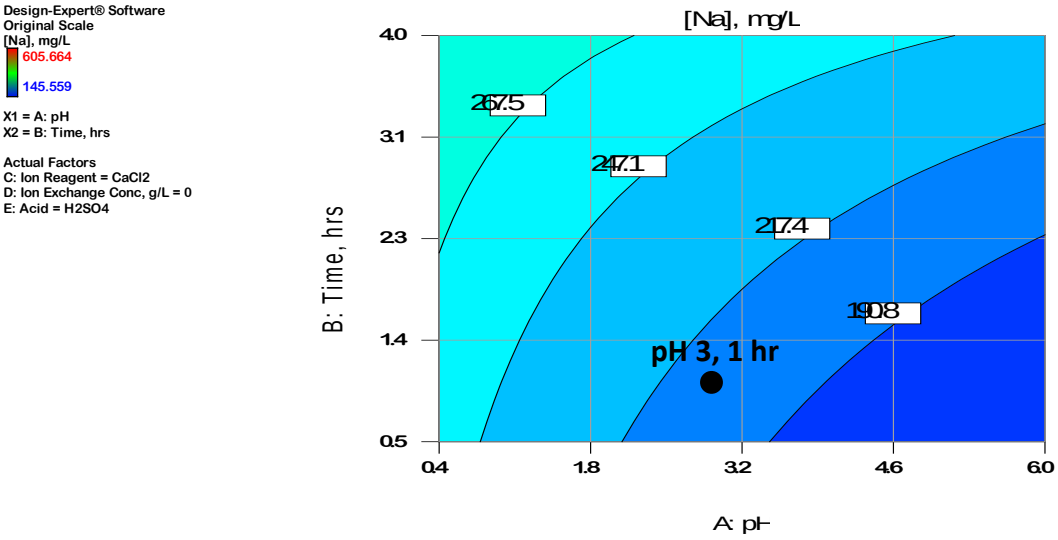

Figure 17. Contour illustration of the influence of time and pH on **sodium content in the leach solution**. Note that the acid reagent is H2SO4 and that there is no CaCl2 present. Sulfuric acid is not as effective as HCl in extracting sodium from the coal (compare to Figure 15).

Optimization of Leach Conditions for Coal B2

Design Expert software allows the user to investigate the effect of variables on the desired responses for any set of chosen conditions. For example Figure 18 is presented to illustrate the conditions that would result in removal of greater than 35%. The selection of time and pH conditions in the dark green area will satisfy the desired result. Additional examples are presented in Appendix E.

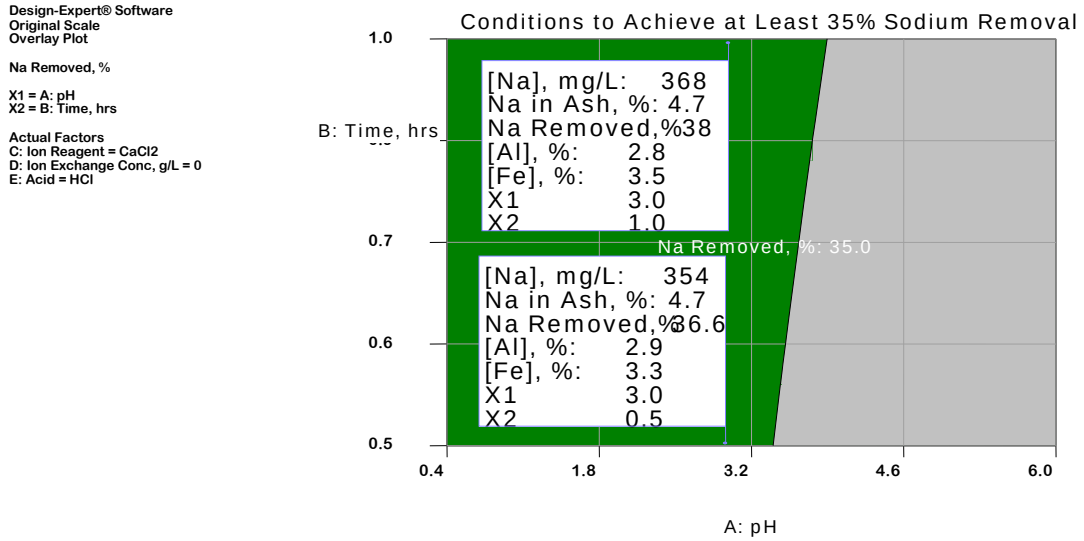

Figure 18. Optimization of time and pH to remove greater than thirty percent of the sodium. This example is based on using HCl acid and no added ion exchange reagent. The selection of time/pH conditions in the dark green region should result in the removal of >35% of the sodium. Note also that two flags have been added to show the amount of sodium in the leach solution, the percent sodium removed, the sodium content in the product ash, and the percent removal of aluminum and iron, for the conditions of pH 3/0.5 hr and pH 3/1 hr.

Coal D2

Based on the STABCAL modeling effort a Three-Level Response Surface Experimental Design Study was formulated for Coal D2. The Coal D2 study was formulated to evaluate the influence of three variables at three different variable levels on the removal of sodium and associated elements from the coal e.g. pH, time, and type of acid.

The specific experimental conditions are presented in Table 23. The range of conditions studied included: pH 1 to 5, time 0.5 to 4 hrs, and type acid either hydrochloric or sulfuric. Midpoint conditions were replicated five times to satisfy our quality control requirement of reproducibility.

Table 23. Response Surface, Three Level Face Centered Cubic Design Matrix for Coal D2

Standard Run Number	A:pH	B:Time, hrs	Type Acid
1	1	0.5	H2SO4
2	5	0.5	H2SO4
3	1	4	H2SO4
4	5	4	H2SO4
5	1	2.25	H2SO4
6a	5	2.25	H2SO4
7a	3	0.5	H2SO4
8	3	4	H2SO4
9	3	2.25	H2SO4
10	3	2.25	H2SO4
11	3	2.25	H2SO4
12	3	2.25	H2SO4
13	3	2.25	H2SO4

Table 23. Response Surface, Three Level Face Centered Cubic Design Matrix for Coal D2			
Standard Run Number	**A:pH**	**B:Time, hrs**	**Type Acid**
14	1	0.5	HCl
15	5	0.5	HCl
16	1	4	HCl
17	5	4	HCl
18	1	2.25	HCl
19	5	2.25	HCl
20	3	0.5	HCl
21	3	4	HCl
22	3	2.25	HCl
23	3	2.25	HCl
24	3	2.25	HCl
25	3	2.25	HCl
26	3	2.25	HCl

Experimental Procedure

The experimental procedure used for conducting the experiments that were presented in Table 23 follows:

- Each coal sample was prepared so that the size fraction distribution was the same as determined by the size distribution test work, see following table.

Size, mesh	Mass, %
+6	24.8
-6,+12	39.9
-12,+20	18.7
-20,+48	16.6

- Place 40 gm coal D2 in a 1-Liter plastic bottle, add 400 mL of DI water
- Place on the shaker table for 30 minutes, measure and record pH
- Collect sample, filter 50 gm of the solution phase through 0.45 um filter disk into a 60 mL scintillation vial, add 1.0 g High Purity Concentrated Nitric acid, cap for analysis.
- Be sure to label the sample correctly both in your lab book and on the scintillation vial.
- The above should be your standard procedure for each of the 26 tests
- After the wash test do the following to each solution in each bottle
    - Adjust the pH to the desired value with the specific acid
    - Record the amount of acid used for each test in your lab book
    - Readjust and maintain pH for the specified time.
    - Collect, filter and preserve samples at times as dictated by the design matrix
- All samples ICP analyzed for Al, Ca, Fe, K, Mg, Na, Si

Discussion of Experimental Design Results for Coal D2

The experimental test results are presented in Tables 24 and 25a. Models have been developed for two responses, e.g. concentration of sodium in the leach solution (mg/L) and percent sodium removed by the leach process. A summary of the design space equations that describe the response results are presented in Appendix E. Also, the modeling results for associated elements are presented in Appendix E. Note that the solution concentration results shown by standard run tests 22 through 26 are quite reproducible.

The evaluation of the percent sodium removed by the leach conditions is, of course, dependent on the initial content of sodium in the feed coal. Several attempts to determine a reproducible head sodium content were made. Samples were supplied to three labs. The results are shown in Table 25. An average of the lithium boride sodium analyses were used as the composition of the coals to determine the percent extractions.

Table 24. Coal D2-Solution Concentration, mg/L

Standard Run Number	Responses: Element Concentration in Final Leach Solution, mg/L						
	[Al]	[Ca]	[Fe]	[K]	[Mg]	[Na]	[Si]
1	11.89	237.01	34.22	4.12	55.96	263.20	2.38
2	0.27	13.66	0.05	1.10	5.16	115.13	0.83
3	42.06	352.44	72.05	6.34	107.42	453.24	4.55
4	0.51	109.82	0.06	3.58	34.34	332.88	1.49
5	18.62	328.90	41.68	4.97	80.68	382.21	2.61
6a	0.63	36.01	0.12	1.96	14.61	235.23	1.30
7a	1.69	107.04	3.22	2.12	24.73	176.22	1.02
8	4.59	321.60	5.83	4.25	69.20	387.66	1.64
9	2.72	219.39	3.87	3.55	50.79	307.26	1.38
10	3.43	208.03	7.09	3.16	45.90	276.58	1.34
11	2.59	194.87	4.41	2.95	44.06	260.76	1.27
12	2.67	195.81	4.38	3.12	44.11	273.24	1.29
13	2.72	180.49	4.98	3.01	41.59	264.59	1.43
14	28.08	576.98	39.64	6.04	110.24	414.33	1.63
15	0.24	21.78	0.05	2.07	9.45	231.86	0.79
16	78.55	757.95	85.69	6.51	136.30	440.74	2.91
17	0.05	75.66	0.01	3.55	32.63	352.36	0.90
18	51.87	643.83	61.37	5.80	118.79	390.88	2.31
19	0.11	39.63	0.02	3.04	17.49	308.18	0.84
20	1.44	131.71	1.37	2.62	31.44	207.92	0.88
21	4.01	425.47	2.06	4.99	94.65	385.51	1.36
22	2.85	306.79	2.30	4.45	71.78	345.52	1.11
23	2.63	283.42	2.50	4.19	67.70	335.49	1.13
24	1.99	230.17	1.83	3.87	56.98	308.86	1.13
25	2.12	250.07	2.01	4.67	62.90	383.12	1.39
26	2.78	278.36	2.49	4.04	64.89	319.69	1.14
Average of tests 22-26	2.5±0.4	269.8±29.9	2.2±0.3	4.2±0.3	64.8±5.5	338.5±28.6	1.2±0.1

The experimental reproducibility for tests has been taken as the average of the midpoint standard run tests 22-26.

Table 25. Coal D2 Head Analyses

Technique/Laboratory	Na Content, %	Comments
Proton Induced X-ray Emission (PIXE), Elemental Analysis, Inc., Lexington, Ky	0.345	Sample mix as used in leaches, based on triplicate analyses for 4 size fractions
Ash analyses , Wyoming	0.408	Sample mix as used in leaches, based on

Table 25. Coal D2 Head Analyses		
Technique/Laboratory	**Na Content, %**	**Comments**
Analytical Lab, Laramie, WY		calculated value from sodium oxide content in ash
Lithium Boride Fusion, CAMP, Butte, MT	0.4191	Size fraction: mesh -6+12
Lithium Boride Fusion, CAMP, Butte, MT	0.4082	Size fraction: mesh -12+20

Table 25a. Coal D2-Element Extracted by Sulfuric and Hydrochloric Acids, %							
Standard Run Number	**Responses: Amount Extracted by Leach Conditions, %**						
	[Al]	**[Ca]**	**[Fe]**	**[K]**	**[Mg]**	**[Na]**	**[Si]**
1	2.97	44.77	26.58	9.74	40.78	79.36	0.36
2	0.07	2.58	0.04	2.61	3.76	34.71	0.12
3	10.51	66.57	55.96	15.00	78.28	136.67	0.69
4	0.13	20.74	0.05	8.48	25.03	100.38	0.22
5	4.65	62.13	32.38	11.76	58.79	115.25	0.39
6a	0.16	6.80	0.09	4.64	10.65	70.93	0.20
7a	0.42	20.22	2.50	5.01	18.02	53.14	0.15
8	1.15	60.75	4.53	10.05	50.43	116.89	0.25
9	0.68	41.44	3.01	8.41	37.01	92.65	0.21
10	0.86	39.29	5.51	7.48	33.45	83.40	0.20
11	0.65	36.81	3.42	6.99	32.11	78.63	0.19
12	0.67	36.99	3.40	7.38	32.15	82.39	0.19
13	0.68	34.09	3.87	7.13	30.31	79.78	0.22
14	7.01	108.99	30.79	14.29	80.34	124.93	0.25
15	0.06	4.11	0.04	4.91	6.88	69.91	0.12
16	19.63	143.17	66.55	15.40	99.33	132.90	0.44
17	0.01	14.29	0.01	8.40	23.78	106.25	0.14
18	12.96	121.61	47.66	13.74	86.57	117.86	0.35
19	0.03	7.48	0.02	7.19	12.74	92.93	0.13
20	0.36	24.88	1.06	6.19	22.91	62.70	0.13
21	1.00	80.37	1.60	11.80	68.98	116.24	0.21
22	0.71	57.95	1.79	10.54	52.31	104.19	0.17
23	0.66	53.54	1.94	9.92	49.34	101.16	0.17
24	0.50	43.48	1.42	9.15	41.52	93.13	0.17
25	0.53	47.24	1.56	11.05	45.84	115.52	0.21
26	0.69	52.58	1.93	9.55	47.29	96.40	0.17
Average of tests 22-26	0.62±0.10	50.96±5.65	1.73±0.23	10.04±0.76	42.26±4.02	102.08±8.34	0.18±0.02

The experimental reproducibility for tests has been taken as the average of the midpoint standard run tests 22-26. The experimental extraction percentages were determined using the extraction solution concentrations and an average coal head concentration based on fusion analyses presented in Table 25.

Leach Solution Sodium Concentration and Percent Extraction-Several figures are presented to illustrate the influence of the studied factors on the amount of sodium extracted. Annotation notes are added to the figure captions to illustrate features of the results shown by each figure.

Influence of Time, pH, and Type Acid (Cubic Visualization)

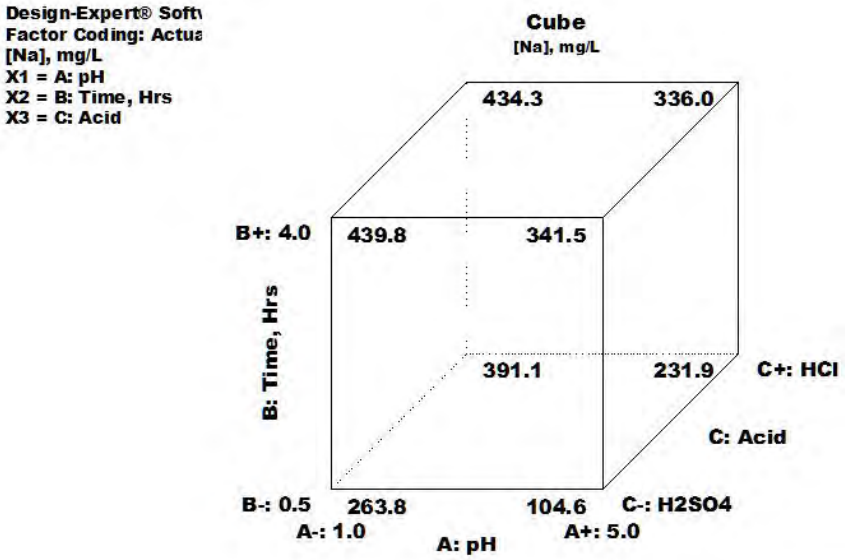

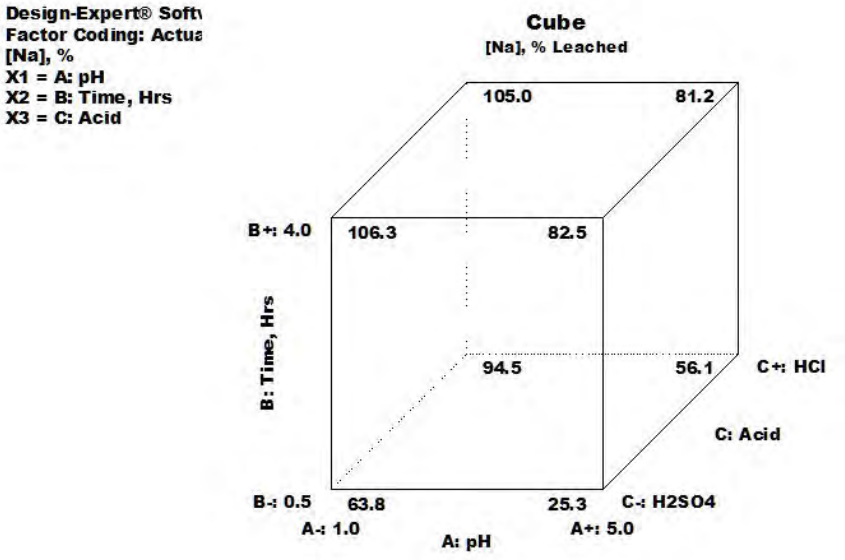

Figure 19. Cubic illustration of the influence of time, pH, and type of acid on **sodium concentration in the leach solution (a) and percent sodium extracted from Coal D2 (b)**. Note that effective leaching of sodium occurs for either acid at the longer residence times. Also, note that considerable sodium is extracted under rather mild conditions. Hydrochloric acid shows better leachability compared to sulfuric acid, although conditions can be chosen where sulfuric acid also shows acceptable leachability.

Comparison of Type of Acid

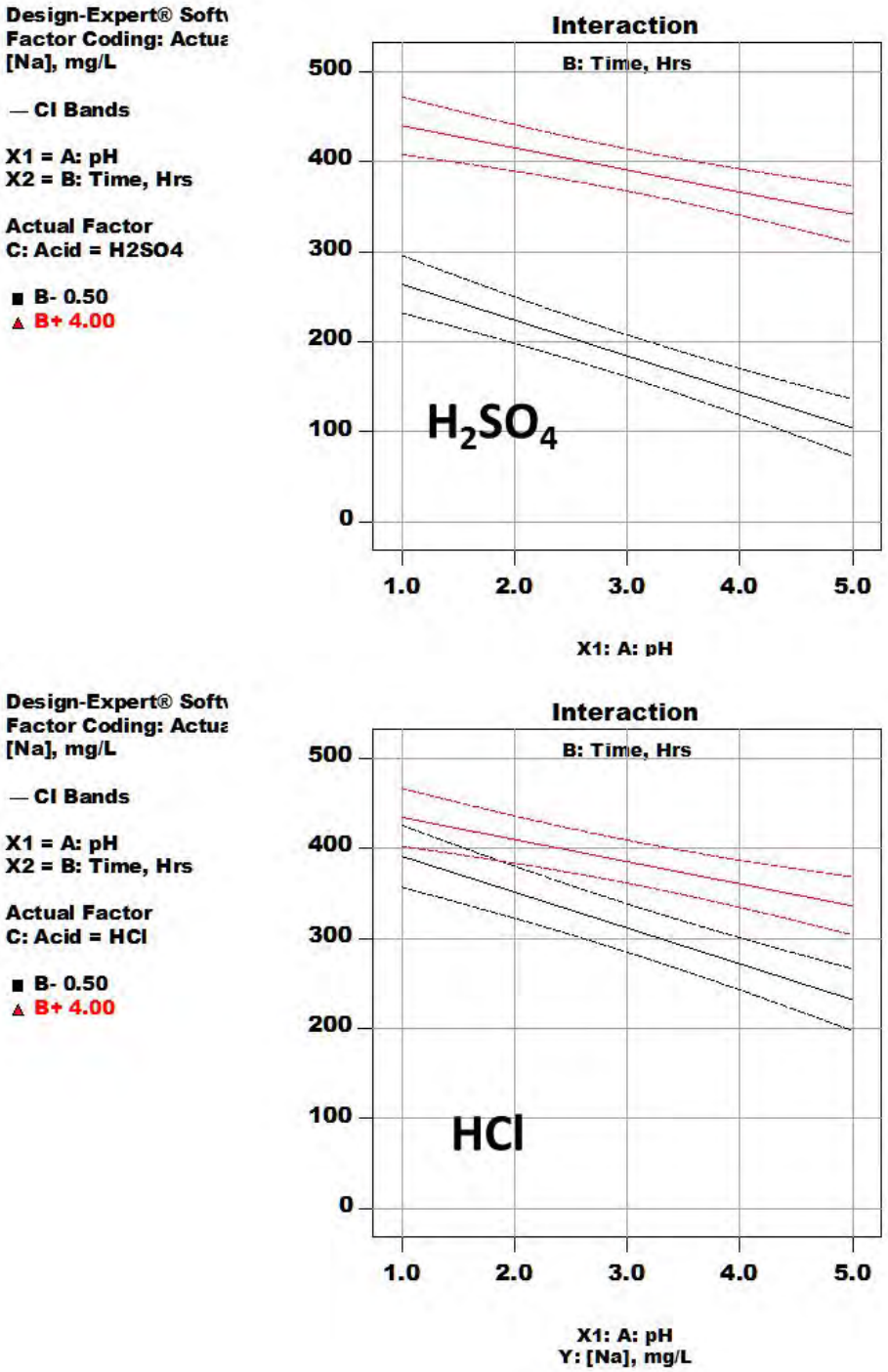

Figure 20. Interaction illustration of the influence of time, pH, and type of acid on **sodium concentration in the leach solution from Coal D2**. Note that effective leaching of sodium occurs for either acid at the longer residence times. Also, note that considerable sodium is extracted under rather mild conditions. Hydrochloric acid shows better leachability compared to sulfuric acid, although conditions can be chosen where sulfuric acid also shows acceptable leachability.

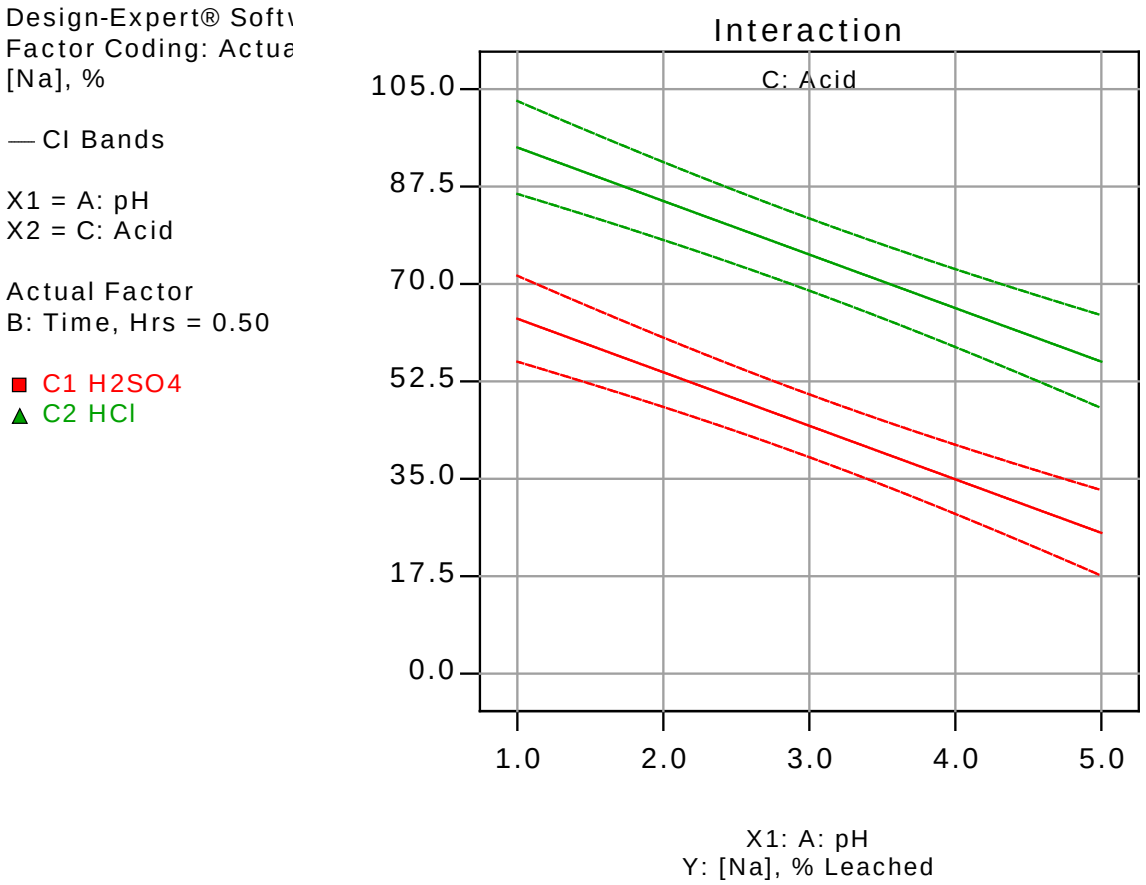

Figure 21. Interaction illustration of the influence of pH, and type of acid on **sodium extracted from Coal D2** at a relatively short exposure time of 0.5-hr. Note that effective leaching of sodium occurs for either acid at relatively short reaction times.

Influence of Time and pH (Contour Visualization)

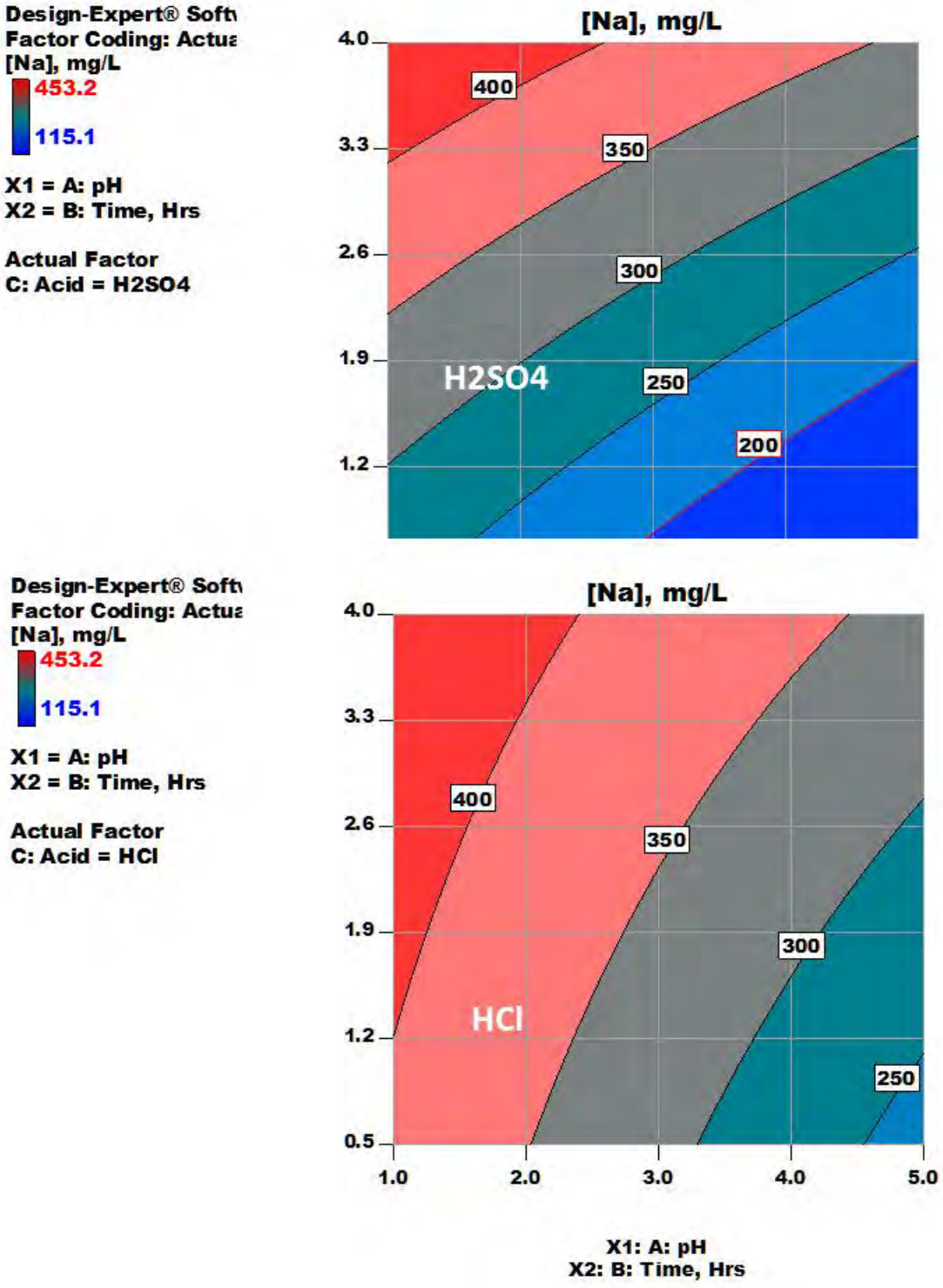

*

Figure 22. Contour illustration of the influence of time, pH, and type of acid on **sodium concentration in the leach solutions for Coal D2**. Note that effective leaching of sodium occurs for either acid at the longer residence times. Also, note that considerable sodium is extracted under rather mild conditions. Hydrochloric acid shows better leachability compared to sulfuric acid, although conditions can be chosen where sulfuric acid also shows acceptable leachability. Similar plots are presented in Figure 23 for percent sodium extracted.

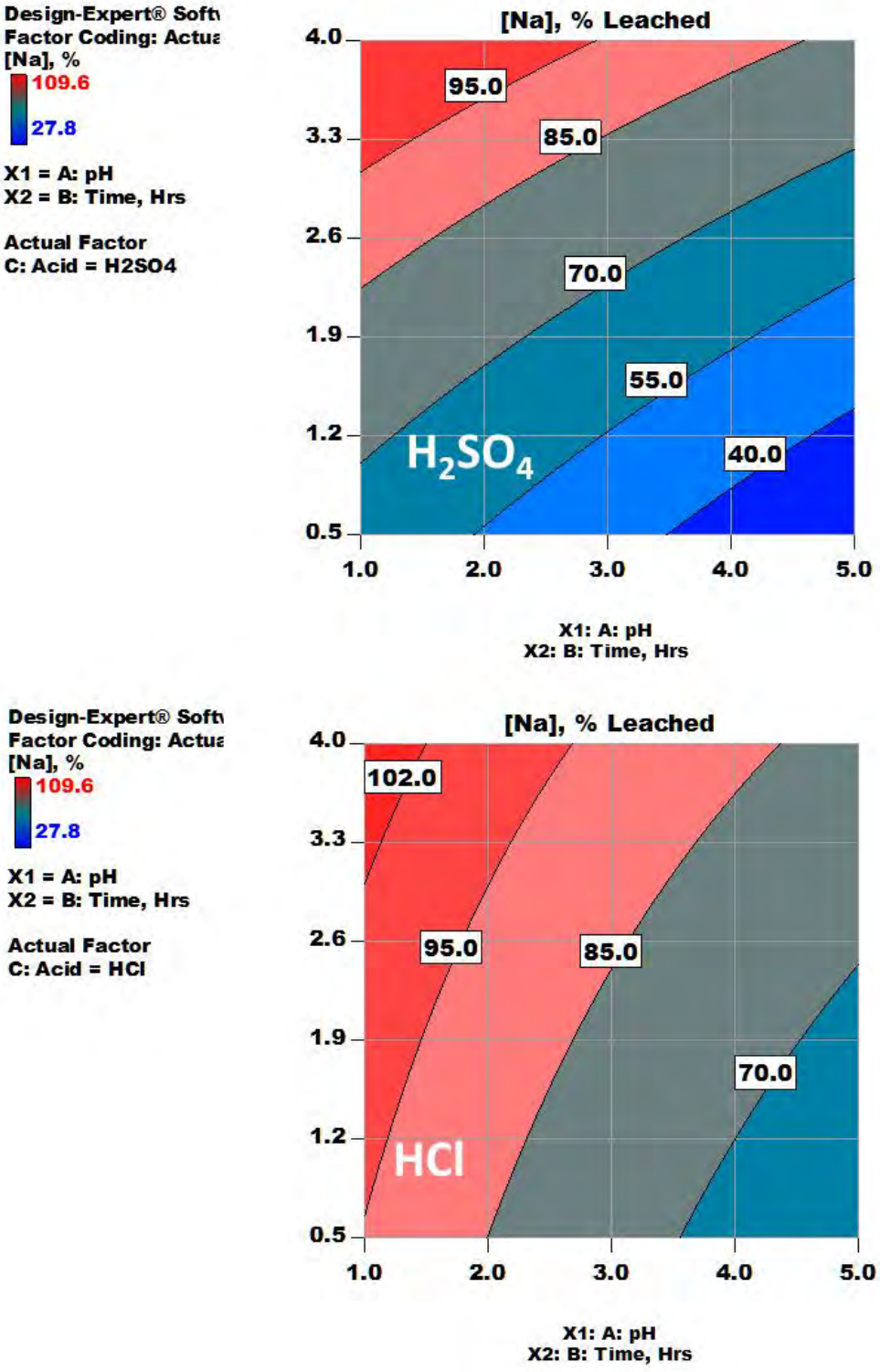

Figure 23. Contour illustration of the influence of time, pH, and type of acid on **sodium extracted (%) from Coal D2**.

Influence of Time and pH (3D Visualization)

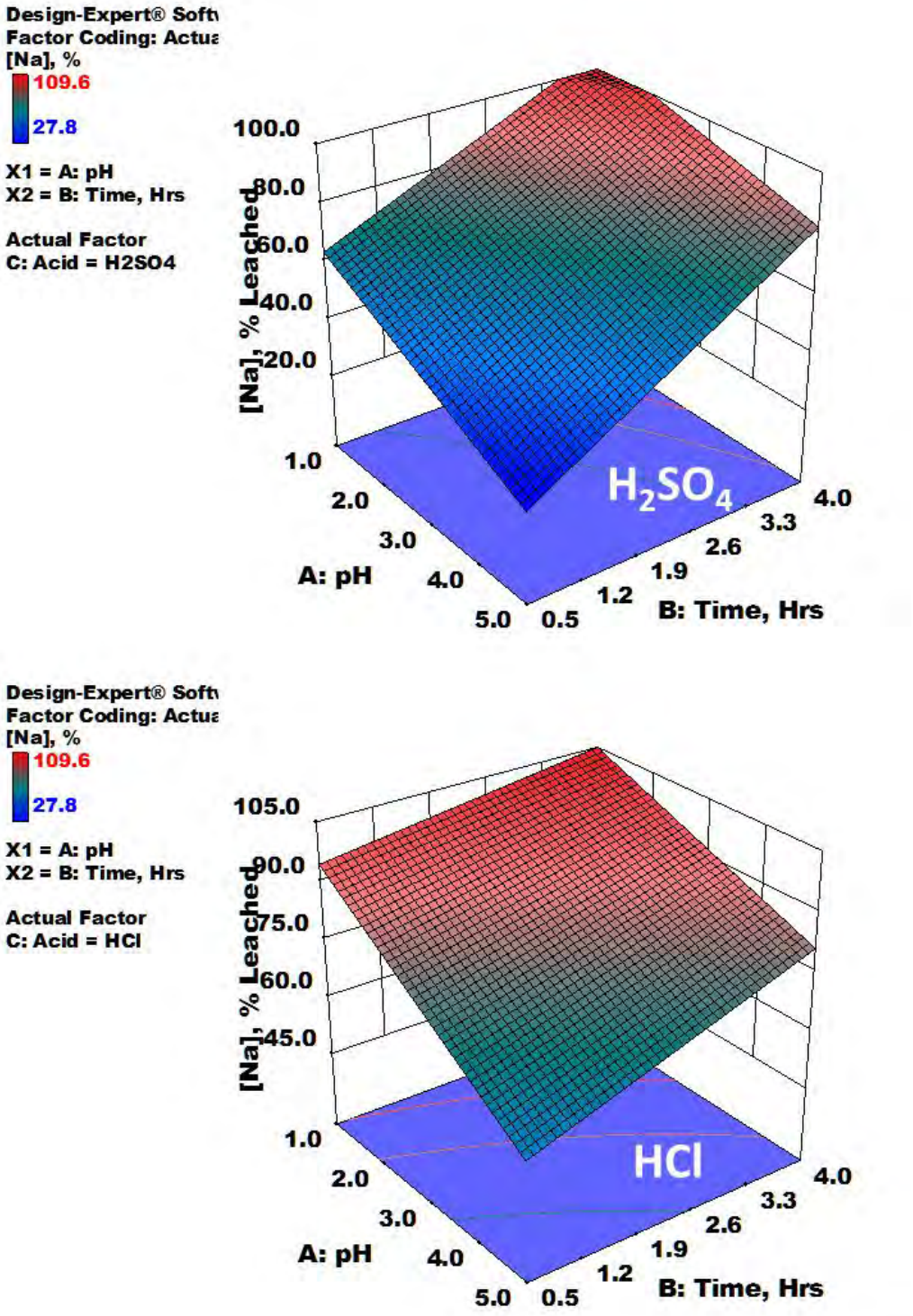

Figure 24. 3-D illustration of the influence of time and pH on **sodium extraction from Coal D2.** At relatively low pH levels and longer reaction times the sodium leached is independent of the type acid but at higher pH values the extraction is a strong function of leach time for both acids.

Optimization of Conditions for Treating Coal D2

Design Expert software allows the user to investigate the effect of variables on the desired responses for any set of chosen conditions. For example Figure 25 is presented to illustrate the conditions that would result in removal of greater than 50% using sulfuric acid and greater that 80% using hydrochloric acid. The selection of time and pH conditions in the dark green area will satisfy the desired result. Tables 26-28 are presented to illustrate the removal of associated elements under selected sodium removal conditions. Note that sulfuric acid is less effective in removing sodium than hydrochloric acid under very mild leach conditions, i.e. 0.5 hours, pH 5. Tables 26 and 27 illustrate the following: sodium is effectively removed using hydrochloric acid under very mild leach conditions (Table 26). Associated elements are not removed which illustrates that a significant fraction of the sodium that is present is contained in the coal as either soluble sodium compounds and/or as constitutes in the maceral material in the coal. The Table 27 results are based on leaching the coal under more severe (lower pH) conditions and illustrates that a greater amount of the sodium is removed and also a significant amount of associated mineral phase elements are removed.

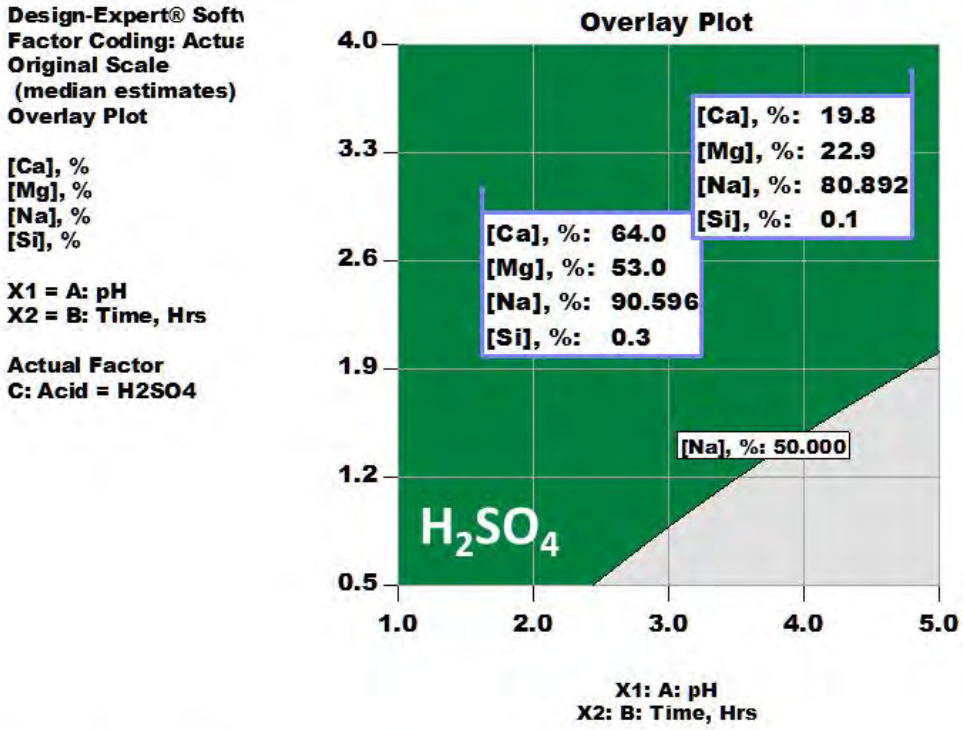

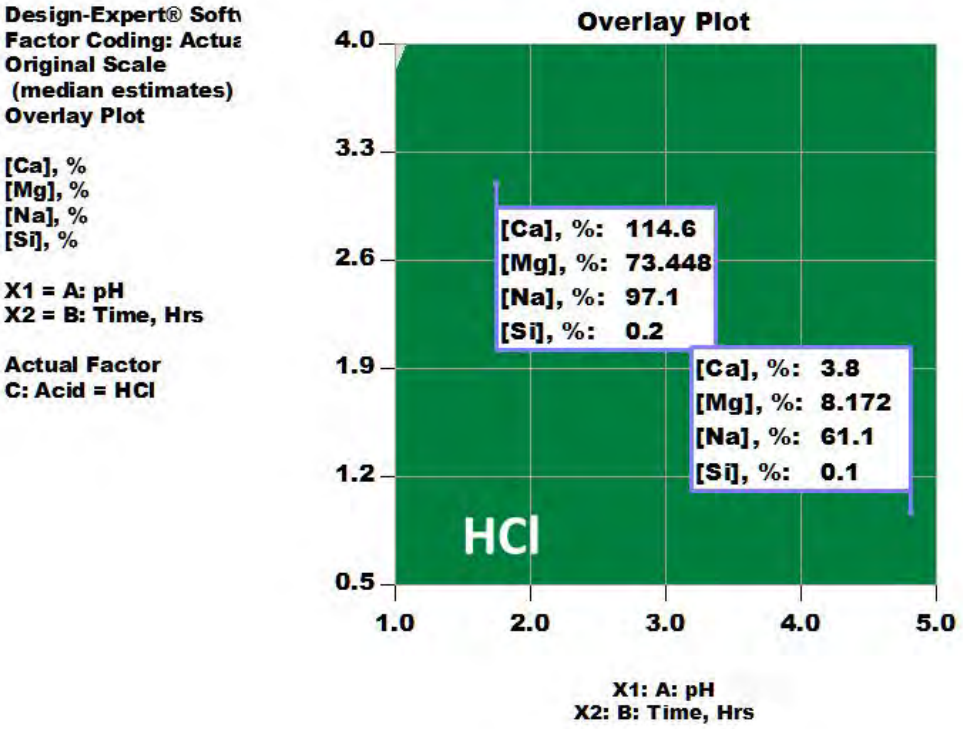

Figure 25. Optimization of time and pH to remove greater than 50 percent of the **sodium from Coal D2** using sulfuric or hydrochloric acid. The selection of time/pH conditions in the dark green region should result in the removal of greater than the specified percentage.

Table 26. Design Expert Model Prediction of Element Extractions from Coal D2 Using Sulfuric Acid under Mild Leach Conditions

Factor	Name	Level	Low Level	High Level
A	pH	5.0	1	5
B	Time, Hrs	0.5	0.5	4
C	Acid	H2SO4	H2SO4	HCl
Response, %	Prediction	95% CI low		95% CI high
[Al]	0	0.0		0.1
[Ca]	2.	2.2		3.0
[Fe]	0.10	0.06		0.18
[K]	2.3	1.3		3.2
[Mg]	3.6	2.0		5.6
[Na]	25.3	17.6		33.0
[Si]	0.1	0.1		0.1

Table 27. Design Expert Model Prediction of Element Extractions from Coal D2 Using Hydrochloric Acid under Mild Leach Conditions

Factor	Name	Level	Low Level	High Level
A	pH	5.0	1	5
B	Time, Hrs	0.5	0.5	4
C	Acid	HCl	H2SO4	HCl
Response	Prediction	95% CI low		95% CI high
[Al]	0	0		0
[Ca]	2.2	1.8		2.6
[Fe]	0.02	0.016		0.03
[K]	5.2	4.3		6.2
[Mg]	4.9	3.0		7.2
[Na]	56.1	47.7		64.4
[Si]	0.1	0.1		0.1

Table 28. Design Expert Model Prediction of Element Extractions for Coal D2 Using Hydrochloric Acid under Low pH Conditions

Model Prediction of Element Extractions Hydrochloric Acid				
Factor	Name	Level	Low Level	High Level
A	pH	2.0	1	5
B	Time, Hrs	0.5	0.5	4
C	Acid	HCl	H2SO4	HCl
Response, %	Prediction	95% CI low		95% CI high
[Al]	1.2	1.3		0.9
[Ca]	55.8	62.3		44.6
[Fe]	5.5	6.9		3.28
[K]	9.0	9		10.6

Model Prediction of Element Extractions Hydrochloric Acid				
Factor	Name	Level	Low Level	High Level
[Mg]	**43.3**	39.0		47.9
[Na]	**84.7**	77.7		91.6
[Si]	**0.1**	0.1		0.1

Task 8b-Water Treatment

Addressing water treatment of sodium or more broadly, salt laden waters is another component of the research being performed as a part of this project. As such, a necessary part of that phase is to relate information as to the primary purpose or driver behind the need for water treatment, provide information regarding current and therefore potential water treatment technologies, and lastly provide research into water treatment technologies that may prove to be the best option for addressing process waters resulting from the first phase of this project.

Dudley (2011) as a part of this project and as a requirement of his Master of Science thesis proposal has conducted an extensive literature review to serve as a working or developing document, highlighting the research done, documenting areas for improved research or more information gathering, and lastly providing a path forward for experimentation and research. The document serves to provide for understanding of the driving force, mainly environmental, behind the need for treatment of process waters, especially in reference to salt/sodium content. Dudley's thesis is presently available in PDF format from the Library at Montana Tech of the University of Montana. A brief summary of the literature review is presented as a part of the project literature review presented as Appendix A.

Path Forward

One of the promising technologies for treating sodium bearing solutions is the formation of artificial zeolite formation. As a condition of the project it is important to not only devise a way to remove the sodium from the coal but be able to treat the waste brine treatment fluid as well. Sodium, although not a large primary pollutant, nonetheless would pose a significant hurdle in the discharge systems of large treatment facilities. Therefore, any treatment of coal to remove sodium must also likewise address what to do with the sodium laden treatment fluid. Current treatment technologies for removal of sodium are costly and heavily energy or material intensive. So much so, that they could be cost prohibitive to a coal facility. Therefore, it is the goal of this project to report and if possible give specifications as to a technology that would be cost effective in treating a sodium brine. The specific intention is to evaluate the use of fly ash for artificial zeolite formation processes performed under non-standard conditions as a viable treatment opportunity for salt laden water produced during coal washing operations.

Chosen Technology

As stated before, many of the technologies that focus on sodium removal from water are heavily energy and material intensive. That said, a promising technology for coal operations has been found within a comprehensive literature review. Formation of artificial zeolite materials from coal fly ash and sodium brine has been proven to be a unique way to treat fly ash from combustion facilities. Previous work focuses much on the fly ash as the primary waste product of concern. This project proposed to increase the scope of such a technology to include the treatment of the process fluid and coal fly ash possibly posing a way to create a saleable material form what would otherwise be considered waste products.

Natural zeolite material is often used as a cation exchange material for treatment of a variety of media ranging from wastewater to soil remediation. Likewise artificial zeolite material can be used in the same manner. A technology such as this represents the establishment of a closed loop process for many materials within a coal facility. This adds many benefits to such a facility including decreased treatment cost, creation of a saleable material, and what one could term as "environmental credit."

Scope of Research

Research as to applicability of this technology to Montana coals will be and is being performed in multiple stages. The first preliminary testing was to determine an optimal brine composition or rather type of brine to treat the fly ash with. Three different brines were tried, the first being a sodium hydroxide brine mixture, seemingly the optimal mixture used in previous research. However, the sodium hydroxide brine showed a limited, if any, formation of a zeolite structure. Next sodium carbonate and sodium sulphate brines were tested. The sodium sulphate brine showed the best results producing an identifiable zeolite structure. Presence of a zeolite structure was determined through the use of x-ray diffraction and associated analysis software. Although, removal of sodium from coals is leaning heavily towards a hydrochloric solution, one's coal facility could incorporate other process streams such as scrubber has to reform the waste brine into the optimal composition.

The next stage of testing should be a bench scale testing matrix, altering brine concentration, temperature, and time to determine the optimal conditions for producing a zeolite structure. Limitations on these tests include a brine concentration of no more than 10,000 ppm NaSO4 (higher concentrations venture into the realm of an increased cost of concentration) and a limitation of reaction temperature of 400 Degrees C. The temperature limitation was imposed by the upper limit of waste heat that could be recovered from a coal fired facility, so as not to incur increased cost of having to produce heat for the treatment procedure.

Once the optimal treatment conditions are determined, a second matrix should be used to determine if outlying factors such as agitation and introduction of alternative carrier gases will have an effect on the type of zeolite structure produced and the magnitude of such a structure. This second matrix is being done to approach a way for determination of process requirements that would allow a pilot scale process to be designed and constructed. This pilot scale, if proceeded with, would resemble an adsorption column producing a saleable zeolite and a clean water discharge.

Task 9-Economic Evaluation of Promising Technologies

This task has not been fully addressed because of the following reasons; a fully conceptual treatment has not been finalized. Mild acidic leaching as a way to remove a portion of the sodium appears to be appropriate; however, only the concept has been validated; there still needs to be further test work to establish what sodium concentration in the leach waters can be attained. Such a study would require that a series of experiments using counter-current coal/leach solution contacts be performed. The present project does not have the funding to conduct such test work. Also, further study is required to determine an appropriate way to remove dissolved sodium and associated metals from the product water or to dispose of the elevated sodium containing water in an environmentally acceptable manner.

Task 10-Final Report

The project final report submitted April 30, 2012.

CONCLUSIONS AND FUTURE WORK

The literature review, modeling, and preliminary test work validates the concept that a mild acidic coal washing technology is appropriate for lowering the sodium content in low-rank coals to acceptable levels.

Study results are summarized below:

- Four Montana coals have been characterized for the parameters that follow:
  - Coal particle mass and size distribution for coarse and fine ground samples
  - Element composition (sodium, potassium and nine other inorganic elements) and mineral identification in as-received and ground coals by X-ray Diffraction (XRD) and Mineral Liberation Analyses (MLA)
  - Element composition as a function of particle size
  - Coal ashing properties including Proximate, Ultimate, Heating value, and T250 softening temperature.
- Good extraction occur using moderately acidic conditions, e.g. 30-40 percent of the sodium in Coal B2 and 80-100 percent of the sodium in Coal D2 can be removed by acidic treatment in the pH range of three to five.
  - In general, hydrochloric acid is better than sulfuric; although acceptable results can be achieved with sulfuric acid.
  - The addition of ion exchange reagents (calcium chloride or ammonium acetate) are not necessary (based on studies on Coal B).
- Sodium removal is from the maceral phase for mild acidic leaching conditions. This is in agreement with published literature results for other low-rank coals.

- Future work should include, but not limited to:
  - Investigation to determine if multiple leach solution contacts with new coals will allow recycle of the leach solution without detrimentally affecting the leachability of the coals and to produce a concentrated sodium bearing solution in order to limit the amount of leach solution that would have to be treated prior to disposal.
  - Water cleanup will be required because of the relatively high sodium and chloride (or sulfate) content. Techniques to accomplish the cleanup are presently being investigated.
  - Evaluation of where and how the leachate could be introduced into the coal preparation treatment system.
  - Evaluation of the consequences of adding leachate reagents to present coal washing equipment, i.e. would treatment of discharge waters be required.

Test work has not been conducted to evaluate the requirements to produce “Clean” coal to be used for liquefaction or gasification processes. However, if the desire of the guidance committee is to produce “Clean” coal from the Montana low-rank coals then aggressive leach studies should be conducted. The approach would be based on the work completed and being presently conducted on Australian “Brown” low-rank coals by Clean Coal Technology, LTD, i.e., very aggressive acidic leach conditions will be used. For example concentrated hydrochloric acid solutions at elevated temperatures will be evaluated using surface-response or two-level factorial experimental design studies to determine the relative importance of a number of variables and to optimize the important variables. Refer to the

LITERATURE REVIEW section on "Clean" coals (*Domazetis, and Domazetis, et al, website:* www.latrobe.edu.au/
chemistry/staff/resfellows/domazetis/gdpubs.html).

REFERENCES

American Coal Foundation, 2007, All About Coal, Coal Reserves, Washington, DC, Website: www.teachcoal.org.

CAMP, 2009, Center for Advanced Mineral and Metallurgical Processing, Montana Tech of the University of Montana, Butte, Montana. J. McCloskey, Director, jmccloskey@mtech.edu, Website: www.Mtech.edu\camp.

Chen, Y., N. Shah, f.E. Huggins, G.P. Huffman, W.P. Linak, C.A. Miller, 2004, Fuel Process Technology, 85,743-61.

Davis, M.B., P.E. Toombs, W.R. Toombs, J. Boyle, G. Hermanas, H. Benisvy, K. Schulz, 2008, Controlling SO_3 Slag and Fouling Resulting in Improved Heat Rates, Better Efficiency and Allowing for Fuel Flexibility - Santee Cooper, Cross Station Case Study**,** Presented at the EUEC Conference, January 2008, Tucson, AZ, Website: www.ftek.com/technicalPapers.php, paper number TPP-581.

Domazetis, Dr. G., 2009, Clean Coals as Fuel for Turbines, Managing Director, Clean Coal Technology Pty Ltd, Website for download: www.autraliancoal.CSIRO.au/pdfs/domazetis.pdf.

Domazetis, G., BD. James, 2006, Molecular models of brown coal containing inorganic species, Organic Geochemistry, 37, 244-259.

Domazetis, G., M. Raoarun, BD. James, J. Liesegang, 2008, Molecular modeling and experimental studies on steam gasification of low-rank coals catalysed by iron species, Applied Catalysis A: General, 340, 105-18.

Domazetis, G., P. Barilla, B.D. James, R. Glaisher, 2008, Treatments of low rank coals for improved power generation and reduction in greenhouse gas emissions, Fuel Processing Technology, 89, 68-76.

Domazetis, G., P. Barilla, BD. James, 2009, Lower emission plant using processed low-rank coals, Fuel Processing Technology, Submitted for publication, Website: www.latrobe.edu.au/chemistry/staff/resfellows/domazetis/gdpubs.html

Domazetis, G., S. Buckman, 1987, Fly ash formation during the combustion of brown coal, Vol 3C, Effects of Aluminum Based Additives on Ash Formation, End of Grant Report, State Electricity Commission of Victoria, Research and Development Department, Report No. ND/87/043.

Dudley, S., 2011. Sodium Removal from Coal Processing Waters, M.Sc. Thesis, Metallurgical/Materials Engineering Department, Montana Tech of the University of Montana, to be awarded in May, 2011.

Electric Power Monthly, 2009, Major US Mines, US Energy Information Administration (EIA), Independent Statistics and Analysis (searchable database), Website: www.eia.doe.gov.

EPA, 2009, Drinking Water Contaminant Candidate List (CCL), Sodium in Drinking Water, www.epa.gov/ogwdw/ccl/sodium.html.

Falcone, S.K., H.H. Schobert,1986, Mineral transformations during ashing of selected low-rank coals, In: K.S. Vorres, Mineral Matter and Ash in Coal, American Chemical Soc., Washington, DC, 114-17.

Gronhovd, G.H., E.A. Sondreal, J.A. Kotowski, G.A. Wiltsee, 1980, Western low-rank coal development analysis,PDF available at Website: http://www.anl.gov/PCS/acsfuel/preprint%20archive/25_1_HOUSTON_03-80.htm. Click on ACS Fuels Volumes, Click on Spring 1980, Click on SYMPOSIUM ON UTILIZATION OF PEAT AND LIGNITE (III). American Chemical Society Meeting Spring, Houston, TX.

Hook, M., K. Aleklett, 2009, Historical trends in American coal production and a possible future outlook, International Journal of Coal Geology, 78 (3), 210-16.

Huang, H.H., 2009, Stability Calculations (STABCAL), Software, Metallurgical and Materials Engineering Department, Montana Tech of the University of Montana, Butte, MT, hhuang@Mtech.edu., www.Chemistry-software.com.

Li, Z., C.R. Ward, L.W. Gurba, 2007, Occurrence of non- mineral inorganic elements in low-rank coal macerals as shown by electron microprobe element mapping techniques, same journal, 70, 137-49.

Lignite Energy Council, 2009, Mines/Plants, Website: www.Lignite.com.

Miranda, P., 2009, Mineral Liberation Analysis applied to Montana Low-Rank coals, Center for Advanced Mineral and Metallurgical Processing (CAMP), Montana Tech of the University of Montana, Butte, MT, pmiranda@Mtech.edu.

Montana Coal Council, 2009, Working for the coal industry of Montana, Helena, MT, Website: www.Montanacoalcouncil.com.

Montana Means Business, 2009, Website: www.business.mt.gov/docs/Coal.pdf.

MRCB, 2008, Montana Research & Commercialization Board Awards $2.3 Million for Biotechnology, Wireless Communications, Clean Coal & Renewable Resources, Production Agriculture, & Environmental Remediation, Montana Associated Technology Roundtable, October 7, 2008, Website: www.MATR.net/article-31008.html.

National Coal Council (NCC), 2006, Coal: America's Energy Future, Volume II, Ed: G.H. Boyce, Website: www.coalamerciasenergyfuture.com/pdf/NCC_Presentation.

NETL, 2009, National Energy Technology Laboratory, Combustion, Combustion Technologies, Website: www.netl.doe.gov/technologies/coal power/combustion/index.html.

Roine, A., 2006, HSC Chemistry 6.0, Chemical reaction and equilibrium software with extensive thermochemical database and flowsheet simulation, outokumpu Research Oy, Pori, Finland, www.outokumputechnology.com/hsc.

Sourcewatch, 2009, Wyoming Mines, Website: www.Sourcewatch.org.

Statease Corporation, 2010, Design Expert Software, Version 8.0, www.statease.com.

Stiegel, G.J., 2008, Integrated Gasification Combined Cycle (Microsoft Powerpoint), National Energy Technology Laboratory, DOE, IGCC Workshop, India, Website: www.indiapower.org/igcc/garyj.pdf.

Thielemann, T., S. Schmidt, J. P. Gerling, 2007, Lignite and hard coal: energy suppliers for worlds needs until the year 2100 - an outlook, International Journal of Coal Geology, 72, 1-14.

Tome, et al., 2009, Towards an understanding of the mutual solubilities of water and hydrophobic ionic liquids in the presence of salts: the anion effect, J. Physical Chemistry, 113, 2815–2825,

Twidwell, L.G., 2009. Personal Database. Center for Advanced Mineral and Metallurgical Processing (CAMP), Montana Tech of the University of Montana, Butte, MT, ltwidwell@mtech.edu.

Twidwell, L.G., S. Dudley, 2010, Literature review sodium removal from Montana low-rank coals, Internal Report, Center for Advanced Mineral and Metallurgical Processing (CAMP), Montana Tech of the University of Montana, Butte, MT, ltwidwell@Mtech.edu

Wagman, D.D., et. al. 1982, 1989. The NBS tables of chemical thermodynamic properties, J. of Physical and Chemical References Data, Vol. 11, Sup. 2 (1982), and Errata. Vol. 18 (1989).

Wyoming Analytical Laboratories, 2009, Wallaramie@wal-lab.com

Zhongsheng, Li, C.R. Ward, L.W. Gurba, 2009, Occurrence of non-mineral inorganic elements in macerals of low-rank coals, International Journal of Coal Geology, in press, available at doi:10.1016/j.coal.2009.02.004. Also see Li, Z., C.R. Ward, L.W. Gurba, 2007, Occurrence of non-mineral inorganic elements in low-rank coal macerals as shown by electron microprobe element mapping techniques, same journal, 70, 137-49.

APPENDIX A. LITERATURE REVIEW-SODIUM REMOVAL FROM LOW-RANK COAL

CAMP Internal Report-LIT 1 June, 2010

LITERATURE REVIEW
SODIUM REMOVAL FROM LOW-RANK COALS

L.G. Twidwell[1], S. Dudley[2]

[1]Professor Emeritus, [2]Research Associate

Montana Tech of the University of Montana, Butte, MT 59701

email ltwidwell@mtech.edu

sdudley@mtech.edu

Literature Search

A detailed, but not comprehensive, literature search (over 220 references) has been conducted and the publications have been reviewed to determine usual treatment approaches for the removal of sodium (and in some cases potassium) from low-rank coal. Annotations of the reviewed literature are presented in this report for the following topics: General Reviews, Solution Leaching, Addition of Metal Compounds (or mineral phases), and Transport of Sodium during Combustion and Gasification. Other elements, such as calcium, magnesium, aluminum, iron and silicon, present in low-rank coals may have an important effect on sodium and potassium removal by chemical leaching processes and on the formation of low-melting mineral phases during the combustion process. However, annotated comments concerning associated elements have not, in most cases, been included in this publication. The user of this document should refer to specific study publications, presented in the bibliography section, for this information. The topic of cleaning leach solutions of elevated concentrations of sodium, other dissolved cationic and anionic species, and dissolved organic species has been the focus of Dudley (2011) as a part of his Master of Science in Metallurgical Engineering research program. A brief summary of this topic is presented in this report. His literature is presented as a part of the project literature review attached as Appendix A.

Background

Lignite and sub-bituminous coal reserves (low-rank coals) are plentiful in the high plains of Montana, North and South Dakota, and Wyoming, see Figure 1 (*American Coal Foundation, 2007*). In general, low-rank coals contain more ash, sodium, potassium, and, in some cases, calcium, magnesium, iron, and aluminum than do the hard coals (anthracites and bituminous). The emphasis of this review has been focused on sodium, potassium removal from low-rank coals.

Multiple mines and power plants exist in the Western states region, e.g. Montana Major Coal mines 6 (5 sub-bituminous, 1 lignite) (*Montana Coal Council, 2009*), coal-fired generating plants 5 (1 major) (*Electric Power Monthly, 2009*); North Dakota Major Lignite mines 4, Lignite coal-fired generating facilities 5 (*Lignite Energy Council, 2009*); Wyoming Major Bituminous and sub-bituminous mines 14 (4 major), Bituminous coal-fired generating facilities 23 (4 major) (*SourceWatch, 2009*).

For interested users of this report The National Coal Council's "Coal: America's Energy Future, Volume II" (NCC, 2006) is recommended as a general review and description of present day coal usage technologies (discussed further in the General Review section). General characterization data are presented for Western and Texas low-rank coals (Figure 2) and a comparison of world coal reserves is presented in Figures 3 (*Stiegel, 2008*) and 4 (*Thielemann, et al, 2007*). The outlook for possible future US coal production,, based on demonstrated reserve base, is presented in Figure 5 (Hook and Aleklett, 2009).

Figure 1. Estimated Coal Reserves in 2005 (American Coal Foundation, 2006)

Properties of U.S. Low-Rank Coals

	Wyoming Subbituminous *Spring Creek*	Montana Subbituminous *Decker*	N. Dakota Lignite *Freedom*	Texas Lignite *S. Hallsville*
Heating Value, kcal/kg (as received)	5,107	5,301	3,940	3,934
Proximate, wt%:				
Moisture	24.1	23.4	33.3	37.7
Volatile matter, dry	43.1	40.8	43.6	45.2
Fixed carbon, dry	51.2	54.0	45.3	44.4
Ash, dry	5.7	5.2	11.1	10.4
Ultimate, wt% moisture free:				
Carbon	70.3	72.0	63.3	66.3
Hydrogen	5.0	5.0	4.5	4.9
Nitrogen	0.96	0.95	1.0	1.0
Sulfur	0.35	0.44	1.1	1.2
Ash	5.7	5.2	11.1	10.4
Oxygen	17.69	16.41	19.0	16.2

Figure 2. General Properties of U.S. Low-Rank Coals (Powerpoint Presentation by Stiegel, US DOE 2008)

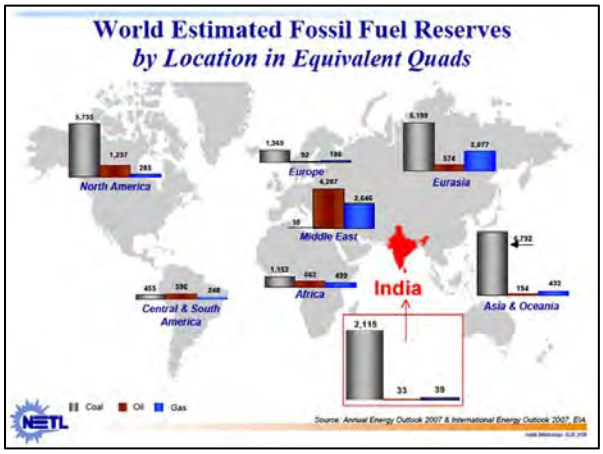

Figure 3 Estimated World Fossil Fuel Reserves in 2005 (Powerpoint Presentation by Stiegel, US DOE 2008)

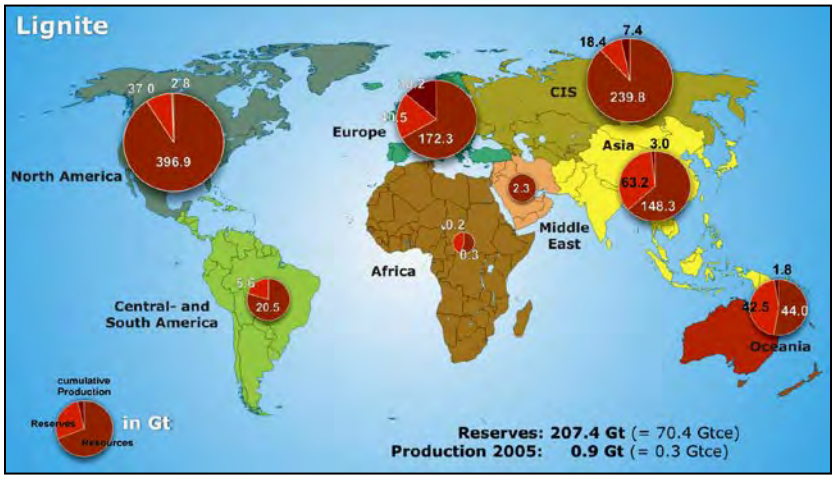

Figure 4. Estimated World Lignite Reserves in 2005 (Thielemann, et al (2007)

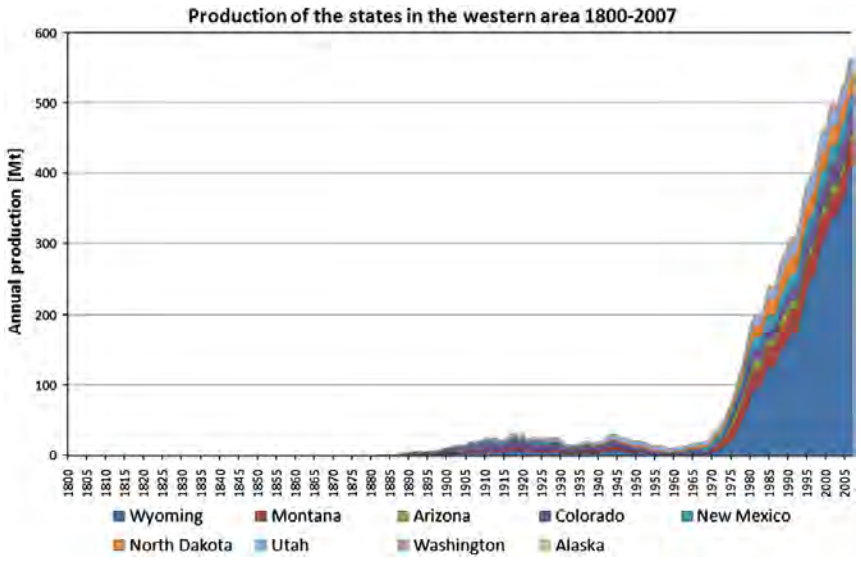

Figure 5. Coal Production in the western United States (Hook and Aleklett, 2009)

Occurrence of Inorganic Constituents in Low-Rank Coals

Inorganic elements can be present as a variety of species in low-rank coals. Primarily they are present as species associated with organic matter (maceral), carbon structural compounds, dissolved in pore moisture, crystalline compounds, and as constituents in mineral phases. The associations in the maceral fraction are cations bound as carboxylate groups, and inorganic complexes coordinated with carboxyl and phenolic groups. The content of inorganic elements, including sodium, potassium, calcium, magnesium, and iron, in low-rank coals is usually concentrated in the maceral matter. Lesser amounts of inorganic elements can be associated with the carbon structure as oxy-hydroxyl polymeric complexes. Low-rank coals that contain appreciable chloride or sulfur contents (like low-rank coals in Australia but not the coals in the Western United States) often contain appreciable amounts of crystalline salts, sodium chloride or sodium sulfate, and elevated sodium content in the moisture component of the coal. Inorganic elements are also associated with mineral phases dispersed throughout the coal matrix.

The Problem with Sodium and Potassium

The detrimental effects of ash forming constituents in low-rank coals are well documented. Alkali constituents and high moisture content are characteristics of low-rank coals. During combustion the alkaline constituents form gaseous and liquid compounds that readily form molten and semi-molten silicates. These molten products (slags) have an adverse effect on boiler and gasification combustors. A long list of detrimental consequences caused by alkaline constituents, especially sodium and potassium, can be quoted, e.g. fireside fouling, inhibition of heat transfer, obstruction of gas flow, excessive corrosion of boiler surfaces, formation of sticky chars that promote particle agglomeration, and formation of fly ash that is readily soluble in outdoor storage ponds.

Reviews and General Interest

National Energy Technology Laboratory

The Department of Energy's National Energy Technology Laboratory (*NETL, 2009*) website should be visited to obtain current information on the U.S. government's coal research efforts; e.g. Clean Coal Demonstrations, Innovations for Existing Plants, Gasification, and Turbines.

National Coal Council

The National Coal Council's "Coal: America's Energy Future, Volume II" (NCC, *2006*) is recommended as a general review and description of present day coal usage technologies, but not specifically sodium or potassium removal technologies. A portion of their report is quoted here to describe the present and potential future usage of coal in combustion systems.

Pulverized Coal (PC) Boiler Combustion (quoted from NCC)-"In a pulverized coal-fueled boiler, coal is dried and ground in grinding mills to face-powder fineness (less than 50 microns). It is transported pneumatically by air and injected through burners (fuel-air mixing devices) into the combustor. Coal particles burn in suspension and release heat, which is transferred to water tubes in the combustor walls and convective heating surfaces. This generates high temperature steam that is fed into a turbine generator set to produce electricity. In pulverized coal firing, the residence time of the fuel in the combustor is relatively short, and fuel particles are not recirculated. Therefore, the design of the burners and of the combustor must accomplish the burnout of coal particles during about a two-second residence time, while maintaining a stable flame.

Pulverized coal combustion is adaptable to a wide range of fuels and operating requirements and has proved to be highly reliable and cost-effective for power generation. Over **2 million MW of pulverized coal power plants** have been operated globally.

Pulverized coal fired supercritical steam cycles (PC/SC) have been in use since the1930s, but material developments during the last 20 years, and increased interest in the role of improved efficiency as a cost-effective means to reduce pollutant emission, resulted in an increased number of new PC/SC plants built around the world. After more than 40 years of operation, supercritical technology has evolved to designs that optimize the use of high temperatures and pressures and incorporate advancements such as sliding pressure operation. Over **275,000 MW of supercritical PC boilers** are in operation worldwide".

Fluidized Bed Combustion Process Description (quoted from NCC)-"In a fluidized bed power plant, coal is crushed (rather than pulverized) to a small particle size and injected into a combustor, where combustion takes place in a strongly agitated bed of fine fluidized solid particles. The term "fluidized bed'' refers to the fact that coal (and typically a sorbent for sulfur capture) is held in suspension (fluidized) by an upward flow of primary air blown into the bottom of the furnace through nozzles and strongly agitated and mixed by secondary air injected through numerous ports on the furnace walls. Partially burned coal and sorbent is carried out of the top of the combustor by the air flow. At the outlet of the combustor, high efficiency cyclones use centrifugal force to separate the solids from the hot air stream and recirculate them to the lower combustor. This recirculation provides long particle residence times in the CFB combustor and allows combustion to take place at a lower temperature. The longer residence times increase the ability to efficiently burn high moisture, high ash, low-reactivity, and other hard-to-burn fuel such as anthracite, lignite, and waste coals and to burn a range of fuels with a given design.

CFB technology has been an active player in the power market for the last two decades. Today, over **50,000 MW of CFB plants** are in operation worldwide".

Gasification of Coal (quoted from NCC)-"Gasification of coal is a process that occurs when coal is reacted with an oxidizer to produce a fuel-rich product. Principal reactants are coal, oxygen, steam, carbon dioxide and hydrogen, while desired products are usually carbon monoxide, hydrogen and methane. Principal reactants are coal, oxygen, steam, carbon dioxide and hydrogen, while desired products are usually carbon monoxide, hydrogen and methane. The resulting synthesis gas, or syngas, consisting primarily of hydrogen and carbon monoxide, is cooled, cleaned and fired in a gas turbine. The hot exhaust from the gas turbine passes through a heat recovery steam generator where it produces steam that drives a steam turbine. Power is produced from both the gas and steam turbine-generators. By removing the emission-forming constituents from the syngas under pressure prior to combustion in the power block, an IGCC power plant can meet stringent emission standards. Oxygen-blown gasifiers typically operate better with **bituminous and lower volatile coal**. In most gasification systems, sulfur content of the coal is only a design consideration for the sulfur-removal system and not an operating limitation on the gasifier.

The composition of coal and some of its physical properties have important influences on the gasification process. Young coals such as **lignite and sub-bituminous coal** generally contain a high percentage of moisture and oxygen, while old coal, such as bituminous coals and anthracite, tend to become sticky as they are heated. As a result, in the entrained flow gasifier the coal must be dried, because if the water enters the gasifier, some of it will react with CO to form hydrogen and CO_2. Moisture content has no effect on the gasification process in the fixed bed gasifier because the hot gas leaving the gasifier dries the coal as it enters the gasifier. Since oxygen is present in the gasification process, coals containing more oxygen will need less oxygen or air to be added. For example, an E-gas gasifier system requires 2,220 tons per day of oxygen for sub-bituminous coal, 2,330 tons per day of oxygen for bituminous coal, and 2,540 tons per day for pet coke. The oxygen in coals is particularly important in air-blown gasification as any oxygen in the coal will reduce the amount of air required for the gasification reaction and thereby reduce the resulting nitrogen in the syngas." (quotation from NCC complete).

An excellent general review of current gasification technologies, is presented (in a Microsoft Office 2007 powerpoint presentation) by the USDOE (*Stiegel, 2008*). The review includes a description of the properties of low-rank coals; the challenges and opportunities for low-rank coals; detailed descriptions of gasifier reactors using low-rank coals; currently operating and future gasification systems in the US and in the world; testing of high sodium coals at the power systems development center (PSDC) at Wilsonville, Alabama; advanced refractory for gasifiers to minimize slag penetration; and capital cost comparisons of various gasification systems.

Coal Properties General Reviews

The literature available for coal characterization, mineralogy, combustion and transport during combustion, elemental content, etc is voluminous and we have not attempted to present a complete review of the available literature. There are a number of relatively recent review papers noted here that are outside the scope of this paper but may be of general interest to the reader. Yudovich, *Yodovich, et al* have published several review articles focused on specific elements in coals. The Yudovich papers provide a wealth of general coal information. Their publications follow the format : a) analytical and historical background, b) some peculiarities in environmental geochemistry, c) estimation of the Clark value, d)

mode of occurrence, e) factors influencing the distribution in coal, and f) origins in coal. The specific elements considered in their reviews include: arsenic in coals (*Yudovich and Ketris, 2005*) and an update and comments to the 2005 arsenic review (*Huggins and Huffman, 2006*); selenium in coals (*Yudovich and Ketris, 2006*) and in the environment (*Lenz and Lens, 2009*); geochemistry of mercury in coal (*Yudovich and Ketris, Part 1, 2005*) and coal use and environmental problems (*Yudovich and Ketris, Part 2, 2005*); chlorine in coals (*Yudovich and Ketris, 2006; Spears, 2005)*, coal inclusions in sedimentary rocks (*Yudovich, 2003*), and metalliferous coals (*Seredin and Finkelman, 2008;, Spears and Tewalt, 2009*);). *Yodovich and Ketris (2002)* have reviewed and published a book "Inorganic Matter in Coal" (in Russian) covering over 970 publications on the subject of coal geochemistry and mineralogy. A general review specific for sodium has not been reported.

An excellent review covering primarily Western low-rank coals previous to 1980, was performed by the US DOE Grand Forks Energy Technology Center (GFETC) and Energy Resources (*Gronhovd, et al, 1980*). The goal of the study was to perform "An analysis o f the technical, environmental, and economic constraints to expanded development o f the U.S. low-rank coal resource is in progress. The primary objective o f the study is t o propose a comprehensive national R&D program focusing on technology development f o r enhanced utilization of lignite and subbituminous coal". A series of papers are attached to this document that provide specific information on coal and ash characterization, inorganic elements, sodium, maceral, and mineral content and their distribution for Montana, North Dakota, and Wyoming coals. This publication will be discussed in subsequent sections. Included in appendices of the reference are a number of papers, presented as a part of their literature review, covering low-rank coal characterization studies: Current Research on the Inorganic Constituents in North Dakota Lignites and Some Effects on Utilization (*Rindt, et al*); Analysis of the Inorganic Constituents in American Lignites (North Dakota, Montana, Texas), (*Morgan, et al*); Removal of Sodium from Lignite by Ion Exchanging with Calcium Chloride Solutions (*Paulson and Futch*); Laboratory Batch Liquefaction of Low Rank Coals (*Souby, et al*), (North Dakota, Montana, Wyoming, Alaska); Characterization of Light Oils from Liquefaction of Lignite (North Dakota), (*Farnum, et al*); Organic Structural Studies of Lignite Coal Tars (*Miller, et al*); and, The Dissolution of Lignite in Anhydrous Liquid Ammonia (Texas), (*Harris, et al*).

COALQUAL (searchable database, 2009)-Geochemical characterization of coals are available for over 13,000 samples and the database is searchable in the United States Geological Society's (USGS) COALQUAL database (*Bragg et al, 1998*). The COALQUAL database was searched by the authors of this review for the sodium and potassium contents for as-received coal samples from all counties in Montana, Wyoming, and North Dakota. The average sodium and potassium concentrations in Western coals and temperatures at which the ash begins to form a liquid phase (initial deformation) and where a large amount of liquid is formed are summarized in Table 1. The presence of other inorganic elements also may have a significant effect on the formation of liquids at combustion and gasification temperatures; therefore, several of the major inorganic species present in low-rank Western coals are presented in Table 2.

Table 1. Sodium and Potassium Concentration in As-Received Coals and Ash Temperatures (COALQUAL Database)

State	Concentration in Raw Coal, mg/kg (no. samples)		Ash Temperature ^{o}C	
	Na	K	Initial Deformation	Liquid
Montana	3069±1928 (274)	818±1319 (274)	1159±61(280)	1253±66 (280)

N. Dakota	3823±2635 (173)	654±867 (173)	1156±63 (169)	1241±65 (169)
Wyoming	1324±851 (411)	708±1087 (411)	1212±95 (453)	1298±91(453)

± standard deviation

Table 2. Element Concentration in As-Received Coals (COALQUAL Database)

State	Concentration in Raw Coal, mg/kg (no. samples)					
	Al	Ca	Fe	Mg	S	Si
Montana(274)	8387±7074	9614±4235	818±1319	2654±1460	4898±3587	16515±15212
N. Dakota (173)	6384±4346	12174±3163	8000±5799	3682±970	8638±4704	16206±16660
Wyoming (411)	8970±7165	9730±5348	5898±6396	2054±987	5234±3629	18499±16686

± standard deviation

MBMG (2009)-The Montana Bureau of Mines and Geology (MBMG) has a searchable chemical characterization database for Montana coals. The database summarizes the elemental content present in 365 coal samples. Sodium contents ranged from near zero to 8,100 mg/kg with an average content of 2,590 and a standard deviation of 2,173. The potassium contents ranged from near zero to 12,000 mg/kg with an average content of 797 and a standard deviation of 1,380.

Montana Means Business (business.mt.gov, 2009)- General contents of ash, sodium, sulfur, and moisture for Montana mine sites and potentially developing coal sites are presented in Table 3.

Table 3. Montana Coal General Characterization for Amounts of Ash, Sodium, Sulfur and Moisture (Montana Means Business, 2009)

Area	Ash %	Sodium, %	Sulfur, %	Moisture, %
1 (Sub-Bituminous)	12.0	0.27	1.0	16.9
2 (Sub-Bituminous	9, 8.2, 9	0.5, 0.3, 1.2	0.7, 0.7, 0.9	25.5, 25.6, 25.7
3 (Sub-Bituminous)	4.1, 4.6,3.6	6.8, 6.4, 8.0	0.38, 0.45,0,32	24.3, 24.2, 25.0
4 (Lignite)	18.5	0.3	0.35	30
5 (Lignite)	7.5	5	-	35
6 (Sub-Bituminous)	5	7	0.17	28

Source: Montana Means Business at website: www.business mt.gov/docs/coal.pdf

Standard Methods for Characterizing Coals-The American Standards for Testing Materials (*ASTM, 2000*) have specified treatment procedures for analyzing coals; they include: D 1757, D 2361, D2492, D 2795, D 3174, d 3682, D 4208, D 4239, D 4326 and d 5016.

Ketris and Yudovich (2009) have collected an extensive world database from which they have summarized what they refer to as geochemical "Clarke" average values for many trace elements in coal. However sodium and potassium are not considered trace elements so Clarke averages were not included. While the Clarke averages are of limited interest in this review they are tabulated here for the interested reader. Clarke averages (in ppm, mg/kg) are presented for lignite and sub-bituminous coals (based on over one

million analyses including the USGS database analyses): copper (15±1), lead (6.6±0.4), manganese (100±6), nickel (9.0±0.9, arsenic (7.6±1.3), selenium (1.0±0.15), mercury (0.1±0.01), chloride (120±20), and phosphorus (200±30).

Coal Mineral and Non-Mineral (Maceral) Content General Reviews

Zhongsheng, et al (2009; also see Li, et al, 2007) have recently studied the occurrence of non-mineral inorganic elements in low-rank coals. The knowledge of the presence of elements in the non-mineral content of coals (macerals) is important because the elements tend to volatilize as atomic species during combustion and they react readily to form low-melting slags and other fouling species (*Falcone and Schobert, 1986*). The Zhonsheng study (eighteen coals were investigated) demonstrated that a significant portion of the Ca (up to 15000 mg/kg), Al (up to 5000 mg/kg), and Fe (up to 7000 mg/kg) occur in low-rank coals and the elements are chemically bonded within the maceral structure.

Other publications that have investigated the containment of inorganic elements in macerals are Ward (2002); Ward, et al (*2008, 2007, 2005*). A description of the procedure for determining the maceral content in coals and the coal rank is presented by *Visser (2004),* i.e. ISO Standard 7404-2, 1985 and ISO Standard 7404-3, 1994, respectively. The influence of chemical structure and physical properties of coal macerals on liquefaction was presented at a recent ICCS&T conference by *Li (October, 2009, too recent to be reviewed here).* Also, *Gesserman, et al (October, 2009)* presented a paper on a petrographic web atlas for bituminous coal macerals (*not reviewed here*).

Ward (2002) has reviewed over two hundred publications and has summarized current technologies used for characterizing coals, especially the mineral and maceral content of coals. Low-rank coals must be treated in a way that non-mineral inorganic species are determined in addition to discrete mineral speciation. Non-mineral inorganic species (such as organic sulfur, sodium salts, sodium organic carboxylate, and organometallic complexes) may react to form artifacts by even low-temperature treatment, thereby forming species not originally present in the coal. Therefore, selective leaching techniques have been developed to determine the abundance and form of the non-mineral inorganic species originally present in coals, especially in low-rank coals, e.g. (quoted by Ward), *Miller and Give (1978, 1986); Benson and Holm (1985); Ward (1991, 1992*), and many more. The techniques that are referenced by Ward that are extensively used for identification of non-mineral elements and mineral phases in coal include: the commonly used techniques of optical microscopy, scanning electron microscopy (especially papers by *Finkelman (1994, 1995)* and *Finkelman et al (1998)*), computer controlled scanning electron microscopy (CCSEM) (details by *Galbreath, et al, 1996*), special adaptations of CCSEM include QEMSEM (quantitative evaluation of materials by scanning electron microscopy (*Creelman and Ward, 1996; Creelman, et al, 1993)*) and MLA (mineral liberation analyses (*Mirand, 2009*), electron probe analysis, x-ray diffraction, and x-ray fluorescence. Ward suggests that non-mineral inorganic elements are best studied by using electron microprobe techniques. *Huggins (2002)* has also reviewed (210 references, 45 p) and presented an "overview" of analytical methods for determining the elemental, maceral, and mineralogical content of coals, and the mode of occurrence of trace elements in coals .

Gronveld, et al, (1980, review and laboratory studies)- These investigators present general characteristics of maseral organic matter, which is primarily Vitrinite, in lignite and sub-bituminous coals. This information is presented in Table 4.

Table 4. Selected analyses of U.S. Coals of Different Rank (Gronhovd, et al 1980)				
Organic Content (Vitrinite Samples)	**Lignite**	**Sub-bituminous**	**Bituminous**	**anthracite**

Moisture, wt.%	40	25	10	<5
Carbon, Wt.% DMMF	69	74.6	83	94
Hydrogen, Wt.% DMMF	5	5.1	5.5	3.0
Vol. Matter, Wt. % DMMF	53	48	38	6
Density (He, g/cc)	1.43	1.39	1.30	1.5
BTU/lb, DMMF	11,600	12,700	14,700	15,200

DMMF, Dry, Mineral-matter-free basis

Fluidization Bed Combustion General Review

Bartel, et al (2008, review) have recently reviewed the world literature for agglomeration in fluid bed combustion of solid carbonaceous fuels (176 publications), with an emphasis on coals, especially low-rank coals. This reference is further discussed in the section **"*Addition or Presence of Metal Compounds or Mineral Phases*".** Bartel discusses the work that has been published on additions of minerals and compounds to combustion systems that have shown positive results for decreasing the stickiness of sodium compounds (and in some cases potassium, calcium, magnesium, and compounds) formed during combustion. Also, the authors summarize studies that have investigated fluid bed combustion systems that use alternative bed materials as substitutes for fine sand.

Drinking Water Contaminant List

The US EPA has included sodium on the Drinking Water Contaminant Candidate List (*CCL, EPA 2008*) which means that there is a low level of concern for its presence in drinking water but the EPA reserved the right to set standards if it is deemed necessary in the future. There is a recommended Drinking Water Equivalency Level (DWEL) for sodium of 10 mg/L. This, however, is not to be considered a required discharge concentration to wastewaters, streams and waterways.

Literature Review-Technologies

The present literature review has shown that two major technological approaches have been investigated to mitigate the sodium problem in coals; e.g., Solution leaching of sodium using reagents to remove sodium salts, and/or organically bound species that are a part of the coal maceral matter or are present as sodium bearing mineral phases; and Addition of metal compounds or mineral phases to react with the sodium and sodium compounds during the combustion process to form compounds that remain solid and/or less-corrosive at combustion temperatures.

Solution Leaching Technologies-There have been only a limited number of investigations to demonstrate partial removal of sodium from low-rank coals by mild solution phase (leaching) treatments on a laboratory scale**. We could not find publications where this technique has advanced to industrial use**. A relatively large number of recent investigations have focused on treating low-rank coals to remove essentially all of the ash forming elements so that ash does not form during combustion. The emphases of these papers are based on the desire to utilize low-rank coals to produce a clean feedstock for gasification processes (aggressive treatments to remove ash formation species, i.e. to produce a "clean" coal). The reviewed literature for solution leaching is discussed below in two sections, i.e. Solution Leaching-General and Solution Leaching-"Clean Coals" from Low-Rank Coals.

Solution Leaching-General

CAMP (2009, laboratory study)-The Center for Advanced Mineral and Metallurgical Processing (CAMP) is presently investigating the removal of sodium from low-rank coals. This work is funded by the US Department of Energy's (DOE) Center for Advanced Separation Technologies (CAST), Great Northern Properties (GN), and the Montana Board Research and Commercialization Technology (MBRCT). The project is being administered and the research directed and conducted at the CAMP location on the campus of Montana Tech of the University of Montana. The intent of the project is to identify, and validate selected currently used (or previously studied) removal and sodium recovery treatment alternative(s) using laboratory bench-scale tests on samples from four Montana coal companies. If the coals cannot be effectively treated by known techniques, alternative treatments will be developed. The evaluation of selected sodium removal technologies are presently underway and the following four stages are being and will be followed in future work: the successful removal of sodium from the coal so that the ash content will be less than three percent sodium oxide, the rate at which the sodium ions are removed, characterization of the waste produced by sodium removal processing, and the overall economics of viable processes. The preliminary results of the study will be reported by *McCloskey, et al (2010)* at the upcoming XVI International Coal Preparation Congress in Kentucky (*ICPC, 2010*).

Domazetis, et al (2009, laboratory study)-An Australian low-rank coal study was conducted by these authors (three coal sources, including a Wyoming coal, with sodium concentrations of 0.1 to 1.8% and ash contents of 2.5 to 14.4%). The investigation focused on the effect of pH adjusted water (pH 0.05 to 1.5) and elevated temperature concentrated hydrochloric acid washing on the removal of ash forming species and the effect of the ash removal on the product compounds formed in the ash. As would be expected decomposition of the mineral phases, including the sodium minerals, significantly increased the removal of sodium, magnesium and calcium content in the ash products. Water leaching lowered the ash contents in the as-received coals as follows, e.g. 2.5 to 2.15; 14.4 to 8.6%, 12.0 to 9.5%. Acid treatment of the coals (70%, hydrochloric acid, 95-100^{o}C, 5 hrs) significantly lowered the ash and sodium contents, ash 2.5 to 1.2%, 14.4 to 3.7%, 12.0 to 3.0% and sodium 0.1 to 0.0%, 1.8 to 0.0%, 1.0 to 0.0%. The leach studies were followed by combustion testing and determination of fouling potential; the as-received coals showed high fouling, water leaching showed moderate fouling, and acid leaching showed no fouling. This study was conducted in support of a program at Clean Coal Technology Pty (*CCT, 2009*) to develop a commercial technology that would upgrade low-rank coals for use in power generation that would have low level greenhouse gas emissions. Additional comments and further test data for development of the CCT technology are presented by *Domazetis (CCT, 2009).*

McCloskey, et al (2009, laboratory study) in a current project have shown that the sodium content in four Montana company coals is evenly distributed throughout ten size fractions between -7 mm and -400 mm. The sodium contents in the four Western coals were (in mg/kg): 374±47, 2509±143, 1425±234, 3293±440. The removal of sodium was investigated by leaching with pH controlled (HCl at pH 3) and calcium chloride containing ion exchange reagent (25 g/L CaCl2, 2 hrs, 10% coal). The results showed 20-40% of the sodium was removed. These removal values relate to the ion exchangeable sodium, the remainder has been identified as being present primarily as the mineral phase albite and sodium amhibole (*Miranda 2009*). Na2(Mg,Fe)3Al2Si8O22(OH)2 . As a part of the McCloskey study Twidwell investigated the potential leachability of sodium from mineral phases using the speciation/titration hydrometallurgical modeling program STABCAL (*Huang, 2009*). The reagents investigated included; no reagent, hydrochloric acid, sulfuric acid, acetic acid, ammonium acetate, sodium hydroxide, and others. The results are in general agreement with the literature

that acidic treatment should be effective for decreasing the sodium and ash solids from the low-rank coals. Sodium hydroxide should also be effective in removing a relatively large portion of the ash, however, high levels of sodium would be added to the leach solution and effective water washing would be necessary. The modeling also shows that leaching with ammonium acetate will not attack the mineral phases and the use of this reagent would likely only remove the sodium that is present as organically bound species.

Bruckard, et al (2008, laboratory study)-Low-rank Australian coal containing approximately one percent sodium was studied. The majority of the sodium was present as sodium chloride which is not true for Montana coals. The authors found that the sodium oxide content in the ash could be lowered to their goal level of <3% by tap water leaching minus 5.6 mm coal for 30 minutes followed by exposure to a solution phase containing a dissolved ion exchangeable specie. The water leach did not remove organically bound sodium. The use of $CaCl_2$ (15 g/L), NH_4Cl (7 g/L) or acid (HCl, 5 g/L; H_2SO_4, 7 g/L) additives showed enhanced sodium removal in a two stage leach. The results were relatively unaffected by pulp densities between 20 and 50 percent. The optimum conditions for removal of greater than ninety percent of the sodium were obtained by water leaching the minus 5.6 mm coal followed by a five minute wash with waters containing dissolved $CaCl_2$ or H_2SO_4.

Paul, et al (2006, laboratory study)-The leaching of coal was studied in sulfuric acid (pH 1.0, 25^{o}C, coal/water 1/10) as a function of time. Thirteen coals were leached (10 mm particles) and they readily responded to element dissolution, over a two day period, to produce a coal deemed "cleaned coal". Their conclusion was that lignites "are ideally suited for direct acid leaching".

Favas and Jackson (2003, laboratory study)-The authors investigated hydrothermal dewatering (HTD) of eighteen sub-bituminous to low-rank coals at 320^{o}C (30 minutes, 1/3 coal to water, 500 mL water). The coals were from Australia, Indonesia, and the U.S. (three US low-rank coals, including Beulah, North Dakota). The intent of the study was to investigate the chemical and physical properties of the treatment. The sodium content in the raw coals ranged from 0.01 to 1.46 % (US coals from 0.02 to 0.74 %); the ash from 0.5 to 14.8% (US coals from 7.7 to14.65). The hydrothermal treatment resulted in wastewaters with pH levels from 4.1 to 6.5 (US 5.3 to 6.5) containing: TOC 1400 to 6400 mg/L (US 3200 to 6400 mg/L); sodium 50 to 920 mg/L (US 70 to 1600 mg/L); chloride 3 to 4400 mg/L (US 90 to 130 mg/L); calcium 110 to 660 mg/L (US 93 to 660 mg/L). The treatment dissolved greater than 70 percent of the sodium into the leach water; therefore the treatment of US coals produced high levels of organic and sodium species in the leach wastewater that would have to cleaned from the leach waters before discharge. There are many other papers on hydrothermal treatments, e.g. *Wilson, et al (1985, 1986); Baker, et al (1985); Li (1990); Guy, et al (1992); Woskoboenko and Allardice (1996). Sev*eral investigators have studied the combination of hydrothermal leaching and treatment of the wastewater, which contain relatively high concentrations of organics, by gasification to recover methane and hydrogen. The end result of the two treatments under identical conditions are recovery of dewatered and upgraded coal and gaseous combustibles; e.g. for more information see the following references *Morimoto, et al (2008), Sakaguchi, et al (2008), Hulston, et al (2005), and, Nakagawa, et al (2004).* However, these papers did not discuss what happens to the sodium and other elements during the processing.

Masuoka, et al (2002, laboratory study)-The authors studied the transformation of alkali species in low-rank coal during combustion and gasification (discussed later). An important ancillary result of their study was that when they applied the usual sequential leaching characterization technique using

water, then ammonium acetate, then strong acidic solutions to determine the presence of soluble sodium and magnesium salts, ion-exchangeable sodium and calcium, and acid soluble mineral phases, it was found that the ammonium acetate reagent removed, not only the ion-exchangeable sodium and calcium but also some of the mineral phases present, especially some calcium mineralization. In the past it has been assumed that ammonium acetate only removes maceral bound calcium and not inorganic mineral phases. Therefore, it is likely that the ion-exchangeable fractions reported in previous studies may not be as high as reported.

Quast (2000, laboratory study)- Quast reported similar results to the Domazetis study on low-rank Australian coals using sulfuric acid at pH 2 for 30 minutes on sized coal (90 percent passing 4 mm coal). The author proposed using continuous counter current washing to minimize the amount of sodium contaminated wastewater creation.

Musich, et al (1992, laboratory and pilot leaching and combustion studies)-The authors investigated the beneficiation of seven low-rank coals (DOE supported study) by physical and chemical cleaning, hydrothermal, and agglomeration techniques. The coals investigated included: lignite coals from North Dakota and Texas, sub-bituminous coals from Montana and Alaska. Variable success was achieved by physical separations including float/sink, froth flotation, and centrifugal washing. Lignites responded well to the washability techniques for removal of all elements analyzed in the ash except for calcium and magnesium. Sub-bituminous coals showed washabilities for ash removal of 25-40%. Chemical cleaning was performed using four strong acids (nitric, hydrochloric, sulfuric, and hydrofluoric) at addition rates of 0.65 to 6.0 weight percent and three strong bases (sodium, potassium, and ammonium hydroxides). The acidic leaches reduced the ash by 40-60 percent. The caustic leaches were unsuccessful because of the difficult solid/liquid separations. Hydrothermal drying techniques resulted in successful moisture reduction but only minor ash removal.

Sharma, et al (1991, laboratory study)- The authors present a method for cleaning low-rank coals using dilute aqueous sodium hydroxide (0.5 N NaOH) under mild atmospheric conditions followed by acid leaching (either 10% HCl or H_2SO_4) and water washing. Their procedure removed 75 percent of the mineralization in low-rank coal.

Finkelman, et al (1990, laboratory study)-The authors treated eight US coals, three of which were low-rank Western coals, in a sequential leach procedure to determine the specie form of sodium. They found that the coals containing the sodium primarily as organically bound species were effectively removed by ammonium acetate (NH_4OAc). The ammonium acetate removed (10g coal, containing 0.038 to 0.52 percent sodium in 50 mL 1-N acetate for 18-24 hrs) over ninety percent of the sodium from the low rank coals.

Blytas, et al (1987, US patent 4,705,530)-Coals were water leached and further treated with dilute carbonate, formic, or acetic acid to remove ion-exchangeable sodium. Treatment with dilute acids at pH values in the range 3-6 may remove 30-40% of the sodium from low-rank coals.

Morgen, et al (1981, laboratory study) studied the response of three lignites (North Dakota, Texas, Montana) to treatment with ammonium acetate. They, as well as others, suggest that ammonium acetate will only remove adsorbed and organically bound sodium and calcium, i.e. it does not dissolve sodium or calcium mineral phases. Their study found that a significant fraction of the sodium, calcium and magnesium were present as organically bound species and that the ammonium acetate treatment procedure can be used to distinguish how the sodium and calcium elements are present in

the coal as organically bound or contained in the mineral phases. The ammonium acetate (0.5 grams of coal in 50 mL of 1N ammonium acetate for three hours) extracted 70-79% of the calcium; 60-84% of the magnesium; 68-100% of the barium; and 74-78% of the strontium. However, as stated above, other investigators have determined that ammonium acetate does remove some mineralization, especially calcium bearing species (*Masuoka, et al 2008, 2002). S*tudies to evaluate whether ammonium acetate will also attack sodium alumino-silicates have not been reported. The *Morgen, et al* results characterized the three lignites as containing 2.2 to 3.2 milliequivalents of carboxyl per gram of mineral free coal. The cation exchangeable content of the mineral free coal was 170 to 245 mg of total cations per gram of coal. The cations present included magnesium, calcium, sodium, potassium, barium, and strontium.

Benson and Holm (1985, pilot study) also studied the response of three low-rank coals, lignites from North Dakota and Texas, and a sub-bituminous coal from Montana to ammonium acetate leaching. The starting coals contained (in mg/kg) Na 4340, K 930; Na 310, K 1970; Na 87, K 120, respectively. The ammonium acetate removed 84%, 75%, 81% of the sodium and 20%, 9%, 2% of the potassium, respectively.

Curtin (1981, US patent 4,268,271)- The authors present a method that consist of crushing the coals (with greater than 0.15% sodium) to produce size fractions that are lower in sodium content to be used without fouling during combustion. The higher sodium content fractions are usually in the minus one-inch coal particulate which can be separated and, if desired, leached by whatever means.

Paulson and Futch (1979, laboratory study)-The authors evaluated the leachability of sodium from a North Dakota lignite using calcium chloride doped waters. They referenced earlier work that stated that "sodium does not occur as in the discrete mineral particles in lignite but is evenly dispersed throughout the coal matrix" (*Tufte et al, 1974; Paulson et al, 1972*). *Paulson and Fowkes (1968)* state that "Sodium, along with calcium, magnesium, iron and aluminum cations, is attached to exchange sites on the lignite structure and can be replaced by ion exchange with other elements". This statement (for calcium) has been supported by the *Chen, et al (2004)* study that the calcium is predominately present as carboxyl-bound calcium species. *Paulson and Futch's study* used 0.05 molar calcium chloride (at a solid/liquid ratio of 1 to 4) as the leachate with five minute exposure time. Their results showed that the sodium removal was a function of particle size (percent removal), e.g. 80% for 40 by 0 mesh; 63% for 8 by 0 mesh; 15% for ½ by 0 mesh. The removal of sodium was also a function of moisture content (highest removal for moisture contents above 28 percent) in the coal, the particle size (less than 80 mesh best), quantity of calcium in solution, solid/liquid ratio, and contact time. The removal was relatively independent of temperature. The sodium content in the coal was, of course, replaced with calcium, which may or may not be a problem during combustion, e.g. calcium may react during combustion to form low melting ternary and/or multi-component compounds (*Chen, et al, 2004*).

Tominaga, et al (1976, US patent 3,948,791)- The authors present a method for treating low-rank coal that consists of sizing the coal to 0.5 to 2 mm then leaching in dilute caustic solution (2-20%), followed by washing in an acid within the pH range of 3-7 percent to remove the caustic and solubilized mineral content from the coal.

Solution Leaching-"Clean Coals" from Low-Rank Coals

A number of studies have been conducted that have the goal of removing essentially all the inorganic element species and mineral phases from low-rank coals. The desire is to provide a "clean coal" that could be used in pulverized coal combustion, gasification, and liquefaction systems. The clean coals would produce less Greenhouse gases, provide a fuel that eliminates the operational difficulties associated with the formation of slagging species, and produce less ash for disposal. Domazetis, et al (2009) have summarized the requirements for making low-rank coals the source for "clean coal": "To maximize the commercial potential of a coal processing technology, it must be able to: (i) remove all the ash related problems, (ii) increase the heating value of the non-fouling coal, and (iii) add effective catalysts to the coal for catalytic steam gasification. The environmental aspects of the coal treatment are also extremely important; for example, it must not produce toxic wastewater. The non-fouling coal may be used in high-efficiency super-critical boilers, and ultra-low ash coal may be used for direct coal-fuelled turbine in combined cycle; such plant would substantially reduce the CO2 produced per unit of power. Coal containing catalysts could be used in lower temperature gasification using a mixture of oxygen and steam, to increase the hydrogen content of syngas."

Domazetis, et al (2009, laboratory study)-An Australian low-rank coal study was conducted by these authors (three coal sources with sodium concentrations of 0.1 to 1.8% and ash contents of 2.5 to 14.4%). The investigation focused on the effect of pH adjusted water (pH 0.05 to 1.5) and elevated temperature concentrated hydrochloric acid washing on the removal of ash forming species and the effect of the ash removal on the product compounds formed in the ash. As would be expected decomposition of the mineral phases, including the sodium minerals, significantly increased the removal of sodium, magnesium and calcium content of the ash products. Water leaching lowered the ash contents in the as-received coals as follows, e.g. 2.5 to 2.15; 14.4 to 8.6%, 12.0 to 9.5%. Acid treatment of the coals (70%, hydrochloric acid, 95-100oC, 5 hrs) significantly lowered the ash and sodium contents, ash 2.5 to 1.2%, 14.4 to 3.7%, 12.0 to 3.0% and sodium 0.1 to 0.0%, 1.8 to 0.0%, 1.0 to 0.0%. The leach studies were followed by combustion testing and determination of fouling potential; the as-received coals showed high fouling, water leaching showed moderate fouling, and acid leaching showed no fouling. This study was conducted in support of a program at Clean Coal Technology Pty (CCT, 2009) to develop a commercial technology that would upgrade low-rank coals for use in power generation that would have low level greenhouse gas emissions. Additional comments and further test data for development of the CCT technology are summarized by *Domazetis (2009).*

Domazetis, et al (2008, laboratory study)-As presented above the CCT company is aggressively developing a technology that would use low-rank coal in gasification reactor power generation. This approach requires that the ash and liquid forming species be removed prior to combustion or gasification. The CCT approach uses aggressive leaching to remove the coal matrix inorganic species and mineral phases. This paper presents the results of doping the acid leached coal with iron species prior to combustion, the coals contained 7.8% ferric iron. The iron species provided catalytic sites for reactions that produce the desired gaseous species, H2, CH4, CO and CO2, in the gasification reactor product. The doping of low-rank coal with iron showed a significant increase in the H_2 content in the gasified product. For addition information with respect to modeling of low-rank coal and the effect of iron doping see the reference *Domazetis and James (2006a).*

Kosminske, et al (2006, laboratory study)-A low-rank coal was studied to determine the fate of sodium in a fluidized gasification reactor. The procedure consisted of pyrolyzing the coal (sized to 38-125 micrometers) in nitrogen followed by gasification of the char in steam or steam and carbon dioxide at 650 to 850^{o}C. Run-of-mine coal (8.6% Na_2O in ash) was leached in concentrated hydrochloric acid to

form a "Clean Coal", then the coal was doped with ion-exchangeble carboxylate sodium acetate (1% sodium in coal) or sodium chloride (1% sodium in coal). The results showed that regardless of the form of sodium in the coal, solid sodium carbonate formed when pyrolyzed (850^{o}C) in the nitrogen atmosphere; less than twenty percent of the sodium volatilized. Gasification of the char in carbon dioxide and in steam at 850^{o}C volatilized about half of the sodium regardless of the initial form of sodium in the coal.

Mukherjee and Borthakur (2003, laboratory study)-This investigation evaluated the use of potassium hydroxide and acid treatment to remove mineral matter from high ash (8.4-10.4%), high sulfur (4.2 %) sub-bituminous coal (India coals). A two-step leaching process consisting of potassium hydroxide leaching at 150^{o}C followed by hydrochloric acid (10% solution) removed most of the inorganic matter and up to thirty-seven percent of the sulfur.

Steel and Patrick (2001, 2003, laboratory studies)- The goal of these studies were to produce an ultraclean coal (defined as containing <0.1% mineral content) from U.K. bituminous stock. Ultraclean coal may be used in coal gasifiers to produce gases to be used in turbines. The starting coal contained 5% ash, 2.4% sulfur. A two-stage process was developed that consisted of leaching with hydrofluoric acid (1.2 M) followed by nitric acid (1.4 to 1.58 M). The results showed that combusted coal containing only 0.2% ash could be produced.

Rubiera, et al (2003, laboratory study)- The goal of this study was to produce an ultraclean coal from high volatile bituminous stock containing 6% ash. A two-stage process was developed that consisted of leaching with hydrofluoric acid (1.2 M) followed by nitric acid (1.4 to 1.58 M). The results showed that coal ash was reduced by ninety-five percent. The authors reference other studies that have also investigated aggressive acidic and caustic reagents to produce "Clean Coals": e.g., nitric acid, *Alvarez, et al (1997);* hydrofluoric acid, *Lloyd and Turner (WO patent, 1986)*; caustic Gravimelt process, *Hycnar, et al (1994)*; hydrofluoric/hydrochloric acid mixtures, *Kinding and Reynolds, (US patent, 1987*), caustic/hydrochloric acid, *Mukherjee and Borthakur (2001)*; calcium hydroxide/ hydrochloric acid mixtures *(Wang, and Tomita, 1998).*

Lloyd, et al (1988, WO patent 4,780,112)- The authors present a method to remove mineral phases from coal. The method requires hydrofluoric acid or hydrogen fluoride at elevated temperatures to convert metal oxides and silicates to fluoride compounds. This procedure would, of course, not be applicable in a cost effective way to low-rank coals.

Addition or Presence of Metal Compounds or Mineral Phases to the Combustion Process

There have been a number of investigations to demonstrate on a laboratory and pilot scale the effect of the addition of aluminum compounds, kaolin, aluminosilicates, dolomite, bauxite, clays and others on the formation and stability of sodium compounds at elevated temperatures. The literature review includes successes using this approach.

Bartel, et al (2008, review) have recently reviewed the world literature for agglomeration in fluid bed combustion of solid carbonaceous fuels (176 publications), with an emphasis on coals, especially low-rank coals. The following references investigated the use of additives for decreasing agglomeration during combustion (i.e. decreasing the presence of liquid or semi-liquid sticky phases) by the presence of sodium: iron oxide *Olofson, et al (2002);* hydrated alumino and magnesium silicates, *Brown (1983, EP patent);* aluminosilicates, *Kyi, et al (1999), Skrifvar, et al (1992), Vuthaluru, et al (1998, 1999, 2000), Vuthaluru (1999), Tangsathitkulchai (2001), Ohman and Nordin (2000),Tran, et al (2005),*

Kosminski, et al (2006); and, dolomite, calcium oxide, and magnesium oxide, *van der Drift and Olsen (1999), Paisley (2002, WO patent), Fan and Walawender (1984).* Additionally, the review presents studies that used substitution bed materials rather than silica sand. The references are not presented here except for naming two commercially available substitute bed materials (materials not specified): *GR Granule (Daavitsinen, et al, 2001*), Agglostop *(Silvennoinen (2003).*

Domazetis, et al (2008, laboratory study)-As presented above the CCT company is aggressively developing a technology that would use low-rank coal in gasification reactor power generation. This approach requires that the ash and liquid forming species be removed prior to combustion or gasification. The CCT approach uses aggressive leaching to remove the coal matrix inorganic species and mineral phases. This paper presents the results of doping the acid leached coal with iron species prior to combustion, the coals contained 7.8% ferric iron. The iron species provided catalytic sites for reactions that produce the desired gaseous species, H2, CH4, CO and CO2, in the gasification reactor product. The doping of low-rank coal with iron showed a significant increase in the H2 content in the gasified product. For addition information with respect to modeling of low-rank coal and the effect of iron doping see the reference *Domazetis and James (2006).*

Vuthaluru and French (2008, laboratory study)-Test work was conducted to evaluate the influence of doping low-rank Indonesian coal with additives on the combustion products produced. Three coals were evaluated, i.e. raw coal (12.1% Na2O in ash, 5.7% mineral matter containing 21.6% kaolinite), coal/additive mixtures (3 % kaolin added which raised the mineral content to 8.6% and the kaolinite content in the mineral phase to 42.1%; or 3% bauxite added which raised the mineral content to 8.6% and the gibbsite content to 33% in the mineral phase), and washed coal. Doping raised the ash slagging temperature from 1218^{o}C (raw coal) to 1252 ^{o}C (kaolin added) and 1324 ^{o}C (bauxite added).The study result conclusions were that bauxite additions produced ashes that contained less glass phase (which means higher slagging temperature). This additive combination was recommended for pilot scale test work.

Schulz and Smyrniotis (2006, industrial scale demonstration)-Fuel Tech markets their Targeted In-Furnace Injection (TIFI) technology that is based on injecting chemical reagents (designed for the specific applications but not specified for sodium control) at critical points in the combustor. The claim is that by using specific injection points the amount of reagent is much less than mixing the reagent with the coal prior to combustion. Several demonstrations have been performed, e.g. South Carolina's Santee Cooper Cross Generating Station (18-month demo) to reduce sulfur and to form a less fouling slag (*Davis, et al, 2008)*; Western Farmers Electric Cooperative Hugo Station in Fort Towson, Oklahoma (3-yr demo, magnesium hydroxide reagent), (*Smyniots, 2005);* PacifiCorp Western Coal Fired Hunter Unit (PRB coal, magnesium hydroxide reagent) demo *(see internet www.ftek.com/pdfs/TPP-568*).

Lignite Energy Council (2007, pilot study)-A 310 hour test (800 tons) was conducted on North Dakota lignite (Beulah mine) in Alabama that used kaolinite additions to the coal. The combustion facility is a syngas test/development system. "favorable results" were obtained.

Takuwa and Naruse (2007),Takuwa, et al (2007 laboratory studies)-Two sodium containing coals (2.4 and 8.4 % Na_2O in the ash) were studied to determine the influence of adding kaolin (mole ratio of kaolin/Na_2O was five) during combustion (up to 1500 C) in an oxidizing atmosphere (stoichiometric air ratio was 1.2). Their results showed that gaseous sodium species, primarily metallic sodium, reacted to form various amounts of solid species over the entire temperature range, e.g. Na_2SiO_3, $Na_2O*2SiO_2$,

$NaAlSiO_4$, $Na2O*3SiO_2$, and $NaAlSi_3O_8$. Gaseous NaOH also formed at 1500°C. Prior to the 2007 studies *Takuwa, et al (2006, laboratory study)* conducted investigations on the same coals to understand the fate of sodium during combustion (without the addition of kaolin). Their conclusions were that the formed ash particles had a bimodal particle size distribution in the less than eleven micrometer particles (<1 micrometer and a few micrometers) and that the sodium was concentrated in the finer less than one micrometer fraction by reaction of gaseous sodium with the raw mineral content in the coals to form new minerals (in the submicron size fraction) in the combustion ash product.

Kosminske, et al (2006a, laboratory study)- A low-rank coal was studied to determine the fate of sodium in a fluidized gasification reactor. The procedure consisted of pyrolyzing the coal (sized to 38-125 micrometers) in nitrogen followed by gasification of the char in steam or steam and carbon dioxide at 650 to 850°C. Run-of-mine coal (8.6% Na_2O in ash) was leached in hydrochloric acid then the coal was doped with ion-exchangeable carboxylate (sodium acetate, 1% sodium in coal) or sodium chloride (1% sodium in coal). Kaolin was also added to the coals so that its content was ten percent. The results were, as would be expected, varied and difficult to interpret. The researchers concluded that: regardless of the initial form of sodium present, the sodium reacts with kaolinite to form a high melting point aluminosilicate, nepheline ($Na_2O*Al_2O_3*2SiO_2$) or carnegietite. In a high temperature steam gasification environment paragonite ($Na_2O*3Al_2O_3*6SiO_2$) may also form. More nepheline forms in a steam atmosphere that in a nitrogen or carbon dioxide environment and "the reaction between kaolin and either forms of sodium present in the coal is more effective in forming a high melting point sodium aluminosilicate nepheline or carnegietite. No sodium silicate or liquid albite formation was detected in any of the samples. It can be expected that during gasification of coal containing sodium in the presence of kaolin, the formation of solid aluminosilicates should help to avoid the formation of liquid silicates and the problems associated with agglomeration and potentially defluidisation of a fluidized bed."

Kosminske, et al (2006b, laboratory study)-The potential for reaction between sodium and silicon minerals to form solid aluminosilicates during gasification was thermodynamically investigated for a low-rank coal. This study was important in interpreting the experimental results presented by *Kosminske, et al* in the references-*Kosminske, et al (2006a, 2006b).* Thermodynamic Multi-Phase Multi-Component Equilibrium (TPCE) calculations were employed. The software package used was CSIRO CHEMIX *(Turnbull and Wadsley).* The initial coal composition was that of a low-rank coal containing 15.7% ash, 1.0% sodium, 3.4% sulfur and 0.5% chloride. The ash contained 31.4% silica, 8.7% sodium oxide, and 8.3% alumina. The temperature range investigated was 450 to 950°C, the gas atmospheres investigated included carbon dioxide, carbon monoxide, steam, hydrogen, or nitrogen. The calculation results are, of course, dependent on, not only the temperature and gas atmosphere, but also on the specific sodium and other gaseous, liquid and solid species chosen as inputs to the program. The reader should refer to the referenced paper to view the species chosen. A variety of results are presented in the paper, e.g. in a system containing sodium carboxylate and kaolin in steam the predicted major sodium solid phase over the entire temperature range would be nepheline (~80 % of the total sodium); albite solid would be the other major phase up to approximately 650°C. The albite would not be expected to be stable as a solid at higher temperatures because it should be converted to liquid silicates. The importance of this example is that a major portion of the sodium would be expected to present as a non-reactive solid which would be desirable in a coal combustion system. However, in a fluidized bed gasification system if twenty percent of the sodium is present as a liquid it may become the "glue" that may destabilize the fluidization process. Other TPCE

calculation software programs have been used to predict the expected outcomes for coal combustion under a variety of conditions, e.g. *Twidwell (2009)* and *Wang, et al (2004).*

Twidwell (2009)-The TPCE programs, HSC *(2006)* and STABCAL *(Huang, 2009)* have been applied to four low-rank Montana coals using analytically determined mineral species (MLA by *Miranda 2009*) and sodium contents (300-3800 mg/kg) in the coal. The results are in qualitative agreement with the CSIRO and FACT modeling results.

Wang, et al (2004) have used the program F*A*C*T to explore the effect of atmosphere and temperature on the formation of mineral phases during combustion. Various coals containing a range of sodium (0.6 to 1.4 percent sodium oxide in the ash) and other inorganic species were considered. Sodium, iron and silicon were predicted to be totally in the solid mineral phases below 1227oC, above that temperature a major portion of the sodium was present in the gas phase as Na(g) and NaOH(g); also present in the gas phase in minor amounts were NaO(g) and NaCl(g).

Vuthaluru (1999, laboratory study)-Low-rank Victorian coals were mixed with eitheraluminum lactate or aluminum lactate plus sodium acetate solutions or mineral additives and fired at 1000-1400 ^{o}C. Additives were effective in reducing ash-related problems. It was demonstrated that 10-20 micrometer kaolin doped to 2-3 percent of the feed coal effectively reduced the ash problem. A number of previous studies showed that fouling can be controlled in low-rank coals by mineral additives: *Vulhaluru and Wall (1998); Vuthaluru, Vleeskens, Wall (1998); Vuthaluru, Domazetis, Wall, Vleeskens, (1996); Lowe, et al (1993); Lindner, et al (1988); Domazeuis and Buckman (1987);* and *Ledger (1987).*

Kyi and Chadwick (1999, laboratory study)-A study similar to the Vuthaluru study investigated the addition of twelve mineral compounds to low-rank coals. The best additives for use as fouling preventatives were kaolin, bentonite, micalay, diatomite, pumice, pyrophylite and overburden.

Linjewile and Manzoori (1999, laboratory study)-The authors investigated the insitu use of four additives, including clays and gibbsite, to tie up the sodium in low-rank high sulfur Australian coal (Western US coals generally have a low sulfur content) during the combustion process. The desire was to evaluate the effectiveness of the additives for controlling ash deposition, agglomeration and defluidization in a fluidized bed combustor. The result of this work concluded that Gibbsite was the most effective additive for tieing up sodium.

Dahlin, et al (2006, laboratory study)-This study was conducted on a North Dakota high sodium lignite in the Power System Development Facility (PSDF) at the Southern Research Institute in Alabama. The study investigated two approaches to reduce agglomeration in a fluid-bed coal/sand gasifier at 900^{o}C. The approaches consisted of adding reagents to block the formation of sodium silicates (dolomite, calcite, and coarse coal ash) and adding mineral species (kaolinite, sand flour, and a paper mill product containing fifty percent kaolinite) to react with gaseous sodium as it formed in the reactor. The conclusion of the study was that agglomeration could most reliably be prevented by using a combination of blockage with dolomite and replacement of a portion of the fluidization sand with finely divided coal ash (thereby reducing the amount of silica but yet having sufficient kaolinite for reaction with the gaseous sodium).

Mwabe and Wendt (1996, laboratory study)-The authors studied the basic characteristics of sodium reaction when coal and kaolinite were injected and combusted together. Their thermodynamic

studies include the following considerations: Kaolinite, $Al_2O_3*2SiO_2*H_2O$, forms metakaolinite, $Al_2O_3*SiO_2$, at temperatures as low as ~500^oC and reacts with NaOH (vapor) to form nephelite, $2Na_2O*Al_2O_3*2SiO_2$, which is solid at temperatures above ~1025^oC. The formation of solid nephelite is desirable so that low melting sticky liquids do not form.

Transformation of Sodium During Combustion and Gasification

Wei, et al (2009, laboratory study)-Lignite coals were washed in water and other samples in a hydrochloric acid solution, then doped with NaCl or NaAc , dried and gasified in steam at 900-950^oC in a fluidized bed reactor. The coals and chars were then subjected to water and acidic leaches to determine the water and acid soluble fractions. The amount of volatilized sodium was calculated from the leached results. Significant sodium was released to the gas phase during gasification. Greater loss to the gas phase occurred as the sodium chloride doping was increased, i.e. approximately forty percent was lost at the lower loading (500 g/L coal soaked in 0.1 mole/L salt solution) and over ninety percent was lost at the higher loading (0.5 mole/L salt solution). Approximately eighty percent sodium loss to the gas phase occurred for both the low and high doped sodium acetate coals.

Sugawara, et al (2009, laboratory study)-Two low-rank (sodium 220 and 580 mg/kg; potassium 170 and 620) and two hard (sodium 330 and 350 mg/kg; potassium 1680 and 250 mg/kg) coals were subjected to pyrolysis in nitrogen at temperatures up to 1200^oC to investigate the transformation during combustion. The investigators subjected the coals and chars to sequential leaching in water (to remove soluble salt in micropores and in sample moisture), ammonium acetate (to remove ion-exchangeable species), hydrochloric acid (to remove readily solubilized mineral species), sulfuric acid with hydrogen peroxide (to remove sulfide minerals), and hydrofluoric/nitric acids (to remove the reminder of mineral species. The low-rank coals showed appreciable water solubility for the sodium, e.g. fifty-five percent dissolved, and seven to nine percent potassium dissolved. The acetate showed only a small amount of dissolution of sodium and potassium, e.g. seven to nine percent and eight to fifteen, respectively. The pyrolysis treatment results were varied and the reader is referred to the paper for details.

Van Dyk, et al (2009, laboratory study)-The authors present a summary of the tests work conducted on samples blended from six coal sources in South Africa. The samples contained a very high ash and maceral content, e.g. 25.8%, and 23%, respectively. The authors point out the importance of determining the coals ash flow temperature (AFT) to indicate the extent that the ash will be likely to agglomerate, clinker, or become completely fluid. *Carpenter (2002)* describes a standard cone test (ASTM D1857) that identifies four important characteristic temperatures, e.g. Initial Deformation where the cone tip shows deformation (IDT), Softening sphere temperature where cone height equals cone width (ST), hemispherical temperature where cone height equals one-half the cone width (HT), and fluid or flow temperature where the cone height equals 1.6 mm (FT). The AFTs for the Dyk study ranged from 1300 (IDT) to 1340^oC (HT).

Pipatmanomai, et al (2009, operating plant study)-The authors studied the relationship between as-received coal characteristics and composition of ashes and slagging. Ash samples from a Thailand operating lignite combustion power plant were studied. The importance of this study is that the lignites contained relatively high ash content (32.2%) with low sodium and potassium content. The characterization showed the importance of controlling the composition of inorganic elements (calcium, aluminum, iron, and silicon) in forming low temperature liquid or semi-liquid ashes. The

conclusions of the studies were that coal blending should be controlled so that they contain the following concentrations: CaO <23%, Fe_2O_3 ~15%, and Al_2O_3 >20%. These concentrations result in keeping the furnace exit gas temperature (FEGT) at the desired level of 150^oC below the initial deformation temperature (IDT) as determined in a reducing atmosphere.

Matsuoka, et al (2008, laboratory study)-Low-rank Australian coal was investigated to determine the transformation of alkali and alkaline earth metals during gasification. Coal was pyrolyzed in nitrogen at 1500^oC, then the char was gasified in CO_2 at 1500^oC. As noted above an important ancillary result of this study (and a previous study by *Matsuoka et al, 2002*) was that when they applied the usual sequential leaching using water, ammonium acetate, then strong acidic solutions to determine the presence of adsorbed sodium and calcium, ion-exchangeable sodium and calcium, and acid soluble mineral phases, it was found that the ammonium acetate reagent removed, not only the ion-exchangeable sodium and calcium but also some of the mineral phases present, especially for calcium. In the past it has been assumed that ammonium acetate only removes adsorbed and organically bound calcium and not inorganic mineral phases. This result is important because the presence of calcium may also contribute to the formation of low-melting ash constituents. However, the low-melting calcium compounds do not readily form at normal combustion temperatures but they do form at elevated gasification temperatures. Therefore, the presence of calcium is less of a problem in normal combustion but may be a serious problem if present during gasification. Particle characterization was performed using computer controlled scanning electron microscopy (CCSEM) analysis. The conclusion of this study with respect to sodium and potassium was that pulverized coal combustion results in the formation of low-melting Na-and K-aluminosilicates whereas at gasification temperatures the sodium and potassium form vaporous species. The greater vaporization of the alkali elements during gasification results from the presence of carbon monoxide in the gasification reactor.

Stiegel (2008, power point presentation on current state of gasification) An excellent general review of current gasification technologies, is presented (in a power point presentation) by the National Energy Technology Laboratory (NETL), US DOE. The review includes a general description of the properties of low-rank coals; the challenges and opportunities for low-rank coals; detailed descriptions of gasification reactors using low-rank coals; currently operating and future gasification systems in the US and in the world; testing of high sodium coals at the power systems development center (PSDC) at Wilsonville, Alabama; advanced refractory for gasification reactors to minimize slag penetration; and capital cost comparisons of various gasification systems.

Kosminske, et al (2006a, laboratory study)-A low-rank coal was studied to determine the fate of sodium in a fluidized gasification reactor. The procedure consisted of pyrolyzing the coal (sized to 38-125 micrometers) in nitrogen followed by gasification of the char in steam or steam and carbon dioxide at 650 to 850^oC. Run-of-mine coal (*8.6% Na_2O in ash) was leached in hydrochloric acid to form a “Clean Coal”, then the coal was doped with ion-exchangeble carboxylate (sodium acetate, 1% sodium in coal) or sodium chloride (1% sodium in coal). The results showed that regardless of the form of sodium in the coal, solid sodium carbonate formed when pyrolyzed (850^oC) in the nitrogen atmosphere; less than twenty percent of the sodium volatilized. Gasification of the char in carbon dioxide and in steam at 850oC volatilized about half of the sodium regardless of the initial form of sodium in the coal.

Matsuoka, et al (2002, laboratory study)-The authors subjected a lignite coal (7.8% sodium oxide in the ash) to gasification (in 1% oxygen/helium) in a fixed bed reactor and investigated the particle size distribution of the ash and mineral formation species formed at 500^oC and 800 ^oC (using CCSEM

analyses). The raw coal major mineral phases were kaolinite (~12%), quartz (~15%), calcite (~22%, and pyrite (~16%). The conclusions for the study were that organically associated sodium reacted significantly with kaolinite and less with quartz.

Neville and Sarofim (1985)-have stated that most coals, irrespective of rank, contain sodium contents in the range 200 to 700 ppm. These investigators studied Montana lignite coal. The coal was sub-bituminous and the sodium content was present mainly as organically bound species (*Miller and Given, 1978*). The Neville study showed that the ash formed during combustion at approximately 1500^{o}C contained seven percent sodium and the concentration of sodium migrated from the larger ash particles to the sub-micrometer size fraction with time. The study conclusions were that the volatility and subsequent sodium content in the ash were dependent on the mode of occurrence in the as-received coal. The sodium present as organically bound sodium readily volatilized and the sodium, that was associated with mineral constituents, was retained in the residual ash, primarily in the sub-micrometer size range.

Environmental Concerns and Wastewater Treatment (Dudley 2011)

Through evaluation it has been determined that pre-treatment poses the best option for control results for eastern Montana coal. Specific removal mechanisms, as well as related study results can be found elsewhere in associated documents. It can be generally assumed here, however, that processing will involve aqueous effluent, primarily sodium or salt laden waters. As such, in order to develop a fully comprehensive understanding of phase two of the project one must understand the driver behind the control of sodium in waste/process waters.

Laws and Regulations-There are a number of laws and regulations, federal and state, through which control of sodium and salt effluent may be promulgated. The primary federal drivers are the Safe Drinking Water Act and the Clean Water Act.

"The Safe Drinking Water Act, originally promulgated in 1974 to protect the public drinking water supply, has grown and evolved through amendments made in 1986 and 1996. The purpose has, however, remained consistent and continues to set national standards for drinking water sources based on human health specific data. Under this legislation, EPA is required to promulgate regulations for human health specific drinking water quality standards if certain criteria are met. These criteria are: 1) "the contaminant may have adverse effects on the health of persons," 2) "the contaminant is known to occur or there is a substantial likelihood that the contaminant will occur in public water systems with a frequency and at levels of public health concern," 3) "in the sole judgement of the Administrator, regulation of such contaminant presents a meaningful opportunity for health risk reduction for persons served by public water systems." As such, it develops what is known as the Contaminant Candidate List (CCL) which serves as a priority check list of supposed contaminants that may pose health-related risks and as such warrant further investigation. Sodium was placed on the 1998 CCL and underwent a Six-Year Review and collection of data to determine if sodium warranted regulation. This review involved a wide spread review of the information available on current sodium present in water and related health concerns. Up to this point EPA had only issued guidance or advisories concerning sodium. A 20 mg/L Drinking Water Equivalent Level, a (non-enforceable) guidance had been in effect as well as the issuance of a 250 mg/L salinity and dissolved solid standard promulgated in 1997 for ambient waters. These guidance levels were the result of key concerns addressed later on in the impacts section, found below. Ultimately, although sodium does represent health concerns to specific portions of the population, the issue is not so wide-spread that would require additional regulation or promulgation of a standard**."(EPA, 2003)**

"The other primary driver behind water quality regulation stems from the Clean Water Act (CWA). First promulgated in 1972, the purpose of the CWA is to protect surface water quality of navigable waters of the US. The act does this through a variety of means, but largely in part due to the water quality standards it promulgates and enforces. Of primary concern is the National Pollution Discharge Eliminations System (NPDES) which regulates what has been termed point-source discharges. These are most closely associated with industrial effluent discharges and are permitted, as defined in CWA Section 402. Often used in concert with CWA regulation is the requirement to develop environmental impact statements of proposed operations and related impairments as promulgated under the National Environmental Protection Act (NEPA).

Permits issued under the NPDES are based on technology based effluent limits to protect water quality to attainment standards. Often the regulating authority is given to individual states that have permitting programs. As such states are required to follow a general process in issuing permits:

- The state establishes water quality standards for a given water body based in intended use and also establishes an anti-degradation policy to prevent significant deterioration of the water body. These are usually in the form of Total Maximum Daily Loads, which outline the maximum contaminant loading a water body may be expected to receive and still achieve attainment status. (TMDL's are usually set in step 4)
- States then assess water bodies to determine attainment status.
- Impaired water bodies are then prioritised for regulation.
- Finally, site specific regulations aimed at limiting degradation and intended reversal of adverse impairment.

With regulations or TMDL's in mind, discharge points into the water body are evaluated for control and issued permits based on effluent treatment plans. This is followed by monitoring of both the entire water body and effluent discharges to ensure compliance.
Note*: Where states are not given permitting authority, Federal agencies are responsible for permitting, and any regulation that an individual state promulgates has to be at least as stringent as the federal standard (if one exists).

It is of note that if a contaminant becomes an increasingly prevalent concern, then EPA will devote resources to develop what is commonly referred to as ELG's or Effluent Limitation Guidelines, these guidelines are the minimum technology based standards that drive much of the NPDES permitting mechanisms. The development and propagation of an ELG does take into account cost and other effects on industrial operations where EPA promulgates guidance as to available technologies for industrial categories. Currently the last guideline for Coal Mining was published in the early 2000's and there does not seem to be a guidance document for coal fired power plants." **(Veil, 2002)**

In close correlation with CWA, at least as far as coal mining developments are the Surface Mining Control and Reclamation Act. Established in 1977 it is the primary means of regulating start up, operation, and closure of coal mining activities (surface). It is administered through the office of Surface Mining Reclamation and Enforcement, within the US Department of the Interior. This office and related permits work in tandem with the EPA and the permits issued under the Clean Water Act, but focus more on end of life planning including water related issues for closure and remediation of surface coal mining sites.

The state of Montana has been given the power to oversee water quality for navigable waters within State-bounds. As such it has developed its rules and regulations, consistent with the requirements of EPA and other governing agencies. The regulatory circular defining effluent standards are known as DEQ 7 – Montana Numeric Water Quality Standards. Within that document it issues such as alkalinity and total dissolved solids are addressed, and one would assume development of issues related to regulatory affairs of conductivity and salinity (sodium) in a narrative fashion:
"Narrative standards are also contained in Montana's rules for ground water (ARM 17.30.1001 through 17.30.1045). The narrative standards cover a number of parameters, such as alkalinity, chloride, hardness, sediment, sulphate, total dissolved solids and nutrients (for surface water), for which sufficient information does not exist to develop specific numeric standards." ***(MT DEQ 7, 2008)***

"Establishing basis for regulation in such a manner leads to multiple conclusions. One, the science is such that development of standards for conductivity, salinity, and more specifically sodium in effluent discharge waters has not progressed far enough to issue specific standards. Secondly, water quality across the state may be such that a specific effluent standard is not applicable and a more site specific approach may be warranted. Given the second issue, in order to ensure non-degradation of receiving waters Montana Pollution Discharge Elimination System permits approach underdeveloped standards areas from the narrative standpoint through the use of Whole Effluent Toxicity limitations. This is evident in the recent permit granted to Westmoreland Resources, Inc. in reference to activities associated with the Absaloka Mine South Extension (Permit No.: MT0030783). Within that document whole effluent toxicity testing is defined the parameters which would constitute a permit violation, in the form of acute lethal concentration (LC50) in which mortality of 50 percent or more of the test species is experienced. If toxicity, either chronic or acute, is detected this enacts permit regulations for additional testing and subsequent reporting to work to correct the issue." **(NPDES – PN: MT0030783, 2009)**

"It is of note, that the Administrative Rules of Montana (ARM) do classify groundwater in accordance with specific conductance measurements. This mechanism would provide added guidance or limitation under the non-degradation approach. Classification is made according to the following (ARM – Environmental Quality, Chapter 30, Water Quality, Subchapter 10:

> Class I: Waters with a specific conductance less than are equal to 1000 microSiemens/cm at 25 degrees Celsius. The quality of such waters must be maintained with little or no treatment and is used primarily for public and private water supplies, culinary and food processing, irrigation, drinking water for livestock and wildlife, commercial and industrial purposes.
>
> Class II: Waters with a specific conductance between 1000 and 2500 microSiemens/cm at 25 degrees Celsius. The quality of such waters must be maintained such that they are marginally acceptable for public and private water supplies, culinary and food processing, irrigation of some agricultural crops, drinking water for livestock and wildlife, most commercial and industrial purposes.
>
> Class III: Waters with a specific conductance between 2500 and 15000 microSiemens/cm at 25 degrees Celsius. The quality of such waters must be maintained such that waters are marginally acceptable for irrigation of some salt tolerant agricultural crops, drinking water for some livestock and wildlife, some commercial and industrial purposes, and drinking, culinary, and food processing where the specific conductance is less than 7000 microSiemens/cm at 25 degrees Celsius.
>
> All waters within the greater Powder River watershed are considered C-3 classification. C-3 classifies waters (mainly in reference to surface) as such to be maintained for bathing, swimming and recreation, growth and propagation of non-salmanoid fish as well as associated aquatic life.

Waters are marginally suitable for drinking, culinary and food processing purposes, agriculture and industrial water supply. Degradation is not permitted." **(EPA & DEQ, 2003)**

The narrative standard applies such that:
"Montana narrative standards address two basic concepts (1) activities that would result in nuisance aquatic life are prohibited, and (2) no increases are allowed over naturally occurring conditions of sediment, settleable solids, oils, or floating solids, which are harmful to public health, recreation, safety, welfare, livestock, wild animals, birds, fish, and other wildlife (ARM, 2002). A summary of the narrative standards that apply to pollutants of concern in the Powder River TPA is shown in Table 3-3 and the full text is included in Appendix C. Aquatic life in the Powder River TPA is protected by several different narrative standards that apply to all of the pollutants of concern. Aquatic life may not be harmed by any anthropogenic source of pollution (ARM 17.30.637(d)), and conditions that produce undesirable aquatic life are prohibited (ARM 17.30.637(e)). Agricultural uses are protected by ARM 17.30.637(d), which states that no anthropogenic source of pollution may create conditions that are harmful to plant or animal life. All of the beneficial uses of a waterbody, whether a direct narrative standard exists or not, must be protected." ***(EPA & DEQ, 2003)***

Additionally as a pre-cursor to the classification, it is stated that effluent discharges are not required to be treated to a purer condition than the receiving waters, but cannot be less than the quality of the receiving waters. Once again highlighting the variability that such industries might see in their permit conditions. This is an ideal segway into a discussion on the site/regions specific standards that do exist for Electrical Conductivity (EC) and Sodium Adsorption Ratio (SAR) of effluent discharges. The table below summarizes the information **(ARM 17.30.670):**

Site	EC (uS/cm) Average (Max)	SAR Average (Max)	Active Timeframe
Rosebud Creek	1500 (2500)	5.0 (7.5)	November-March
	1000 (1500)	3.0 (4.5)	March - October
Tongue River	1500 (2500)	5.0 (7.5)	November-March
	1000 (1500)	3.0 (4.5)	March - October
Powder River	2500 (2500)	6.5 (9.7)	November-March
	2000 (2500)	5.0 (7.5)	March - October
Little Powder River	2500 (2500)	6.5 (9.7)	November-March
	2000 (2500)	5.0 (7.5)	March - October
All tributaries and surface waters related to above watersheds	500 (500)	5.0 (7.5)	November - March
	500 (500)	3.0 (4.5)	March – October
Tongue River Reservoir	1000 (1500)	3.0 (4.5)	All Year

Current Conditions-The Powder River Basin, as can be seen above, is a well-defined regulatory area within the state of Montana. The watershed planning area was put on the fast track for establishment of TMDL standards and therefore established the previous mentioned standards. A status report of development was issued in 2003 and summarized various progress steps as well as data collected thus far. A few things were of note from that report.

"A survey conducted of irrigators in the area led to the conclusion that nearly 40% had experienced irrigation problems in reference to crop yield, and over 50% reported soil salinization issues.

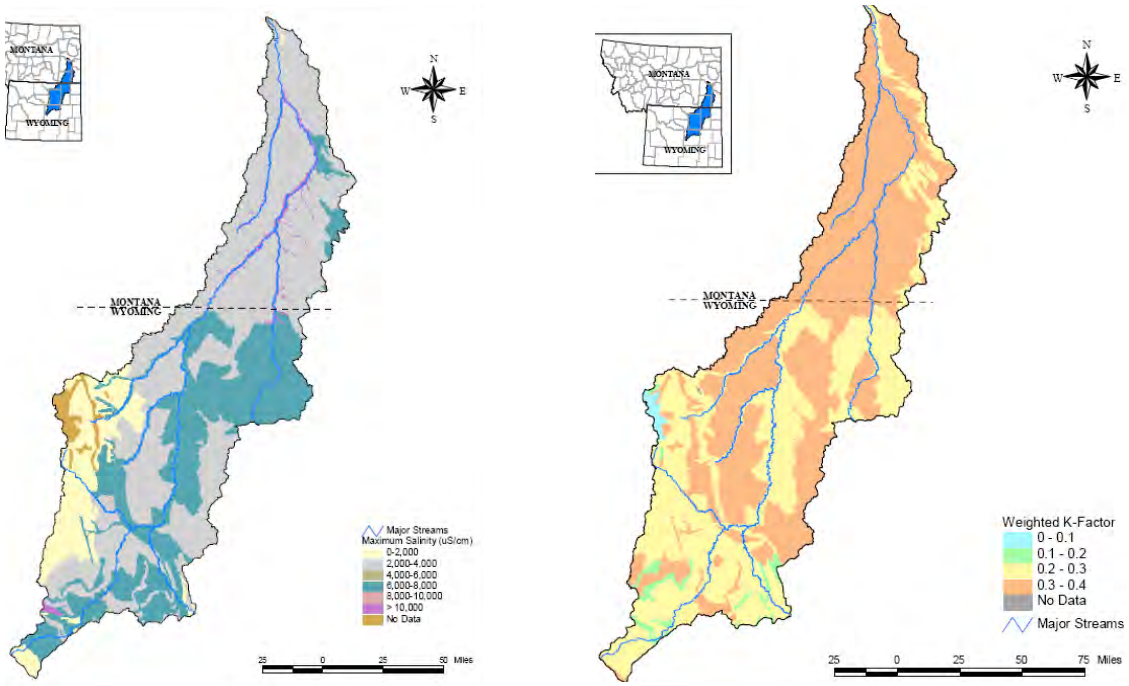

Soil quality shows increased degradation potential towards the lower end of the watershed area, which would correlate to increased presence of sodium and subsequent destabilization effects. Soil erodability can be quantified by what is known as a K factor. The higher the k factor, the higher the potential for degradation. Looking specifically at salinity of soils, EC ranged from 2000 to 8000 uS/cm, corresponding to soil that inhibits plant growth through the inhibition of available water. One would expect that the highest regions of potential erosion would coincide with the highest salinity value areas. Not the case, as can be seen from the comparison of the two maps above. None-the-less the higher erosion soils are considered saline or moderately saline, as well as show SAR value in the 5-10 range, this may constitute the perfect storm of soil parameters, being that the combination in the lower regions may be optimal for erosion with limited calcium and magnesium and increased sodium presence.

Relation of aquatic areas to fishery status is such that most of the Powder River Basin has been classified as a high value fishery, even under current water conditions. Impairments have been a cause for concern since listing in 1996, most notably, for the purpose of this paper, are salinity and total dissolved solids considerations. These parameters include ions beyond sodium, and include sulphates and chlorides. All of which have an additive effect on the water column quality. Impacts relative to these parameters are discussed later on.

As a reference point, for the Powder River Basin data was collected in 2007 detailing specific conductance and sodium adsorption ratios for coal bed methane wells, and while not indicative of the process that will be implemented in this study, one can draw conclusions on relative sodium content and subsequent discharge. Specific conductance measurements ranged from 1000 to 4300 uS/cm and SAR values ranged from 8-35. Therefore none of these produced waters would meet average requirements under SAR and may meet requirements under conductivity. That said, the study concluded that, for the most part, no statistically significant impact has been seen because of the produced waters. The study does note that as development increases, impacts may become more prevalent." **(Dawson, 2007)**

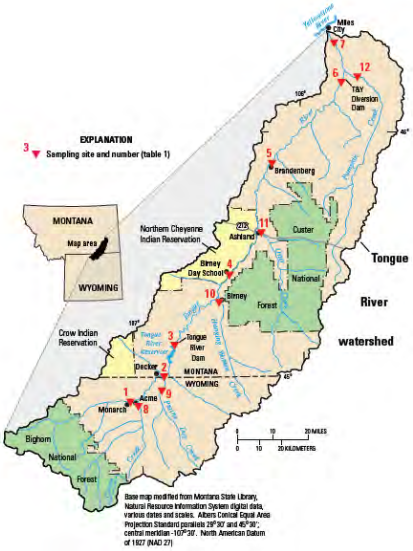

"The Tongue River, which flows through the Powder River basin and handles drainage for approximately 5,400 square miles, has long been used for irrigation of approximately 86,000 acres. A major study performed by the United State Geological Service (USGS) starting in 2004 and continuing through 2006 looked as measured and estimated values for sodium adsorption ratios for the Tongue River and its tributaries. One should refer to the study for details of the individual results for sampling stations, but for the purpose of this document a higher level summary will be presented. Looking at the data, there is a general trend of steadily increasing specific conductance and sodium adsorption ratios from Monarch to Miles City. Although there are variances, such as peaks with seasonal flows and at tributary additions, the data does show that for the most part the values are in-line with Montana regulations, but do not represent an ideal source of water for irrigation purposes. Ranking consistently around a class 3 water (as detailed later on) based on specific conductance, but conversely SAR values are such that waters would be acceptable for irrigation. Therefore generalizing water quality the source would be suitable for irrigation from a ground stabilization standpoint but would most likely result in toxicity issues based on specific conductance." **(USGS 2007)**

***Recent Developments*-**EPA's plan for standards development and focus was summarized best in their guideline factsheet with the excerpt below, highlighting increased regulator concerns in reference to facilities such as coal fire power plants.

"This notice first presents EPA's 2009 review of its existing effluent guidelines. Second, it presents EPA's evaluation of indirect dischargers without effluent guidelines to identify potential new categories for standards. Third this notice presents the ***preliminary 2010 effluent guidelines*** *program plan as required under CWA section 304(m).*

EPA used its 2009 annual review of existing effluent guidelines and pre-treatment standards to identify the Steam Electric Power Generating category for an effluent guidelines rulemaking. EPA made this selection in part due to the potential hazard to human health and the environment by the industry's toxic and non-conventional pollutant discharges.

This notice also provides a status update on three studies supporting the Agency's review of effluent guidelines: Coal bed Methane Extraction, Unused Pharmaceutical Management in the Health Care Industry, and Ore Mining and Dressing. Finally, this notice also discusses plans for conducting the 2010 annual review of existing effluent guidelines. The current schedule is to publish the final 2010 Plan in the Federal Register in October 2010." ***(EPA, October 2009)***

As of July 13, 2010 the US Department of the Interior, the EPA, and the US Army (specifically the Corp of Engineers) entered into a memorandum of understanding regarding review of CWA NPDES permits for coal mines in the Appalachian states. "The intention is to strengthen regulations promulgated under an individual states authority to increase regulation under NPDES permits. A report summarizing the findings and recommendations was published detailing path forwards steps to strengthen regulation. Detailed within this report were the following recommendations (US EPA Memorandum, April 1, 2010):
A more regional based approach to effluent limitations should be undertaken, including correlated efforts with neighboring states to ensure attainment status even where regulating boundaries inhibit action from the other entity. EPA regional authority is primarily responsible for ensuring a correlated response.

Permitting authorities should try to limit the use of NPDES general site permits and focus more on effluent limitations addressing receiving water conditions on a case –by-case basis. In essence, permit issues should be more specific to operations and impairment conditions.
Closer attention and increased documentation should be implemented concerning baseline water quality data and consideration of similar operations in a given area. In short, cumulative impact analysis should be considered. Increased coordination and accumulation of water quality data should be implemented for various permitting exercises including SMCRA permitting, NDPES permitting, and other related permitting mechanisms.

Closer attention should be given to the development of proposed effluent discharge points. Mainly in consideration of extent of impact a facility will have. Quantitative data from similar facilities can and should be used to develop comprehensive estimates of loading rates in the discharge.
Regulating authorities are required to promulgate effluent limitations to control ALL pollutants or related pollutant parameters, including those related to narrative or numerically based water quality standards. It was found that the majority of states involved did not have numeric standards that address conductivity and total dissolved solids, among other things. As such, regulation would fall under the narrative standard to protect waters from degradation, and development or enforcement of effluent limitations should be undertaken to address these issues. Narrative criteria, even those as general as prevention of degradation, have the same weight and force of law as numeric standards. According to **federal code,** narrative standards must be established in one of three ways summarised below:
Establish effluent limits using a calculated numeric water quality criterion for the pollutant which the permitting authority demonstrates will attain and maintain applicable narrative water quality criteria and will fully protect the designated use. Such a criterion may be derived using a proposed state criterion, or an explicit state policy or regulation interpreting its narrative water quality criterion, supplemented with other relevant information which may include: EPA's Water Quality Standards Handbook, October 1993, risk assessment data, exposure data, information about the pollutant from the Food and Drug Administration, and current EPA criteria documents; or,

Establish effluent limits on a case-by-case basis, using EPA's water quality criteria, published under §304(a) of the CWA, supplemented where necessary by other relevant information; or
In certain circumstances, establish effluent limitations on an indicator parameter for the pollutant of concern.

It was found that permits adequately addressed discharges where numeric standards existed, however other quality parameters were left unaddressed. As such increased regulation should be enforced through the narrative promulgation of criteria to prevent degradation of water quality.

With the inadequacies of current permitting conditions, the EPA recommended that authorities include whole effluent toxicity limitations or chemical-specific limitations when issuing or re-issuing a permit in order to protect water for intended uses, i.e. anti-degradation.
It was recommended that more resources be given to development of the afore mentioned standards, including monitoring and enforcement.

A key parameter, within the issued memorandum, is that EPA and its relative scientific offices are performing extensive research to ascertain impacts from previously under-represented pollutants when it comes to applicable regulations. Specifically, the pursuit of new water quality criteria for conductivity is on the horizon. This action has been brought on by increased frequency of reports of impaired waterways in reference to conductivity and dissolved solid presence. This has been especially prevalent operations related to coal mining operations. Specific studies on impacts are discussed within the impacts section. In addition to examining impacts, EPA conducted a widespread review of permitting practices and found that protection of downstream water quality was being effectively ignored. This ultimately was found to related back to inadequacies of enforcement of the anti-degradation clause. EPA has now ramped up efforts to address such shortfalls in the permitting and regulatory process.

As a part of these increased efforts, EPA is requesting states to ensure that narrative anti-degradation portions of their water quality standards are being properly addressed in issuance of NPDES permits If not properly address; EPA is working to ensure that future steps will address these shortcomings. Anti-degradation policy approaches protection from a tiered water classification viewpoint. Tier 1 policy requires limits within the permit are sufficient to maintain existing uses, Tier 2 policies are used for high quality waters that can sufficiently accommodate impact from added loading, Tier 3 are for those impacted waters that can see no additional loading. Anti-degradation policy also requires that alternatives to effluent discharge be addressed. Similar requirements exist throughout the Clean Water Act, SMCRA, and NEPA.

Much of the memorandum centers on increased regulation of discharge, and relates much of its increased regulation to section 404 of the CWA. Section 404 promulgates regulation of dredge fill material into navigable waterways. Development of regulations, specifically in relation to conductivity and total dissolved solids is only the starting point of establishment of regulations to be promulgated under section 303 of the CWA or the general anti-degradation policy. One does not expect that this increased development will remain strictly in the Appalachian region, but rather will be extended to all regions, including EPA Region 8, operable region for Montana. Montana has the permitting authority in regards to administering regulations under the Clean Water Act.

As of July 30, 2010, a memo of understanding concerning increased efforts under section 404 of the clean water act for the Appalachian region was issued. This memo underlines increased focus on determination of effect of discharge on aquatic ecosystems and organisms. This increased focus comes from joint operations of the US Army Corp of Engineers (who have final regulatory capacity over coal mining operation and navigable waters) and the US Environmental Protection Agency." **(Sliva & Darcy, 2010)**

Impacts-"Impacts of sodium presence, like regulation, can really be broken down into two categories, human health impacts, therefore those that are related to drinking water, and environmental release impacts, those related to effluent discharge. As such discussion related to impacts will be developed along these two lines.

Human Health: Sodium is a necessary component for a balanced health register and contributed to maintenance of fluid volume within the body, blood pressure, and basic cell function. Most sodium is obtained from food supply and recommended daily consumption ranges from 120 mg for infants and 500 mg for 10 year olds and on. Maximum consumption should not exceed 2,400 mg, but often normal intake ranges from 3,500 to 4,500 mg/day. The primary cause for concern is the development of hypertension or high blood pressure, characterized by drowsiness, headaches and nausea and has been linked to coronary artery disease and stroke (included by reference Stamler, 1991). At risk populations, are the primary groups of concern. Infants may experience toxicity and death if sodium intake is too high because kidneys are unable to process the increased presence (included by reference Sax, 1975). Expecting mothers can see decreased pregnancy rates and decreased body mass gain, while the fetus may experience toxicity and death (included by reference Karr-Dullien and Bloomquist, 1979). Other adverse health effects have linked sodium to possible influence on increased tumour development, especially in the gastrointestinal tract. As stated above, EPA has decided to forego promulgation of regulation under the Safe Drinking Water Act, even with the related health concerns, primarily because only 8% of the population is at risk of being exposed to waters above the evaluation level of 120 mg/L." **(EPA, 2003)**

Environmental Impairment*:* Much of the information related to environmental impairment from sodium comes from studies and information gathered in regard to Coal bed Methane (CBM) activities. Control of sodium and other pollutants for CBM activities is often done under bulk parameter control such as total dissolved solids or conductivity. The EPA defines these bulk parameters as:
Conductivity*: "Conductivity is a measure of the ability of water to pass an electrical current. Conductivity in water is affected by the presence of inorganic dissolved solids such as chloride, nitrate, sulphate, and phosphate anions (ions that carry a negative charge) or sodium, magnesium, calcium, iron, and aluminum cations (ions that carry a positive charge).*

The basic unit of measurement of conductivity is the mho or siemens. Conductivity is measured in micromhos per centimeter (µmhos/cm) or microsiemens per centimeter (µs/cm). Distilled water has conductivity in the range of 0.5 to 3 µmhos/cm. The conductivity of rivers in the United States generally ranges from 50 to 1500 µmhos/cm. Studies of inland fresh waters indicate that streams supporting good mixed fisheries have a range between 150 and 500 µhos/cm. Conductivity outside this range could indicate that the water is not suitable for certain species of fish or macro invertebrates. Industrial waters can range as high as 10,000 µmhos/cm." **(EPA, LA July 2010)**

Total Dissolved Solids*: "Total dissolved solids means the total dissolved (filterable) solids present in a fluid as determined by use of the method specified in Title 40 of the Code of Federal Regulations (40 CFR) Part 136. UIC regulations protect water which has less than 10,000 milligrams per liter (mg/l) total dissolved solids. To put this value into perspective, most drinking water averages between 200 and 300 milligrams per liter total dissolved solids and water with TDS greater than 500 milligrams per liter is not recommended for human consumption. Therefore 10,000 mg/l is a very conservative value."* (**EPA, LA 2010)**

Sodium Adsorption Ratio: *"Is the expression of relative activity of sodium ions in exchange reactions within soil and is an index of sodium or alkali hazard to the soil. Sodium hazard in water is an index that can be used to evaluate the suitability of water for irrigating crops."* (USGS, LA 2010)
There are many means to measure salt content, the tables below summarize some of the units and related conversions (tables taken from the reference **(EPA, LA 2010):**

Definitions

Abbrev.	Meaning
mg/L	milligrams per liter
meq/L	milliequivalents per liter
ppm	parts per million
dS/m	deciSiemens per meter
µS/cm	microSiemens per centimeter
mmho/cm	millimhos per centimeter
TDS	total dissolved solids

Table 3. Conversion factors for irrigation water quality laboratory reports.

Component	To Convert	Multiply By	To Obtain
Water nutrient or TDS	mg/L	1.0	ppm
Water salinity hazard	1 dS/m	1.0	1 mmho/cm
Water salinity hazard	1 mmho/cm	1,000	1 µmho/cm
Water salinity hazard	EC (dS/m) for EC <5 dS/m	640	TDS (mg/L)
Water salinity hazard	EC (dS/m) for EC >5 dS/m	800	TDS (mg/L)
Water NO_3N, SO_4-S, B applied	ppm	0.23	lb per acre inch of water
Irrigation water	acre inch	27,150	gallons of water

In 2006, the CBM sector was identified as a primary sector for further investigation concerning surface water discharge quality. To date phase one of this investigation has been completed which was to review scientific journal articles in reference to impacts of produced waters and possible beneficial uses. Phase 2, document retrieval from state and federal agencies, universities, websites, and non-governmental organizations, and Phase 3, environmentally sustainable beneficial uses of produced water are still to be completed. In the 2006 technical support document for effluent guidelines a quality review of adverse impacts of produced water discharges was published. Although this discussion centers on coal-bed methane production, much of the adverse impacts of effluent discharge translate horizontally to coal mine and coal combustion facilities. **(EPA, 2006)** Discharge of effluent waters without treatment is of primary concern. The development of research centers on what can be termed "what if" scenarios. In essence, "if effluent waters laden with sodium are used in such a manner what are the related effects that may be seen."

Impoundment: "One option for disposal is impoundment of produced waters. Healy et al undertook a study on changing sediment chemistry through a ten month period. Sediment cores were obtained before and after operation of the impoundment commenced. Depth analysis showed that among exchange site contaminants, calcium was predominant at shallow depths while sodium concentration increased with increasing depth. The underlining result being that sodium is more highly transported to deeper sediment depths. Initial produced waters were of sodium-bicarbonate type with a total dissolved solids concentration of about 2275 mg/L. As suspected, sediment deposits had a concentrating effect as depth increased. Samples were taken at the 3, 5, and 7 meter depths. At a depth of 3 meters sodium concentration increased to double that of impounded produced waters. The five meter depth measurement showed an initial spike of sodium concentrations but equalized to that of the 3 meter depth as time progressed. Lastly, the 7 meter depth sample (once water was detected in the sample area) peaked at twice the concentration of the 5 meter depth samples. This general trend of increasing sodium trend was confirmed when modeled with exchangeable sites consistent with geological formations of the impoundment site. This increase in sodium presence with increasing depth was characteristic of a contaminant plume, the high TDS concentration appeared to be a result of cation exchange and additional release of sodium was spurred by calcium exchange. The plume is of concern because it is slowly migrating towards water ways in which it would negatively impact and cause subsequent degradation." **(Healy et al, 2008)**

"Montana's current water quality regulations align with class 2 waters, aimed at keeping waters suitable for crop irrigation. Another way to qualify waters is according to sodium hazard, typically quantified by the sodium adsorption ratio (SAR). The value takes into account competition between sodium, which will disperse soil particles resulting in decreased permeability due to loss of infiltration panels, with calcium and magnesium which tend to flocculate soil particles creating void spaces for movement of water. The problem is further compounded because as soil is continually destabilised and compacted, leaching or flushing of saline constituents cannot be accomplished (through natural means) and the soil continues to increase in salinity." **(Smart, 2003)** "One should not look at SAR alone, EC combined with

SAR measurements have shown different trends. SAR with low EC tends to have a greater effect on dispersion of soil than does SAR with high EC. In general however the following table can be used to describe irrigation water based on SAR values:

Table 4. General classification of water sodium hazard based on SAR values.

SAR values	Sodium hazard of water	Comments
1-9	Low	Use on sodium sensitive crops must be cautioned.
10-17	Medium	Amendments (such as gypsum) and leaching needed.
18-25	High	Generally unsuitable for continuous use.
>26	Very high	Generally unsuitable for use.

The presence of chloride in irrigation water, much like sodium will also have adverse impacts and can serve to compound impacts resulting in toxicity issues for crops. The following table shows a general trend in reference to suitability to various crops.

Table 5. Susceptibility ranges for selected crops to foliar injury from saline sprinkler water.

	Na or Cl concentration (mg/L) causing foliar injury			
Na concentration	<46	46-230	231-460	>460
Cl concentration	<175	175-350	351-700	>700
	Apricot	Pepper	Alfalfa	Sugarbeet
	Plum	Potato	Barley	Sunflower
	Tomato	Corn	Sorghum	

Foliar injury is influenced by cultural and environmental conditions. These data are presented only as general guidelines for daytime irrigation. Source: Mass (1990) Crop salt tolerance. In: Agricultural Assessment and Management Manual. K.K. Tanji (ed.). ASCE, New York. pp. 262-304.

In Wyoming, especially within the Powder river Basin, (which Montana shares) it is required that produced waters be used for beneficial purposes. To meet this requirement many of the well production waters are being integrated into irrigation systems. Brink and Frost conducted an examination to determine extent of salinization/sodification of soils where agriculture water was derived from produced water operations. Salinization refers primarily to the concentration of salt constituents in the root zone. Determination as to if a soil is saline, depends primarily on the end use of the soil, in essence what crop is going to be present there. Some crops can fully accommodate increased salt presence from produced water and are not considered saline for their end-use purposes, however, others grow more sensitive crops and use of CBM waters will result in the soils being saline. This saline soil effectively inhibits plant growth and crop yield by limiting the availability of adequate water. Sodification refers to accumulation of Sodium on the cation exchange complex of the soil. A soil is said to be sodic when sodium negatively impacts the structural qualities. Sodium may cause the soil, clay and organic matter to disperse and or swell, effectively reducing macro porosity and inhibits the avenue of water infiltration to the root zone for uptake by plants. That said, sodification is not a generalized effect, it is very much dependent upon the geologic and biological characteristics of the soil, but is generally considered sodic when the Exchangeable Sodium Percentage (ESP) is 15% or more. This translates to 15% of available cation exchange sites of the soil are effectively occupied by sodium.

One major parameter for evaluation of irrigation water and its application to irrigation is the Sodium Adsorption Ratio (SAR). SAR is a measure of the ratio of sodium to magnesium and calcium, and relays information about the possibility and extent to which sodium will replace other ionic constituents, namely calcium, in structural exchange sites of the soil. Once again acceptable SAR values vary by region and related geological characteristics but in general waters with SAR values of 0 to 6 are considered acceptable for irrigation purposes. As a reference co-produced water from the Powder River Basin measures a 14 on the SAR index. Baseline soil samples were taken from the experimental sites, and it was found that irrigation with CBM production waters increased the SAR, ESP, and Electro conductivity values of the soils well above baseline. Additional sampling showed trends of increased

values seen at 30 cm depths ceased to continue below 60 to 90 cm depth. High SAR values combined with a higher EC value leads to destabilization of the soil structure and loss of flocculation, sodium presence is the primary driver behind this. Loss of flocculation leads, in kind to loss of aggregate material in the soils structure. This aggregate material allows adequate infiltration between aggregates and is a good indicator of soil quality, while dispersed soil will be characterized by pooling and loss of infiltration capacity. This loss of infiltration would effectively damage organic matter by limiting the amount of water available to them in the root zone. Therefore, increased sodium values used in waters for irrigation is a major cause for concern, and treatment of water would have to be enacted before discharge is plausible." **(Brink et al, 2009)**

Figure 2. Relationship of EC with SAR for desirable soil conditions *(Hanson, et al. 1999)*

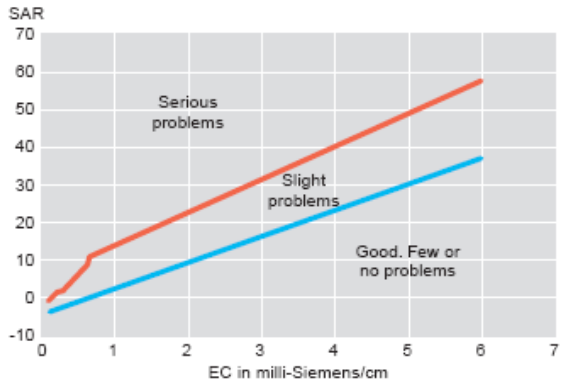

"It may have been highlighted best in a study performed by Johnston et al in 2008, looking at impacts to soils and crops using saline water as irrigation source. It was shown that increasing conductivity may temper the impacts of high sodium content. This further confirmed studies by Van Olphen, 1977, Arora and Coleman, 1979, Shanmuganathan and Oades, 1983, and Sumner et al, 1998. EC, which includes magnesium and calcium presence, may provide the necessary structural support that prevents significant degradation of soil structure. Increased EC comes at a trade-off. Values need to be kept high enough to prevent soil destabilisation but low enough to be suitable for irrigation and not adversely affect yield. (Johnston et al, 2008) This relationship was graphically (shown above) in a report published by Jangbarwala in 2007." **(Jangbarwala, 2007)**

Table 3. Livestock response to water quality limits

TDS (mg/L)	Livestock watering comment *(National Academy of Sciences)*
Less than 1,000	Excellent for all classes of livestock.
1,000 to 2,999	Very satisfactory for all classes of livestock. May cause temporary and mild diarrhea in livestock not accustomed to them.
3,000 to 4,999	Satisfactory for livestock, but may cause temporary diarrhea or be refused at first by animals not accustomed to them.
5,000 to 6,999	Can be used with reasonable safety for dairy and beef cattle, sheep, swine and horses. Avoid use for pregnant or lactating animals.
7,000 to 10,000	Considerable risk in using for pregnant or lactating cows, horses or sheep or for the young of these species. In general, use should be avoided although older ruminants, horses, poultry and swine may subsist on them under certain conditions.
Over 10,000	This water is considered unsatisfactory for all classes of livestock.

"In a summary report published by the Montana Department of Environmental Quality in 2001, Abe Horpestad gave generalised conclusions regarding acceptable levels of water quality constituents in relation to soils, crops, and aquatic life. It was concluded that EC and SAR would only need to be heavily regulated during irrigation season from March 1 through September 30. Values of EC up to 1000 uS/cm were considered to have no negative impact on crop yields and values above result in increasingly decreased crop yields. Control is recommended somewhere between 900 to 1100 uS/cm for the Tongue River and Little Big Horn Rivers, while Rosebud Creek was between 1000 to 1300 uS/cm. Conversely SAR values vary widely based on location from .6 to 7." (**Horpestad, 2001)**

Irrigation may also be used for livestock operations. Such applications have their limited capability to accept highly saline or sodic waters, summarised by this table. **(Jangbarwala, 2007)**

Water Quality & Fish Species: "Salinity and total dissolved solids are of concern for the Powder River Watershed area. These parameters are of concern to aquatic life because salt content regulates the balance of water flowing in and out of a cell through osmosis and therefore relates to a primary biological factor and adaptability mechanism for fish within the region. This region represents a high value fishery and the fish present have become adapted to the current conditions, but conditions are such that changes to salinity values, including increases from effluent discharges if left uncontrolled would result in alteration of the aquatic ecosystem and preferred native species presence**." (EPA & DEQ, 2003)**

"Weber-Scannell and Duffy give representative research to move from TDS regulatory controls to specific regulations for individual ions, especially in relation to salmonoid species. Currently TDS is the primary means of measuring ionic presence in effluent and natural waters, on average most waters measure 9 ppm sodium and any water greater than 1000 ppm is considered brackish. This values is a cumulative ionic value for TDS also includes ions such as silica, sulfate, bicarbonate, and calcium. Increased TDS and associated salinity have shown shifts in biotic communities, biodiversity limitation, and other acute and chronic developments at various aquatic life stages. Additionally, changes in salinity will not only alter aquatic life but vegetative life near the aqueous area as well. Shifts can go as far as altering the ecosystem of the impacted area, altering delicate balances that once existed. That said each species of aquatic life or vegetation has its own specific limitation as to the amount of variance it can tolerate in ionic concentration alterations. This specific study performed a comprehensive literature research to determine existing recommendations concerning ionic concentration exposure as well as identify gaps in the process of identifying ionic specific regulatory standards.

Results concerning the species studies showed high variability in tolerance over differing life stages, and found that developed fish or in some early developing stages increased TDS showed no adverse effect, that being said significant evidence showed increased mortality rates on species during fertilization resulting in highly increased mortality rates for eggs exposed to TDS ranges from 1875 – 2500 ppm. Other studies found that the Lowest Observed Effect Concentration to start at around 254 ppm. The lowest concentration of sodium chloride with adverse effects was found to be around 735 ppm for zooplankton aquatic species reported by Hooke et al. The primary findings from this exercise was that regulatory issues have many hurtles given the wide range of species both biotic and aquatic that have to be addressed. There are three modes of addressing this situation: 1) set a standard low enough to protect all species at all stages of development, 2) set a standard to protect most species against most ions and combinations of ions, 3) set differing limits for differing combinations of ionic species. One cannot only look at ion specific regulations all the time, since often effects are additive for certain ionic species, regulations have to cover cumulative aquatic and biotic effects as well as address such issues as bio-concentration/accumulation. It was determined that approach 1 may be overly restrictive, 2 may leave gaps in regulations and adversely impact species, while 3 was determined to be the most comprehensive but conversely the most complicated to institute. (Weber-Scannell & Duffy, 2007) Approach 3 becoming the way of the future, from a regulatory standpoint. More often industrial discharges are being required to conduct site specific studies to determine the presence of aquatic and biotic species as well as threshold concentrations for adverse impacts. Subsequent permit regulations are based on these studies. Therefore, regulatory scope is going from set standards for all impacted waters to site specific effluent standards based on site specific conditions. Both costly and time consuming but may provide added benefit if the discharger can prove that widespread standard is too stringent and in fact the receiving waters can accept a greater level of impact than was previously thought.

A study performed by **Clearwater et al, in 2002** had many highlights to add to the conversation on water quality in the Powder River basin and one can draw subsequent conclusions. Water quality significantly varies across the state of Montana, for example Powder River surface waters are significantly more saline than others such as the Tongue to Little Powder River, or those in entirely different basins/watersheds. That further reinforces the approach to regulatory affairs being a case-by-case basis for effluent dischargers as opposed to a widespread set standard. In addition to the surface water differing, produced waters from various wells differ depending on geography, which leads one to conclude that, although the geology of the area is said not to show any correlation. The groundwater is such that consistent water quality is not guaranteed and process water for any operation drawing from these aquifers would be cause for concern in reference to the associated salinity and impacts or treatment that would be needed.

Surface water sources have relatively high benchmark water quality characterised by low-salinity values, important as a viable habitat for salmonid species. In reference to testing species, it was found that effluent discharges to these water bodies may negatively impact aquatic species through the increase of salinity to that of lethal dosage. Another parameter that could negatively impact native species is the abatement of seasonal water flow and quality. In essence, native aquatic species are accustomed to seasonal changes in flow patterns and therefore have adaptable mechanisms, increased effluent discharge would tend to stabilise flow in receiving water bodies and effectively remove these seasonal variances. With their removal, no longer are native species adaptively competitive and non-native species can now move in and compete directly. This leads to other subsequent changes, including the reorganization of the aquatic ecosystems hierarchy and loss of native species.

Characteristic surface waters in the Powder River basin, specifically those close to the Montana-Wyoming border, show high levels of conductance and salinity, linked primarily to a high sodium concentration (300 ppm), chloride concentration (210 ppm), and sulphate concentration (810 ppm). This characteristic salinity tapers off in other surface waters downstream, going from a conductivity measurement of 2480 uS/cm to around 450 uS/cm. In general the study summarises the water quality trend as follows:
"Conventional wisdom is that product water quality differs significantly across the PRB. The general trend is thought to range from so-called "drinking-water quality" in the southeast portion of the basin to more saline, non-potable waters in the northwest portion of the basin. Below we test that conventional wisdom using four datasets from a variety of sources." **Weber-Scannell and Duffy**

The study further went on to recommend preferred methods of aquatic impact characterisation, given the unique characteristics of the parameters to be looked at and the Powder River Basin itself. The first recommendation uses a common biological evaluation test for fresh water quality. Daphnia magna, D. Pulex, and Ceriodaphnia dubia, along with fish species of fathead minnow, rainbow trout, and brook trout are recommended for use due to their ability to give characterisation because of their natural sensitivity to the proposed pollutants. A second approach would capitalise on the nearly 32 species of fish and 19 species of aquatic invertebrates to conduct an in-situ study, but was noted that this method would pose difficulty because of its underdeveloped procedures as compared to the first method. Lastly, a statistically vigorous in-situ testing method developed by O'Neil and Harris was proposed for the area. This method focuses on comparison of in-situ specimens from both pre-discharge and post discharge condition to determine the relative response to effluent concentrations and pollutant constituents.

A study looking at mining operations in Appalachian Coal Fields highlights other important considerations when examining toxicity impacts due to effluent discharges. One cannot look at control from an individual ion perspective, interplay, which is still as of yet largely not understood, must be considered. Cumulative impacts of simultaneous operations should be considered. As was shown above in the examination of the Powder River basin by USGS the interconnectivity of tributaries and their cumulative toxicity, especially concerning specific conductance and sodium adsorption ratios is enough to warrant concern. **(EPA 2009)** Therefore leaving control of ionic species including sodium in the realm of non-degradation policy may constitute the best approach to controlling and mitigating impacts due to increased sodium concentration discharge into receiving water for Montana.

The primary purpose of the development of this section was to highlight current regulatory trends and the purpose of phase two of the project for removal of sodium from eastern Montana coals. If current trends in the Appalachian region are any indicator of where regulations are going, then Montana will soon start to institute more stringent reviews of how it handles effluent discharges and consequently sodium presence. Much of the discussion above focused on CBM produced waters and effluents related to mining operations. This was mainly because these areas have the most widely available information regarding effluent discharges and regulation when it comes to sodium presence. Whether the discharge is coming from the mine or from the coal fired power plant, effluent criteria will still have to be met. It is likely that Montana will continue to control, at-least for the time being, sodium through narrative standard enforcement and widespread application of whole effluent toxicity characterisation. Given eastern Montana's dependence on irrigation water, the effluent toxicity parameters may be expanded to include analysis and testing to determine site specific discharges that will not degrade soil stability or crop yields as well. Therefore it is only prudent to have a plan of action concerning abatement of the impacts due to sodium treatment options and the subsequent effluent discharges.

The next part of this document is to provide an overview of current technologies that may prove to be avenues to treat process waters. It has to be noted that there are sections within this part that are still to be researched and filled in, but once completed should provide comprehensive overview of the state of salt treatment technologies.

Water Treatment Technologies

A detailed description of water treatment technologies are summarized by **Dudley in his Master of Science Thesis (2011).** Detailed descriptions of the various technologies are beyond the scope of the present literature review. The reader is encouraged to use the Dudley reference as a guide to the literature covering this topic. A brief list of the technologies discussed by Dudley are presented here and include:

"Distillation/Thermal Technologies-The basic principle of the distillation process relies on the fact that when a solution containing salt components is boiled the salt itself will remain in solution, subsequently the vapour that is produced can be taken from the system and condensed as a pure water source, in essence containing none of the previous salts.

According to examination of the distillation process by the Bureau of Reclamation the main factor that drives design of distillation processes, as with any process design, is cost. However, distillation processes are heat transfer processes and therefore can become quite energy intensive. The optimal design component is to build a system that efficiently transfers heat and provides an economical clean water source. Another component that is often capitalized on is the adjustment of pressures at which the source is treated, this will be discussed further below. With this in mind there are primary technologies that are worth discussing within the topic of distillation processes. These include multi-effect distillation, multi-stage flash distillation, and vapour compression. A paper published by Younos

and Tulou included a brief summary table of information collected from published works of El-Dessouky and Ettouney **(Younos & Tulou, 2005).**

Table 2. Summary of processes of typical thermal technologies

Technology	Brief Description – Advantages and Disadvantages	Feedwater
Solar Distillation(SD)	A pond of saltwater with a clear lid takes advantage of solar heat. The saltwater evaporates and condenses on the lid. The brine stays in the pool and condensation forms potable water Low energy costs, low material and equipment costs / requires large amounts of land and direct sunlight, low productivities	SW/BW
Multistage-Flash	Combination of many flashing stages. One flashing stage: Saltwater traveling through tubes is cooler than the vapor surrounding the tubes. Heat exchange preheats the saltwater. The saltwater is emptied to the brine pool, where it evaporates and fills the vapor space that preheats the incoming saltwater. The vapor is condensed to form potable water, and the brine becomes the feed water for the next stage Proven reliable for years, can operate using waste thermal energy, can handle large capacities / requires highest amount of energy of all technologies	SW
Multiple Effect Evaporation(MEE)	Combination of many effects. One effect: Saltwater is sprayed overtop of hot tubes. It evaporates and the vapor is collected to run through the tubes in the next effect. As the cool saltwater is sprayed over the vapor filled tubes, the vapor condenses and is collected as potable water. The resulting brine collects in the bottom of each effect, and is either circulated to next effect or exited from system Requires less energy than MSF, can operate using waste thermal energy, can handle large capacities / high amounts of energy, scaling on tubing	SW
Thermal Vapor Compression(TVC)	Works as first effect of multiple effect evaporation. The steam jet ejector is used to compress the vapor for the tubes in the first effect. A condenser is responsible for condensing the vapor to the final productIncreases MEE performance ratio when combined with MEE.	SW
Mechanical Vapor Compression(MVC)	Works the same as thermal vapor compression except that mechanical compressors are used instead of steam jet ejectors Meet needs in remote areas, transportable.	SW/BW
Adsorption Vapor Compression	Pressure differences occur between two tanks as a fluid mixture is transferred between them. This drives the heat exchange for evaporation and condensation of saltwater to form potable water Heat is released from an exothermic reaction between blending of feed water with a solution such as LiBr, which preheats the feed water that is sent to the evaporator	SW/BW

Sources: El-Dessouky and Ettouney 2002, El-Dessouky et al. 2000

Membrane Processes-In a paper by **Younos and Tulou (2005)** the following was included by reference from Duranceau and summarises the major details concerning established membrane processes.

Table 1. Characteristics of Applications of Pressure-Driven Membrane Processes

Membrane Process	Applied Pressure psi (kPa)	Minimum Particle Size Removed	Application (type, average removal efficiency %)
Microfiltration	4-70 (30-500)	0.1-3 µm	- Particle/turbidity removal (>99%) - Bacteria/protozoa removal (>99.99 %)
Ultrafiltration	4-70 (30-500)	0.01-0.1 µm	- Particle/turbidity removal (>99 %) - Bacteria/protozoa removal (>99.999 %) - TOC removal (<20%) - Virus removal/(partial credit only)
Nanofiltration	70-140 (500-1000)	200-400 daltons	- Turbidity removal (>99%) - Color removal (>98%) - TOC removal (DBP control) (>95%) - Hardness removal (softening) (>90%) - Synthetic organic contaminant (SOC) removal (500 daltons and up) (0-100%) - Sulfate removal (>97%) - Virus removal (>95%)
Hyperfiltration (Reverse Osmosis)	140-700 (1000-5000)	50-200 daltons	- Salinity removal (desalination) (>99%) - Color and DOC removal (>97%) - Radionuclide removal (not including radon) (>97%) - Nitrate removal (85 to 95%) - Pesticide/SOC removal (0 to 100%) - Virus removal (>95%) - As, Cd, Cr, Pb, F removal (40 to >98%)

Source: Duranceau 2001

Representing the forefront of both development and implement of desalination technologies, membrane separation technologies (especially that of RO) are a growing trend in systems being implemented for purification of process waters. Future improvements are those that can be made to the membranes and those that can be made to the category of energy efficiency. Membrane improvements need to focus on increased life resistance to fouling mechanisms, and ability to handle increased flux rates with lower pressure differentials. Energy efficiency improvements are intended to discover opportunities for energy recovery and decreased polarisation phenomena. ***(MIT OpenCourseWare 2009, included by reference Miller, 2003*)**

Membrane Distillation

Emerging as an alternative to reverse osmosis, membrane distillation can be characterised by the following: 1) porous membrane, 2) non-wetted process membrane, 3) pores of membrane lack capillary condensation, 4) vapour-liquid equilibrium is not altered by membrane, 5) at least one side of the membrane contact process flow, 6) partial pressure gradient is the driving force for operation. This partial pressure gradient is supplied in a variety of ways: direct contact – the condensation side of the membrane is occupied by a flowing solution, air gap – air occupies the space between the membrane and the condensation surface, sweeping gas – gas flows on the opposing membrane side and removes vapour while maintaining vapour pressure gradient, Vacuum – an applied vacuum atmosphere provides the necessary gradient. Regardless of how the gradient is maintained, water vapour migrates across the hydrophobic membrane and is subsequently removed and condensed on the permeate side leaving behind dissolved ions as they cannot or are unlikely to migrate with the vapour. This process has the ability to completely reject ionic impurities. This technology has the propensity to increase water recovery, but also increase energy costs and has few opportunities to integrate energy capture and

recycle. Research concludes that many hurdles need to be overcome to make membrane distillation a viable technology, especially for large scale application. **(Evans & Miller, 2002)**

Nano filtration

Nano filtration is typically only applicable to remove low concentrations of dissolved solids or salts, but cannot operate at large salt concentrations because the larger pore size that characterises Nano filtration membranes and allows it to operate at lower pressures than traditional reverse osmosis processes is not sufficient at treating high salt content brine. **(Younos & Tulou, 2005)**

Pervaporation Proceses

Ion Exchange Membranes/Resins-Using solid materials, ion exchange will purify process waters by preferentially absorbing desired constituents and at the same time releasing another constituent to take its place. In essence displacement is the primary treatment driver, entrapping the constituent of concern for a less harmful substance. Resins or membranes can be designed for specific constituents, but is a costly process and therefore has not been widely implemented in industry. A process known as the Surotherm process aimed to make the economics of such systems more attractive by using weakly basic and acidic exchangers capable of being regenerated by relatively low-cost moderately-hot water. It was proven to be successful in treating waters by reducing 2000 ppm brine by 75%, but large scale economics are still prohibitive. **(MIT OpenCourseWare 2009, included by reference Miller, 2003)**

Reverse Osmosis-relies on the principles of chemical equilibria. When two solutions, one without salt and the other a concentrated salt solution, are put into contact with each other the system will work to equilibrate. Reverse osmosis uses this principle known as osmotic pressure coupled with a semi-permeable membrane system to provide a source of purified water. Applying pressure greater than the osmotic pressure, or pressure at which no net migration of water takes place through the membrane, to the salt feed solution provides a motive force for the migration of purified product water across the membrane and out of the system. Salt migration across the membrane will still occur, but with optimized settings, salt migration can be minimized.

In addition to the pressure component of such a system there are other components or factors that mitigate salt transfer through the membrane, these include: 1) as a salts valence structure increases so does its rejection to movement through the membrane (i.e. higher valence salts have higher hindrance), 2) the higher a salts molecular size the higher the rejection, 3) the higher a salt binds (bond strength) with hydrogen the smaller the rejection, 4) dissolved gases. Generally two common types of membranes are employed in RO processes, Cellulose Acetate and non-cellulose acetate membranes. Cellulose acetate membranes are thought to be resistant to fouling due to their relatively smooth nature. Non-cellulose acetate membranes are more applicable to large scale water systems and can be used in a more broad range of PH waters, but allow breakthrough of lower salt concentrations and are highly susceptible to chlorine content. (**Younos & Tulou, 2005)**

A modification of the reverse osmosis process was developed as a response to effluent mine waters in Africa. This modification known as the SPARRO, Slurry Precipitation and Recycle Reverse Osmosis process is a form of seeded reverse osmosis (SRO). SRO was developed by a Seattle based company in the 1970's and involves the introduction seed crystals within the RO

system to serve as agglomeration sites for constituents as their solubility limits are exceeded in concentrating brine in the RO process. Preferential agglomeration on the crystals extends the life and efficiency of the membranes. SPARRO is simply an extension of the SRO process with modifications including lowered linear velocity to reduce energy consumption, lower seed concentrations to reduce wear on pumps, use of tapered membrane stacks to improve efficiency, separated seed crystal and brine blow down systems for increased process control. SRO is seen as a primary alternative for waters that are prone to fouling. (Juby & Shutte, 2000)
RO is used for brine water ranging from 100 to 1000 ppm, but the widespread development of membranes, and even tailored membranes, means that for a price RO can be integrated to a wider range of applications. **(Office of Technology Assessment – US Congress, 1988)**

Pre-treatment is typically integrated in RO processes to eliminate fouling possibilities from suspended solids and is usually followed by post treatment to ensure proper pH and degassing of waters. Disadvantages of RO systems include the fact that they are typically only applicable to low salinity waters and are expensive in relation membrane costs. **(Wardeh, ND)**

Electro-dialysis (Electro-dialysis Reversal) Process-Electro dialysis integrates anion and cation selective membrane with the application of DC current generating an electric field to remove ionic constituents. Unlike other distillation technologies ED is only successful at removing ionic constituents. The general process consists of brine being fed into channels with the application of the voltage across the cell. Ionic interaction with membranes leads to concentration of anions and cations in separate along with channels of purified water. A stack or cell consists of hundreds of these alternating channels and therefore to increase efficiency separation is done in a series of successive steps. As a design parameter ED also has a correlation between removal efficiency and concentration, in short the higher the concentration the higher energy required to treat the process water. ED is subject to fouling, same as reverse osmosis membranes are, and therefore influent usually requires pre-treatment. ED can treat higher concentration process waters in reference to suspended solids than reverse osmosis because lack of flow of water entraining fouling constituents on membrane surfaces (no flow across membranes). None-the-less fouling will occur, to try and combat this electrodialysis reversal was developed. EDR effectively reverses polarity of the applied electric field, this results in the switch from fresh water channels to ionic channels and allows the fouling constituents to be flushed**. (MIT OpenCourseWare 2009, included by reference Miller, 2003)**
The following conclusions were presented in an openware course offered by MIT covering the subject of electro membrane processes (MIT OpenCourseWare, 2009):

- Electrodialysis is a mature process used mainly for water desalination, brine concentration, demineralization of food products and treatment of industrial effluents
- Membrane and membrane stack production costs must be reduced
- The use of electro membrane processes is changing from conventional electrodialysis to hybrid processes and catalytic reactors with specific industrial applications
- Donnan-and diffusion-dialysis serve presently only small market segments and piezodialysis and reverse electrodialysis are still highly uneconomicalLife analysis is needed for components in and EDR system. Typically, electrode will need to be replaced every 2-3 years, and membranes will last around 10 years if proper techniques are undertaken to prevent scaling and fouling.

Electrodialysis units are successful at treating waters with high sodium and chloride contents because of the relative attractive forces that these ions experience when electrical current is

applied to the stack membrane unit. Electro dialysis has high treatment efficiency from 75-98%, but not as consistently high as electrodialyiss reversal, which alternates current to force alteration of water/ionic equilibria flow. This reversal serves to increase circulation an deduced membrane fouling, increasing lifespan. Both technologies are able to withstand a range of pH conditions and can treat relatively high salt content waters**. (Younos & Tulou, 2005)**

Table 3. Summary of processes of desalination technologies under research and development

Technology	Brief Description – Advantages and Disadvantages	Feedsource
Electrodeionization(EDI)	EDI is a combination of ion exchange and electrodialysis. Electric charge is applied to plates outside of membranes with resin beads between them. Saltwater passes between membranes. Saltwater ions take place of ions on resin then are pulled out through membranes in front of electrically charged plates. Water passes through resin and is free from ions, thus producing purified water Can produce ultra-pure water	BW
Membrane Distillation(MD)	A temperature difference occurs on opposing sides of the membrane. Differences in vapor pressure drive the system and only vapor passes through the membrane. Salt is not vaporized so it cannot pass through pores Requires high amounts of energy / not fully developed	Researched using 15,000-300,000 mg/L TDS
Freeze Separation(FS)	Freezing of saltwater forms pure water ice crystals, which have to be separated from brine and then melted to get potable water Less energy required than evaporation techniques / not fully developed	SW
Capacitive Deionization(CDI)	Salt water passes through plates coated with carbon aerogel material. Carbon aerogel absorbs ions, thus producing potable water Applicable to special needs / not fully developed.	BW
Rapid Spray Evaporation(RSE)	Saltwater is sprayed through nozzles at high velocity. As it exits, it is vaporized and salt is not, thus producing potable waterPotential to process brine and high salinities, can use waste energy, high recovery / not used for large applications	Brine/SW/BW
Freezing With Hydrates(FH)	A saltwater vapor/gas mixture is cooled. Hydrates are formed and separated from the brine. Hydrates are decomposed to form potable water and the hydrate former gasPotential for future use because of research of hydrates developing / still being researched and not developed	SW
Vacuum Distillation(VD)	By subjecting saltwater to vacuum, the boiling temperature is reduced. Saltwater is vaporized at lower temperatures and is condensed to form potable waterLow amounts of energy, ability to run off of waste energy, no scaling because of low temperatures / being researched and not developed	Researched using 32,100 mg/L TDS

Sources: El-Dessouky and Ettouney 2002, El-Dessouky et al. 2000

Other/Developing Technologies-Various technologies are being developed when it comes to salt removal from water feedstock. The following technologies are currently being researched and may be possible development avenues for treatment technologies. They have various benefits over the standard technologies previously mentioned, including greater throughput and lower energy requirements. Once again Younos and Tulou included a summary table of developing technology congregated from information from the works of El-Dessouky and Ettouney, of which more details are provided in the paragraphs below**. (Younos & Tulou, 2005).**

Although these technologies are being developed, there remain hurdles to their widespread implementation including: solids handling, efficiency issues, inability to handle increased volumes, resources being given to development of improvement of more mainstream technologies such as RO. **(MIT OpenCourseWare 2009, included by reference Miller, 2003)**

BIBLIOGRAPHY

Access Science by McGraw Hill, LA 7/12/2009, Ion Exchange, http://www.accessscience.com.mtproxy.lib.umt.edu:3048/content.aspx?id=351600&searchStr=electrodialysis#searchTerm

Access Science by McGraw Hill, LA 7/12/2009, Water Desalination, http://www.accessscience.com/content.aspx?id=598900

Alvarez, R., C. Clemenie, D. Gomez-Limon, 1997, Environmental Science Technology, 31, 3148.

Ambient, Commissió de Medi, Associació d'Enginyers Industrials de Catalunya, Dario Breschi, 2005, Paper prepared for the meeting "Jornada sobre la dessalació d'aigües"

American Coal Foundation, 2007, All About Coal, Coal Reserves, Washington, DC, Website: www.teachcoal.org.

American Standards for Testing Materials (ASTM), 2000, Gaseous Fuel, Coal and Coke, ASTM, Philadelphia, PA, Vol. 05.06, 600p.

Aqua Chem, Inc, LA July 2010, Theory of Operation, Multi Effect Spray Film Evaporator, Once Through System, Technical Bulletin 750-1037, http://sections.asme.org/milwaukee/history/40-EvaporatorTheory.pdf

AquaChem, Inc, LA July 2010, Theory of Operation, Multistage Flash Evaporator, Once Through System, Technical Bulletin 750-1007, http://sections.asme.org/milwaukee/history/40-EvaporatorTheory.pdf

ARM, LA 2010, Administrative Rules of Montana 17.30.670, NUMERIC STANDARDS FOR ELECTRICAL CONDUCTIVITY (EC) AND SODIUM ADSORPTION RATIO (SAR)

Baker, G.G., R.E. Sears, D.J. Maas, T.A. Potas, W.G. Wilson, S.A. Farnum, 1985, Technical report DOE/FE/60181-133 for presentation at Newer Coal Technologies: Implications for Energy and Development Policies in Asia and the Pacific Conference, Honolulu, Hawaii, April.

Banat, Fawzi, June 2007, Economic and Technical Assessment of Desalination Technologies (Presentation), Economic and Technical Assessment of Desalination Technologies, http://www.desline.com/Geneva/Banat.pdf

Barnstead informational pamphlet, No Date Presented, What is Reverse Osmosis?

Bartels, M., W. Lin, J. Nijenhuis, F. Kapteijn, J. Ruud van Ommen, 2008, Agglomeration in fluidized beds at high temperatures: Mechanisms, detection, and prevention, Progress in Energy and Combustion Science, 34, 633-66.

Benson, S. A., P. L. Holm, 1985, Comparison of inorganic constituents in three low-rank coals, Ind. Eng. Chem. Prod. Res. Dev. 24, 145-9.

Blytas, GC., FJ. Trogus, 1987, Reduction of sodium in coal by water wash and change with a weak electrolyte, US Patent, 4,705,530.

Bou-Raad, M., M.D. Hobday, C.J. Rix, 2000, Aqueous extraction of oxalate and other anions from coal, Fuel, 79, 1185-93.

Bragg, L.j., JK. Oman, SJ. Tewalt, SL. Oman, NH. Rega, PM. Washington, RB. Finkelman, 1998, Coal Quality (COALQUAL) Database: Version 2.0. U.S. Geological Survey (USGS), Open File Report, 97-134 (2009). Website: http\\energy.er.usgs.gov/products/databases/coalqual/intro.htm.

Brinck, E., C. Frost, 2009, Evaluation of amendments used to prevent sodification of irrigated fields, Applied Geochemistry – Elsevier, http://faculty.gg.uwyo.edu/cfrost/pdfs/2009%20Brinck%20and%20Frost%20ApGeoch.pdf

Brown, LD, 1983, Fluidised bed gasification of Carbonaceous Solids - with Alumino- or Magnesium Silicate addition to Inhibit ash sintering, EP Patent 88194-A.

Bruckard, WJ., JT. Woodcock, R. Williams, 2008,Sodium chloride removal from Lake Phillipson low rank coal by aqueous leaching, Proceedings: XXIV International Mineral Processing Conference, September 24-28, 2008 Beijing, China, p 1908-17. W.J. Bruckard (warren.bruckard@CSIRO.com).

Buader, RM Waskom, JG Davis, March 2007, Irrigation Water Quality Criteria (no. 0.506), Crop Series – Irrigation, Colorado State University, http://www.ext.colostate.edu/pubs/crops/00506.pdf

Budhiraja, Parmod and Asma Ahmed Gares, 2008, Studies of scale formation and optimization of anti-scalant dosing in multi-effect thermal desalination units, Presented at the conference on Desalination and the Environment. Sponsored by the European Desalination Society and Center for Research and Technology Hellas (CERTH), Sani Resort, Halkidiki, Greece, April 22–25, 2007

Butt, F.H., A.G. Maadhah, F. Rahman, and U. Baduruthamal, November 1994, Relative Energy Consumption of Reverse Osmosis and Multi-Stage- Flash Desalination Processes, Proc. Second Saudi Symposium on Energy Utilization and Conservation, KFUPM, Dhahran, Saudi Arabia

CAMP, 2009, Center for Advanced Mineral and Metallurgical Processing, Montana Tech of the University of Montana, Butte, Montana. J. McCloskey, Director, jmccloskey@mtech.edu, Website: www.Mtech.edu\camp.

Carpenter, A.M., 2002, Coal Quality Assessment-the validity of empirical tests, IEA, Clean Coal Centre, p 1-100. CCT, 2009, Clean coal as fuel for turbines, Clean Coal Technology Pty. Ltd, www.australiancoal.csiro.au/pdfs/domazetis.pdf, 8 p.

Chen, Y., N. Shah, f.E. Huggins, G.P. Huffman, W.P. Linak, C.A. Miller, 2004, Fuel Process Technology, 85,743-61.

Creelman, R.A., C.R. Ward, 1996, A scanning electron microscope method for automated, quantitative analysis of mineral matter in coal, International Journal Coal Geology, 30 249-69.

Creelman, R.A., N. Argon-Olshina, P. Gottlieb, 1993, The characterization of coal and the products of coal combustion using QEM*SEM, Final Report, Project 1467, National energy Research, Development and Demonstration Program, Australian Department of Primary Industries and Energy, Canberra, 135p.

Curtin, DJ, 1981, Reduction of the fouling potential of high sodium coal, US Patent, 4268271.

Daavitsainen, J.H., R.S. Laitinen, L.H. Nuutinen, H.J. Ollila, M.s. tiamen, M.E. Virtanen, 2001, Effect of GR granule used as bed material to reduce agglomeration in BFB combustion of biomass with high alkali metal content, In: Progress in Thermofchemical biomass Conversion, IEA Bioenergy, Bridgwater AV, p 705-12.

Dahlin, RS., WW. Peng, M. Nelson, P. Vimalchand, G. Liu, 2006, Formation and prevention of agglomeration deposits during the gasification of high sodium lignite, Energy and Fuels, 20, 2465-70.

Davis, M.B., P.E. Toombs, W.R. Toombs, J. Boyle, G. Hermanas, H. Benisvy, K. Schulz, 2008, Controlling SO_3 Slag and Fouling Resulting in Improved Heat Rates, Better Efficiency and Allowing for Fuel Flexibility - Santee Cooper, Cross Station Case Study, Presented at the EUEC Conference, January 2008, Tucson, AZ, Website: www.ftek.com/technicalPapers.php, paper number TPP-581.

Dawson, Helen, March 2007, Powder River Watershed Stream Water Quality Pre-and Post CMB Development, U.S. EPA, Region 8, Denver, CO, http://www.epa.gov/region8/water/monitoring/TongueRiverReportDraftFinal11Jul2007.pdf

Department of the Interior- Bureau of Reclamation, THE DESALTING AND WATER TREATMENT MEMBRANE MANUAL: A GUIDE TO MEMBRANES FOR MUNICIPAL WATER TREATMENT - Water Treatment Technology Program Report No. 1, U.S., SEPTEMBER 1993

Domazetis, Dr. G., 2009, Clean Coals as Fuel for Turbines, Managing Director, Clean Coal Technology Pty Ltd, Website for download: www.autraliancoal.CSIRO.au/pdfs/domazetis.pdf.

Domazetis, G., BD. James, 2006, Molecular models of brown coal containing inorganic species, Organic Geochemistry, 37, 244-259.

Domazetis, G., M. Raoarun, BD. James, J. Liesegang, 2008, Molecular modeling and experimental studies on steam gasification of low-rank coals catalysed by iron species, Applied Catalysis A: General, 340, 105-18.

Domazetis, G., P. Barilla, B.D. James, R. Glaisher, 2008, Treatments of low rank coals for improved power

generation and reduction in greenhouse gas emissions, Fuel Processing Technology, 89, 68-76.
Domazetis, G., P. Barilla, BD. James, 2009, Lower emission plant using processed low-rank coals, Fuel Processing Technology, Submitted for publication, Website: www.latrobe.edu.au/chemistry/staff/resfellows/domazetis/gdpubs.html
Domazetis, G., S. Buckman, 1987, Fly ash formation during the combustion of brown coal, Vol 3C, Effects of Aluminum Based Additives on Ash Formation, End of Grant Report, State Electricity Commission of Victoria, Research and Development Department, Report No. ND/87/043.
Electric Power Monthly, 2009, Major US Mines, US Energy Information Administration (EIA), Independent Statistics and Analysis (searchable database), Website: www.eia.doe.gov.
EPA, 2009, Drinking Water Contaminant Candidate List (CCL), Sodium in Drinking Water, www.epa.gov/ogwdw/ccl/sodium.html.
European Communities, 2009, Sustainable Agriculture and Soil Conservation, Soil Degradation Processes – Fact Sheet Number 4, http://soco.jrc.ec.europa.eu/documents/ENFactSheet-04.pdf
Evans, Lindsey R. and James E. Miller, January 2002, Sweeping Gas Membrane Desalination Using Commercial Hydrophobic Hollow Fiber Membranes, Sandia National Laboratories, SAND REPORT - SAND 2002-0138, http://prod.sandia.gov/techlib/access-control.cgi/2002/020138.pdf
Falcone, S.K., H.H. Schobert,1986, Mineral transformations during ashing of selected low-rank coals, In: K.S. Vorres, Mineral Matter and Ash in Coal, American Chemical Soc., Washington, DC, 114-17.
Fan, L., WP. Walawender, 1984, Pyrolysis of carbonaceous solids in fluidised bed of quartz sand - using e.g. ground limestone as anti-agglomerant, US Patent 4448589-A.
Farnum, S.A., E.S. Olson, B.W. Farnum, W.G. Wilson, 1980, Characterization of light oils from liquefaction of lignite, Attached paper to Gronhovd, et al (1980); see their reference for source.
Favas, G., W.R. Jackson, 2003, Hydrothermal dewatering of lower rank coals. 2. Effects of coal characteristics for a range of australian and international coals, Fuel, 82, 59-69.
Finkelman, R.B., 1994, Abundance, source, and mode of occurrence of the inorganic constituents in coal, In: Kural, I. (Ed.), "Coal" Instanbul Technical University, 115-25.
Finkelman, R.B., 1994, Modes of occurrence of environmentally sensitive trace elements in coal: In Swaine, D.J., Goodarzi, F. (Eds.), Environmental Aspects of Trace Elements in Coal, Kluwer Academic Publishing, Dordrecht, p 24-50.
Finkelman, R.B., C.A. Palmer, M.R. Krasnow, P.J. Aruscavage, G.A. Sellers, F.T. Dulong, 1990, Combustion and leaching behavior of elements in the Argonne premium coal samples, Energy and Fuels, 4(6), 755-66.
Finkelman, R.B., N.H. Bostick, F.T. Dulong, F.E. Senftle, A.N. Thorpe, 1998, Influence of an igneous intrusion on the inorganic geochemistry of bituminous coal from Pitkin County, Colorado, International Journal of Coal Geology, 36, 223-41.
Gabelich, Christopher J., Fredrick W. Gerringer, John C. Franklin, Junbo Gao, Yoram Cohen,3 and I. H. "Mel" Suffet, 2004, REVERSE OSMOSIS PRETREATMENT: CHALLENGES WITH CONVENTIONAL TREATMENT, 2004 AWWA ACE, Orlando, Florida, http://www.watercenter.ucla.edu/Publications/2004%20AWWA%20ACE%20Gabelich%20Proceeding.pdf
Galbreath, K., C. Zygarlicke, G. Casuccio, T. Moore, P. Gottlieb, N. Agron-Olshina, G. Huffman, A. Shah, N. Yang, J. Vleeskens, G. Hamburg, 1996, Collaborative study of quantitative coal mineral matter analysis using computer-controlled scanning electron microscopy, Fuel, 75, 424-30.
Gesserman, RM., EA. Morrissey, PC. Hackley, 2009, Petrographic web atlas for metallurgical mituminous coal Macerals, Portland Conference-2009 Portland Geological Society of America (GSA), Abstracts, 41 (7), 334.
Gronhovd, G.H., E.A. Sondreal, J.A. Kotowski, G.A. Wiltsee, 1980, Western low-rank coal development analysis, PDF available at Website:

http://www.anl.gov/PCS/acsfuel/preprint%20archive/25_1_HOUSTON_03-80.htm, ACS Fuels Volumes, Spring 1980, SYMPOSIUM ON UTILIZATION OF PEAT AND LIGNITE (III), ACS Meeting Spring, Houston, TX. Also google search Western low-rank coal sodium removal.

Guy, P., G.I. Perry, D.J. Allardice, T. Yoshida, H. Kitanmura, 1992, Proceedings: Fifth Austrasian Coal Science Conf, Melbourne, Victoria, p 103.

Harris, R.L., L.H. Simons, J.J. Iagowski, 1980, Organic structural studies of lignite coal tars, Attached paper to Gronhovd, et al (1980); see their reference for source.

Healy, Richard W., Cynthia A. Rice, Timothy T. Bartos, and Michael P. McKinley, 2008, Infiltration from an impoundment for coal-bed natural gas, Powder River Basin, Wyoming: Evolution of water and sediment chemistry, WATER RESOURCES RESEARCH, VOL. 44, W06424, 16 PP., 2008

Hook, M., K. Aleklett, 2009, Historical trends in American coal production and a possible future outlook, International Journal of Coal Geology, 78 (3), 210-16.

Horpestad, Abe (Montana Department of Environmental Quality), October 2001, Water Quality Analysis of the Effects of CBM Produced Water on Soils, Crop Yields and Aquatic Life, MDEQ, http://deq.mt.gov/CoalBedMethane/pdf/Criteria-sar-EC-h.pdf

Huang, H.H., 2009, Stability Calculations (STABCAL), Software, Metallurgical and Materials Engineering Department, Montana Tech of the University of Montana, Butte, MT, hhuang@Mtech.edu.

Huggins, F.E., 2002, Overview of analytical methods for inorganic constituents in coal, International Journal of Coal Geology, 50, 169-214.

Huggins, F.E., G.P. Huffman, 2006, Comment on and addenda to "Arsenic in Coal: A Review" by Yudovich and Ketris, international Journal of Coal Geology, 66, 148-50.

Hulston, J., G. Favas, A.L. Chaffee, 2005, Physico-chemical properties of Loy Yang Lignite dewatered by mechanical thermal expression, Fuel, 84, 1940-8.

Hycnar, J., K. Rondio, M. Sciazko,, 1994, Tests on demineralization of high sulfur steam fines in TRW Gravimelt process, The 12th International Coal Preparation Congress, 425-31.

ICPC, 2110, XVI International Coal Preparation Congress, Lexington, Kentucky, April 26-29.

Jangbarwala, Juzer, December 2007, CBM-Produced Water – A Synopsis of Effects and Opportunities, Water Conditioning & Purification, http://www.wcponline.com/pdf/0712Jangbarwala.pdf

Johnston, Christopher R., George F. Vance b, Girisha K. Ganjegunte, November 2008, Irrigation with coalbed natural gas co-produced water, Agricultural Water Management, Volume 95, Issue 11, Pages 1243-1252

Juby, GJG and CF Schutte, April 2000, Membrane life in a seeded-slurry reverse osmosis system, Division of Water Utilisation Engineering, Department of Chemical Engineering, University of Pretoria, Pretoria 0002, South Africa, http://www.wrc.org.za/Knowledge%20Hub%20Documents/Water%20SA%20Journals/Manuscripts/2000/02/WaterSA_2000_02_1171.pdf

Kamali, R.K. *, A. Abbassi, S.A. Sadough Vanini, M. Saffar Avval, 2008, Thermodynamic design and parametric study of MED-TVC, Desalination, Volume 222, Issues 1-3, 1 March 2008, Pages 596-604, European Desalination Society and Center for Research and Technology Hellas (CERTH), Sani Resort 22 –25 April 2007, Halkidiki, Greece, European Desalination Society and Center for Research and Technology Hellas (CERTH), Sani Resort

Kamali, Ramin K., S. Mohebbinia, 2007, OPTIMIZATION OF THE TUBE SIZE AND THE ARRANGEMENT OF EVAPORATOR TUBE BUNDLE TO IMPROVE THE PERFORMANCE OF MED-TVC SYSTEMS, Eleventh International Water Technology Conference, IWTC11 2007 Sharm El-Sheikh, Egypt, http://www.water-observatory.net/sources/iwtc2007/4-7.PDF

Ketris, MP., YE. Yudovich, 2009, Estimations of Clarkes for carbonaceous biolithes: World averages for trace element contents in black shales and coals, International Journal of Coal Geology, 78, 135-48.

Kinding, J.K., J.E. Reynolds, 1987, Integrated coal cleaning process with mixed acid regeneration, US patent

4695290.
Koch Membrane Systems, 2009, System Information, http://www.kochmembrane.com/
Kosminski, A, D.P. Ross, J.B. Agnew, 2006b, Transformations of sodium during gasification of low-rank coal, Fuel Processing Technology, Volume 87, 1051-1062,
Kosminski, A., D.P. Ross, J.B. Agnew, 2006a, Reactions between sodium and kaolin during gasification of a low-rank coal, Fuel Processing Technology, 87, Pages 1051-1062,
Kyi, S., BL. Chadwick, 1999, Screening of potential mineral additives for use as fouling preventatives in Victorian Brown Coal combustion, Fuel, 78(7), 845-55.
Ledger, RC., 1989, Short term combustion tests using additives, State Electricity Commission of Victoria, Research and Development Department, Report No. SO/89/158.
Lenz, M., P. N. L. Lens, 2009, The Essential Toxin: the changing perception of selenium in environmental sciences, Science of the Total Environment, 407, 3620-33.
Li, Y.F., 1990, MSc Thesis, University of Alaska, Fairbanks, Alaska.
Li, Y.F., 2009, Influence of chemical structure and hydrogenated-coal-liquefaction, International Conf on Coal Science and Tech (ICCS&T), Oct 26-29, Cape Town, South Africa.
Li, Z., C.R. Ward, L.W. Gurba, 2007, Occurrence of non- mineral inorganic elements in low-rank coal macerals as shown by electron microprobe element mapping techniques, International Journal of Coal Geology, 70, 137-49.
Lignite Energy Council, 2009, Mines/Plants, Website: www.Lignite.com.
Lindner, ER., A. Kosminski, C. Taylor, RG. Williams, May 1988, Effects of additives on fouling behavior characteristics of South Australian Brown Coal, Proceedings of Australian Coal Science Conference, B2:11.1-11.14.
Linjewile, TM., AR. Manzoori, 1999, Role of additives in controlling agglomeration and defluidization during fluidized bed combustion of high-sodium, high-sulphur low rank coal, Impact of Mineral Impurities in Solid Fuel Combustion, 319-31.
Liu, Clark C.K. and Krispin Fernandes, No Date Present, Wind and Solar Energy Driven RO Brackish Water Desalination, University of Hawaii at Manoa
Lloyd, R., M.J. Turner, 1986, Method for the continuous chemical reduction and removal of mineral matter contained in carbon structures, Worldwide Patent, WO 86/04917.
Lowe, AJ. DJA. McCaffrey, DG. Richards, 1993, Fuel Process Technology, 36, 47-53
Mabrouk, AA, AS Nafey, HES Fath, 2007, Analysis of a new design of a multi-stage flash –mechanical vapour compression desalination process, Desalination, Volume 204, Issues 1-3, 5 February 2007, Pages 482-500, EuroMed 2006 - Conference on Desalination Strategies in South Mediterranean Countries
Matsuoka, K., E. Rosyadi, A. Tomita, 2002, Mode of occurrence of Calcium in various coals, Fuel, 81, 1433-38.
Matsuoka, K., T, Yamashita, K. Kuramoto, Y. Suzuki, A. Takaya, A. Tomita, 2008, Transformation of alkali and alkaline earth metals in low rank coal during gasification, Fuel, 87, 885-93.
McCloskey, J., L.G. Twidwell, P. Miranda, C. Young, D. Cameron, S.Dudley, B. Pascoe, 2010, Enhancement of Montana coal, sodium removal technology evaluation and development, XVI International Coal Preparation Congress, Lexington, Kentucky, April 26-29.
Miller, D.J., J.K. Olson, H.H. Schobert, 1980, The dissolution of lignite in anhydrous liquid ammonia, Attached paper to Gronhovd, et al (1980); see their reference for source.
Miller, R. N., P. H. Given, 1978, A geochemical study of inorganic constituents in some low rank coals', Pennsylvania State University, Report PSU-TR-IL, USDOE, Coal Research Section, 314p.
Miller, R. N., P. H. Given, 1986, The association of major, minor, and trace elements with lignites: 1 Experimental approach and study of a North Dakota lignite, Geochimica et Cosmochimica Acta, 50, 2033-43.A geochemical study of inorganic constituents in some low rank coals', Pennsylvania State

University
Miranda, P., 2009, Mineral Liberation Analysis applied to Montana Low-Rank coals, Center for Advanced Mineral and Metallurgical Processing (CAMP), Montana Tech of the University of Montana, Butte, MT, pmiranda@Mtech.edu.
Mittelman, Gur, Ornit Mouchtar, Abraham Dayan, 2007, Large-Scale Solar Thermal Desalination Plants: A Review, Heat Transfer Engineering, http://www.informaworld.com/smpp/content~db=all~content=a780836700~frm=titlelink
Mohammadia, Toraj, Mohtada Sadrzadehb, Ahmad Mohebb, Amir Razmia, 2005, ZINC ION REMOVAL FROM WASTEWATER BY ELECTRODIALYSIS, Ninth International Water Technology Conference, IWTC9 2005, Sharm El-Sheikh, Egypt
Montana Bureau Mines and Geology (MBMG), Personal Communications with J. Gungerson, Montana Tech of the University of Montana, Butte, MT, Website: www.mbmg.Mtech.edu
Montana Coal Council, 2009, Working for the coal industry of montana, Helena, MT, Website: www.Montanacoalcouncil.com.
Montana Means Business, 2009, Website: www.business.mt.gov/docs/Coal.pdf.
Mora Associates - Wagner, Linda, December 2007, Water Desalination – Tap into the Liquid Gold, Research Report , http://www.moraassociates.com/publications/0712%20Water%20desalination.pdf
Morgan, M. E., R. G. Jenkins, P. L. Walker, Jr, 1981, Inorganic constituents in American lignites, Fuel, 60, 189-93.
Morgan, M.E., R.G. Jenkins, P.L. Walker, 1980, Analysis of the inorganic constituents in American lignites, Attached paper to Gronhovd, et al (1980); see their reference for source.
Morimoto, M., H. Nakagawa, K. Miura, 2008, Hydrothermal extraction and hydrothermal gasification process for brown coal conversion, Fuel, 87, 546-51.
MRCB, 2008, Montana Research & Commercialization Board Awards $2.3 Million for Biotechnology, Wireless Communications, Clean Coal & Renewable Resources, Production Agriculture, & Environmental Remediation, Montana Associated Technology Roundtable, October 7, 2008, Website: www.MATR.net/article-31008.html.
Mukherjee, S., P.C. Borthakur, 2001, Effect of leaching high sulphur subbituminous coal by potassium hydroxide and acid on removal of mineral matter, Fuel, 80, 2037.
Mukherjee, S., P.C. Borthakur, 2003, Effect of leaching high sulphur subbituminous coal by potassium hydroxide and acid on removal of mineral matter and sulphur, Fuel, 82, 783-8.
Musich, MA., CM. Anderson, RA. DeWall, 1992, Benefication of low-rank coals, Final Technical Progress Report for Period April 1986 to December 1992, USDOE, Pittsburg Energy Technology Center, Cooperative Agreement with Energy and Environmental Research Center, University of North Dakota.
Mwabe, PO., JOL. Wendt, 1996, Mechanisms governing trace sodium capture by kaolinite in a downflow combustor, Twenty-Sixth International Symposium on Combustion/The Combustion Institute, p2447-53, Authors-Department of Chemical and Environmental Engineering, University of Arizona, Tucson, AZ
Myers, James E., Kathryn M. Hogan and John M. Pederson, January 2009, An Introduction to Water Reuse in the Petroleum Industry, http://www.spe.org/events/dl/Myers.php
Nafey , A. S., H. E. S. Fath, and A. A. Mabrouk, 2006, THERMOECONOMIC ANALYSIS OF MULTI STAGE FLASHTHERMAL VAPOR COMPRESSSION (MSF-TVC) DESALINATION PROCESS, Tenth International Water Technology Conference, IWTC10 2006, Alexandria, Egypt, http://www.iwtc.info/2006_pdf/03-2.pdf
Nakagawa, H., A. Namba, M. Bohlmannm, K. Miura, 2004, hydrothermal dewatering of brown coal and catalytic hydrothermal gasification of the organic compounds dissolving in the water using a novel ni/carbon catalyst, Fuel, 83, 719-25.
National Coal Council (NCC), 2006, Coal: America's Energy Future, Volume II, Ed: G.H. Boyce, Website:

www.coalamerciasenergyfuture.com/pdf/NCC_Presentation.
NETL, 2009, National Energy Technology Laboratory, Combustion, Combustion Technologies, Website: www.netl.doe.gov/technologies/coal power/combustion/index.html.
Neville, M., A. F. Sarofim, 1985, The fate of sodium during pulverized coal combustion, Fuel, 64, 384-90.
Office of Technology Assessment – US Congress, March 1988, Desalination Technologies for Water Treatment, NTIS order #PB88-193354, http://www.fas.org/ota/reports/8842.pdf
Ohman, M., A. Nordin, 2000, The role of kaolin in prevention of bed agglomeration during fluidized bed combustion of biomass fuels, Energy Fuels, 14, 618-24.
Olofson, G., Y. Z, I. Bjerle, A. Andersson, 2002, Bed agglomeration problems, Ind. Eng. Chem. Res., 41, 2888-94.
Ophir, A., A. Gendel, 2007, Steam driven large multi effect MVC (SD MVC) desalination process for lower energy consumption and desalination costs, Desalination, Volume 205, Issues 1-3, 5 February 2007, Pages 224-230
Paisley, M.A., 2002, Reduction of ash agglomeration in parallel entrainment fluidized bed gasifier/combustor system involves introducing feedstock into system, WO Patent 200250214-A. Future Energy Resourcess Corporation and Ferco Enterprises, Inc, and JAW Enterprises, LLC.
Paul, M., M. Seferinoglu, GA. Aycik, A. Sandstrom, ML. Smith, J. Paul, 2006, Acid leaching of ash and coal: time dependence and trace element occurrences, International Journal of Mineral Processing, 79, 27-41.
Paulson, L. E. and J. R. Futch, No Date Presented, REMOVAL OF SODIUM FROM LIGNITE CY ION EXCHANGING WITH CALCIUM CHLORIDE SOLUTIONS, Grand Forks Energy Technology Center, DOE, http://www.anl.gov/PCS/acsfuel/preprint%20archive/Files/25_1_HOUSTON_03-80_0224.pdf
Paulson, L.e., J.r. Futch, 1980, Removal of sodium from lignite by ion exchanging with calcium chloride solutions, Attached paper to Gronhovd, et al (1980); see their reference for source.
Paulson, L.E., JR. Futch, 1980, Removal of Sodium From Lignite By Ion Exchanging with Calcium Chloride Solutions, Grand Forks DOE Energy Technology Center, Grand Forks, North Dakota, American Chemical Society, Vol 25:1; Conference: 179 American Chemical Society, Houston, TX, USA, 23 Mar 1980, 224-32.
Paulson, L.E., W. Bickering, W.W. Fowkes, 1972, Separation and identification of Minerals from Northern Great Plains Lignites, Fuel, 51 (3), p 224.
Paulson, L.E., W.W. Fowkes, 1968, Changes in ash composition of North Dakota lignite treated by ion exchange, USBM Report of Investigation 7176.
Petersen, H.I., Rosenberg, P., H.P. Nytoft, 2008, Oxygen groups in coals and alginate-rich kerogen revisited, International Journal of Coal Geology, 93-113.
Pipatmanomal, S., B. Fungtammasan, S. Bhattacharya, 2009, characteristics and composition of lignites and boiler ashes and their relation to slagging: the case of Mae Moh PCC boilers, Fuel, 88, 116-23.
Quast, KB, 2000, Technical note counter-current ion exchange for the removal of organically bound sodium from low-rank coals, Minerals Engineering, 13(13), 1423-28
Rindt, D.K., R.R. Karner, W. Beckering, H.H. Schobert, 1980, Current research on the inorganic constituents in north dakota lignites and some effects on utilization, Attached paper to Gronhovd, et al (1980); see their reference for source.
Roine, A., 2006, HSC Chemistry 6.0, Chemical reaction and equilibrium software with extensive thermochemical database and flowsheet simulation, outokumpu Research Oy, Pori, Finland, www.outokumputechnology.com/hsc.
Rubiera, F., A. Arenillas, B. Arias, J. J. Pis, I. Suárez-Ruiz, K. M. Steel, J. W. Patrick, 2003, Combustion behaviour of ultra clean coal obtained by chemical demineralisation, Fuel, 82, (15-17), 2145-51.
Sakaguchi, M., k. Laursen, H. Nakagawa, K. Miura, 2008, Hydrothermal upgrading of Loy Yang Brown Coal - effect of upgrading conditions on the characteristics of the products, Fuel Processing

Technology, 89, 391-6.
Schulz, K.W., C.R. Smyrniotis, 2006, Analyzing the use of chemical technology for controlling and/or influencing opacity, fouling, and slagging in coal-fired utility boilers, Presentation: Clean Coal Conference, Clearwater, FL, Website: www.ftek.com/technicalPapers.php, paper number TPP-571.
Sears, Stephen, November 2006, Vapour Compression Distillation, Adding High Tech Understanding to Natures Process, Water Conditioning & Purification, http://www.wcponline.com/PDF/0611_Sears.pdf
Seredin, V.V., RB. Finkelman, 2008, Metalliferous coals: A review of the main genetic and geochemical types, International Journal of Coal Geology, 70, 253-289.
Sharma, DK., S. Gihar, 1991, Chemical cleaning of low grade coals through alkali-acid leaching employing mild conditions under ambient pressure, Fuel, 70 (5), 663-5.
Silva, Peter, Jo-Ellen Darcy, July 30, 2010, MEMORANDUM FOR U.S. Army Corps of Engineers Headquarters, Directorate of Civil Works, Districts and Divisions, and U.S. Environmental Protection Agency Regional Offices
Silvennoinen, J.A., 2003, A new method to inhibit bed agglomeration problems in fluidized bed boilers. In: Proceedings of the 17th International Conference on Fluidized Bed Combustion, American Society of Mechanical Engineer, 377-85.
Singh, Rajindar, 2009, Analysis of High Recovery Brackish Water Desalination Processes using Fuel Cells, Separation Science & Technology, Volume 45, Issue 1 January 2010 , page 148
Skrifvars, BJ., M. Hupa, M. Hiltunen, 1992, Sintering of ash during fluidized bed combustion, Ind. Eng. Chem. Res., 31, 1026-30.
Smart, MK., 9/1/2003, Effects of long-term irrigation with reclaimed water on soils of the Northern Adelaide Plains, South Australia, Australian Journal of Soil research, http://waterquality.montana.edu/docs/methane/long_term_irrigation_S_Australia.pdf
Smyrniotis, C.R., 2005, Slag Inhibition Success Utilizing Targeted In-Furnace Injection at a PRB Coal Burning Utility Boiler, Presented at the Clearwater, Fl 2005 Conference, TPP-568, Website: www.ftek.com/technicalPapers.php, paper number TPP-568.
Sonune, Amit *, Rupali Ghate, 2004, Developments in wastewater treatment methods, Desalination, Volume 167, 15 August 2004, Pages 55-63, Desalination Strategies in South Mediterranean Countries
Souby, A.M., T.C. Owens, D.E. Severson, 1980, Laboratory batch liquefaction of low rank coals, Attached paper to Gronhovd, et al (1980); see their reference for source.
Sourcewatch, 2009, Wyoming Mines, Website: www.Sourcewatch.org.
Spears, DA., 2005, A review of chlorine and bromine in some United Kingdom coals, International Journal of Coal Geology, 64, 257-265.
Spears, DA., S.J. Tewalt, 2009, The geochemistry of environmental important trace elements in UK coals, with speial reference to the Parkgate coal in the Yorkshire-Nottinghamshire Coalfield, UK, International Journal of Coal Geology, 80, 157-66.
Steel, K.M., J. Besida, T.A. O'Donnell, D.G. Wood, 2001, Production of ultra clean coal Part I - Dissolution Behavior of mineral matter in black coal toward hydrochloric and hydrofluoric acids, Fuel Processing Technology, 70, 171-92
Steel, K.M., J.W. Patrick, 2003, Production of ultra clean coal by sequential leaching with HF followed by HNO3, Fuel, 82, 1917-20.
Stiegel, G.J., 2008, Integrated Gasification Combined Cycle (Microsoft Powerpoint), National Energy Technology Laboratory, DOE, IGCC Workshop, India, Website: www.indiapower.org/igcc/garyj.pdf.
Sugawara, K., T. Kato, T. Karuishi, November 10, 2009, Dynamic behavior of sodium and potassium during pyrolysis of coals, Energy and Fuels, ACSJ Review,
Takuwa, T., I. Naruse, 2007, Detailed kinetic and control of alkali metal compounds during coal combustion, Fuel Processing Technology, 88, 1029-34.

Takuwa, T., I. Naruse, 2007, Emission control of sodium compounds and their formation mechanisms during coal combustion, Proceedings of the Combustion Institute, 31, 2863-70

Takuwa, T., ISN. Mkilaha, I. Naruse, 2006, Mechanisms of fine particulates formation with alkali metal compounds during coal combustion, Fuel, 85, 671-8.

Tangsathitkulchai, C., Tangsathitkulchai, M., 2001, Effect of bed materials and additives on the sintering of coal of coal ashes relevant to agglomeration in fluidized bed combustion, Fuel Process Technology, 72(3), 163-83.

Thielemann, T., S. Schmidt, J. P. Gerling, 2007, Lignite and hard coal: energy suppliers for worlds needs until the year 2100 - an outlook, International Journal of Coal Geology, 72, 1-14.

Tominaga, M., M. Mimori, K. Okuda, April 6, 1976, Ion exchanger and method for the production therof, US Patent, 3948791.

Tran, K.Q., K. Lisa, B-M. steenari, O. Lindqvist, 2005, A kinetic study of gaseous alkali capture by kaolin in the fixed bed reactor equipped with an alkali detector, Fuel, 84(2-3), 169-75.

Tufte, P.H., W. Beckering, 1974, A proposed mechanism for ash fouling burning northern Great Plains Lignite, Annual Meeting American Society of Mechanical Engineers, N.Y., November 17-22.

Turnbull, A.G., M.W. Wadsley, The CSIRO-MONASH thermochemistry system, CSIRO Division of Minerals.

Twidwell, L.G. Dudley, 2009, Removal of sodium from Montana low-rank coals, Internal Report, Center for Advanced Mineral and Metallurgical Processing (CAMP), Montana Tech of the University of Montana, Butte, MT, pmiranda@Mtech.edu.

Twidwell, L.G., 2009, Personal Communications,, Center for Advanced Mineral and Metallurgical Processing (CAMP), Montana Tech of the University of Montana, Butte, MT, ltwidwell@Mtech.edu.

Twidwell, L.G., S. Dudley, 2009, Literature review sodium removal from montana low-rank coals, Internal Report, Center for Advanced Mineral and Metallurgical Processing (CAMP), Montana Tech of the University of Montana, Butte, MT, ltwidwell@Mtech.edu.

United States Department of the Interior - Bureau of Reclamation, July 2003, Desalting Handbook for Planners - 3rd Edition

University of New South Wales, No Date Present, Reverse Osmosis-Capable Subsurface Drip Irrigation, http://www.nsinnovations.com.au/industry/technologies/renewables/07_2178~reverse~osmosis.pdf

US Department of the Interior and USGS, 2007, Measured and Estimated Sodium-Adsorption Ratios for Tongue River and its Tributaries, Montana and Wyoming, 2004–06, Scientific Investigations report 2007-5072

US Environmental Protection Agency , October 2009, Technical Support Document for the Preliminary 2010 Effluent Guidelines Program Plan, http://water.epa.gov/lawsregs/guidance/cwa/304m/archive/upload/2009_11_17_guide_304m_2010_tsdplan.pdf

US Environmental Protection Agency, October 2009, Preliminary Effluent Guidelines Plan for 2010, http://www.epa.gov/waterscience/guide/304m/2010/factsheet2010.html

US Environmental Protection Agency, April 1, 2010, US EPA Memorandum, Detailed Guidance: Improving EPA Review of Appalachian Surface Coal Mining Operations Under the Clean Water Act, National Environmental Policy Act, and the Environmental Justice Executive Order, http://water.epa.gov/lawsregs/guidance/wetlands/upload/2010_04_01_wetlands_guidance_appalachian_mtntop_mining_detailed.pdf

US Environmental Protection Agency, December 2006, Technical Support Document for the 2006 Effluent Guidelines Program Plan, EPA-821R-06-018, http://water.epa.gov/lawsregs/lawsguidance/cwa/304m/upload/2007_01_10_guide_304m_2006_2006-TSD-whole.pdf

US Environmental Protection Agency, July 13, 2010, US EPA Memorandum, Review of Clean Water Act 402 Permitting for Surface Coal Mines by Appalachian States: Findings and Recommendations

US Environmental Protection Agency, July 2003, Contaminant Candidate List Regulatory Determination Support Document for Sodium, Standards and Risk Management Division, EPA-815-R-03-15, http://www.epa.gov/ogwdw000/ccl/pdfs/reg_determine1/support_cc1_sodium_ccl_regdet.pdf

US Environmental Protection Agency, LA 7/25/2010, Understanding the Safe Drinking Water Act, http://water.epa.gov/lawsregs/guidance/sdwa/basicinformation.cfm

US Environmental Protection Agency, September 1996, Reverse Osmosis Process, Capsule Report, EPA/625/R-961009 , Center for Environmental Research Information, National Risk Management Research Laboratory, Office of Research and Development http://www.epa.gov/nrmrl/pubs/625r96009/625r96009.pdf

Van der Drift, A., A. Olsen, 1999, Conversion of biomass, prediction and solution methods for ash agglomeration and related problems, Report ECN-C-99-090.

Van Dyk, J.C., S.A. Benson, M.L. Laumb, B. Waanders, 2009, Coal and coal ash characteristics to understand mineral transformations and slag formation, Fuel, 88, 1057-63.

Veil, John A., February 2002, REGULATORY ISSUES AFFECTING MANAGEMENT OF PRODUCED WATER FROM COAL BED METHANE WELLS, U.S. DEPARTMENT OF ENERGY, OFFICE OF FOSSIL ENERGY, UNDER CONTRACT W-31-109-ENG-38

Visser, P., 2004, Coal and Minerals, Secunda, South Africa, available from piet.visser@coalandminerals.com.

Vuthaluru H.B.; Vleeskens J.M.; Wall T.F., May 1998, Reducing fouling from brown coals by sodium binding additives, Fuel Processing Technology, 55, (2), 161-73.

Vuthaluru, H.B., D. French, 2008, Ash chemistry and mineralogy of an Indonesian coal during combustion - part 1 drop-tube observations, Fuel Processing Technology, 89, 595-607.

Vuthaluru, H.B., DK. Zhang, TM. Linjewile, 2000, Behavior of inorganic constituents and ash characteristics during fluidised-bed combustion of several australian low-rank coals, Fuel Process Technology, 67(3), 165-76

Vuthaluru, HB., 1999, Remediation of ash problems in pulverised coal fired boilers, Fuel, 78, 1789-1803.

Vuthaluru, HB., G. Domasetis, TF. Wall, JM. Vleeskens, 1996, Reducing fly ash deposition by pretreatment of brown coal: Effect of aluminium on ash character, Fuel Processing Technology, 46, 117-32.

Vuthaluru, HB., JM. Vleeskens, TF. Wall, 1998, Reducing fouling from brown coals by sodium-binding additives, Fuel Process Technology, 55(2), 161-73.

Vuthaluru, HB., TF. Wall, 1998, Ash formation and deposition from a Victorian Brown Coal: Modeling and prevention, Fuel Process Technology, 53, 215-33.

Vuthaluru, HB., TM. Linjewil, DK. Zhang, AR. Manzoori, 1999, Investigation into the control of agglomeration and defluidisation during fluidised bed combustion of low rank coals, Fuel, 78(4), 419-25.

Vuthaluru, NB., 1999, Remediation of ash problems in pulverised coal-fired boilers, Fuel, 78, 1789-803.

Wang, Q., J. Qiu, Y. Liu, C. Zheng, 2004, Effect of atmosphere and temperature on the speciation of mineral in coal combustion, Fuel Processing Technology, 85, 1431-41.

Ward, C. R., 1991, Mineral matter in low-rank coals associated strata of the Mae Moh Basin, northern Thailand. International Journal of Coal Geology, 17, 69-93.

Ward, C. R., 1991, Mineral matter in low-rank coals from South Australia, International Journal of Coal Geology, 20, 185-208.

Ward, C. R., 2002, Analysis and significance of mineral matter in coal seams, International Journal of Coal Geology, 50, 135-68.

Ward, C. R., Z. Li, W. Gurba, 2005, Variations in coal maceral chemistry with rank advance in the German

Creek and Moranbah coal measures of the Bowen Basin, Australia, International Journal of Coal Geology, 63, 117-29.

Ward, C. R., Z. Li, W. Gurba, 2007, Variations in elemental composition of maceral with Vitrinite reflectance and organic sulphur in the Greta Coal Measures, New South Wales, International Journal of Coal Geology, 69, 205-19.

Ward, C. R., Z. Li, W. Gurba, 2008, Comparison of elemental composition of maceral determined by electron microprobe to whole-coal ultimate analysis data, International Journal of Coal Geology, 75, 157-65.

Wardeh, S., H.P. Morvan and N.G. Wright, No Date Provided, DESALINATION FOR SYRIA, School of Civil Engineering, the University of Nottingham, http://ressources.ciheam.org/om/pdf/a65/05002228.pdf

Waters, Susan J. Clearwater, Ph.D., Brady A. Morris, B.S., Joseph S. Meyer, Ph.D., May 2002, A Comparison of Coalbed Methane Product Water Quality Versus Surface Water Quality in the Powder River Basin of Wyoming, and An Assessment of the Use of Standard Aquatic Toxicity Testing Organisms for Evaluating the Potential Effects of Coalbed Methane Product, Department of Zoology and Physiology, University of Wyoming

Webb, Charlie – Chevron, Rich Franks - Hydranautics, LNSP Nagghappan - Veolia Water S&T, Gerald Smart - Veolia Water, John Hoblitzel - Veolia Water, No Date Present, Desalination of Oilfield Produced Water at the Chevron San Ardo Water Reclamation Facility

Weber-Scannell, Phyllis K., and Lawrence K. Duffy, 2007, Effects of Total Dissolved Solids on Aquatic Organisms: A Review of Literature and Recommendation for Salmonid Species, American Journal of Environmental Sciences, Veolia Water Solutions & Technologies

Wei, Xiao-fang, Jie-jie Huang, Yi-tian Fang, Yang Wang, 2009, Transformation of sodium during gasification of a lignite with addition of NaCl and NaAc, Journal of Fuel chemistry and Technology, 37 (1), 6-10.

Westmoreland Resources, Inc , May 1, 2009, AUTHORIZATION TO DISCHARGE UNDER THE NATIONAL POLLUTANT DISCHARGE ELIMINATION SYSTEM, PN: MT0030783

Wilson, W.G., G.G. Baker, S.A. Farnum, S.A., D.J. Maas, T.A. Potas, R.E. Sears, D.N. Baria, R.A. Hasan, 1986, Energy Power Research Institute (EPRI), Report AP-4905.

Wilson, W.G., G.G. Baker, S.A., D.J. Maas, T.A. Potas, R.E. Sears, D.N. Baria, R.A. Hasan, 1985, Energy Power Research Institute (EPRI), Report AP-4262.

Woskoboenko, F., D.J. Allardice, 1996, Australia n-Indonesian Low Rank Coal Science and Technology Workshop, Melbourne, Australia, May.

Younos, Tamim, Kimberly E. Tulou, 2005, Overview of Desalination Techniques, UNIVERSITIES COUNCIL ON WATER RESOURCES, JOURNAL OF CONTEMPORARY WATER RESEARCH & EDUCATION, ISSUE 132, PAGES 3-10, DECEMBER 2005, http://www.ucowr.siu.edu/updates/132/2.pdf

Yudovich, Ya.E., 2003, Coal inclusions in sedimentary rocks: a geochemical phenomenon. A review, International Journal of Coal geology, 56, 203-22.

Yudovich, Ya.E., M.P. Ketris, 2002, Inorganic Matter in Coal, Russian Academy of Science, Ural Division, Ekaterinburg, 422p

Yudovich, Ya.E., M.P. Ketris, 2005, Arsenic in Coal: A review, International Journal of Coal Geology, 61, 141-96.

Yudovich, Ya.E., M.P. Ketris, 2006, Selenium in Coal: A Review, international Journal of Coal Geology, 67, 112-26.

Yudovich, YaE., MP. Ketris, 2005, Mercury in Coal: A Review - Part 2. Coal use and environmental problems, International Journal of Coal Geology, 62, 135-65.

Yudovich, YaE., MP. Ketris, 2005, Mercury in Coal: A Review - Part I. Geochemistry, International Journal of Coal Geology, 62, 107-34.

Yudovich, YaE., MP. Ketris, 2006, Chlorine in Coal: A Review, International Journal of Coal Geology, 67,

127-144.

Zhongsheng, Li, C.R. Ward, L.W. Gurba, 2009, Occurrence of non-mineral inorganic elements in macerals of low-rank coals, International Journal of Coal Geology, in press, available at doi:10.1016/j.coal.2009.02.004. Also see Li, Z., C.R. Ward, L.W. Gurba, 2007, Occurrence of non-mineral inorganic elements in low-rank coal macerals as shown by electron microprobe element mapping techniques, same journal, 70, 137-49.

APPENDIX B-COAL CHARACTERIZATION DATA

SIEVE ANALYSIS FOR COAL FINES (As-Received Non-Dried coals)

Table I: Coal A2 Fines

Size (Tyler Mesh)	Size (mm)	Mass (g)	% Retained	% Passing
+7	2.8	0	0%	0.00%
-7/+12	1.7	1.7	0%	0.23%
-12/+20	0.85	20	3%	2.95%
-20/50	0.3	225.7	31%	33.67%
+140	0.106	233.8	32%	65.49%
-140/+200	0.075	76.4	10%	75.88%
-200/+325	0.045	87.6	12%	87.81%
-325/+400	0.038	60.6	8%	96.05%
-400	<.038	29	4%	100.00%
Total		734.8		

Table II: Coal B2 Fines

Size (Tyler Mesh)	Size (mm)	Mass (g)	% Retained	% Passing
+7	2.8	0.2	0%	0%
-7/+12	1.7	4.4	1%	1%
-12/+20	0.85	69.1	8%	9%
-20/50	0.3	307.2	37%	46%
+140	0.106	218	27%	73%
-140/+200	0.075	63.5	8%	81%
-200/+325	0.045	76.4	9%	90%
-325/+400	0.038	41.4	5%	95%
-400	<.038	40.4	5%	100%
Total		820.6		

Table III: Coal C2 Fines

Size (Tyler Mesh)	Size (mm)	Mass (g)	% Retained	% Passing
+7	2.8	2.6	0%	0%
-7/+12	1.7	14	1%	2%
-12/+20	0.85	75.8	7%	9%
-20/50	0.3	291.5	27%	36%
+140	0.106	346.3	33%	69%
-140/+200	0.075	89.1	8%	77%
-200/+325	0.045	100	9%	86%
-325/+400	0.038	46.6	4%	91%
-400	<.038	97.7	9%	100%
Total		1063.6		

Table IV: Coal D1 Fines

Size (Tyler Mesh)	Size (mm)	Mass (g)	% Retained	% Passing
+7	2.8	0	0%	0%
-7/+12	1.7	2.1	1%	1%
-12/+20	0.85	10.5	4%	5%
-20/50	0.3	61.8	23%	27%
+140	0.106	97.7	36%	64%
-140/+200	0.075	41.1	15%	79%
-200/+325	0.045	39.4	15%	93%
-325/+400	0.038	13.1	5%	98%
-400	<.038	5	2%	100%
Total		270.7		

Table V: Coal D2

Size (Tyler Mesh)	Size (mm)	Mass (g)	% Retained	% Passing
+6	3.36	140.1	23%	77%
-6/+12	1.41	225.0	36%	41%
-12/+20	0.841	105.6	17%	24%
-20/+48	0.297	93.5	15%	9%
-48/+150	0.105	32.1	5%	3%
-150/+250	0.063	7.7	1%	2%
-250/+325	0.044	3.2	1%	2%
-325/+400	0.037	1.4	0%	1%
-400	-0.037	8.7	1%	0%
Total		270.7		

ELEMENTAL CONTENT IN SIZE FRACTIONS FOR COAL FINES (As-Received Non-Dried coals)

The elemental content in the various size fractions are presented in the following tables. The following data identification is Coal A (sample 2); Coal B (sample 5); Coal C (sample 9); Coal D1 (sample 14). All analyses were performed by the Wyoming Analytical Laboratories using XRF on supplied coals.

The more recent (2012) sample Coal D2 was analyzed by Photon Induced X-Ray Emission (PIXE performed by Elemental Analysis, Inc., Lexington, Kt) and the results are presented in the last table in this appendix.

Jay McCloskey
Montana Tech
1300 West Park St.
Butte, MT. 59701

Date: October 19, 2009
Request Number: 27215
Matrix: Coal

REPORT OF ANALYSIS

Lab Number	M0422	M0421	M0405	M0404	M0403
Sample ID	**Sample 2 +140**	**Sample 2 -140+200**	**Sample 2 -200+325**	**Sample 2 -325+400**	**Sample 2 -400**
Arsenic, mg/kg	0.176	0.809	1.340	1.240	1.370
Lead, mg/kg	4.50	24.9	34.5	59.1	81.9
Aluminum, mg/kg	1,561	1,520	1,380	1,720	1,284
Silica, mg/kg	209	218	288	298	466
Phosphorus, mg/kg	134	133	151	159	199
Calcium, mg/kg	10,200	12,040	13,300	15,500	15,400
Iron, mg/kg	1,797	3,070	3,490	3,620	1,012
Magnesium, mg/kg	1,460	1,430	1,600	1,790	1,820
Sodium, mg/kg	327	341	364	340	335
Potassium, mg/kg	34.6	24.5	34.3	34.3	39.1
Chloride, mg/kg	0.001	0.002	0.003	0.001	0.002
Sulfur, As determined wt.%	0.56	0.66	0.66	0.59	0.42

Jay McCloskey
Montana Tech
1300 West Park St.
Butte, MT. 59701

Date: October 19, 2009
Request Number: 27215
Matrix: Coal

REPORT OF ANALYSIS

Lab Number	M0410	M0409	M0408	M0407	M0406
Sample ID	**Sample 5 +140**	**Sample 5 -140+200**	**Sample 5 -200+325**	**Sample 5 -325+400**	**Sample 5 -400**
Arsenic, mg/kg	1.66	2.7	3.78	5.16	6.48
Lead, mg/kg	9.97	7.34	17.7	29.8	61.9
Aluminum, mg/kg	1,935	2,020	2,078	2,064	2,290
Silica, mg/kg	225	263	296	313	403
Phosphorus, mg/kg	400	393	403	425	518
Calcium, mg/kg	4,400	4,180	3,980	4,280	4,880
Iron, mg/kg	1,790	1,790	984	1,230	2,460
Magnesium, mg/kg	505	526	519	584	640
Sodium, mg/kg	2,740	2,570	2,370	2,350	2,520
Potassium, mg/kg	48.7	45.1	37.6	55.1	67.8
Chloride, mg/kg	0.001	0.002	0.002	0.002	0.002
Sulfur, As determined wt.%	0.64	0.72	0.78	0.78	0.76

Jay McCloskey
Montana Tech
1300 West Park St.
Butte, MT. 59701

Date: October 19, 2009
Request Number: 27215
Matrix: Coal

REPORT OF ANALYSIS

Lab Number	M0415	M0414	M0413	M0412	M0411
Sample ID	**Sample 9 +140**	**Sample 9 -140+200**	**Sample 9 -200+325**	**Sample 9 -325+400**	**Sample 9 -400**
Arsenic, mg/kg	0.214	0.814	1.3	1.85	1.5
Lead, mg/kg	4.58	7.87	86.9	138	164
Aluminum, mg/kg	1,280	1,330	1,270	1,234	1,170
Silica, mg/kg	170	264	324	432	490
Phosphorus, mg/kg	77.2	80.2	74.4	69.6	74.4
Calcium, mg/kg	14,400	13,000	14,800	12,990	11,800
Iron, mg/kg	1,930	2,790	3,280	2,753	2,680
Magnesium, mg/kg	1,280	1,230	1,430	1,100	1,070
Sodium, mg/kg	1,460	1,420	1,510	1,150	1,123
Potassium, mg/kg	47.9	55.9	69.0	87.3	106
Chloride, mg/kg	0.001	0.002	0.002	0.002	0.002
Sulfur, as determined wt.%	0.54	0.64	0.69	0.58	0.50

REPORT OF ANALYSIS

Lab Number	M0877	M0878	M0879	M0880
Sample ID	**Sample 2 -12+20**	**Sample 2 - 20+50**	**Sample 2 -50**	**Sample 5 -12+20**
Arsenic, mg/kg	0.849	0.371	0.392	1.450
Lead, mg/kg	4.43	4.12	4.36	1.27
Aluminum, mg/kg	1,551	1,628	1,590	2,154
Silica, mg/kg	178	145	130	136
Phosphorus, mg/kg	164	174	171	488
Calcium, mg/kg	10,170	10,990	11,390	3,900
Iron, mg/kg	3,220	564	865	1,430
Magnesium, mg/kg	1,625	1,740	1,710	650
Sodium, mg/kg	410	445	428	2,450
Potassium, mg/kg	46	64	64	106
Chloride, mg/kg	2.6	1.7	0.9	2.5
Sulfur, As determined wt.%	0.82	0.41	0.45	0.65

Lab Number	M0881	M0882	M0883	M0884
Sample ID	**52 -20+50**	**Sample 5 -50**	**Sample 9 -12+20**	**Sample 9 -20+50**
Arsenic, mg/kg	1.47	1.98	0.53	1.47
Lead, mg/kg	1.74	16.4	8.50	4.05
Aluminum, mg/kg	2,115	2,054	1,429	1,476
Silica, mg/kg	152	114	209	233
Phosphorus, mg/kg	495	479	93.3	106
Calcium, mg/kg	4,080	3,670	9,840	10,360
Iron, mg/kg	1,500	1,410	1,510	1,260
Magnesium, mg/kg	680	620	1,150	1,310
Sodium, mg/kg	2,670	2,400	1,366	1,500
Potassium, mg/kg	98	59	75	91
Chloride, mg/kg	1.8	2.1	2.5	1.1
Sulfur, As determined wt.%	0.67	0.67	0.59	0.44

REPORT OF ANALYSIS

Lab Number	M0885	M0886	M0887
Sample ID	**Sample 9 -50**	**Sample 14 -20+50**	**Sample 14 -50**
Arsenic, mg/kg	1.42	0.545	0.592
Lead, mg/kg	5.36	2.71	3.79
Aluminum, mg/kg	1,450	2,200	2,230
Silica, mg/kg	212	148	158
Phosphorus, mg/kg	98.2	131	150
Calcium, mg/kg	12,760	6,140	6,140
Iron, mg/kg	1,300	1,040	1,040
Magnesium, mg/kg	1,700	1,220	1,220
Sodium, mg/kg	1,870	3,700	3,690
Potassium, mg/kg	128	62	46
Chloride, mg/kg	1,100	1,300	1,100
Sulfur, as determined wt.%	0.47	0.1	0.12

Element Content in Coal D2 by PIXE				
Element	**6**	**-6/+12**	**-12/+20**	**-20/+48**
Sodium	0.326%	0.347%	0.346%	0.366%
Magnesium	0.122%	0.148%	0.164%	0.190%
Aluminum	0.399%	0.414%	0.591%	0.816%
Silicon	0.460%	0.754%	1.170%	1.750%
Sulfur	0.155%	0.171%	0.159%	0.166%
Potassium, ppm	94.820	280.248	639.246	1070.000
Calcium	0.535%	0.550%	0.571%	0.540%

Titanium, ppm	192.377	247.434	311.487	388.605
Manganese, ppm	21.386	28.612	34.570	39.957
Iron	0.111%	0.140%	0.201%	0.303%
Copper, ppm	3.795	4.377	7.688	10.676
Zinc, ppm	3.378	3.462	5.757	8.602

All analyses performed by Elemental Analysis, Inc., Lexington, Kt

MINERAL CONTENT IN MONTANA COALS

The mineral content in each coal was examined by Mineral Liberation Analyses at Montana Tech. The reported percentages relate to the content in the mineral phase not the content in the coal.

Table 1. MLA Mineralogy for Coal A2 Fines		
Mineral/Phase	**Compound**	**Content (wt.%)**
K-Feldspar	$KAlSi_3O_8$	73.34
Quartz	SiO_2	25.39
Amphibole	$(Mg,Fe)_3Al_2Si_8O_{22}(OH)_2$	0.43
Na-Amphibole	$Na_2(Mg,Fe)_3Al_2Si_8O_{22}(OH)_2$	0.40
Zircon	$ZrSiO_4$	0.19
Pyrite	FeS_2	0.15
Apatite-Albite	$Ca_5(PO_4)_3OH$ $NaAlSi_3O_8$	0.03
Barite	$BaSO_4$	0.02
Calcite	$CaCO_3$	0.01
Apatite	$Ca_5(PO_4)_3OH$	0.01

Table 2. Mineral Content in Coal B2 Fines		
Mineral/Phase	**Compound**	**Content (wt.%)**
Quartz	SiO_2	51.90
Apatite	$Ca_5(PO_4)_3OH$	26.71
Apatite-Albite	$Ca_5(PO_4)_3OH$ $NaAlSi_3O_8$	8.47
Kyanite	Al_2OSiO_4	5.69
Pyrite	FeS_2	2.74
Na-Amphibole	$Na_2(Mg,Fe)_3Al_2Si_8O_{22}(OH)_2$	1.50
K-Feldspar	$KAlSi_3O_8$	1.48
Barite	$BaSO_4$	1.37
Amphibole	$(Mg,Fe)_3Al_2Si_8O_{22}(OH)_2$	0.11
Ilmenite	$FeTiO_3$	0.02
Calcite	$CaCO_3$	0.01

Table 3. MLA Mineralogy for Coal C1 Course		
Mineral/Phase	**Compound**	**Content (wt.%)**
K-Feldspar	$KAlSi_3O_8$	41.03
Quartz	SiO_2	29.87
Na Amphibole	$Na_2(Mg,Fe)_3Al_2Si_8O_{22}(OH)_2$	9.54
Kyanite	Al_2OSiO_4	9.44
Calcite	$CaCO_3$	5.87
Pyrite	FeS_2	3.58
Lollingite	$FeAs_2$	0.61
Corrundum	Al_2O_3	0.06

Table 4. MLA Mineralogy for Coal D1 Fines		
Mineral/Phase	**Compound**	**Content (wt.%)**
Na-Amphibole	$Na_2(Mg,Fe)_3Al_2Si_8O_{22}(OH)_2$	36.32
Amphibole	$(Mg,Fe)_3Al_2Si_8O_{22}(OH)_2$	25.07
Kyanite	Al_2OSiO_4	17.76
Quartz	SiO_2	16.64
Apatite-Albite	$Ca_5(PO_4)_3OH$ $NaAlSi_3O_8$	2.15
K-Feldspar	$KAlSi_3O_8$	0.59
Lollingite	$FeAs_2$	0.53
Ilmenite	$FeTiO_3$	0.50
Barite	$BaSO_4$	0.26
Pyrite	FeS_2	0.11
Corrundum	Al_2O_3	0.02
Calcite	$CaCO_3$	0.02
Apatite	$Ca_5(PO_4)_3OH$	0.01
Zincite	ZnO	0.01

CHEMICAL CHARACTERISTICS OF MONTANA COAL ASH

The following data identifications are for ashes formed from coal fines: Coal A (sample 2); Coal B (sample 5); Coal C (sample 9); Coal D (sample 14). All analyses performed by the Wyoming Analytical Laboratories using XRF on supplied coals.

Coal D2 was received late in the present study. The characterization data are presented as the last table in this appendix.

Jay McCloskey
Montana Tech
1300 West Park St.
Butte, MT. 59701

Date: June 1, 2009
Request Number: 26660
Lab Number: L8829
Sample ID: #2 Coal Fine 4-15-09

REVISED
REPORT OF ANALYSIS

Proximate Analysis ASTM D-5142	As Received Wt%	Moisture Free wt%	MAF Basis wt%
Moisture	20.55	******	******
Ash	10.19	12.83	******
Volatile Matter	32.23	40.57	46.54
Fixed Carbon	37.03	46.60	53.46
Total	100.00	100.00	100.00

Ultimate Analysis/ Method: ASTM D5142/5373			
Moisture	20.55	******	******
Hydrogen	2.52	3.17	3.64
Carbon	52.93	66.62	76.43
Nitrogen	0.92	1.16	1.33
Sulfur	0.57	0.72	0.83
Oxygen	12.32	15.50	17.77
Ash	10.19	12.83	******
Total	100.00	100.00	100.00

Heating Value, Btu/lb Method: ASTM D-5865			
	9,013	11,344	13,014

Coal Ash Analysis, wt% Ignited Basis	
Silicon Dioxide, % as SiO2	45.16
Aluminum Oxide, % as Al2O3	15.12
Iron Oxide, % as Fe2O3	5.16
Calcium Oxide, % as CaO	17.81
Magnesium Oxide, % as MgO	2.96
Sodium Oxide, % as Na2O	0.64
Potassium Oxide, % as K2O	0.14
Titanium Dioxide, % as TiO2	1.62
Manganese Dioxide, % as MnO2	0.07
Phosphorus Pentoxide, % as P2O5	0.33
Strontium Oxide, % as SrO	0.62
Barium Oxide, % as BaO	0.13
Sulfur Trioxide, % as SO3	10.24
Alkalies as Na20	0.73
Base to Acid Ratio	0.43
Silica Ratio	0.64
T250, °F	2375

Trace Element, mg/kg Method: D6357	As Rec. Basis	Dry Basis
Beryllium	0.11	0.138
Vanadium	3.65	4.594
Chromium	2.90	3.650
Manganese	29	36.501
Cobalt	0.345	0.434
Nickel	1.18	1.485
Zinc	2.49	3.134
Arsenic	0.435	0.548
Molybdenum	0.255	0.321
Cadmium	0.059	0.074
Lead	25.4	31.97
Sodium	370	466
Uranium	0.431	0.542
Potassium	25	31

Jay McCloskey
Montana Tech
1300 West Park St.
Butte, MT. 59701

Date: June 1, 2009
Request Number: 26660
Lab Number: L8832
Sample ID: #5 Coal Fine 4-15-09

REVISED
REPORT OF ANALYSIS

Proximate Analysis ASTM D-5142	As Received Wt%	Moisture Free wt%	MAF Basis wt%
Moisture	20.74	******	******
Ash	4.62	5.83	******
Volatile Matter	32.42	40.90	43.43
Fixed Carbon	42.22	53.27	56.57
Total	100.00	100.00	100.00

Ultimate Analysis/ Method: ASTM D5142/5373			
Moisture	20.74	******	******
Hydrogen	3.01	3.80	4.04
Carbon	56.83	71.70	76.14
Nitrogen	0.96	1.21	1.28
Sulfur	0.61	0.77	0.82
Oxygen	13.23	16.69	17.72
Ash	4.62	5.83	******
Total	100.00	100.00	100.00

Heating Value, Btu/lb Method: ASTM D-5865	9,950	12,554	13,331

Coal Ash Analysis, wt% Ignited Basis	
Silicon Dioxide, % as SiO2	29.39
Aluminum Oxide, % as Al2O3	15.72
Iron Oxide, % as Fe2O3	6.59
Calcium Oxide, % as CaO	14.21
Magnesium Oxide, % as MgO	2.87
Sodium Oxide, % as Na2O	7.66
Potassium Oxide, % as K2O	0.81
Titanium Dioxide, % as TiO2	0.77
Manganese Dioxide, % as MnO2	0.04
Phosphorus Pentoxide, % as P2O5	1.91
Strontium Oxide, % as SrO	0.88
Barium Oxide, % as BaO	1.27
Sulfur Trioxide, % as SO3	17.88

Alkalies as Na20	8.19
Base to Acid Ratio	0.7
Silica Ratio	0.55
T250, ^{o}F	2000

Trace Element, mg/kg Method: D6357	As Rec. Basis	Dry Basis
Beryllium	0.181	0.228
Vanadium	4.52	5.703
Chromium	2.73	3.444
Manganese	7.85	9.904
Cobalt	0.609	0.768
Nickel	1.42	1.792
Zinc	4.11	5.185
Arsenic	1.11	1.400
Molybdenum	0.215	0.271
Cadmium	0.061	0.077
Lead	3.70	4.668
Sodium	9750	12329
Uranium	0.167	0.211
Potassium	126	159

REVISED 7-22-09; Added Potassium, and corrected sodium values.

Jay McCloskey
Montana Tech
1300 West Park St.
Butte, MT. 59701

Date: June 1, 2009
Request Number: 26660
Lab Number: L8836
Sample ID: #9 Coal Fine 4-15-09

REVISED
REPORT OF ANALYSIS

Proximate Analysis ASTM D-5142	As Received Wt%	Moisture Free wt%	MAF Basis wt%
Moisture	21.97	******	******
Ash	13.51	17.31	******
Volatile Matter	30.76	39.42	47.67
Fixed Carbon	33.76	43.27	52.33
Total	100.00	100.00	100.00

Ultimate Analysis/ Method: ASTM D5142/5373			
Moisture	21.97	******	******
Hydrogen	2.45	3.14	3.80
Carbon	49.81	63.83	77.19
Nitrogen	0.98	1.26	1.52
Sulfur	0.53	0.68	0.82
Oxygen	10.75	13.78	16.67
Ash	13.51	17.31	******
Total	100.00	100.00	100.00

Heating Value, Btu/lb Method: ASTM D-5865	8,383	10,743	12,992

Coal Ash Analysis, wt% Ignited Basis	
Silicon Dioxide, % as SiO2	54.92
Aluminum Oxide, % as Al2O3	14.42
Iron Oxide, % as Fe2O3	3.07
Calcium Oxide, % as CaO	14.35
Magnesium Oxide, % as MgO	2.12
Sodium Oxide, % as Na2O	1.58
Potassium Oxide, % as K2O	1.41
Titanium Dioxide, % as TiO2	1.01
Manganese Dioxide, % as MnO2	0.17
Phosphorus Pentoxide, % as P2O5	0.12
Strontium Oxide, % as SrO	0.37
Barium Oxide, % as BaO	0.13
Sulfur Trioxide, % as SO3	6.33

Alkalies as Na20	2.51
Base to Acid Ratio	0.32
Silica Ratio	0.74
T250, ^{O}F	2517

Trace Element, mg/kg Method: D6357	As Rec. Basis	Dry Basis
Beryllium	0.147	0.188
Vanadium	3.54	4.537
Chromium	3.06	3.922
Manganese	84.3	108
Cobalt	0.25	0.320
Nickel	0.854	1.094
Zinc	1.58	2.025
Arsenic	0.238	0.305
Molybdenum	0.282	0.361
Cadmium	0.087	0.111
Lead	4.71	6.036
Sodium	582	746
Uranium	0.560	0.718
Potassium	270	347

Jay McCloskey
Montana Tech
1300 West Park St.
Butte, MT. 59701

Date: June 1, 2009
Request Number: 26660
Lab Number: L8841
Sample ID: #14 Coal Fine 4-15-09

REVISED
REPORT OF ANALYSIS

Proximate Analysis ASTM D-5142	As Received Wt%	Moisture Free wt%	MAF Basis wt%
Moisture	29.28	******	******
Ash	4.06	5.74	******
Volatile Matter	31.41	44.41	47.11
Fixed Carbon	35.25	49.85	52.89
Total	100.00	100.00	100.00

Ultimate Analysis/ Method: ASTM D5142/5373			
Moisture	29.28	******	******
Hydrogen	2.67	3.78	4.01
Carbon	49.91	70.58	74.88
Nitrogen	0.82	1.16	1.23
Sulfur	0.07	0.09	0.10
Oxygen	13.19	18.65	19.78
Ash	4.06	5.74	******
Total	100.00	100.00	100.00

Heating Value, Btu/lb Method: ASTM D-5865			
	8,508	12,031	12,764

Coal Ash Analysis, wt% Ignited Basis	
Silicon Dioxide, % as SiO2	26.06
Aluminum Oxide, % as Al2O3	20.21
Iron Oxide, % as Fe2O3	4.32
Calcium Oxide, % as CaO	23.4
Magnesium Oxide, % as MgO	4.9
Sodium Oxide, % as Na2O	10.72
Potassium Oxide, % as K2O	0.29
Titanium Dioxide, % as TiO2	0.84
Manganese Dioxide, % as MnO2	0.03
Phosphorus Pentoxide, % as P2O5	0.6
Strontium Oxide, % as SrO	0.94
Barium Oxide, % as BaO	1.25
Sulfur Trioxide, % as SO3	6.44

Alkalies as Na20	10.91
Base to Acid Ratio	0.93
Silica Ratio	0.44
T250, ^{O}F	2139

Trace Element, mg/kg Method: D6357	As Rec. Basis	Dry Basis
Beryllium	0.029	0.037
Vanadium	2.47	3.165
Chromium	2.87	3.678
Manganese	7.74	9.919
Cobalt	0.198	0.254
Nickel	0.971	1.244
Zinc	1.75	2.243
Arsenic	0.457	0.586
Molybdenum	0.189	0.242
Cadmium	0.077	0.099
Lead	1.97	2.525
Sodium	9795	12553
Uranium	0.259	0.332
Potassium	48	68.3

Brian Park
Montana Tech
1300 West Park St.
'te, MT. 59701

Date: March 30, 2012
Request Number: 30281
Lab Number: N3261
Sample ID: OC-Head 3-9-12

REPORT OF ANALYSIS

Proximate Analysis ASTM D-5142	As Received Wt%	Moisture Free wt%	MAF Basis wt%
Moisture	5.38	******	******
Ash	8.93	9.44	******
Volatile Matter	37.73	39.87	44.03
Fixed Carbon	47.96	50.69	55.97
Total	100.00	100.00	100.00

Ultimate Analysis/ Method: ASTM D5142/5373			
Moisture	5.38	******	******
Hydrogen	3.60	3.80	4.20
Carbon	65.56	69.29	76.51
Nitrogen	1.00	1.06	1.17
Sulfur	0.21	0.22	0.25
Oxygen	15.32	16.19	17.87
Ash	8.93	9.44	******
Total	100.00	100.00	100.00

Heating Value, Btu/lb Method: ASTM D-5865			
	10,858	11,475	12,671

Trace Element, mg/kg	Method: D6357)
...ryllium	0.442
...nadium	3.88
Chromium	19
Manganese	43.2
Cobalt	1.36
Nickel	5.79
Copper	12
Zinc	11.8
Arsenic	1.03
Molybdenum	0.504
Cadmium	0.11
Antimony	0.11

Coal Ash Analysis, wt% Ignited Basis	
Silicon Dioxide, % as SiO2	48.15
Aluminum Oxide, % as Al2O3	15.78
Iron Oxide, % as Fe2O3	4.18
Calcium Oxide, % as CaO	14.39
Magnesium Oxide, % as MgO	3.66
Sodium Oxide, % as Na2O	6.16
Potassium Oxide, % as K2O	1.09
Titanium Oxide, % as TiO2	0.76
Manganese Dioxide, % as MnO2	0.08
Phosphorus Pentoxide, % as P2O5	0.18
Strontium Oxide, % as SrO	0.47
Barium Oxide, % as BaO	0.69
Sulfur Trioxide, % as SO3	4.41

Alkalies as Na20	6.88
Base to Acid Ratio	0.46
Silica Ratio	0.68
T250	2350

Forms of Sulfur (Method: ASTM D-2492)

Sulfate Sulfur	Pyretic Sulfur	Organic Sulfur
0.01%	0.04%	0.23%

X-Ray Diffraction of Coal D2

Analysis Results for Coal D2, -6+20 mesh

General Information

Analysis date	1/9/2012 1:52:26 PM		
Sample name	Otter_6	Measurement date	2011/12/27 12:03:42
File name	Otter_6.raw	Operator	Administrator

Measurement profile

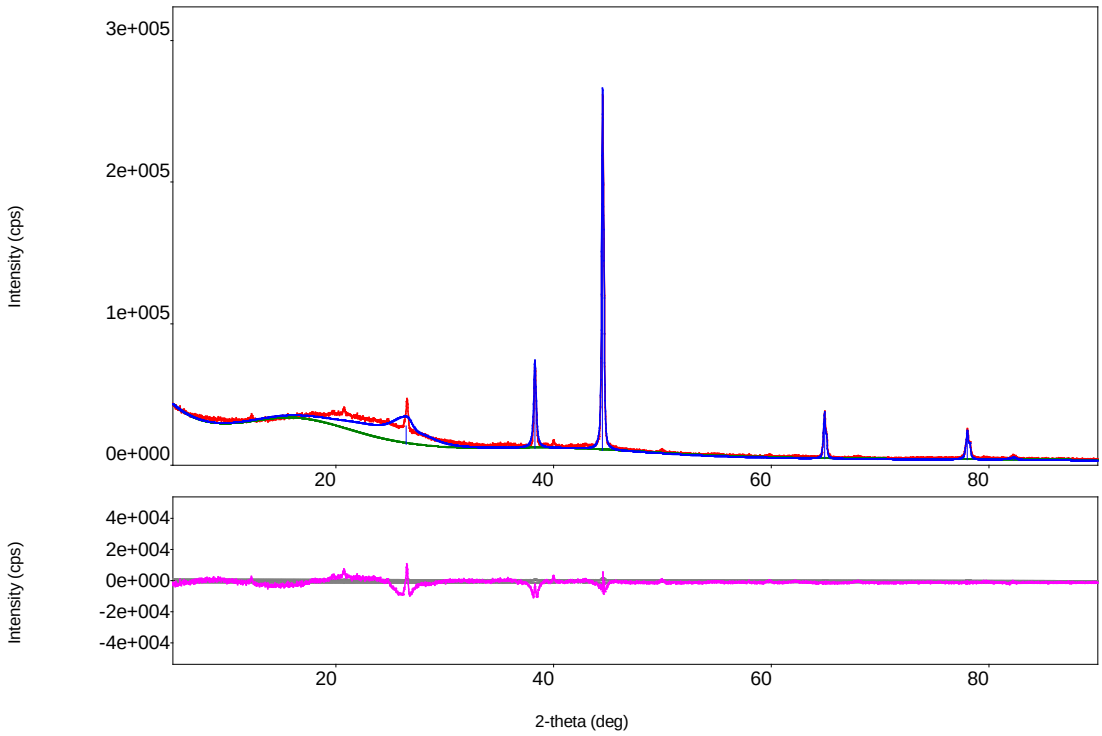

Qualitative analysis results

Phase name	Formula
Aluminum Magnesium	Al0.95 Mg0.05
Albite (heat-treated)	Na (Al Si3 O8)

Peak list

No.	2-theta(deg)	d(ang.)	Height(cps)	FWHM(deg)
1	26.48(7)	3.363(8)	12826(462)	3.5(2)
2	38.278(6)	2.3494(4)	47191(887)	0.21(2)
3	44.501(4)	2.03425(16)	216119(1898)	0.165(4)
4	64.912(3)	1.43534(6)	28668(691)	0.201(3)
5	78.043(5)	1.22343(7)	18154(550)	0.241(6)
6	82.31(2)	1.1704(3)	1435(155)	0.52(14)

Analysis results

File name	a(A)	b(A)	c(A)
Otter_6	4.063964	4.063964	4.063964
Otter_6	8.168543	12.815403	7.137465
Otter_6	0.000000e+000	0.000000e+000	0.000000e+000

Phase name	a(A)	b(A)	c(A)
Aluminum Magnesium	4.063964	4.063964	4.063964
Albite (heat-treated)	8.168543	12.815403	7.137465
Unknown	0.000000e+000	0.000000e+000	0.000000e+000

Quantitative analysis results (RIR)

Phase name	Content(%)

Aluminum Magnesium	100.0(19)
Albite (heat-treated)	0.000000e+000
Unknown	0.000000e+000

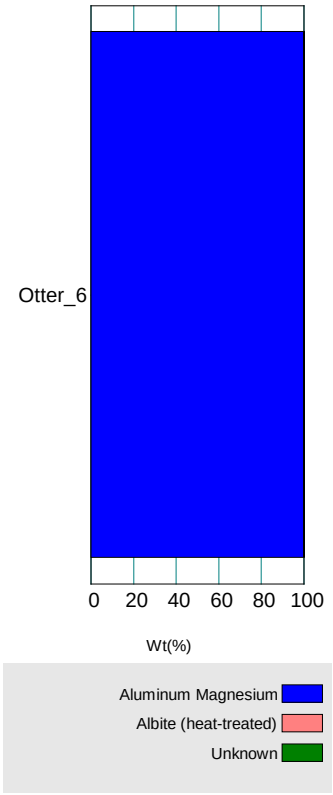

Analysis Results, -12+20 mesh

General Information

Analysis date	1/9/2012 1:50:19 PM		
Sample name	Otter_12	Measurement date	2011/12/27 12:57:04
File name	Otter_12.raw	Operator	Administrator
Comment			

Measurement profile

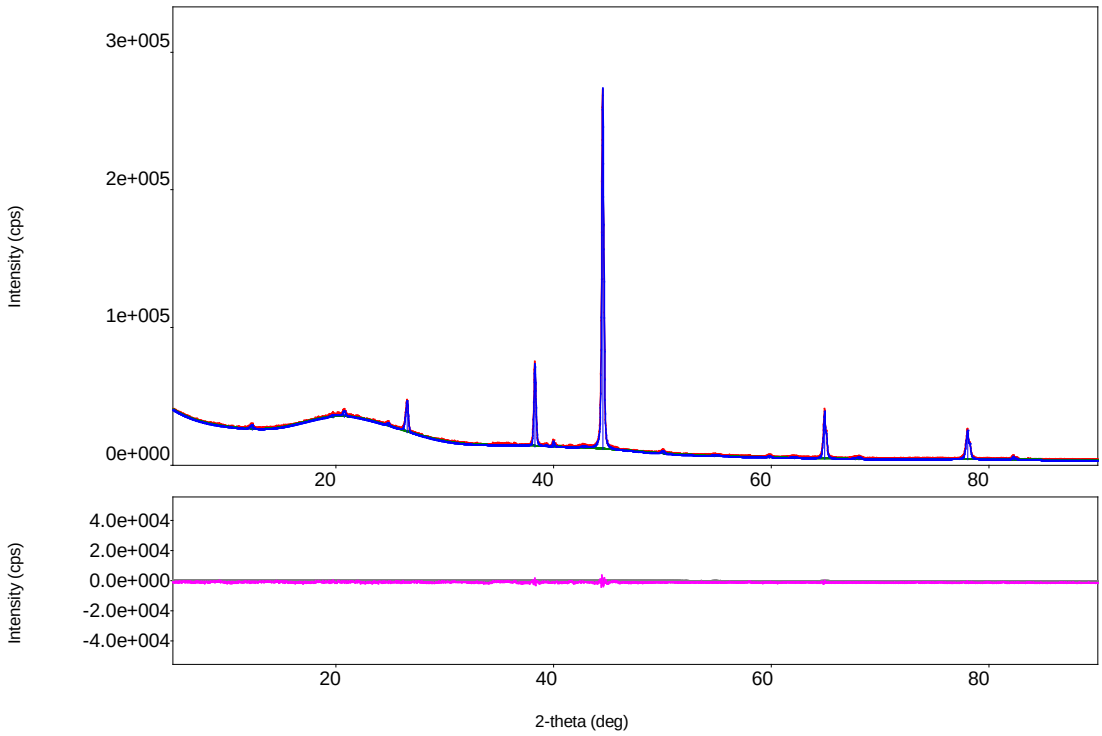

Measurement conditions

X-Ray	40 kV , 44 mA	Scan speed / Duration time	4.0000 deg./min.
Goniometer		Step width	0.0200 deg.
Attachment	-	Scan axis	2Theta/Theta
Filter	K-beta filter	Scan range	5.0000 - 90.0000 deg.
CBO selection slit	BB	Incident slit	2/3deg.
Diffrected beam mono.		Length limiting slit	-
Detector	D/teX Ultra	Receiving slit #1	8.00mm
Scan mode	CONTINUOUS	Receiving slit #2	Open

Qualitative analysis results

Phase name	Formula	Figure of merit	Phase reg. detail	DB card number
Aluminum Magnesium	Al0.95 Mg0.05	1.045	ICDD (PDF2010)	01-074-5237
Quartz alpha, alpha-Si O2	Si O2	0.843	ICDD (PDF2010)	01-089-8936

Peak list

No.	2-theta(deg)	d(ang.)	Height(cps)	FWHM(deg)	Phase name
1	12.294(19)	7.193(11)	2031(82)	0.33(3)	Unknown
2	19.69(3)	4.505(7)	912(55)	1.54(12)	Unknown
3	20.72(2)	4.284(4)	2313(88)	0.249(17)	Quartz alpha, alpha-Si O2(1,0,0)
4	24.77(4)	3.591(6)	1533(71)	0.25(4)	Unknown
5	26.521(3)	3.3581(4)	15604(228)	0.266(3)	Quartz alpha, alpha-Si O2(0,1,1)
6	38.250(3)	2.3511(2)	46446(393)	0.181(3)	Aluminum Magnesium(1,1,1)
7	39.30(3)	2.2905(1	677(48)	0.24(9)	Quartz alpha, alpha-Si O2(1,0,2)

8	39.961(12)	2.2543(6)	3367(106)	0.139(14)	Unknown
9	42.74(11)	2.114(5)	740(50)	0.63(9)	Quartz alpha, alpha-Si O2(2,0,0)
10	44.4771(12)	2.03528(	216950(850)	0.1698(12)	Aluminum Magnesium(2,0,0)
11	50.03(3)	1.8216(9)	1473(70)	0.34(3)	Quartz alpha, alpha-Si O2(1,1,2)
12	54.75(7)	1.675(2)	689(48)	0.90(11)	Quartz alpha, alpha-Si O2(0,2,2)
13	59.815(18)	1.5449(4)	1033(59)	0.27(3)	Quartz alpha, alpha-Si O2(1,2,1)
14	62.09(6)	1.4936(1	562(43)	0.65(7)	Unknown
15	64.8871(19)	1.43584(	29931(316)	0.201(2)	Aluminum Magnesium(2,2,0)
16	67.69(2)	1.3831(4)	761(50)	0.36(3)	Quartz alpha, alpha-Si O2(1,2,2)
17	68.03(3)	1.3769(5)	1196(63)	0.31(3)	Quartz alpha, alpha-Si O2(2,0,3)
18	78.029(3)	1.22360(	18341(247)	0.247(3)	Aluminum Magnesium(3,1,1)
19	82.235(13)	1.17135(	2140(84)	0.249(15)	Aluminum Magnesium(2,2,2)

Analysis results

Phase name	a(A)	b(A)	c(A)
Aluminum Magnesium	4.065863	4.065863	4.065863
Quartz alpha, alpha-Si	4.932005	4.932005	5.421667
Unknown	0.000000e+000	0.000000e+000	0.000000e+000
Unknown			

Crystallite size and lattice strain

Williamson-Hall method

Phase name	Crystallite size(A)	Strain (%)
Aluminum Magnesium	528.73(8)	0.0948(8)
Quartz alpha, alpha-Si O2	324.3(9)	0.16(2)

Quantitative analysis results (RIR)

Phase name	Content(%)
Aluminum Magnesium	100.0(6)
Quartz alpha, alpha-Si O2	0.000000e+000
Unknown	0.000000e+000

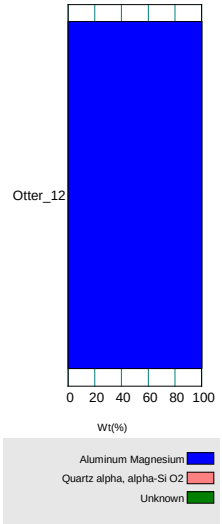

Analysis Results, -12+48 mesh

General Information

Analysis date	1/9/2012 1:46:51 PM		
Sample name	Otter_48	Measurement date	2011/12/27 13:44:39
File name	Otter_48.raw	Operator	Administrator
Comment			

Measurement profile

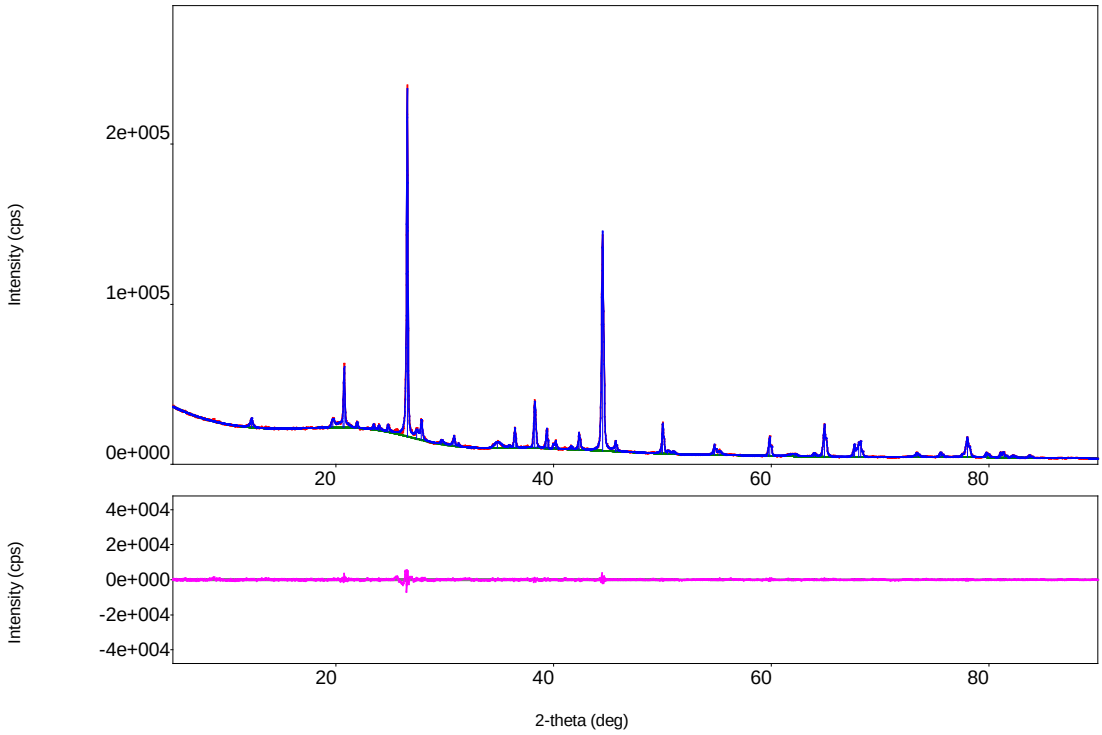

Measurement conditions

X-Ray	40 kV , 44 mA	Scan speed / Duration time	4.0000 deg./min.
Goniometer		Step width	0.0200 deg.
Attachment	-	Scan axis	2Theta/Theta
Filter	K-beta filter	Scan range	5.0000 - 90.0000 deg.
CBO selection slit	BB	Incident slit	2/3deg.
Diffrected beam mono.		Length limiting slit	-
Detector	D/teX Ultra	Receiving slit #1	8.00mm
Scan mode	CONTINUOUS	Receiving slit #2	Open

Qualitative analysis results

Phase name	Formula	Figure of merit	DB card number
pyrope, high, syn, trimagnesium	Mg3 Al2 (Si O4)3	1.640	01-086-0151
sodium magnesium aluminum	Na1.78 (Mg1.87 Al0.13) (Si2	1.512	01-070-7264
Celsian	Ba Al1.94 Si2.06 O8	1.356	01-074-1677

albite, high, sodium tecto-	Na (Al Si3 O8)	1.939	01-083-1612
Jadeite	Na Al (Si2 O6)	1.563	01-076-6328
sodium alumosilicate	Na6 Al6 Si10 O32	2.092	01-074-1787

Peak list

No.	2-theta(deg)	d(ang.)	Height(cps)	FWHM(deg)	Phase name
1	12.238(10)	7.227(6)	3931(114)	0.248(13)	sodium alumosilicate(1,1,0)
2	19.699(15)	4.503(3)	3186(103)	0.30(2)	albite, high, sodium tecto-
3	20.64(5)	4.300(10)	2528(92)	1.12(6)	sodium magnesium aluminum
4	20.752(3)	4.2769(6)	24602(286)	0.136(2)	Jadeite(1,1,-1)
5	21.919(17)	4.052(3)	2560(92)	0.159(14)	Celsian(2,1,-1),albite, high,
6	23.457(12)	3.789(2)	2373(89)	0.14(2)	Celsian(1,3,0)
7	23.923(17)	3.717(3)	2184(85)	0.15(3)	albite, high, sodium tecto-
8	24.76(5)	3.593(7)	3220(104)	0.16(6)	sodium magnesium aluminum
9	26.541(3)	3.3557(4)	165834(743)	0.123(4)	Celsian(2,2,0)
10	27.39(4)	3.254(5)	3459(107)	0.32(8)	Celsian(2,0,-4),albite, high,
11	27.811(16)	3.2052(18	9575(179)	0.17(2)	sodium magnesium aluminum
12	29.66(2)	3.010(2)	1853(79)	0.27(4)	Celsian(1,3,2)
13	30.843(5)	2.8967(5)	5228(132)	0.120(9)	pyrope, high, syn,
14	31.260(13)	2.8590(12	1705(75)	0.06(2)	Celsian(2,0,2),albite, high,
15	34.81(3)	2.5751(18	2514(92)	0.76(3)	pyrope, high, syn,
16	35.86(5)	2.502(4)	922(55)	0.25(5)	sodium magnesium aluminum
17	36.445(5)	2.4632(3)	9501(178)	0.162(6)	pyrope, high, syn,
18	38.255(5)	2.3508(3)	21765(269)	0.186(4)	Unknown
19	38.37(4)	2.344(3)	510(41)	0.92(16)	pyrope, high, syn,
20	39.376(5)	2.2864(3)	9456(178)	0.153(6)	albite, high, sodium tecto-
21	39.962(12)	2.2542(6)	2626(94)	0.131(16)	Celsian(1,3,4)
22	40.188(6)	2.2421(3)	4325(120)	0.120(9)	Celsian(0,5,3),albite, high,
23	41.573(11)	2.1705(5)	1710(75)	0.127(19)	Celsian(0,0,6),albite, high,
24	42.320(3)	2.13391(1	9416(177)	0.109(8)	sodium magnesium aluminum
25	44.4832(9)	2.03502(4	113587(615)	0.1702(10)	pyrope, high, syn,
26	45.67(6)	1.985(2)	1206(63)	0.54(6)	sodium magnesium aluminum
27	45.695(5)	1.9838(2)	3995(115)	0.110(9)	albite, high, sodium tecto-
28	50.010(2)	1.82228(7	16739(236)	0.138(3)	pyrope, high, syn,
29	50.46(4)	1.8072(13	1355(67)	0.33(6)	Celsian(1,7,0),albite, high,
30	50.96(4)	1.7904(13	1216(64)	0.31(7)	pyrope, high, syn,
31	54.788(5)	1.67414(1	5457(135)	0.138(9)	Celsian(2,7,-
32	55.20(2)	1.6626(6)	2034(82)	0.29(5)	pyrope, high, syn,
33	59.868(4)	1.54364(9	10115(184)	0.188(4)	pyrope, high, syn,
34	62.16(3)	1.4922(7)	1058(59)	0.87(4)	sodium magnesium aluminum
35	63.947(11)	1.4547(2)	1883(79)	0.195(14)	sodium magnesium aluminum
36	64.890(3)	1.43578(5	17553(242)	0.203(3)	sodium magnesium aluminum
37	67.646(3)	1.38384(5	6873(151)	0.169(4)	Celsian(2,6,-8),albite, high,
38	68.036(4)	1.37685(7	7715(160)	0.199(12)	pyrope, high, syn,
39	68.206(4)	1.37382(8	4965(129)	0.123(13)	Celsian(0,3,9)
40	73.370(10)	1.28936(1	2200(86)	0.22(2)	pyrope, high, syn,
41	75.567(9)	1.25724(1	2580(93)	0.196(9)	pyrope, high, syn,
42	77.555(13)	1.22989(1	1495(71)	0.20(2)	pyrope, high, syn,

43	78.016(3)	1.22378(4	10805(190)	0.245(4)	sodium magnesium aluminum
44	79.780(6)	1.20109(8	2703(95)	0.216(10)	Celsian(4,9,-3),Jadeite(6,4,-
45	81.077(6)	1.18512(7	3115(102)	0.169(6)	Celsian(4,0,-12),sodium
46	81.396(8)	1.18129(1	2085(83)	0.209(14)	Celsian(5,8,-3),Jadeite(3,5,2)
47	82.244(12)	1.17123(1	1254(65)	0.279(16)	Celsian(5,8,-5),sodium
48	83.754(10)	1.15392(1	1490(70)	0.229(10)	pyrope, high, syn,

Phase name	a(A)	b(A)	c(A)
pyrope, high, syn,	11.532447	11.532447	11.532447
sodium magnesium	4.979931	4.979931	6.396083
Celsian	8.602703	13.048730	14.378747
albite, high, sodium	8.181180	12.852744	7.083620
Jadeite	9.234474	8.403517	5.120004
sodium alumosilicate	10.180680	10.180680	10.180680
Unknown	0.000000e+000	0.000000e+000	0.000000e+000

Crystallite size and lattice strain

Williamson-Hall method

Phase name	Crystallite size(A)	Strain (%)
pyrope, high, syn, trimagnesium dialuminum tris(silicate)	504.4(3)	0.069(4)
sodium magnesium aluminum disilicate	299.17(9)	0.062(8)
Celsian	678(5)	0.138(15)
albite, high, sodium tecto-alumotrisilicate	489.0(2)	0.068(4)
Jadeite	337.1(10)	0.15(3)
sodium alumosilicate	546.7(16)	0.097(13)

Quantitative analysis results (RIR)

Phase name	Content(%)
pyrope, high, syn, trimagnesium dialuminum tris(silicate)	45.219421
sodium magnesium aluminum disilicate	26.147317
Celsian	5.992637
albite, high, sodium tecto-alumotrisilicate	17.875074
Jadeite	4.759377
sodium alumosilicate	0.006173
Unknown	0.000000e+000
albite, high, sodium tecto-alumotrisilicate	
sodium magnesium aluminum disilicate	
Celsian	
albite, high, sodium tecto-alumotrisilicate	
sodium alumosilicate	
Jadeite	
albite, high, sodium tecto-alumotrisilicate	
Jadeite	
Celsian	
Celsian	

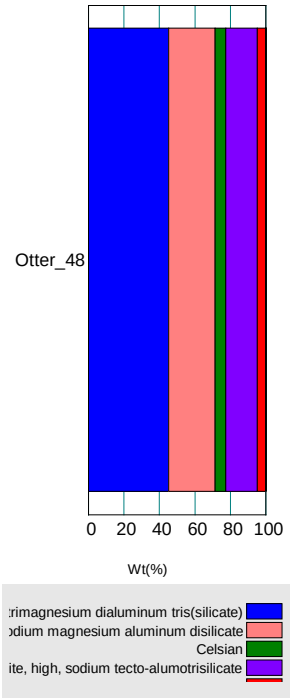
Otter_48
0
20
40
60
80
100
Wt(%)
rimagnesium dialuminum tris(silicate)
odium magnesium aluminum disilicate
Celsian
ite, high, sodium tecto-alumotrisilicate

APPENDIX C. SUMMARY OF STABCAL MODELING RESULTS

Coals from four site locations were collected by CAMP personnel. The collected samples included coarse, fine, and waste samples. These samples were provided for ashing and elemental analyses to the Wyoming Analytical Laboratories (Wallaramie@wal-lab.com) and a portion was provided to CAMP's laboratory for Mineral Liberation Analyses (MLA for phase identification, Miranda 2009).

A preliminary modeling study was conducted to understand what reagents may be effective in lowering the sodium and potassium concentrations to less than three percent in the final ash solids. Therefore, the influence of incremental reagent titration on the stability of coal ash solids was modeled using the speciation/titration equilibrium calculational program developed by H.H. Huang (STABCAL, 2009). Six standard free energies of formation databases are available to the user of the STABCAL program. We used the National Bureau of Standards (NBS) and Twidwell Personal databases. The reagents modeled included hydrochloric acid, sulfuric acid, sulfurous acid, carbonic acid, and acetic acid. The results for hydrochloric and sulfuric acids are presented for samples 4 (coarse) and 5 (fine); 8 (coarse) and 9 (fine); and 14 (fine).

The speciation/titration modeling effort was based on the following:

- The Wyoming Laboratories (WY) analyses were performed on each coal ash solids by x-ray fluorescence instrumentation (XRF). The WY results were reported as oxides for each element present. The oxide data was used to calculate the elemental content used in the modeling program.
- The CAMP MLA analyses were performed on sized as-received coals. Therefore, the results reflect the mineralization present in the original coals. The MLA phase identification was used to determine what compound assemblages should be used in the modeling program, including especially the sodium and potassium bearing compounds.
- The National Bureau of Standards (NBS, Wagman, et al) and Twidwell Personal databases were used to provide the required necessary thermodynamic data (standard free energies of formation) for the modeling program. The databases were also used to select the aqueous and solid species to be considered in the equilibrium calculations.
- The initial solution pH was selected to be six and all calculations were conducted using data at an ambient temperature of 25^{o}C.
- The Reduction/Oxidation Potential (E_H) was chosen based on the S(VI)/S(II) couple (slightly reducing).
- A variety of additive acidic reagents were chosen for the titration process.

Multiple outputs are possible with the STABCAL program. The outputs chosen for inclusion in this report were 1) the distribution of sodium (and in some cases potassium) species within the solution and solid compounds; 2) the amount (in grams/liter) of each solid formed; and 3) the amount of anionic reagent species (chloride or sulfate, in grams/liter) added to the treated water. Using these data the conditions necessary for removal of sodium plus potassium were specified, in order, to attain a solid product that contained less than three percent. However, be aware that the modeling results are based on equilibrium considerations and does not reflect the possibility of slow kinetic reaction rates.

COAL A

Coal A contained such a low concentration of sodium and potassium in the ash (based on the Table 1 analytical data) that these samples were not modeled.

Table 1. Elemental makeup based on ash chemistry for Coal A fines

Wyoming Lab	Concentration, g/L										
	%	Al	Ca	Mg	Fe	K	Na	O	P	S	Si
SiO2	45.2							24.1		21.1	
Al2O3	15.1	8.0						7.1			8.0
Fe2O3	5.2				3.6			1.6			
CaO	17.8		12.7					5.1			
MgO	3.0			1.8				1.2			
Na2O	0.6						0.5	0.2			
K2O	0.1					0.1		0.0			
SO3	10.2							6.1	4.1		
Total	**97.2**	**8.00**	**12.73**	**1.79**	**3.61**	**0.12**	**0.47**	**45.30**	**4.10**	**21.11**	**8.00**

Source: Mellis (Wyoming Analytical Laboratory, 2009). Results reported as oxides in the coal ash. Coal A (coarse) ash had a similar composition.

Table 2. Phase makeup for Coal B fines

Mineral/Phase	Phase Stoichiometry	Relative Concentration, %
K-Feldspar	$KAlSi_3O_8$	73.34
Quartz	SiO_2	25.39
Amphibole	$(Mg,Fe)_3Al_2Si_8O_{22}(OH)_2$	0.43
Na-Amphibole	$Na_2(Mg,Fe)_3Al_2Si_8O_{22}(OH)_2$	0.4
Zircon	$ZrSiO_4$	0.19
Pyrite	FeS_2	0.15
Apatite-Albite	$Ca_5(PO_4)_3OH$ $NaAlSi_3O_8$	0.03

Source: Miranda, MLA (Center for Advanced Mineral and Metallurgical Processing, 2009)

COAL B

The data used for the modeling studies are presented in Tables 3 and 4. The sodium bearing phases were albite, $NaAlSi_3O_8$ (major) and sodium amphiboles $Na_2(Mg,Fe)_3Al_2Si_8O_{22}(OH)_2$ (minor). The sodium amphiboles were assumed to be present even though their relative presence in the analyzed ash was found to be low.

Table 3. Elemental makeup based on ash chemistry for Coal B fines

Wyoming Lab	Concentration, g/L										
	%	Al	Ca	Mg	Fe	K	Na	O	P	S	Si
SiO2	29.39							15.7			13.7
Al2O3	15.72	8.3						7.4			
Fe2O3	6.59				4.6			2.0			
CaO	14.21		10.2					4.1			
MgO	2.87			1.7				1.1			
Na2O	7.66						5.7	2.0			
K2O	0.81					0.7		0.1			

P2O5	1.91							0.8	1.1		
SO3	17.88							10.7		7.2	
Total	97.57	8.32	10.16	1.73	4.61	0.67	5.68	44.03	1.08	7.16	13.74

Source: Mellis (Wyoming Analytical Laboratory, 2009). Results reported as oxides. in the coal ash. Coal B (coarse) ash was from the same company site and had a similar composition to Coal B (fines).

Table 4. Phase makeup for Coal B fines

Mineral/Phase	Phase Stoichiometry	Relative Concentration, %
Quartz	SiO_2	51.9
Apatite	$Ca_5(PO_4)_3OH$	26.71
Apatite-Albite	$Ca_5(PO_4)_3OH\ NaAlSi_3O_8$	8.47
Kyanite	Al_2OSiO_4	5.69
Pyrite	FeS_2	2.74
Na-Amphibole	$Na_2(Mg,Fe)_3Al_2Si_8O_{22}(OH)_2$	1.5
K-Feldspar	$KAlSi_3O_8$	1.48
Barite	$BaSO_4$	1.37
Amphibole	$(Mg,Fe)_3Al_2Si_8O_{22}(OH)_2$	0.11
Ilmenite	$FeTiO_3$	0.02
Calcite	$CaCO_3$	0.01

Source: Miranda, MLA (Center for Advanced Mineral and Metallurgical Processing

SPECIATION/TITRATION RESULTS

The reagents modeled included hydrochloric acid, sulfuric acid, sulfurous acid, carbonic acid, and acetic acid. The results for hydrochloric and sulfuric acid are presented below.

HCl

The influence of HCl titration is presented in Figures 1-3 to define the solubility of the sodium and potassium bearing compounds i.e. albite, $NaAlSi_3O_8$ (major), sodium amphiboles $Na_2Mg_3Al_2Si_8O_{22}(OH)_2$ (glacuophane) and $Na_2Fe_3Al_2Si_8O_{22}(OH)_2$ (ferroglacuophane), and potassium feldspar, $KAlSi_3O_8$. All titration results are based on beginning the titration at a solution pH of six. Annotation notes are added the figure captions to illustrate the results shown by each figure.

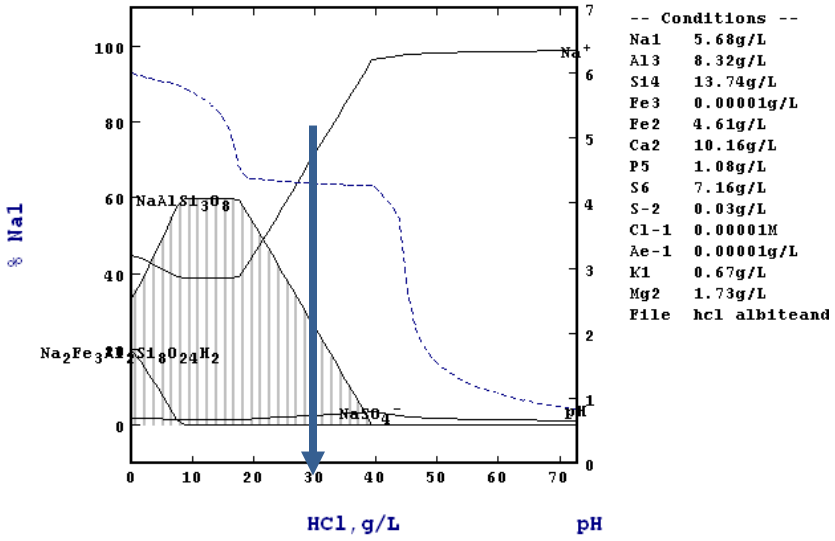

Figure 1. An illustration of the influence of titrating HCl acid on the distribution of sodium species. Note that a significant amount of HCl is required to completely dissolve the albite. However, it is not necessary to remove all the sodium to attain the project goal concentration in the ash solids (discussed later).

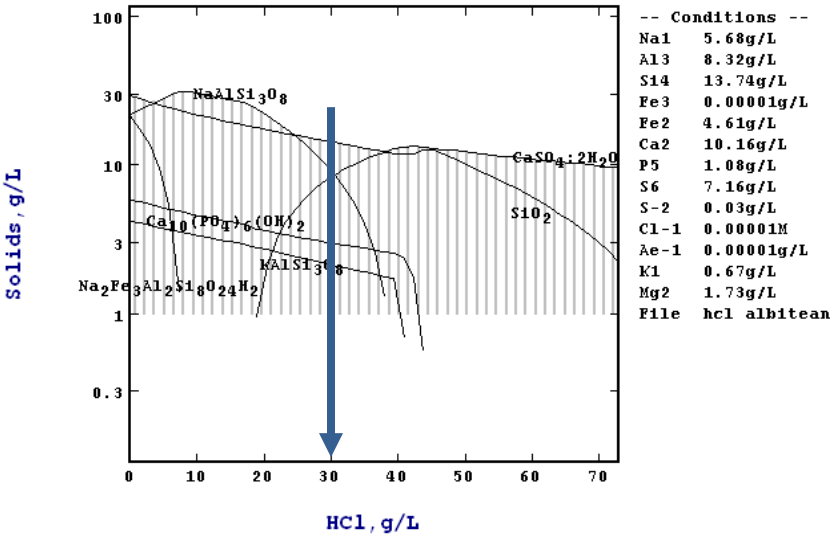

Figure 2. An illustration of the influence of titrating HCl acid on the presence of solids. The conditions to achieve a combination of sodium and potassium that is less than three percent concentration in the final ash solids is marked on the diagram (30.6 g/L HCl).

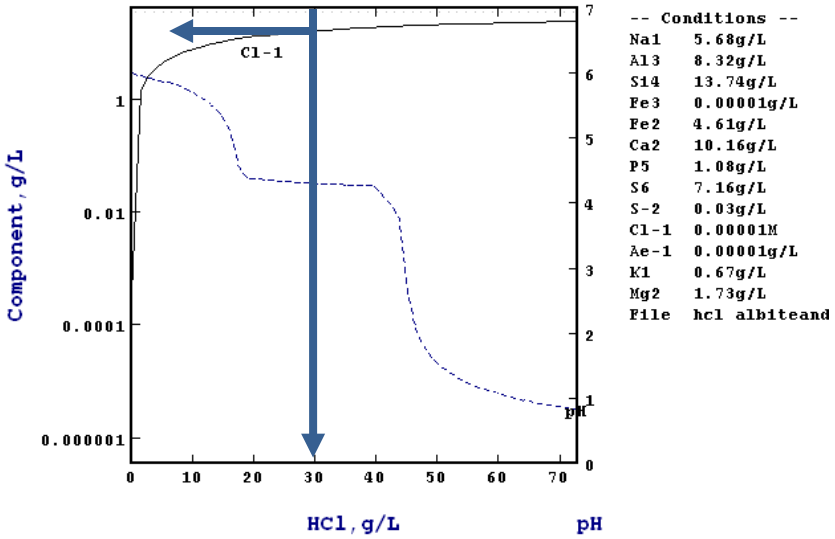

Figure 3. An illustration of the influence of titrating HCl acid on the increase in chloride content in the final leach solution. The chloride content (at three percent sodium plus potassium in the final ash solids) is marked on the diagram (16.2 g/L Cl^-).

H_2SO_4

The influence of H_2SO_4 titration is presented in Figures 4-6 to define the solubility of the sodium and potassium bearing compounds i.e. albite, $NaAlSi_3O_8$ (major), sodium amphiboles $Na_2Mg_3Al_2Si_8O_{22}(OH)_2$(glacuophane) and $Na_2Fe_3Al_2Si_8O_{22}(OH)_2$ (ferroglacuophane), and potassium feldspar, $KAlSi_3O_8$. All titration results are based on beginning the titration at a solution pH of six.

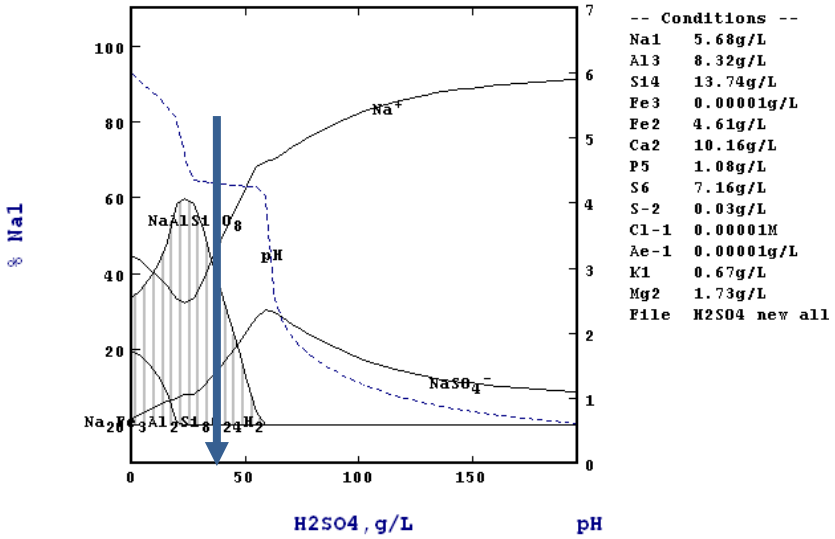

Figure 4. An illustration of the influence of titrating H2SO4 acid on the distribution of sodium species. Note that a significant amount of sulfuric acid is required to completely dissolve the albite.

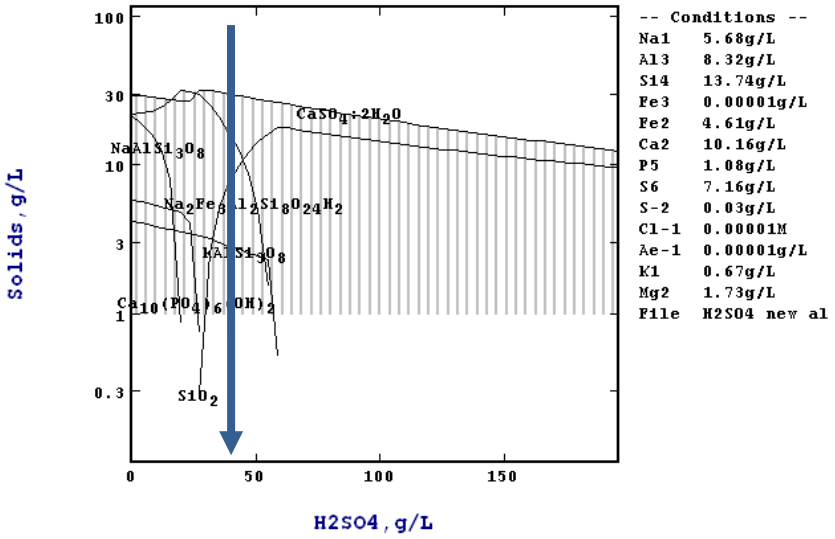

Figure 5. An illustration of the influence of titrating H2SO4 acid on the presence of solids. The conditions to achieve less than three percent sodium and potassium concentration in the final acid solids is marked on the diagram (43.1 g/L H2SO4).

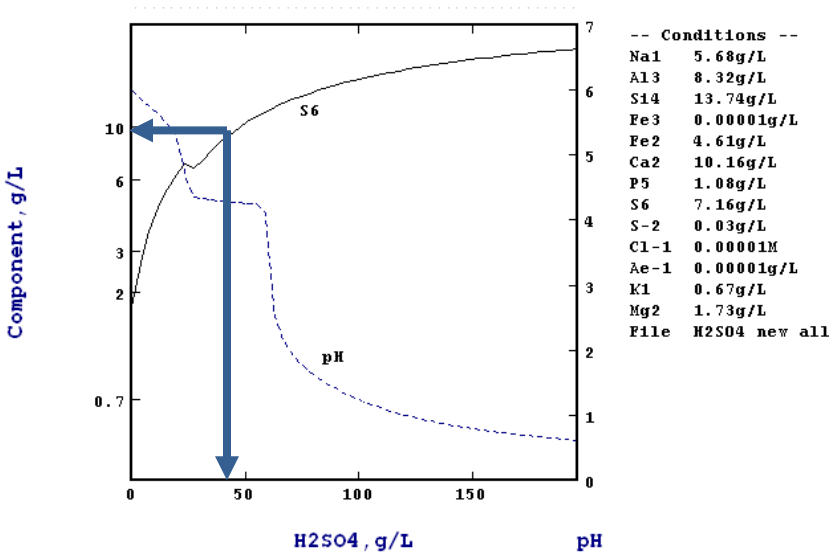

Figure 6. An illustration of the influence of titrating H2SO4 acid on the increase in sulfur (not sulfate) content in the final leach solution. The sulfur content (at three percent sodium plus potassium in the final solids) is marked on the diagram (9.3 g/L S; 27.9 g/L SO_4^{2-} in solution).

COAL C

The data used for the following modeling studies are presented in Tables 5 and 6. An assumption was made that albite was not present and only sodium amphiboles were present, e.g. $Na_2Mg_3Al_2Si_8O_{22}(OH)_2$(glacuophane) and $Na_2Fe_3Al_2Si_8O_{22}(OH)_2$ (ferroglacuophane). Potassium was included as $KAlSi_3O_8$. If these assumptions prove to be valid then coal C should respond to slightly acidic leaching to produce a coal product with less than three percent sodium plus potassium in the ash (see figures below). Note that based on the ash chemistry in the untreated state the sodium plus potassium concentration is less than the project goal concentration of three percent.

Table 5. Elemental makeup based on ash chemistry for Coal C fines

Wyoming Lab	%	Concentration, g/L									
		Al	Ca	Mg	Fe	K	Na	O	P	S	Si
SiO2	54.92							29.2			25.7
Al2O3	14.42	7.6						6.8			
Fe2O3	3.07				2.1			0.9			
CaO	14.35		10.3					4.1			
MgO	2.12			1.3				0.8			
Na2O	1.58						1.2	0.4			
K2O	1.41					1.2		0.2			
SO3	6.33							3.8		2.5	
Total	98.20	**7.6**	**10.3**	**1.3**	**2.1**	**1.2**	**1.2**	**46.3**	**0.0**	**2.5**	**25.7**

Source: Mellis (Wyoming Analytical Laboratory). Results reported as oxides in the coal ash. An assumption was made for the modeling that albite was not present and only sodium amphiboles were present, e.g. $Na_2Mg_3Al_2Si_8O_{22}(OH)_2$ (glacuophane) and $Na_2Fe_3Al_2Si_8O_{22}(OH)_2$ (ferroglacuophane). Potassium was assumed to be present as potassium feldspar. Coal C (coarse) was from the same company site and the ash had a similar composition to Coal C (fines).

Table 6. Phase makeup for Coal C fines

Mineral/Phase	Phase Stoichiometry	Relative Concentration, %
K-Feldspar	$KAlSi_3O_8$	41.03
Quartz	SiO_2	29.87
Na-Amphibole	$Na_2(Mg,Fe)_3Al_2Si_8O_{22}(OH)_2$	9.54
Kyanite	Al_2OSiO_4	9.44
Calcite	$CaCO_3$	5.87
Pyrite	FeS_2	3.58

Source: Miranda, MLA (Center for Advanced Mineral and Metallurgical Processing, 2009).

SPECIATION/TITRATION RESULTS

The reagents modeled included hydrochloric acid, sulfuric acid, sulfurous acid, carbonic acid, acetic acid. The results for hydrochloric and sulfuric acid are presented below.

HCl

The influence of HCl titration is presented in the Figures 7-10 to define the solubility of the primary sodium bearing compounds, i.e. sodium amphiboles, $Na_2Mg_3Al_2Si_8O_{22}(OH)_2$(glacuophane) and $Na_2Fe_3Al_2Si_8O_{22}(OH)_2$ (ferroglacuophane). All titration results are based on beginning the titration at a solution pH of six. Annotation notes are added the figure captions to illustrate the results shown by each figure.

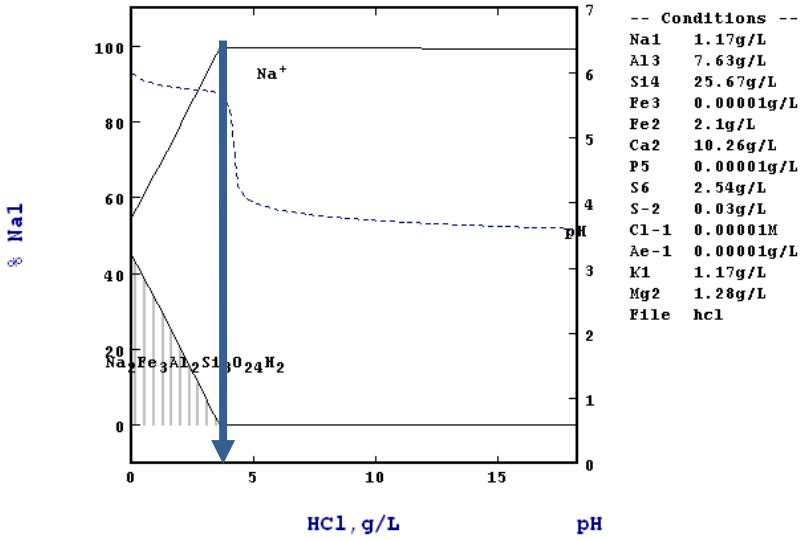

Figure 7. An illustration of the influence of titrating HCl acid on the distribution of sodium species. Note that rather dilute acidic conditions remove a significant amount of sodium, e.g. approximately 4 g/L HCl acid should remove essentially all the sodium.

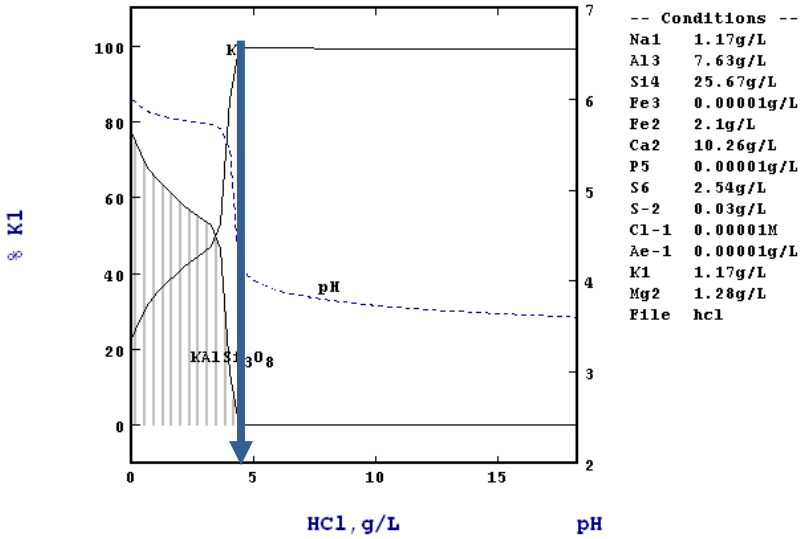

Figure 8. An illustration of the influence of titrating HCl acid on the distribution of potassium species. Note that rather dilute acidic conditions remove a significant amount of potassium, e.g. approximately 5 g/L HCl acid should remove essentially all the potassium.

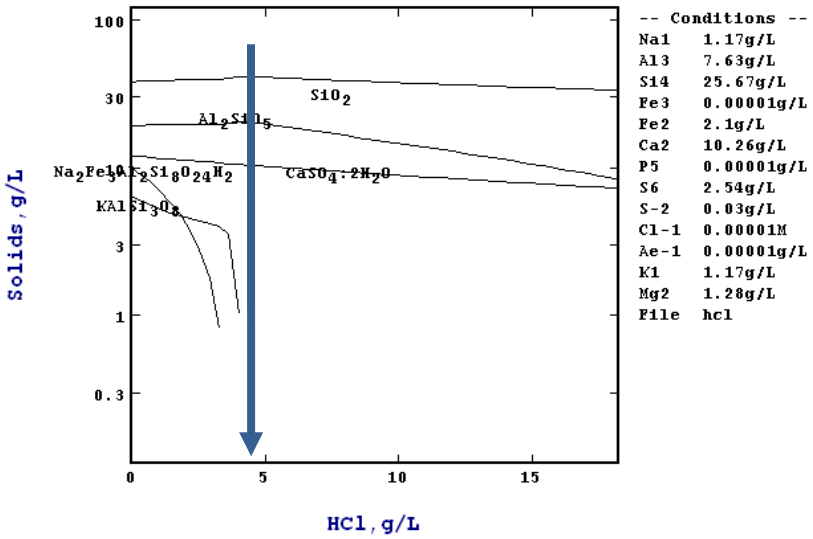

Figure 9. An illustration of the influence of titrating HCl acid on the presence of solids. The conditions to achieve essentially all the sodium and potassium are shown on the figure.

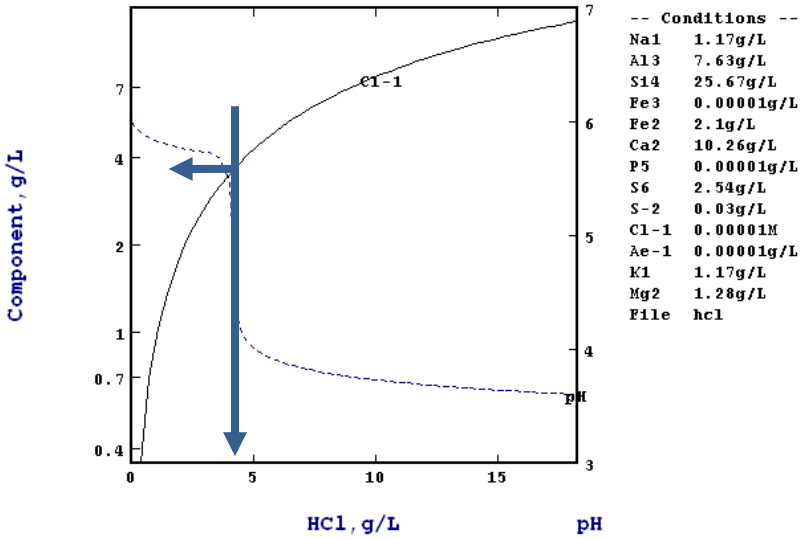

Figure 10. An illustration of the influence of titrating HCl acid on the increase in chloride content in the final leach solution.

H_2SO_4

The influence of H_2SO_4 titration is presented in the Figures 11-14 to define the solubility of the alkali compounds, i.e. sodium amphiboles, $Na_2Mg_3Al_2Si_8O_{22}(OH)_2$(glacuophane) and $Na_2Fe_3Al_2Si_8O_{22}(OH)_2$ (ferroglacuophane) and $KAlSi_3O_8$ (potassium feldspar). All titration results are based on beginning the titration at a solution pH of six.

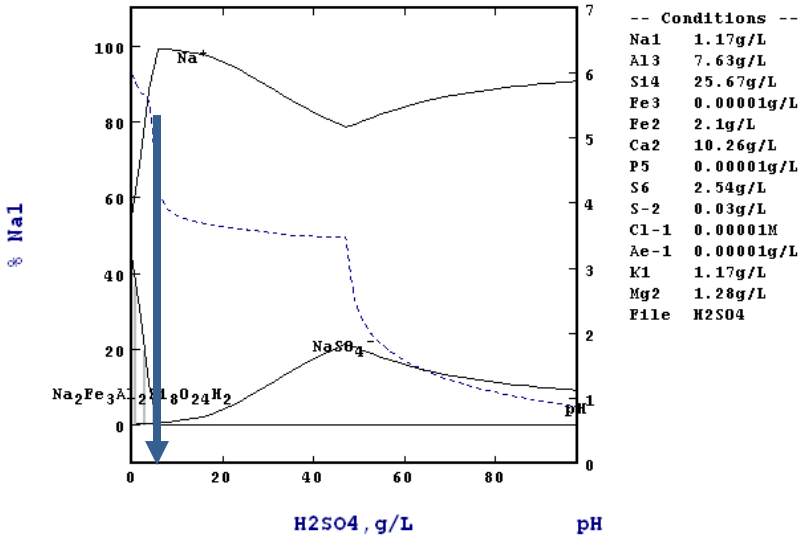

Figure 11. An illustration of the influence of titrating H_2SO_4 acid on the distribution of sodium species. Note that rather dilute acidic conditions remove a significant amount of sodium, e.g. approximately 4-5 g/L H_2SO_4 acid should remove essentially all the sodium.

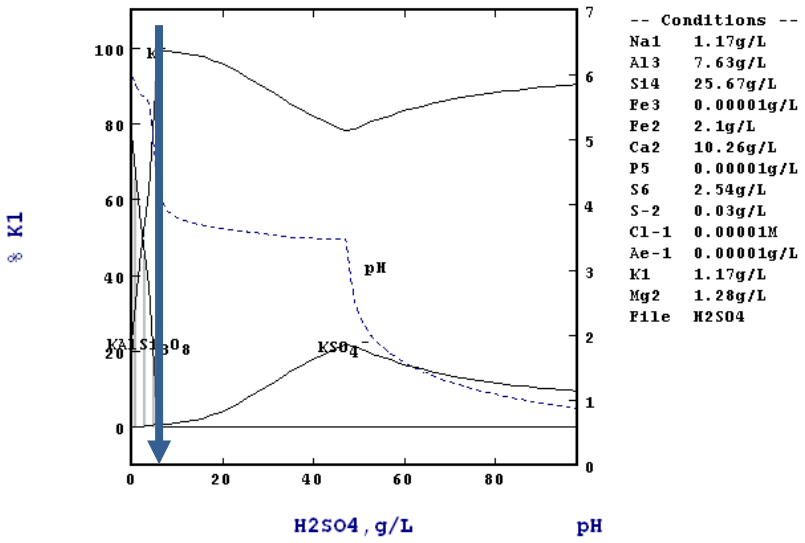

Figure 12. An illustration of the influence of titrating H2SO4 acid on the distribution of potassium species. Note that rather dilute acidic conditions remove a significant amount of sodium, e.g. approximately 4-5 g/L H_2SO_4 acid should remove essentially all the potassium.

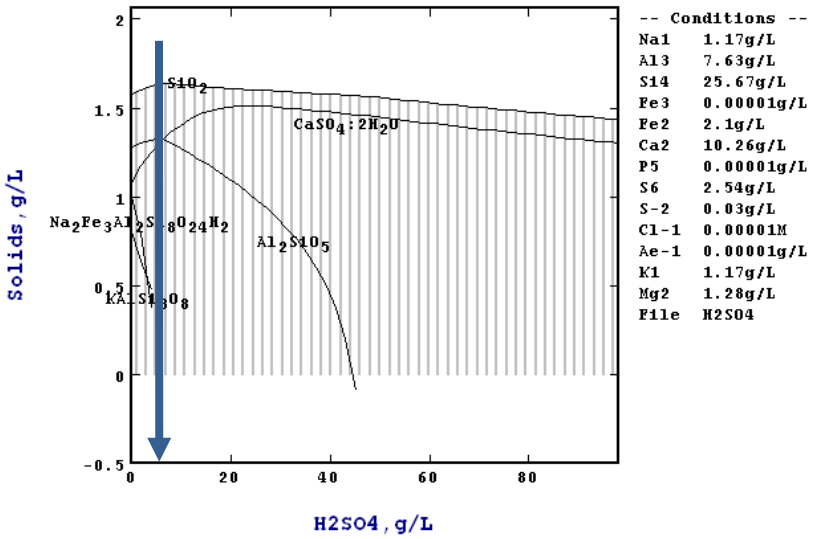

Figure 13. An illustration of the influence of titrating H_2SO_4 acid on the presence of solids. The conditions to achieve essentially all the sodium and potassium are shown on the figure.

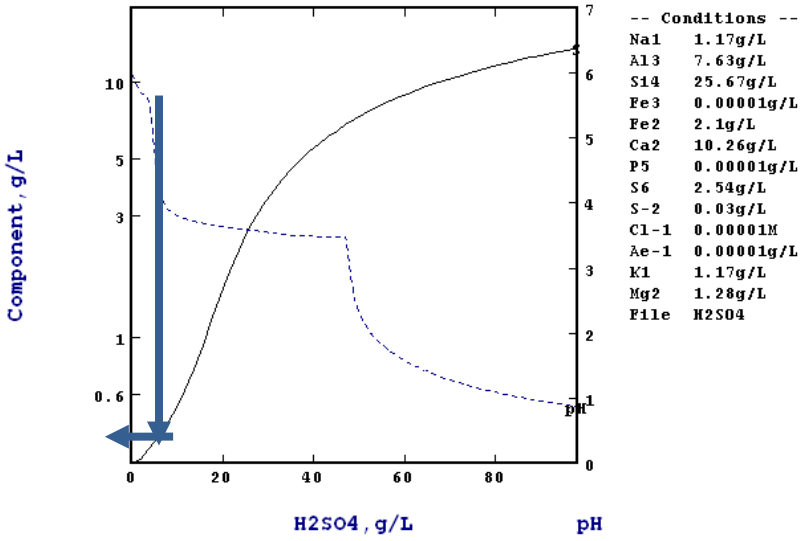

Figure 14. An illustration of the influence of titrating H_2SO_4 acid on the increase in sulfur (not sulfate) content in the final leach solution.

COAL D

The data used for the following modeling studies are presented in Tables 7 and 8. An assumption was made that the albite (which was a major phase in some of the other coals but was only a minor constituent as shown by MLA analyses) was not present and only sodium amphiboles would be present, e.g. $Na_2Mg_3Al_2Si_8O_{22}(OH)_2$(glacuophane) and $Na_2Fe_3Al_2Si_8O_{22}(OH)_2$ (ferroglacuophane). If these assumptions prove to be valid then coal 14 should respond to slightly acidic leaching to produce a coal product with less than three percent sodium in the ash (see figures below).

Table 7. Elemental makeup based on ash chemistry for Coal D fines

Wyoming Lab	%	Concentration, g/L									
		Al	Ca	Mg	Fe	K	Na	O	P	S	Si
SiO2	26.06							13.9			12.2
Al2O3	20.21	10.7						9.5			
Fe2O3	4.32				3.0			1.3			
CaO	23.4		16.7					6.7			
MgO	4.9			3.0				1.9			
Na2O	10.72						8.0	2.8			
K2O	0.29					0.2		0.0			
P2O5	0.6					0.2		0.4	0.3		
SO3	6.44							3.9		2.6	
Total	**96.94**	**10.7**	**16.72**	**2.96**	**3.02**	**0.24**	**7.95**	**40.25**	**0.34**	**2.58**	**12.18**

Source: Mellis (Wyoming Analytical Laboratory, 2009). Results reported as oxides in the coal ash. An assumption was made that the major sodium phases were amphiboles, e.g. $Na_2Mg_3Al_2Si_8O_{22}(OH)_2$(glacuophane) and $Na_2Fe_3Al_2Si_8O_{22}(OH)_2$ (ferroglacuophane).

Table 8. Phase makeup for Coal D fines

Mineral/Phase	Phase Stoichiometry	Relative Concentration, %
Quartz	SiO_2	16.64
Apatite	$Ca_5(PO_4)_3OH$	0.01
Apatite-Albite	$Ca_5(PO_4)_3OH\ NaAlSi_3O_8$	2.15
Kyanite	Al_2OSiO_4	17.76
Pyrite	FeS_2	0.11
Na-Amphibole	$Na_2(Mg,Fe)_3Al_2Si_8O_{22}(OH)_2$	36.32
K-Feldspar	$KAlSi_3O_8$	0.59
Barite	$BaSO_4$	0.26
Amphibole	$(Mg,Fe)_3Al_2Si_8O_{22}(OH)_2$	25.07

Source: Miranda, MLA (Center for Advanced Mineral and Metallurgical Processing, 2009.) Free energy of formation for amphibole was unavailable and only sodium amphiboles were included in the modeling.

SPECIATION/TITRATION RESULTS

The reagents modeled included hydrochloric acid, sulfuric acid, sulfurous acid, and carbonic acid. The results for only hydrochloric and sulfuric acid are presented below.

HCl

The influence of HCl titration is presented in the Figures 15-17 to define the solubility of the primary sodium bearing compounds, i.e. sodium amphiboles, $Na_2(Mg,Fe)_3Al_2Si_8O_{22}(OH)_2$ (major). Both amphibole species were included in the modeling; i.e. $Na_2Mg_3Al_2Si_8O_{22}(OH)_2$(glacuophane) and $Na_2Fe_3Al_2Si_8O_{22}(OH)_2$ (ferroglacuophane). All titration results are based on beginning the titration at a solution pH of six.

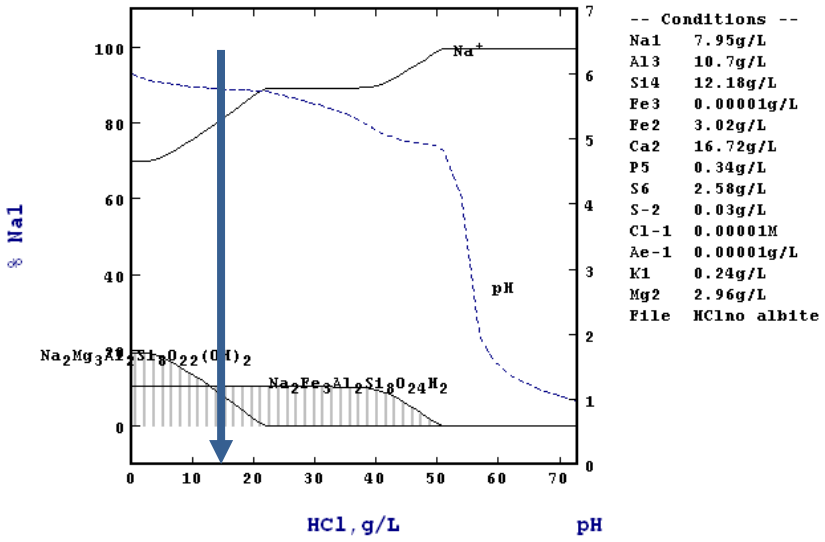

Figure 15. An illustration of the influence of titrating HCl acid on the distribution of sodium species. Note that rather dilute acidic conditions remove a significant amount of sodium.

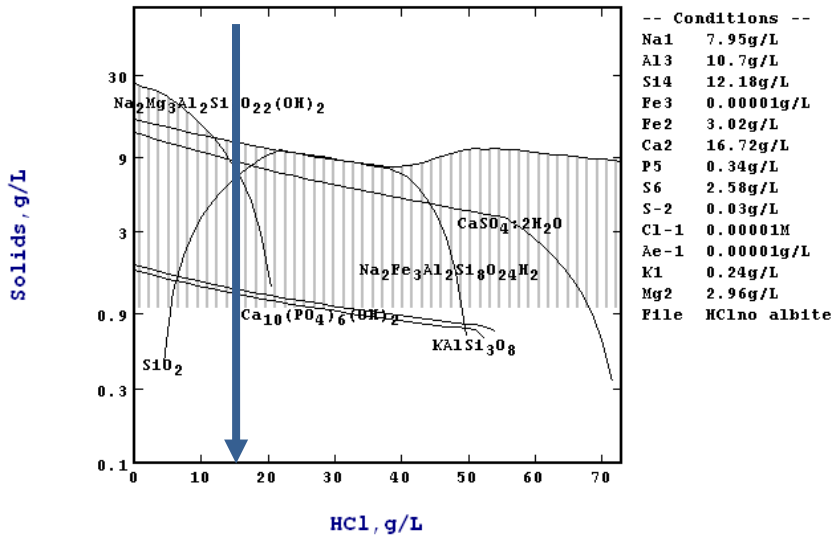

Figure 16. An illustration of the influence of titrating HCl acid on the presence of solids. The conditions to achieve less than three percent sodium concentration in the final ash solids is marked on the diagram (14.6 g/L HCl).

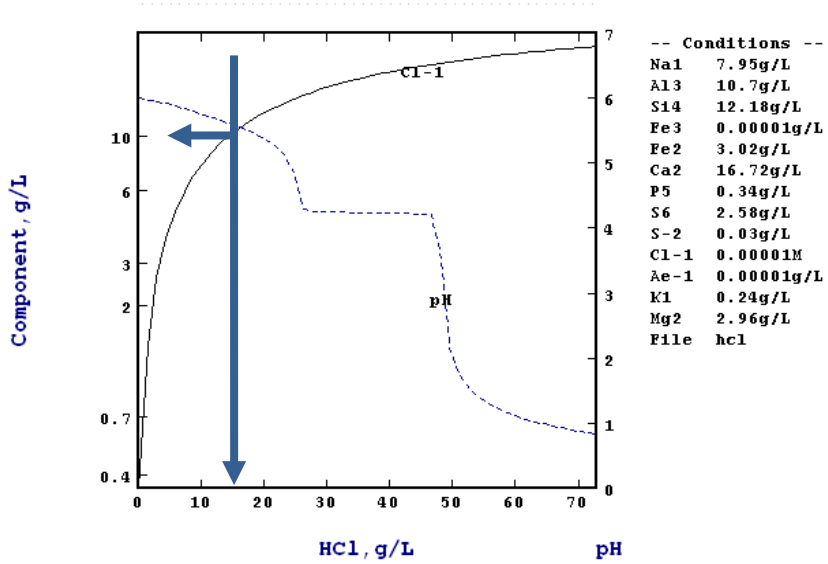

Figure 17. An illustration of the influence of titrating HCl acid on the increase in chloride content in the final leach solution. The chloride content (at three percent sodium in the final ash solids) is marked on the diagram (10.1 g/L Cl^-).

H_2SO_4

The influence of H_2SO_4 titration is presented in the Figures 18-20 to define the solubility of the primary sodium bearing compounds, i.e. sodium amphiboles, $Na_2(Mg,Fe)_3Al_2Si_8O_{22}(OH)_2$ (major). Both amphibole species were included in the modeling; i.e. $Na_2Mg_3Al_2Si_8O_{22}(OH)_2$(glacuophane) and $Na_2Fe_3Al_2Si_8O_{22}(OH)_2$ (ferroglacuophane). All titration results are based on beginning the titration at a solution pH of six.

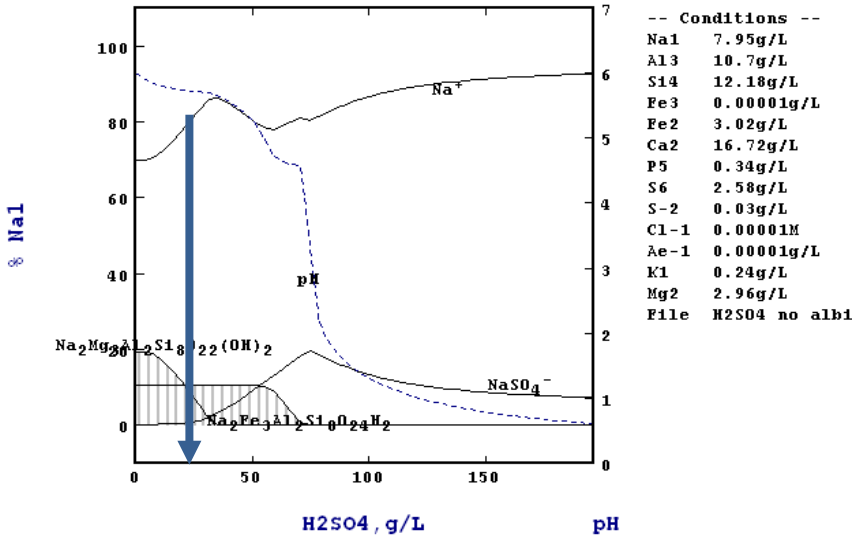

Figure 18. An illustration of the influence of titrating H_2SO_4 acid on the distribution of sodium species. Note that rather dilute acidic conditions remove a significant amount of sodium.

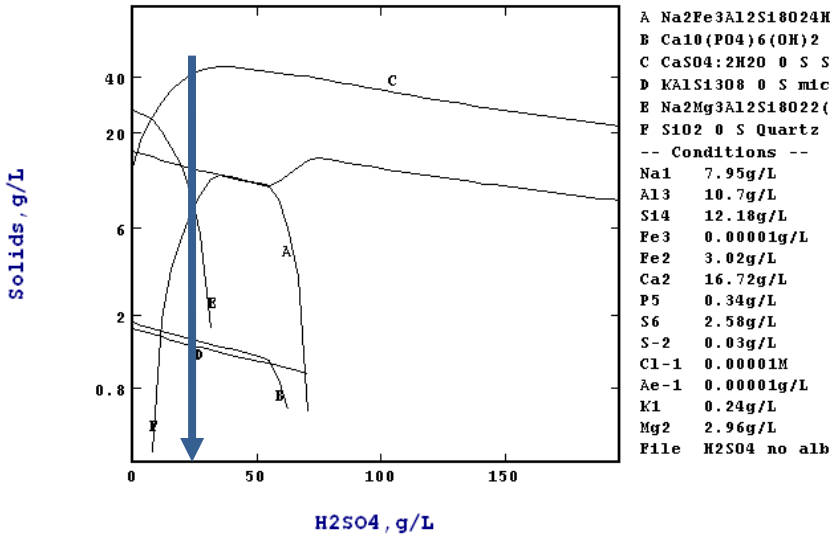

Figure 19. An illustration of the influence of titrating H_2SO_4 acid on the presence of solids. The conditions to achieve less than three percent sodium concentration in the final solids is marked on the diagram (11.8 g/L H_2SO_4).

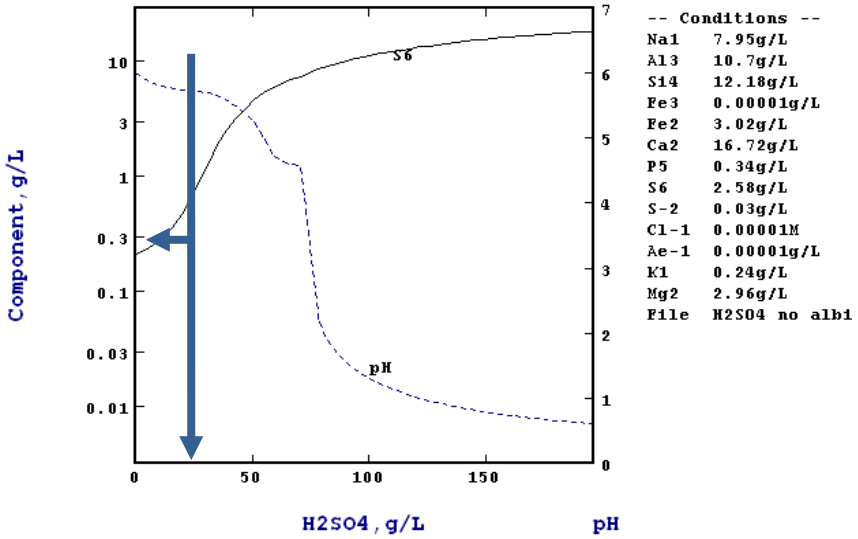

Figure 20. An illustration of the influence of titrating H_2SO_4 acid on the increase in sulfur (not sulfate) content in the final leach solution. The sulfur content (at three percent sodium in the final ash solids) is marked on the diagram (0.3 g/L S, 0.9 g/l $SO4^{2-}$).

CONCLUSIONS

The thermodynamic equilibrium modeling result conclusions are presented in Table 9. However, be aware that the modeling results are based on equilibrium considerations and does not reflect the possibility of slow kinetic reaction rates. Therefore, these results must be subjected to laboratory verification or non-verification.

Table 9. Summary conclusion results for STABCAL speciation/titration modeling

Coals	Anticipated Na and K Response for Reagent Type		Comments
	HCl	H_2SO_4	
A	Ash from as-received coal already below project goal	Ash from as-received coal already below project goal	Modeling not performed
B	Requires significant acid to achieve an ash with <3%	Required significant acid to achieve as ash with <3%	Treated water would be relatively high in anionic species
C	Good response at low acid additions	Good response at low acid additions	Ash from as-received coal already below project goal but near enough that modeling performed. Laboratory verification required.

D	Good response at low acid additions	Good response at low acid additions	Laboratory verification required

APPENDIX D. SUMMARY OF HSC ELEVATED TEMPERATURE MODELING RESULTS

HSC 6.0 (Reine 2006) Preliminary Modeling for Combustion of Coal B2

Basic Assumptions:

- 1000 kg of Coal B2
- Wyoming Lab Analyses for Coal Used for Water, Carbon, Nitrogen, Sulfur, and Ash Inputs to Model

Ultimate Analysis/ Method: ASTM D5142/5373		
Moisture	20.74	
Hydrogen	3.01	
Carbon	56.83	
Nitrogen	0.96	
Sulfur	0.61	
Oxygen	13.23	
Ash	4.62	
Total	100.00	

Values given in weight %, amounts used in the modeling was based on 1000 kg of Coal C2

- Wyoming Lab Analyses for Ash Used for Ash Element Content (their data given as oxides which were converted to kg of elements)

Lab Number: L8832
Sample ID: #5 Coal Fine 4-15-09

Coal Ash Analysis, wt% Ignited Basis	
Silicon Dioxide, % as SiO2	29.39
Aluminum Oxide, % as Al2O3	15.72
Iron Oxide, % as Fe2O3	6.59
Calcium Oxide, % as CaO	14.21
Magnesium Oxide, % as MgO	2.87
Sodium Oxide, % as Na2O	7.66
Potassium Oxide, % as K2O	0.81
Titanium Dioxide, % as TiO2	0.77
Manganese Dioxide, % as MnO2	0.04
Phosphorus Pentoxide, % as P2O5	1.91
Strontium Oxide, % as SrO	0.88
Barium Oxide, % as BaO	1.27
Sulfur Trioxide, % as SO3	17.88

Alkalies as Na20	8.19
Base to Acid Ratio	0.7
Silica Ratio	0.55
T250, °F	2000

Values given in weight % of oxides in ash, amounts used in the modeling was based on calculated elements in 46.2 kg Ash

- Miranda MLA Analysis Used for Selection of Potential Solid Species Present

Mineral/Phase	Chemistry

Quartz	SiO_2
Apatite	$Ca_5(PO_4)_3OH$
Apatite-Albite	$Ca_5(PO_4)_3OH\ NaAlSi_3O_8$
Kyanite	Al_2OSiO_4
Pyrite	FeS_2
Na-Amphibole	$Na_2(Mg,Fe)_3Al_2Si_8O_{22}(OH)_2$
K-Feldspar	$KAlSi_3O_8$
Barite	$BaSO_4$
Amphibole	$(Mg,Fe)_3Al_2Si_8O_{22}(OH)_2$
Ilmenite	$FeTiO_3$
Calcite	$CaCO_3$

Major solids present based on Miranda (2009) analysis of Coal B2

- Potential Vapor Species Selected Based on Eyk, et al Publication (Eyk, et al 2009)
- Temperature and Air Input Values Also Taken from Eyk, et al

Summary of Results

Influence of Temperature at 1.3 Times the Stoichiometric Requirement for Air to Combust All the Carbon

The influence of temperature on the thermodynamically stable solids formed and the distribution of sodium and potassium species at ashing and combustion temperatures are shown in Figures 1 and 2, respectively. The distribution of other species in the system are also presented in this appendix.

Ashing-The solid species as reported by Miranda are verified by the HSC modeling to be thermodynamically stable (Figure 1) , i.e. kyanite, albite, quartz, potassium feldspar, and apatite can thermodynamically coexist at the ashing temperature. Note that a significant amount of sodium is likely lost from the system during ashing as $Na_2SO_4(g)$.

Combustion- At combustion temperatures the sodium and potassium will be present as solid albite, potassium feldspar, a liquid slag phase, and a gas phase. A greater amount of the sodium and potassium will be present within the solids and liquid slag phases; although a smaller but significant amount will be evolved as $Na_2SO_4(g)$, NaOH(g),Na(g), and KOH(g) (Figure 3).

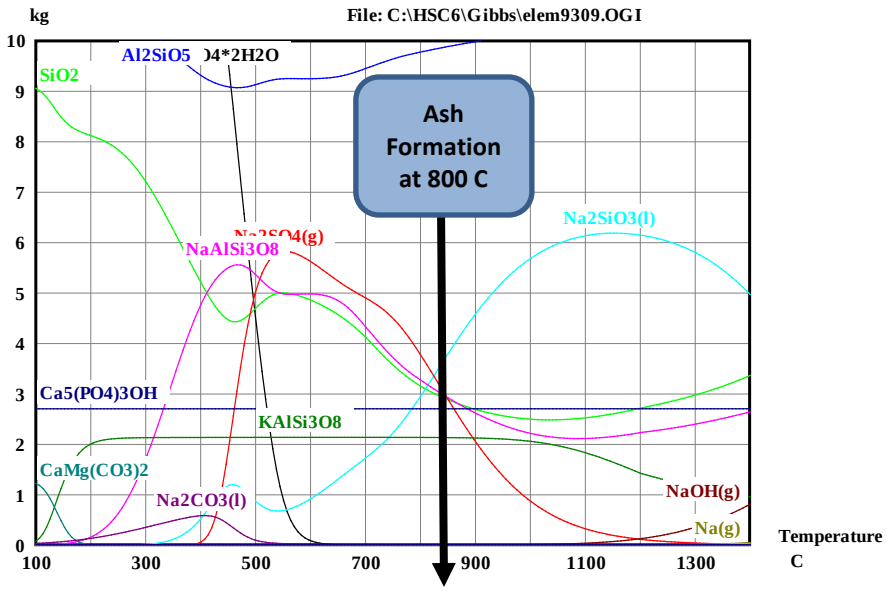

Figure 1. The influence of temperature on the formation of thermodynamically stable phases using 1.3 times the stoichiometric amount of air required for the combustion of carbon (1000 kg coal). Anticipated species when coal is ashed at 800°C are: Al_2SiO_5 (kyanite), Na_2CO_3(g), NaAlSi3O8 (albite), SiO_2 (quartz), $KAlSi_3O_8$ (feldspar), $Ca_5(PO_4)_3(OH)$ (apatite), Na2SiO3(liquid) begins to form at about 780°C. Note that a significant amount of the sodium is expected to be lost to the gas phase as Na_2SO_4(g) at ashing temperature.

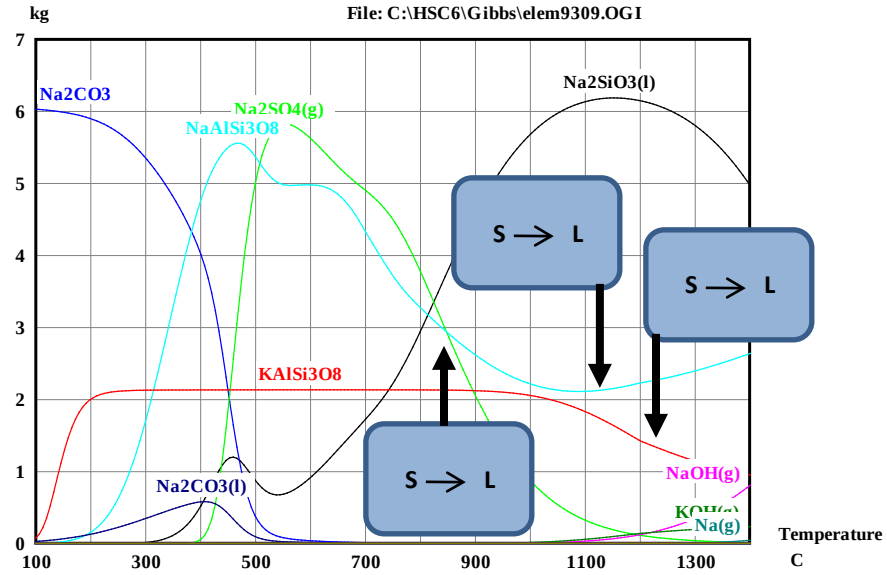

Figure 2. The influence of temperature on the formation of thermodynamically stable sodium and potassium species using 1.3 times the stoichiometric amount of air required for the combustion of carbon (1000 kg coal). Anticipated sodium and potassium species are shown when coal is combusted at temperatures of 1150°C and above. Al_2SiO_5 (kyanite) and $Ca_5(PO_4)_3OH$ remain stable as solids, A sodium (and potassium) rich liquid (molten slag) forms and gaseous NaOH(g) and KOH(g) species form at combustion temperatures.

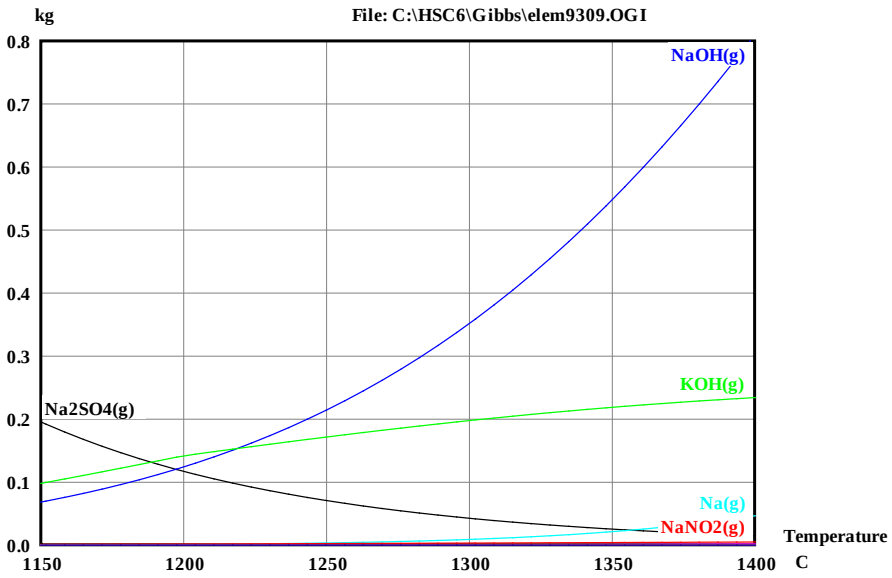

Figure 3. The influence of temperature on the formation of thermodynamically stable sodium and potassium vapor species during the combustion of coal 5 using 1.3 times the stoichiometric amount of air. Anticipated sodium and potassium vapor species include Na2SO4(g), NaOH(g), KOH(g), Na(g), and a minor amount of NaNO2(g).

Distribution of Specific Individual Species for Combustion of Coal B2

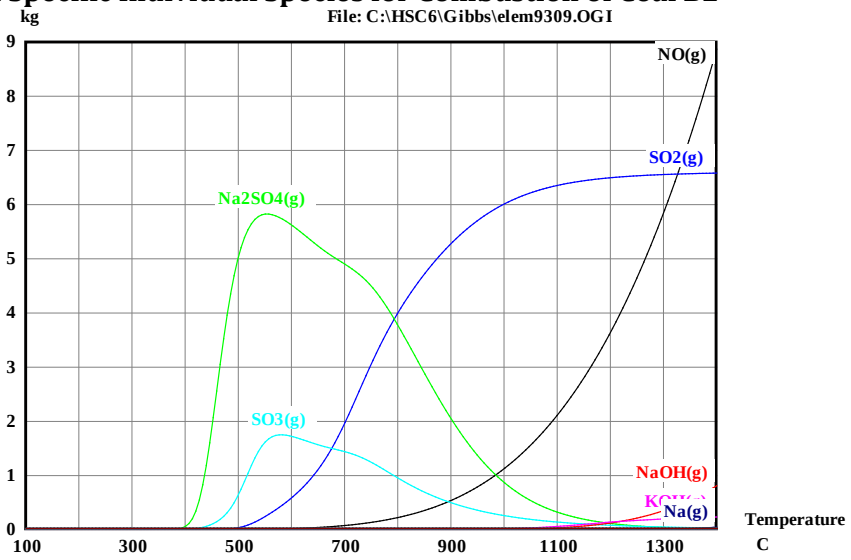

Gas Species (except N_2, CO, CO_2, H_2O, O_2)

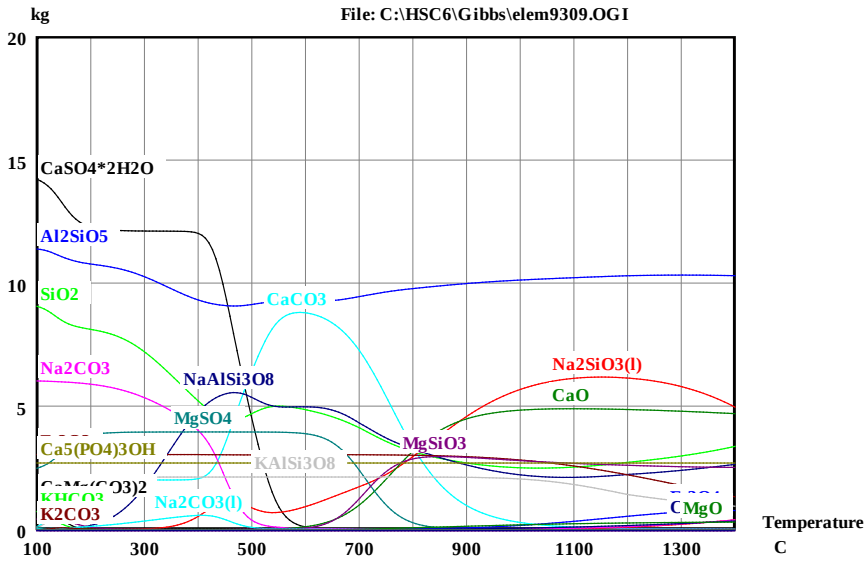

Condensed Species

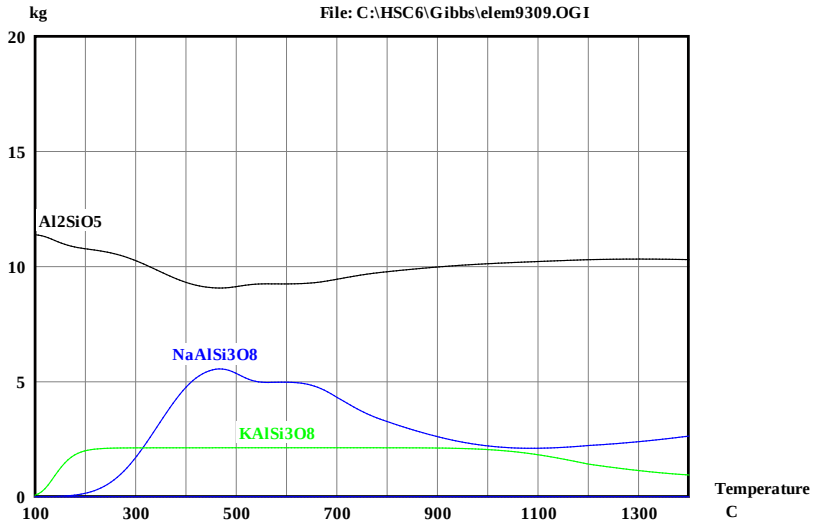

Aluminum Species

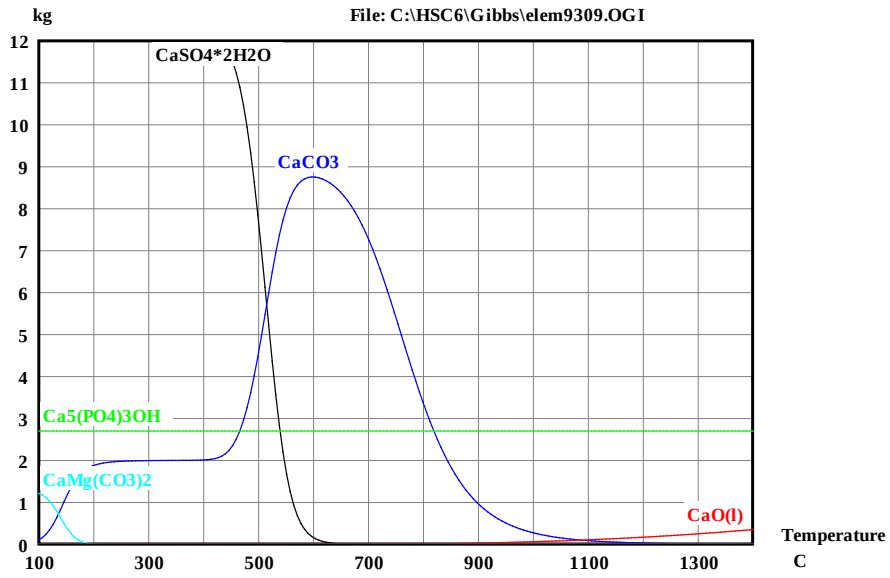

Calcium Species

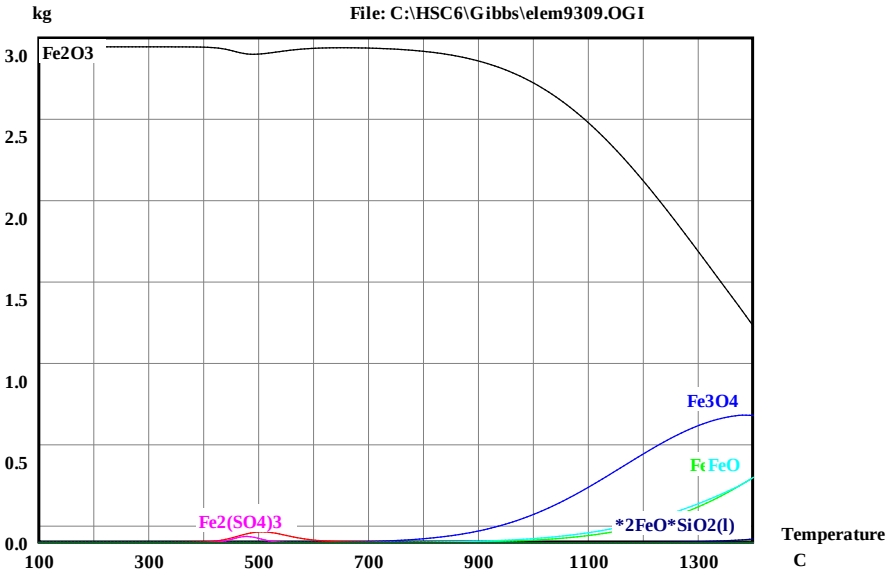

Iron Species

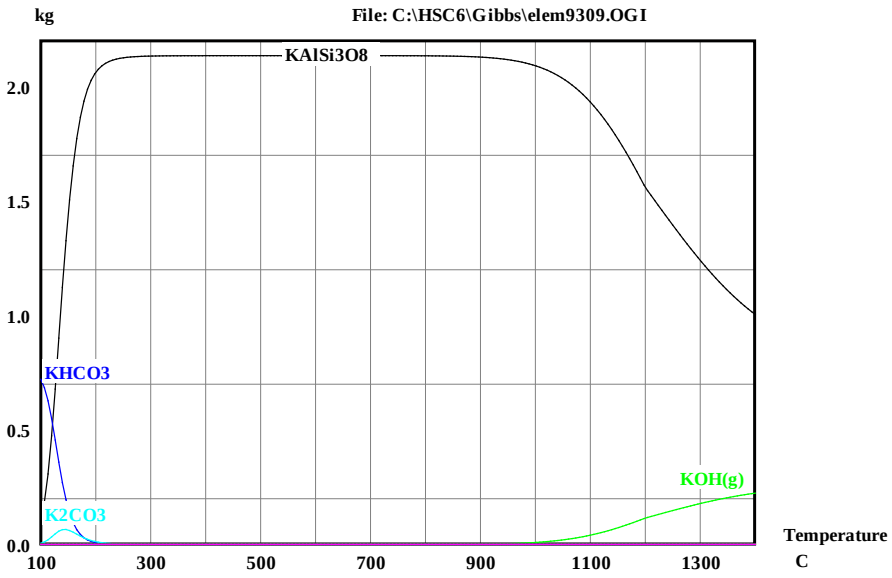

Potassium Species

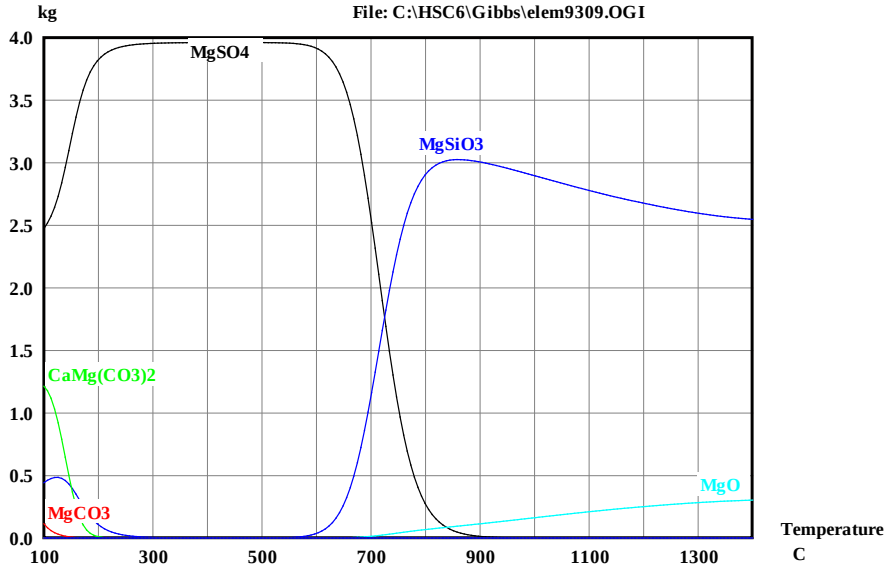

Magnesium Species

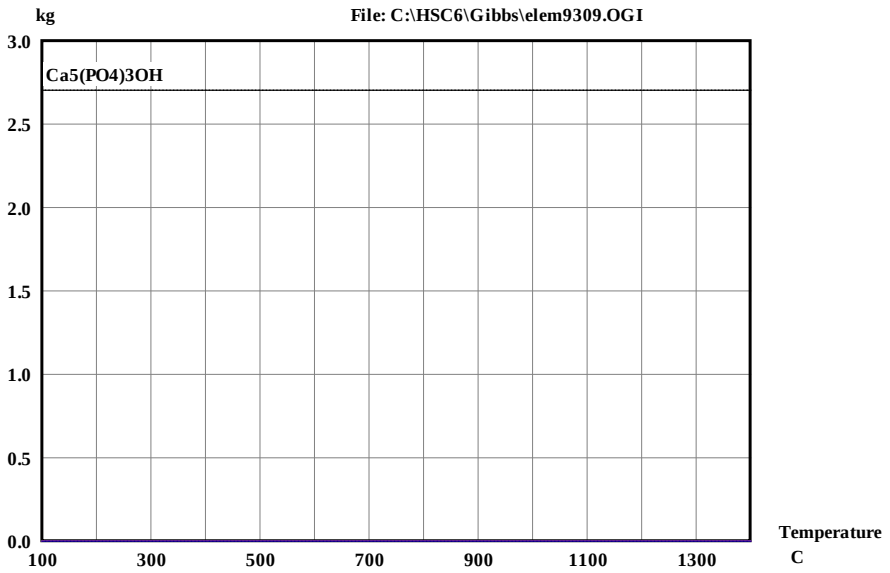

Phosphate Species

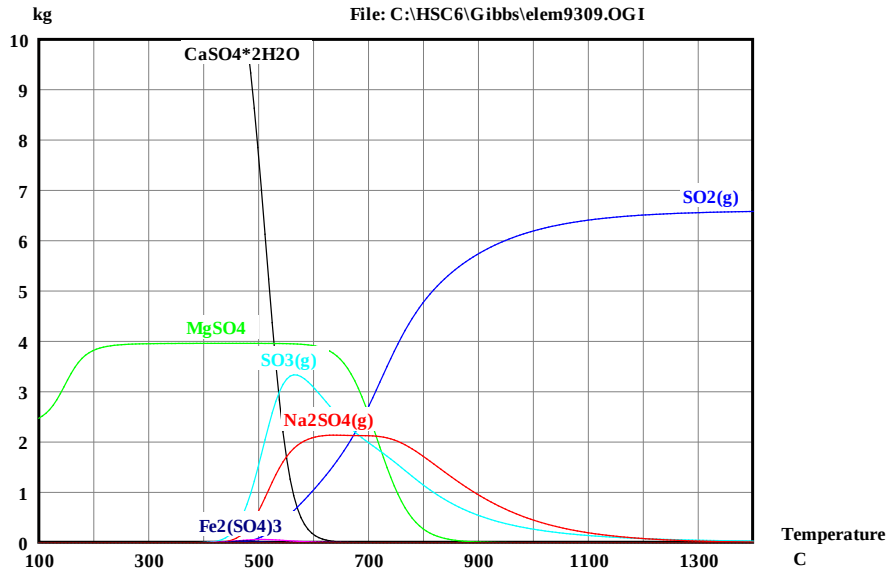

Sulfur Species

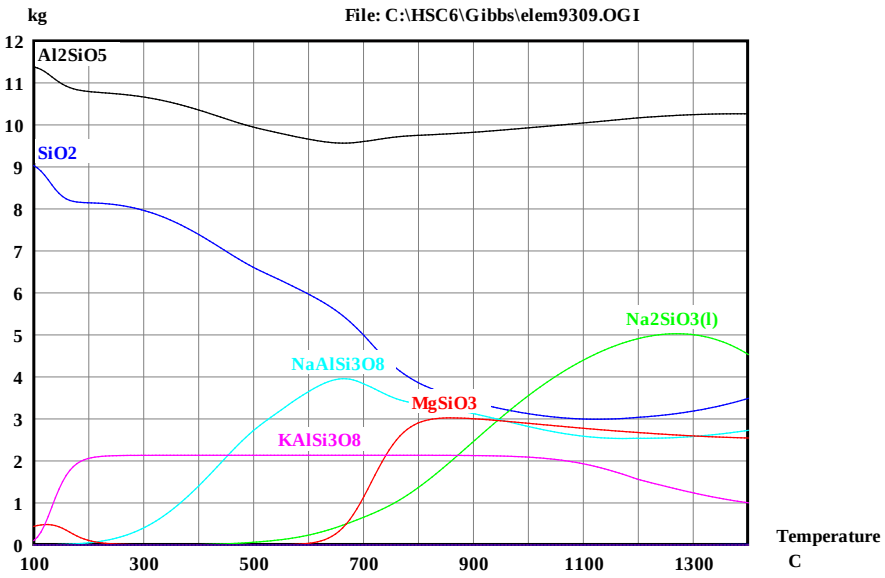

Silicate Species

APPENDIX E. DESIGN EXPERT EVALUATION OF STATISTICALLY DESIGNED STUDIES FOR THE LEACHABILITY OF COAL B2

Optimization of Leach Conditions for Coal B2

Based on the STABCAL modeling effort and the preliminary test work a Two-Level Experimental Design Study was formulated for Coal B2. Other coals will be evaluated by future studies. The Coal B design study was formulated to evaluate the influence of five variables on the removal of sodium from the coal e.g. pH, time, type of ion exchange reagent, concentration of the ion exchange reagent, and type of acid.

Design Expert software (Version 8.0, 2010) marketed by STATEASE (2010) was used to formulate a the two-level Experimental Design Matrix (Text Table 21). The specific software program used in this study is referred to by STATEASE as Resolution V. The value of using the Resolution V matrix is that it is statistically formulated so that the main and binary factors (variables) can be identified. None of the main factors or binary factors are aliased, i.e., the main factors and binary interaction factors are not influenced by other factors. This allows the study responses to be optimized, maximized, minimized, etc.

The specific experimental results for sodium are presented in Text Table 22.

Experimental Procedure

The experimental procedure used for conducting the experiments denoted in Text Table 21 follows:

- Place 10.0 gm coal 5 fines in a 200 mL plastic bottle (equivalent to 100 gm/Liter), add 100 mL of DI water
- Place on the shaker table for 30 minutes, measure and record pH
- Collect sample, filter 20 gm of the solution phase through 0.45 um filter disk into a 20 mL scintillation vial, add 1.0 g High Purity Concentrated Nitric acid, cap for analysis.
- Be sure to label the sample correctly both in your lab book and on the scintillation vial.
- The above should be your standard procedure for each of the 14 tests
- After the wash test do the following to each solution in each bottle
- Adjust the pH to the desired value with the specific acid
- Record the amount of acid used for each test in your lab book
- If specified by the design matrix add the ion reagent (CaCl2 or Ammonium Acetate), readjust and maintain pH for the specified time.
- All samples will be ICP analyzed for Na, K, Ca, Fe, Mg, Al
- Some solutions will be sampled at 30 minutes, then again at 4 hours. For those to be sampled at 4 hrs, readjust pH every 15 minutes over the 4 hour period.
- Collect sample, filter 20 gm of the solution phase through 0.45 um filter disk into a scintillation vial, add 1.0 g High Purity Concentrated Nitric acid, cap for analysis.

Philosophy of Statistical Evaluation

Statistical analyses of the data were conducted using the software Design-Expert Version 7.1.1 (Stat Ease 2009). The procedure was as follows:

- The data was input into the statistically designed experimental matrix.

- A transformation model was selected from seven available options, including none, natural log, base ten log, square root, inverse square root, inverse, power, and logit.
- The factors considered significant was selected using either a half-normal versus percent probability plot or Pareto chart.
- An Analysis of Variance (ANOVA) evaluation was performed and a P-Test was used to evaluate whether the model and factors were significant or not.
    - The model was deemed appropriate if the p-value test was <0.05; if the value was not less than this value then the selection process was started over and a new transformation model was selected. If the p-value test was <0.05 then the evaluation process was continued.
    - The individual factors were deemed appropriate if the p-value test was <0.10
- The Analysis of Variance (ANOVA) evaluation was continued to ascertain that the selected model and factors could be used to "navigate the design space". This was accomplished by evaluating several statistically calculated parameters:
    - R-squared (should be as high as possible and near 1.0 as possible)
    - Adjusted R-squared (as near R-squared as possible)
    - Predicted R-squared (within 0.2 of the Adjusted R-squared value and >0.6)
    - Adequate Precision (as large as possible but at least >4).
- If the evaluation was not satisfactory then the process of model selection, effects selection, ANOVA recalculation was repeated until the above p-test and R-squared evaluation was satisfactory. If the evaluation did not find a satisfactory solution this result was noted. If the ANOVA evaluation was satisfactory then further diagnostic evaluations were performed (example plots are presented for each DOE study), including:
    - Normal probability versus Internally Studentized Residuals
    - Externally Studentized Residuals versus Standardized Run Number
    - Leverage
    - Cook' Distance.

Discussion of Experimental Design Results

Models have been developed for three responses, e.g. concentration of sodium in the leach solution (mg/L); percent sodium removal by the leach process; and anticipated sodium content in the ash after leaching. A summary of the design space equations that describe the response results are presented in Table 1.

A series of figures are presented for the percent sodium removal results not discussed in the text of this report. Other conditions can be explored if the reader so desires (ltwidwell@mtech.edu).

Table 1. Design Space Equations for the Leaching of Coal B2

Sodium in Leach Solution, mg/L	Sodium Removal, %	Sodium in Ash, %
Ion Reagent CaCl2; Acid HCl ([Na], mg/L)^-0.13=0.448+0.00689*pH-0.0011 *Time, hrs+0.000608*Ion Exchange Conc, g/L-.0012 * pH * Time, hrs Ion Reagent Am Ac; Acid HCl ([Na], mg/L)^-0.13 =0.464+0.00286*pH+0.0038* Time, hrs+0.000608*Ion Exchange Conc, g/L-0.0013 * pH * Time, hrs	Ion Reagent CaCl2: Acid HCl (Na Removed, %)^-0.13=0.60243+0.00917 * pH-0.00160 *Time, hrs+0.00086*Ion Exchange Conc, g/L-0.00171* H * Time, hrs Ion Reagent Am Ac; Acid HCl (Na Removed, %)^-0.13=0.6246+0.00361*pH0.00491 * Time, hrs+0.00086*Ion	Ion Reagent CaCl2; Acid HCl (Na in Ash, %)^3=78.03+11.595 * pH-0.2068 * Time, hrs Ion Reagent Am Ac; Acid HCl (Na in Ash, %)^3 =141.08+ 0.9252 * pH-7.2068 * Time, hrs Ion Reagent CaCl2; Acid H2SO4 (Na in Ash, %)^3 =146.79+11.595 * pH-7.207 * Time, hrs

Table 1. Design Space Equations for the Leaching of Coal B2		
Sodium in Leach Solution, mg/L	**Sodium Removal, %**	**Sodium in Ash, %**
Ion Reagent CaCl2; Acid H2SO4 ([Na], mg/L)^-0.13 =0.484+0.00689*pH-0.0011*Time, hrs-0.000308*Ion Exchange Conc, g/L-0.00129 * pH * Time, hrs Ion Reagent Am Ac; Acid H2SO4 ([Na], mg/L)^-0.13 =0.477+0.00287*pH+0.00381*Time, hrs-0.000309*Ion Exchange Conc, g/L-0.0013*pH* time, hrs	Exchange Conc, g/L-0.00171* pH * Time, hrs Ion Reagent CaCl2; Acid H2SO4 (Na Removed, %)^-0.13=0.6511+0.00917*pH-0.00160 *Time, hrs-0.00039 * Ion Exchange Conc, g/L-0.00171 * pH * Time, hrs Ion Reagent Am Ac; Acid H2SO4 (Na Removed, %)^-0.13=0.6418+0.00361 * pH+0.00491 *Time, hrs-0.00039 *Ion Exchange Conc, g/L-0.00171 * pH * Time, hrs	Ion Reagent Am Ac; Acid H2SO4 (Na in Ash, %)^3 =151.51+0.9252 * pH-7.207 *Time, hrs

HCl, Ammonium Acetate (AmAc)

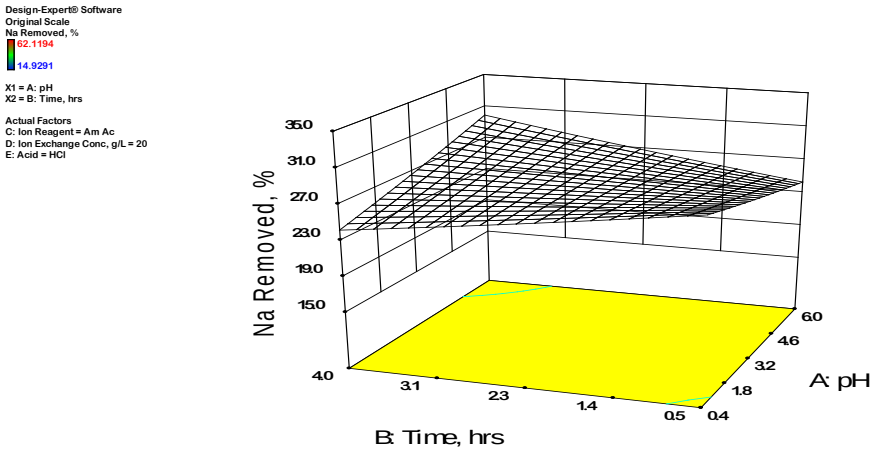

H2SO4, Ammonium Acetate (AmAc)

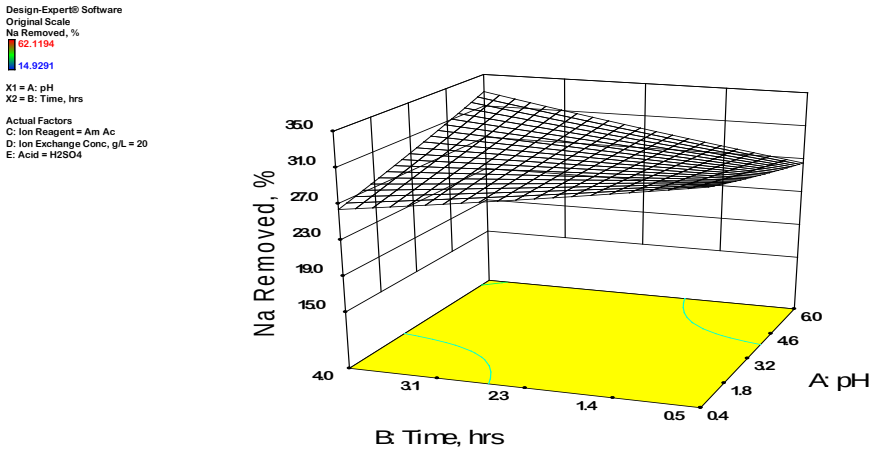

H2SO4, Calcium Chloride

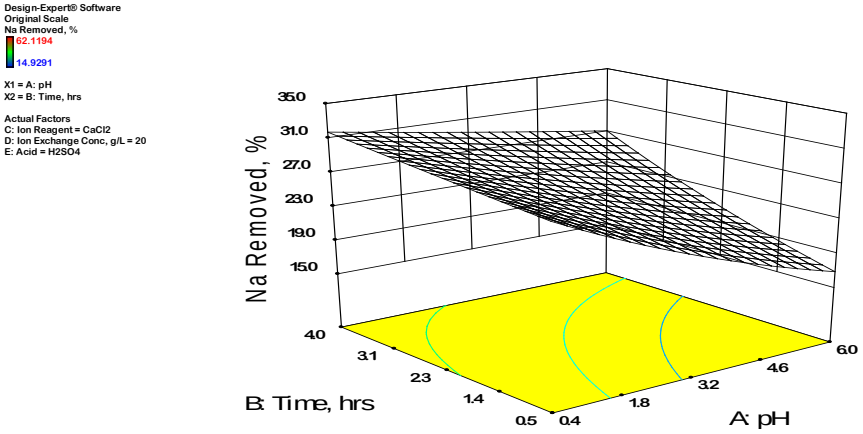

HCl, AmAc at pH 3

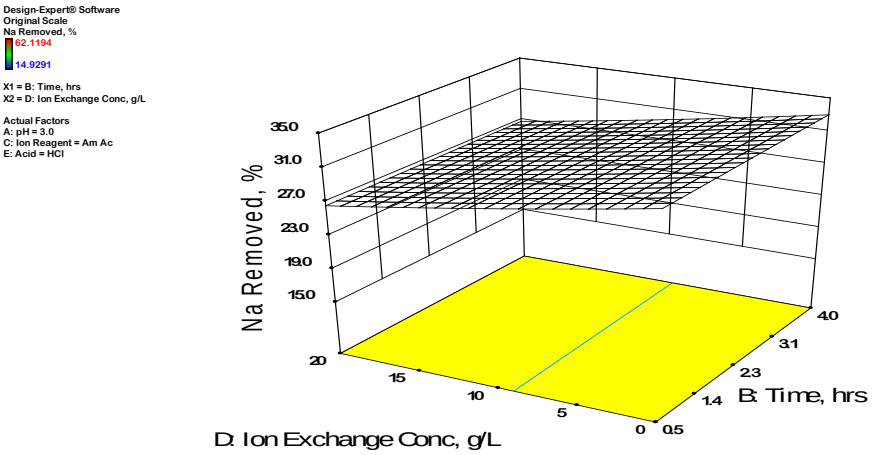

H2SO4, AmAc at pH 3

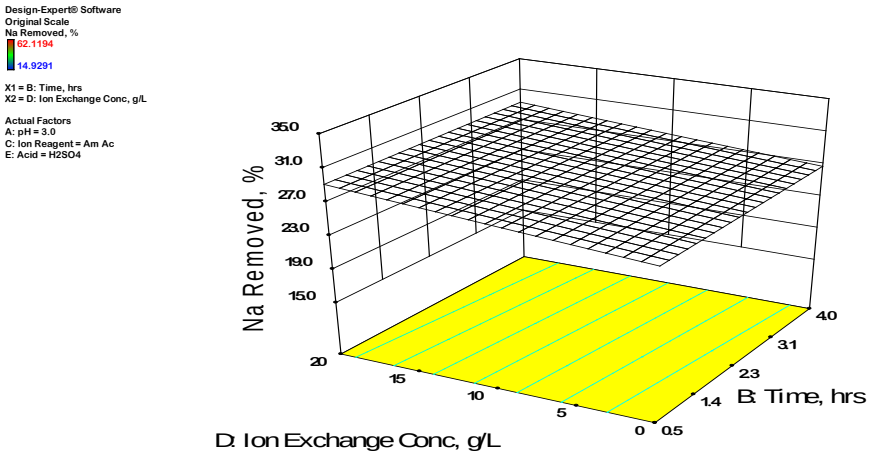

APPENDIX F. PUBLICATIONS RESULTING FROM THIS STUDY

Presentations and Publications

Jay McCloskey, Larry Twidwell, Paul Miranda, Doug Cameron, Courtney Young, Sean Dudley, Bill Pascoe, **Enhancement of Montana Coal Sodium Removal Technology Evaluation and Development**, PROCEEDINGS OF THE XVI INTERNATIONAL COAL PREPARATION CONGRESS, Editor, Rick Honaker, SME, Lexington, KY, 2010, pp 622-33.

Abstract: Montana has approximately 120 billion tons of coal reserves, more than any other state in the U.S. However, Montana ranks only 6th among the states in coal production. Various factors including coal quality, mining conditions and resulting economics, transportation costs, taxation and environmental regulations have contributed to Montana lagging behind other coal producing states. One factor that has historically limited the market for certain Montana coal reserves is the relatively high sodium content. Because elevated levels of sodium may cause excessive slagging in some power plant boilers, high sodium coal can only be marketed to power plants with specially designed boilers. Coal gasification, rather than direct firing of coal in boilers, is seen by many as the future of the coal industry in an increasingly carbon-conscious society. Unfortunately, some of the most promising gasification processes cannot utilize high sodium coal. Thus, the future "clean coal" market for Montana high sodium coal is expected to be restricted much as the traditional power plant market has been in the past. The intent of the project at CAMP is to identify and physically duplicate selected sodium removal and sodium recovery treatment alternative(s) for laboratory bench-scale evaluations. The overall objectives of the project are to develop and implement viable sodium removal and sodium recovery treatment alternatives for the Montana Coal Industry. The project work progress will be presented and discussed in this presentation.

Sean P. Dudley, Jay McCloskey, Larry Twidwell, Brian Park, **Issues Related to Montana Coal Development,** PROCEEDINGS OF THE XVI INTERNATIONAL COAL PREPARATION CONGRESS (Editor, Rick Honaker, SME, Lexington, KY, 2010, 18p)

Montana has roughly 120 billion tons of coal reserves, more than any other state in the U.S. However, Montana ranks typically low among states in coal production. Various factors including coal quality, mining conditions and resulting economics, transportation costs, taxation and environmental regulation have contributed to Montana lagging behind other coal producing states. One factor that has historically limited the market for certain Montana coal reserves is high-sodium content and resulting degradation of combustion systems. Furthering to compound the issue is increased focus on control of minor pollutants, including sodium, in industrial effluents and the already limited capacity of major coal reserve areas such as the Powder River Basin (PRB) to absorb increased salt presence. This document is intended to give and overview of sodium removal technologies, steps done to investigate applicability of those technologies to Montana coal reserves, and mitigation options for salt in effluent streams will have to become an integral part of process operations if increased coal production in Montana is to be a viable prospect for the future.

Thesis

Dudley, Sean, 2011. **Evaluation of Fly Ash Based Artificial Zeolite Formation as Treatment for Salt Laden Process Water from Eastern Montana Coal Operations**, Master of Science Thesis, Montana Tech of the University of Montana, Butte, MT., 155p. dudleysweb@gmail.com.

Abstract: Montana has roughly 120 billion tons of coal reserves, more than any other state in the U.S. However, Montana ranks low among coal-producing states. Various factors including coal quality, mining conditions, resulting economics, transportation costs, taxation and environmental regulation contribute to Montana's lag. A major factor that has historically limited the market for certain Montana coal reserves is high-sodium content and resulting degradation of combustion systems. The issue is compounded by the increased focus on control of minor pollutants, including sodium, in industrial effluents and the already limited capacity of major coal reserve areas such as the Powder River Basin (PRB) to absorb increased salt presence. This thesis presents the work related to coal development for eastern Montana, specifically focusing on wastewater issues associated with the processing and removal of sodium from coal matrices. A variety of means exist to remove sodium from process waters, but most options are economically disadvantaged and still produce waste streams for subsequent disposal. This work focuses on a technology that, if applicable, has the propensity to combine waste streams and produce a by-product that is not only beneficial but saleable. Artificial zeolite formation was evaluated as the primary means to treat effluent, hoping to capitalize on the characteristic aluminosilicate structure of fly-ash by product and the ability of sodium, to not only act as a structure formation director, but be included in those structures effectively combining waste streams, cleaning process water, and producing a by-product that is a benefit to operations. Results indicated that process variables are still widely not understood, but formation of a zeolite phase (or conversely a geopolymer) favours conditions of high pH, moderate sodium solution concentration, low solid to liquid ratios, and low temperatures.

Reports

Twidwell, L.G., S. Dudley, **Literature Review-Sodium Removal from Low-Rank Coals,** CAMP Internal Report-LIT 1, June, 2010.

Abstract- A detailed, but not comprehensive, literature search (over 220 references) has been conducted and the publications have been reviewed to determine usual treatment approaches for the removal of sodium (and in some cases potassium) from low-rank coal. Annotations of the reviewed literature are presented in this report for the following topics: General Reviews, Solution Leaching, Addition of Metal Compounds (or mineral phases), and Transport of Sodium during Combustion and Gasification. Other elements, such as calcium, magnesium, aluminum, iron and silicon, present in low-rank coals may have an important effect on sodium and potassium removal by chemical leaching processes and on the formation of low-melting mineral phases during the combustion process. However, annotated comments concerning associated elements have not, in most cases, been included in this publication. The user of this document should refer to specific study publications, presented in the bibliography section, for this information. The topic of cleaning leach solutions of elevated concentrations of sodium, other dissolved cationic and anionic species, and dissolved organic species has been the focus of Dudley (2011) as a part of his Master of Science in Metallurgical Engineering research program. A brief summary of this topic is presented in this report.

Dudley, S., **Environmental Concerns and Wastewater Treatment**, CAMP Internal Report-LIT 2, June 2011.

Abstract-Through evaluation it has been determined that pre-treatment poses the best option for control results for eastern Montana coal. Specific removal mechanisms, as well as related study results can be found elsewhere in associated documents. It can be generally assumed here, however, that processing will involve aqueous effluent, primarily sodium or salt laden waters. As such, in order to develop a fully comprehensive understanding of phase two of the project one must understand the driver behind the control of sodium in waste/process waters.

McCloskey, J., et al., **Enhancement of Montana Coal to Support Future Expansion Sodium Removal Technology Development,** Montana Board of Research and Commercialization Technology Task 10 Project, Final Report for Period Ending: March 30, 2012, Report Date: April 30, 2012. Interim Reports September 2009, September 2010.

McCloskey, J., et al., **Enhancement of Montana Coal to Support Future Expansion Sodium Removal Technology Development**, Center for Advanced Separation Technology (CAST) Montana 2009 Final Report, March 30, 2012, Report Date: April 30, 2012. Interim Reports January 2009; January 2010.

McCloskey, j., et al., **Report to Stakeholders**, CAMP Internal Report-LIT 4 June 15, 2010, Presentation in Billings, MT.

APPENDIX 18-Development of a 3D Lattice-Boltzman Model for Fluid Flow Simulation Under Partially-Saturated Conditions in Packe Particle Beds. (UT007)

FINAL TECHNICAL REPORT

Contract Title and Number:
Continuation in Crosscutting Technology Development at CAST. (DE-FC26-05NT42457)

Period of Performance:
Starting Date: 10/1/2005
Ending Date: 9/30/2009

Sub-Recipient Project Title:
Development of a 3D Lattice-Boltzmann Model for Fluid Flow Simulation under Partially-Saturated Conditions in Packed Particle Beds

Principal Investigators:
J.D. Miller & M. Sukop

Report Information:
Type: Final
Number:
Period: 10/01/05-09/30/08
Date: 7/31/08
Code: UT007-Final

Contact Address:
University of Utah
135 South 1460 E. Room 412
Salt Lake City UT 84112

Contact Information:
Phone: (801) 581-5160
Fax: (801) 581-8119
E-Mail: jdmiller@mines.utah.edu

Subcontractor Address:
Department of Earth Sciences
Florida International University
Office: 305-348-3117
Fax: 305-348-3877

Subcontractor Information:
Mike Sukop

DISCLAIMER

ABSTRACT

The research has been designed to develop software capable of simulating the fluid flow of a leaching solution through a packed bed of particles under partially-saturated conditions. The results from the 1st year of study are presented as a final report for the CAST II program. The 2nd year of the research will be completed under the CAST III program. The software uses the Lattice Boltzmann Method (LBM), which has numerous advantages over other approaches. The research involves consideration of the mechanics of the heap leaching system as influenced by particle size distribution, pore-network structures, solution flow rate, oxygen flow rate, and moisture content. In a broader sense, this research is part of a long range program using X-Ray Microtomography (XMT) to determine to what extent the rate and practical recovery from heap leaching is limited by: (1) mineral exposure, (2) fluid flow/transport phenomena and (3) chemistry. It is expected that the results from the research will help to design heap leaching operations for more effective utilization of our mineral resources.

During this 1st year, a three dimensional (3D) Lattice-Boltzmann Model (LBM) has been developed for one component fluid flow simulations through packed particle beds under totally saturated conditions. The software has been used to predict saturated permeability using real X-ray computed tomography (XMT) images of packed beds of sand, glass beads, and ore particles. Comparison with empirical equations as well as with experimental results has been done showing good agreement between theory and experiment.

TABLE OF CONTENTS

EXECUTIVE SUMMARY

The University of Utah in an effort to improve our understanding in the particle technology area and separation processes has developed an X-ray Microtomography facility in order to capture three dimensional (3D) images of real particle samples for further digital analysis. In particular, with the objective to improve the understanding for control of heap leaching operations, mathematical and physical modeling are indispensable for analysis of problems which can not be done on an experimental scale. In this regard, the 3D scientific visualization opens a complete new area of research where the porous structure of a packed particle bed of multiphase particles can be completely characterized and used for scaling up the micro phenomena that drive and control the whole leaching process of reactant transport, chemical reaction/dissolution and transport of solubilized products. In a broader sense, this research is part of a long range program using X-Ray Microtomography (XMT) to determine to what extent the rate and practical recovery from heap leaching is limited by: (1) mineral exposure, (2) fluid flow/transport phenomena and (3) chemistry. It is expected that the results from the research will help to design heap leaching operations for more effective utilization of our mineral resources.

A first step in this direction was to develop software capabilities of a complex model with mathematical and multi-physical phenomena such as being able to capture the basic phenomena of the whole process. In this regard, the Lattice Boltzmann Model (LBM) is an emergent mathematical technique able to handle the complex boundary conditions of flow in porous structures of actual ore samples and to simulate the process in a reasonable amount of time.

In fact, during this 1st year of research under CAST II a single component model was constructed and the analytical verification with simple pipe flow was accomplished with excellent agreement between theory and experiment under laminar flow conditions. Familiarization with the method has been achieved and more complex tasks are about to start in the next phase of the research.

The same model has been modified and used for calculation and comparison of the permeability for packed beds of glass beads, sands and ore samples with different particle sizes. The results show again an excellent agreement between experimental results obtained from constant head experimental tests and those results obtained from LBM simulation of the flow using 3D images obtained from micro CT analysis of packed particle beds.

The next phase of the research during the 2nd year under CAST III corresponds to the development of the multiphase Shan and Chen model. First, code parallelization will be required because intensive computing will need to be divised for several processors to make the memory requirements affordable and the time of simulation practical for the multiphase flow problem. Second, verification of the code with the analytical solution of Laplace's law will be done to verify the agreement with the surface tension model necessary to describe wetting and capillary filling of small pores. The verification of the interaction between solid and fluid phases will be done by verification with the analytical solution for the flow of two fluids of different viscosity/density in a pipe. And finally, the applicability of the method to analysis of actual packed particle beds will be determined by determination of a solid-water saturation curve for a simple sample of particles.

INTRODUCTION

The fluid flow condition through the packed particle bed is an important consideration in the design and operation of the heap leaching process. In fact, for a given particle size distribution the moisture content, the geometry of the porous structure in the particle bed, and the local fluid velocity conditions will determine the extent of leaching and transport of solution from which the metal will be finally recovered.

Until recently it has not been possible to accomplish fluid flow analysis in such packed particle beds under partially-saturated conditions due to the lack of models to simulate multiphase (gas-liquid) flow behavior with very complex boundary conditions (pore network structure/geometry). Now such analysis may be possible by using X-Ray Micro CT (XMT) to capture the complex geometry involved in a particle bed structure and using Lattice Boltzmann methods (LBM) to simulate the fluid dynamic behavior of unsaturated flow.

The pore structure and the connectivity of the pore space are important features which determine fluid flow in a packed particle bed during heap leaching. In this regard, the X-Ray Microtomography technique is the best noninvasive nondestructive technology available today to characterize complex pore structures. XMT allows the capture of the shape and connectivity of the void space in three dimensions of a randomly organized particle bed through the 3D image reconstruction of the sample under analysis.

The image digitalization of the particle beds allows us to obtain the porous network structure characteristic of a given ore and particle size distribution. Computer simulation can then be used to calculate macro variables of the flow. However, in this regard the use of conventional FEM (Finite Element Method) or FDM (Finite Difference Method) for simulation of flow in the complex porous network structure of a porous media has not found practical application because the use of a small grid size is necessary making the computational time unacceptable.

In contrast to FEM or FDM methods, LBM has computational aspects that make it a particularly strong method for fluid flow simulations in complex pore structures due to its particular bottom-up approach. Also, it has recently been shown that LBM can simulate multi-phase (gas-solid-liquid) multi-component interactions with excellent results (Chen, 2003; Martys & Chen, 1996; Shan & Chen, 1993; Zhang & Chen, 2003). However, so far applications have been largely limited to 2D problems or 3D fluid flow models under saturated conditions. This research will focus on the development and implementation of software able to handle 3D multiphase fluid flow under partially saturated conditions for use in the analysis and control of optimum conditions for recovery of copper and/or gold from heap leaching operations. It is expected that the software to be developed will have great utility and be extended to nano flow simulation, granular flow, and colloidal flow analysis.

OBJECTIVES AND APPROACH

A two-year research program is in progress to develop a 3D Lattice Boltzmann Model for fluid flow simulation under partially-saturated conditions in packed particle beds in order to help identify optimum flow conditions for copper and/or gold recovery in heaps. This is the continuation of research developed by Dr. J.D. Miller and Dr. C.L. Lin using LBM in 3D problems in order to improve the understanding of the phenomena associated with fluid flow in packed particle beds (Lin & Miller, 2004; Miller et al., 2003a; Miller et al., 2003b).

Development of the multiphase 3D LBM is a difficult and complex task. References and literature in this regard are limited. It is not expected to develop optimized and final-end-user software in the first approach. Instead, it is expected to develop as fast as possible a first prototype software to evaluate the capabilities and applicability of this technique for unsaturated flow assessment and characterization.

In order to accomplish the final goal the project has been divided into the following sequential steps: single component flow, surface interactions, and two-phase fluid flow. Each step consists of software development and experimental verification in order to gain confidence and assure reliability in the technique.

The first stage of the project involves the software development of a single component 3D flow model. This software will be the corner-stone for the development of the next stages and it will give us important insights about implementation issues. In this stage, the 3D simulation results will be compared to analytical solutions of Stokes-Flow in a pipe. Also, the 3D LBM simulation results through porous solids will be verified with Darcy's Law for flow in porous media. Real XMT image samples obtained from packed particle beds will be used in this regard.

The second stage will incorporate the wettability property of the fluid into the model. For this effect a fluid-solid interaction potential (Shan & Chen, 1993) will be used. Verification with experimental data will be carried out.

The third stage of the research will involve the incorporation of an additional fluid into the model and description of the interface interactions. We need to simulate the interface between two fluids of significantly different viscosity as is the case of water and air. Up to this moment we are evaluating two different approaches: The multicomponent model as proposed by Shan and Chen (1993) and the Free Energy Method as explained by Swift et al. (1995, 1996). The final version of this software will be applied to complex 3D pore spaces in packed beds of irregularly shaped particles imaged from real samples using a unique high-resolution cone-beam X-Ray Microtomography system (XMT) installed at the University of Utah. New insights regarding the relation between pore geometry, air ventilation, and water saturation are expected to be found. Further tests of the model will include verification of the ability to reproduce Darcy's Law in appropriate laminar flow regimes, saturated and unsaturated permeability measurements, and water potential/particle size/moisture content relationships.

EXPERIMENTAL

Over the last few years, the Lattice Boltzmann Model (LBM) has become a promising numerical technique for the simulation of fluid flows under complex boundaries geometries. This property is making the LBM an important tool for research for the case of flow in porous media. It is also becoming popular for its capability to incorporate additional physical complexities, making multiphase flow problems computationally more feasible (Chen & Doolen, 1998). Unlike the conventional Computer Fluid Dynamics (CFD), a 'top-down' approach based on discretization of macroscopic continuum equations, the LBM method is based on a 'bottom-up' approach where constructed kinetic models incorporate microscopic model interactions and mesoscopic kinetic equations so that the macroscopic averaged properties obey the desired macroscopic equations.

In the original lattice gas cellular automata (LGCA) model from which the LBM evolved, the mass and momentum are conserved locally in a discrete space-time model. The space is discretized in a lattice arrangement and particles are defined at each node of the lattice by a Boolean variable. During the streaming step, particles are only allowed to move one lattice unit along the lattice directions during each time step. During the collision step, two particles arriving at the same node collide and a collision rule is followed by the particles involved changing their directions but conserving local mass and momentum. Frish (Frish et al., 1986) found that sufficient symmetry of the lattice was necessary for the recovery of the Navier-Stokes equation at the macroscale. For example, in two dimensions a square lattice does not provide enough symmetry whereas hexagonal symmetry is sufficient to recover the Navier-Stokes equation.

In spite of the remarkable progress achieved in the LGCA, the difficulties related to lack of Galilean invariance, anomalous velocity dependency of the fluid pressure, statistical noise, exponential complexity and spurious invariants plus the interest to develop 3D models and high Reynolds numbers simulations led to the development of the LBM (Succi, 2001). The LBM evolved from the lattice gas cellular automata (LGCA) to overcome its difficulties but keeping many of the intrinsic advantages such as the locality equilibrium, space-time discretization, and the streaming and collision structure.

The Lattice Boltzmann Model.

The first LBM was developed by (Macnamara & Zanetti, 1988). The fundamental difference between LGCA and LBM is that the later replaced the Boolean variable by a particle distribution function f_α which eliminates the statistical noise problem present at that moment in its ancestor. Later, Higuera and Jimenez (1989) made a great simplification when they linearized the collision term around the local equilibrium state by using a single relaxation term. The model using this type of relaxation term is known as the LBGK model for the Bhatnagar-Gross-Krook operator (Bhatnagar et al., 1954). The Bhatnagar-Gross-Krook (BGK) approximation and discretization of the Boltzmann Equation leads to the following explicit equation:

$$f_\alpha(x+\vec{e}_\alpha, t+\Delta t) - f_\alpha(x,t) = -\frac{1}{\tau}\left[f_\alpha(x,t) - f_\alpha^e(x,t)\right] \qquad \text{(equation 1)}$$

which is equivalent to:

$$f_\alpha(x+\vec{e}_\alpha, t+\Delta t) = (1-\frac{1}{\tau})\, f_\alpha(x,t) + \frac{1}{\tau}\, f_\alpha^e(x,t) \qquad \text{(equation 2)}$$

where ,

$f_\alpha(x,t)$: gives the probability of finding a particle with the velocity $\vec{e}_\alpha$ at lattice site x at the time t.

$f_\alpha^e(x,t)$: is the equilibrium distribution function.

τ : is known as the relaxation time and controls the rate of approach to the dynamic equilibrium. Typical values are $0.5 < \tau < 2.0$. The lower limit is dictated by numerical stability conditions.

Currently, there are two different ways of showing that this discretization approximates the Navier-Stokes equations – either by the method of Chapman-Enskog expansion from statistical physics (Frisch et al., 1987), or by direct discretization of the Boltzmann equation as proposed by (He and Luo, 1997).

In the LBGK model the local equilibrium distribution is chosen in such a way that the micro-dynamics converge to the governing Navier-Stokes macroscopic equations. Qian (Qian et al., 1992) provided a whole family of solutions for this matter. We have selected the D3Q19 model for use in this research because it is a good compromise between stability and performance.

Overview of a Single Component LBM – The D3Q19 Model.

The D3Q9 model denomination comes from the three dimensional lattice representation and nineteen velocities according with Qian's notation. Depending on the dimensions and the number of velocity directions different models can be used. Figure 1 shows the sketch of a D3Q19 model.

The D3Q19 model consists of nineteen velocity vectors where one is in the center, six along the axis and twelve for all combinations of two axes. For each velocity vector a particle distribution function (DF) f_α is stored where the DF represents the amount of fluid molecules moving in the direction e_α. Therefore, in the D3Q19 model there are particles not moving at all (f_0), moving with speed 1 ($f_2, f_3, f_4, \ldots f_7$) and moving with speed $\sqrt{2}$ ($f_8, f_9, f_{10}, \ldots f_{19}$). This is particularly important in terms of computational requirements because each node of the lattice will need to store at least 19 float variables with the population moving in each velocity for each component, therefore a three dimensional problem is very computationally demanding.

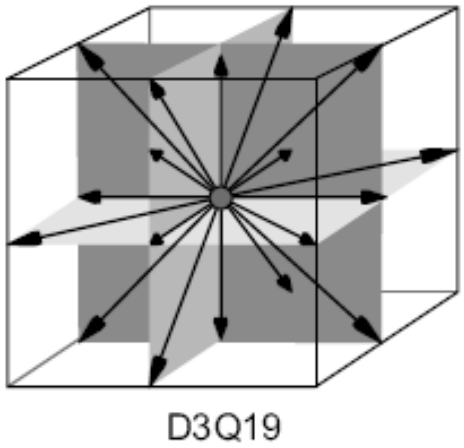

Velocity vectors:

e_1 = (0,0,0)

$e_{2,3}$ = (+/-1,0,0)

$e_{4,5}$ = (0,+/-1,0)

$e_{6,7}$ = (0,0,+/-1)

$e_{8..11}$ = (+/-1,+/-1,0)

$e_{12..15}$ = (+/-1,0,+/-1)

$e_{16..19}$ = (0,+/-1,+/-1)

Figure 1. Sketch of a three dimensional lattice with nineteen velocities (D3Q19).

As mentioned above, the LBM consist of two basic steps, streaming and collision. The streaming step represents the advection of the particles in the fluid and if the size of a cell Δx and the length of the time step Δt are normalized to 1 (as is usually the case for computing practice), the streaming DF ($f_\alpha^{|S}$) can be easily represented by copying each DF to its adjacent cell along the corresponding velocity vector.

$$f_\alpha^{|S}(x,t+\Delta t) = f_\alpha(x+e_\alpha,t) \qquad \text{(equation 3)}$$

The collision step describes the evolution of a system towards equilibrium by relaxing the streamed DFs of a cell towards the equilibrium distribution function. It has been shown that LBGK approximation with a Maxwell-Boltzmann equilibrium distribution recovers the Navier-Stokes equations at low Mach number in the equilibrium limit (He & Luo, 1997). For a D3Q19 lattice, a second order expansion of the equilibrium distribution function is commonly used:

$$f_\alpha^{eq}(x) = w_\alpha \rho(x)\left[1+3\frac{\vec{e}_\alpha \bullet \mathbf{u}}{c^2}+\frac{9}{2}\frac{(\vec{e}_\alpha \bullet \mathbf{u})^2}{c^4}-\frac{3}{2}\frac{\mathbf{u}^2}{c^2}\right], \text{ for } \alpha \ 1, 2,3 \ldots.19. \qquad \text{(equation 4)}$$

Where,

w_α : Weight values depending on the velocity direction. For the D3Q19 model they are defined as

$$w_1 = 1/3$$

$$w_\alpha = 1/18 \quad \text{for } \alpha \text{ i} = 2, ..7$$
$$w_\alpha = 1/36 \quad \text{for } \alpha = 8,\ldots 19$$

c : The lattice speed given by $\Delta x_{lattice} / \Delta t_{lattice}$. For simplicity it is defined as 1.

$\rho(x)$: The macroscopic fluid density at the cell x.

u : The macroscopic fluid velocity at the cell x.

This functional form of the equilibrium distribution assures that up to the fourth order momentum equations are identical to the respective velocity moments over the Maxwell distribution (Wolf-Gladrow, 1991). Also, the LBGK model defined as shown above assures mass and momentum conservation laws.

During iteration the macroscopic density and velocity fluid variables are computed at each node as the first and second momentum of the distribution functions. Then,

$$\rho = \sum_{\alpha=1}^{19} f_\alpha \qquad \text{and} \qquad u = \sum_{\alpha=1}^{19} e_\alpha f_\alpha \qquad \text{(equation 5)}$$

Moreover, the following relations are associated with the pressure (P) and kinematic shear viscosity (v) according with the following formulas:

$$P = \frac{\rho}{3} \qquad \text{(equation 6)}$$

$$v = \frac{1}{3}\left(\tau - \frac{1}{2}\right) \qquad \text{(equation 7)}$$

More details about the LBM, treatment of boundary conditions, applications and techniques can be found at (Succi, 2001).

Software Development

3D software has been developed for analysis of fluid flow through porous media. The software is based on a single component Lattice Boltzmann Model as explained previously. The software is composed of two major structures: the 3D LBM software and a SILO translator. The former is the main core of the program and it performs the three dimensional Lattice Boltzmann simulation. The latter uses the output files of the 3D LBM to make a SILO format file which can be finally imported from the open source VISIT platform for Scientific Visualization. The major structure of the code is shown in Figure 2.

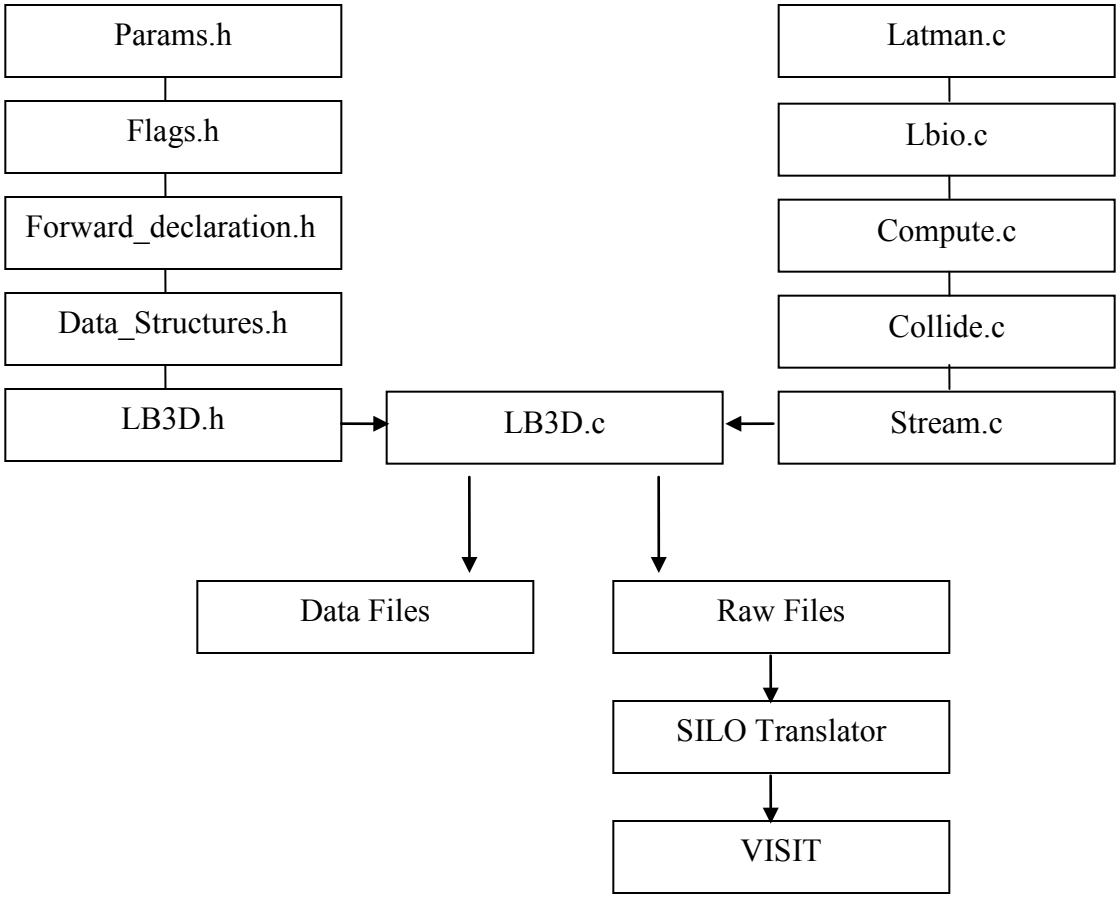

Figure 2. Software structure for flow simulation.

The sequential process for the iteration of the 3D LBM is shown in the following pseudo-code below. First the memory is allocated and the problem is initialized based on the initial condition of velocity and density which are evaluated in the equilibrium distribution functions for this matter. Then the iterative process of streaming and collision is executed until convergence or until the maximum step iteration is reached. Macro variables, such as velocity components and density, are computed based on the new values of the velocity distribution function after streaming during each time step. Then the resulting macro variables for each node in the lattice are saved in files from which the data can be visualized for further analysis.

Pseudo Code for 3D LB Computation

==========LB3D.c==========

```
#include "LB3D.h"

int main (int argc, char **argv)
{
        Locate memory and initialize variables.

        Iteration: If maximum iteration or convergence has not been reached continue
        {
                Execute streaming step.

                Compute macro variables such as density and velocity.

                Execute collision step.

                Add the volume –force to mimic pressure gradient.

                Save outputs files.
        }

        Free memory.

        Return 0.

}
```

==========

Due to the collision step, the resulting distributions are modified with the volume force component so as to mimic the equivalent gradient pressure used to force the flow in a particular direction as shown in equation 8.

$$\rho u = \sum_{i=1}^{19} f_i e_i + \tau g \qquad \text{(equation 8)}$$

Analytical Verification - Stokes Flow in a Pipe

The Stokes Flow through a pipe has a well-known analytical solution. For this reason it was selected to verify the function of the software. The fluid enters the pipe from the left side and exits to the right under the effect of a constant pressure drop (ΔP) between the inlet and outlet section as shown in figure 3.

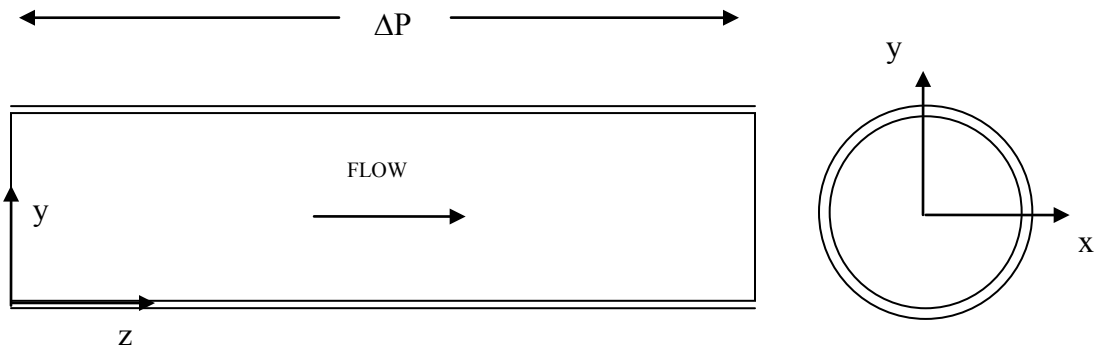

Figure 3. Laminar flow in a pipe.

A non-slip boundary condition is assumed at the walls. Therefore, the fluid velocity is assumed to be zero at the boundary walls because of the drag force of the wall exerted on the fluid. Under moderate-to-low Reynolds number flow conditions the solution is easily determined and it is given by (Bird et al., 2002):

$$V_x(y) = V_{\max}\left[1-\left(\frac{y}{R}\right)^2\right] \qquad \text{(equation 8)}$$

With,

$$V_{\max} = \frac{R^2 \Delta P}{4\mu L} \qquad \text{(equation 9)}$$

Where,

$V_x(y)$: Velocity in the x direction at y position.
$V_{\max}$: Maximum velocity in the x direction.
R : Radius of the pipe.
L : Length of the pipe
μ : Dynamic viscosity.

Since in the LBM presented above the pressure depends on the density (see equation 6) the model is considered a non exact incompressible method. To simulate a change in

pressure requires a change in density. Therefore this LBM is known as a weakly compressible model. In this type of model, we can generate the gradient pressure with the application of an equivalent volume force added to the DFs designed in such a way to produce the same momentum input to the flow as the true gradient. This volume-force model does not allow us to recover an exact Reynolds number and/or the internal structure of the pressure field point-wise, however it is extremely efficient to recover the universal behavior of the fluid system in the range of the Reynolds numbers to be studied.

Figure 4 shows a comparison between the analytical solution of the pipe flow problem described above and the result for a simulation in a 64x64x64 lattice. Because of the symmetry of the problem Figure 4 only shows the profile of the velocity along a line perpendicular to the flow. As is evident there is very good agreement between the analytical solution and the results from the 3D LBM simulation for low Mach number and low Reynolds number conditions.

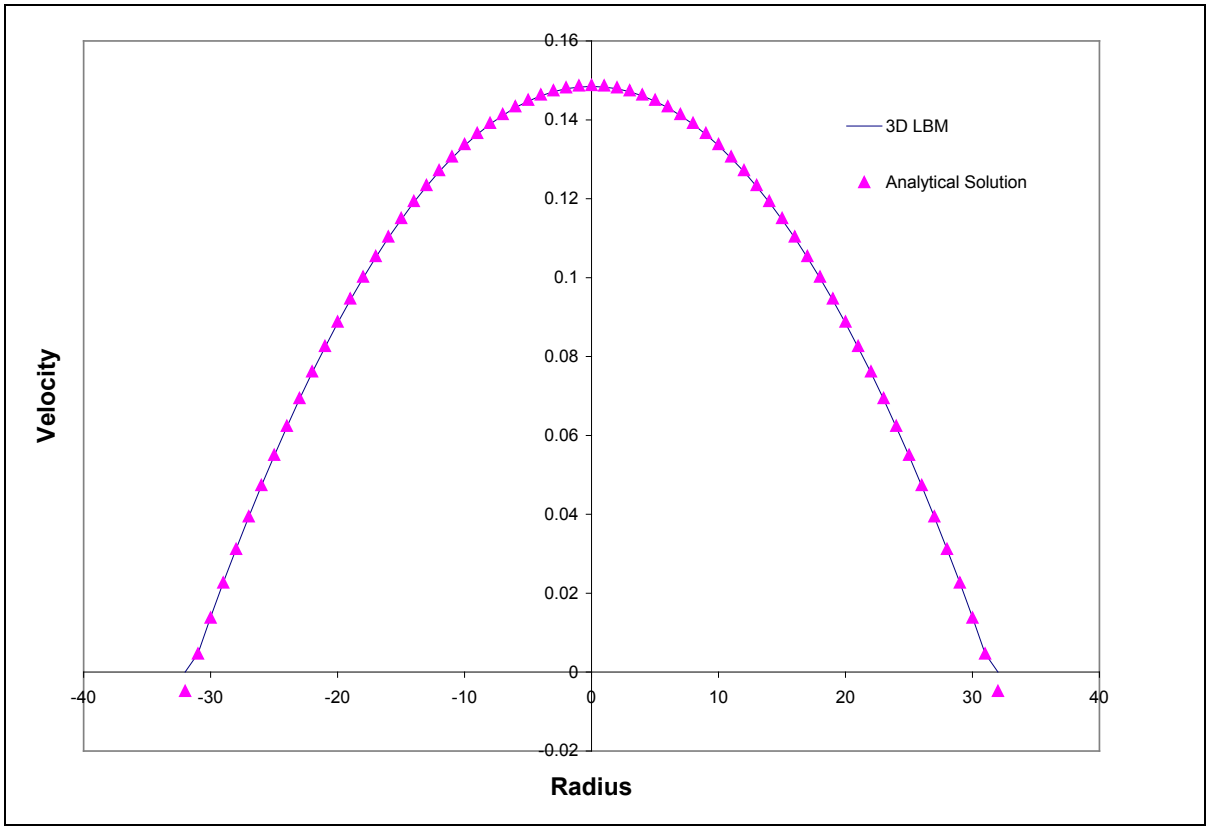

Figure 4. Comparison between analytical solution and a 3D LBM simulation for a 64x64x64 lattice.

Determination of Saturated Permeability using XMT Images

In this part of the research the utility of the 3D LBM to predict saturated permeability for packed particle beds is evaluated. In this regard, different particle samples of sand, glass beads, and ore (identified as C4) have been used for X-ray tomography analysis. The reconstructed 3D image is then used for LBM flow simulation to calculate the expected permeability based on the porous structure of the sample. The samples used for analysis have porosities from 25% to 40%. Table 1 shows the particle size characteristics of the samples used in this study.

Sample	Dmin μm	Dmax μm	Diameter μm
Filtersand	300	425	357.07
Limestone	710	2000	1191.64
Acusand	420	595	499.90
C4	2000	3175	2519.92
C4	420	2000	916.52
C4	149	420	250.16
glass beads	210	250	229.13
glass beads	300	420	354.96
glass beads	420	600	502.00

Table 1. Particle samples.

Darcy's Law.

Darcy's law established that the flow rate passing through a granular material is proportional to the constant cross sectional area, proportional to the difference in piezometric head and inversely proportional to the length of the sample. A formal equation of Darcy's law is given by (Bear, 1972):

$$Q = KA\frac{(\varphi_1 - \varphi_2)}{L} \qquad \text{(equation 10)}$$

$$\varphi_i = z_i + \frac{p_i}{\rho g} \qquad \text{(equation 11)}$$

and,

$$K = \frac{kg}{\nu} \qquad \text{(equation 12)}$$

Where,

Q is the flow rate in [cc/sec].

A is the cross sectional area [cm^2].

$\frac{(\varphi_1 - \varphi_2)}{L}$ is the hydraulic gradient [non dimensional].

K is the hydraulic conductivity and has units [cm/sec].

k is the permeability coefficient of the porous matrix [cm^2]

Experimental Set-Up

The experimental determination of the coefficient of permeability is done by a constant-head method for laminar flow through granular samples. The experimental set-up follows the recommendations given in ASTM D 2434 "Standard Test Method for Permeability of Granular Soils".

A cylindrical container of around 10 cm length and 2.6 cm in diameter holds the sample which is fitted between two screens to contain the sample. A fiber of high porosity is attached to each screen to prevent movement of particles. The top screen has a spring attached for applying a light pressure load to hold the placement density and volume of the sample. The system consists of 60 cc syringes as containers and CO_2 has been used for filling the void space before saturation with water. Figure 5 shows a diagram of the experiment.

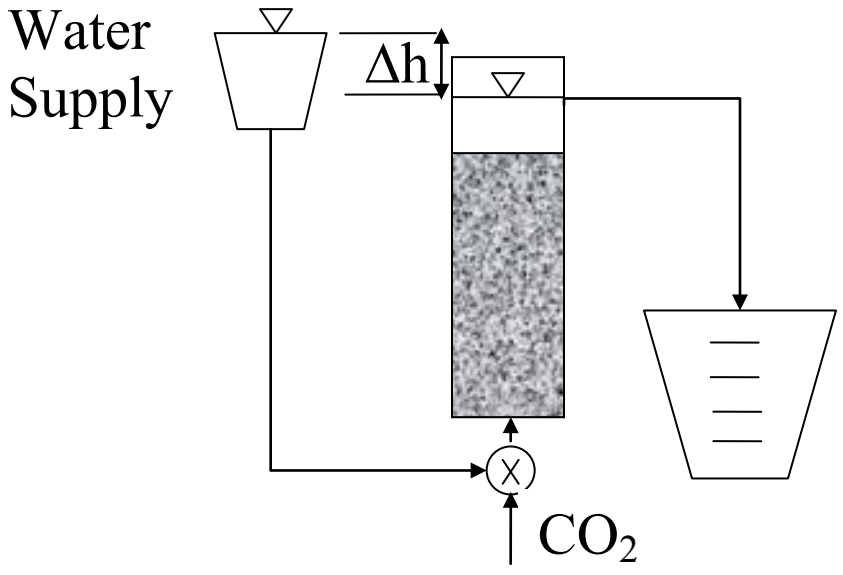

Figure 5. Test apparatus for permeability measurements.

A constant head of water was kept on the inlet and the outlet of the sample so the head difference was constant during the experiment. The diameter and length of the sample were also measured. Experiments were run at different head differences but being careful to keep a laminar flow condition. The flow was driven with different hydraulic gradients, so a line could be fitted for the different flow rate v/s hydraulic gradient data. Once the hydraulic conductivity was calculated from the slope of the line, then the permeability was calculated from its relation with hydraulic conductivity according to equation 20. Because the fluid used was water at 20 C degrees, the viscosity used for calculation was 1.0 cPoise.

LBM Permeability Estimation

Calculation of permeability from a 3D image captured with XMT analysis requires the simulation of fluid flow through the porous structure of the particle bed. In this regard, it is important to recall that the properties of the fluid are not important because the permeability is a characteristic of the tortuous path that the flow must follow through the particle bed and not a property which will depend on the fluid characteristics. Because of the latter, the flow simulation can be done with any type of fluid. Therefore in all our simulations the fluid properties are defined by a relaxation time of one given a lattice viscosity of 0.166 lattice units.

The flow is assumed to be vertical and it is forced for a constant pressure-model through the application of a volume force. Since the flow is at steady state and at a constant pressure, then the volume force can be balanced to the pressure according to the following equation:

$$g_x \rho L^3 = \left(P_{in} - P_{out}\right) * L^2 = -\frac{\Delta P}{\Delta x} * L^3 \qquad \text{(equation 13)}$$

Then by substitution in equation (10) and (12) we get

$$k = -\left(\frac{q\mu}{dP/dx}\right) = \frac{q\nu}{g} \qquad \text{(equation 14)}$$

In LBM, the initialization is not critical for steady-state flows because the system will converge to that condition whatever the initial condition. Therefore, the initial conditions in all our simulations are set with velocities equal to zero and density equal to one in the whole domain.

The flow is constrained to the left and right sides with an artificial box, and the flow is only allowed in one direction, where the bottom and top are open. The flows in the inlet and outlet are treated with a periodic boundary condition to allow the departing particle to reenter the flow domain. The first four layers at the bottom and top of the flow direction are

empty and they are initialized with fluid at the beginning of the simulation so the periodic boundary condition can be applied.

The standard bouncing back boundary condition is applied at the solid boundaries, including the artificial container around the porous matrix. The standard bounce-back scheme requires that when a particle distribution streams to a solid boundary node it is scattered back to the node from which it came. This treatment is independent of the direction of the particle distribution and is very easy to implement.

Once the flow reaches steady state, the flow rate (q) can be calculated from the average of the flow velocity along the flow direction and then the permeability can be calculated according to equation 14 using the viscosity and gravity force values used for the simulation. Since the lattice permeability needs to be translated to physical units [cm^2], the calculated lattice permeability has to be scaled to physical units with a relationship given by the following equation

$$k_{physical} = k_{lattice*} * L_x^2 \qquad \text{(equation 14)}$$

Where,

L_x is the voxel resolution of the image, usually 20 μm.

During the LB simulation, the particles of the single fluid enter the porous media from the inlet face and flow towards the outlet face. The flow occurs through the connected parts of the porous structure and the simulation is finished when the flow achieves steady state or the time of simulations reaches 5000 iterations, whichever happens first.

Figure 6 shows the results of a 128x128x128 glass bead sample used to calculate the permeability under saturated flow. The vectors shown in red display the path followed by the liquid around the solid particles. It is evident that the simulation is able to capture the underlying physics of the system.

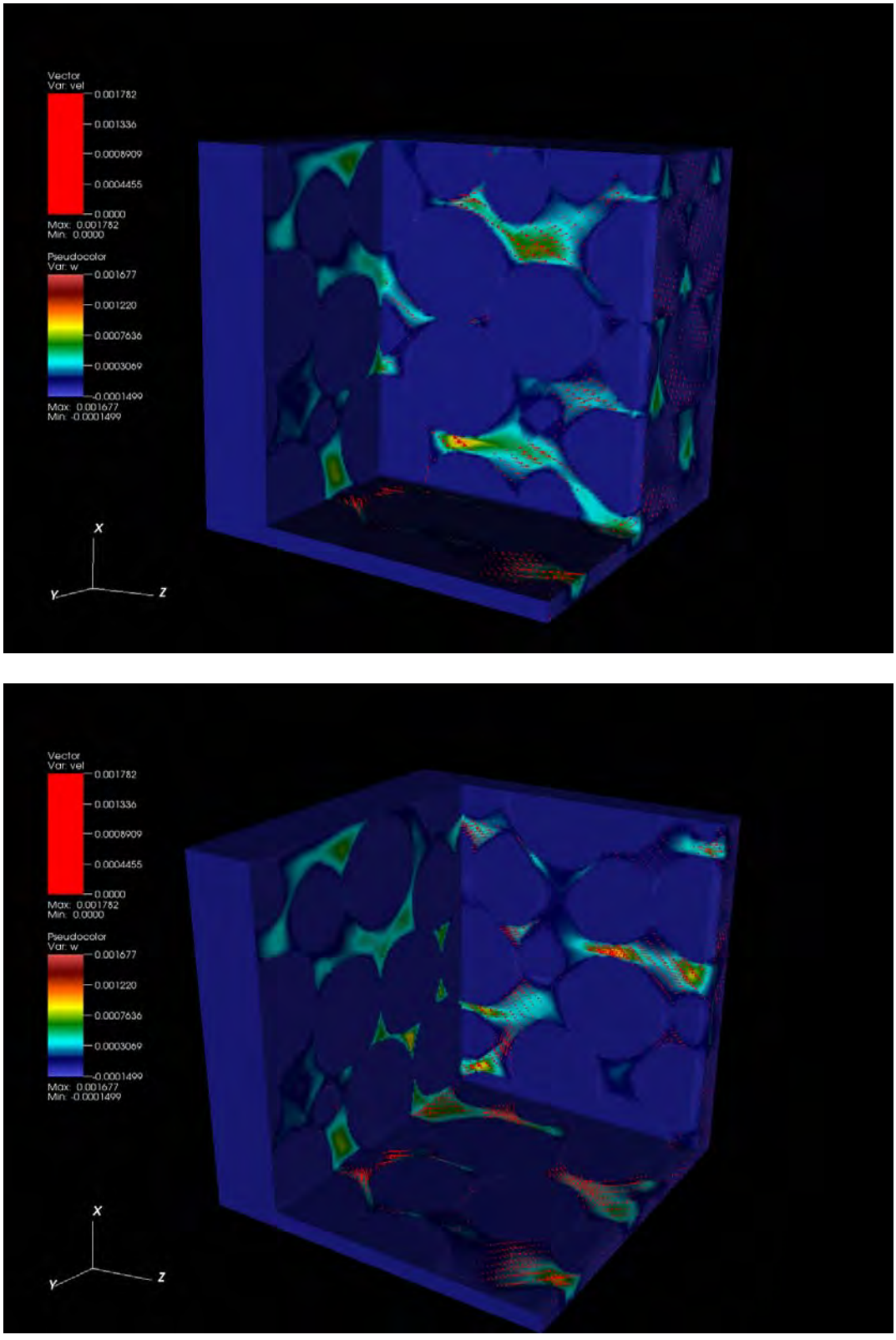

Fig 6. Velocity profiles along the flow direction (left to right) in a 3D XMT image. The vectors (in red) show the flow of the fluid through the pore network structure of glass beads.

RESULTS AND DISCUSSION

We have made several permeability measurements from LBM simulations and from experimental tests. The methods have been explained above and here we will show a comparison between these results.

Figure 7, 8, 9 and 10 show the experimental results used for calculation of the hydraulic conductivity for Limestone, Acusand, Filtersand, and Ore. The slope corresponds to the hydraulic conductivity measured from different driving pressure gradients. The permeability is calculated using equation 12 for water at 20 C degrees (viscosity equals 1 cPoise). The correlation value is excellent showing good agreement between theory (Darcy's Law) and experimental tests.

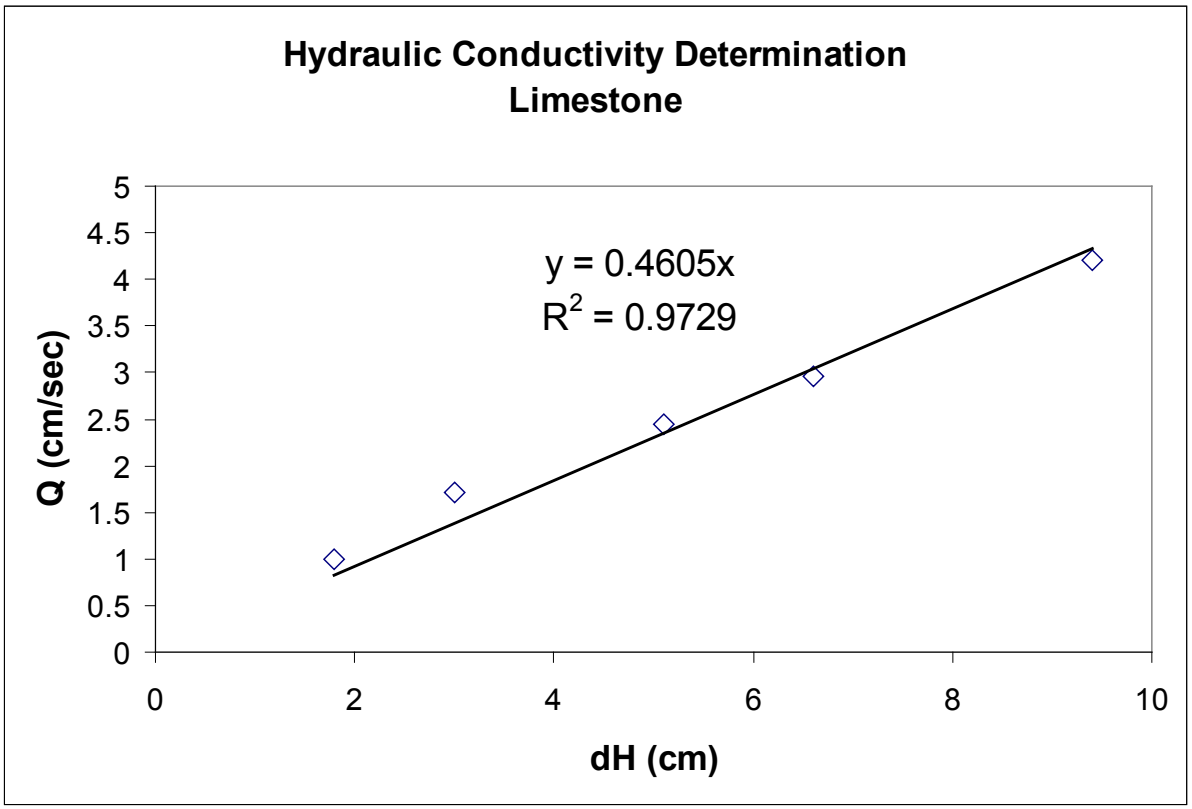

Figure 7. Relation between flow rate and pressure differential (cm of water) for Limestone.

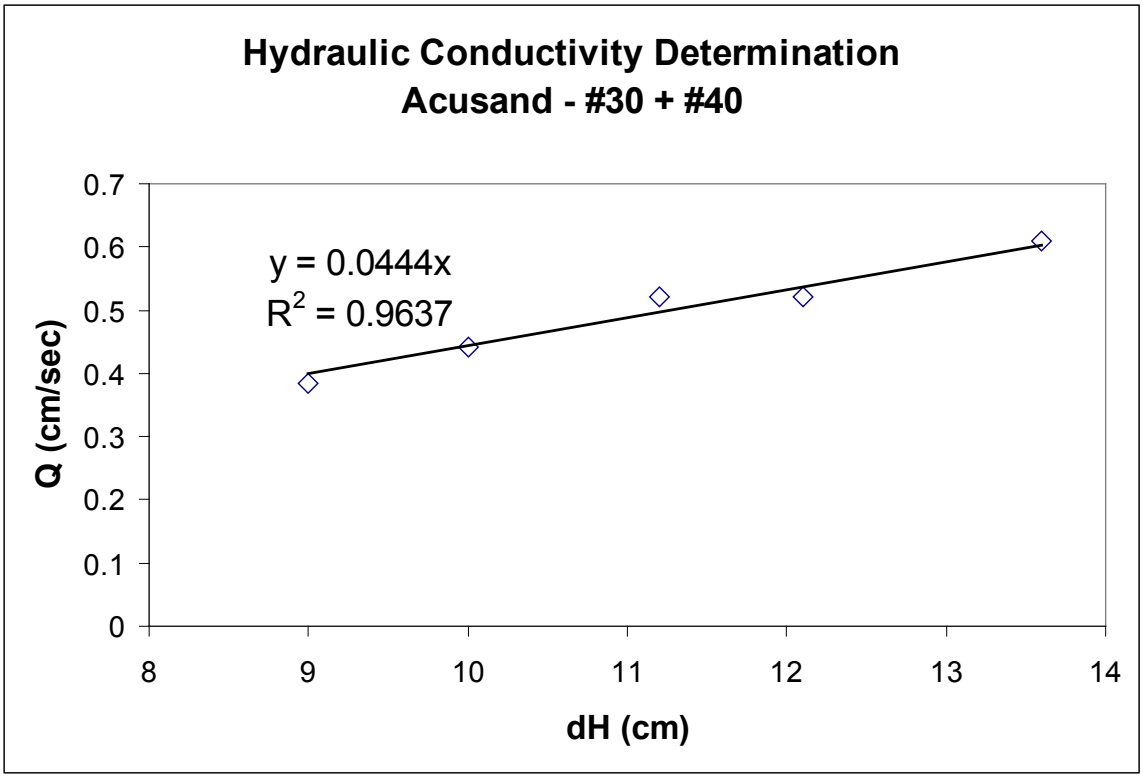

Figure 8. Relation between flow rate and pressure differential (cm of water) for Acusand.

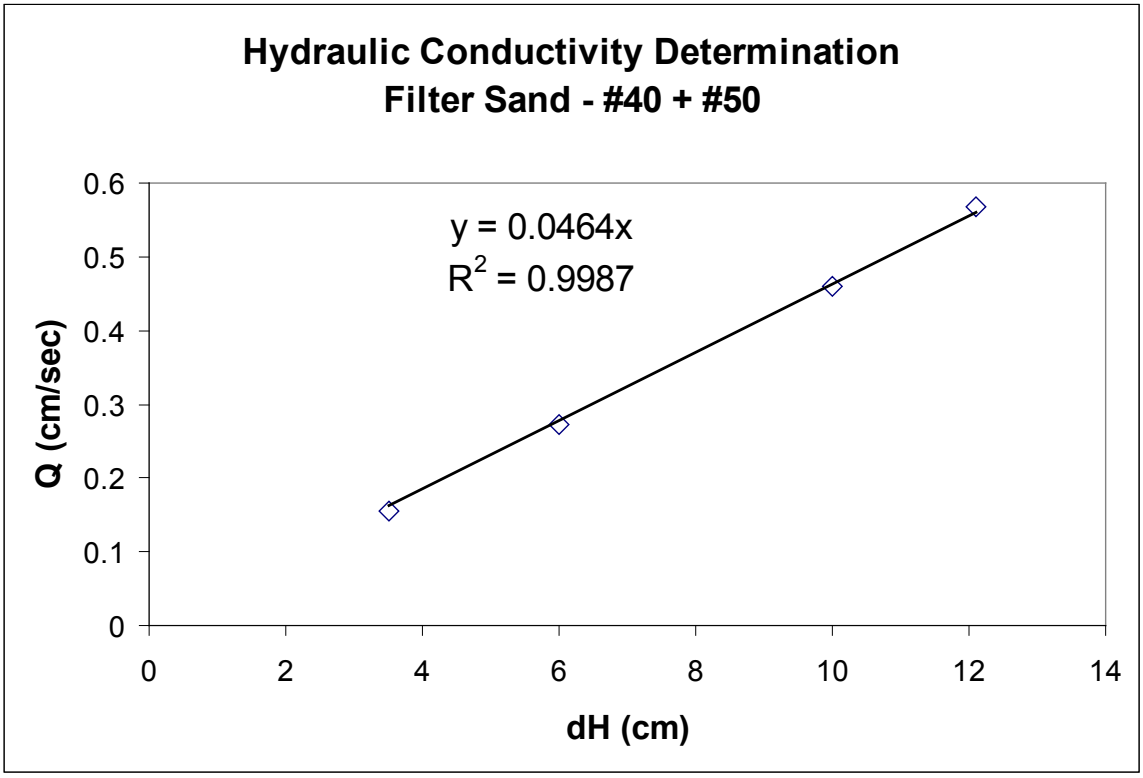

Figure 9. Relation between flow rate and pressure differential (cm of water) for Filter Sand.

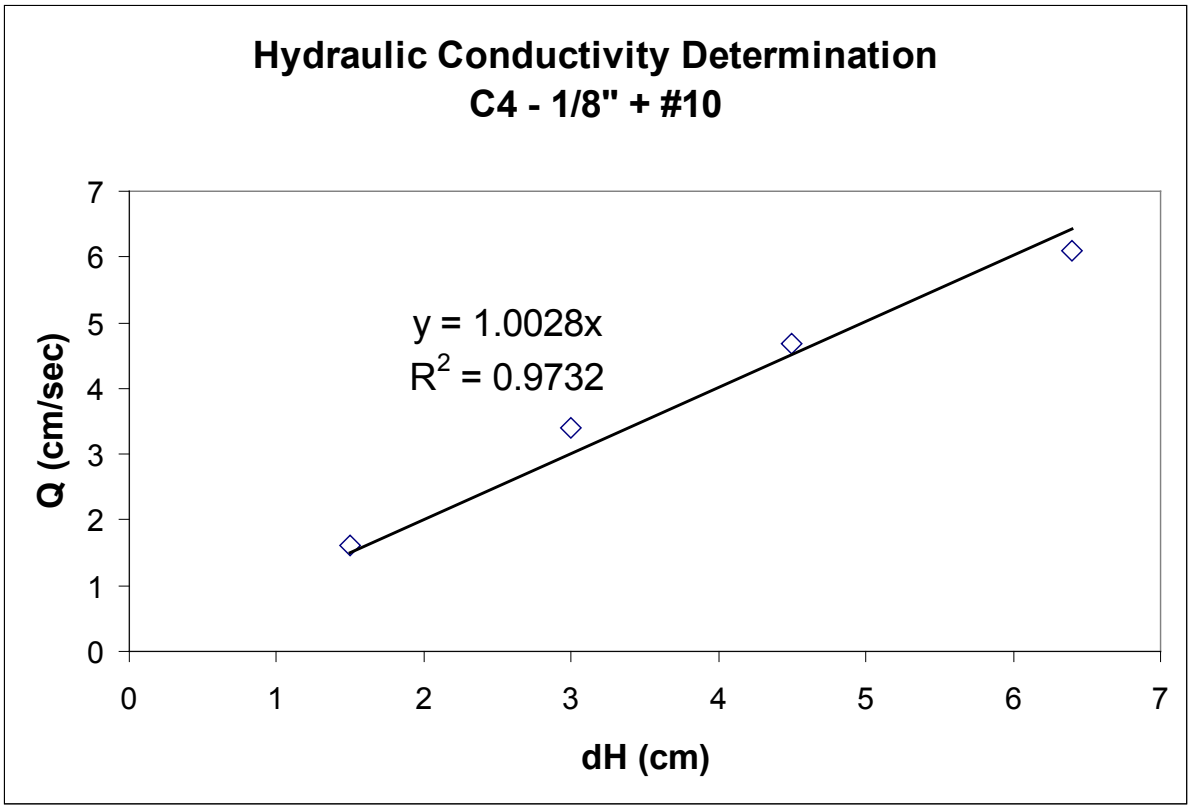

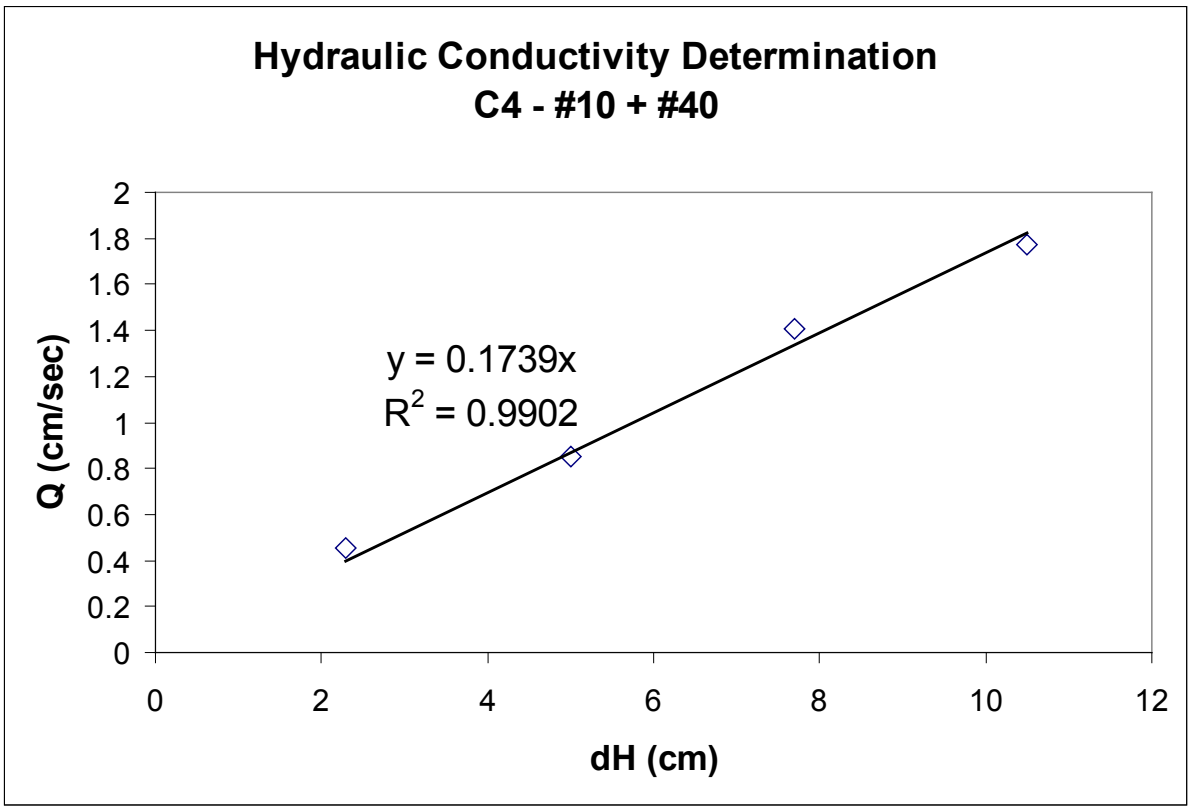

Figure 10. Relation between flow rate and pressure differential (cm of water) for different particle sizes of ore.

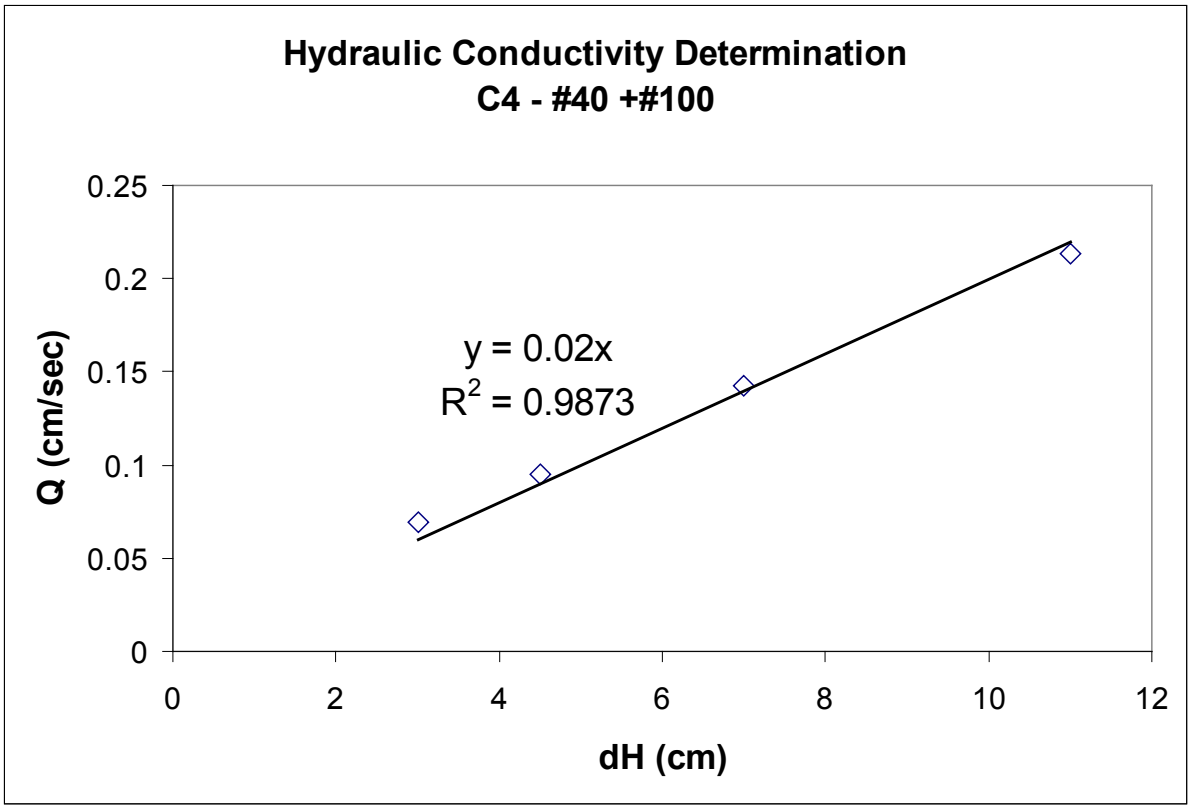

Figure 10 (continued). Relation between flow rate and pressure differential (cm of water) for different particle sizes of ore.

The permeability obtained from LBM simulation tends to change with the size of the sample and the resolution of the image. A compromise must be found between resolution and complexity, because a better resolution increases enormously the number of voxels to be used for getting a representative volume size of the sample. In this regard, a 20 μm resolution has been a good compromise for most of the samples under analysis. When the amount of sample is very small as in the case of the glass beads which vary in size from 210 to 250 μm, then a 10 μm resolution has been used.

Depending on the particle size, the size of the images used for simulation varies from 128x128x128 voxels to 256x256x256 voxels. To reduce the effect of the anisotropy, the permeability of the flow is simulated in the three major directions x, y and z. Table 2 shows a summary of the result of the simulations. The resolution of the voxels and the particle sizes are indicated for each sample. The porosity corresponds to the fraction of void space measured from the 3D image.

Sample	Resolution μm	Dmin μm	Dmax μm	Porosity	K_x (cm^2)	K_y (cm^2)	K_z (cm^2)	K (cm^2)	Image Size
Filtersand	20	300	425	0.421	1.393E-06		1.928E-06	1.660E-06	200x200x200
Acusand	20	420	595	0.379	1.014E-06	1.143E-06	1.144E-06	1.100E-06	200x200x200
Limestone	20	710	2000	0.392	8.300E-06	9.570E-06	1.020E-05	9.357E-06	256x256x256
C4	20	149	420	0.323	2.015E-07	2.711E-07	2.368E-07	2.365E-07	256x256x256
C4	20	420	2000	0.367	3.406E-06	4.580E-06	4.910E-06	4.299E-06	256x256x257
C4	20	2000	3175	0.407	2.133E-05	2.078E-05	1.767E-05	1.993E-05	256x256x256
glass beads	10	210	250	0.363	4.288E-07	4.515E-07	4.556E-07	4.453E-07	256x256x256
glass beads	20	300	420	0.293	6.630E-07	6.954E-07	6.849E-07	6.811E-07	128x128x128
glass beads	20	420	600	0.388	2.275E-06	2.425E-06	2.459E-06	2.386E-06	128x128x128

Table 2. Permeability obtained from the LB simulations in the x, y and z directions. K is the average value obtained from the three major directions.

Table 3 shows a comparison between the average permeability calculated from LB simulations and the experimental value obtained from the tests as explained above. The relative error decreases for coarser particle sizes because the permeabilities are higher and the relative error is less sensitive for these differences. In general, good agreement is obtained between the LB simulation and the experimental values even for irregular particle shapes. Figure 11 shows the results as a function of particle size. The agreement is good for a wide spectrum of particle sizes.

Sample	Average Diameter μm	K_{LB} (cm^2)	$K_{Experimental}$ (cm^2)	Relative Error
Filtersand	357	1.660E-06	9.449E-07	76%
Acusand	500	1.100E-06	9.212E-07	19%
Limestone	1192	9.357E-06	9.024E-06	4%
C4	250	2.365E-07	4.034E-07	41%
C4	917	4.299E-06	3.475E-06	24%
C4	2520	1.993E-05	2.023E-05	1%
glass beads	229	4.453E-07	4.872E-07	9%
glass beads	355	6.811E-07	1.101E-06	38%
glass beads	502	2.386E-06	1.507E-06	58%

Table 3. Comparison between experimental and LB permeabilities.

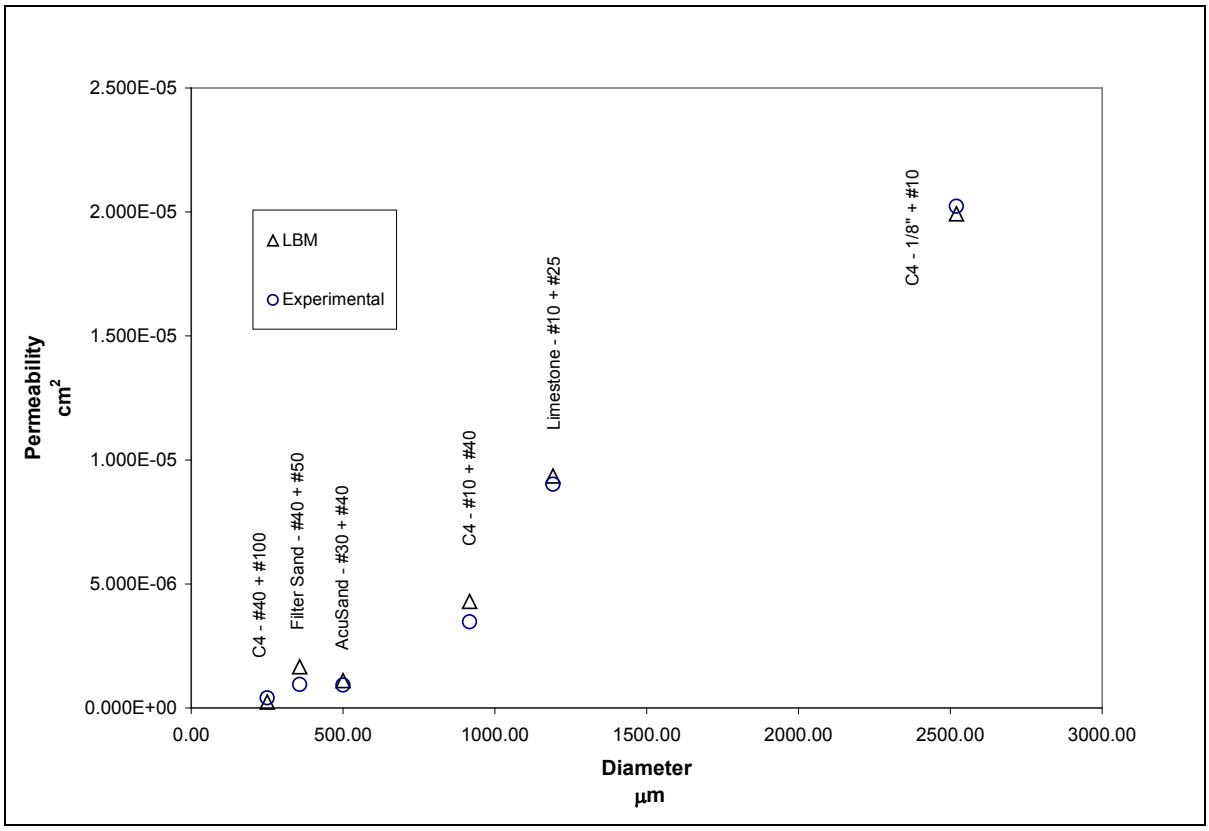

Figure 11. LB permeability and experimental permeability for irregularly shaped particles.

CONCLUSION

Up to this moment 3D LBM for saturated flow in packed particle beds has been developed. Comparison of the results with analytical solutions for pipe flow under laminar fluid flow conditions and with permeability measurements show good agreement. In fact, we are able to predict the permeability of the porous media with certain accuracy.

In general we will follow the approach explained before in the Objective and Approach section. We are now working on the parallelization of the model in order to make it scalable. This work is necessary in order to be able to handle development of a multiphase model in the next step of the research since this problem is at least twice as computer intensive as the single fluid component model.

In the near future we intend to implement the Shan and Chen model and evaluate the performance of the model with known analytical solutions. Two problems will be evaluated. One is the verification of the Law of Laplace and the second problem is the countercurrent flow of two fluids of different viscosity or density or both in pipe flow.

REFERENCES

Bear J., *Dynamics of Fluids in Porous Media*, Dover Publications, New York, 1988.

Bhatnagar P., E. Gross, and M. Krook, A model for collision processes in gases. I: Small amplitude processes in charged and neutral one-component system. Phys. Rev., 94:511-525, 1954.

Chen H., Discrete Boltzmann systems and fluid flows. J. Comp. in Phys., Nov/Dec:632-637, 1993.

Chen S., G. Doolen, Lattice Boltzmann Method for fluid flows. Ann. Rev. Fluid. Mech., 30:329-64, 1998.

Frish U., B. Hasslacher, and Y. Pomeau, Lattice-gas automata for the Navier-Stokes equation, Phys. Rev. Lett., 56:1505-1508, 1986.

Frish U., D. d'Humieres, B. Hasslacher, P. Lallemand, Y. Pomeau, and J. Rivert, Lattice Gas Hydrodynamics in Two and Three Dimensions, Complex Syst., 1:649-707, 1987.

He X., L. Luo, A priori derivation of the Lattice Boltzmann equation, Phys. Rev. E, 55(60): R6333-R6336, 1997.

Higuera F., J. Jimenez, Boltzmann approach to lattice gas simulations, Europhys. Lett., 9:663-668, 1989.

Lin, C.L., J.D. Miller, Pore structure analysis of particle beds for fluid transport simulation during filtration, Int. J. Min. Proc., 73:281-294, 2004.

Macnamara G., G. Zannetti, Use of Boltzmann equation to simulate lattice-gas automata, Phys. Rev. Lett., 61:2332-2335, 1988.

Martys N., H. Chen, Simulation of multicomponent fluids in complex three-dimensional geometries by the Lattice Boltzmann Model, Phys. Rev. E, E 53:743-750, 1996.

Miller J.D., C.L. Lin, C. Roldan, and C. Garcia, Characterization and analysis of copper heap leaching by x-ray computed tomographic techniques, *Proc. 3nd World Congress on Industrial Process Tomography*, Banff, Canada, 2-5 September 2003:707-712, 2003a.

Miller J.D., C.L. Lin, C. Roldan, and C. Garcia, Particle size distribution for copper heap leaching operations as established from 3D mineral exposure analysis by x-ray microCT, Copper 2003, Santiago, Chile, VI – Hydrometallurgy of Copper: 83-97, 2003b.

Qian Y., D d'Humieres, and P. Lallemand, Lattice BGK models for Navier-Stokes equation, Europhys. Lett., 17:479-484, 1992.

Shan X., H. Chen, Lattice Boltzmann model for simulating flows with multiple phases and components, Phys. Rev. E, 47, 1993. Page Nos.

Succi S. *The Lattice Boltzmann Equation for Fluid Dynamics and Beyond*, Oxford University Press, New York, 2001.

Zhang R., H. Chen, Lattice Boltzmann method for simulations of liquid-vapor thermal flows, Phys. Rev. E, 67:066711, 2003.

PUBLICATIONS/PRESENTATIONS

X-ray microtomography and the LB method to measure permeability through particle packed beds, Presented at the International Conference of Mesoscopic Methods, Hampton, Virginia, 2006. Name of presenter?

APPENDIX 19 – Development of a Turbulent Flotation Model Model and Computer Simulator (VA015)

TECHNICAL PROGRESS REPORT

Contract Title and Number:	Period of Performance:
Continuation of Crosscutting Technology Development at CAST (DE-FC26-05NT42457)	Starting Date: 7/26/2006 Ending Date: 09/30/2010

Sub-Recipient Project Title:	Report Information:
Development of a Turbulent Flotation Model and a Computer Simulator	Type: Semi-Annual Number: 1 Period: 07/26/06-9/30/10 Date: 11/15/10 Code: VA015-FINAL
Principal Investigators: Yoon, Luttrell, Vlachos. Teleonis	
Contact Address:	Contact Information: Phone: Fax: E-Mail: ryoon@vt.edu
Subcontractor Address: No subcontracts issued.	Subcontractor Information: Phone: Fax: E-Mail:

ABSTRACT

Flotation is a process of separating particulate materials of different surface properties in a hydrodynamic environment, and is used extensively for separating different minerals from each other in the mining industry. In this process, air bubbles are introduced at the bottom of a particulate suspension (pulp), so that bubbles coated with hydrophobic particles rise to the top and form a froth phase while hydrophobic particles stay in suspension. The selectivity of the flotation process is determined by the hydrophobicity of the particulate materials involved, while the kinetics of the process is controlled by the hydrodynamic conditions and the disjoining pressures in the thin aqueous films between air bubbles and particles.

In the present work, a mathematical model for the flotation process has been developed by considering both the hydrodynamic and surface chemical parameters. The model can describe the events occurring in both the pulp and froth phases of a mechanically-agitated flotation cell. The pulp-phase model is based on predicting the kinetics of bubble-particle attachment using the DLVO extended to include contributions from hydrophobic force and the theory of turbulent collision. The froth-phase model is based on predicting the rate of bubble-particle detachment by considering bubble coarsening and water recovery. The predictions from the overall flotation model are in general agreement with the results obtained in single-bubble flotation experiments and the flotation test results reported in literature. Since the model has been developed largely from first principles, it has predictive and diagnostic capabilities.

TABLE OF CONTENTS

LIST OF FIGURES

Chapter 2

A flotation model under turbulent flow conditions

Chapter 3

Induction time measurement for single-particle flotation

Chapter 4

Developing a drainage model in foams incorporating hydrophobic force

Chapter 5

Predicting the critical rupture thickness of free foam films

Chapter 6

Developing a froth-phase recovery model from first principles

LIST OF TABLES

Chapter 5

Predicting the critical rupture thickness of free foam films

Chapter 1. Introduction

1. Fundamentals on Flotation Modeling

Flotation is a process for separating finely divided solids from each other using air bubbles under hydrodynamic environment [1]. Regarding its application in the mining industry, it has been used for more than 100 years for separating valuable minerals from raw ore. This popularity is due to its low operation cost, simplicity and versatility. Virtually any mineral present in an ore can be separated from other minerals by flotation. Minerals to be floated must be either naturally hydrophobic or rendered hydrophobic by judicious use of hydrophobizing reagents (collectors). Therefore, when bubbles are introduced into the bottom of a flotation cell in which an ore pulp is contained, hydrophobic mineral particles are selectively attached to the bubbles while hydrophilic mineral particles are left unattached. The bubble-particle aggregates formed as a result of the attachment process then rise to the top of the slurry and exit the flotation cell, and thereby be separated from the hydrophilic minerals left in the cell.

For the bubble-particle attachment to occur, the Gibbs free energy change (ΔG) must be negative. The free energy change associated with the attachment process can be by considering the changes in interfacial tensions at the solid-liquid, solid-vapor, and liquid-vapor interfaces [2]. By relating the changes in interfacial tensions to the Young's equation, one obtains the flowing relation,

$$\Delta G = \gamma_{lv}(\cos\theta - 1) < 0 \qquad (1)$$

as the thermodynamic criterion for bubble-particle attachment, or flotation. In Eq. (1), γ_{lv} is the interfacial tension between liquid and vapor, and θ is the contact angle at the three phase contact. From this relation it is clear that the process of bubble-particle attachment is thermodynamically possible only when the contact angle is greater than zero. The larger the value of θ is, the more negative the value of ΔG becomes. Therefore the contact angle has often been used as a measure of floatability. Parameters such as θ or γ_{lv} vary depending on the chemical conditions such as collector and concentrations employed during flotation.

While the thermodynamic criterion for floatation is determined by chemistry parameters, hydrodynamic parameters such as bubble size, particle size, and energy dissipation rate in a flotation cell also affect the process. Flotation machines are designed to optimize the hydrodynamic conditions to maximize bubble-particle collision, which is a prerequisite for the attachment process discussed above, and to keep particles in suspension and move forward from one cell to another. It is difficult, however, to experimentally measure collision frequencies as it is a stochastic process particularly under turbulent flow conditions.

Many investigators developed collision models and used them to predict coagulation of colloidal particles [3-9]. The various collision models developed to date are of different forms, but may be represented in the following generalized form:

$$Z_{12} = CN_1N_2(d_{12})^n \quad (2)$$

in which Z_{12} is the number of collisions between species **1** and species **2**, N_1 and N_2 are the number densities of particles **1** and **2**, d_{12} is the sum of the radius of the two particles, which is referred to as collision radius, and C and *n* are parameters varying with the boundary conditions involved in the derivation of the models. It is a challenge to use Eq. (2) developed for the interaction between small, colloidal size particles in liquid or gaseous phases for flotation, in which **1** is solid and **2** is air bubble and particle sizes are well beyond the length scales involved colloidal and aerosol interactions. Many investigators adapted Eq. (2) for the bubble-particle interactions in flotation by introducing adjustable parameters such as probability (or efficiency) of collision (P_c), attachment (P_a) and detachment (P_d) [10-12]. Modeling flotation is complicated further by the fact that bubble-particle aggregates form a froth phase (three-phase foam) on top of the flotation pulp and that some of the bubble-particle aggregates break up during the course of entering and rising in the froth phase. Thus, it would be necessary to consider the probability of the hydrophobic particles not being dropped out of the froth phase and exit the flotation cell and be recovered in the forth launder (P_f).

Many investigators showed that flotation can be represented as first-order rate process, in which case the following flotation rate equation may be used [13, 14]:

$$\frac{dN_1}{dt} = -kN_1 = -Z_{12}P \quad (3)$$

Eq. (3) states that the rate of flotation is proportional to the number density (N_1) of particles in a flotation cell and flotation time *t*, with *k* being the flotation rate constant. Its shows also that flotation rate is simply the product of collision frequency (Z_{12}) and the probability of flotation (P). Sutherland [13] proposed that P should be a function of various subprocesses discussed above, *i.e.*, P_c, P_a, P_d, and P_f. Most of the investigators derived the probability functions of some of these sub-processes by considering hydrodynamic parameters. Others, however, considered both hydrodynamic and surface chemistry parameters [9, 14-16]

So far, most researchers on flotation modeling laid foundations for predicting flotation rate either by using chemistry or hydrodynamic parameters. Not many studied the effects of both parameters partuclarly for the flotation under turbulent flow conditions. Serious attempts to account for both parameters were few [9, 16]. More recently, however, increasing number of researchers have challenged the subject of modeling flotation by taking advantages of the recent advances in fluid mechanics, particularly CFD simulations, and in colloid chemistry, particularly on the role of hydrophobic force in the thin films of water between air bubble and particles, which are referred to as wetting films. Recent interest in flotation model development may stem also from ever increasing demands for natural resources. Developing a good flotation model should lead to the development of a computer simulator that can be used to optimize the process, train plant operators and engineers, and help better understand the complex three-phase phenomenon.

2. Research Objectives

The objectives of the present work are restated as follows:

1) To develop a turbulent flotation model from first principles by considering both chemistry and hydrodynamic parameters.

2) To study bubble-particle attachment kinetics by conducting induction time measurements under different chemical and hydrodynamic conditions.

3) To develop a foam drainage model from first principles and compare the model predictions with experimental results.

4) To develop a model to predict the critical rupture thicknesses for free foam films, and use the model to predict bubble coarsening in foam columns.

5) To develop a froth recovery model and incorporate it into the flotation model to be developed in Chapter 1.

3. Literature Review

The first aggregation kinetics model was in higher order since it was derived for colloidal particles subject to Brownian motion [17]. However, flotation system is less influenced by Brownian motion, and accordingly many investigators used the first order equation shown in Eq.(3) [9, 12-16, 18-22].

Equation (3) is interpreted such that the rate constant k indicates how fast the floatable particles are recovered. So many various parameters are involved in the constant, but largely, it has been found a function of the number of bubble-particle collisions taking place (Z_{12}), and the probability (P) of the collision's follow-up sub-processes, *i.e*.

$$k = f(Z_{12}, P) \tag{4}$$

Z_{12} is termed as collision frequency. As the name purports, Z_{12} presents the number of encounters between bubbles (subscript 2) and particles (subscript 1) occurring in their relative motions. Regarding this, earlier models in the literature used the simple idea that a bubble meets particles in the way when it sweeps through, and reached an approximate relation of Z_{12} with bubble size and superficial gas flow rate [12, 15]. According to the relation the frequency increases as gas flow rate increases, and inversely to the bubble size. However, this relation may not fit well for turbulent flow conditions.

In turbulent flow environment, modeling Z_{12} and P will be substantially different from what is for relatively quiescent flow conditions because bubbles and particles may influence each other's adjacent streamlines. In fact, researchers like Pyke *et al*.[9] extended to turbulent flow conditions the model originally derived from the streamline assumption around a bubble in quiescent flow

[22]. On the other hand, Sherrell and Yoon [16] suspected this idea and incorporated turbulence properties into calculating *P* based on surface energy estimate. The model, however, showed a result indicating that flotation kinetics is controlled more by bubble-particle detachment, rather than attachment [21].

Turbulence is composed of eddies of various length scales. Turbulent kinetic energy is known to be distributed along these different length scales, and the energy input at the largest scale is transferred successively to smaller scales until it dissipates out. One of the most significant properties of turbulence is the energy dissipation (or specific energy input), ε_{sp}. It involves along with the liquid viscosity in determining the statistically universal form of the dissipation length scale [23]. In some turbulent systems where inertial effects are ignored, the root mean squared (r.m.s) value of fluid's velocity gradients is proportional to the square root of the ratio of energy dissipation to liquid viscosity [24]. In such systems, collision frequencies are derived using the relation [3, 8]. For the case of systems where inertial effects are not ignored, collisions are not due to shear mechanism only. Therefore, Abrahamson [4] implied the r.m.s velocities of suspended particles 1 and 2 directly into the model as the following.

$$Z_{12} = 2^{3/2}\pi^{1/2}N_1N_2d_{12}^2\sqrt{\overline{u_1}^2 + \overline{u_2}^2} \tag{5}$$

with notations meaning the same as in Eq.(2). $\overline{u_1}^2$ and $\overline{u_2}^2$ are the mean squared fluctuation velocities. This has been frequently referenced in describing aggregations in flotation systems. In the application of mineral flotation, Schubert [25] regarded the particles as minerals (subscript 1) and bubbles (subscript 2), and replaced the velocity term with the one proposed by Liepe and Moeckel [26]. Recently, Brady *et al*.[27] verified experimentally several models describing particle velocities in homogeneous turbulence. In their model comparison, Liepe and Moeckel [26]'s expression fit best for describing particle velocities. This information may be useful in modeling bubble-particle interactions in flotation system. However, there exists a limitation that the models are valid only for homogenous turbulence. In practical flotation tank, it is well known that near-impeller regions have higher energy dissipations than the remainders, and even with certain ratio relative to the average energy dissipation [9, 28, 29]

In turbulent flow conditions, neither the probability *P* of sub-processes nor the number of collisions is independent of hydrodynamic influence. On the other hand, unlike the collision frequency, surface chemistry also plays equivalently important role in evaluating *P*. The most important phenomenon implied in *P* is the bubble-particle attachment. Luttrell and Yoon [11] suggested the following expression for estimating the probability of bubble-particle attachment, P_a.

$$P_a = \exp\left(-E_1/E_k\right) \tag{6}$$

,where E_1 is the energy barrier or activation energy for bubble-particle attachment determined by colloidal forces, and E_k is the kinetic energy of collision. For objects in liquid medium, the hydrodynamic resistance increases as two surfaces approach closer [30, 31]. Due to this resistance, the kinetic energy exerted on particles in flotation system should reduce at sufficiently small separation distance to a comparable degree to the order of activation energy.

In aggregation kinetics modeling, Derjaguin and Dukhin [14] were the first who used surface forces in modeling bubble-particle interactions. Their work, however, was intriguing for mineral processing applications because what they considered were only repulsive forces while for mineral flotation to occur attractive force is responsible [32]. Therefore, Luttrell and Yoon [11] modified the classical DLVO theory that is used to describe the bubble-particle interaction energy. After adding attractive energy term due to hydrophobic force, the extended DLVO theory is as follows.

$$V_T = V_E + V_D + V_H \tag{7}$$

,where V_T is the total potential energy summed up by the potential energies due to electrostatic repulsion(V_E), Van der Waals dispersion (V_D), and hydrophobic force attraction (V_H). The value of energy barrier E_1 in Eq.(6) is found at the local maximum of the potential *vs*. separation distance curve portrayed by Eq.(7). Regarding the term V_H, no general analytical expressions is available because the origin of hydrophobic force is still at a loss. However, the evidences for its existence can be found easily in other literature [33-35].

Similar to P_a, the probability of detachment was also suggested as follows [15].

$$P_d = \exp\left(-(W_a + E_1)/E'_k\right) \tag{8}$$

,where W_a is the work of adhesion and E_k' is the detachment kinetic energy. The work of adhesion is derived from the force balance on the particle area in contact with bubble surface, and accordingly surface tension, contact area, and contact angles are involved.

After Sutherland [13]'s pioneering work, most of flotation models adopted the idea of the sub-process probability P as a product of collision (P_c), attachment (P_a), and detachment probability (P_d) as follows.

$$P = P_c P_a (1 - P_d) \tag{9}$$

Many flotation models in the literature estimate flotation rate constants based on this relationship. However, it may be appropriate only for describing batch flotation test where 100% recovery of mineral within the froth is usually assumed [36, 37]. The rate constants obtained in this way may be regarded 'apparent' rate constant since the pulp-to-froth transport process of particles collected in the pulp is ignored.

To be realistic, the transfer process needs to be considered. Noting that froth-pulp interface behaves like a barrier before the bubble-particle aggregates transfer, the probability of aggregates being transferred into froth (P_f) is incorporated with P as follows.

$$P = P_c P_a (1 - P_d) P_f \tag{10}$$

The same idea dates back as old as the work by Schumann [38]. However, the post-attachment sub-processes were not specified as the author simply put them in one parameter defined as froth stability factor. Clear distinction was not made until Tomlinson and Flemming's work [20] where the authors first suggested P_f as a probability of the attached particle reaching the pulp-froth interface without detachment. A clearer picture to this statistical aspect has been shown by Waters *et al*. recently [39]. In their experiment, the authors used positron emission particle tracking method to follow particles in flotation cells, and observed particles entering the froth after attaching to an air bubble, detaching from the froth, and re-entering. For all this experimental advances, incorporating P_f into P doesn't seem easy either empirically or analytically, because of the complex characteristics of froth [16, 20, 38]. According to the recent work by Koh and Schwarz [40, 41], froth phase is a significant contributor to the overall recovery. Aided by a Computational Fluid Dynamics (CFD) program for the first time, they could predict the temporal changes of total particle numbers in a lab-scale cell, which were used to infer the flotation rate constant.

As it was well reviewed in other literature, kinetic modeling of flotation critically depends on the assumptions made for the mixing conditions of the flow in the cell [42, 43]. Typically, two perfectly mixed flow regimes are defined: pulp and froth phase. With this regard, the first order kinetic modeling is valid only in the pulp phase, and the process in the froth phase needs to be studied separately if interested. Nevertheless, many researchers did not account for this in modeling flotation. At best, froth recovery was investigated separately while setting the 'apparent' rate constant proportional to froth recovery [12, 44-46]. In other words,

$$k = k_p R_f \tag{11}$$

,where k is the overall (apparent) flotation rate constant, k_p is the rate constant concerning the collection mechanism in pulp phase only, and R_f is defined as the froth recovery factor. R_f is interpreted as the fraction of particles recovered after they are transferred into froth [12]. While k is inferred from the recovery data in flotation tests, k_p is evaluated by extrapolating rate constants plot obtained from the same recovery data with various froth depths. However, the relation in Eq.(11) is not strictly valid because it is derived assuming the particles collection in the pulp phase is a first order process with 100% maximum recovery, that is ideal case [36, 43].

Many researchers do not differentiate k with k_p in interpreting recovery data. One common mistake is that they obtain the "apparent" rate constant k from recovery data, then wrongfully use it for validating the model derived for pulp phase only [9, 47, 48]. To conduct more precise validation, the overall recovery data needs to be directly compared with the model prediction, not the rate constant. Finch and Dobby [12] suggested the following to estimate the overall flotation recovery when the recovery in the pulp phase and froth phase are discrete.

$$R = \frac{R_c R_f}{R_c R_f + 1 - R_c} \tag{12}$$

,where R is the overall recovery, and R_c and R_f ar the recovery in the pulp and froth phase respectively. R_c can be estimated using the rate constant k_p, and R_f needs to be defined independently.

The fractional recovery in the froth phase, R_f, may be modeled in a broader sense by the following aspects. Since air bubbles are hydrophobic [49] as well as mineral particles, the mechanisms governing froth recovery can be attributed to attachment. This is called true froth recovery because only hydrophobic particles are recovered along with the surviving bubble-particle aggregates from the froth. Because froth bubbles are hydrophobic and in 3 phase some researchers could model the recovery in empirical ways only [50, 51]. However, more analytical froth recovery model may be developed by investigating liquid drainage and bubble coarsening in froth. It is well known that non-hydrophobic particles are also recovered from froth, being carried by the froth without attachment. This is called entrainment, and it is not directly related to the chemistry but well known to play significant roles in the fine mineral particles recovery [52, 53].

Recovery mechanisms in relation with froth structure may be more simplified if one is to apply the same physical interpretations to foams. *Foams* is the term used to distinguish the 2 phase system from the 3 phase (*froths*) [54]. A foam is a two-phase system where gas cells are enclosed by liquid, and accordingly the structure looks like a network of pipe-like channels (called Plateau Border) and thin film walls (called lamellae) [55]. The drainage along this structure has been a popular research topic for a long time because foams are commonly observed in many practical applications. Most of foam drainage models in the literature assume that liquids in foams flow mainly through the channels, and set the following continuity equation as the basis for the model [56-60]

$$\frac{\partial \varepsilon}{\partial t} + \frac{\partial (\varepsilon u)}{\partial x} = 0 \tag{11}$$

,where ε is the liquid fraction defined as the ratio of wet area over the whole column cross-sectional area and u is the average velocity of the flow through plateau borders. This equation basically states that the rate of change of the liquid mass flow inside the volume is balanced by the changes induced by the flow velocity through the surface area. Knowing that the pressure difference between liquid and gas bubble is described by the Young's equation, an expression for u can be found after manipulating the Euler equation [59, 60]. The models in the literature were derived only for dry and stable foams. In reality, however, foam bubbles grow, break and coalesce into larger sizes. Those models fail to comprise the coalescence of bubbles. Combining coalescence with drainage model is challenging because the factors causing foam's instability are not clear yet. The most convincing factor so far is the hydrophobic force in foam films. In many experiments on foam films drainage, it has been shown that foam films thin faster than the prediction by the Reynolds lubrication equation and it was ascribed to the hydrophobic force [61, 62]. Thin water films tend to rupture at different thicknesses for different surfactant concentrations or certain chemical conditions. This particular thickness is termed as critical rupture thickness h_{cr}. The film thinning rate down to h_{cr} in those systems is well predictable with the help of the extended DLVO theory [62], but a good theory to predict the approximate time of rupture or corresponding rupture thickness is still missing. Majority of researchers on film rupture models think that the rupture results from capillary waves due to the forces at the water-air interface [63-65], but those models also deviate from actual observations when hydrophobic force is influential [61, 66].

4. Dissertation Outline

The results of the present work are presented in five chapters in the same order as listed under Research Objectives.

Chapter 1 gives an overview and justification of the present research along with literature review.

Chapter 2 presents the model developed in the present work. The model consists of two parts, including i) the model describing the bubble-particle attachment and detachment processes occurring in the pulp phase of a flotation cell and ii) the transport of resulting bubble-particle aggregates and entrained particles through the froth phase.

Chapter 3 shows i) the effects of chemical and hydrodynamic parameters affecting flotation, and ii) the role of surface forces affecting the kinetics of bubble-particle attachment by conducing induction time measurements.

Chapter 4 describes a foam drainage model derived from first principles. The model can predict bubble coarsening as functions of the hydrophobic force parameter (K_{232}), which in turn is a function of surfactant (frother) additions.

Chapter 5 gives a theoretical model that can predict the critical rupture thickness of free foam films.

Chapter 6 presents derivation of thefroth recovery model that is used in Chapter 1.

Chapter 7 suggests possible future work in developing a comprehensive flotation model.

All of the chapters have been written in journal paper formats for publications with appropriate amendments in the near future.

5. References

1. Gaudin, A.M., *Flotation*. 1957: McGraw Hill.
2. Laskowski, J., ed. *The relationship between floatability and hydrophobicity*. Advances in Mineral Processing, ed. P. Somasundaran. 1986, SME publication.
3. Saffman, P.G.a.T., J.S., *On the collision of drops in turbulent coluds.* Journal of Fluid Mechanics, 1956. **1**: p. 16-30.
4. Abrahamson, J., *Collision rates of small particles in a vigorously turbulent fluid.* Chemical Engineering Science, 1975. **30**(11): p. 1371-1379.
5. Levins, D.M. and J.R. Glastonbury, *Particle-liquid hydrodynamics and mass transfer in a stirred vessel.* Chemical Engineering Research and Design, 1972. **50A**: p. 32-41.
6. Kruis, F.E. and K.A. Kusters, *The collision rate of particles in turbulent flow.* Chemical Engineering Communications, 1997. **158**: p. 201-230.

7. Bloom, F. and T.J. Heindel, *On the structure of collision and detachment frequencies in flotation models.* Chemical Engineering Science, 2002. **57**(13): p. 2467-2473.
8. Camp, P.R. and P.C. Stein, *Velocity gradients and internal work in fluid motion.* Journal of the Boston Society of Civil Engineers, 1943. **30**(4): p. 219-237.
9. Pyke, B., D. Fornasiero, and J. Ralston, *Bubble particle heterocoagulation under turbulent conditions.* Journal of Colloid and Interface Science, 2003. **265**(1): p. 141-151.
10. Weber, M.E. and D. Paddock, *Interceptional and gravitational collision efficiencies for single collectors at intermediate Reynolds numbers.* Journal of Colloid and Interface Science, 1983. **94**(2): p. 328-335.
11. Luttrell, G.H. and R.-H. Yoon, *A hydrodynamic model for bubble-particle attachment.* Journal of Colloid and Interface Science, 1992. **154**(1): p. 129-137.
12. Finch, J.A. and G.S. Dobby, *Column flotation*. 1990: Pergamon press.
13. Sutherland, K.L., *Physical Chemistry of Flotation. XI. Kinetics of the Flotation Process.* The Journal of Physical and Colloid Chemistry, 1948. **52**(2): p. 394-425.
14. Derjaguin, B.V. and S.S. Dukhin, *Theory of flotation of small and medium-size particles.* Transactions of Institutions of Mining and Metallurgy, 1961. **70**: p. 221-246.
15. Yoon, R.-H. and L. Mao, *Application of Extended DLVO Theory, IV: Derivation of Flotation Rate Equation from First Principles.* Journal of Colloid and Interface Science, 1996. **181**(2): p. 613-626.
16. Sherrell, I. and R.-H. Yoon. *Development of a turbulent flotation model*. in *Centenary of flotation symposium*. 2005. Barisbane, Australia.
17. Smoluchowski, M., *Mathematical theory of the kinetics of the coagulation of colloidal particle.* Z. phys. Chem, 1917. **92**: p. 129.
18. Kelsall, D.F., *Application of probability assessment of flotation systems.* Transactions of Institutions of Mining and Metallurgy, 1961. **70**(3): p. 191.
19. Arbiter, N. and C.C. Harris, *Flotation kinetics*, in *Froth Flotation 50th Anniversary Volume*, D.W. Fuerstenau, Editor. 1962, AIME. p. 215-246.
20. Tomlinson, H.S. and M.B. Flemming, *Flotation rate studies*, in *6th International Mineral Processing Congress*. 1963. p. 563.
21. Sherrell, I., *Development of a flotation rate equation from first principles under turbulent flow conditions*, in *Mining and Minerals Engineering*. 2004, Virginia Tech: Blacksburg.
22. Ralston, J., S.S. Dukhin, and N.A. Mishchuk, *Inertial hydrodynamic particle-bubble interaction in flotation.* International Journal of Mineral Processing, 1999. **56**(1-4): p. 207-256.
23. Kolmogorov, A.N., *Dissipation of energy in locally isotropic turbulence (in russian).* Dokl. Alad. Nauk SSSR, 1941. **32**: p. 19-21.
24. Taylor, G.I., *Statistical theory of turbulence: Parts I-III.* Proceedings of Royal Society, Series A, 1935. **151**: p. 421-464.
25. Schubert, H., *On the turbulence-controlled microprocesses in flotation machines.* International Journal of Mineral Processing, 1999. **56**(1-4): p. 257-276.
26. Liepe, F. and H.O. Moeckel, *Untersuchungen zum Stoffvereinigen in Flüssiger Phase.* Chemical Technology, 1976. **28**.
27. Brady, M.R., et al., *Evaluation of multiphase flotation models in grid turbulence via Particle Image Velocimetry.* International Journal of Mineral Processing, 2006. **80**(2-4): p. 133-143.

28. Lu, S., Y. Ding, and J. Guo, *Kinetics of fine particle aggregation in turbulence.* Advances in Colloid and Interface Science, 1998. **78**(3): p. 197-235.
29. Okamoto, Y., M. Nishikawa, and K. Hashimoto, *Energy dissipation rate distribution in mixing vessels and its effects on liquid-liquid dispersion and solid-liquid mass transfer.* International Chemical Engineering, 1981. **21**(1): p. 88-94.
30. Goren, S.L. and M.E. O'Neill, *On the hydrodynamic resistance to a particle of a dilute suspension when in the neighbourhood of a large obstacle.* Chemical Engineering Science, 1971. **26**(3): p. 325-338.
31. Davis, R.H., J.A. Schonberg, and J.M. Rallison, *The lubrication force between two viscous drops.* Physics of Fluids A: Fluid Dynamics, 1989. **1**(1): p. 77-81.
32. Yoon, R.H., *The role of hydrodynamic and surface forces in bubble-particle interaction.* International Journal of Mineral Processing, 2000. **58**(1-4): p. 129-143.
33. Yoon, R.-H. and S.A. Ravishankar, *Long-Range Hydrophobic Forces between Mica Surfaces in Dodecylammonium Chloride Solutions in the Presence of Dodecanol.* Journal of Colloid and Interface Science, 1996. **179**(2): p. 391-402.
34. Christenson, H.K. and P.M. Claesson, *Cavitation and the Interaction Between Macroscopic Hydrophobic Surfaces.* Science, 1988. **239**(4838): p. 390-392.
35. Stevens, H., et al., *Effects of Degassing on the Long-Range Attractive Force between Hydrophobic Surfaces in Water.* Langmuir, 2005. **21**(14): p. 6399-6405.
36. Yianatos, J.B., et al., *Froth recovery of industrial flotation cells.* Minerals Engineering, 2008. **21**(12-14): p. 817-825.
37. Mathe, Z.T., M.C. Harris, and C.T. O'Connor, *A review of methods to model the froth phase in non-steady state flotation systems.* Minerals Engineering, 2000. **13**(2): p. 127-140.
38. Schumann, R., *Flotation kinetics: I. Moethods for steady state study of flotation problems.* Journal of physical chemistry, 1942. **46**: p. 891-902.
39. Waters, K.E., et al., *Positron emission particle tracking as a method to map the movement of particles in the pulp and froth phases.* Minerals Engineering, 2008. **21**(12-14): p. 877-882.
40. Koh, P.T.L. and M.P. Schwarz, *CFD modelling of bubble-particle collision rates and efficiencies in a flotation cell.* Minerals Engineering, 2003. **16**(11): p. 1055-1059.
41. Koh, P.T.L. and M.P. Schwarz, *CFD modelling of bubble-particle attachments in flotation cells.* Minerals Engineering, 2006. **19**(6-8): p. 619-626.
42. Harris, C.C., *Multiphase models of flotation machine behaviour.* International Journal of Mineral Processing, 1978. **5**(2): p. 107-129.
43. Yianatos, J.B., *Fluid Flow and Kinetic Modelling in Flotation Related Processes: Columns and Mechanically Agitated Cells--A Review.* Chemical Engineering Research and Design, 2007. **85**(12): p. 1591-1603.
44. Vera, M.A., J.P. Franzidis, and E.V. Manlapig, *Simultaneous determination of collection zone rate constant and froth zone recovery in a mechanical flotation environment.* Minerals Engineering, 1999. **12**(10): p. 1163-1176.
45. Seaman, D.R., J.P. Franzidis, and E.V. Manlapig, *Bubble load measurement in the pulp zone of industrial flotation machines--a new device for determining the froth recovery of attached particles.* International Journal of Mineral Processing, 2004. **74**(1-4): p. 1-13.
46. Alexander, D.J., J.P. Franzidis, and E.V. Manlapig, *Froth recovery measurement in plant scale flotation cells.* Minerals Engineering, 2003. **16**(11): p. 1197-1203.

47. Duan, J., D. Fornasiero, and J. Ralston, *Calculation of the flotation rate constant of chalcopyrite particles in an ore.* International Journal of Mineral Processing, 2003. **72**(1-4): p. 227-237.
48. Ralston, J., et al. *Flotation rate constant prediction for metal sulfide particles*. in *Centenay of flotation symposium*. 2005. Brisbane, Australia.
49. Craig, V.S.J., B.W. Ninham, and R.M. Pashley, *The effect of electrolytes on bubble coalescence in water.* The Journal of Physical Chemistry, 1993. **97**(39): p. 10192-10197.
50. Gorain, B.K., et al., *The effect of froth residence time on the kinetics of flotation.* Minerals Engineering, 1998. **11**(7): p. 627-638.
51. Mathe, Z.T., et al., *Review of froth modelling in steady state flotation systems.* Minerals Engineering, 1998. **11**(5): p. 397-421.
52. Maachar, A. and G.S. Dobby, *Measurement of feed water recovery and entrainment solids recovery in flotation columns.* Canadian Metallurgical Quarterly, 1992. **31**(3): p. 167-172.
53. Savassi, O.N., et al., *An empirical model for entrainment in industrial flotation plants.* Minerals Engineering, 1998. **11**(3): p. 243-256.
54. Pugh, R.J., *Experimental techniques for studying the structure of foams and froths.* Advances in Colloid and Interface Science, 2005. **114-115**: p. 239-251.
55. Weaire, D. and S. Hutzler, *The physics of foams*. 1999: Oxford university press.
56. Leonard, R.A. and R. Lemlich, *A study of interstitial liquid flow in foam. Part I. Theoretical model and application to foam fractionation.* AIChE Journal, 1965. **11**(1): p. 18-25.
57. Koehler, S.A., S. Hilgenfeldt, and H.A. Stone, *A Generalized View of Foam Drainage: Experiment and Theory.* Langmuir, 2000. **16**(15): p. 6327-6341.
58. Verbist, G., D. Weaire, and A.M. Kraynik, *The foam drainage equation.* Journal of Physics: Condensed Matter, 1996. **8**(21): p. 3715-3731.
59. Gol'dfarb, I.I., K.B. Kann, and I.R. Shreiber, *Liquid flow in foams.* Fluid Dynamics, 1988. **23**(2): p. 244-249.
60. Verbist, G. and D. Weaire, *A Soluble Model for Foam Drainage.* EPL (Europhysics Letters), 1994. **26**(8): p. 631-634.
61. Angarska, J.K., et al., *Detection of the Hydrophobic Surface Force in Foam Films by Measurements of the Critical Thickness of the Film Rupture.* Langmuir, 2004. **20**(5): p. 1799-1806.
62. Wang, L. and R.-H. Yoon, *Hydrophobic forces in thin aqueous films and their role in film thinning.* Colloids and Surfaces A: Physicochemical and Engineering Aspects, 2005. **263**(1-3): p. 267-274.
63. Vrij, A., *Possible mechanism for the spontaneous rupture of thin, free liquid films.* Discussions of Faraday Society, 1966. **42**: p. 23-33.
64. Ruckenstein, E. and R.K. Jain, *Spontaneous rupture of thin liquid films.* Journal of Chemical Society, Faraday Transactions 2, 1974. **70**: p. 132-147.
65. Ivanov, I.B., et al., *Theory of the critical thickness of rupture of thin liquid films.* Transactions of Faraday Society, 1970. **66**: p. 1262-1273.
66. Wang, L. and R.-H. Yoon, *Effects of surface forces and film elasticity on foam stability.* International Journal of Mineral Processing, 2008. **85**(4): p. 101-110.

CHAPTER 2

A FLOTATION MODEL UNDER TURBULENT FLOW CONDITIONS

ABSTRACT

Flotation is designed to separate hydrophobic and hydrophilic particles by selectively attaching the former on the surfaces of air bubbles. The process has been modeled by many investigators mostly using parameters affecting the hydrodynamics of bubble-particle interactions occurring in the pulp phase of a flotation cell, while the efficiency of the process is critically affected by various chemical parameters, particularly the hydrophobicity of particles. In a previous work, the effect of particle hydrophobicity was incorporated into a flotation model using the DLVO theory extended to include the contributions from hydrophobic force. However, the model was applicable only for the bubble-particle interactions occurring under laminar flow conditions without consideration of the separation processes occurring in the froth phase formed on top of the pulp phase. In the present communication, a comprehensive flotation model has been developed to describe the events occurring both in the pulp and froth phases of a flotation cell operating under turbulent flow conditions. The model predictions are consistent with typical industrial mineral flotation results reported in the literature.

1. INTRODUCTION

Froth flotation is an important separation process that is widely used in the minerals, coal, oil, recycling, and environmental industries. It is designed to separate hydrophobic particles from hydrophilic ones by selectively attaching the former to the surface of rising stream of air bubbles in aqueous media (pulp), leaving the latter behind. The air bubbles carrying the hydrophobic particles form a froth (three-phase foam) phase, in which some of the particles drop back to the pulp phase due to bubble coarsening and drainage. The parameters affecting the process may be divided into hydrodynamic (*e.g.*, bubble size, particle size, turbulence, energy dissipation) and chemical parameters (*e.g.*, hydrophobicity, surface tension, ζ-potentials). Most of the models derived until recently incorporated only the hydrodynamic parameters, which made it impossible to predict the efficiency of separation. In general, hydrodynamic parameters affect recovery, while chemical parameters control both recovery and separation efficiency.

The first theory of modeling flotation was developed by Sutherland [1] based on Gaudin's hypothesis [2, 3]. The theory described the process as dependent on the probabilities of bubble-particle collision, attachment and detachment occurring under the environment of inviscid fluid. Some models also took similar approach with more detailed considerations in the interpretation of bubble-particle attachment. For example, Derjaguin and Dukhin [4] considered interfacial forces in determining the flotation rate of fine particles settling onto a rising bubble in a quiescent flow. As interests extended to the aggregation of larger particles, the hydrodynamic effect of particle inertia was also incorporated with flotation kinetics by other researchers [5-8]. Finch and Dobby [7] developed their flotation model using Weber and Paddock's theory on collection efficiency [6], where only hydrodynamic effect of small stokes number particles and intermediate Reynolds number flow was investigated. The bubble-particle attachment efficiency was determined by the induction time (the time required for film rupture) and particle's sliding time on bubble surface.

While Finch and Dobby [7] modeled flotation kinetics in hydrodynamics' aspects only, Yoon and Mao [9] derived a first-order flotation rate equation using both the hydrodynamic and chemical parameters. The model estimated kinetic energies of particles using the empirical flow streamline around a bubble derived for intermediate Reynolds numbers by Yoon and Luttrell [8]. In an attempt to derive the model from first principles, the model was limited to describing frothless flotation under laminar flow conditions. On the other hand, most of the industrial flotation machines operate under turbulent flow conditions, and the froth phase plays a critical role in determining the efficiency of hydrophobic and hydrophilic separation and also the recovery, particularly that of coarse particles.

In flotation, turbulence plays an important role. It is used to disperse air in water, induce bubble-particle collision, keep solid particles in suspension, and to transport the suspension from one flotation cell to another. Recently, Pyke *et al*. [10] derived a flotation model for such environment. Their model was in essence the extended version of Ralston *et al*.[11]'s flotation model to turbulent flow conditions. In the latter, the authors used the BBO equation to describe the particle moving along the streamline around a bubble. The collision efficiency and attachment efficiency were calculated based on the induction time and the angle of bubble-particle contact obtained by solving the BBO equation.

On the other hand, Sherrell and Yoon [12] suspected Pyke *et al.'*[10]s approach realizing that flow streamlines may be affected by turbulent flows in the presence of particles of high inertia. Therefore, Sherrell and Yoon [12] extended Yoon and Mao's [9] model to turbulent flow conditions, with the aspect of bubble-particle interaction energies in turbulence. The model, however, showed a result indicating that flotation kinetics is controlled more by bubble-particle detachment, rather than attachment [13]. More recently, Koh and Schwarz [14, 15] applied Yoon and Luttrell [8]'s sub-process probabilities into their flotation model. Aided by a Computational Fluid Dynamics (CFD) program for the first time, they could predict the temporal changes of total particle numbers in a lab-scale cell, which were used to infer the flotation rate constant. Their results showed that froth phase is a significant contributor to the overall recovery.

As well as the models stated above, most of the flotation models [10, 11, 16-18] addressing turbulence used the collision model derived by Abrahamson [19], which was based on the assumption of infinite Stokes number (*i.e.*, bubbles and particles are in random motion independently of fluid flow) and, hence, of hardcore collision. During the process of bubble-particle collision, a particle can approach the surface of an air bubble within the distance range where surface forces can affect the attachment process. Derjaguin and Dukhin [4] were in fact the first to consider the effects of surface forces in flotation. They suggested that during the course of bubble-particle interaction, a particle passes through three successive zones, *i.e.*, hydrodynamic, diffusio-phoretic and wetting zones. As the particle reaches the wetting zone, it would experience three surface forces, namely, electrostatic, van der Waals dispersion, and *structural* forces. The structural force was considered hydrophilic, which was considered repulsive but becomes zero when bubble-particle adhesion is to occur. In a later publication, Derjaguin and Dukhin [20] suggested that the bubble-particle adhesion can occur without penetrating the wetting film, a process referred to as 'contactless flotation'.

Mika and Fuerstenau [21] developed a detailed flotation model by considering various sub-processes, including collision, attachment and detachment. These authors considered that the attachment sub-process is controlled by the double-layer and dispersion forces, and that the wetting film is thinned by turbulent force. They also noted that the diffusiophoretic phenomena suggested by Derjaguin and Dukhin [4] cannot be justified when the essentially turbulent character of the fluid in the neighborhood of the bubble is recognized.

It is interesting to note here that all of the surface forces by Derjagiun and Dukhin [4, 20] and Mika and Fuerstenau [21] are repulsive under typical flotation conditions. It is likely that electrostatic forces are repulsive as both bubbles and particles are often negatively charged particularly in alkaline solutions. Knowing that the van der Waals dispersion forces are also repulsive in bubble-particle interactions, as are the hydrophilic structural (or hydration) forces, it is difficult to explain the process of bubble-particle attachment. It was probably these reasons that Derjagiun and Dukhin suggested the concept of contactless flotation, which means that bubble-particle attachment can occur without forming a three-phase contact. This mechanism may provide an explanation for the flotation of submicron particles but not for the flotation of larger particles that are commonly processed in the minerals and coal industries. If the wetting film between bubble and particle does not rupture, the energy of holding a particle onto the surface of a bubble, which is proportional to the area of the three-phase contact, becomes too

weak to withstand the turbulence created in an industrial flotation machine. Furthermore, the repulsive surface forces will create a large energy barrier, which should cause the process to be slow. In colloid chemistry, coagulation is considered to be 'slow' or 'fast' depending on the presence or absence of energy barrier, respectively [22-24]. In flotation, the bubble-particle adhesion is a fast process, with the wetting films rupturing within the time frame of tens of milliseconds or less [25, 26].

Israelachvili and Pashley's work [27] on surface force measurements may shed a light to the dilemma in explaining flotation, that is, the bubble-particle adhesion is fast despite the high energy barrier. These investigators measured the surface forces between two mica surfaces hydrophobized by cetyltrimethylammounium bromide (CTAB), and discovered a hitherto unknown attractive force that was approximately ten times stronger than the van der Waals force. The follow-up experiments conducted by numerous other investigators also showed the presence of the extraneous force, which was appropriately referred to as hydrophobic force, as described in a recent review paper by Christenson and Claesson [28]. It was shown that the hydrophobic force increases with increasing water contact angle [29, 30]. Other investigators showed, on the other hand, that the long-range attractions measured between hydrophobic surfaces are due to bridging bubbles [31, 32]. In support of this mechanism, Tyrell and Attard [33] and Ishida *et al*. [34] observed nanobubbles on hydrophobic surfaces by means of atomic force microscope (AFM), while Mao *et al*.[35] failed to detect nanobubbles (or vapor cavities) on hydrophobic surfaces by means of ellipsometry. Also, Sakamoto *et al*. [36] showed that the long-range attractions observed with silica surfaces coated with octadecyltrimethyl ammonium chloride (C_{18}TAC) disappeared completely when the force measurements were conducted in degassed solutions. Zhang, *et al.* [37] showed, however, that the measurements conducted under the same conditions showed long-range attractions both in air-saturated and degassed solutions. Meyer *et al.* [38] also observed strong attractive forces between mica surfaces in degassed C_{18}TAC solutions.

The role of the hydrophobic force in flotation may be to reduce the energy barrier for bubble-particle interaction so that flotation can become a fast process. It was shown previously that coagulation of hydrophobic particles requires much less kinetic energy than required to overcome the energy barriers calculated using the DLVO theory [39-41]. In relating the kinetic energy of bubble-particle collision to the energy barrier, it is important to consider the hydrodynamic resistance to film thinning, which causes deceleration of the particles approaching bubbles in close proximity [9, 42, 43].

It was the objective of the proposed work to derive a turbulent flotation model using both hydrodynamic and chemical parameters based on the concepts presented above. The model describes the events occurring in the pulp phase and froth phase separately. The model predictions are compared with the general trends reported in the literature with regards to the effects of particle size, bubble size, energy input, particle hydrophobicity, surface tension, and the ζ-potentials of particles and bubbles, all of which are recognized as important parameters affecting flotation.

2. MODEL

2.1 Collision Frequency

The process of flotation commences with bubble-particle collision, followed by adhesion. Camp and Stein [44] were the first to derive a collision model under turbulent flow consitions,

$$Z_{12} = \frac{4}{3} N_1 N_2 d_{12}^3 \sqrt{\frac{\varepsilon}{\nu}} \tag{1}$$

where Z_{12} is the collision frequency between particles 1 and 2, N_1 and N_2 are the number densities of particles, d_{12} (= r_1 + r_2) is the collision radius with r_1 and r_2 being the radii of the particles, ε the energy dissipation rate, and ν is the kinematic viscosity of the medium. Eq. (1) is of the same form as Smoluchowski's model [24] which was derived for collision under laminar flow conditions. The model derived by Saffman and Turner [45] was the same as Eq. (1) with a slightly different constant, *i.e.*, $\sqrt{8\pi/15}$ rather than 4/3. These models are applicable for small particles that follow fluid flow, which makes it difficult to be used for modeling flotation involving coarse particles.

Abrahamson [19] derived a turbulent collision model based on the assumption that particle velocities are independent of fluid flow. The simplest form of his model is given by

$$Z_{12} = 2^{3/2} \pi^{1/2} N_1 N_2 d_{12}^2 \sqrt{\bar{u}_1{}^2 + \bar{u}_2{}^2} \tag{2}$$

where $\sqrt{\overline{U_1^2}}$ and $\sqrt{\overline{U_2^2}}$ represent the root-mean-square (RMS) velocity fluctuations of the particles 1 and 2, respectively. Eq. (2) was derived with an infinite Stokes number, which makes it applicable for large particles. For small particles, however, an appropriate correction may be necessary.

2.2 Flotation Kinetics

Eq. (2) can be used as a basis for writing a second-order flotation rate equation as follows,

$$\frac{dN_1}{dt} = -Z_{12} P \tag{3}$$

where P is the probability of flotation, which may be considered a product of collision (P_c), adhesion (P_a) and detachment (P_d) probabilities [1]:

$$P = P_c P_a (1 - P_d) \tag{4}$$

Use of Eq. (4) for a flotation model presumes that bubble-particle aggregates formed in the pulp phase enter the froth phase automatically, which is unlikely.

When a bubble-particle aggregate rises in a flotation pulp, it will encounter the froth-pulp interface and may break up depending on the hydrodynamic conditions at the interface. Thus, it

would be necessary to consider the probability of bubble-particle aggregates successfully entering the froth phase (P_f). Therefore, Eq. (4) may be rewritten as follows,

$$P = P_c P_a (1 - P_d) P_f \tag{5}$$

as suggested by Schumann [46] and Tomlinson and Flemming [47].

Substituting Eqs. (2) and (5) into Eq. (3), one obtains,

$$\frac{dN_1}{dt} = -2^{3/2}\pi^{1/2} N_1 N_2 (r_1 + r_2)^2 \sqrt{\bar{u}_1{}^2 + \bar{u}_2{}^2} P_c P_a (1 - P_d) P_f \tag{6}$$

which is a second-order rate equation with respect to N_1 and N_2. If $N_2 >> N_1$ or N_2 remains constant during flotation, one can write a pseudo-first-order flotation rate equation as follows:

$$\frac{dN_1}{dt} = -k_p N_1 \tag{7}$$

where

$$k_p = 2^{3/2}\pi^{1/2} N_2 (r_1 + r_2)^2 \sqrt{\bar{u}_1{}^2 + \bar{u}_2{}^2} P_c P_a (1 - P_d) P_f \tag{8}$$

In the present work, the particle RMS velocities were calculated using the following empirical relation [18, 48]:

$$\sqrt{\bar{u}_1{}^2} = 0.4 \frac{\varepsilon^{4/9} d_1^{7/9}}{\nu^{1/3}} \left(\frac{\rho_1 - \rho_3}{\rho_3}\right)^{2/3} \tag{9}$$

in which ε is energy dissipation rate, d_1 particle diameter, ν kinematic viscosity, ρ_1 particle density, and ρ_3 is water density. Recently, Brady *et al*. [49] measured particle velocities using a digital particle image velocimetry (PIV) technique and compared the results with those calculated using Eq. (9). For 80 μm particles under grid turbulence, the errors were within 12%.

On the other hand, the mean squared velocity of bubbles, $\bar{u}_2{}^2$, were calculated using the following relationship [50]:

$$\bar{u}_2{}^2 = C_0 (\varepsilon d_2)^{2/3} \tag{10}$$

where d_2 is bubble diameter and C_0 (=2) is a constant.

2.3. Probabilities of Attachment and Detachment

In the flotation model developed by Yoon and Mao [9] for laminar flow conditions, the probability of attachment, P_a, was considered to be a function of the energy barrier (E_1) for bubble-particle attachment and the kinetic energy of attachment (E_k) as follows,

$$P_a = \exp\left(-E_1/E_k\right) \quad (11)$$

while P_d is a function of E_1, work of adhesion (W_a), and the kinetic energy of detachment (E'_k) as follows:

$$P_d = \exp\left(-(W_a + E_1)/E'_k\right) \quad (12)$$

It was shown that [9]

$$W_a = \gamma_{lv}\pi r_1^2(1-\cos\theta)^2 \quad (13)$$

where γ_{lv} is the surface tension of water and θ is the water contact angle of the particle with radius r_1.

Eq. (11) is analogous to the Arrhenius equation for chemical kinetics and to coagulation models for colloidal particles. Derjaguin *et al*. [51] derived an expression for coagulation efficiency, which is an exponential function of $-E_1/k_bT$, where the denominator represents the kinetic energy due to thermal motion. For the heterocoagulation of macroscopic particles, *i.e*., between bubbles and particles in flotation, it would be appropriate to substitute the k_bT with the kinetic energies (E_k) due to hydrodynamic interactions. The use of Eq. (11) implicitly recognizes that bubbles and particles in a flotation cell have distributed kinetic energies.

The approach taken in this communication to determining P_a is distinguished from that of Ralston *et al.* [17, 52] who used induction time rather than E_1. In their approach, it is assumed that bubble-particle attachment occurs when the sliding time of a particle on the surface of a bubble is longer than the induction time. The induction time, which is defined as the minimum time required for bubble-particle attachment, is usually determined experimentally, although a predictive model is available [53, 54].

2.4. Energy Barrier

In the present work, the energy barrier (E_1) has been determined using the extended DLVO theory,

$$V = V_E + V_D + V_H \quad (14)$$

where V is the free energy of interaction between bubble and particle, V_E the contribution from electrostatic interaction, V_D the same from van der Waals-dispersion interaction, and V_H is from hydrophobic interaction. Under most flotation conditions particularly at alkaline pH, both V_E and V_D are repulsive, while V_H is attractive as shown in Fig. 1.

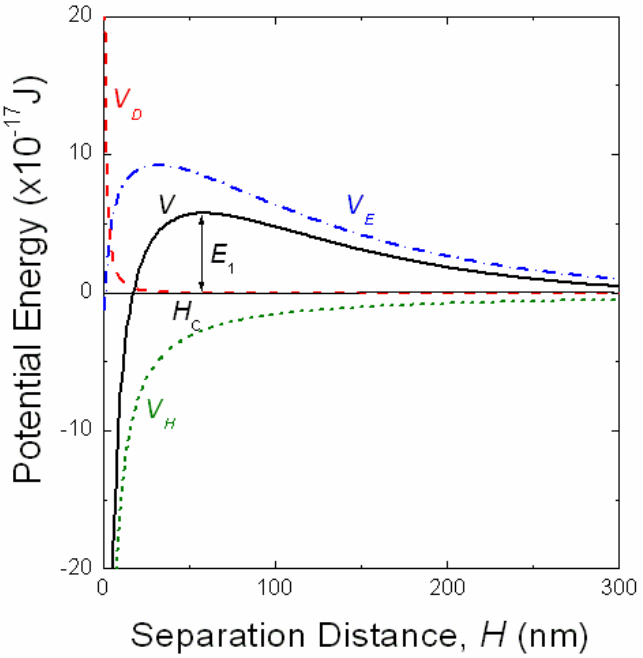

Fig.1. A plot of Eq. (14) with Ψ_1 = -63.9 mV, Ψ_1 = -32.8 mV, A_{132} = -7.08 x10^{-20} J, K_{132} = 4.14 x10^{19} J, r_1 = 0.05mm, r_2 = 0.5 m. E_1 represents the energy barrier for bubble particle attachment and H_c is the critical rupture thickness of the wetting film.

The electrostatic interaction energy (V_E) can be calculated using the model derived by Hogg, Healey and Fuerstenau [55],

$$V_E = \frac{\pi\epsilon_0\epsilon r_1 r_2(\Psi_1^2+\Psi_2^2)}{(r_1+r_2)}\left[\frac{\Psi_1^2\Psi_2^2}{\Psi_1^2+\Psi_2^2}\ln\left(\frac{1+e^{-\kappa H}}{1-e^{-\kappa H}}\right)+\ln(1+e^{-2\kappa H})\right] \quad (15)$$

where ϵ_0 is the permittivity in vacuum, ϵ the dielectric constant of the medium, Ψ_1 and Ψ_2 are the double layer potentials for particle and bubble, respectively, κ the inverse Debye length, and H is the closest separation distance between particle and bubble. As an approximation, Ψ_1 and Ψ_2 may be substituted by ζ–potentials.

The dispersion interaction energy can be calculated using the following relation [56],

$$V_D = -\frac{A_{132}r_1r_2}{6H(r_1+r_2)}\left[1-\frac{1+2bl}{1+bc/H}\right] \quad (16)$$

where A_{132} is the Hamaker constant for the interaction between particle **1** and bubble **2** in a medium **3**. The second term of Eq. (16) is a correction factor for the retardation effect, where b (= 3x10^{-17} s for most materials) is a parameter characterizing materials of interacting particles, l (= 3.3x10^{15} s^{-1} for water) is a parameter characterizing the medium, and c is the speed of light [9].

The hydrophobic interaction energy (V_H) between bubble and particle may be calculated using the following equation [9]

$$V_H = -\frac{r_1 r_2 K_{132}}{6(r_1+r_2)H} \tag{17}$$

which is of the same form as Eq. (16). The hydrophobic interaction constant, K_{132}, can be obtained using the combining law [57]:

$$K_{132} = \sqrt{K_{131}K_{232}} \tag{18}$$

in which K_{131} and K_{232} represent the hydrophobic force constant between two particles **1** and the bubbles **2** in a medium **3**, respectively.

Many investigators showed that the long-range attractive force between two hydrophobic surfaces increases with increasing hydrophobicity. Pazhianur and Yoon [29] showed that K_{131} increases with increasing water contact angle (θ), a measure of hydrophobicity. The log K_{131} vs. θ plots given by these investigators may be used to obtain the values of the hydrophobic force constants from the contact angles that can be readily measured in experiment. The plot shows three different regions of contact angles, in which one can obtain the value of K_{131} from θ using the following relation:

$$K_{131} = ae^{b_k\theta} \tag{19}$$

in which a and b_k are fitting parameters whose values are: a = 2.732x10^{-21} and b_k = 0.04136 at θ < 86.89°; a = 4.888x10^{-44}, b_k = 0.6441 at 86.89° < θ < 92.28°; and a = 6.327x10^{-27}, b_k = 0.2172 at θ > 92.28°.

The values of K_{131} obtained using Eq. (19) were then combined with the value of K_{232} = 2.5x10^{-18}, representing the hydrophobic force constant of the bubble-bubble interactions occurring in the absence of surfactant, to obtain the value of K_{132} using Eq. (18). It was shown previously that K_{232} decreases with increasing concentration of surfactants (cationic, anionic, and non-ionic)[58, 59].

2.5 Kinetic Energy for Attachment

To calculate P_a using Eq. (11), it is necessary to know the kinetic energy, E_k, of the particles colliding with bubbles. The kinetic energy may be calculated using the following equation,

$$E_k = 0.5m_1\bar{u}_1{}^2 \tag{20}$$

where m_1 is particle mass, $\bar{u}_1{}^2$ is the mean-square velocity of the particle relative to fluids that can be obtained from Eq. (9). As a particle approaches a bubble, the distance (H) separating the

two decreases with time. In time, the particle will reach the critical rupture distance (H_c), where the wetting film ruptures spontaneously to form a three-phase contact line. It is necessary, therefore, to compare E_k with the energy barrier E_1 at H_c, which in turn requires the velocity of the particle at the rupture thickness rather than in the bulk of the solution. According to the Reynolds lubrication theory, a spherical particle of radius r_1 should experience a hydrodynamic resistance force, F_{hyd}, during the approach:

$$F_{hyd} = 6\pi\mu r_1 U\beta \tag{21}$$

where U is the velocity of the sphere at H, μ the viscosity, and β is a drag coefficient in the boundary layer. For a small sphere approaching a large sphere, Goren and O'Neil [60] calculated the values of β numerically, which may be represented by the following relationship found by Luttrell and Yoon [61, 62],

$$\beta = 0.37(r_1/H)^{0.83} \tag{22}$$

By equating the hydrodynamic resistance force ($F_{hyd} = 6\pi\mu r_1 U_H\beta$) at H_c to the Stokes drag force ($F_{drag} = 6\pi\mu r_1\sqrt{\bar{u}_1{}^2}$), one obtains the following relation [61],

$$U_{H_c} = \sqrt{\bar{u}_1{}^2}/\beta \tag{23}$$

which may be used to determine the velocity of the particles (U_{H_c}) colliding with bubbles at H_c. It is this velocity rather than the velocity in the bulk solution that is used to calculate E_k.

2.6 Kinetic Energy for Detachment

It has been suggested that particles are detached from bubbles by the centrifugal force in a vortex rotating in a turbulent flow [63, 64]. The shear rate in a vortex has been given as $\sqrt{\varepsilon/\nu}$ by Camp and Stein [44] (see Eq. (1)). The following equation may thus be used to calculate the kinetic energy for detachment,

$$E'_k = 0.5m_1\left((d_1 + d_2)\sqrt{\varepsilon/\nu}\right)^2 \tag{24}$$

2.7 Energy Dissipation Rate in two different region

Energy dissipation rate plays a critical role in determining the particle and bubble velocities and the detachment kinetic energy, as shown in Eqs. (9), (10) and (24). One could use a mean energy dissipation rate ($\bar{\varepsilon}$), which can be obtained by dividing the power input (W) with the mass (M) of the slurry in a flotation cell, for the values of ε in these equations. It has been shown, however, that the value of ε in the vicinity of an impeller (or a rotor-stator mechanism) is much larger than in the bulk of a flotation pulp [10, 65, 66]. Therefore, it would be more realistic to subdivide the volume of a flotation cell into two different zones, *i.e.*, one near an impeller where bubbles are generated (bubble generation zone), and the other away from it where bubbles

and particles may interact with each other (collection zone). One can then use the following relation,

$$\bar{\varepsilon} = \frac{W}{M}(f_b\varphi_b + f_c\varphi_c) = f_b\varepsilon_b + f_c\varepsilon_c \tag{25}$$

where φ_b and φ_c are the multiplication factors representing the intensity of agitation in the bubble generation and collection zone, respectively; f_b and f_c are the respective volume fractions; and ε_b and ε_c are the dissipation rates. In the present work, it is assumed that φ_b=15, φ_c=0.5, and the corresponding volume fractions are: f_b=0.035 and f_c=0.965.

It has been assumed that bubble-particle attachment is controlled by ε_c, bubble-particle detachment by $\bar{\varepsilon}$, and bubble generation by ε_b. In the present work, the bubble generation model

$$d_2 = \left(\frac{2.11\gamma_{lv}}{\rho_3\varepsilon_b^{0.66}}\right)^{0.6} \tag{26}$$

reported by Schulze [64] was used. According to this model, bubble size decreases approximately as $\varepsilon_b^{-0.4}$ and $\gamma_{lv}^{0.6}$.

2.8 Probability of Collision

The Abrahamson's collision model (Eq. (2)) was derived with an assumption of infinitely large Stokes number. Therefore, bubbles and particles move independently of fluid flow, in which case collision probability (P_c) should be unity. This may be the case with particles larger than approximately 100 μm at energy dissipation rates in the order usually found in pumping fluids in industry [19]. Much of the particles subjected to flotation are finer than 100 μm, and the energy dissipation rates in the collection zones are substantially lower. Therefore, it would be necessary to consider that P_c<1 for small particles, which may be regarded a correction for of Eq. (2). Indeed, the numerical simulations carried out by Sundaram and Collins [67] showed that the Abrahamson's model is not applicable at Stokes numbers below approximately 15.

In the present work, the collision efficiency model derived by Webber and Paddock [6, 61] was used,

$$P_c = \frac{3}{2}\left(\frac{d_1}{d_2}\right)^2\left[1 + \frac{\frac{3}{16}Re}{1+0.249Re^{0.56}}\right] \tag{27}$$

in which *Re* is the Reynolds number of the bubble. One problem in using Eq. (25) is that P_c becomes larger than 1 at $d_1/d_2 > 0.1$ and $0 < Re \leq 300$. Therefore, Eq. (27) has been modified as follows,

$$P_c = \tanh^2\left(\sqrt{\frac{3}{2}\left(1 + \frac{\frac{3}{16}Re}{1+0.249Re^{0.56}}\right)}\left(\frac{d_1}{d_2}\right)\right) \tag{28}$$

so that the condition of $P_c < 1$ can be met. Despite the different functional forms involved, Eqs. (27) and (28) give essentially the same values of P_c for smaller particles, as shown in Figure 2.

2.9 Probability of Aggregates Transferring to Froth

As a bubble-particle aggregate is formed, it rises in the pulp phase with a velocity of U_0 and hit the pulp-froth interface. The bubble laden with hydrophobic particles can bounce back to the pulp phase due the elasticity of the bubble. Many investigators observed the phenomenon as free bubbles rise to the air-water or solid-water interfaces [68-73]. Also, the bubble-particle aggregate may break up and lose particles depending on the kinetic energy imparted by the interface onto the aggregate. It is, therefore, necessary to consider the probability (P_f) for the aggregate to successfully enter the froth phase without losing hydrophobic particles, which may be described as follows,

$$P_f = P_i(1 - P_r) \tag{29}$$

where P_i is the probability of the aggregate to be at the interface after bouncing n times, and P_r is the probability of rupture.

If a bubble-particle aggregate bounces n times to a halt, P_i should be $1/n$. Let us assume that the aggregate has a kinetic energy E_{ai} as it approaches the interface initially, and that it is reduced to E_{af} after n bounces. Assuming that the bubble retains its kinetic energy by a factor of

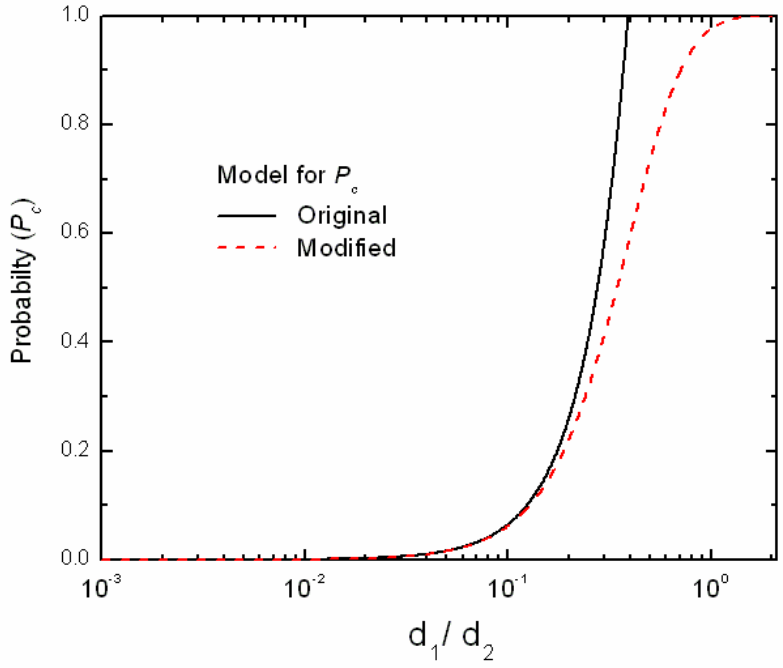

Fig.2. Comparison of Eq.(27) and Eq.(28). Both give the same values of P_c at $d_1/d_2 <$ 0.1, while the latter corrects the over-prediction of the former for larger particles.

α after each bounce, one obtains the following relation,

$$E_{a,f} = \alpha^n E_{a,i} \tag{30}$$

It has been shown that at the air-water interface U_0 decreases by approximately ten-fold after bouncing *n* time, in which case the bubble should retain only 1% of its kinetic energy when it is ready to penetrate the air-water interface [74]. Zenit and Legendre [68] derived an expression for α as follows,

$$\alpha = \exp\left(-60\sqrt{\frac{9\mu^2}{d_2\gamma_{lv}\rho_3}}\right) \tag{31}$$

From Eqs. (30) and (31), one can derive an expression for *n* and hence P_i as follows:

$$P_i = 13\sqrt{\frac{9\mu^2}{d_2\gamma_{lv}\rho_3}} \tag{32}$$

Regarding the probability of aggregate rupture (P_r) at the pulp-froth interface, it is necessary to know the kinetic energy (E_{iw}) imparted by the wave motion at the interface relative to the kinetic energy (E_{ka}) of the bubble-particle aggregate after bouncing *n* times. The former may be considered to be the square of the wave propagation velocity at the smallest wavelength η, *i.e.* the kolmogorov's length scale, while the latter can be estimated form a momentum balance. In the present work, the wave velocity has been estimated assuming fluids above and below the interfacial wave is relatively quiescent in horizontal direction. For the interface formed between two fluids of different densities, *i.e.*, water with a density of ρ_3 at the bottom and the foam with a density of $\rho_f \sim 0.33\rho_3$ on the top, one can readily obtain the following [75],

$$E_{iw} = \left(\sqrt{\frac{g\eta}{2\pi}\left(\frac{\rho_3-\rho_f}{\rho_3+\rho_f}\right)}\right)^2 = \frac{g}{4\pi}\left(\frac{\nu^3}{\varepsilon_b}\right)^{1/4} \tag{33}$$

where g is gravity, and ν is the kinematic viscosity of water.

For a bubble whose surface is 50% covered by hydrophobic particles, one obtains the following relation from a momentum balance:

$$E_{ka} = \frac{\left(m_2\sqrt{\bar{u}_2{}^2} - 2\left(\frac{d_2}{d_1}\right)^2 m_1\sqrt{\bar{u}_1{}^2}\right)^2}{10^2\left(m_2+2\left(\frac{d_2}{d_1}\right)^2 m_1\right)^2} \tag{34}$$

where m_2 is the bubble mass, m_1 is particle mass. In the present work, the RMS velocities have been determined using the energy dissipation rates in the collection zone. Also, it has been assumed that a bubble-particle aggregate loses its kinetic energy by a factor 10^2 after *n* bounces at the froth-pulp interface. Note here that the $2(d_2/d_1)^2$ term of Eq. (34) represents the number

of particles adhering on the surface of the bubble of diameter d_2. Note also that E_{iw} and E_{ka} have been normalized by mass.

Conceptually, the probability of bubble-particle aggregate penetrating the pulp-froth interface (P_r) should increase as the ratio between E_{iw} and E_{ka} decreases. Thus, it is assumed that,

$$P_r = exp\left(-\frac{E_{iw}}{E_{ka}}\right) \tag{35}$$

Substituting Eqs. (32) and (35) into Eq. (29), one can determine the probability of bubble-particle aggregates entering the froth phase without losing particles.

3. NUMERICAL SIMULATION

Simulations were run to show the effect of different variables on the flotation rate constant. The variables studied were: the particle diameter (d_1), bubble diameter (d_2), surface tension (γ_{lv}), contact angle (θ), zeta potentials of particles (ζ_1) and of bubbles (ζ_2), and mean energy dissipation rate ($\bar{\varepsilon}$).

Unless otherwise stated, the values of the different parameters used for the simulations were as follows: $\bar{\varepsilon}$ = 2.0 W/kg (=2.5kW/m^3 as the specific energy input), ζ_1 = -15 mV, ζ_2 = -30 mV, γ_{lv} = 68.0 mN/m. The specific gravity (SG) of the particle was 4.1 (chalcopyrite). The pulp density of the flotation pulp was 20% by weight, and the air hold-up was 20% by volume. It was assumed also that the water contact angle (θ) of the floatable particles is 60^o, from which one obtains the value of K_{131} = 3.27x10^{-20} J using Eq. (19).

The Hamaker constants used in the present work were 3.0x10^{-19} J for chalcopyrite, 0 for air, and 4.38x10^{-20} J for water, from which the value of A_{132} = -7.13x10^{-20} J was obtained using the geometric mean combining law. Substituting the value of A_{132} obtained in this manner to Eq. (16), one can calculate the repulsive dispersion interaction energy (V_D) for bubble-particle interaction. The electrostatic interaction energy (V_E) was calculated using Eq. (15) using different values of Ψ_1 and Ψ_2 (or ζ_1 and ζ_2) and κ^{-1} = 96 nm. The hydrophobic interaction energy (V_H) was calculated using Eq. (17) with the value of K_{132} = 3.65x10^{-19} J, which was obtained using Eq. (18) from the values of K_{131} = 3.27x10^{-20} J and K_{232} = 4.07x10^{-18} J.

It should be noted here that the flotation rate constants (k_p) predicted from Eq. (8) represent the results of the events occurring in the pulp phase only. On the other hand, the rate constants obtained from experiment include the events occurring both in the pulp and froth phases. One can relate the k predicted from Eq. (8) to flotation recovery from the fraction froth recovery. If the fractional recovery in the pulp and froth phases are R_p and R_f, respectively, the overall fractional recovery (R) should be the product of the two, *i.e.*, $R = R_pR_f$. The recovery for a bank of n flotation cells, the recovery becomes [7, 76],

$$R = 1 - \left(1 - \frac{R_pR_f}{R_pR_f + 1 - R_p}\right)^n \tag{36}$$

For a single flotation cell or a batch flotation cell, R_c is given by[7, 77, 78],

$$R_p = 1 - \left(1 + k_p t\right)^{-1} \tag{37}$$

where t is the retention of the particles in the cell. R_f, on the other hand, has been given by the following relation [79, 80].

$$R_f = \frac{d_{2-0}}{d_{2-f}} exp\left(-N\frac{6h_f}{d_{2-0}}\left(1 - \frac{d_{2-0}}{d_{2-f}}\right)\left(\frac{d_1}{d_{2-0}}\right)^2\right) + R_W exp\left(-0.0325(\frac{\rho_3}{\rho_1} - 1) - 6.3 \times 10^4 d_1\right) \tag{38}$$

where $d_{2\text{-}0}$ and $d_{2\text{-}f}$ are bubble diameters at the bottom and top of a froth phase, respectively, h_f is the height of the froth phase under consideration, N is an adjustable constant, and R_w is the fractional water recovery. Most of the variables in Eq. (38) are input parameters, R_w and $d_{2\text{-}f}$ are obtained *a posteriori* from bubble coarsening and drainage models [79, 80].

Fig. 3-A shows a typical plot of flotation rate constant (k_p) versus particle diameter (d_1) as predicted by Eq. (8). The values of the various model parameters used in the simulation are given in the inset. As shown, k_p reaches a maximum at d_1 of approximately 200 μm, and the plot shows difficulties in floating ultrafine and coarse particles. Note here that the k_p values given in this plot are for pulp phase recovery. Therefore, the k_p values should be higher than those reported from experimental data. Nevertheless, the simulation results are generally in the same range as those reported in the literature. Trahar and Warren[81] reported, for example, the k_p values in the range of 0.2 to 5 min^{-1} for copper flotation, while Ahmed and Jameson [82] reported the k_p in the range of 0.01 to 3 min^{-1} for the flotation of quartz.

Fig. 3-B shows the recovery (R) as a function of particle size with t = 2 minutes and n = 15 and 30. Also shown for comparison are the plant operation data reported by Gaudin *et al*. [83], and Lynch *el al.* [77]. The shapes of the R *vs*. d_1 curves are typical of what has been observed in many flotation plants worldwide. The solid and dashed lines represent model predictions from Eq. (36) using appropriate fitting parameters. As the references from which the experimental data have been extracted do not give information on operational details, the predictions were made for 15-cell bank (dashed line) and 30-cell banks (solid line) with a 4-minute retention time in each cell. The fractional froth recovery (R_f) was adjusted to fit the experimental data. In estimating R_f using Eq. (38), the values of $d_{2\text{-}0}/d_{2\text{-}f}$ = 0.25, R_w = 0.51, N = 2 were used at a superficial gas rate of 2.3cm/s. Both the simulation and experimental data presented in Figure 3-B demonstrate difficulties in floating mineral particles below 10 μm and above 200 μm.

While Figure 3-B shows the recovery data converted from the flotation rate constants, the direct comparison between the data of the flotation rate constants along particle size change and the model is given in Fig.4. Duan *et al*.[84] obtined the overall flotation rate constant of chalcopyrite particles using the size- to-recovery data. Realizing that the data were obtained from

a lab-scale batch cell test, the overall flotation rate constant, *k*, for this comparison was obtained using the following expression [7],

$$k = k_p R_f \tag{39}$$

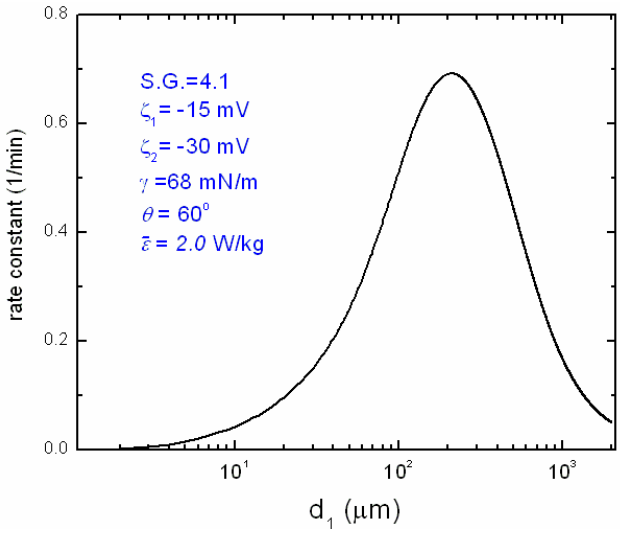

Fig. 3-A. The flotation rate constants (k_p) *vs.* particle size (d_1) as predicted from Eq. (8). It was assumed that the energy dissipation rate in the collection zone was 50% of the mean energy dissipation ($\bar{\varepsilon}$), and the one in the bubble generation zone was 15 times higher than $\bar{\varepsilon}$.

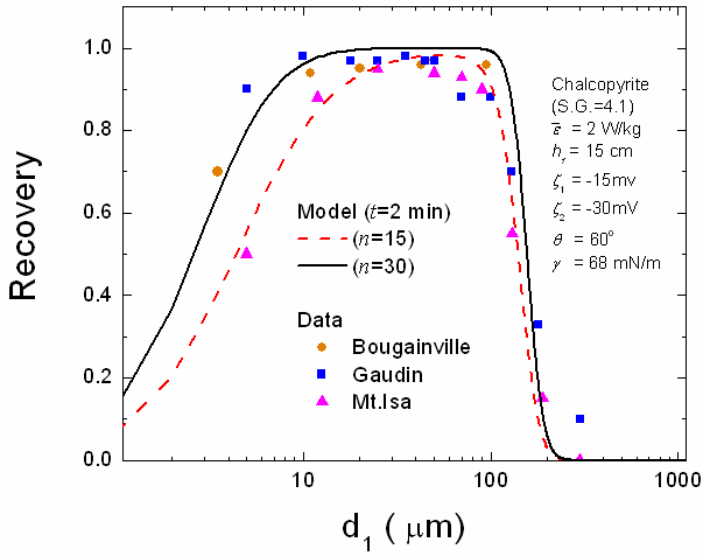

Fig. 3-B. Fractional recovery of chalcopyrite as predicted from Eq. (36) on the basis of the k_p values given in Figure 3-A. The data points represent the size-by-size recoveries obtained at operating plants as reported by Gaudin (1931) and Lynch *et al*. (1981). As these references did not specify the operational details, the predictions were made for fifteen-cell bank (n=15) and thirty-cell banks (n=30) with a 2-minute retention time in each cell.

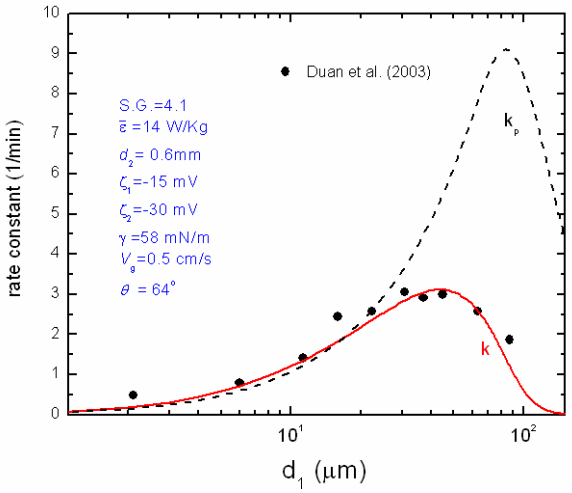

Fig. 4. Comparison of the rate constants predicted using Eq.(8) and Eq.(39) and the experimental data obtained by Duan *et al.*[84] for the flotation of chalcopyrite using a laboratory-scale Rushton flotation cell at the superficial gas rate of 0.5 cm/s.

where k_p and R_f were defined in Eqs.(8) and (38) respectively. In the simulation, all the components were evaluated using the information given in the experimental work, while several unknown parameters had to be assumed. Therefore, the following were used for estimating k : $\bar{\varepsilon}$=14 W/kg, ζ_1=-15mV, ζ_2=-30 mV, γ=58 mN/m, V_g=0.5 cm/s, θ =65°, h_f =2cm, $d_{2\text{-}0}/d_{2\text{-}f}$ = 0.9, R_w = 0.5, N = 3.5. The difference between k and k_p in Fig.4, especially in the range of coarse particle sizes, indicates that coarse particles recovery is hindered in the presence of froth phase.

Fig. 5 shows the effects of the various parameters on the k and R values presented in Figs.

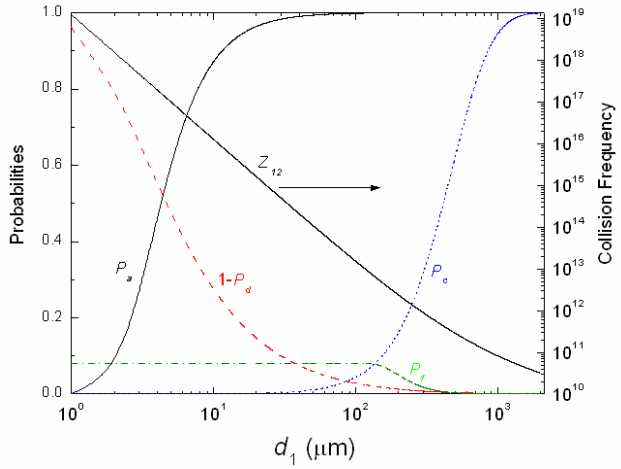

Fig.5. Effect of particle size on collision frequency (Z_{12}), collision efficiency (P_c), probability of adhesion (P_a), probability of detachment (P_d), and probability of particles transferring to froth. The hydrodynamic and surface chemistry parameters are the same as shown in Figure 3.

3-A and -B, respectively. It is shown that collision probability (Z_{12}) which is represented by Eq. (2), increases with decreasing particle size. This is due to the increase in the number density of particles (N_1) with decreasing particle size. Therefore, the changes in Z_{12} alone do not explain the difficulty in floating fine particles. On the other hand, the probability of collision (P_c) decreases sharply with decreasing particle size. Thus, the difficulty in floating fine particles can be attributed to the changes in the product of Z_{12} and P_c, which means that the hard-core collision model of Abrahamson [19] alone is not adequate for modeling flotation. His model is based on the random collision at high Stokes numbers, and ignores the likelyhood that smaller particles follow fluid flow or the stream lines around bubbles. Ralston *et al*, [11, 17] calculated the trajectories of particles around bubbles using the Basset-Boussinesq-Ossen (BBO) equation, and calculated the collision efficiencies. They showed that P_c was less than unity even under potential flow conditions. However, the values of P_c obtained in the present work are much smaller than predicted by Ralston *et al*.

It is shown also that the probability of adhesion (P_a) decreases with decreasing particle size. This can be attributed to the decrease in the kinetic energy (E_k) of the particles colliding with air bubbles. At low E_k, particles would have difficulties in overcoming the energy barriers created by the repulsive double-layer force. Fig. 3 shows also that the probability of the particles not being detached, *i.e.*, (1-P_d), decreases as particle size increases, which is the main reason that coarse particles are difficult to float. At the larger particle sizes, the RMS velocity increases (Eq.

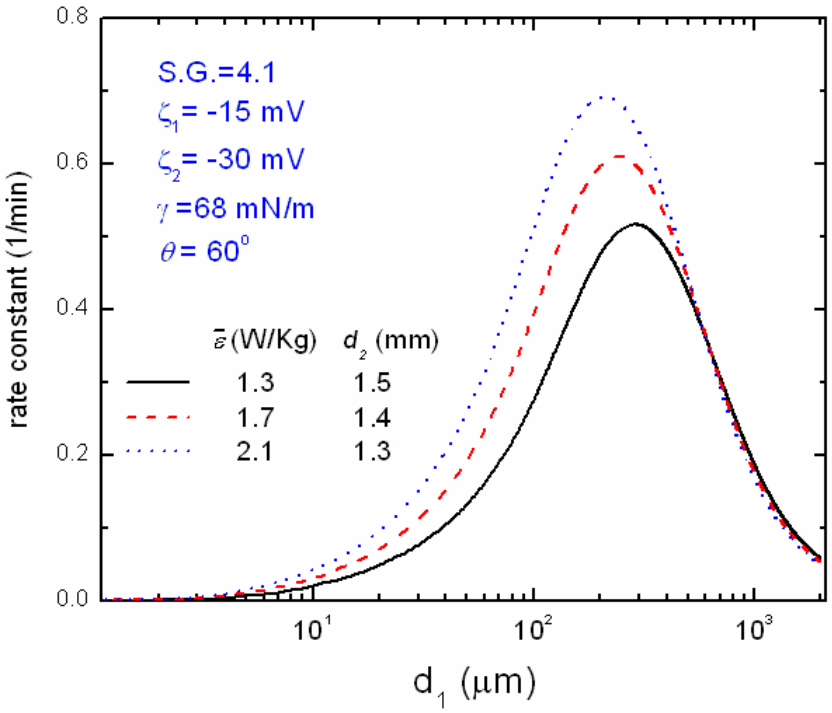

Fig.6. Effect of energy dissipation rate ($\bar{\varepsilon}$) and bubble size (d_2) on flotation rate constant (k). Higher energy dissipations generate smaller bubbles, and they give higher rates at a given particle size (d_1). The optimum particle size for flotation shifts to smaller sizes, indicating that smaller bubbles are beneficial for fine particle flotation.

(9)) and the kinetic energies of detachment (E'_k) increases as square of particle velocity, causing an increase in the probability of detachment (P_d). Also shown in Fig. 5 is the probability (P_f) of aggregates transferring bubble-particle aggregates to froth phase.

As shown in Figure 5, the probabilities of transferring bubble-particle aggregates to froth phase (P_f) are much smaller than those of other sub-processes. They do not change much at particle sizes below approximately 100 μm, but decreases significantly for coarser particles. This finding suggests that the difficulty in floating coarse particles is partly due to the sharp decrease in P_f with increasing particle size above 100 μm. It should be noted, however, that in predicting P_f it was assumed that the velocity of bubble-particle aggregate is reduced by approximately tenfold after n bounces at the pulp-froth interface, which entails a hundredfold decrease in kinetic energy. This assumption was based on the experimental result reported in the literature for free air bubbles with no particles attached [74]. For bubbles coated with hydrophobic particles, however, could have higher inertia and hence higher P_f . Unfortunately, there are no experimental results reported in the literature for bubble-particle aggregates bouncing at the pulp-froth interface. Further work is, therefore, necessary to gather additional information.

Fig. 6 shows the effects of changing the mean energy dissipation rate ($\bar{\varepsilon}$) on flotation rate constant (k) in the pulp phase. The simulation results are plotted versus particle size (d_1). As $\bar{\varepsilon}$ increases, bubble size (d_2) decreases according to Eq. (26) as shown in the inset. The results

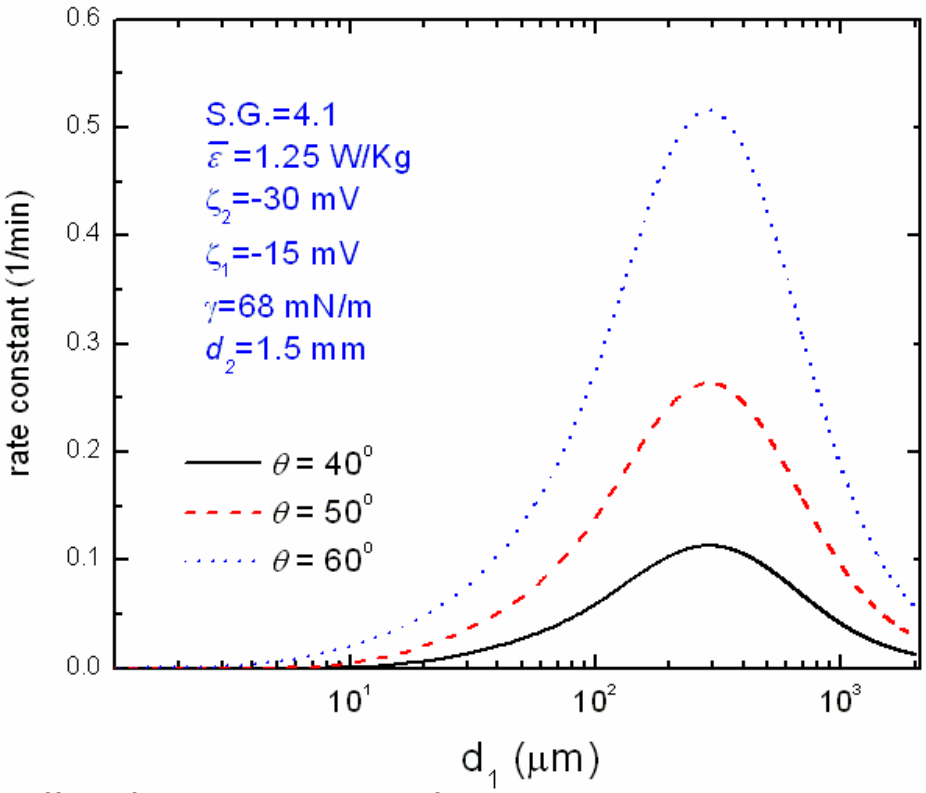

Fig.7. Effect of contact angle (θ) on flotation rate constant (k). An increase in contact angle causes the energy barrier (E_1) to decrease and the work of adhesion (W_a) to increase, both contributing to increased rate constant.

show that as $\bar{\varepsilon}$ increases k increases in general, which can be attributed to the increase in the kinetic energy for attachment (E_k). This finding is in agreement with the work of Ahmed and Jameson [82], who showed that an increase in agitation caused an increase in the rate of flotation of latex particles. Note here that an increase in energy input shifts the k vs. d_1 curves toward the finer particle sizes, which suggests that a higher energy input is helpful for the flotation of finer particles. This observation can be explained by the fact that fine particles do not have sufficient kinetic energies to overcome the energy barrier (E_1), which is one of the main causes for the difficulty in floating fine particles. This problem can be overcome by increasing the specific energy input for flotation. The increase in k with increasing $\bar{\varepsilon}$ may also be attributed to the corresponding decrease in bubble size. However, the changes in bubble size are too small to account for the large decrease in k.

Figs. 7 and 8 show the effects of various surface chemical parameters. The results of varying the contact angle (θ), along with particle size (d_1), have been plotted *vs.* the latter in Fig. 7. As shown, the flotation rate constant (k) increases with increasing particle hydrophobicity. An increase in hydrophobicity should have triple benefits. First, it causes an increase in the work of adhesion (W_a) and, hence, a decrease in the probability of detachment (P_d) as suggested by Eqs. (13) and (12), respectively. Second, an increase in hydrophobicity should increase the hydrophobic force constant (K_{131}), which should in turn reduce the energy barrier (E_1) and, hence, the probability of adhesion (P_a) as suggested by Eq. (11). Third, an increase in hydrophobicity should increase the critical rupture thickness (H_c), which should decrease the

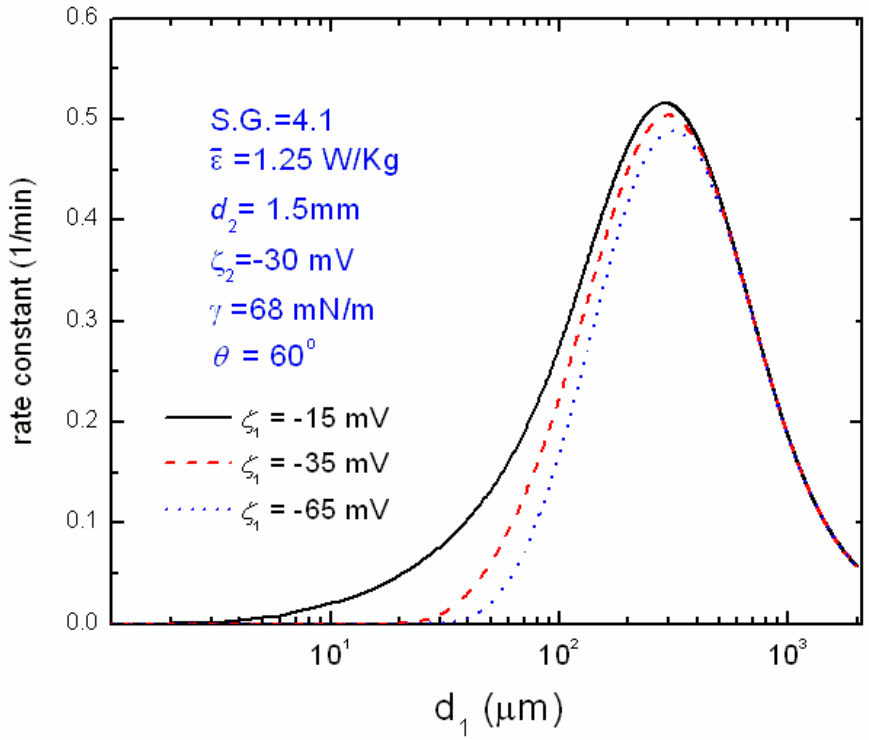

Fig.8. Effect of particle zeta potential (ζ_1) on flotation rate constant (k). k increases with a decrease in the negative zeta-potential of the particles due to a decrease in energy barrier (E_1).

extent of decrease in the particle velocity due the hydrodynamic resistance. This should in turn increase the kinetic energy of attachment (E_k) and, hence, the probability of attachment (P_a) as suggested by Eq. (11).

Fig. 8 shows the simulation results obtained by varying the zeta-potentials (ζ_1) of particles at different particle sizes. The results show that k increases substantially as ζ_1 becomes less negative. Since the zeta-potential of air bubbles is negative, a decrease in the magnitude of the negative zeta-potential of particles should result in a decrease in the electrostatic repulsion between bubble and particle, which should in turn decrease the energy barrier (E_1) and, hence, increase k. This finding is in agreement with the work of many investigators, who showed that flotation recovery is maximum when the magnitude of zeta-potential is minimum [5, 85-89]. A decrease in the negative zeta-potential should also increase in the critical rupture thickness (H_c). At a larger H_c, the velocity of the particle approaching an air bubble becomes larger due to a decrease in the hydrodynamic resistance as discussed in the foregoing paragraph. This should also increase the kinetic energy of attachment (E_k) and, hence, the flotation rate. Thus, some of the beneficial effects of controlling zeta-potentials of bubbles and particles are the same as those obtainable by control of particle hydrophobicity. The benefits of controlling zeta-potentials are more readily discernable at smaller particle sizes. With larger particles, the beneficial effects are overcome by the larger detachment probabilities (P_d) and lower probabilities of pulp-to-froth

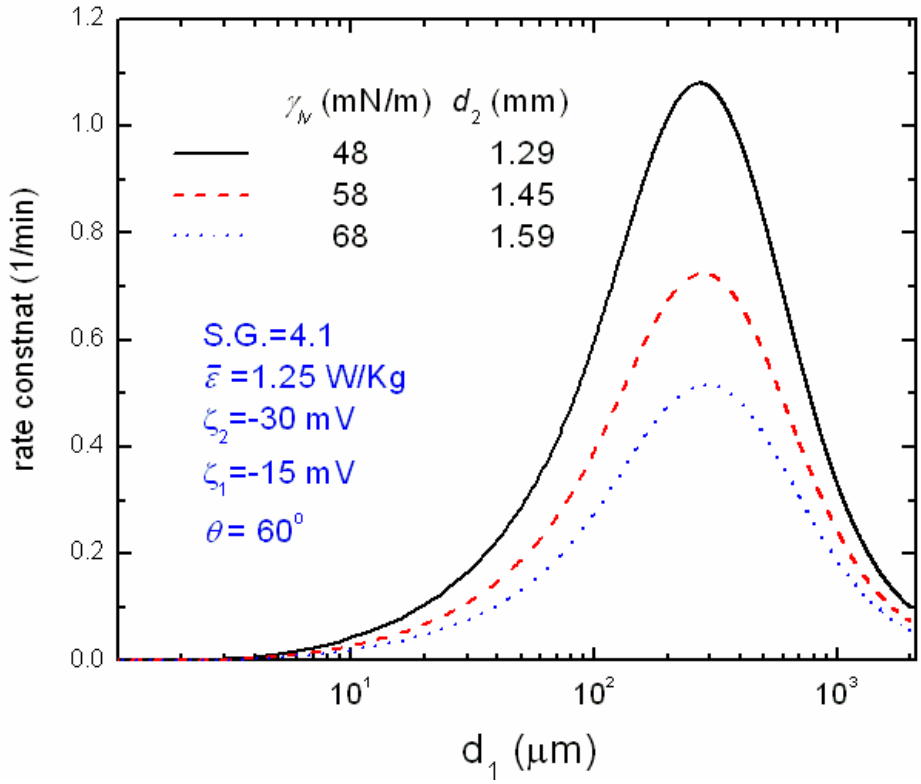

Fig.9. Effect of surface tension (γ_{lv}) on flotation rate constant (k). A higher surface tension causes larger bubble sizes and deteriorated flotation rate.

transfer probability (P_f).

Fig. 9 shows the simulation results obtained by changing the surface tension of water (γ_{lv}) and particle size (d_1). The results show that as surface tension is decreased flotation rate is increased at the entire particle size range investigated. This finding can be explained by the decrease in bubble size (d_2) with decreasing surface tension (γ_{lv}) in accordance to the bubble generation model represented by Eq. (26) and as shown in the inset. On the other hand, a decrease in γ_{lv} should cause a decrease in work of adhesion (W_a) according to Eq.(13) and hence cause an increase in the probability of detachment (Eq.(12)). Obviously, change in γ_{lv} affects d_2 more than W_a in terms of flotation recovery.

4. DISCUSSION

The model developed in the present work is by no means complete, as flotation is a complex three-phase phenomenon, and much is still unknown. The most difficult part of modeling flotation under turbulent flow conditions is to accurately determine the kinetic energies involved in the sub-processes of bubble-particle attachment and detachment sub-processes, both of which are related to energy dissipation rates. In the present work, a flotation cell was subdivided into two compartments, *i.e.*, high and low energy dissipation zones. It may be necessary, however, to use a multi-compartment model for energy dissipation. Better still may be to use the local energy dissipation rates that can be readily determined from CFD simulation.

Many investigators studied the kinetics of thinning of the wetting films of water formed on flat and well-defined surfaces of solids [27, 90, 91]. The changes in film thickness can be monitored accurately using the optical interference technique. The results showed that as an air bubble is pressed against a flat solid surface in a horizontal orientation, the air bubble deforms to produce a plane-parallel wetting film. The change in curvature associated with this process creates a pressure difference between the liquid in the film and the bulk solution, causing the film to thin spontaneously. As the film thinning continues to a thickness of approximately 200 nm, the process is controlled by the disjoining pressure (Π), which is created by the forces acting between the two surfaces, *i.e.*, solid and air bubble, facing each other in the wetting film. If Π is positive (repulsive), the film thinning stops at an equilibrium thickness (H_e), and the film does not rupture. If the Π is negative (attractive), then the film ruptures at a critical rupture thickness (H_c), creating an air/solid interface. In general, both H_c and the kinetics of film thinning increases with increasing hydrophobicity (contact angle) of the solid [26].

In flotation, air bubbles collide with mineral particles and create wetting films between them. For a successful flotation, the films must rupture during the short contact times allowed under highly dynamic conditions. Thus, the basic mechanisms involved in bubble-particle attachment should be the same as those of the wetting films discussed above. To model the attachment process, one must consider all of the forces involved, including the hydrodynamic, capillary, and surface forces. During the initial stages of film thinning, the first two forces are important, while the surface forces become important during the latter stages. Whether a film ruptures or not and how fast it thins are determined mainly by the surface forces. As has already

been discussed, the DLVO forces, *i.e.*, the van der Waals-dispersion force and the double-layer force are often repulsive under most flotation conditions. Thus, it is necessary to consider the presence of hydrophobic force, as in Eq. (14). Figure 1 shows a plot of the extended DLVO theory for a hypothetical case. It gives a value of the energy barrier (E_1) to be $5\text{x}10^{-17}$ J, which needs to be overcome by the hydrodynamic forces available in a cell for a successful flotation. It would, therefore, be of interest to determine E_1 experimentally and compare the results with that obtainable by an extended DLVO plot.

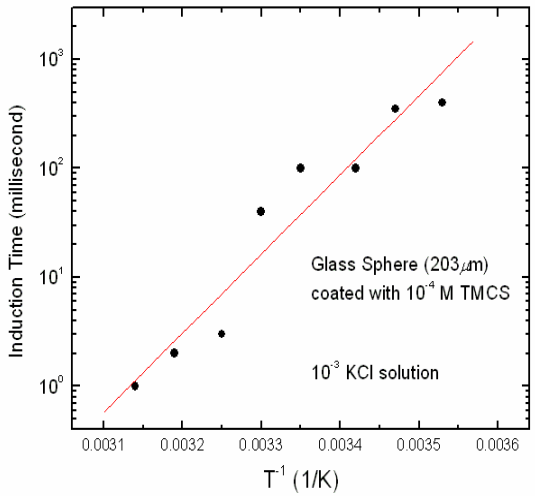

Fig. 10-A. Temperature effect on induction time. The slope of the plot yields $E_1 = 3\times10^{-17}$ J at 25^{o}C from Eq.(39).

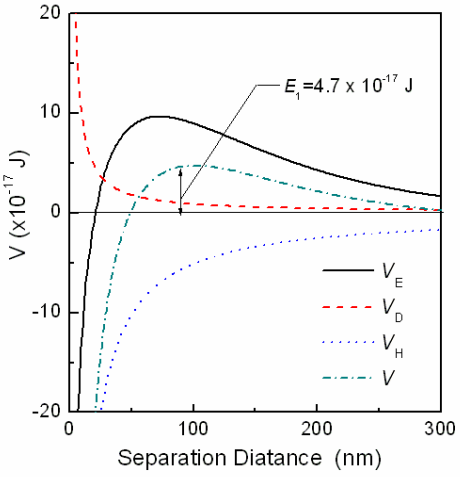

Fig. 10-B. The potential energy curves showing the extended DLVO theory in the corresponding system with Fig.9-A. The parameters used in the theoretical predictions were as follows: Ψ_1= -60 mV, Ψ_1= -15mV, A_{132}= -7.08 $\text{x}10^{-20}$ J, K_{132}= $2.3\text{x}10^{-19}$J, r_1=0.1mm, r_2=1 mm.

In the present work, E_1 has been determined from the induction time measurements conducted at different temperatures. Figure 10-A shows the results obtained with the glass spheres (d_1 = 203 μm) hydrophobized with TMCS (10^{-4} M) to obtain $\theta = 50^o$. The measurements were conducted in a 10^{-3} M KCl solution at fixed speeds for bubbles approaching and retreating to and from a bed of particle. The results have been plotted according to the Arrhenius equation [92, 93],

$$t = t_0 \exp\left(\frac{E_1}{k_b T}\right) \tag{39}$$

where t is the induction time, t_0 a constant, k_b the Boltzmann's constant, and T is the absolute temperature. The induction time is found to decrease substantially with increasing temperature. From the slope, one obtains $E_1 = 3\times10^{-17}$ J at 25°C, which agrees well with that (= 4.7×10^{-17} J) obtained from an extended DLVO plot given in Figure 9-B. The plot was made with the following parameters: ζ_1 = -60 mV [94], ζ_2 = -15 mV [95], and $K_{132} = 2.3\times10^{-19}$ J. The hydrophobic force constant was obtained using the combining rule (Eq. (18)) with $K_{131} = 2.16\times10^{-20}$ J and $K_{232} = 2.5\times10^{-18}$ J. The former was obtained using Eq. (19) from $\theta = 50^o$ for the glass spheres used in the induction time measurement. The value of the bubble zeta-potential (ζ_2) may appear lower than those (-30 to -15 mV) reported in the literature [9, 40, 96]. In the present work, the lowest limit of -15 mV was chosen in view of the relatively large bubble size (2 mm) used in the induction time measurements. It has been shown that bubble zeta-potentials decrease considerably with increasing bubble size [95]. The agreement between the calculated and experimental values of E_1 justifies the approach taken in the present work in modeling flotation.

It has been found that the pulp-phase flotation rate constant, k, predicted from Eq. (8) are considerably higher than those reported in the literature from batch flotation experiments. This is particularly the case for coarse particles, which can be attributed to the fact that froth phase recovery drops off sharply with increasing particle size. Another reason for the discrepancy between the predicted and laboratory experimental results is that the energy dissipation rates employed in the model calculations are substantially lower than those used in laboratory flotation experiments.

5. SUMMARY AND CONCLUSION

A flotation model has been derived to predict flotation recovery under turbulent flow conditions from both hydrodynamic and surface chemistry parameters. The model can predict the flotation rate constants in the pulp phase of a flotation cell, which will allow predicting the corresponding flotation recovery. By combining such information with those in the froth phase, it is possible to predict the overall flotation recovery. It has been found that the model can be used to successfully simulate the industrial flotation results reported in the literature.

The simulation results obtained under typical operating conditions employed for the flotation of chalcopyrite show that flotation becomes difficult at particle sizes below 10 μm and above approximately 200 μm, which are consistent with the upper and lower particle size limits reported in the literature. The difficulty in floating fine particles is due to the low collision

efficiency (P_c) rather than collision frequency (Z_{12}). In fact, the latter increases with decreasing particle size. That fine particles have low kinetic energies also contribute to the low P_a and hence low flotation recovery. This problem can be overcome by increasing the specific energy input to a flotation cell. On the other hand, the difficulty in floating coarse particles is due to the high probability of detachment under turbulent flow conditions and the low probability of bubble-particle aggregates entering froth phase.

The simulation results show also that flotation rate is critically dependent on contact angle, ζ-potential, and surface tension, as demonstrated amply in the literature and in flotation practice. In general, flotation rate increases with increasing contact angle at all particle sizes. When the ζ-potentials of air bubbles are negative, flotation rate increases with a decrease in the negative ζ-potentials of particles. The simulation results suggest that proper control of ζ-potentials helps the flotation of finer particles rather than that of coarser particles. Simulation results obtained by changing the surface tension of water show that flotation rare increases with decreasing surface tension, which in turm causes a decrease in bubble size. The induction time measurements were conducted at different temperatures to determine the energy barrier for bubble-particle attachment. The result is similar to that obtained using the extended DLVO theory.

6. REFERENCES

1. Sutherland, K.L., *Physical Chemistry of Flotation. XI. Kinetics of the Flotation Process.* The Journal of Physical and Colloid Chemistry, 1948. **52**(2): p. 394-425.
2. Schuhmann, R., *Flotation Kinetics. I. Methods for steady-state study of flotation problems.* The Journal of Physical Chemistry, 1942. **46**(8): p. 891-902.
3. Gaudin, A.M., *Flotation*. 1932, New York: McGraw Hill.
4. Derjaguin, B.V. and S.S. Dukhin, *Theory of flotation of small and medium-size particles.* Transactions of Institutions of Mining and Metallurgy, 1961. **70**: p. 221-246.
5. Reay, D. and G.A. Radcliff, *Removal of fine particles from water by dispersed air flotation: effects of bubble size and particle size on collection efficiency.* Canadian Journal of chemical engineering, 1973. **51**: p. 178-185.
6. Weber, M.E. and D. Paddock, *Interceptional and gravitational collision efficiencies for single collectors at intermediate Reynolds numbers.* Journal of Colloid and Interface Science, 1983. **94**(2): p. 328-335.
7. Finch, J.A. and G.S. Dobby, *Column flotation*. 1990: Pergamon press.
8. Yoon, R.H. and G.H. Luttrell, *The effect of bubble size on fine particle flotation.* Mineral Processing and Extractive Metallurgy Review, 1989. **5**: p. 101-122.
9. Yoon, R.-H. and L. Mao, *Application of Extended DLVO Theory, IV: Derivation of Flotation Rate Equation from First Principles.* Journal of Colloid and Interface Science, 1996. **181**(2): p. 613-626.
10. Pyke, B., D. Fornasiero, and J. Ralston, *Bubble particle heterocoagulation under turbulent conditions.* Journal of Colloid and Interface Science, 2003. **265**(1): p. 141-151.
11. Ralston, J., S.S. Dukhin, and N.A. Mishchuk, *Inertial hydrodynamic particle-bubble interaction in flotation.* International Journal of Mineral Processing, 1999. **56**(1-4): p. 207-256.

12. Sherrell, I. and R.-H. Yoon. *Development of a turbulent flotation model*. in *Centenary of flotation symposium*. 2005. Barisbane, Australia.
13. Sherrell, I., *Development of a flotation rate equation from first principles under turbulent flow conditions,* in *Mining and Minerals Engineering*. 2004, Virginia Tech: Blacksburg.
14. Koh, P.T.L. and M.P. Schwarz, *CFD modelling of bubble-particle collision rates and efficiencies in a flotation cell.* Minerals Engineering, 2003. **16**(11): p. 1055-1059.
15. Koh, P.T.L. and M.P. Schwarz, *CFD modelling of bubble-particle attachments in flotation cells.* Minerals Engineering, 2006. **19**(6-8): p. 619-626.
16. Bloom, F. and T.J. Heindel, *On the structure of collision and detachment frequencies in flotation models.* Chemical Engineering Science, 2002. **57**(13): p. 2467-2473.
17. Ralston, J., et al. *Flotation rate constant prediction for metal sulfide particles*. in *Centenay of flotation symposium*. 2005. Brisbane, Australia.
18. Schubert, H., *On the turbulence-controlled microprocesses in flotation machines.* International Journal of Mineral Processing, 1999. **56**(1-4): p. 257-276.
19. Abrahamson, J., *Collision rates of small particles in a vigorously turbulent fluid.* Chemical Engineering Science, 1975. **30**(11): p. 1371-1379.
20. Derjaguin, B.V. and S.S. Dukhin. in *13th international mineral processing congress.* 1969.
21. Mika, T.S. and D.W. Fuerstenau. *A microscopic model of the flotation process*. in *8th international mineral processing congressqLeningrad, U.S.S.R.* 1968. Leningrad.
22. Hunter, R.J., *Fundamentals of colloid science*. 1986: Oxford science publications.
23. Overbeek, J.T.G., *Colloid science*. 1952: Elsevier.
24. Smoluchowski, M., *Mathematical theory of the kinetics of the coagulation of colloidal particle.* Z. phys. Chem, 1917. **92**: p. 129.
25. Jowett, A. and S.M.M. Safvi, *Refinements in methods of determining flotation rates.* Trans. AIME, Metallurgical and petroleum engineers, 1960. **217**: p. 351-357.
26. Yoon, R.H. and J.L. Yordan, *The critical rupture thickness of thin water films on hydrophobic surfaces.* Journal of Colloid and Interface Science, 1991. **146**(2): p. 565-572.
27. Israelachvili, J. and R. Pashley, *The hydrophobic interaction is long range, decaying exponentially with distance.* Nature, 1982. **300**(5890): p. 341-342.
28. Christenson, H.K. and P.M. Claesson, *Direct measurements of the force between hydrophobic surfaces in water.* Advances in Colloid and Interface Science, 2001. **91**(3): p. 391-436.
29. Pazhianur, R. and R.H. Yoon, *Model for the origin of hydrophobi force.* Minerals and Metallurgical processing, 2003. **20**(4): p. 178-184.
30. Yoon, R.-H. and S.A. Ravishankar, *Long-Range Hydrophobic Forces between Mica Surfaces in Dodecylammonium Chloride Solutions in the Presence of Dodecanol.* Journal of Colloid and Interface Science, 1996. **179**(2): p. 391-402.
31. Considine, R.F., R.A. Hayes, and R.G. Horn, *Forces Measured between Latex Spheres in Aqueous Electrolyte:??Non-DLVO Behavior and Sensitivity to Dissolved Gas.* Langmuir, 1999. **15**(5): p. 1657-1659.
32. Meagher, L. and V.S.J. Craig, *Effect of Dissolved Gas and Salt on the Hydrophobic Force between Polypropylene Surfaces.* Langmuir, 1994. **10**(8): p. 2736-2742.

33. Tyrrell, J.W.G. and P. Attard, *Atomic Force Microscope Images of Nanobubbles on a Hydrophobic Surface and Corresponding Force?岚eparation Data.* Langmuir, 2002. **18**(1): p. 160-167.
34. Ishida, N., et al., *Nano Bubbles on a Hydrophobic Surface in Water Observed by Tapping-Mode Atomic Force Microscopy.* Langmuir, 2000. **16**(16): p. 6377-6380.
35. Mao, M., et al., *Is There a Thin Film of Air at the Interface between Water and Smooth Hydrophobic Solids?* Langmuir, 2004. **20**(5): p. 1843-1849.
36. Sakamoto, M., et al., *Origin of Long-Range Attractive Force between Surfaces Hydrophobized by Surfactant Adsorption.* Langmuir, 2002. **18**(15): p. 5713-5719.
37. Zhang, J., et al., *Effects of Degassing and Ionic Strength on AFM Force Measurements in Octadecyltrimethylammonium Chloride Solutions.* Langmuir, 2005. **21**(13): p. 5831-5841.
38. Meyer, E.E., Q. Lin, and J.N. Israelachvili, *Effects of Dissolved Gas on the Hydrophobic Attraction between Surfactant-Coated Surfaces.* Langmuir, 2005. **21**(1): p. 256-259.
39. Xu, Z. and R.-H. Yoon, *The role of hydrophobia interactions in coagulation.* Journal of Colloid and Interface Science, 1989. **132**(2): p. 532-541.
40. Xu, Z. and R.-H. Yoon, *A study of hydrophobic coagulation.* Journal of Colloid and Interface Science, 1990. **134**(2): p. 427-434.
41. Chia, Y.H. and P. Somasundaran, *A theoretical approach to flocculation in carrier flotation for beneficiation of clay.* Colloids and Surfaces, 1983. **8**(2): p. 187-202.
42. Schimmoller, B.K., G.H. Luttrell, and R.H. Yoon. *A combined hydrodynamic-surface force model for bubble-particle collection.* in *18th international mineral processing congress*. 1993. Sydney, Australia.
43. Mao, L. and R.-H. Yoon, *Predicting flotation rates using a rate equation derived from first principles.* International Journal of Mineral Processing, 1997. **51**(1-4): p. 171-181.
44. Camp, P.R. and P.C. Stein, *Velocity gradients and internal work in fluid motion.* Journal of the Boston Society of Civil Engineers, 1943. **30**(4): p. 219-237.
45. Saffman, P.G.a.T., J.S., *On the collision of drops in turbulent coluds.* Journal of Fluid Mechanics, 1956. **1**: p. 16-30.
46. Schumann, R., *Flotation kinetics: I. Moethods for steady state study of flotation problems.* Journal of physical chemistry, 1942. **46**: p. 891-902.
47. Tomlinson, H.S. and M.B. Flemming, *Flotation rate studies,* in *6th International Mineral Processing Congress*. 1963. p. 563.
48. Liepe, F. and H.O. Moeckel, *Untersuchungen zum Stoffvereinigen in Flüssiger Phase.* Chemical Technology, 1976. **28**.
49. Brady, M.R., et al., *Evaluation of multiphase flotation models in grid turbulence via Particle Image Velocimetry.* International Journal of Mineral Processing, 2006. **80**(2-4): p. 133-143.
50. Lee, C.A. and L.E. Erickson, *Bubble breakup and coalescence in turbulent gas-liquid dispersions.* Chemical Engineering Communications, 1987. **59**: p. 65-84.
51. Derjaguin, B.V., N.V. Churaev, and V.M. Muller, *Surface Forces*. 1987, New York: Consultatn Bureau-Plenum.
52. Ralston, J., S.S. Dukhin, and N.A. Mishchuk, *Wetting film stability and flotation kinetics.* Advances in Colloid and Interface Science, 2002. **95**(2-3): p. 145-236.

53. Luttrell, G.H. and R.H. Yoon. *Determination of the probability of bubble-particle adhesion using induction time measurements*. in *International symposium on the production and processing of fine particles*. 1988. Montreal, Canada.
54. Dobby, G.S. and J.A. Finch. in *114th annual AIME meeting*. 1985. New York.
55. Hogg, R., T.W. Healy, and D.W. Fuerstenau, *Mutual coagulation of colloidal dispersions.* Transactions of Faraday Society, 1966. **62**: p. 1638-1651.
56. Rabinovich, Y.I. and N.V. Churaev, *Effect of electromagnetic delay on the forces of molecular attraction.* Kolloidnyi Zhurnal, 1979. **41**(3): p. 468-474.
57. Yoon, R.-H., D.H. Flinn, and Y.I. Rabinovich, *Hydrophobic Interactions between Dissimilar Surfaces.* Journal of Colloid and Interface Science, 1997. **185**(2): p. 363-370.
58. Yoon, R.-H. and B.S. Aksoy, *Hydrophobic Forces in Thin Water Films Stabilized by Dodecylammonium Chloride.* Journal of Colloid and Interface Science, 1999. **211**(1): p. 1-10.
59. Wang, L. and R.-H. Yoon, *Hydrophobic Forces in the Foam Films Stabilized by Sodium Dodecyl Sulfate:Effect of Electrolyte.* Langmuir, 2004. **20**(26): p. 11457-11464.
60. Goren, S.L. and M.E. O'Neill, *On the hydrodynamic resistance to a particle of a dilute suspension when in the neighbourhood of a large obstacle.* Chemical Engineering Science, 1971. **26**(3): p. 325-338.
61. Luttrell, G.H. and R.-H. Yoon, *A hydrodynamic model for bubble-particle attachment.* Journal of Colloid and Interface Science, 1992. **154**(1): p. 129-137.
62. Luttrell, G.H., *Hydrodynamic studies and mathematical modeling of fine coal flotation*, in *Mining and Minerals Engineering*. 1986, Virginia Polytechnic Institute and State University: Blacksburg, Virginia.
63. Jowett, A. *Formation and disruption of particle-bubble aggregates in flotation*. in *Fine particle processing: Proceedings of International symposium on fine particles*. 1980: SME.
64. Schulze, H.J., *Physicochemical elementary processes in flotation*. 1983: Elsevier.
65. Lu, S., Y. Ding, and J. Guo, *Kinetics of fine particle aggregation in turbulence.* Advances in Colloid and Interface Science, 1998. **78**(3): p. 197-235.
66. Okamoto, Y., M. Nishikawa, and K. Hashimoto, *Energy dissipation rate distribution in mixing vessels and its effects on liquid-liquid dispersion and solid-liquid mass transfer.* International Chemical Engineering, 1981. **21**(1): p. 88-94.
67. Sundaram, S. and L.R. Collins, *Collision statistics in an isotropic particle-laden turbulent suspension. Part 1. Direct numerical simulations.* Journal of Fluid Mechanics, 1997. **335**(-1): p. 75-109.
68. Zenit, R. and D. Legendre, *The coefficient of restitution for air bubbles colliding against solid walls in viscous liquids.* Physics of Fluids, 2009. **21**(8): p. 083306-12.
69. Sanada, T., M. Watanabe, and T. Fukano, *Effects of viscosity on coalescence of a bubble upon impact with a free surface.* Chemical Engineering Science, 2005. **60**(19): p. 5372-5384.
70. Sunol, F. and R. Gonzalez-Cinca, *Rise, bouncing and coalescence of bubbles impacting at a free surface.* Colloids and Surfaces A: Physicochemical and Engineering Aspects, 2010. **In Press, Corrected Proof**.
71. Krzan, M., K. Lunkenheimer, and K. Malysa, *Pulsation and Bouncing of a Bubble Prior to Rupture and/or Foam Film Formation.* Langmuir, 2003. **19**(17): p. 6586-6589.

72. Malysa, K., M. Krasowska, and M. Krzan, *Influence of surface active substances on bubble motion and collision with various interfaces.* Advances in Colloid and Interface Science, 2005. **114-115**: p. 205-225.
73. Boulton-Stone, J.M. and J.R. Blake, *Gas bubbles bursting at a free surface.* Journal of Fluid Mechanics Digital Archive, 1993. **254**(-1): p. 437-466.
74. Barnocky, G. and R.H. Davis, *The lubrication force between spherical drops, bubbles and rigid particles in a viscous fluid.* International Journal of Multiphase Flow, 1989. **15**(4): p. 627-638.
75. Currie, I.G., *Fundamental mechanis of fluids*. 2nd ed. 1993: McGraw Hill.
76. Harris, C.C., *Flotation machines*, in *Flotation-A.M. Gaduin Memorial volume*, M.C. Fuerstenau, Editor. 1976, AIME. p. 753-815.
77. Lynch, A.J., M.W. Johnson, and E.V. Manlapig, eds. *Mineral and coal flotation circuits: their simulation and control*. Developments in mineral processing 3. 1981, elsevier.
78. MacMullin, P.B. and M. Weber, *The theory of short-circuiting in continuous flow mixing vessels in series and the kinetics of chemical reactions in such systems.* Transactions of Americal Isntitute of Chemical Engineeris, 1935. **31**: p. 409-458.
79. Do, H., *Development of a turbulent flotation model from first principles*, in *Engineering Science and Mechanics*. 2010, Virginia Polytechnic Institute and State University: Blacksburg.
80. Do, H. and R.H. Yoon, *A model for froth-phase recovery in a flotation cell.* International Journal of Mineral Processing, 2010. **to be submitted**.
81. Trahar, W.J. and L.J. Warren, *The flotability of very fine particles -- A review.* International Journal of Mineral Processing, 1976. **3**(2): p. 103-131.
82. Ahmed, N. and G.J. Jameson, *The effect of bubble size on the rate of flotation of fine particles.* International Journal of Mineral Processing, 1985. **14**(3): p. 195-215.
83. Gaudin, A.M., J.O. Groh, and H.B. Henderson, AIME Eng. Tech. Pub, 1931. **414**.
84. Duan, J., D. Fornasiero, and J. Ralston, *Calculation of the flotation rate constant of chalcopyrite particles in an ore.* International Journal of Mineral Processing, 2003. **72**(1-4): p. 227-237.
85. Devivo, D.G. and B.L. Karger, *Studies in the Flotation of Colloidal Particulates: Effects of Aggregation in the Flotation Process.* Separation Science and Technology, 1970. **5**(2): p. 145 - 167.
86. Baker, H.F. and K.J. Miller, *Zeta poetntial contro: its application in coal preparation.* Mining congress journal, 1968. **55**: p. 43-44.
87. Chander, S. and D.W. Fuerstenau, Trans. AIME, 1972. **252**.
88. Fuerstenau, D.W., Trans. AIME, 1957. **208**: p. 1365.
89. Jacock, M.J. and R.H. Ottewill, Trans. Inst. Min. & Metall., 1963. **72**: p. 497.
90. Laskowski, J. and J.A. Kitchener, *The hydrophilic--hydrophobic transition on silica.* Journal of Colloid and Interface Science, 1969. **29**(4): p. 670-679.
91. Blake, J.R. and J.A. Kitchener, *Stability of aqueous films on hydrophobic methylated silica.* Journal of Chemical Society, Faraday Transactions 1: Physical chemistry in condensed phases, 1972. **68**: p. 1435-1442.
92. Eigeles, M.A. and M.L. Volova. *Kinetic investigation of effect of contact time, temperature and surface condition on the adhesion of bubble to mineral surfaces*. in *5th International Mineral Processing Congress*. 1960. London: Inst. Min. Metall.

93. Yoon, R.-H. and J.L. Yordan, *Induction time measurements for the quartz--amine flotation system.* Journal of Colloid and Interface Science, 1991. **141**(2): p. 374-383.
94. Ducker, W.A., Z. Xu, and J.N. Israelachvili, *Measurements of Hydrophobic and DLVO Forces in Bubble-Surface Interactions in Aqueous Solutions.* Langmuir, 1994. **10**(9): p. 3279-3289.
95. Usui, S., H. Sasaki, and H. Matsukawa, *The dependence of zeta potential on bubble size as determined by the dorn effect.* Journal of Colloid and Interface Science, 1981. **81**(1): p. 80-84.
96. Blake, P. and J. Ralston, *Controlled methylation of quartz particles.* Colloids and Surfaces, 1985. **15**: p. 101-118.

CHAPTER 3

INDUCTION TIME MEASUREMENT FOR SINGLE-PARTICLE FLOTATION

Abstract

Bubble and particle attachment plays the most important role in flotation because it is the prerequisite for successful flotation. With regard to the bubble-particle attachment, the effect of various parameters on floatability has been studied in this report by measuring the time required for completing the attachment. The time, called induction time, showed significant changes with changing parameters such as bubble size, particle size, moving speed of bubble, surface tension, and electrolyte concentration of the solution. The overall experimental results agreed with the prediction by the flotation model which was developed in another work by the present authors. The effect of temperature on induction time was also studied, and the corresponding results could verify the extended DLVO theory which was used in the flotation model.

1. Introduction

Flotation is a separation technique which has been used in the mining industry for more than a century for the recovery of valuable minerals. Of the various subprocesses of flotation, attachment of hydrophobic mineral particles to air bubbles is the most important. For the attachment to be accomplished, the liquid film intervening between bubble and particle surfaces should rupture. The time required for this rupture process is referred to as induction time in flotation research, and it has been considered as a good indicator for the floatability of minerals under a given chemical condition. Floatability is also evaluated by contact angle of particles. Of the two, evaluating floatability by induction time is more reliable because the measurement is conducted in a dynamic environment while contact angle represents only the property of equilibrium state. Generally, the shorter the induction time is, the higher the floatability [1].

The first experiment on induction time may date back to Sven-Nilson [2]'s work in which a method was devised for estimating relatively short induction time. In this report, a captive bubble was vibrated with varying frequencies against a submerged mineral surface. The time it took for the interfacial film to rupture at a sufficiently low frequency was considered as the induction time, and it was found to be 0.01~0.1 seconds for typical minerals. Since then, many investigators used different techniques to determine induction time [3-7]. Nevertheless, the number of references on induction time measurement does not correspond to its significance in flotation research. It seems due to the limitations of experimental techniques used, as well as the ambiguity concerning the definition of actual induction time. Several researchers considered induction time as the resultant time of three discrete steps to complete attachment: drainage of liquid film between particle and air bubble surfaces followed by the rupture time of the film, and the spreading of contact area after the rupture [2, 8, 9]. Those three steps may be distinguishable for the case when particles are large relative to bubble because the attachment commences in a relatively long timescale due to large contact area. However, the steps may have less meaning in actual flotation systems where attachment timescale is generally very short due to smaller particle sizes than bubbles. Therefore, the term 'induction time' may well be used interchangeably with 'attachment time' in the experiment that simulates bubble-particle attachment of actual flotation [3].

Regarding the timescales, the work by Ye *et al*. [10] may indicate the particular difference of timescale between the induction time measured on a polished mineral surface and the one on a particle bed of the same material. They found that induction time measured on a polished surface is orders of magnitude greater than that measured on a particle bed. However, there is a blemish in their comparison that the authors compared two systems that are dynamically dissimilar. The data on polished mineral surfaces were obtained by analyzing the images at the interface between the mineral surface and a bubble kept underneath the surface by its buoyant force. On the other hand, the bubble's motion and contact time with a particle bed was well controlled by an electromechanical driver.

Eigeles and Volova [11] were the first who conducted induction time experiments at a particle bed. Induction time was measured by moving a bed of small mineral particles in a solution toward and then away from a fixed captive bubble. The same approach was adopted by other researchers with modified and improved induction timer apparatus [1, 10, 12]. Using

similar apparatus, Ye *et al*.[10] measured induction time in coal flotation systems while Yoon and Yordan [1] did in quartz-Amine flotation systems especially with extensive investigation on the effects of flotation chemistry. Hewitt *et al*. [13] also measured induction time in an environment more dynamically similar to actual flotation. In their experiments, a video camera was used to record hydrophobic particles settling onto a rising bubble. However, their induction time was not measured directly but inferred from the analysis of the collection efficiency data determined by measuring the number of attached particles per bubble. Recently, Wang *et al*.[3] measured induction time between a hydrophobic solid sphere and a bubble using the same technique as Gu *et al*. [12]. However, the radius of sphere was exaggerated to the extent as large as the bubble radius in order to detect the attachment more clearly.

In the present work, induction time measurements have been carried out for several systems: quartz-amine, and quartz-silane systems. The effects of different physical parameters such as bubble size, particle size, and bubble's approaching speed have been investigated as well as the effect of chemical properties such as surface tension, contact angle, and electrolyte concentrations.

2. Experimental

The methodology for measuring induction time was originally adopted from other literature that had successfully proved its validity for assessing floatability in certain systems [1].

2.1 Sample preparation

Particles of various hydrophobicties were obtained using two different methods. First, different sizes of glass spheres obtained from Potters Industries Inc. were hydrophobized by submerging them in solutions of trimethylchlorosilane (TMCS) in cyclohexane by following the method descrined in literature [14-16]. Samples of desired sizes were first preheated in a convection oven at 80^{o}C for 24 hours, and kept immersed in designated TMCS solutions at ambient temperature for another 24 hours. After supposedly complete reaction, particles were removed from the solution to be washed twice with pure cyclohexane, and then dried in a convection oven at 100^{0}C. At the same time with the particle preparation, glass plates of 1.5x1.0 cm^2 were also immersed in the same solution so that the contact angles of the plate and sphere were the same.

In addition to the glass-TMCS system, another system was considered as well. Spherical glass particles of various sizes obtained from Potters Industries Inc. were hydrophobized by submerging in solutions of 5×10^{-6}M C_{18}TACl. This particular concentration was found to yield the strongest hydrophobicity of silica surface according to Zhang *et al.* [17]. Samples had to be immersed for at least 2 hours for the adsorption to reach equilibrium. At the same time, glass plates of 1.5x1.0 cm^2 were also prepared under the same conditions, representing particles of infinite size. The plate samples were prepared in case the particle samples would be too small beyond the equipment's 1 millisecond sensitivity. It should be also noted here that cleaning sample surfaces was a crucial factor in the experiment as dirty surfaces caused inhomogeneous adsorptions on them and hence poor reproducibility. The cleaning process is well described elsewhere [17].

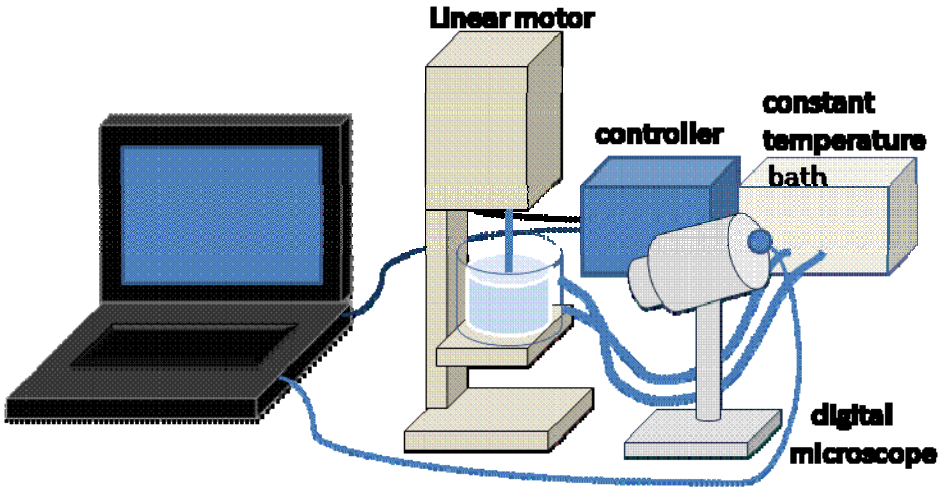

Figure.1. Experimental setup for induction time measurement

2.2 Equipment and procedure

The experimental setup is shown in Fig.1. A programmable linear D.C. motor was assembled atop a glass capillary tube. Then single air bubble of approximately 1,1.5 or 2 mm diameter was generated in each test by injecting constant volume of air through a syringe connected to the inlet of the tube. The motor mount was designed such that the tube tip can be dipped in a small solution container placed on a rack where the bubble motion was observed more closely by a digital microscope. A glass titration vessel with thermostatic jacket was chosen as the container, so that the solution could be kept in constant temperature of certain degrees by circulating water into the jacket from a constant temperature bath.

The tube tip's moving speed, distance, and the contact time were programmable. The contact time was adjusted in several trials, from which the minimum was sought. The minimum contact time at which the bubble successfully picked up more than one particle with reproducibility of at least 5 out of 10 trials was defined as the induction time, as has been in the original experiments by Yoon and Yordan [1].

3. Experimental Results

Previously, a flotation model was developed by considering both the hydrodynamic and chemical properties [18, 19]. The following experimental results agreed with some of what the model predicted when those properties were changed.

3.1 Effect of particle size

Figure 2 shows the effect of particle sizes on induction time. The results obtained with two different samples are plotted in one figure. Bubble diameter in both experiments was 2mm. For the glass-TMCS samples, the glass spheres were hydrophobized in 10^{-4} % by volume TMCS-in-

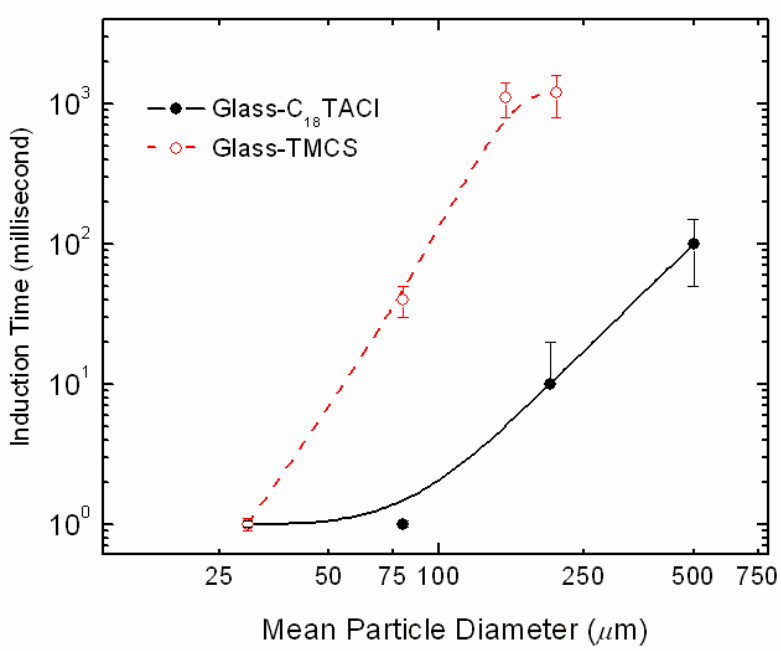

Figure.2. Effect of particle sizes on induction time

cyclohexane solutions, and immersed in pure water with 0.1 M NaCl. Approaching and retracting speed of the bubble were both 7.8 cm/s. For the glass-C_{18}TACl samples, glass spheres were immersed in 5×10^{-6} M C_{18}TACl solutions with 0.01 M NaCl, and bubble moved at 315 cm/s in both approaching and retracting directions. The results show higher induction times for larger particle sizes. This agrees with the general observation that large particles are difficult to float.

3.2 Effect of bubble size

In figure 3, the effects of bubble size on induction time are shown. Bubble size control was possible by injecting different air volume. Approximately 1.0 mm, 1.5 mm, and 2.0 mm diameter bubbles were made to compare. Particle samples were the same as those used in the experiment for Figure 2, but the diameter was fixed at 203 μm. The moving speed of bubble was 315 cm/s in both approaching and retracting directions. Electrolyte concentration was 10^{-3} M of NaCl.

As Figure 3 indicates, particles attach more quickly to smaller bubbles than to larger bubbles. This result agrees with the predictions of the flotation model by Do and Yoon [18-20] that small bubbles are beneficial to flotation. This result also corresponds to the theoretical prediction by the Reynolds equation that is commonly used to estimate the thinning rate of wetting films [21]. The thinning rate is proportional to the pressure difference between the liquid and gas phase. Therefore, small bubbles should induce faster film thinning because the pressure difference is inversely proportional to the radius of air drop, according to the Laplace equation.

3.3 Effect of bubble speed

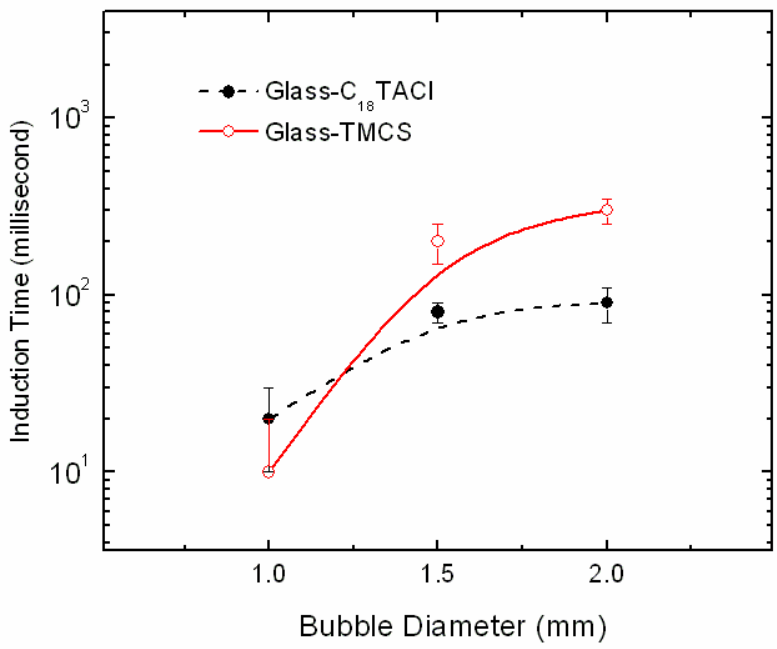

Figure.3. Effect of bubble sizes on induction time

In figure 4, the effects of the approaching speed of a bubble are shown. The retracting speed may be of interest as well. However, only the approaching speed is studied because the present work focuses on bubble-particle attachment only. In fact, the effect of retracting speed was not observable because its change did not cause any difference in induction time. It may be because

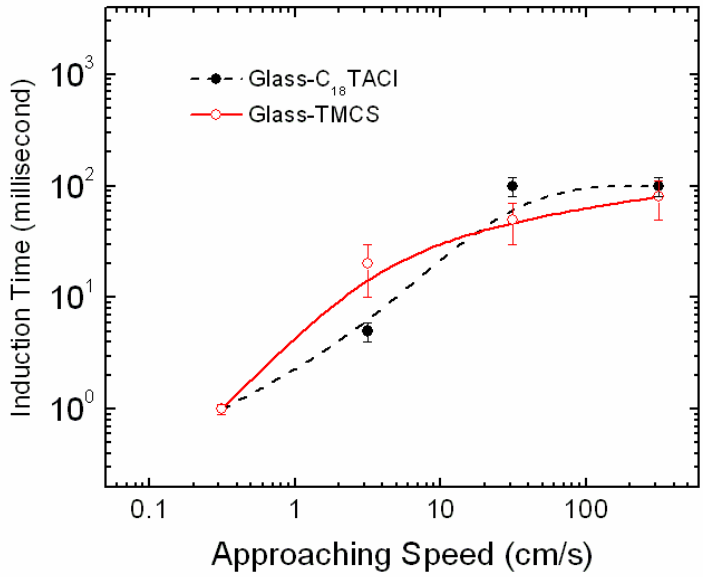

Figure.4. Effect of the approaching speed of the bubble on induction time

particles require much higher energy to be detached from bubble surfaces, and the present experimental setup could not reach up to the necessary speed.

For the particles of glass-C_{18}TACl system, the particle diameter was 500 μm, and the retracting speed was 315 cm/s. The particles of glass-TMCS system were hydrophobized in solutions of 80% Cyclohexane and 20% TMCS by volume, and the experiments were conducted in the presence of 1 M NaCl. The diameter was 156 μm, and the retracting speed was 315 cm/s as well.

The results in figure 4 show that induction time gets longer as the approaching speed of a bubble increases. This was contrary to the intuition that the intervening liquid film between air bubble and particle might drain faster at high approaching speed. However, the results conform to physical insight in that bubble surfaces are deformable. Bubbles are more likely to deform at high moving speed. Therefore, the contact area between air bubble and particle bed is large at high approaching speed of a bubble, and the liquid film should take a long time to drain off. The results also agree with Arbiter and Harris's statement that induction time generally decreases as the relative velocity between bubble and particles become smaller [9].

3.4 Effect of surface tension

Figure 5 shows that induction time decreases with increasing surface tension. The surface tension was controlled by adding a surfactant, MIBC. The results can be understood with the help of the Reynolds equation as well. The thinning rate of liquid film between air bubble and particle is proportional to the pressure difference. In turn, the pressure difference is proportional to surface tension as the Laplace equation suggests. Therefore, thinning rate is faster at higher

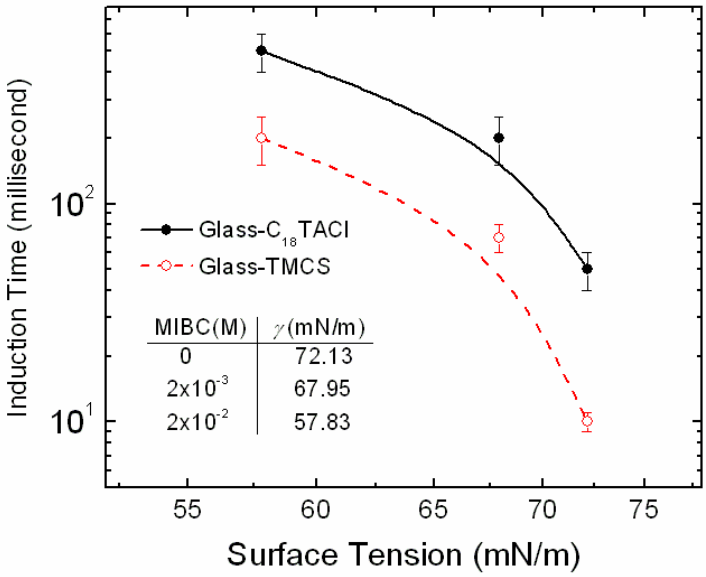

Figure.5. Effect of surface tension on induction time

surface tension. Finch and Smith [22] measured the time-dependent surface tension and observed similar results that particles attach better at higher surface tensions.

Nevertheless, the results are contrary to the prediction made in Chapter 2 that high surface tension deteriorates flotation performance. The discrepancy is because the flotation model developed in Chapter 2 considered the interdependency between bubble size and surface tension, while in the present experiment surface tension was controlled independently.

3.5 Effect of electrolyte concentration

Figures 6 and 7 show the change of induction time with the increase of NaCl concentration. Higher electrolyte concentration has an effect of compressing electrical double layers, which should diminish the repulsion force between bubble and particles. In that case, the induction time has to get shorter with higher NaCl concentrations. Figure 6 shows this effect for relatively low contact angles of particles (less than 50 degrees) hydrophobized in the glass-TMCS system. On the other hand, for relatively higher contact angles (above 50 degrees), it shows the opposite. This indicates that the change in hydrophobic force due to electrolyte concentration change is more dominant than the other effect, *i.e.*, double-layer compression. This agrees with the observation in other literature that hydrophobic force decreases significantly with increasing NaCl concentrations [17, 23].

For the case of glass-C_{18}TACl system, the results indicate this conclusion more clearly, as shown in figure 7. The samples were hydrophobized in $5x10^{-6}$ M C_{18}TACl, which yielded the contact angle above 60 degrees. In the plot, each line represents two different particle sizes and the results are in very different time scales. While particles attached in the timescale of milliseconds,

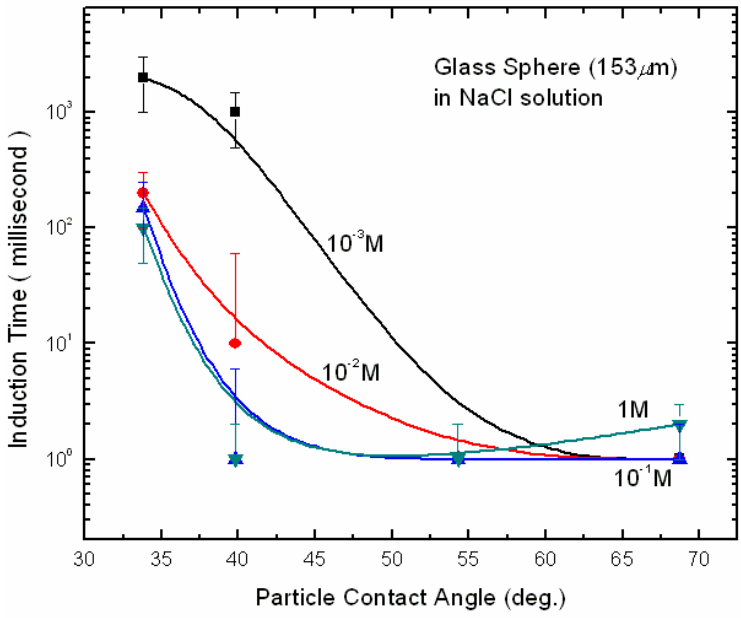

Figure. 6. The change of induction time with NaCl concentration for particles of various contact angles.

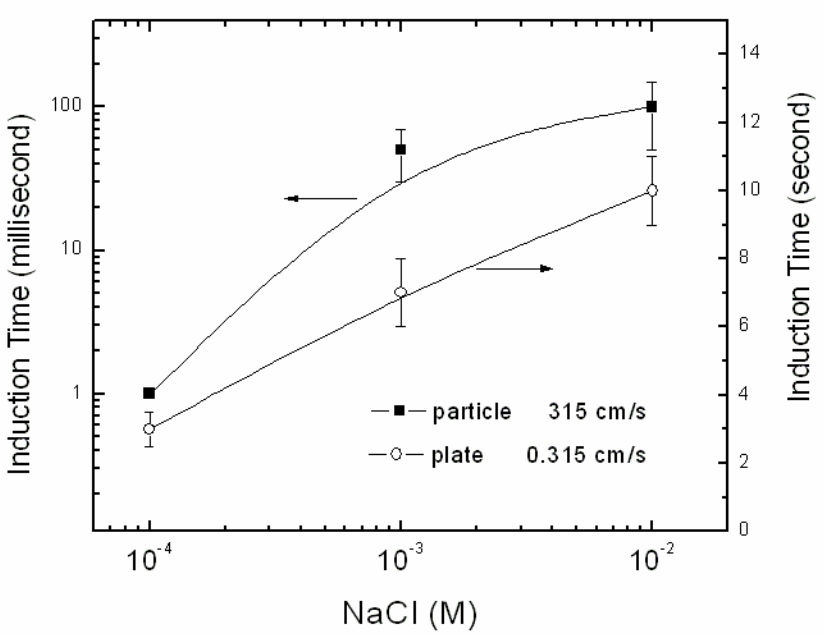

Figure.7. Effect of electrolyte concentration on induction time for glass particles (■) and glass plate (○). Moving speed of bubbles for each case was 315cm/s and 0.315 cm/s, respectively.

plates did in seconds. This result agrees with the recent observation in the same condition that putting more electrolyte in the solution reduces hydrophobic force [17], hence longer induction time.

3.6 Effect of temperature

The temperature effect on induction time is shown in Figure 8. The samples of glass-C_{18}TACl system were 500 μm in diameter and hydrophobized in the solution of 10^{-5}M C_{18}TACl. The bubbles moved at 315 cm/s. On the other hand, the samples of glass-TMCS sytem were 203 μm in diameter, and immersed in 10^{-3} M KCl solution during the measurement. Bubble moving speed was 315cm/s and the particles were hydrophobized by 10^{-4} M TMCS solution.

As shown in figure 8, induction time decreases as temperature increases. This result can be interpreted in several different aspects. For example, unless the results are attributed to surface forces present between bubble and particles, they may be due to surface tension and viscosity changes with temperature. However, for the temperature range of this experiment (10~40 ^{o}C), surface tension of pure water decreases only by 6.2% while viscosity decreases by 50%. Therefore, the induction time change of this experiment can be attributed partly to the decrease of viscosity, while the surface tension effect regarding the temperature change is minimal. The Reynolds equation also helps understanding this interpretation in that the film intervening bubble and particle thins in an inverse proportion to viscosity.

On the other hand, if the surface forces are responsible, the result can be interpreted by the aspect of the critical rupture thickness. Critical rupture thickness is defined as the thickness at which thin liquid film breaks down and the two surfaces separated by the film make a contact. There are several models for critical rupture thickness [24-26], and they assume there is instability at the air-water interface due to interfacial forces. The rupture model by Ivanov and Dimitrov [24] describes this thickness as proportional to the square root of the absolute temperature if all other properties are set equal. At higher temperature, the critical thickness is higher and accordingly induction time is shorter because particles attach to bubble at earlier stage.

4. Discussion

In the flotation model developed by Do and Yoon [18-20], the activation energy of bubble-particle attachment was the key parameter in determining floatability. The activation energy was estimated by the extended DLVO theory that describes the combined effect of the interfacial energies due to van der Waals-dispersion force, the double-layer force, and the hydrophobic force. In other words,

$$V = V_E + V_D + V_H \tag{1}$$

where V is the free energy of interaction between bubble and particle, V_E the electrostatic interaction energy, V_D the van der Waals-dispersion interaction energy, and V_H is the hydrophobic interaction energy.

The electrostatic interaction energy (V_E) between a particle of radius r_1 and a bubble of radius r_2 can be calculated using the model derived by Hogg, Healey and Fuerstenau [27]

$$V_E = \frac{\pi\epsilon_0\epsilon r_1 r_2(\Psi_1^2+\Psi_2^2)}{(r_1+r_2)}\left[\frac{\Psi_1^2\Psi_2^2}{\Psi_1^2+\Psi_2^2}\ln\left(\frac{1+e^{-\kappa H}}{1-e^{-\kappa H}}\right)+\ln(1+e^{-2\kappa H})\right] \tag{2}$$

where ϵ_0 is the permittivity in vacuum, ϵ the dielectric constant of the medium, Ψ_1 and Ψ_2 are the double layer potentials for particle and bubble, respectively, κ the inverse Debye length, and H is the closest separation distance between particle and bubble. As an approximation, Ψ_1 and Ψ_2 may be substituted by ζ–potentials.

The dispersion interaction energy can be calculated using the following relation [28],

$$V_D = -\frac{A_{132}r_1r_2}{6H(r_1+r_2)}\left[1-\frac{1+2bl}{1+bc/H}\right] \tag{3}$$

where A_{132} is the Hamaker constant for the interaction between particle **1** and bubble **2** in a medium **3**. The second term of Eq. (3) is a correction factor for the retardation effect, where b (=3x10^{-17} s for most materials) is a parameter characterizing materials of interacting particles, l (=3.3x10^{15} s^{-1} for water) is a parameter characterizing the medium, and c is the speed of light [29].

The hydrophobic interaction energy (V_H) between bubble and particle may be calculated using the following equation [29]

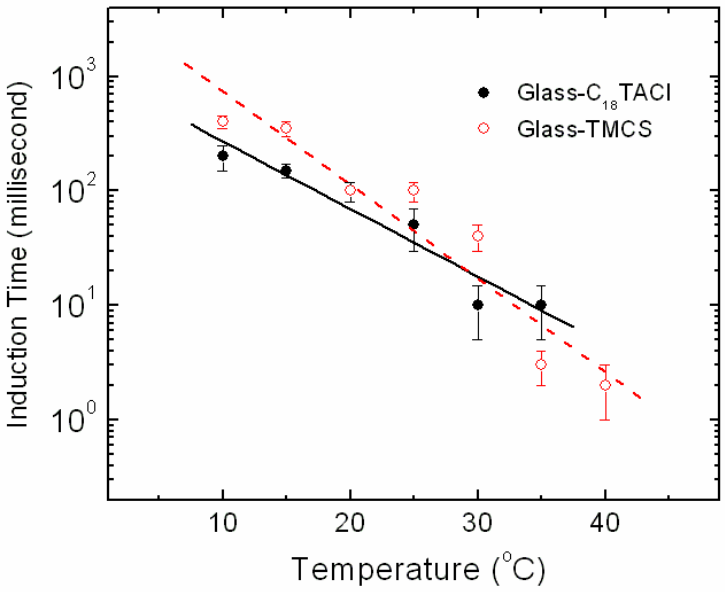

Figure.8. Effect of temperature on induction time

$$V_H = -\frac{r_1 r_2 K_{132}}{6(r_1+r_2)H} \quad (4)$$

where K_{132} is the hydrophobic force constant with the subscript 132 meaning the same as A_{132}.

Although the theory was used in Do and Yoon [18-20]'s the flotation model, it has not been validated yet. The validation may be possible in the following sense.

It has been shown in other literature that the activation energy can be obtained by analyzing the experimental data of induction time change with temperature, which may be described by an Arrhenius type equation as follows [1, 11].

$$t = t_0 \exp\left(\frac{E_1}{k_b T}\right) \quad (5)$$

where t is the induction time, t_0 a constant, k_b the Boltzmann's constant, and T is the absolute temperature of the solution. Manipulating Eq.(5), it is found that the slope of the log t *vs.* T^{-1} plot corresponds to E_1/k_b. The data obtained with glass-TMCS system in figure 8 was rearranged in this way. Then the log t vs. T^{-1} plot yielded E_1=2.99×10^{-17} J at 25^{o}C. This value represents the experimentally obtained activation energy, which can be compared with the calculated value of E_1 to validate the extended DLVO theory.

Figure 9 shows the potential energy vs. distance curve described by the extended DLVO theory, using input parameters as follows: r_1 = 100 μm, r_2 = 1 mm, ζ_1 = -60 mV [30], ζ_2 = -15 mV [31], and K_{132} = 2.3×10^{-19} J. The hydrophobic force constant (K_{132}) was obtained using the

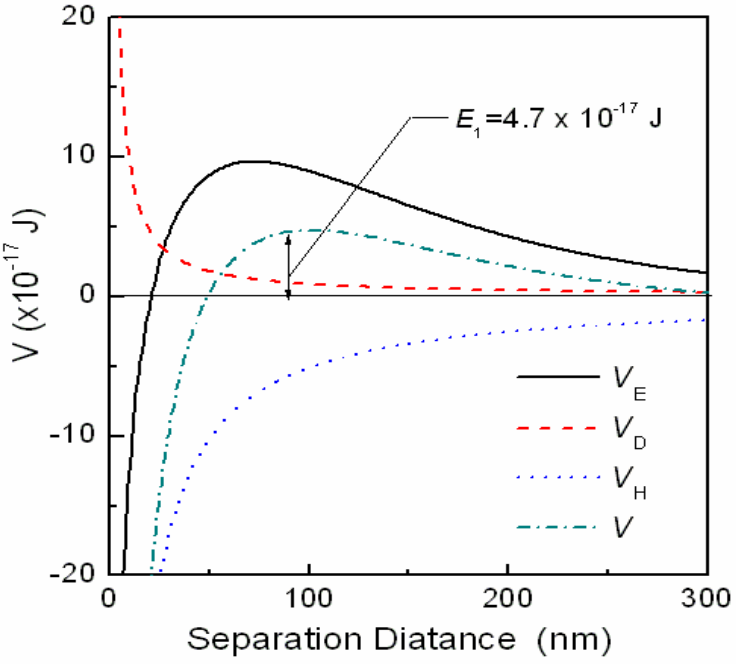

Figure. 9. The potential energy curves showing the extended DLVO theory in the corresponding samples of glass-TMCS system in Figure 8. The parameters used in the theoretical predictions were as follows: Ψ_1= -60 mV, Ψ_1= -15mV, A_{132}= -7.08 x10^{-20} J, K_{132}= 2.3x10^{-19}J, r_1=0.1mm, r_2=1 mm.

combining rule proposed by Yoon *et al.* [32]. The value of the bubble zeta-potential (ζ_2) used for the curve was somewhat lower than those (-30 to -15 mV) reported in the literature [14, 29, 33]. The lowest limit of -15 mV was chosen in view of the relatively large bubble size (2 mm) used in the induction time measurements. It has been shown that bubble zeta-potentials decrease considerably with increasing bubble size [31].

In figure 9, the curve shows the maximum potential energy, the activation energy, of 4.7×10^{-17} J. This agrees well with the one experimentally obtained (= 2.99 ×10^{-17} J). Therefore, this agreement between the two justifies the extended DLVO theory used in the flotation model by Do and Yoon.

5. Summary and conclusions

Induction times of glass-TMCS and glass-C_{18}TACl systems have been measured using an apparatus that simulates the single-bubble flotation. Some measurements were conducted to see the effect of physical parameters on induction time. As a result, it was found that induction time increases when particle or bubble sizes are large, and also when the approaching speed of bubble is high. Induction time measurements were also conducted under different chemical conditions in terms of surface tension and electrolyte concentration. The results showed that induction time decreases as surface tension increases, while the effects of electrolyte concentration varied

depending on the hydrphobicity of particles. Finally, it was also shown that the activation energy of the bubble-particle attachment can be assessed by analyzing the induction time change with temperature. The value of activation energy obtained from the data analysis agreed well with the value predicted by the extended DLVO theory. This agreement suggests that that hydrophobic force is the driving force for bubble-particle attachment, and that asymmetric hydrophobic force can be predicted using the geometric mean combining rule.

6. References

1. Yoon, R.-H. and J.L. Yordan, *Induction time measurements for the quartz--amine flotation system.* Journal of Colloid and Interface Science, 1991. **141**(2): p. 374-383.
2. Sven-Nilsson, I., *Einfluß der Berührungszeit zwischen Mineral und Luftblase bei der Flotation.* Colloid & Polymer Science, 1934. **69**(2): p. 230-232.
3. Wang, W., et al., *An induction time model for the attachment of an air bubble to a hydrophobic sphere in aqueous solutions.* International Journal of Mineral Processing, 2005. **75**(1-2): p. 69-82.
4. Eigeles, M.A., *Selective flotation and the effect of flotation reagents on it*. 1950, Moscow: Science Press.
5. Glembotsky, V.A., *The time of attachment of air bubble to minerals in flotation and ints measurement.* Izv, Akad, Naukk USSR, Otd. Teh. Nauk., 1953. **11**: p. 1524-1531.
6. Evans, L.F., *Bubble-mineral attachment in flotation.* Ind. Eng. Chem., 1954. **46**: p. 2420-2431.
7. Leja, J., *Surface chemistry in froth flotation*. 1982, New York: Plenum press.
8. Nguyen, A.V., H.J. Schulze, and J. Ralston, *Elementary steps in particle--bubble attachment.* International Journal of Mineral Processing, 1997. **51**(1-4): p. 183-195.
9. Arbiter, N. and C.C. Harris, *Flotation kinetics*, in *Froth Flotation 50th Anniversary Volume*, D.W. Fuerstenau, Editor. 1962, AIME. p. 215-246.
10. Ye, Y., S.M. Khandrika, and J.D. Miller, *Induction-time measurements at a particle bed.* International Journal of Mineral Processing, 1989. **25**(3-4): p. 221-240.
11. Eigeles, M.A. and M.L. Volova. *Kinetic investigation of effect of contact time, temperature and surface condition on the adhesion of bubble to mineral surfaces*. in *5th International Mineral Processing Congress*. 1960. London: Inst. Min. Metall.
12. Gu, G., et al., *Effects of physical environment on induction time of air-bitumen attachment.* International Journal of Mineral Processing, 2003. **69**(1-4): p. 235-250.
13. Hewitt, D., D. Fornasiero, and J. Ralston, *Bubble-particle attachment.* Journal of Chemical Society, Faraday Transactions, 1995. **91**: p. 1997-2001.
14. Blake, P. and J. Ralston, *Controlled methylation of quartz particles.* Colloids and Surfaces, 1985. **15**: p. 101-118.
15. Xu, Z. and R.-H. Yoon, *The role of hydrophobia interactions in coagulation.* Journal of Colloid and Interface Science, 1989. **132**(2): p. 532-541.
16. Mao, L. and R.-H. Yoon, *Predicting flotation rates using a rate equation derived from first principles.* International Journal of Mineral Processing, 1997. **51**(1-4): p. 171-181.
17. Zhang, J., et al., *Effects of Degassing and Ionic Strength on AFM Force Measurements in Octadecyltrimethylammonium Chloride Solutions.* Langmuir, 2005. **21**(13): p. 5831-5841.

18. Do, H., *Development of a turbulent flotation model from first principles*, in *Engineering Science and Mechanics*. 2010, Virginia Polytechnic Institute and State University: Blacksburg.
19. Do, H. and R.H. Yoon, *A flotation model under turbulent flow conditions.* Journal of Colloid and Interface Science, 2010. **submitted**.
20. Do, H. and R.H. Yoon, *A turbulent flotation model derived from first principles*, in *23rd International Mineral Processing Congress*. 2006: Istanbul, Turkey.
21. Pan, L. and R.H. Yoon, *Hydrophobic forces in wetting films of water formed on Xanthate-coated gold surfaces.* Faraday discussion, 2010. **146**: p. xxx-xxx.
22. Finch, J.A. and G.W. Smith, *Bubble-solid attachment as a function of bubble surface tension.* Canadian Metallurgical Quarterly, 1975. **14**(1): p. 47-51.
23. Wang, J. and R.H. Yoon. *Surface forces measured between Xanthate-coated gold surfaces*. in *ECS meeting*. 2010. Vancouber, Canada.
24. Ivanov, I.B. and D.S. Dimitrov, *Hydrodynamics of thin liquid films.* Colloid & Polymer Science, 1974. **252**(11): p. 982-990.
25. Ruckenstein, E. and R.K. Jain, *Spontaneous rupture of thin liquid films.* Journal of Chemical Society, Faraday Transactions 2, 1974. **70**: p. 132-147.
26. Vrij, A. and J.T.G. Overbeek, *Rupture of thin liquid films due to spontaneous fluctuations in thickness.* Journal of the American Chemical Society, 1968. **90**(12): p. 3074-3078.
27. Hogg, R., T.W. Healy, and D.W. Fuerstenau, *Mutual coagulation of colloidal dispersions.* Transactions of Faraday Society, 1966. **62**: p. 1638-1651.
28. Rabinovich, Y.I. and N.V. Churaev, *Effect of electromagnetic delay on the forces of molecular attraction.* Kolloidnyi Zhurnal, 1979. **41**(3): p. 468-474.
29. Yoon, R.-H. and L. Mao, *Application of Extended DLVO Theory, IV: Derivation of Flotation Rate Equation from First Principles.* Journal of Colloid and Interface Science, 1996. **181**(2): p. 613-626.
30. Ducker, W.A., Z. Xu, and J.N. Israelachvili, *Measurements of Hydrophobic and DLVO Forces in Bubble-Surface Interactions in Aqueous Solutions.* Langmuir, 1994. **10**(9): p. 3279-3289.
31. Usui, S., H. Sasaki, and H. Matsukawa, *The dependence of zeta potential on bubble size as determined by the dorn effect.* Journal of Colloid and Interface Science, 1981. **81**(1): p. 80-84.
32. Yoon, R.-H., D.H. Flinn, and Y.I. Rabinovich, *Hydrophobic Interactions between Dissimilar Surfaces.* Journal of Colloid and Interface Science, 1997. **185**(2): p. 363-370.
33. Xu, Z. and R.-H. Yoon, *A study of hydrophobic coagulation.* Journal of Colloid and Interface Science, 1990. **134**(2): p. 427-434.

CHAPTER 4

DEVELOPING A DRAINAGE MODEL IN FOAMS INCORPORATING HYDROPHOBIC FORCE

Abstract

A foam drainage model that can predict bubble coarsening has been derived by considering that drainage rate increases with increasing the hydrophobic force. Hydrophobic force is the force that attracts two surfaces of air bubbles and reduces the interstitial liquid amount to a critical value for bubble coalescence. Therefore, hydrophobic force should be considered in the modeling of foam drainage, but no model in the literature addresses its significance. In the present report, however, the flow rates with and without hydrophobic force considerations have been compared to derive the relation between the flow increase and hydrophobic force. As a result, it was found that the average flow velocity increases by the relative significance of the hydrophobic force to Van der Waals force. The change of the number of bubbles due to coalescence was coupled to the drainage model by assuming that the number decreases exponentially with the local changes of liquid fraction.

1. Introduction

1.1 Foam Drainage Equation

Foam is a colloidal system where gas bubbles are separated by thin liquid films. It has a wide range of applications such as food processing, sanitary systems, chemical reactors, froth flotation and so forth. Despite a wide applicability, the mechanisms for controlling foam stability are not fully understood due to complexities involved. A theoretical model is required to understand spatial and temporal kinematics of gas-liquid distributions and to describe the instability, which would be of great advantage to some industrial applications. For example, mining industries will benefit especially from such advancement because the properties of foam are critical controlling parameters that determine the rate of froth flotation, the industry's most important separation process.

The fluid in a foam flows through the network of channels, known as *plateau borders* (PB), which serves as the predominant channels of fluid flow. The PBs are randomly oriented and inter-connected through nodes where the segments of PBs meet. The bubble films osculated to the PBs are called the *lamellae*, but they are not considered to play important role in most of drainage models developed to date. It is assumed that channel (or PB) flow is dominant [1-4].

The flow through the channels is described by the continuity equation,

$$\frac{\partial \varepsilon}{\partial t} + \frac{\partial (\varepsilon U)}{\partial x} = 0 \quad , \tag{1}$$

where ε is the local liquid fraction defined as the ratio of area occupied by liquid to total cross-sectional area, U is the average velocity of flow through PBs, and x is the draining direction. Equation (1) basically states that the rate of change of the liquid mass flow inside a PB is balanced by the changes induced by the flow velocity through the surface area. Typically, U is derived assuming the Poiseuille flow in a pipe, *i.e*. no slip at the interfacial wall [1-6] while some, but not many, derived U assuming plug flow inside PBs [7, 8]. In either case, the assumptions are valid depending on the characteristics of foam. For example, no-slip at the plateau border wall is valid when the foam is made from high concentration surfactant solutions [9]. On the other hand, no-slip boundary condition is not strict valid. Flexible boundary conditions may also be useful, depending on the amounts of liquids held and the chemicals used [10].

Following the definition of ε, Eq.(1) can be expressed in terms of the total number of PBs (N_{PB}) and the average cross-sectional area of a single PB (A).

$$\frac{\partial N_{PB} A}{\partial t} + \frac{\partial (N_{PB} A U)}{\partial x} = 0 \tag{2}$$

In foams, thin fluid film breakage causes bubble coarsening and change in N_{PB}. However, the dynamics of coarsening bubbles has not been fully understood, but it is necessary to

incorporate bubble coarsening in modeling foam drainage. Most of the drainage models developed to date assume that N_{PB} is constant, which has been shown to be the case for dry and stable mono-dispersed foams of polyhedral bubbles. However, foam drainage models developed without considering dynamics of coarsening are not useful in a sense that drainage rates of industrial foams are much faster than predicted by the models. An attempt has been made recently to relate foam drainage equation with the dynamics of N_{PB} by Cox *et al*.[11]. The authors explained qualitatively how drainage is affected by changing bubble sizes by considering N_{PB} as a random distribution function. Using a similar approach, one can obtains the following equation.

$$\frac{\partial A}{\partial t} + \frac{\partial (AU)}{\partial x} + A\left(\frac{\partial \ln N_{PB}}{\partial t} + U\frac{\partial \ln N_{PB}}{\partial x}\right) = 0 \qquad (3)$$

Using Eq.(3), foam drainage is generalized by taking into account the dynamics of coarsening. Details are discussed in the following sections.

1.2 Film and node contribution in foam drainage

The role of lamellae films in foam drainage has not been fully understood yet, but it is obvious that drainage is generally disturbed due to film drainage and ruptures. Many models of film drainage and film rupture have been introduced [12-14], but none of them can be considered generic or sufficiently verified in experiment. It is partly because so many variables are involved in film dynamics under various conditions, and also because the present understandings are based on many controversial evidences. Because those models mostly consider horizontal films, employing them to foam drainage is inappropriate in that foam films have various orientations. In addition, let alone the film dynamics modeling, incorporating the drainage and rupture inside films with drainage model is another challenge.

Of those few who took this challenge, some succeeded in the modeling, only with boundary conditions that liquids flow from films into PBs [15-17]. However, these conditions may betray the real phenomena according to the observation by Carrier *et al.*[18]. The authors found liquids in vertical films flow across from the upper node to the lower, and left the possibility of liquid flowing through films.

In addition to the interpretation of the film's role in foams, the role of PB nodes is also intriguing. The importance of nodes in foam drainage was first posed by Koehler *et al*. [19] who studied both experimentally [10, 19] and numerically [11, 18]. Koehler *et al*. [19] observed the significant change of the correlation between liquid influx rate and the flow's front wave velocity in foams under certain conditions. The authors then attributed the change to the transition of flow characteristics between the PB-dominated flow and the node-dominated flow. In fact, the latter was devised to explain the unexpected flow enhancement by relaxing the no-slip boundary condition at the plateau border walls.

The two, films and nodes in foam, play significant roles in changing the flow characteristics because films, nodes, and plateau borders dynamically interplay with each other. However, the present work regard films and nodes simply as extra fluid volume, hence, substitute the term N_{PB} with N^* which is newly defined as the *effective* number of PBs comprising film's and node's contribution. Eq.(3) may then be rewritten as follows.

$$\frac{\partial A}{\partial t} + \frac{\partial (AU)}{\partial x} + A\left(\frac{\partial \ln N^*}{\partial t} + U\frac{\partial \ln N^*}{\partial x}\right) = 0 \qquad (4)$$

1.3 Various views on foam drainage

The average draining velocity U in Eq. (4) can be expressed analytically by integrating the axial flow profiles in a single plateau border [3, 20-22], or by an analogy with Darcy's law for flows in porous media [2, 7, 23]. Since Darcy's law does not describe the details of flows but indicates only the effective permeability as the coefficient of the correlation between flow velocity and pressure gradient, U's in the corresponding references are based on the semi-empirical relation for the coefficient of Darcy's equation. The coefficient is hard to obtain analytically since foam permeability interplays with so many variables [24]. As a matter of fact, there is no report that verified the theoretical value of U in an isolated plateau border. The closest may be the work by Pitios *et al.* [25] in which PB channels had to be exaggerated for experimental convenience. On the other hand, some researchers measured flow rates in a volume of foam and later showed the validity of theoretically estimated U [2, 7, 23]. In both cases, it was found that the theoretical value of U is lower than the experimentally obtained value in certain systems.

The discrepancy is explained in several different aspects. One prevalent aspect is that foam's rheological property, i.e., surface viscosity, is responsible for the difference. Surface viscosity was originally postulated by Boussinesq [26] to explain the unexpected retardation in fluid droplet's settling velocity, and it had invoked many researchers for many decades into the controversy over its real identity. In fact, the surface viscosity may be phenomenally identical to the Marangoni effect but simply observed in different aspects, as it was stated in the historical review of interfacial rheology by Edwards *et al* [27]. Under the premise that surface viscosity is a unique physical property of a fluid interface, some models for the average flow velocity introduced a mobility parameter [3, 22, 28] or its inverse, the Boussinesque number [20], to fit the model to the actual experimental data. However, the parameter can be considered an adjustable constant because there is not a good method yet to measure the surface viscosity of practical foams [29]. In addition, the surface viscosity measurement may be erroneous due to the intimate coupling of bulk and interfacial viscous effects [27].

With a more general aspect on the problem, Durand and Langevin [23] analyzed the average flow velocity in a way that the mobility parameter can be related to the interfaces' diffusivity, surfactant solubility, elasticity, and so on. As a result, their drainage model coupled

with the average PB flow velocity conformed to the drainage model of Koehler *et al.* [7] when the parameter was large, and to the model by Verbist *et al*. [1] when the parameter was small. The model, however, did not provide good verification.

For all the different aspects, solving drainage equation in consideration of such various parameters may not be a good approach because it requires too many independent variables to be estimated, as well as precise experimental technique. Therefore, the current work will simplify the problem after ignoring the dynamical change of fluids in films and nodes by lumping them into N^* as seen in Eq.(4). On the other hand, the foam drainage is incorporated with bubble coalescence and the *slip* velocity inside PBs. *Slip* is defined as any situation in dynamics of fluids where the value of tangential component of the velocity appears to be different from that of the solid surface immediately in contact with it [30]. Slip velocity is a controversial topic also, especially in foam.

However, the relationship between the slip and wetting property of interface, the contact angle, is relatively well known even though the origin of slip velocity is ambiguous. According to various experimental data, slip is more apparent in the flows on the surface that induces high contact angle [30]. This observation may be interpreted such that the same relationship exists between slip and the hydrophobicity, because contact angle is commonly regarded as an indicator for the degree of *hydrophobic* force. Hydrophobic force is an attractive interfacial force that is known to enhance the flow between two hydrophobic surfaces immersed in water [31]. The air-water interface is also a hydrophobic surface [32-35], but no good theory on the origin of hydrophobic force is yet to emerge. Nevertheless, the force should be considered in the modeling of foam drainage so that one can have more practical approach. Regarding this, the present work will show that slip is in fact a reasonable way to account the role of hydrophobic force in foam drainage. In conjunction with the hydrophobic force, the change in PB numbers due to coarsening and the slip velocity will be derived in the following as well, so that they can be combined with the drainage model.

2. Model Development

To incorporate the hydrophobic force in foam drainage model, it is first necessary to introduce the disjoining pressure in foams. By definition, disjoining pressure is the difference between the pressure in the bulk of one phase and the pressure at the intervening phase between two surfaces. It is a common concept in colloid science and can be predicted by the DLVO theory [36]. DLVO theory accounts for the total surface interaction energy as the combined effect of well-known surface forces: electrostatic force and Van der Waals dispersion force. However, this theory is not applicable for the thin water films confined between two hydrophobic surfaces as in foams [37, 38]. Therefore, additional attraction force between hydrophobic surfaces needs to be considered. In this regard, the disjoining pressure in a foam film may be given as [38, 39],

$$\Pi = \Pi_E + \Pi_W + \Pi_H \quad (5)$$

where Π_E is the pressure due to electrostatic repulsion force, Π_W is the pressure due to the Van der Waals force, and Π_H is the same due to hydrophobic force. Given H as the separation distance between two surfaces, Π_E is expressed by the following equation for simplicity [40].

$$\Pi_E = \alpha \exp(-\kappa \cdot H), \quad (6)$$

where κ is the inverse Debye length, and α is a constant determined by the system properties.

The disjoining pressure due to Van der Waals force is also given by [40]

$$\Pi_W = -\frac{A_{232}}{6\pi(H)^3}, \quad (7)$$

where A_{232} is the Hamaker constant with the subscript 232 meaning that two air bubbles **2** interact across an aqueous media **3** (water).

It is assumed here that the magnitude of disjoining pressure due to hydrophobic force decays with the separation distance H by the same power law as in Π_W, *i.e*.

$$\Pi_H = -\frac{K_{232}}{6\pi(H)^3}, \quad (8)$$

where K_{232} is the hydrophobic force constant with the subscript meaning the same as in Eq. (7). At present, no one knows the origin of the hydrophobic force. Under this situation, it may be acceptable to represent Π_H in the same form as with Π_W [41].

2.1 Average velocity of flow inside PBs

The model represented by Eq. (4) can be simplified if the average velocity of flow through PBs (U) is expressed in terms of PB area (A). U has been analytically modeled by many investigators [2, 3, 5, 6, 20, 22, 42]. The various models converge to the following fundamental expression,

$$U = \frac{A}{3\varphi\mu}\frac{dP}{dx} \quad (9)$$

where the PB cross sectional area, A, is a variable that changes with the position and time in a foam, μ is viscosity, and φ is a factor determined solely by the cross-sectional shape [43]. For example, the factor is 8π for a circular section, 34.6 for a triangular section [4, 22], and 49.1 for the cross section of PBs [3]. The factor, 1/3, in Eq. (9) used because U is an average of all possible PB orientations [4, 23]. P is the pressure inside PB, and typically it consists of gravitational and capillary forces. In addition, disjoining pressure is also taken into consideration. Thus,

$$P = \rho g x + \frac{\gamma}{r_{PB}} - \Pi \tag{10}$$

where ρ is liquid density, g is gravity, A is the PB cross-sectional area, γ is surface tension, r_{PB} is the radius of curvature of PB. The PB cross-sectional area can be as $A = C^2 r_{PB}^2$, where C is approximately 0.4 for a tricuspid-shaped PB cross-section and r_{PB} is the PB radius Π is the disjoining pressure represented by Eq. (5). Assuming for simplicity that hydrophobic force component is the most dominant term in Π and the unit length of the separation distance between two PB walls is $2r_{PB}$, one obtains,

$$\Pi \approx \beta \frac{K_{232}}{(2r_{PB})^3} \tag{11}$$

where β is the coefficient taking into account the geometry of PB. Differentiating the disjoining pressure with respect to x,

$$-\frac{d\Pi}{dx} = \beta K_{232} \frac{3}{(2r_{PB})^4} \frac{d2r_{PB}}{dx} = \frac{3\beta K_{232} C^{3/2}}{16} \frac{1}{A^2\sqrt{A}} \frac{dA}{dx} \tag{12}$$

Therefore, from Eqs. (9), (10) and (12), the average flow velocity is obtained as follows.

$$U = \frac{1}{3\varphi\mu}\left[\rho g A - \left(\frac{C\gamma}{2} - \frac{3\beta K_{232} C^3}{16A}\right)\sqrt{A}\frac{\partial A}{\partial x}\right] \tag{13}$$

Although Eq. (13) is the correct expression incorporating the effect of hydrophobic force component of disjoining pressure, it is necessary to compare the order of magnitude of each term. Noting that K_{232}/A is typically in the order of 10^{-11}~10^{-12} N/m^2 while γ is in 10^{-3} N/m$_2$, the disjoining pressure term is negligible and Eq. (9) reduces to:

$$U = \frac{1}{3\varphi\mu}\left[\rho g A - \frac{C\gamma}{2}\sqrt{A}\frac{\partial A}{\partial x}\right] \tag{14}$$

A contribution from the surface tension gradient may have to be added to Eq. (10), as authors like Stein and Laven [9] criticized, but it is excluded for this research because there is yet no good analytical formula describing surface tension gradient in foam systems. In fact, Eq.(10) corresponds to the model for U that was derived under no-slip boundary condition without considering the disjoining pressure terms [43, 44]. This may indicate that hydrophobic force or disjoining pressure has no significant effect on the flows through PB channels. However, this conclusion is contrary to the observation that hydrophobized porous media reveal enhanced flow rate [45-47]. Therefore, the discrepancy may be compensated by introducing slip velocity at PB walls.

2.2 Slip velocity on hydrophobic interfaces

Flows in foam PBs are analogous to the one through micro channels of solid walls. The slip velocity in micro channels of solid walls has been well reviewed in other literature, and the

controversy on various possible origins of slip has been numerated [30]. For example, surface roughness is suspected as one of possibilities because rough surfaces produce the regions where gas molecules are trapped, and the regions are regarded responsible for the slip of liquids flowing over the gas layer [30, 48]. In the same context, the slip is also presumed coming from the nanobubbles present near hydrophobic surfaces [30, 49].

On the contrary, if there is no gas trapped between the wall troughs or dissolved in the liquid, surface roughness should suppress the slip because rough surface induces resistance of the fluid at the interface. On the other hand, many experimentalists observed slip on solid surfaces with special treatment even after degassing the liquid [45, 50, 51]. This suggests that the slip may not result from gas layers on the surface, but from special surface treatment. The surface treatment mentioned here indicates controlling the wetting property of the surface. The wetting property is typically estimated by measuring contact angles, which is a criterion for evaluating the degree of hydrophobicity. Therefore, hydrophobicity of the surface seems to have strong correlations with the slip velocity in micro channels. The effect of hydrophobic interaction related to slip phenomena has been reviewed [52].

According to the data on solid surfaces of various contact angles, the average flow velocity in micro channels should be augmented by slip velocities by means of a factor f ,

$$f = 1 + \frac{4\lambda}{a} \tag{15}$$

where λ is the slip length and a is the radius of the flow channel [30]. The slip length is defined as the extrapolation of channel radius at which zero fluid velocity is imposed. The value of λ is usually measured from experiments either directly or indirectly, but the ratio λ/a may be approximated once the surface interaction forces in the channel are known.

The factor, f, given by Eq. (15) is applicable to solid hydrophobic surfaces. However, it is assumed that the foam PB walls also follow the same relationship between the hydrophobicity and slip. Given that the contact angle or hydrophobic force parameter of the channel wall is an indicator for slip velocity [30], this assumption is valid because liquid-air interface is highly hydrophobic [32-35]. Based on this assumption, λ/a in Eq. (15) may be estimated as described below.

Suppose a PB in a foam. For simplicity's sake, consider an axis-symmetric Poiseulle flow problem for a circular pipe of radius a as shown in Fig.1. Solving the Navier-Stokes equations with no-slip conditions at the pipe walls, one obtains the velocity profile as follows (profile 1),

$$u_1(R) = -\frac{1}{4\mu}\frac{\partial P_1}{\partial x}(a^2 - R^2) \tag{16}$$

where μ is the viscosity of the fluid, R is the distance from the pipe center in vertical direction, and P_1 is the driving pressure.

One obtains another velocity profile for the case of slip by applying the boundary condition that u is zero at the imaginary position outside the channel perimeter as described in Fig. 1 (profile 2). One can find in this case that

$$u_2(R) = -\frac{1}{4\mu}\frac{\partial P_2}{\partial x}((a+\lambda)^2 - R^2)\,, \tag{17}$$

where λ is again the slip length defined as the fictitious distance outside the surface where the no-slip boundary condition is satisfied.

The heads of the flow profiles, u_1 and u_2, are considered equal because the disjoining pressure in PB channel is considered negligible in deriving Eq. (14). Therefore, the profile of $u_2(R)$ is simply a translation of $u_1(R)$ in x direction by the value u_2 at $R = a$ [53]. On this ground, λ can be approximated by comparing the integrands of the two velocity profiles, *i.e.*,

$$\int_{-a-\lambda}^{a+\lambda} u_2(R)dR - \int_{-a}^{a} u_1(R)\,dR = (\lambda + 2a)u_2(a) \tag{18.1}$$

$$\therefore \lambda = \sqrt[3]{-4 + 4\frac{\partial P_1}{\partial P_2}}\,a \tag{18.2}$$

The driving pressures P_1 and P_2 have the following expressiond considering both the capillary pressure and interfacial forces [21].

$$P_1 = -\frac{\gamma}{r_{PB}} + P_g + \Pi_{\mathrm{W,E,H}} \tag{19.1}$$

$$P_2 = -\frac{\gamma}{r_{PB}} + P_g + \Pi_{\mathrm{W,E}} \tag{19.2}$$

Here, γ is the surface tension, r_{PB} the radius of curvature of PBs, P_g the gas pressure, and Π is the

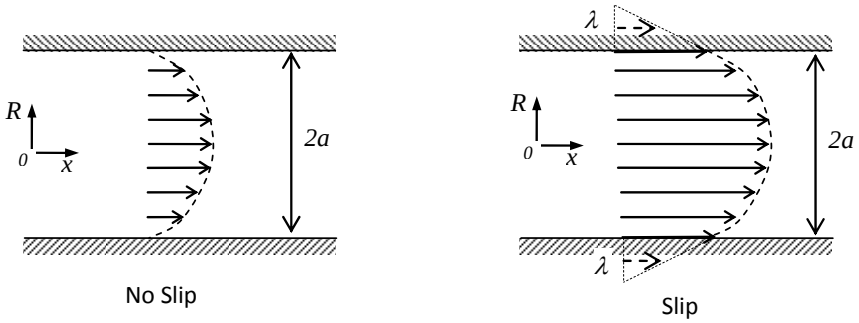

Figure. 1. Poiseulle flow in a cylindrical pipe. Velocity profile 1 with no slip boundary condition (left) and profile 2 with slip (right).

disjoining pressures. Π is th sum of the pressures due to the attractive van der Waals force (W), repulsive electrostatic force (E), and attractive hydrophobic force (H). The van der Waals and hydrophobic components of Π are given as follows:

$$\Pi_{\mathrm{W}} = -\frac{A_{232}}{6\pi(2a)^3} \tag{20}$$

$$\Pi_{\mathrm{H}} = -\frac{K_{232}}{6\pi(2a)^3} \tag{21}$$

The values of A_{232} and K_{232} are easily available in the literature, including those of Wang and Yoon [54-56].

Assuming P_g to be constant, and taking the partial derivatives of P_1 and P_2 with respect to the separation distance $2a$,

$$\frac{\partial P_1}{\partial P_2} = \frac{\partial P_1/\partial 2a}{\partial P_2/\partial 2a} = \frac{\frac{\gamma}{r_{PB}{}^2}\frac{\partial r_{PB}}{\partial 2a} - \kappa\alpha\exp(-\kappa\cdot 2a) + \frac{A_{232}}{2\pi(2a)^4} + \frac{K_{232}}{2\pi(2a)^4}}{\frac{\gamma}{r_{PB}{}^2}\frac{\partial r_{PB}}{\partial 2a} - \kappa\alpha\exp(-\kappa\cdot 2a) + \frac{A_{232}}{18\pi(2a)^4}} \tag{22}$$

Here, the value for A_{232} = 2.95×10^{-21}J is considered to be constant, although there is a degree of variations for different systems [37, 57]. Since the double layer force term and $\partial r_{PB}/\partial 2a$ are negligible, Eq.(22) may be simplified further as,

$$\frac{\partial P_1}{\partial P_2} \approx 1 + \frac{K_{232}}{A_{232}} \tag{23}$$

After substituting Eq. (23) into Eq. (18.2), one finds the ratio between λ and a to be,

$$\frac{\lambda}{a} = \sqrt[3]{\frac{4K_{232}}{A_{232}}} \tag{24}$$

Eq. (24) indicates that PB wall's no slip condition is valid when there is no hydrophobic interaction in PB or much less than the Van der Waals force, and hydrophobic surfaces induce faster drainage due to slip.

2.3 Bubble coalescence in foam

Although the present drainage model represented by Eq.(4) does not show any parameter representing film rupture process, it certainly describes the effect due to flows in lamella films and film rupture by introducing additional term, *i.e.*, effective number of PBs (N*). Knowing that N* is simply a modification of N_{PB}, the relation between N_{PB} and the number of bubbles, N_{B}, should be the first concern. There are no functional relations between $N_{\mathrm{B,}}$ and N_{PB}. Nevertheless, it is general known that N_{PB} is proportional to N_{B} by a factor n_{pb}, which is defined as the average number of PBs per a bubble. n_{pb} should actually be a variable for topological properties. For example, n_{pb} = 2 if foam is packed with spherical bubbles, and n_{pb} = 10 for pentagonal

dodecahedra cells [42]. However, in the present model, it is considered to be a constant for simplicity. It will eventually be shown that the value of $n_{pb}$is trivial in the final form of drainage model.

Aside from the argument for actual numbers of N_{PB}, n_{pb}, and N_{B}s, one useful form describing the bubble population change may be the exponential decay in time [58]. On this basis, the following is suggested for predicting N^* in Eq.(4).

$$N^* = n_{pb}^* N_b = n_{pb}^* \times N_{B,0} \exp\left(-C\sqrt{\frac{A_{crit}}{A}}\right) \tag{25}$$

where n_{pb}^* is the effective number of PBs per cell, $N_{B,0}$ is the initial number of bubbles, and the term in the bracket is devised to incorporate the instability of the bubble. Again, n_{pb}^* should end up trivial in the final drainage model. A_{crit}, is the critical PB area, a threshold value for A at which bubbles are more likely to rupture due to instability. C is an adjustable parameter. Although arbitrary value is given in the present report, A_{crit} may be determined by chemical characteristics such as surfactant concentration. This will be addressed in the discussion section. By Eq.(25), local values of the average bubble size can be predicted as well, using the resultant liquid holdup profile. Examples will be given in the later sections of this report.

2.4 Foam drainage equation

Substituting Eq.(25) into Eq.(4) and rearranging, the following is obtained.

$$\frac{\partial A}{\partial t} + \frac{1}{1+C\sqrt{\frac{A_{crit}}{A}}}\frac{\partial}{\partial x}(AfU) + \left(\frac{C\sqrt{\frac{A_{crit}}{A}}}{1+C\sqrt{\frac{A_{crit}}{A}}}\right) fU\frac{\partial A}{\partial x} = 0 \tag{26}$$

Eq. (26) can be solved numerically, along with U in Eq. (14). Note that this equation is reduced to the classical foam drainage equation widely cited and reviewed in the literature [1], when there is no-slip at the PB walls (f=1), and bubbles are stable in size (C=0).

It is necessary to non-dimensionalize the governing equations for numerical accuracy and also for obtaining generality in comparing with any data available in various systems. Given $x_0 = \sqrt{0.4\gamma/\rho g}$ and $t_0 = 3\mu_{eff}/\sqrt{0.4\gamma\rho g}$, Eqs.(14) and (26) are nondimensionalized using the following variables.

$$A = \alpha {x_0}^2 \qquad x = \xi x_0 \qquad t = \tau t_0 \qquad u = v(t_0/x_0) \tag{27}$$

Therefore, the final non-dimensional forms of Eqs. (14) and (26) are,

$$\frac{\partial \alpha}{\partial \tau} + \frac{1}{1+C\sqrt{\frac{\alpha_{crit}}{\alpha}}} \frac{\partial}{\partial \xi}(\alpha f v) + \left(\frac{C\sqrt{\frac{\alpha_{crit}}{\alpha}}}{1+C\sqrt{\frac{\alpha_{crit}}{\alpha}}} \right) f v \frac{\partial \alpha}{\partial \xi} = 0 \tag{28.1}$$

$$v = \alpha - \frac{1}{2\sqrt{\alpha}} \frac{\partial \alpha}{\partial \xi} \tag{28.2}$$

3. Simulation Results and Model Verification

The drainage model represented by Eqs. (28.1) and (28.2) was solved numerically using the finite difference method. Figure 2 shows the results of the numerical simulations of free drainage in the proposed model. The model parameters were arbitrarily chosen. Comparing the liquid profiles along the foam column at the drainage time of τ=100, figure 2A shows that hydrophobic force enhances the drainage. The bubble size changes along the foam column corresponding to the liquid drainage are plotted together, as shown in Figure 2B. Therefore, Figure 2 suggests that bubbles grow with lower liquid fraction, as it was intended in the coalescence model in Eq. (25). The conclusion is that larger bubbles induce faster drainage, which is also consitent with experimental observations in other literature [59, 60]. Figure 3 indicates this typical observation more clearly by the simulated plot of the liquid fraction and bubble size change in time. The time at which liquid fraction start diminishing corresponds approximately to the point at which bubble size starts increasing.

In addition to the numerical example, the model simulation is verified with experiment. The wetness of coarsening foam was estimated by measuring the local and temporal changes of

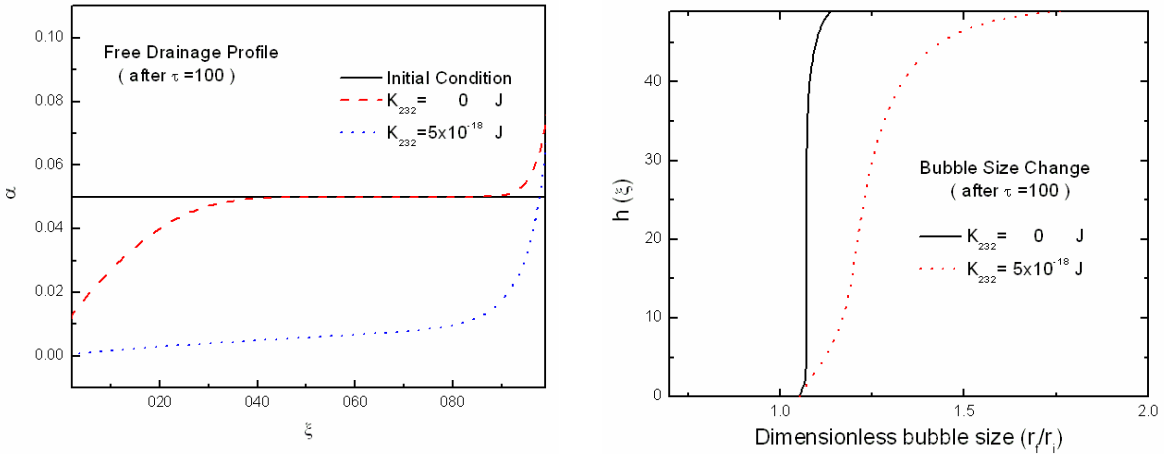

Figure. 2. A) An example of the free drainage profile (left). It indicates that hydrophobic force enhances flow rate. ξ represents the distance from the top of the foam, α represents the amount of liquids held. B) the bubble size change corresponding to the liquid fraction change along the foam column heigh *h* (right). The bubble sizes were normalized by the initial size.

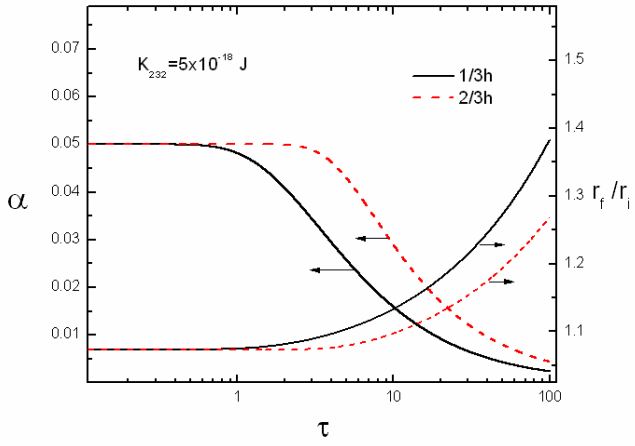

Figure. 3. Liquid fraction and bubble size change in time at the position 1/3 (solid line) and 2/3 (dashed line) of foam height. The time at which liquid fraction α starts diminishing corresponds approximately to the point at which the dimensionless bubble size (r_f/r_i) grows. Input parameters are the same with those used for Fig. 2.

capacitance in a foam column. The details of the methodology are described in the work by Do *et al*. [60]. In the present experiment, foam was made from the solution of 5×10^{-6} M Neodol 23-6.5 (molecular weight =480), allowing significant coarsening but the drainage to occur slow enough. Local changes of bubble sizes representing top, middle, and bottom of foam column were also recorded repeatedly, and averaged.

Figure 4 shows a comparison of the model with the data obtained. Given initial conditions,

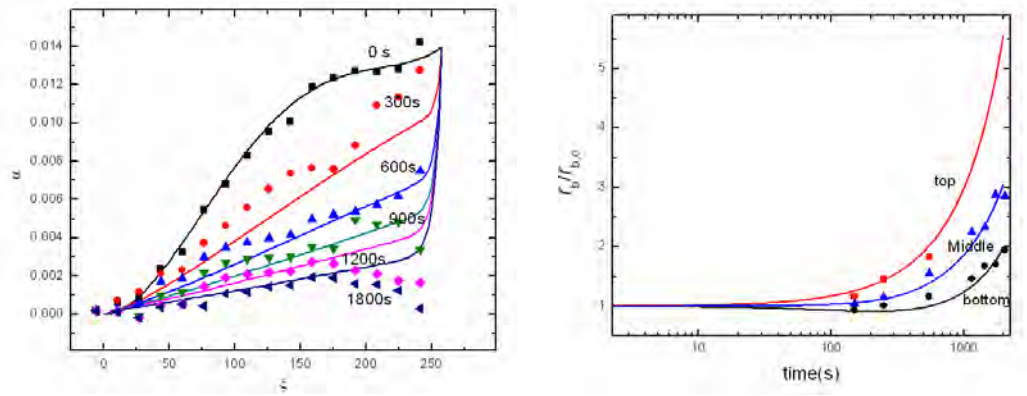

Figure. 4. Free drainage of coarsening foam compared with experimental data. The drainage profile (left), and bubble coarsening (right). The model used the following parameter values: $K_{232}=5\times10^{-19}$J. C=0.4, A_{crit}=0.1

and fitting parameters, i.e., A_{crit}=0.1 and C=0.4, the model predicted the changes in liquid profile as well as the bubble size change, which are in good agreements with experimental results. The results are also consitent with the typical observations that drier foams have higher rate of coarsening, or that large bubbles induce faster drainage [59-61].

4. Discussion

It should be noted again that A_{crit} in Eq.(26) is a parameter used in the present work as a measure of instability of foams at finite liquid fraction. The same concept has been employed for experimental studies [59]. However, critical rupture thickness (h_{cr}) is a more widely used measure for foam instability. Therefore, it may be used to derive a relation between A_{cr} and h_{cr}. The relationship between the film thickness and the radius of curvature of PB for dry, flowing foam was given by Hartland and Barber [62]. Their expression can be modified as follows,

$$\sqrt{A_{cr}} = 2.8\left(\frac{\mu R_s d_{2-max}^2}{\rho g}\right)^{1/4} h_{cr}^{1/4} \tag{29}$$

A and h have been replaced by A_{cr} and h_{cr}, respectively. Other parameters used in Eq. (29) include liquid density (ρ), dynamic viscosity (μ), and gravity (g). Also, R_s is the superficial surface area rate defined as the changes of bubble surface area per time per unit cross-sectional area, and $d_{2\text{-max}}$ is the maximum bubble size. R_s and $d_{2\text{-max}}$ may be considered adjustable parameters to correlate A_{cr} and h_{cr}, because they are not determined by the system properties. Therefore, as shown in this example, converting A_{cr} to h_{cr} does not have a particular advantage in applying to foam drainage equation as it will bring in additional parameters into the model. In fact, A_{cr} may be more convenient to use than h_{cr}, as the latter is useful for horizontal films only. Moreover, h_{cr} is especially difficult to measure if the foam is unstable and its measurement requires sophisticated instrumentation, while A_{cr} can be measured optically.

5. Summary and conclusion

A foam drainage model that can predict bubble coarsening has been developed. The model can be used to predict the changes in bubble size along the foam height. It has been a challenge to couple foam drainage and bubble coarsening. The model requires only two adjustable parameters to fit foam bubble size data, and is based on the premise that hydrophobic force is a significant factor in determining the drainage rate. The relation between hydrophobic force and slip length inside a plateau border has been derived and use to predict the changes in liquid fraction. The model shows the interdependency among hydrophobic force, liquid fraction, and bubble size and predicts that drainage rate becomes faster when bubble size becomes larger. The model predictions are in agreement with the experimental data.

6. References

1. Verbist, G., D. Weaire, and A.M. Kraynik, *The foam drainage equation.* Journal of Physics: Condensed Matter, 1996. **8**(21): p. 3715-3731.
2. Neethling, S.J., H.T. Lee, and J.J. Cilliers, *A foam drainage equation generalized for all liquid contents.* Journal of Physics: Condensed Matter, 2002. **14**(3): p. 331-342.
3. Leonard, R.A. and R. Lemlich, *A study of interstitial liquid flow in foam. Part I. Theoretical model and application to foam fractionation.* AIChE Journal, 1965. **11**(1): p. 18-25.
4. Gol'dfarb, I.I., K.B. Kann, and I.R. Shreiber, *Liquid flow in foams.* Fluid Dynamics, 1988. **23**(2): p. 244-249.
5. Haas, P.A. and H.F. Johnson, *A Model and Experimental Results for Drainage of Solution between Foam Bubbles.* Industrial & Engineering Chemistry Fundamentals, 1967. **6**(2): p. 225-233.
6. Koehler, S.A., et al., *Dynamics of foam drainage.* Physical Review E, 1998. **58**(2): p. 2097.
7. Koehler, S.A., S. Hilgenfeldt, and H.A. Stone, *A Generalized View of Foam Drainage: Experiment and Theory.* Langmuir, 2000. **16**(15): p. 6327-6341.
8. Kann, K.B., *Steady filtration through foam.* Fluid Dynamics, 1986. **21**(3): p. 420-425.
9. Stein, H.N. and J. Laven, *On the Validity of the Foam Drainage Equation.* Journal of Colloid and Interface Science, 2001. **244**(2): p. 436-438.
10. Durand, M., G. Martinoty, and D. Langevin, *Liquid flow through aqueous foams: From the plateau border-dominated regime to the node-dominated regime.* Physical Review E, 1999. **60**(6): p. R6307.
11. Cox, S.J., et al., *Applications and Generalizations of the Foam Drainage Equation.* Proceedings: Mathematical, Physical and Engineering Sciences, 2000. **456**(2002): p. 2441-2464.
12. Vrij, A. and J.T.G. Overbeek, *Rupture of thin liquid films due to spontaneous fluctuations in thickness.* Journal of the American Chemical Society, 1968. **90**(12): p. 3074-3078.
13. Ruckenstein, E. and R.K. Jain, *Spontaneous rupture of thin liquid films.* Journal of Chemical Society, Faraday Transactions 2, 1974. **70**: p. 132-147.
14. Ivanov, I.B. and D.S. Dimitrov, *Hydrodynamics of thin liquid films.* Colloid & Polymer Science, 1974. **252**(11): p. 982-990.
15. Desai, D. and R. Kumar, *Liquid holdup in semi-batch cellular foams.* Chemical Engineering Science, 1983. **38**(9): p. 1525-1534.
16. Bhakta, A. and E. Ruckenstein, *Decay of standing foams: drainage, coalescence and collapse.* Advances in Colloid and Interface Science, 1997. **70**: p. 1-124.
17. Ramani, M.V., R. Kumar, and K.S. Gandhi, *A model for static foam drainage.* Chemical Engineering Communications, 1993. **48**(3): p. 455-465.
18. Carrier, V., S. Destouesse, and A. Colin, *Foam drainage: A film contribution?* Physical Review E, 2002. **65**(6): p. 061404.
19. Koehler, S.A., S. Hilgenfeldt, and H.A. Stone, *Liquid Flow through Aqueous Foams: The Node-Dominated Foam Drainage Equation.* Physical Review Letters, 1999. **82**(21): p. 4232.
20. Nguyen, A.V., *Liquid Drainage in Single Plateau Borders of Foam.* Journal of Colloid and Interface Science, 2002. **249**(1): p. 194-199.
21. Bhakta, A. and E. Ruckenstein, *Drainage of a Standing Foam.* Langmuir, 1995. **11**(5): p. 1486-1492.

22. Desai, D. and R. Kumar, *Flow through a plateau border of cellular foam.* Chemical Engineering Science, 1982. **37**(9): p. 1361-1370.
23. Durand, M. and D. Langevin, *Physicochemical approach to the theory of foam drainage.* The European Physical Journal E: Soft Matter and Biological Physics, 2002. **7**(1): p. 35-44.
24. Stone, H.A., et al., *Perspectives on foam drainage and the influence of interfacial rheology.* Journal of Physics: Condensed Matter, 2003. **15**(1): p. S283-S290.
25. Pitois, O., C. Fritz, and M. Vignes-Adler, *Liquid drainage through aqueous foam: study of the flow on the bubble scale.* Journal of Colloid and Interface Science, 2005. **282**(2): p. 458-465.
26. Boussinesq, M.J., *Sur l'existance d'une viscosite' superficielle, dans la mince couche de transition separant un liquide d'une autre fluide contigu. .* Ann. Chim. Phys., 1913. **29**: p. 349-357.
27. Edwards, D.A., M.P. Brenner, and D.T. Wasan, *Interfacial transport process and rheology*. Butterworth-Heinemann series in chemical engineering. 1991.
28. Koehler, S.A., S. Hilgenfeldt, and H.A. Stone, *Foam drainage on the microscale: I. Modeling flow through single Plateau borders.* Journal of Colloid and Interface Science, 2004. **276**(2): p. 420-438.
29. Stevenson, P., *Dimensional analysis of foam drainage.* Chemical Engineering Science, 2006. **61**(14): p. 4503-4510.
30. Lauga, E., M.P. Brenner, and H.A. Stone, *Microfluidics: The No-Slip Boundary Condition*, in *Handbook of experimental fluid dynamics*, C. Tropea, A. Yarin, and J.F. Foss, Editors. 2007, Springer: New-York. p. 1219-1240.
31. Israelachvili, J. and R. Pashley, *The hydrophobic interaction is long range, decaying exponentially with distance.* Nature, 1982. **300**(5890): p. 341-342.
32. Craig, V.S.J., B.W. Ninham, and R.M. Pashley, *The effect of electrolytes on bubble coalescence in water.* The Journal of Physical Chemistry, 1993. **97**(39): p. 10192-10197.
33. Deschenes, L.A., et al., *Inhibition of Bubble Coalescence in Aqueous Solutions. 1. Electrolytes.* The Journal of Physical Chemistry B, 1998. **102**(26): p. 5115-5119.
34. Du, Q., E. Freysz, and Y.R. Shen, *Surface Vibrational Spectroscopic Studies of Hydrogen Bonding and Hydrophobicity.* Science, 1994. **264**(5160): p. 826-828.
35. van Oss, C.J., R.F. Giese, and A. Docoslis, *Hyperhydrophobicity of the Water-Air Interface*, in *Journal of Dispersion Science & Technology*. 2005, Taylor & Francis Ltd. p. 585-590.
36. Derjaguin, B.V. and S.S. Dukhin, *Theory of flotation of small and medium-size particles.* Transactions of Institutions of Mining and Metallurgy, 1961. **70**: p. 221-246.
37. Wang, L. and R.-H. Yoon, *Role of hydrophobic force in the thinning of foam films containing a nonionic surfactant.* Colloids and Surfaces A: Physicochemical and Engineering Aspects, 2006. **282-283**: p. 84-91.
38. Yoon, R.H. and L. Wang, *Hydrophobic forces in foam films*, in *colloids and interface science series*, Tadros, Editor. 2007, Wiley-VCH. p. 161-186.
39. Yoon, R.H., *The role of hydrodynamic and surface forces in bubble-particle interaction.* International Journal of Mineral Processing, 2000. **58**(1-4): p. 129-143.
40. Yoon, R.-H. and B.S. Aksoy, *Hydrophobic Forces in Thin Water Films Stabilized by Dodecylammonium Chloride.* Journal of Colloid and Interface Science, 1999. **211**(1): p. 1-10.

41. Wang, L., *A Response to the Comment on "Hydrophobic Forces in the Foam Films Stabilized by Sodium Dodecyl Sulfate: Effect of Electrolyte"*. Langmuir, 2008. **24**(9): p. 5194-5196.
42. Narsimhan, G. and E. Ruckenstein, *Structure, drainage and coalescence of foams and concentrated emulsions*, in *Foams: Theory, Measurments, and Applications*, R.K. Prud'homme and K.B. Kann, Editors. 1995, Marcel Dekker: New York.
43. Nguyen, A.V. and H.J. Schulze, *Colloidal Science of Flotation*. Surfactant science series. 2003: CRC Press.
44. Prud'homme, R.K. and S.A. Khan, eds. *Foams: theory, measurement, and applications*. surfactant science series. 1995, Marcel Dekker.
45. Henniker, J.C., *Retardation of flow in narrow capillaries.* Journal of Colloid Science, 1952. **7**(4): p. 443-446.
46. Pfahler, J., et al., *Liquid transport in micron and submicron channels.* Sensors and Actuators A: Physical, 1989. **22**(1-3): p. 431-434.
47. Hasegawa, T., M. Suganuma, and H. Watanabe, *Anomaly of excess pressure drops of the flow through very small orifices.* Physics of Fluids, 1997. **9**(1): p. 1-3.
48. Choi, C.-H. and C.-J. Kim, *Large Slip of Aqueous Liquid Flow over a Nanoengineered Superhydrophobic Surface.* Physical Review Letters, 2006. **96**(6): p. 066001.
49. Tretheway, D.C. and C.D. Meinhart, *A generating mechanism for apparent fluid slip in hydrophobic microchannels.* Physics of Fluids, 2004. **16**(5): p. 1509-1515.
50. HUANG, P., J.S. GUASTO, and K.S. BREUER, *Direct measurement of slip velocities using three-dimensional total internal reflection velocimetry.* Journal of Fluid Mechanics, 2006. **566**(-1): p. 447-464.
51. Huang, P. and K.S. Breuer, *Direct measurement of slip length in electrolyte solutions.* Physics of Fluids, 2007. **19**(2): p. 028104-3.
52. Meyer, E.E., K.J. Rosenberg, and J. Israelachvili, *Recent progress in understanding hydrophobic interactions.* Proceedings of the National Academy of Sciences, 2006. **103**(43): p. 15739-15746.
53. Tabeling, P., *Introduction to microfluidics*. 2005: Oxford university press.
54. Wang, L. and R.-H. Yoon, *Hydrophobic Forces in the Foam Films Stabilized by Sodium Dodecyl Sulfate:??Effect of Electrolyte.* Langmuir, 2004. **20**(26): p. 11457-11464.
55. Wang, L. and R.-H. Yoon, *Hydrophobic forces in thin aqueous films and their role in film thinning.* Colloids and Surfaces A: Physicochemical and Engineering Aspects, 2005. **263**(1-3): p. 267-274.
56. Wang, L. and R.-H. Yoon, *Effects of surface forces and film elasticity on foam stability.* International Journal of Mineral Processing, 2008. **85**(4): p. 101-110.
57. Israelachvili, J.N., *Intermolecular & surface forces*. 2nd ed. 1992: Academic press.
58. Szekrenyesy, T., K. Liktor, and N. S?dor, *Characterization of foam stability by the use of foam models 1. Models and derived lifetimes.* Colloids and Surfaces, 1992. **68**(4): p. 267-273.
59. Carrier, V. and A. Colin, *Coalescence in Draining Foams.* Langmuir, 2003. **19**(11): p. 4535-4538.
60. Do, H., et al., *Coarsening foam- Numerical modeling and experimental results*, in *Flotation 07 symposium*. 2007: Cape town, South Africa.
61. Saint-Jalmes, A. and D. Langevin, *Time evolution of aqueous foams: drainage and coarsening.* Journal of Physics: Condensed Matter, 2002. **14**(40): p. 9397-9412.

62. Hartland, S. and A.D. Barber, *A model for a cellular foam.* Trans. Instn Chem. Engrs, 1974. **52**: p. 43-52.
63. Saint-Jalmes, A., Y. Zhang, and D. Langevin, *Quantitative description of foam drainage: Transitions with surface mobility.* The European Physical Journal E: Soft Matter and Biological Physics, 2004. **15**(1): p. 53-60.
64. Saint-Jalmes, A., *Physical chemistry in foam drainage and coarsening.* Soft Matter, 2006. **2**(10): p. 836-849.

CHAPTER 5

PREDICTING THE CRITICAL RUPTURE THICKNESS OF FREE FOAM FILMS

ABSTRACT

A thin film ruptures when a fluid layer gets thinner than a critical thickness. In other literature, this critical thickness has been attempted to predict using the instability criteria for a wavy interface of the film. However, the predictions of those models deviate from experimental observations in the case of aqueous films at low surfactant concentrations. The discrepancy results from the hydrophobic force in the film, but the origin of the force has not been well understood yet. The force can be typically evaluated from film thinning kinetics data. On the other hand, there has been no model yet to incorporate it with the rupture. In this chapter, a model for predicting the critical rupture thickness has been derived by assuming that the hydrophobic force causes the instability of air-water film interfaces. As a result, the model could predict the rupture thickness and the time of rupture in the presence of the hydrophobic force.

1. Introduction

The drainage and rupture in thin liquid films have been of great interest among many researchers because understanding the subject is critical to the productivity improvement in certain industries. For example, the mining industry has been active in studying this subject because liquid film's thinning rate and rupture determine the efficiency of the flotation [1], the most widely practiced mineral separation technique in the industry.

With regard to the thinning of films in such applications, some interests remained only in the physics of film thinning due to the hydrodynamic forces between two approaching bubbles or spheres [2-4]. On the other hand, some researchers studied film thinning in the scale where interfacial forces is as significant as hydrodynamic forces, by incorporating the disjoining pressure to the Reyonolds equation [5, 6]. Disjoining pressure is practically the difference between the pressure in the bulk of liquid film and the pressure at the air-water interface. It is usually negligible in the large scale physical phenomena, but becomes significant in analyzing the colloidal scale problems such as foam films. However, in foam films, this approach was under criticism because the Reynolds equation had been derived originally for tangentially immobile surfaces while foam films may be regarded mobile. Therefore, many researchers relaxed the boundary condition of the Reynolds equation to match the theory and true experimental observations [7-9].

Even though it is still controversial whether foam film surface is mobile or immobile, the present work assumes the immobile boundary of foam films based on experimental evidences. Recently, Valkovska *et al*. [10] showed by a thinning rate model that the effect of disjoining pressure is more significant in film drainage / rupture than the effect of the interfacial mobility. Angaraska *et al*. [11] also checked the effect of surface mobility in small, thin aqueous films experimentally, but found it negligible even with the tiny amount of surfactant.

1.1 Thin film rupture models

The thinning rate of foam films may well be predictable on the premise that the Reynolds equation is valid with or without mobility considerations. On the contrary, predicting when films rupture is still a mystery. In general, film gets unstable as it thins down, but the actual thickness of rupture or the rupture time is hardly predictable because there is no universal criterion. This threshold of thickness at which films tend to break is defined as the critical rupture thickness, H_{cr}. Although the exact mechanisms of this instability are not vindicated so far, many authors [9, 12, 13] followed the criterion to reach H_{cr} suggested by Vrij [5]. Vrij's criterion is based on the idea that films fail when the waves on the air-water interfaces grow substantially, as first posed by Scheludko [14]. After observing scattered light on soap films, Vrij suggested that the reflections were possibly due to irregular corrugations of the film interface [15]. Then a theory for the rupture was made out of this hypothesis [5]. However, in finalizing the model equation for H_{cr},

he introduced an empirical correction factor to make the rupture thickness correspond with specific experimental examples [5, 16]. On the other hand, some authors took more mathematical account for the rupture with the same idea of 'fluctuating interfaces' [17-19]. In theory, their wave evolution was resulting from boundary disturbances, but no practical examples were given except for the numerical simulations based on arbitrary initial conditions.

The wave-induced instability also inspired other notable researchers like Ivanov *et al*. [9, 20]. Their rupture criterion was such that films break when the amplitude of the wave on each faces of the film is tall enough to touch each other. In their approach, the surface mobility was thought to be the most contributing factor to the rupture, but later the leading author had to contradict himself in the work with Valvoska *et al*.[10] by showing that mobility was insignificant. In addition, their own experimental data did not agree well with predictions [9]. In a similar approach, Ruckenstein and Jain [12] put in the derivation an extra potential energy term other than the energy due to Vand der Waals force. This term was regarded as perturbations of the surface potential due to fluctuating nature. In the authors' approach, all aspects such as surface viscosity, diffusion effect, and purity were implied in the model. Having a parameter subject to the surfactant's solubility and concentration, the model became identical with Vrij's model [5] when the concentration was high.

While the rupture criteria for the above-mentioned models were such that the critical thickness equals twice the amplitude of surface wave itself, Sharma and Ruckenstein [13, 21] set slightly different criterion. Assuming that rupture is caused by the relatively small 'thermal' fluctuations riding on the thinnest trough of the 'hydrodynamic' surface waves, the authors found numerically the relationship between film thickness and thermal fluctuation. Then a model was developed based on this relation [21]. The thermal fluctuation was also implemented within the model by Radoev *et al*. [8], who saw the problem as attaining the state of instability due to the Brownian motion on the surface, unlike the else who saw it as the consequence of the instability evolution.

The film rupture models introduced above are hardly universal since each model was verified only numerically or, at best, compared to data of specific conditions where interfacial forces were relatively well-understood. Moreover, for the interesting case of aqueous surfactant films, none of those models are close to practical observations because the films are much more unstable than expected due to an additional attractive force called hydrophobic force [22-25]. Hydrophobic force seems eminent in aqueous films of low surfactant concentrations in particular, and therefore it holds importance in areas like mineral processing where such a low concentration is commonly employed.

1.2 Hydrophobic force in aqueous surfactant films

The drainage rate or rupture of foam films is usually predicted by the Reynolds equation in the literature. However, many researchers had overlooked the existence of the attractive '*hydrophobic*' force in applying the disjoining pressure into the equation. Because the DLVO theory, that is used to calculate the interaction energies of colloidal scale interfaces, has been failing to conform with certain experimental data especially in the examples of hydrophobic surfaces [26], many researchers ascribed the discrepancy to this unveiled force. The force had been first observed between hydrophobic solid surfaces [27], but later, air bubbles forming liquid films were found strongly hydrophobic as well [28-31]. However, hydrophobic force in foam films has been particularly questioned by strong-believers of the DLVO theory [32]. Despite of this controversy, there are more evidences for the flaws of the obsolete theory than the unconvincing evidences of hydrophobic force [33, 34].

In the experiments on foam films by Wang and Yoon [22-25], the authors modified the DLVO theory by introducing the additional disjoining pressure induced by hydrophobic force (Π_H). The pressure term was assumed following the same power-law decay rule as the van der Waals force, such that

$$\Pi_H = -\frac{K_{232}}{6\pi H^3} \tag{1}$$

where K_{232} is the hydrophobic force constant ,and H is the film thickness. It should be noted that subscript 232 was devised for conveniently implying that the force exists in media 3 squeezed between media 2s, *i.e.* in the liquid film held between two air bubbles. Due to lack of complete theory, there is no direct measurement method of K_{232} value yet, but it can be found indirectly by analyzing the foam film thinning kinetics data [22-25]. The assumption that Π_H takes after the disjoining pressure induced by Van der Waals force has several advantages [34]. First, it is easy to compare hydrophobic force with the Van der Waals force, by simply assessing K_{232} and the Hamaker constant. In addition, as simple it is and has fewer variables, the given form in Eq.(1) may simplify the derivation of film rupture model. Therefore, Eq.(1) will be used in describing hydrophobic force in the present film rupture model. Details of model derivation shall be described in the next.

2. Modeling the rupture of thin films

It has been noted in the introduction that the film thinning velocity predicted by the Reynolds equation, V_{Re}, deviates from the practical observations in aqueous surfactant films [22-25]. This finding may be represented by the following relationship [9, 10],

$$V = f^3 V_{Re} \tag{2}$$

where V is the actual film thinning velocity, and f^3 is the coefficient that represents the difference between V and V_{Re}.

Substituting into Eq.(2) the Reynolds equation, one obtains the following.

$$\frac{2H^3}{3\mu R_f^2}\Delta P = f^3\frac{2H_{Re}^3}{3\mu R_{f_{Re}}^2}\Delta P \tag{3}$$

In Eq.(3), H is the film thickness, R_f is the film radius, μ is viscosity, and ΔP is the pressure difference. H and R_f with subscript Re indicate that they are the parameters pertaining to the ideal cases of Reynolds equation assumption: flat film, no-slip at the interface. Therefore, the actual film thickness observed at certain time can be expressed in terms of theoretical prediction after manipulating Eq.(3).

$$H = \left(R_f/R_{f_{Re}}\right)^{2/3} f H_{Re} \tag{4}$$

Based on this relationship, the actual critical rupture thickness H_{cr} may be estimated since all the terms in the right hand side of Eq.(4) at the time of rupture can be evaluated theoretically. In other words:

$$H_{cr} = \left(R_f/R_{f_{Re}}\right)^{2/3} f H_0 \tag{5}$$

where H_0 is the rupture thickness predicted from the film thinning kinetics using the Reynolds equation. In assessing H_0 theoretically, major assumption is that the film interfaces are stable and flat. However, it should be noted that, in the present work, thin liquid films are thought to be unstable due to fluctuations growing at the interfaces, and therefore their interfaces are not flat at least. Accordingly, a proper modification of the prediction theory for H_0 is necessary. This is described in the following section.

2.1 The rupture thickness predicted by the ideal theory

The major assumption in the present derivation of film rupture thickness is the film's fluctuating interfaces. The key idea was originally adopted from other researchers [5, 9, 12, 16], but more practical and statistical accounts are added.

In Figure 1, an example of a thin liquid film of median thickness H_{m} is presented with its corrugated surface profile superposed. For simplicity, the wave is assumed steady and to be represented by the following 2D profile (y).

$$y = \eta\sin\left(\frac{2\pi x}{\lambda}\right) \tag{6}$$

where η is the amplitude of the wave, λ is the wavelength, and x is the propagating direction.

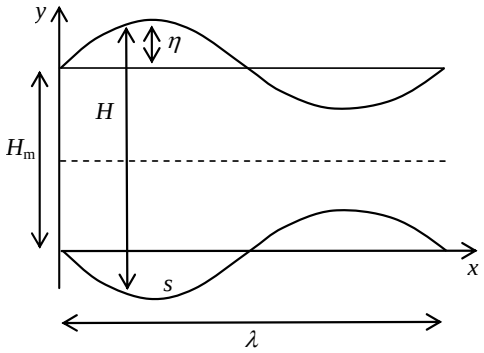

Figure.1. Waves on the film surface. H_m is the mean thickness. η is the amplitude of the wave which has the wavelength of λ.

In their approach of Vrij and Overbeek [16], the critical wavelength λ_c was defined as the representative wavelength at which the film interfaces get critically unstable causing the waves' sudden growth. Then λ_c was derived by equating the total Gibbs energy change (ΔG) to the extra energy induced by the corrugated area and other interaction energy, such that

$$\lambda_c = \sqrt{-2\pi^2\gamma\frac{dH^2}{d^2G}} \tag{7}$$

in which γ is surface tension, H is the gap between film interfaces and G is the total Gibbs energy. Eq.(7) is the wavelength criterion above which the total Gibbs energy becomes negative and fluctuation is more likely to grow [16, 20]. Vrij and Overbeek [16] took only the Van der Waals force into this account and incorporated it with the Reynolds film thinning velocity subject to capillary pressure and the extra, finally obtaining the characteristic time τ as follows where the fluctuation's most rapid growth is expected [16].

$$\tau = 96\pi^2\mu\gamma A_{232}^{-2}H_m^5 \tag{8}$$

Here, A_{232} is the Hamaker constant, again the subscript 232 meaning the same as in K_{232} (see Eq.(1)). Eq.(8) characterizes the time the film stays unstable until it fails. It should be noted here that τ gets shorter as film gets thin, meaning that the film is so unstable when it is critically thin that it can readily break.

Now one may view the total time of film thinning until the rupture as the sum of the stable 'draining' time t_d and n times the characteristic time of 'unstable fluctuating' τ [16]. Then the rate of change in H_m at the time of rupture should be infinite, and equivalently the inverse should be zero. From this, one obtains the following.

$$\frac{dt_d}{dH_m} = -n\frac{d\tau}{dH_m} \tag{9}$$

The inverse of the thinning rate on the left hand side can be substituted by the Reynolds equation with film radius R_f and pressure difference as P_c, the capillary pressure. Manipulating Eqs.(8) and (9), the final expression for H_m at the time of rupture can be derived as the following.

$$H_m = \sqrt[7]{\frac{A_{232}^2 R_f^2}{n320\pi^2\gamma P_c}} \tag{10}$$

In Vrij and Overbeek's work [16], the authors arbitrarily set n =6 based on empirical data. However, it is interesting to note that its effective is in fact comparable to the case when one takes the r.m.s. value of H_m of n=1. Since $\sqrt[7]{6} \approx \sqrt{2}$, their empirically chosen value (n=6) agrees interestingly well with the statistical account. This indicates that H_m without considering n (or with n=1) is the upper limit of the predicted rupture thickness, and H_m with n=6 is the statistical average at the particular state. In addition to this, several authors on the vibrations and waves in liquid films discuss that there are two major modes of film thinning, namely the bending mode and the squeezing mode [35-37]. The bending mode is when the wave profiles on the upper and lower interfaces of film are symmetric each other, while the squeezing mode is anti-symmetric. This may work as an additional aspect to be considered other than taking the root-squared-mean only of H_m. Considering the two modes, one half of the r.m.s value of the upper-limit H_m is the most probable value of mean film thickness, namely H_0. Therefore, one may substitute into Eq.(5) the following expression.

$$H_0 = \frac{1}{2\sqrt{2}} \sqrt[7]{\frac{A_{232}^2 R_f^2}{320\pi^2\gamma P_c}} \tag{11}$$

2.2 The role of hydrophobic force

In the next, one needs to revisit Eq.(1) to find the yet-unknown factor f related to the critical rupture thickness of aqueous surfactant films. It has been derived earlier by the same authors [1] that the increase of flow velocity in a micro channel with hydrophobic walls can be evaluated based on the relative dominance of hydrophobic force over the Van der Waals force *i.e.*, K_{232}/A_{232}. In the derivation, an assumption was made that hydrophobic force is responsible for the slip at the air-water interface [38]. The drainage inside a foam film may have an analogy with this, because the flow resembles the channel flow in 2 dimensional view if the mean film thickness is considered as channel diameter. Therefore, f can be expressed as follows.

$$f = \left(1 + 8\sqrt[3]{4K_{232}/A_{232}}\right)^{1/3} \tag{12}$$

It is assumed in the literature that film radius between two small air drops does not change while thinning [6, 11, 22-25], and at least it is not of any concern for the case of high-concentration surfactant films [7]. However, there may exist any difference between the initial film radius and the resultant radius one really observes, especially when the instability is so virulent. To account for this, the ratio between R_f and $R_{f\,\mathrm{Re}}$ was introduced in Eq.(3).

As shown in Figure 1, suppose that the ratio (R_f / $R_{f\,\mathrm{Re}}$) equals to the ratio of the wave arc length, *s*, to the corresponding wavelength, $\lambda/2$, *i.e.*

$$\frac{R_f}{R_{f_{Re}}} = \frac{s}{\lambda/2} \tag{13}$$

Then the curve length *s* is given the expression:

$$s = \int_0^{\lambda/2} \sqrt{1 + \eta^2 \left(\frac{2\pi}{\lambda}\right)^2 \cos^2\left(\frac{2\pi x}{\lambda}\right)}\, dx \tag{14}$$

Substituting Eq.(14) into Eq.(13), one obtains the following.

$$\frac{R_f}{R_{f_{Re}}} = \frac{1}{\pi}\sqrt{4\pi^2(\eta/\lambda)^2 + 1} \cdot E(\pi|\kappa) \tag{15.1}$$

$$\kappa = \frac{4\pi^2(\eta/\lambda)^2}{4\pi^2(\eta/\lambda)^2+1} \tag{15.2}$$

Here, $E(\phi|\kappa)$ is the incomplete elliptic integral of the second kind defined as [39]

$$E(\phi|\kappa) = \int_0^{\phi} \sqrt{1 - \kappa^2 \sin^2\theta}\, d\theta \tag{16}$$

where the parameter κ is in the range of 0 ~1. To determine κ from Eq.(15.2), the following relationship is required in the evaluation.

$$\frac{\eta}{\lambda} = C_1 \frac{K_{232}}{A_{232}} / C_2 \tag{17}$$

In Eq.(17), C_1 is a constant that varies with surfactant type or the system and C_2 is the reference value of K_{232}/A_{232}. C_2 was found 40~50 from the typical experimental data, and this indicates the consideration of film radius variation is particularly meaningful when the hydrophobic force is 40~50 times or more larger than the Van der Waals force. Assume high concentration of surfactants such that the film interfaces behave like immobile flat surface, *i.e.*, η/λ=0. Then the value for R_f / R_{fRe} = $E(\pi|\,0)\,/\pi$ = 1. This is also interesting to note because it indicates the assumption of invariable film radius for high surfactant concentration is valid as cited in many other works [22-25].

2.3 Prediction of critical rupture thickness and coalescence time

From Eqs. (4), (10), (11), and (14), one can derive an expression of critical rupture thickness as follows.

$$H_{cr} = \left(\frac{1}{\pi}\sqrt{4\pi^2(\eta/\lambda)^2 + 1} \cdot E(\pi|\kappa)\right)^{2/3} \left(1 + 8\sqrt[3]{4K_{232}/A_{232}}\right)^{1/3} \frac{1}{2\sqrt{2}} \sqrt[7]{\frac{A_{232}^2 R_f^2}{320\pi^2\gamma P_c}} \tag{18}$$

where the elliptic integral of the second kind E, and the parameter κ was defined in Eqs.(16) and (17), respectively. Eq. (18) reduces to Eq. (11) when K_{232} becomes much smaller that A_{232} or negligibly small.

In addition to the thickness of film rupture, one can also find the film rupture time or bubble coalescence time by integrating the Reynolds equation over the thickness variation. In other words,

$$t_c = -\frac{3\mu R_f^2}{2}\int_{H_i}^{H_{cr}} \frac{1}{H^3 \Delta P}\, dH \tag{19}$$

where H_i is the initial thickness of film. Conducting the integration for the case of high electrolyte solutions, for example, the electrostatic disjoining pressure term is negligible and the coalescence time may be predictable by the following.

$$t_c = \frac{\mu R_f^2}{4\sqrt[3]{P_c}\left(\frac{A_{232}+K_{232}}{6\pi}\right)^{\frac{2}{3}}}\left[2\sqrt{3}\tan^{-1}\left(\frac{1}{\sqrt{3}} - \frac{2}{\sqrt{3}}\sqrt[3]{\frac{6\pi P_c}{A_{232}+K_{232}}}H_i\right) - 2\sqrt{3}\tan^{-1}\left(\frac{1}{\sqrt{3}} - \frac{2}{\sqrt{3}}\sqrt[3]{\frac{6\pi P_c}{A_{232}+K_{232}}}H_{cr}\right) - \log\left(\frac{\sqrt[3]{P_c}H_{cr}+\sqrt[3]{\frac{A_{232}+K_{232}}{6\pi}}}{\sqrt[3]{P_c}H_i+\sqrt[3]{\frac{A_{232}+K_{232}}{6\pi}}}\right) + \log\left(\frac{P_c^{\frac{2}{3}}H_{cr}^2 - \sqrt[3]{P_c\left(\frac{A_{232}+K_{232}}{6\pi}\right)}H_{cr} + \left(\frac{A_{232}+K_{232}}{6\pi}\right)^{\frac{2}{3}}}{P_c^{\frac{2}{3}}H_i^2 - \sqrt[3]{P_c\left(\frac{A_{232}+K_{232}}{6\pi}\right)}H_i + \left(\frac{A_{232}+K_{232}}{6\pi}\right)^{\frac{2}{3}}}\right)\right] \tag{20}$$

3. Model verification

In the following, various experimental works are compared with the critical rupture thickness and coalescence time predicted by the model. The present model incorporated hydrophobic force with the film rupture by introducing the hydrophobic force constant K_{232}. Wang and Yoon [22-25] were the first to implement this idea, and their work may be the only reference where the values of K_{232} for certain foam films can be found directly. However, the value of K_{232} can be assessed also from other references that have film thinning kinetics or coalescence time data. For example, the predicted coalescence time shown in Figure 2 was obtained using the K_{232} values inferred from the data presented by Li [40]. Li suggested an analytical model to predict the coalescence time by studying the dynamics of film thinning in recognition of Van der Waals force and electrostatic double layer force. Then the coalescence time (t_c) model can be simplified as the following [41],

$$t_c = 0.729\left(\frac{k}{A_{232}{}^{0.46}}\right) \tag{20}$$

where A_{232} is the Hamaker constant, and k is a constant determined by the system properties such as viscosity, surface tension, and bubble diameter. The details for estimating constant k is given in Li's work where the information for all necessary parameters is available [40].

Even though it was concluded in Li's work that there was a good agreement between the theoretical calculation of t_c by Eq.(20) and the experimental results, his conclusion seems unconvincing in that the two show discrepancy in the range of 8 to 13 seconds. This range is considerably larger than the coalescence time of bubbles measured in pure water at low surfactant concentrations. Therefore, the data are necessary to be reevaluated by introducing the hydrophobic force. Assuming the coalescence between two bubble drops of equal size, Eq.(20) for this purpose can be rewritten as [41]

$$t_c = 0.729\left(\frac{k}{(A_{232}+K_{232})^{0.46}}\right) \tag{21}$$

where the hydrophobic force constant K_{232} is simply added to A_{232} since surface forces are additive. As a consequence, K_{232} can be back-calculated from the difference in t_c between theory and experiment. First, the values of k are determined following the details presented by Li's model [40]. Then the k values are substituted into Eq.(21) to calculate K_{232} by fitting the values of t_c calculated by Eq.(21) to the experimental data. K_{232} values obtained in this way are presented in Table 1.

The values have been used in the calculation of t_c by the present model (Eq.(19)), and the results are shown in Figure 2. The present model is in much better agreement with data than Li's model is.

While the values of K_{232} had to be back-calculated in the present model, values of K_{232}

Antifoam EA 146 (g/l)	K_{232} (J) BSA 0.0 g/l	BSA 0.2 g/l	BSA 1.0 g/l
1.0×10^{-2}	6.0×10^{-18}	5.0×10^{-18}	5.5×10^{-18}
2.5×10^{-2}	2.2×10^{-18}	5.0×10^{-18}	4.0×10^{-18}
8.0×10^{-2}	1.5×10^{-18}	6.5×10^{-19}	2.9×10^{-19}
1.0×10^{-1}	6.2×10^{-19}	5.0×10^{-19}	3.6×10^{-19}
2.5×10^{-1}	5.3×10^{-19}	4.4×10^{-19}	4.0×10^{-19}

Table 1. K_{232} values obtained from the data presented by Li (1994) for foam films stabilized with Bovine Serum Albumin (BSA) solutions with commercial antifoam EA142 of the polypropylene glycol type.

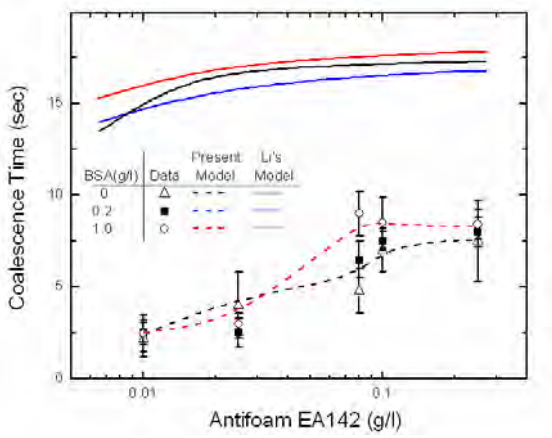

Figure. 2. Coalescence time (t_c) of a foam film made of Bovine Serum Albumin (BSA) solutions with commercial antifoam EA142 of the polypropylene glycol type. Model calculations were conducted using the K_{232} values presented in Table1. Other input parameters were: C_1=1, C_2=40, A_{232} =1×10^{-19} J, H_i=200 nm. The effects of electrostatic forces were ignored because the data were given in the presence of high electrolyte concentration (0.1 M NaCl).

obtained using different methods are also available. Wang and Yoon have reported the values of K_{232} and A_{232} for several surfactant systems [23, 24]. Using their values, the critical rupture thickness and coalescence time of the same system can be predicted by the model developed. The comparisons between the model and the experiment by Wang and Yoon are made in figures 3 and 4. As one can see, the present model is in good agreement with experimental data, even

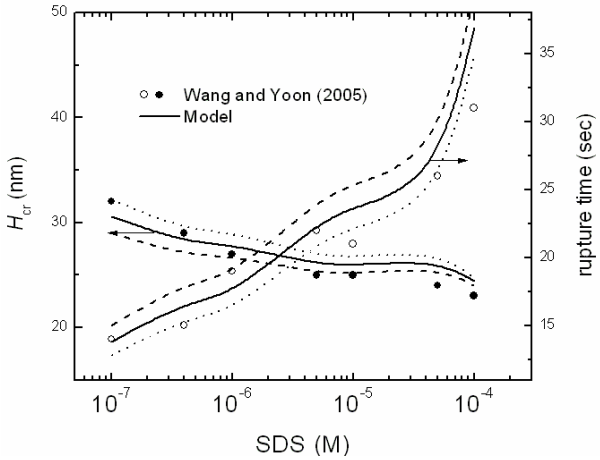

Figure. 3. Critical rupture thickness (H_{cr}) and corresponding rupture time (t_c) with surfactant SDS concentration change, in the presence of 0.3M NaCl. Input parameters were: C_1=0.07, C_2=40, H_i =250 nm. Dashed line represents the model prediction with 10% higher value of K_{232} reported by Wang and Yoon (2005), and dotted line represents the one with 10% lower value.

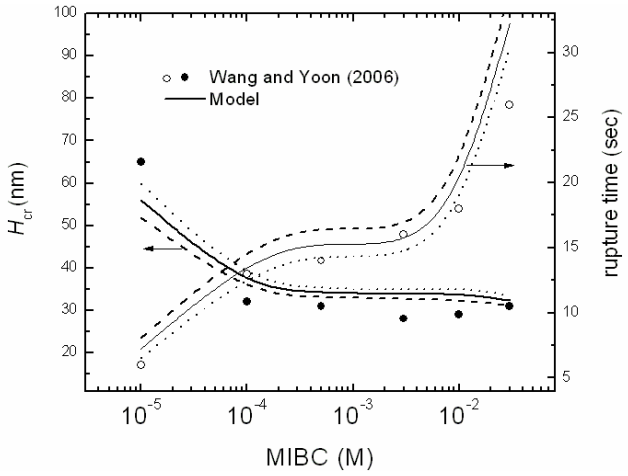

Figure. 4. Critical rupture thickness (H_{cr}) and corresponding rupture time (t_c) with surfactant MIBC concentration change, in the presence of 0.1M NaCl. Input parameters were: C_1=0.125, C_2=40, H_i =250 nm. Dashed line represents the model prediction with 10% higher value of K_{232} reported by Wang and Yoon (2006), and dotted line represents the one with 10% lower value.

with changes of K_{232} value 10% higher and lower.

Another comparison between the model and experimental data by Manev *et al.* [42] is presented in Figure 5. The authors studied the stability of emulsion and foam films. The critical rupture thickness was obtained for several different systems, but the corresponding coalescence time was not presented. Instead, they measured the drainage time for a constant range of

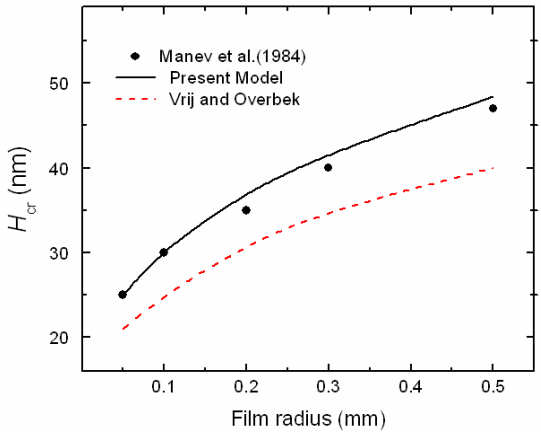

Figure. 5. Critical rupture thickness (H_{cr}) change according to the film radius change. Model calculations were conducted for the same system as Figure 3. Input parameters were same as Figure 3. : C_1=0.07, and C_2=40. The value of K_{232} was chosen 2×10^{-20} J, by extrapolating Wang and Yoon (2005)'s K_{232} vs. SDS concentration data. Dashed line represents the prediction by Vrij and Overbeek's model.

thickness, and observed slower drainage at higher surfactant concentrations in which electrostatic force was suppressed. Although their experimental conditions given by Manev et *al*.[42] are insufficient for the purpose of the present model comparison, all the necessary properties such as K_{232} and surface tension were referenced from the experimental work by Wang and Yoon [23] in which experiments were conducted in the similar environment on SDS foam films. As shown in Figure 5, the present model prediction agrees better with the experimental data than the model by Vrij and Overbeek [16]. It also agrees with the general observation that small films are much more stable than large films in a similar system [11].

4. Summary and conclusion

A model for predicting the critical rupture thickness of thin liquid film and corresponding rupture time has been derived. In the literature, no other model incorporated the hydrophobic force with the phenomena, but the present model has succeeded by applying the hydrophobic force constant in film, K_{232}. The basic assumption of the model was that thin liquid film has interfaces fluctuating due to interfacial forces, as many other models in the literature have assumed. Unlike others, the present model does not necessarily imply that the critical rupture thickness is equal to twice the amplitude of the critical interfacial wave. This was possible because the velocity increase factor and film radius change ratio were introduced to correct the rupture thickness to real practice. The model was verified by experimental data reported in other literature. Although not many presented the value of K_{232} as a direct value, K_{232} could be inferred from the given data. As a result, the model was in good agreement with experimental data reported in various references.

5. References

1. Do, H., *Development of a turbulent flotation model from first principles*, in *Engineering Science and Mechanics*. 2010, Virginia Polytechnic Institute and State University: Blacksburg.
2. Davis, R.H., J.A. Schonberg, and J.M. Rallison, *The lubrication force between two viscous drops.* Physics of Fluids A: Fluid Dynamics, 1989. **1**(1): p. 77-81.
3. Barnocky, G. and R.H. Davis, *The lubrication force between spherical drops, bubbles and rigid particles in a viscous fluid.* International Journal of Multiphase Flow, 1989. **15**(4): p. 627-638.
4. Fuentes, Y.O., S. Kim, and D.J. Jeffrey, *Mobility functions for two unequal viscous drops in Stokes flow. I. Axisymmetric motions.* Physics of Fluids, 1988. **31**(9): p. 2445-2455.
5. Vrij, A., *Possible mechanism for the spontaneous rupture of thin, free liquid films.* Discussions of Faraday Society, 1966. **42**: p. 23-33.
6. Sheludko, A., *Thin liquid films.* Advances in Colloid and Interface Science, 1967. **1**(4): p. 391-464.
7. Karakashev, S.I. and A.V. Nguyen, *Effect of sodium dodecyl sulphate and dodecanol mixtures on foam film drainage: Examining influence of surface rheology and*

intermolecular forces. Colloids and Surfaces A: Physicochemical and Engineering Aspects, 2007. **293**(1-3): p. 229-240.
8. Radoev, B.P., A.D. Scheludko, and E.D. Manev, *Critical thickness of thin liquid films: Theory and experiment.* Journal of Colloid and Interface Science, 1983. **95**(1): p. 254-265.
9. Ivanov, I.B. and D.S. Dimitrov, *Hydrodynamics of thin liquid films.* Colloid & Polymer Science, 1974. **252**(11): p. 982-990.
10. Valkovska, D.S., K.D. Danov, and I.B. Ivanov, *Stability of draining plane-parallel films containing surfactants.* Advances in Colloid and Interface Science, 2002. **96**(1-3): p. 101-129.
11. Angarska, J.K., et al., *Detection of the Hydrophobic Surface Force in Foam Films by Measurements of the Critical Thickness of the Film Rupture.* Langmuir, 2004. **20**(5): p. 1799-1806.
12. Ruckenstein, E. and R.K. Jain, *Spontaneous rupture of thin liquid films.* Journal of Chemical Society, Faraday Transactions 2, 1974. **70**: p. 132-147.
13. Sharma, A. and E. Ruckenstein, *Critical thickness and lifetimes of foams and emulsions: Role of surface wave-induced thinning.* Journal of Colloid and Interface Science, 1987. **119**(1): p. 14-29.
14. Scheludko, A., Proc. K. Akad. Wetensch, B, 1962. **65**: p. 76.
15. Vrij, A., *Light scattering by soap films.* Journal of Colloid Science, 1964. **19**(1): p. 1-27.
16. Vrij, A. and J.T.G. Overbeek, *Rupture of thin liquid films due to spontaneous fluctuations in thickness.* Journal of the American Chemical Society, 1968. **90**(12): p. 3074-3078.
17. Williams, M.B. and S.H. Davis, *Nonlinear theory of film rupture.* Journal of Colloid and Interface Science, 1982. **90**(1): p. 220-228.
18. Erneux, T. and S.H. Davis, *Nonlinear rupture of free films.* Physics of Fluids A: Fluid Dynamics, 1993. **5**(5): p. 1117-1122.
19. Ida, M.P. and M.J. Miksis, *Thin Film Rupture.* Applied Mathematics Letters, 1996. **9**: p. 35-40.
20. Ivanov, I.B., et al., *Theory of the critical thickness of rupture of thin liquid films.* Transactions of Faraday Society, 1970. **66**: p. 1262-1273.
21. Sharma, A. and E. Ruckenstein, *Stability, critical thickness, and the time of rupture of thinning foam and emulsion films.* Langmuir, 1987. **3**(5): p. 760-768.
22. Wang, L. and R.-H. Yoon, *Hydrophobic Forces in the Foam Films Stabilized by Sodium Dodecyl Sulfate:Effect of Electrolyte.* Langmuir, 2004. **20**(26): p. 11457-11464.
23. Wang, L. and R.-H. Yoon, *Hydrophobic forces in thin aqueous films and their role in film thinning.* Colloids and Surfaces A: Physicochemical and Engineering Aspects, 2005. **263**(1-3): p. 267-274.
24. Wang, L. and R.-H. Yoon, *Role of hydrophobic force in the thinning of foam films containing a nonionic surfactant.* Colloids and Surfaces A: Physicochemical and Engineering Aspects, 2006. **282-283**: p. 84-91.
25. Wang, L. and R.-H. Yoon, *Effects of surface forces and film elasticity on foam stability.* International Journal of Mineral Processing, 2008. **85**(4): p. 101-110.
26. Yoon, R.H., *The role of hydrodynamic and surface forces in bubble-particle interaction.* International Journal of Mineral Processing, 2000. **58**(1-4): p. 129-143.
27. Israelachvili, J.N. and R.M. Pashley, *The hydrophobic interaction is long range, decaying and exponentially with distance,* in *Nature*. 1988: London. p. 341-342.

28. Craig, V.S.J., B.W. Ninham, and R.M. Pashley, *The effect of electrolytes on bubble coalescence in water.* The Journal of Physical Chemistry, 1993. **97**(39): p. 10192-10197.
29. Deschenes, L.A., et al., *Inhibition of Bubble Coalescence in Aqueous Solutions. 1. Electrolytes.* The Journal of Physical Chemistry B, 1998. **102**(26): p. 5115-5119.
30. Du, Q., E. Freysz, and Y.R. Shen, *Surface Vibrational Spectroscopic Studies of Hydrogen Bonding and Hydrophobicity.* Science, 1994. **264**(5160): p. 826-828.
31. van Oss, C.J., R.F. Giese, and A. Docoslis, *Hyperhydrophobicity of the Water-Air Interface*, in *Journal of Dispersion Science & Technology*. 2005, Taylor & Francis Ltd. p. 585-590.
32. Stubenrauch, C., et al., *Comment on 'Hdrophobic Forces in the Foam Films Stabilized by Sodium Dodecyl Sulfate:Effect of Electrolyte' and Subsequent Criticism.* Langmuir, 2007. **23**(24): p. 12457-12460.
33. Ninham, B., *The Present State of Molecular Forces*, in *Smart Colloidal Materials*. 2006. p. 65-73.
34. Wang, L., *A Response to the Comment on "Hydrophobic Forces in the Foam Films Stabilized by Sodium Dodecyl Sulfate: Effect of Electrolyte"*. Langmuir, 2008. **24**(9): p. 5194-5196.
35. Feather, N., *An introduction to the physics of vibrations and waves*. 1962: Edinburgh university press.
36. Hansen, R.H. and E.J. Derderian. *Plenary lecture-Problems in foam origin, drainage and rupture*. in *Symopsium on foams*. 1975. Brunel University: Academic press London.
37. Joosten, J.G.H., *Light scattering from thin liquid films*, in *Thin liquid films- fundamentals and applications*, I.B. Ivanov, Editor. 1988, Marcel Dekker.
38. Tabeling, P., *Introduction to microfluidics*. 2005: Oxford university press.
39. Abramowitz, M. and I.A. Stegun, in *Handbook of mathematical functions with formulas, graphs, and mathematical tables*. 1972, Dover: New York. p. 587-607.
40. Li, D., *Coalescence between Two Small Bubbles or Drops.* Journal of Colloid and Interface Science, 1994. **163**(1): p. 108-119.
41. Aksoy, B.S., *personal note*. 1998.
42. Manev, E.D., S.V. Sazdanova, and D.T. Wasan, *Emulsion and foam stability--The effect of film size on film drainage.* Journal of Colloid and Interface Science, 1984. **97**(2): p. 591-594.

CHAPTER 6

DEVELOPING A FROTH-PHASE RECOVERY MODEL FROM FIRST PRINCIPLES

ABSTRACT

In flotation, hydrophobic particles are selectively collected by air bubbles, and the bubble-particle aggregates enter the froth phase. However, less hydrophobic particles drop off from the froth phase, while more hydrophobic particles are recovered. The latter is referred to as true flotation in a sense that the recovery is achieved *via* bubble-particle attachment. The froth recovery model incorporating this mechanism has been developed by considering particle drop rate and the carrying capacities of bubbles. On the other hand, non-hydrophobic particles are also recovered, being carried by water entrained among bubbles. The particle recovery due to the entrainment mechanism water has also been incorporated in the model by considering water recovery as functions of bubble coarsening and the stability of bubble-particle aggregates during lateral transport to overflow lip. In addition, the entrainment model incorporates empirical parameters for particle size and density effects. The model predictions are in good agreement with experiments.

1. Introduction

Flotation is the most widely used separation process used in the mining industry. In this process, air bubbles are used to selectively collect hydrophobic particles and rise to the surface of a pulp, forming a froth phase. The bubbles laden with hydrophobic particles are removed from the top of a flotation cell, while hydrophilic particle are removed at the bottom. It has been shown recently that some of the bubble-particle aggregates break up upon encountering the pulp-froth interface, causing the particles return to the pulp phase [1] Thus, the pulp-froth interface behaves like a barrier. It has also been shown that much of the particles that have successfully entered the froth phase drop back to the pulp phase, as bubbles coalesce while rising in the froth phase and thereby cause a decrease in bubble surface area on which particle can be attached. A particle tracking method based on positron emission spectroscopy [2] clearly showed that drop back is an important sub-processes of flotation. It may appear, therefore, that both the pulp-froth interface and froth phase hinder the recovery process. On the other hand, they serve as important basis for achieving high degree of selectivity.

The stability of froth plays an important role in flotation, as it determines the final grade, recovery and throughput. Despite its importance, there are no models that can comprehensively account for all of the subprocesses occurring in the froth phase. It has been suggested that nearly twenty different physical and chemical factors influencing the froth recovery process [3]. However, the fractional recovery in the froth may be modeled in a broader sense by the following aspects. It was reported that hydrophobic force plays the most important role in determining the flotation recovery [4]. Since air bubbles are hydrophobic as well as mineral particles are [5], the froth recovery mechanisms can be grouped by two, largely. One is the recovery due to attachment [6, 7]. This is called true froth recovery because only hydrophobic particles are recovered along with the aggregates entering the froth. Through this mechanism, the collection of minerals was shown to have strong correlations with the hydrophobicity of particles and bubble surface area available for attachment. Some researchers modeled the recovery in empirical ways only, because froth bubbles are in the complicated 3 phases (solid-gas-liquid) [3, 7]. On the other hand, non-hydrophobic particles are also recovered from froth, being carried without attachment by the water in the froth [6, 7]. This is called the recovery due to entrainment [8, 9]. It is not directly related to the chemistry but is well known to play significant roles in the fine mineral particles recovery [10, 11]. Some empirical models for this recovery are also available [8, 9, 12], and generally the models include water recovery and particle size as parameters. The froth recovery models stated above have shortcomings in that their empirical parameters have complex relationship with each other and no governing criterion was given. The criterion may be found if a froth recovery model is developed in analytical way. This is possible by investigating both the drainage and bubble coarsening, because liquids drain and bubbles coalesce consistently in the froth.

The recovery mechanisms in relation to froth structure may be further simplified by regarding froth as foam. *Foam* is the term used to distinguish the liquid-gas dispersions from the liquid-gas-solid dispersions (*froths*) [13]. A foam is a two-phase system where gas cells are enclosed by liquid, and accordingly the structure looks like a network of pipe-like channels (called plateau border) and thin film walls (called lamellae) [14]. The drainage along this

structure has been a prevalent research topic for a long time because foams are commonly observed in many practical applications. Most of foam drainage models in the literature assume that liquids in foams flow mainly through the channels, and set the mass balance as the basis for the model [15-19]. The models in the literature were derived only for stable foams. In reality, foam bubbles grow, break and coalesce into larger sizes. Those models do not include the coalescence of bubbles. Relating coalescence with drainage model is challenging because the factors destabilizing foams are all interplaying with each other. For all that, the modeling effort to incorporate bubble size change has been tried recently [20].

The most convincing factor for coalescence in foam, so far, is the hydrophobic force [21]. Thin water films tend to rupture at different thicknesses for different surfactant concentrations or certain chemical conditions. In many experiments on foam film drainage, it has been shown that foam films thin faster than the prediction by the Reynolds lubrication equation and it was ascribed to hydrophobic force [21, 22]. Despite the findings, a good theory to predict the approximate time of rupture or corresponding rupture thickness is still missing. Many of the film rupture models available in the literature were good enough to predict the rupture of stable foams [23-25]. The models were derived by assuming that the rupture results from capillary waves due to the forces at the water-air interface but hydrophobic force was not considered. Therefore, the models were valid only for foam films of high surfactant concentrations at which hydrophobic force is significantly diminished [22, 26]. On this ground, the models are inappropriate for predicting the coalescence of practical foam films in such applications as mining industry, where hydrophobic force is apparent [27].

There are two different types of flotation cells used in the mining industry, *i.e.*, mechanically agitated flotation cells and flotation columns. Traditionally, flotation had been conducted in the mechanically agitated cells until columns were first used in practice in Canada in 1980 [28]. The characteristics of froths observed in the two may not be too much different from each other in essence. Therefore, the froth recovery model to be developed in this report should work for both. However, the model developed in the present work is more suitable for in mechanically agitated cells. Operated in deeper froth than mechanical cells, columns have advantages of improving product grade after introducing wash water into the froth. On the other hand, the hydrodynamics in columns becomes more complex than the one in mechanically agitated cells because the resultant froth instability from adding the wash water and deeper froth induce convective flow inside [29], which is not considered in the present model. Efforts have been made to develop the model from first principles.

2. Froth recovery model development

2.1 Overall froth recovery

The present froth recovery model accounts for two independent mechanisms, *i.e.*, recovery due to attachment and recovery due to entrainment. Thus, the overall froth recovery, R_F, becomes,

$$R_F = R_{F-a} + R_{F-e} \tag{1}$$

where $R_{F\text{-}a}$ is the recovery due to attachment, and $R_{F\text{-}e}$ is the recovery due to entrainment. Warren [9] has shown experimentally that the two are independent, and found $R_{F\text{-}a}$ changes with mineral type and particle size, while $R_{F\text{-}e}$ changes with water recovery and particle size.

2.1.1. Froth recovery due to attachment

Gorain *et al*. [7] proposed an empirical expression for overall froth recovery after analyzing numerous experimental data. The authors found that froth recovery decreases with longer residence time of air in a froth phase. Therefore, one can write the following relation,

$$R_{F-a} = R_{F-max}\exp\left(-\alpha t_f\right) \tag{2}$$

where t_f is the retention time of air in froth phase, and $R_{F\text{-}max}$ represents the maximum fractional recovery in the froth. In Gorain's model, $R_{F\text{-max}}$ was taken to be unity, In the present model it is considered to change with bubble size along the depth of a froth phase. As is well known, bubble size is small at the base of a froth phase but increases as the bubbles rise along the height due to coalescence. Therefore, the surface area rate of the bubbles, S_b, will decrease along the height and so will the capacity of the froth to carry particles upward. The surface area rate can be given as follows [30].

$$S_b = \frac{6V_g}{d_2} \tag{3}$$

where V_g is the superficial gas velocity, and d_2 is bubble diameter. In the present work, $R_{F\text{-}max}$ is considered to be the ratio of the surface area rate at the top of the froth to the one at the pulp-froth interface [31], *i.e*.,

$$R_{F-max} = \frac{S_{b-f}}{S_{b-0}} = \frac{d_{2-0}}{d_{2-f}} \tag{4}$$

where the subscripts -0 and *–f* indicates that the parameters are pertaining to the bottom and top of the froth, respectively. Eq. (4) suggests that the froth recovery can be maximized by minimizing bubbles coalesce, which can be achieved by increasing frother dosage. Forth recovery can also be increased by employing shallow froth depth to minimize bubble coalescence.

It has been shown that froth recovery increases as the froth residence time decreases [7]; therefore, α may be considered the rate constant for particles dropping back to the pulp phase due to coarsening. Assuming that each bubble carried *N* particles initially, α may be given as,

$$\alpha = -\left(\frac{Nd_1^2}{d_{2-0}^2}\right)\left(S_{b-f} - S_{b-0}\right) \tag{5}$$

where d_1 is particle diameter, $d_{2\text{-}0}$ is the initial bubble diameter (at the bottom). The second term in the parenthesis represents the change in surface area rate (S_b) as bubble size grows from $d_{2\text{-}0}$ at the bottom to $d_{2\text{-}f}$ at the top. Substituting Eq.(3) into (5), one obtains:.

$$\alpha = N\frac{6V_g}{d_{2-0}}\left(1-\frac{d_{2-0}}{d_{2-f}}\right)\left(\frac{d_1}{d_{2-0}}\right)^2 \tag{6}$$

Note here that N should vary depending on both physical (e.g., bubble size, particle size, turbulence) and chemical (e.g.,hydrophobicity, surface tension) properties of the system. Therefore, it may be treated as as an adjustable parameter.

As for the retention time, t_f, in Eq.(2), one may use the retention time of air, which can be given as the froth height (h_f) divided by superficial gas velocity, i.e., $t_f = h_f/V_g$, in the same manner as Gorain *et al*.'s [7]. Eq.(2) can then be rewritten as,

$$R_{F-a} = R_{F-max}\exp\left(-\alpha\frac{h_f}{V_g}\right) = \frac{d_{2-0}}{d_{2-f}}\exp\left(-N\frac{6h_f}{d_{2-0}}\left(1-\frac{d_{2-0}}{d_{2-f}}\right)\left(\frac{d_1}{d_{2-0}}\right)^2\right) \tag{7}$$

According to Eq. (7), $R_{F\text{-}a}$ should be a function of the ration between the bubble sizes at the base ($d_{2\text{-}0}$) and at the top ($d_{2\text{-}f}$) of a froth, where $d_{2\text{-}0} < d_{2\text{-}f}$. In a froth (or foam), bubbles coarsen due to drainage and rupture of intervening water films. The drainage occurs primarily in plateau borders [15, 17, 18], although drainage through plateau border junctions and lamella films may also be significant depending on bubble sizes involved. When the thickness of the lamella film becomes smaller than the critical rupture thickness (H_{cr}), the film ruptures and bubbles become coarser.

The number of plateau borders per unit cross-sectional area of foam should be proportional to the number of bubbles. Therefore, one can derive the following relationship,

$$\frac{N_{PB-f}}{N_{PB-0}} = \frac{4S/\pi {d_{2-f}}^2}{4S/\pi {d_{2-0}}^2} = \left(\frac{d_{2-0}}{d_{2-f}}\right)^2 \tag{8}$$

where N_{PB} is the number of plateau borders at a cross-section, S the cross-sectional area of a foam column, and d_2 is the bubble diameter with the subscripts -0 and *–f* representing the same as in Eq.(4).

It has been shown experimentally that the number of bubbles in a foam changes exponentially with time [32]. Therefore, the number of plateau borders may be estimated as follows,

$$N_{PB} = n_0\exp\left(-C\sqrt{A_{cr}/A}\right) \tag{9}$$

where N_{PB} is the total number of plateau borders at a given cross-sectional area of a flotation cell, n_0 the initial number of plateau borders, C a fitting parameter representing bubble coalescence, A the plateau border cross-sectional area, and A_{cr} is the critical value of A at which bubbles

coalesce. It has been shown experimentally that foam bubbles coarsen at a critical liquid fraction [33]. It would, therefore, be reasonable to assume that there is a critical value of A, i.e., A_{crit}, at which the lamella film between two bubbles rupture at a critical rupture thickness (H_{cr}) and become one [22, 26, 34, 35] The use of A_{cr} may be convenient in modeling foam (or froth) stability, as plateau boarders can be related to liquid fraction or measured optically. The measurement of $H_{cr,}$ on the other hand, requires sophisticated devices such as thin-film pressure balance (TFPB) [36].

Substituting Eq.(9) into Eq.(8), and assuming that A_{cr} is approximately the same as the plateau border area (A_f) at the top of a foam, one can write the following relation,

$$\frac{d_{2-0}}{d_{2-f}} = \sqrt{\exp\left(C\sqrt{A_f/A_0} - C\right)} \tag{10}$$

where A_0 the plateau border areas at the bottom of the foam. The plateau boarder area can be related to the average drainage velocity (U) in the plateau boarders [17, 18, 37],

$$U = \frac{1}{\mu}\left(\rho g A - \frac{f\gamma}{2}\frac{1}{\sqrt{A}}\frac{\partial A}{\partial x}\right) \tag{11}$$

where ρ is the liquid density, g the gravity, γ surface tension, and μ is dynamic viscosity of liquid, and f is a parameter related to plateau border shape. For well-structured, mono-dispersed foams, f = 0.4. In the present work, where coarsening foams (or froth) are considered, it is assumed that f = 2.

At steady state, the downward liquid velocity (U) given by Eq. (11) should be equal to the superficial gas velocity, $-V_g$, which is upward. One can, therefore, derive the following relation,

$$\frac{dA}{dx} = \frac{\rho g}{\gamma} A\sqrt{A} + \frac{\mu V_g}{\gamma}\sqrt{A} \tag{12}$$

which can be solved to obtain,

$$\sqrt{A_f} = \sqrt{\frac{V_g\mu}{\rho g}}\tan\left(\tan^{-1}\left(\sqrt{\frac{\rho g A_0}{V_g\mu}}\right) - \frac{h_f}{2}\frac{\sqrt{\rho g \mu V_g}}{\gamma}\right) \tag{13}$$

with boundary conditions: $A = A_f$ at $x = 0$ (top of a froth), and $A = A_0$ at $x = h_f$ (bottom of a forth). Eq. (13) can be used to obtain the value of $\sqrt{A_f/A_0}$, which in turn can be substituted into Eq.(10) to predict the coarsening of foam (or froth) bubbles. All of the parameters of Eq. (14) are known except A_0. In the present work, it is considered that $\sqrt{A_0} \approx d_{2-0}$, which is an approximation based on the observation that for stable foams the radius of curvature of plateau border ($\sqrt{A}$) is proportional to the radius of the bubbles by a factor less than 2, depending on the wetness of a foam under consideration [38].

2.1.2. Froth recovery due to entrainment

Fine particles in a flotation cell flow with water due to their small masses. In principle, therefore, the recovery ($R_{F\text{-}e}$) due to entrainment for fine particles should be the same as water recovery (R_w). The latter should in turn be a function of the liquid fraction of the foam at the top, which should decrease as bubbles coarsen along the height of a froth phase. Once a group of bubbles reach the top, however, they will start flowing laterally toward the overflow lip, during which time bubble coarsening continues and, hence, the liquid fraction decreases further. Thus, R_w should be given as,

$$R_W = F_W F_B \tag{14}$$

where F_W is the liquid fraction at the top of a foam as soon as bubbles arrive at the top, and F_B is the fraction of bubbles that do not burst during their lateral flow.

In principle, F_w should be a function of the surface area rate of the bubbles ($S_{b\text{-}f}$) at the top of a froth phase. This relationship may be given as follows,

$$F_W = \varepsilon_0 \mathrm{S}_{b-f} t_{cf} = \varepsilon_0 \frac{6V_g}{d_{2-f}} \frac{4\mu h_f}{\rho g \delta^2} \tag{15}$$

where ε_0 is the liquid fraction at the bottom of a froth phase, t_{cf} is the time scale over which a thick liquid film thins to a thickness δ [39], and h_f is the froth height. Typically, ε_0 varies in the range of 0.26-0.36, depending on the packing condition of bubbles at the bottom [40]. In the present work, a value of 0.33 has been chosen for ε_0 [14, 41], while δ has been approximated by the following relation,

$$\delta = \frac{3}{4}\left(\frac{\varepsilon_0}{1-\varepsilon_0}\right) d_{2-0} \tag{16}$$

which has been derived assuming that all of the bubbles at the pulp-froth interface have diameter $d_{2\text{-}0}$ and film thickness δ.

As for F_B in Eq. (15), one may use the following form,

$$F_B = \exp\left(-\frac{h_f}{L}\right) \tag{17}$$

where h_f is the froth height at a steady state, and L is a length scale representing transport of froth across a flotation cell, which may be represented by,

$$L = \frac{\mu}{\rho_2 U_f} \tag{18}$$

where μ is the liquid viscosity, ρ_2 is air density, and U_f is the velocity of froth moving laterally toward overflow lip. Eqs. (17) and (18) suggest that as froth height increases the lateral velocity of froth should decrease, which is consistent with industrial experience.

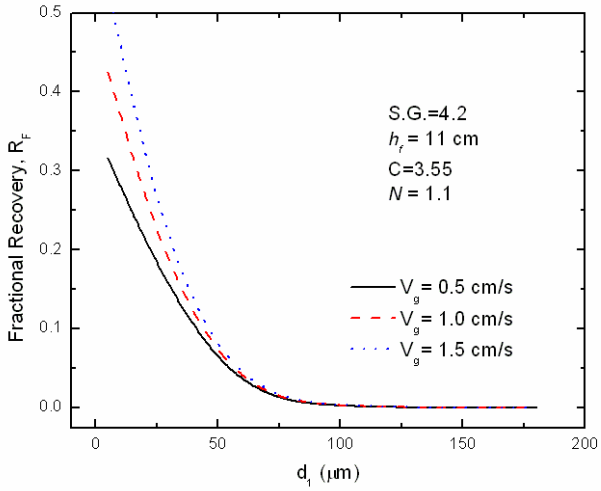

Figure 1. Effect of superficial gas flow rate on froth recovery. Higher superficial gas flow is beneficial to fine particles froth recovery.

As discussed above, Eq. (14) gives the water recovery (R_w), which should be equal to the recovery of fine particles. However, coarse particles deviate from fluid flow due to inertia force; therefore, Eq. (14) may be rewritten as follows,

$$R_{F-e} = F_W F_B \exp\left(-0.0325\Delta\rho - 0.063 d_1\right) \tag{19}$$

where $\Delta\rho$ is the specific gravity difference between mineral and medium (water), and d_1 is particle diameter in μm. The terms in the parenthesis are designed to make corrections for the S.G. and size of particles, as determined empirically by Maachar and Dobby [10].

Substituting Eqs. (7) and (19) into Eq. (1), one obtains an expression for the overall froth recovery as follows:

$$R_F = \frac{d_{2-0}}{d_{2-f}} \exp\left(-\alpha \frac{h_f}{V_g}\right) + R_W \exp\left(-0.0325\Delta\rho - 0.063 d_1\right) \tag{20}$$

Most of the parameters of Eq.(20) are readily available from operating conditions.

3. Effect of Various Parameters on Froth Recovery

In the following, the effects of various parameters used in the model are presented. Figure 1 shows the effect of particle size on froth recovery at different superficial gas flow rates. As shown, froth recovery increases with decreasing particle size mostly due to increased entrainment of fine particles. As particle size (d_1) becomes smaller, the recovery due to entrainment ($R_{f\text{-}e}$) increases as shown in Eq. (19). Eq. (15) shows that as the superficial gas velocity (V_g) increases, water recovery (F_w) increases, which in turn causes an increase in the

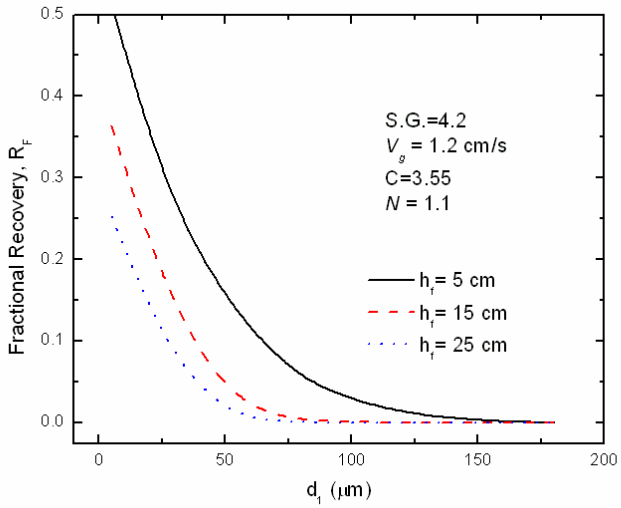

Figure 2. Effect of froth height on froth recovery. Shallow froth height is helpful for froth recovery of coarse particles.

overall froth recovery (R_f), as shown in Eq. (20). An increase in V_g should also increase the recovery due to attachment ($R_{F\text{-}a}$) as shown in Eq. (20). Its benefit is small, however, at larger particle sizes, which can be attributed to the high detachment probabilities associated with coarse particles.

Figure 2 shows the effect of changing froth heights. As shown in Eq. (17), a decrease in froth height causes F_B increase, which in turn causes the entrainment recovery ($R_{F\text{-}e}$) to improve as

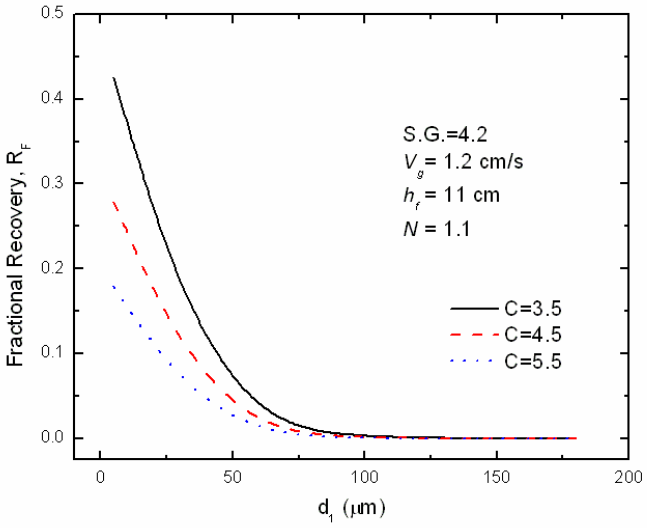

Figure 3. Effect of coarsening on froth recovery. Higher coarsening factor, meaning unstable froth, shows lower froth recovery.

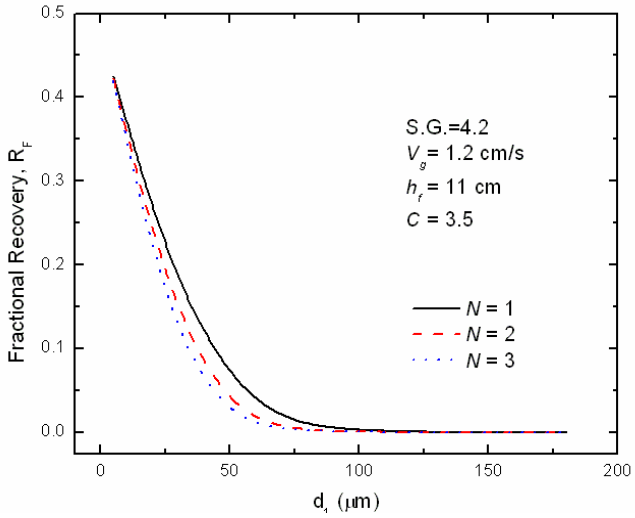

Figure 4. Effect of mineralization on froth recovery. The degree of mineralization in fine particles and coarse particles has less significant effect than other particle sizes.

shown in Eq. (19). The predictions shown in Figs. 1 and 2 agree with industrial experience that increasing superficial gas velocity and decreasing froth height in flotation is beneficial to froth recovery [30]. It should be noted here that the simulation results presented in Figures 1 and 2 have been obtained by assuming that the lateral velocity (U_f) of froth on the top of a froth phase is 1 cm/s. It has been reported that for a 50 m^3 conventional flotation cell U_f is in the range 2~12 cm/s [42].

The effects of coarsening and the degree of mineralization of bubbles are presented in

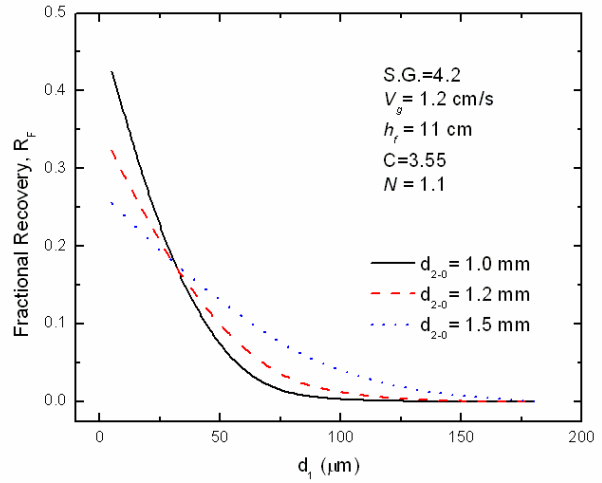

Figure 5. Effect of bubble size entering the interface (d_{2-0}) on froth recovery. Small entering bubbles are helpful for the froth recovery of particles as fine as 25μm, while large entering bubbles are for larger particles than 25 μm.

Figures 3 and 4, represented by the changes of parameters C in Eq.(9), the fitting parameter representing coalescence, and N in Eq.(6), the fitting parameter representing the number of particles returning to the pulp. Eq. (9) suggests that higher values of C represent less stable froth, and hence the froth recovery should decrease with increasing C. This is shown to be the case in Fig. 3.

On the other hand, as the drop-back rate (Eq.(6)) increases with increasing N. N represents the number of particles dropping back to pulp-phase. Thus, froth recovery decreases with increasing N, as shown in Fig. 4. However, the effect of changing N is minimal when particles are very fine (<1μm) or coarse (>100μm). This may be because at fine particle sizes particle drop rate is low regardless of the degree of mineralization, and the drop-back rate is high at coarse particle sizes. Parameters C and N work as independent parameters in the present model, although the two may have certain relationship to each other. However, the present work did not account for this relationship.

The effect of bubble size entering froth is shown in Figure 5. Eqs.(4) and (7) suggests that small bubbles entering the froth should yield low froth recovery. In figure 5, on the contrary, smaller entering bubbles are shown to be beneficial for the recovery at d_1<25 μm. Therefore, the simulation results for particles for those sizes are attributed to the recovery due to entrainment ($R_{F\text{-}e}$), rather than due to attachment. As shown in Eq.(14)~(16), small entering bubbles induce high water recovery, and hence high $R_{F\text{-}e}$. This model prediction agrees well with Ata *et al.*'s [43] experiment, in which fine silica particles showed significantly low recovery rate with large bubbles entering the froth, while the recovery of hydrophobic particles did not change much in the same environment.

The various parameters studied in the present work are interdependent with each other in practical froths. Therefore, the predictions made in Figures 1~5 may not be valid for certain cases, because the present model has been derived by assuming that all the parameters are independent from each other. Experimental data for verifying the model for all of the parameters are not available as yet. In the following section, some of the model predictions will be compared with experimental data reported in the literature.

4. Comparison with experimental work

In this section, the model for overall froth recovery is compared with experimental data reported in other literature. Seaman *et al*. [1] reported size-by-size froth recovery data. The authors measured froth recovery using two different methods and found that the pulp-froth interface is responsible for the recovery loss of recovery. Their device could effectively capture particles subject to true flotation, and corresponding data showed that true froth phase recovery varies with particle sizes. The data may be helpful for verifying the present model, but may not be the best because entrainment should give rise to the total recovery. Therefore, the entrainment part of the model is compared with other data reported by Zheng *et al*.[44, 45]. Both authors used the Outokumpu 3m^3 (OK3) cell. Typical operational values of OK3 cell such as specific air rate, and specific area were used in the simulation to provide the same conditions with the report. Any

physical conditions of OK3 may be found in the literature [46]. Any unspecified information but necessary for the current model was selected from other references.

In model predictions, the bubble size entering the froth was assumed to be 1 mm. The coalescence parameter *C* in Eq.(10) was chosen 3.55 for chalcopyrite flotation and 4 for galena flotation. These values are close to the data obtained for beer foams, for which the equivalent empirical parameter vary between 3 and 5 [47]. The model predictions for the froth recoveries of chalcopyrite are shown in Figures 6-A and 6-B, and those for galena are shown in Figures 7-A and 7-B. As shown, the model shows good agreement with experimental data represented by

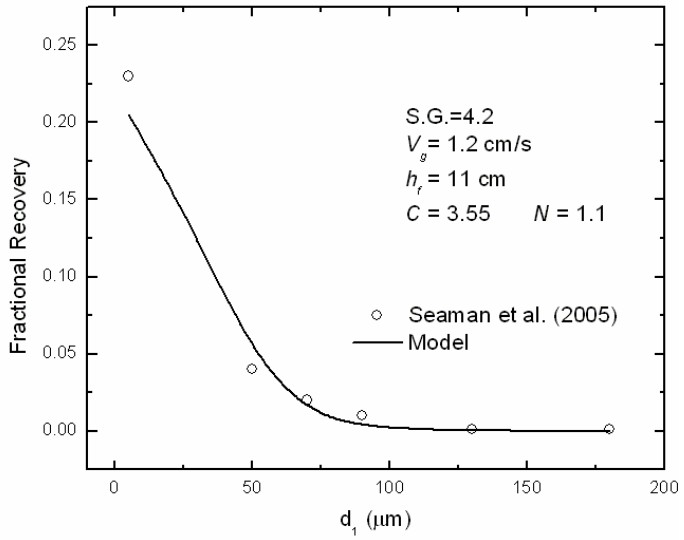

Figure 6-A. Comparison of the model, froth recovery due to attachment, with the chalcopyrite froth recovery data reported by Seaman et al.

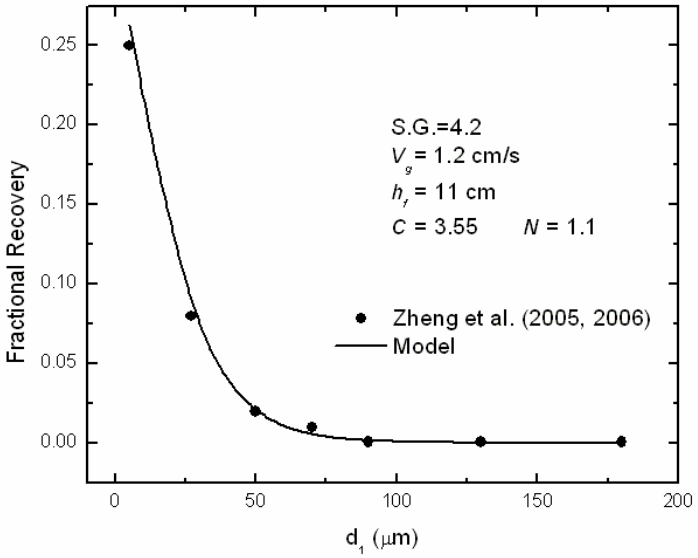

Figure 6-B. Comparison of the model, froth recovery due to entrainment, with the chalcopyrite froth recovery data reported by Zheng et al.

symbols. As shown, the recovery due to entrainment is as significant as attachment recovery when particles are small, but the significance diminishes as particles become as large as 50μm. This observation is consistent with what is reported in the literature [8, 48]. The predictions for the recovery due to attachment are not as good as those for the recovery due to entrainment, which may be attributed to the possibility that the adjustable parameter N from Eq.(7) may actually be a variable.

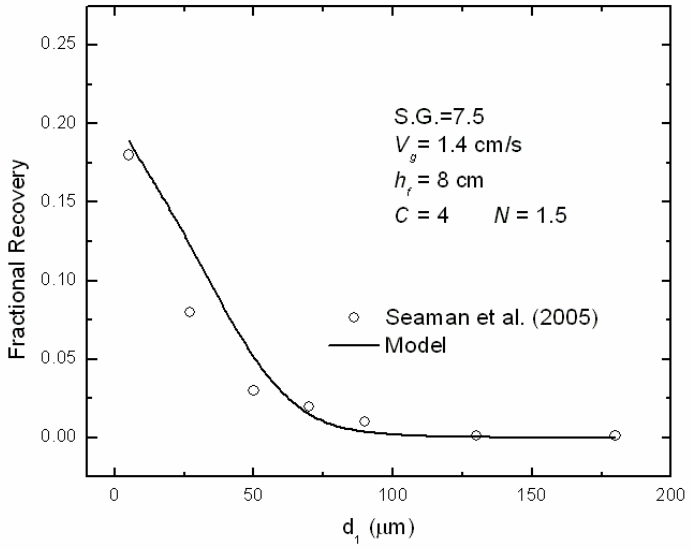

Figure 7-A. Comparison of the model, froth recovery due to attachment, with the galena froth recovery data reported by Seaman et al.

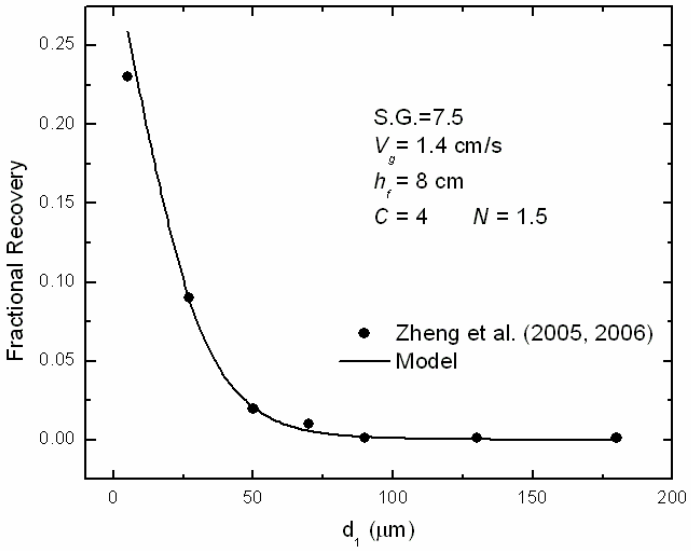

Figure 7-B. Comparison of the model, froth recovery due to entrainment, with the galena froth recovery data reported by Zheng et al.

5. Summary and conclusion

A froth recovery model for the conventional flotation cell has been developed and compared with experimental data. The model includes two major mechanisms for froth recovery, i.e., bubble-particle attachment and particle entrainment. For the froth recovery by attachment, a maximum recovery factor was considered from the idea that attachment is proportional to available surface area. A new definition of the particle drop-back rate in the froth was derived to account for the changes in bubble surface area and froth retention time for air bubbles. The recovery due to entrainment has been modeled by deriving a relationship between water recovery and fraction of water at the top of a froth phase and the fraction of bubble unburst during the process of bubble-particle aggregates being transported to overflow lip. The model predictions show that entrainment becomes significant with fine particles.

The model predictions show also that froth recovery decreases with increasing particle size due to detachment of particles, which in turn can be related to the decrease in bubble surface area as bubbles rise along the height of a froth phase due to bubble coalescence. Thus, coarse particle recovery in the froth phase can be improved by decreasing froth height or letting large bubbles enter the froth, as Eq.(7) indicates in case of high particle dropping rates.

6. References

1. Seaman, D.R., E.V. Manlapig, and J.P. Franzidis, *Selective transport of attached particles across the pulp-froth interface.* Minerals Engineering, 2005. **19**(6-8): p. 841-851.
2. Waters, K.E., et al., *Positron emission particle tracking as a method to map the movement of particles in the pulp and froth phases.* Minerals Engineering, 2008. **21**(12-14): p. 877-882.
3. Mathe, Z.T., et al., *Review of froth modelling in steady state flotation systems.* Minerals Engineering, 1998. **11**(5): p. 397-421.
4. Yoon, R.H., *The role of hydrodynamic and surface forces in bubble-particle interaction.* International Journal of Mineral Processing, 2000. **58**(1-4): p. 129-143.
5. Craig, V.S.J., B.W. Ninham, and R.M. Pashley, *The effect of electrolytes on bubble coalescence in water.* The Journal of Physical Chemistry, 1993. **97**(39): p. 10192-10197.
6. Ata, S., N. Ahmed, and G.J. Jameson, *Collection of hydrophobic particles in the froth phase.* International Journal of Mineral Processing, 2002. **64**(2-3): p. 101-122.
7. Gorain, B.K., et al., *The effect of froth residence time on the kinetics of flotation.* Minerals Engineering, 1998. **11**(7): p. 627-638.
8. Trahar, W.J., *A rational interpretation of the role of particle size in flotation.* International Journal of Mineral Processing, 1981. **8**(4): p. 289-327.
9. Warren, L.J., *Determination of the contributions of true flotation and entrainment in batch flotation tests.* International Journal of Mineral Processing, 1985. **14**(1): p. 33-44.
10. Maachar, A. and G.S. Dobby, *Measurement of feed water recovery and entrainment solids recovery in flotation columns.* Canadian Metallurgical Quarterly, 1992. **31**(3): p. 167-172.

11. Savassi, O.N., et al., *An empirical model for entrainment in industrial flotation plants.* Minerals Engineering, 1998. **11**(3): p. 243-256.
12. Lynch, A.J., M.W. Johnson, and E.V. Manlapig, eds. *Mineral and coal flotation circuits: their simulation and control*. Developments in mineral processing 3. 1981, elsevier.
13. Pugh, R.J., *Experimental techniques for studying the structure of foams and froths.* Advances in Colloid and Interface Science, 2005. **114-115**: p. 239-251.
14. Weaire, D. and S. Hutzler, *The physics of foams*. 1999: Oxford university press.
15. Leonard, R.A. and R. Lemlich, *A study of interstitial liquid flow in foam. Part I. Theoretical model and application to foam fractionation.* AIChE Journal, 1965. **11**(1): p. 18-25.
16. Koehler, S.A., S. Hilgenfeldt, and H.A. Stone, *A Generalized View of Foam Drainage: Experiment and Theory.* Langmuir, 2000. **16**(15): p. 6327-6341.
17. Verbist, G., D. Weaire, and A.M. Kraynik, *The foam drainage equation.* Journal of Physics: Condensed Matter, 1996. **8**(21): p. 3715-3731.
18. Gol'dfarb, I.I., K.B. Kann, and I.R. Shreiber, *Liquid flow in foams.* Fluid Dynamics, 1988. **23**(2): p. 244-249.
19. Verbist, G. and D. Weaire, *A Soluble Model for Foam Drainage.* EPL (Europhysics Letters), 1994. **26**(8): p. 631-634.
20. Do, H., et al., *Coarsening foam- Numerical modeling and experimental results*, in *Flotation 07 symposium*. 2007: Cape town, South Africa.
21. Wang, L. and R.-H. Yoon, *Hydrophobic forces in thin aqueous films and their role in film thinning.* Colloids and Surfaces A: Physicochemical and Engineering Aspects, 2005. **263**(1-3): p. 267-274.
22. Angarska, J.K., et al., *Detection of the Hydrophobic Surface Force in Foam Films by Measurements of the Critical Thickness of the Film Rupture.* Langmuir, 2004. **20**(5): p. 1799-1806.
23. Vrij, A., *Possible mechanism for the spontaneous rupture of thin, free liquid films.* Discussions of Faraday Society, 1966. **42**: p. 23-33.
24. Ruckenstein, E. and R.K. Jain, *Spontaneous rupture of thin liquid films.* Journal of Chemical Society, Faraday Transactions 2, 1974. **70**: p. 132-147.
25. Ivanov, I.B., et al., *Theory of the critical thickness of rupture of thin liquid films.* Transactions of Faraday Society, 1970. **66**: p. 1262-1273.
26. Wang, L. and R.-H. Yoon, *Effects of surface forces and film elasticity on foam stability.* International Journal of Mineral Processing, 2008. **85**(4): p. 101-110.
27. Yoon, R.H. and L. Wang, *Hydrophobic forces in foam films*, in *colloids and interface science series*, Tadros, Editor. 2007, Wiley-VCH. p. 161-186.
28. Habashi, F., *A short history of mineral processing*, in *23rd International Mineral Processing Congress*. 2006: Istanbul, Turkey. p. 3-8.
29. Hutzler, S., D. Weaire, and R. Crawford, *Convective instability in foam drainage.* EPL (Europhysics Letters), 1998. **41**(4): p. 461-466.
30. Finch, J.A. and G.S. Dobby, *Column flotation*. 1990: Pergamon press.
31. Sherrell, I. and R.-H. Yoon. *Development of a turbulent flotation model*. in *Centenary of flotation symposium*. 2005. Barisbane, Australia.
32. Szekrenyesy, T., K. Liktor, and N. S?dor, *Characterization of foam stability by the use of foam models 1. Models and derived lifetimes.* Colloids and Surfaces, 1992. **68**(4): p. 267-273.

33. Carrier, V. and A. Colin, *Coalescence in Draining Foams.* Langmuir, 2003. **19**(11): p. 4535-4538.
34. Yoon, R.-H. and B.S. Aksoy, *Hydrophobic Forces in Thin Water Films Stabilized by Dodecylammonium Chloride.* Journal of Colloid and Interface Science, 1999. **211**(1): p. 1-10.
35. Hartland, S. and A.D. Barber, *A model for a cellular foam.* Trans. Instn Chem. Engrs, 1974. **52**: p. 43-52.
36. Scheludko, A. and D. Exerowa, Kolloidnyi Zhurnal, 1959. **165**: p. 148.
37. Nguyen, A.V., *Liquid Drainage in Single Plateau Borders of Foam.* Journal of Colloid and Interface Science, 2002. **249**(1): p. 194-199.
38. Narsimhan, G. and E. Ruckenstein, *Structure, drainage and coalescence of foams and concentrated emulsions*, in *Foams: Theory, Measurments, and Applications*, R.K. Prud'homme and K.B. Kann, Editors. 1995, Marcel Dekker: New York.
39. Mysels, K.J., K. Shinoda, and S. Frankel, *Soap films, studies of their thinning and a bibliography*. 1959, New York: Pergamon Press.
40. Neethling, S.J., H.T. Lee, and J.J. Cilliers, *The recovery of liquid from flowing foams.* Journal of Physics: Condensed Matter, 2003. **15**(10): p. 1563-1576.
41. Prud'homme, R.K. and S.A. Khan, eds. *Foams: theory, measurement, and applications*. surfactant science series. 1995, Marcel Dekker.
42. Zheng, X. and L. Knopjes, *Modelling of froth transportation in industrial flotation cells: Part II. Modelling of froth transportation in an Outokumpu tank flotation cell at the Anglo Platinum Bafokeng-Rasimone Platinum Mine (BRPM) concentrator.* Minerals Engineering. **17**(9-10): p. 989-1000.
43. Ata, S., N. Ahmed, and G.J. Jameson, *A study of bubble coalescence in flotation froths.* International Journal of Mineral Processing, 2003. **72**(1-4): p. 255-266.
44. Zheng, X., N.W. Johnson, and J.P. Franzidis, *Modelling of entrainment in industrial flotation cells: Water recovery and degree of entrainment.* Minerals Engineering, 2006. **19**(11): p. 1191-1203.
45. Zheng, X., et al., *Modelling of entrainment in industrial flotation cells: the effect of solids suspension.* Minerals Engineering, 2005. **18**(1): p. 51-58.
46. Fallenius, K., *Turbulence in flotation cells.* International Journal of Mineral Processing, 1987. **21**(1-2): p. 1-23.
47. Sauerbrei, S., E.C. Haß, and P.J. Plath, *The Apollonian decay of beer foam bubble size distribution and the lattices of young diagrams and their correlated mixing functions.* Discrete Dynamics in Nature and Society, 2006: p. 1-35.
48. Smith, P.G. and L.J. Warren, *Entrainment of particles into flotation froths.* Mineral Processing and Extractive Metallurgy Review, 1989. **5**: p. 123-145.

Chapter 7. Summary and Suggestions for Future Research

1. Original Contributions

Five different topics have been presented in each chapter of this dissertation. However, all were in a consistent purpose: incorporating hydrophobic force into a flotation model. Therefore, the dissertation comprised mostly mathematical models pertaining to the fundamental theory of flotation. The original contributions by the present research are summarized as follows.

- ☐ Modeling flotation
  - A comprehensive turbulent flotation model has been developed for the first time.
  - The model incorporates both surface forces and hydrodynamic forces.
  - The model includes input parameters changing interdependently.
  - Extended DLVO theory has been verified from induction time measurement
- ☐ Modeling foam
  - The drainage equation incorporates bubble coalescence and PB area change for the first time.
  - Foam film rupture is modeled by incorporating hydrophobic force with fundamental theories.
- ☐ Froth recovery model
  - The model considers two distinctive mechanisms: particle attachment and entrainment.
  - Attachment mechanism is a function of bubble coarsening, which can be predicted from A_{cr} and h_{cr} models.
  - Entrainment mechanism is a function of water recovery, which can be predicted from a model.
- ☐ Dynamic simulator development
  - Flotation model and froth recovery model are ready to be implemented to the simulator.
  - Models can be used for circuit simulation, plant optimization and control.

2. Suggestions for Future Research

Even though experimental evidences were given to verify the models developed in this dissertation, they may be insufficient. In addition, the models are not complete since a lot of assumptions and simplifications were made to render the model work. In this regard, several suggestions are made for further research.

In chapter 2, the probability of aggregates entering froth (P_f) was introduced for the first time. It has been well known that the pulp-froth interface behaves like a barrier, and some particles collected by bubbles in the pulp phase fail to be recovered and hence fall back. However, there are no reports in the literature yet, that has systematically investigated the drop-back phenomenon in a flotation cell. Therefore, it is suggested that the P_f model may be validated by using an experimental technique similar to Heweitt *et al.'s* [1]. In a similar sense, the modified model for P_c may be validated as well if proper experimental method is present to account for all ranges of d_1/d_2.

In the flotation model, the value of K_{132} was estimated by known contact angles using an empirical relationship between the contact angle and hydrophobic force. However, this process may be substituted by a first principle since we have the extended DLVO theory. If the potential energy between bubble and mineral surfaces can be predicted by the theory, it may be incorporated with the Frumkin-derjaguin equation [2] to calculate the contact angle, when system properties are given. The reverse relationship may be found also because the original relationship would be derived from first principles.

The velocity increase factor of the flow inside a channel of hydrophobic walls was derived in chapter 4, but it was not validated by an independent experiment. However, it may be possible by a simple experiment. For example, one can evaluate the increase by studying the flow rate of water through a cylindrical plug made of a bunch of capillary glass tubes or sintered glass with certain porosity. Because glass surface can be hydrophobized and corresponding interfacial forces are relatively well known, flow through the hydrophobized media can be analyzed and compared with the untreated media.

In the foam drainage model, the interchangeability between the critical plateau border area (A_{cr}) and the critical rupture thickness (h_{cr}) was discussed. A_{cr} was preferred in the model because the other required more unknown parameters to be substituted in the drainage model. The number of unknown parameters may be reduced if one can devise an equation to correlate them. It can be done by analyzing the relationship between foam lifetime data and the critical rupture thickness data obtained from independent experiments.

References

1. Hewitt, D., D. Fornasiero, and J. Ralston, *Bubble-particle attachment.* Journal of Chemical Society, Faraday Transactions, 1995. **91**: p. 1997-2001.
2. Churaev, N.V. and V.D. Sobolev, *Physical chemistry of wetting phenomena*, in *Colloid stability: the role of surface forces, part 2*, F. Tadros, Editor. 2007, Wiley-VCH. p. 130.

APPENDIX 20 – Development of a Comprehensive Model for the Simulation, Scale-Up and Design of Large Flotation Machines (VA018)

FINAL TECHNICAL REPORT

Contract Title and Number:	Period of Performance:
Continuation in Crosscutting Technology Development at CAST. (DE-FC26-05NT42457)	Starting Date: 10/1/05 Ending Date: 3/31/12

Sub-Recipient Project Title: Development of a Comprehensive Model for the Simulation, Scale-UP and Design of Large Flotation Cells	Report Information: Type: Final Number: VA018-Final Period: Date: 8/1/2012 Code:
Principal Investigators: Roe-Hoan Yoon	
Contact Address: CAST 146 Holden Hall Blacksburg VA 24061	Contact Information: Phone: 540-231-7056 Fax: 540-231-3948 E-Mail: ryoon@vt.edu
Subcontractor Address: No subcontracts issued.	Subcontractor Information: Phone: Fax: E-Mail:

ABSTRACT

In flotation, particulate materials are separated by controlling the hydrophobicity of the particles using appropriate collectors. In this regard, contact angle (θ) is the most important process variable. However, the flotation models used in industry today do not include θ as a parameter. As result, flotation circuits are designed on the basis of the first-order flotation rate constants (k) determined from laboratory experiments. A problem with this approach is that laboratory experiments usually give substantially higher k values than achievable in full-scale operations, which makes it difficult to use the model for plant design. In the present work, we have developed a model from first principles using both surface chemistry and hydrodynamic parameters, such as θ, ζ-potentials, surface tension (γ), particle size, energy dissipation rate, etc.

The basic approach is similar to the one developed previously for bubble-particle interactions under laminar flow conditions (Yoon and Mao, *J. Colloid and Interface Science*, **181**, 61, 1996) except that the model parameters have been modified by considering the turbulence in a flotation cell. In addition, the model describes the recovery processes in froth phase, including bubble-coarsening due to coalescence. Based on this model, we have developed a computer simulator (FloteSim) that can be used to design flotation circuits from the mineralogical (or liberation) data on the feed and the hydrodynamic characteristics of a flotation machine. Since the model is dynamic, it can also be used for process control. Further, the simulator has predictive capacity as it is based on a first-principles model. The model-based simulator has been validated in a carefully controlled bench-scale flotation experiments.

Keywords: flotation kinetics; flotation model; contact angle; ζ-potential; size-by-size recovery; liberation; DLVO theory

INTRODUCTION

Flotation is widely used for upgrading run-of-the mine (ROM) ores and coal and is arguably the most important separation process used in the mining industry. The process is based on separating hydrophobic particles from hydrophilic ones dispersed in water by selectively attaching the former on the surface of air bubbles. Since the particles are collected on the surface of air bubbles, flotation kinetics and throughput should increase with bubble surface area rate (S_b) and decreasing bubble size (Yoon and Mao, 1996). Smaller air bubbles also give higher collision efficiencies (Ahmed and

Jameson, 1985; Luttrell and Yoon, 1992) and shorter induction times due to the higher Laplace pressure and smaller length scales involved (Yang, *et al*., 2011).

It has been shown recently that air bubbles in water are hydrophobic (Yoon and Aksoy, 1999; Yoon and Wang, 2006). Therefore, bubble-particle interaction may be considered a hydrophobic interaction operating at macroscopic scale. Recent studies showed also that the thin liquid films (TLF) of water formed between air bubble and xanthate-coated gold surfaces thin fast and rupture at critical film thicknesses (H_c) due to the presence of the attractive hydrophobic forces present in TLFs (Pan and Yoon, 2010; Pan, *et al*., 2011, 2012). In wetting films, both the van der Waals and double-layer forces are repulsive; therefore, the hydrophobic force should exceed these forces for the film to rupture, which is a prerequisite to bubble-particle attachment during flotation.

At Virginia Tech, we have been developing flotation models from first principles by considering both hydrodynamic and surface forces (Yoon and Mao, 1996; Sherrell and Yoon, 2005; Do, H, 2010). The parameters affecting the former include particle size, bubble size, energy dissipation rate, *etc*., while the parameters affecting the latter include contact angle (θ), ζ-potential, Hamaker constant (A_{131}), and surface tension (γ). Thus, the model can predict flotation recovery and grade from both physical and chemical parameters. The objective of the present communication is to present a model-based simulator that can be used to predict flotation performance from both hydrodynamic and surface chemistry parameters. Since the model is derived from first principles, the simulator has predictive and diagnostic capabilities.

MODEL

Derivation of First-Order Rate Equation

Many researchers modeled flotation as a first-order process (Sutherland, 1948; Tomlinson and Fleming, 1963),

$$\frac{dN_1}{dt} = -kN_1 \qquad [1]$$

in which the flotation rate is shown to be proportional to the number of particles **1 (**N_1) in a cell, with k representing its rate constant. It has been shown that k is given by the following relationship (Mao and Yoon, 1996),

$$k = \frac{1}{4} S_b P \qquad [2]$$

where S_b is the superficial bubble surface area rate and P is the probability of flotation. In general, P is given by

$$P = P_a P_c (1 - P_d) P_f \qquad [3]$$

where P_a is the probability of attachment, P_c the probability of collision, P_d the probability of detachment in pulp phase, and P_f is the probability of particles surviving froth phase.

Under quiescent conditions, P_c can be readily determined from stream functions for water around air bubbles (Luttrell and Yoon, 1992). Under turbulent conditions, however, most investigators use Abrahamson's collision model (1975),

$$Z_{12} = 2^{3/2} \pi^{1/2} N_1 N_2 d_{12}^2 \sqrt{\overline{u_1^2} + \overline{u_2^2}} \qquad [4]$$

which was derived for random collision under highly turbulent conditions and is applicable for particles whose Stokes numbers are very large. In Eq. [4], Z_{12} is the collision frequency between particles **1** and bubbles **2**, N_1 and N_2 are the number densities of particles and bubbles, respectively, d_{12} is the collision diameter (sum of radii of bubbles and particles), and $\bar{u}_1$ and $\bar{u}_2$ are the RMS velocities of the particles and bubbles, respectively.

The flotation rate equation for the turbulent flow conditions can then be written as

$$\frac{dN_1}{dt} = -Z_{12} P \qquad [5]$$

Substituting Eqs. [3] and [4] into Eq. [5], one obtains,

$$\frac{dN_1}{dt} = -2^{3/2} \pi^{1/2} N_1 N_2 (r_1 + r_2)^2 \sqrt{\overline{u_1^2} + \overline{u_2^2}} P_c P_a (1 - P_d) P_f \qquad [6]$$

which is a second-order flotation rate equation with respect to N_1 and N_2 and is applicable for large particles with high Stokes numbers. In flotation, bubble-particle collision is not completely random. Smaller particles follow the stream lines around bubbles; therefore, appropriate corrections are necessary particularly in areas away from impeller. In effect, the P_c of Eq. [6] serves as a correction factor for the hard-core, random collision model of Abramson (Eq. [4]). Eq. [21] below gives an expression for P_c used in the present work.

If N_2>>N_1 or N_2 remains constant during flotation, Eq. [6] becomes a pseudo-first-order flotation rate equation with respect to N_1. From Eqs. [1] and [6], one can then write an expression for the first-order rate constant (k) in the following form,

$$k = 2^{3/2}\pi^{1/2}N_2(r_1+r_2)^2\sqrt{\overline{u_1^2}+\overline{u_2^2}}P_cP_a(1-P_d)P_f$$
$$= Z_{12}/N_1P \qquad [7]$$

Bubble Generation Model

In using Eq. [7], the diameters of bubbles ($2r_2$) were calculated using the bubble generation model derived by Schulze(1984),

$$d_2 = \left(\frac{2.11\gamma_{lv}}{\rho_3\varepsilon_b^{0.66}}\right)^{0.6} \qquad [8]$$

where γ_{lv} is the surface tension of the water in a flotation cell, ρ_3 is the density of the water, and ε_b is the energy dissipation rate in the bubble generation zone. In the present work, it is assumed that air bubbles are generated at the high energy dissipation zone in and around the rotor/stator assembly, which has 5 to 30 times larger energy dissipation rates than the mean energy dissipation rate ($\bar{\varepsilon}$) of a cell (Schulze 1984). In the present work, we assumed that the energy dissipation rate in the bubble generation zone is 15 times larger than the mean.

RMS Velocities

The RMS velocity of the particles is calculated using the following relationship,

$$\overline{u_1} = 0.4\frac{\varepsilon^{4/9}d_1^{7/9}}{v^{1/3}}\left(\frac{\rho_1-\rho_3}{\rho_3}\right)^{2/3} \qquad [9]$$

where ε is the energy dissipation rate, d_1 is the particle diameter, v is the kinematic viscosity of water, ρ_1 is the density of the particle, and ρ_3 is the density of water (Schubert 1999).

For bubbles, the RMS velocity has been calculated using the equation derived by Lee and Erickson (1987),

$$\overline{u_2} = \left(C_0(\varepsilon d_2)^{2/3}\right)^{1/2} \qquad [10]$$

where C_0 (= 2) is a constant, and d_2 is bubble diameter.

Probability of Flotation

Probability of Attachment

In calculating P of Eq. [2], the probability of attachment is given by (Yoon and Mao, 1996),

$$P_a = exp\left(\frac{-E_1}{E_k}\right) \quad [11]$$

where E_1 is the energy barrier and E_k is the kinetic energy available during attachment process.

The value of E_1 of Eq. [11] can be obtained using the extended DLVO theory (Xu and Yoon, 1989; Yoon and Ravishankar, 1996),

$$E_1 = V_E + V_D + V_H \quad [12]$$

where V_E, V_D and V_H are the potential energies due to electrostatic, van der Waals and hydrophobic interactions, respectively. In the present work, we used the HHF model (Hogg, Healy, and Fuerstenau, 1966) to obtain,

$$V_E = \frac{\pi\varepsilon_0\varepsilon r_1 r_2(\psi_1^2+\psi_2^2)}{r_1+r_2}\left[\frac{\psi_1^2\psi_2^2}{\psi_1^2+\psi_2^2} ln\left(\frac{1+e^{-\kappa H}}{1-e^{-\kappa H}}\right) + ln(1+e^{-2\kappa H})\right] \quad [13]$$

where ε_0 is the permittivity in vacuum, ε the dielectric constant of the medium, ψ_1 the surface potential of the particle, ψ_2 the surface potential of the bubble, κ the reciprocal Debye length, and H is the separation distance between the bubble and particle. ψ_1 and ψ_2 can be substituted with ζ-potentials.

The van der Waals dispersion energy can be calculated using the following relationship,

$$V_D = -\frac{A_{132} r_1 r_2}{6H(r_1+r_2)}\left[1 - \frac{1+2bl}{1+bc/H}\right] \quad [1]$$

where A_{132} is the Hamaker constant for the bubble-particle interaction in the medium, b and l are characterization parameters for the materials involved, and c is the speed of light (Rabinovich and Churaev, 1979).

In the present work, the hydrophobic interaction energy has been calculated using the following relation,

$$V_{\mathrm{H}} = -\frac{K_{132} r_1 r_2}{6H(r_1+r_2)}$$

[15]

where K_{132} is the hydrophobic force constant between the bubble and particle (Rabinovich and Churaev, 1979), which can be obtained using the following relationship

$$K_{132} = \sqrt{K_{131} K_{232}} \qquad [16]$$

where K_{131} is the hydrophobic force constant between two particles, and K_{232} is the hydrophobic force constant between two bubbles (Yoon et al., 1997). It has recently been shown that Eq. [16] can be used for bubble-particle interactions (Pan and Yoon, 2010).

In using Eq. [16], we obtained the hydrophobic force constant (K_{131}) between two hydrophobic surfaces using the following relation,

$$K_{131} = ae^{b_k \theta} \qquad [17]$$

where a and b_k are constants which vary with contact angle, θ (Pazhianur and Yoon, 2003). Table 1 gives the values of a and b_{k} at different ranges of contact angles.

In determining P_a using Eq. [11], we calculated E_{k} using the following relation,

$$E_{\mathrm{k}} = 0.5 m_1 \left(U_{\mathrm{H_c}}\right)^2 \qquad [18]$$

where m_1 is the mass of the particle, and U_{Hc} is the velocity of a particle approaching a bubble at the critical rupture distance (H_{c}). This velocity may be found by the following relation,

$$U_{H_c} = \frac{\overline{u}_1}{\beta} \qquad [19]$$

where β is the drag coefficient in the boundary layer of the bubble (Goren and O'Neill, 1971), which in turn can be obtained as follows (Luttrell and Yoon, 1992),

$$\beta = 0.37 \left(\frac{r_1}{H}\right)^{0.83}$$

[2]

which has been derived from the Reynolds lubrication theory.

Probability of Collision

Luttrell and Yoon (1992) derived an expression for P_c, which has been modified slightly to ensure that $P_c < 1$(Do 2010),

$$P_c = tanh^2\left(\sqrt{\frac{3}{2}\left(1+\frac{\frac{3}{16}Re}{1+0.249Re^{0.56}}\right)}\left(\frac{d_1}{d_2}\right)\right)$$

[3]

where *Re* is the Reynolds number.

Probability of Detachment

The probability of detachment was calculated using the following expression (Yoon and Mao, 1986),

$$P_d = exp\left(\frac{-W_a+E_1}{E_k'}\right) \quad [22]$$

where W_a is the work of adhesion, and E'_k is the kinetic energy of detachment. W_a can be obtained from the following relation,

$$W_a = \gamma_{lv}\pi r_1^2(1-cos\,\theta)^2 \quad [23]$$

where γ_{lv} is the surface tension of water, r_1 is the radius of the particle, and θ is the contact angle.

In using Eq. [22], the kinetic energy of detachment (E_k') has been calculated using the following relation(Do 2010),

$$E'_k = 0.5m_1\left((d_1+d_2)\sqrt{\varepsilon/\nu}\right)^2$$

[24]

where ε is the energy dissipation rate and ν is the kinematic viscosity.

Froth Recovery Model

Once particles enter the froth phase, the more hydrophobic particles survive the froth phase and reach the launder while the less hydrophobic particles drop back to the pulp phase. The probability of survival (P_f) is given as (Do, 2010),

$$R_f = \frac{d_{2,0}}{d_{2,f}}e^{-N\frac{6h_f}{d_{2,0}}\left(1-\frac{d_{2,0}}{d_{2,f}}\right)\left(\frac{d_1}{d_{2,0}}\right)^2} + R_w e^{-0.0325\left(\frac{\rho_3}{\rho_1}-1\right)-63000d_1}$$

[25]

where $d_{2,0}$ is the diameter of the bubbles entering the froth phase at the bottom, d_{2f} the bubble diameter at the top, N the number of particles attached to each bubble, h_f the froth height, R_w the maximum theoretical water recovery, ρ_3 the density of water, and ρ_1 is the particle density. The first term of Eq. [25] represents the recovery due to attachment, while the second term represents the recovery due to entrainment (Do 2010).

By considering flow balance, one can derive the following relationship,

$$R_w = \frac{Q_{out}^{air}/Q_{in}^{liq}}{1/E_l - 1} \quad [26]$$

where Q_{out}^{air} is the volumetric flow rate of air leaving the cell, Q_{in}^{liq} the flow rate of pulp entering the cell, and E_l is the fraction of water entering a froth launder. The values of these parameters can be readily measured or are readily available in operating plants.

SIMULATION

Standalone Simulator

As shown in the foregoing section, the model is based on first principles (with the exception of entrainment), incorporating both hydrodynamic and surface chemistry parameters. The latter parameters including θ, A_{131} and ζ-potentials chemistry. Note here that the Hamaker constants (A_{131}) are inherent characteristics of minerals and water that do not change with operating conditions, while θ and ζ-potentials change with collector addition rate and pulp pH, respectively. Thus, the simulator is capable of predicting flotation from i) mineralogical characteristics of flotation feed that can be readily obtainable using QEM*SAM or MLA, ii) reagent dosage rates, iii) hydrodynamic characteristics of flotation machines, and iv) circuit arrangement. Conversely, the simulator can also be used to predict optimal flotation circuits for a given flotation feed. No laboratory flotation experiments are necessary to design a flotation circuit using a given set of flotation machines on the basis of such input dada as mineral liberation and reagent type and dosage rates.

More specifically, input parameters include specific power input, superficial gas rate, specific gravity (SG) of particles, air fraction (air holdup), slurry fraction (%solids), contact angle, froth height, frother type and concentration, particle and bubble ζ-potentials, the number of flotation cells and retention time, and volumetric feed rates of air and ore slurry. The permittivity of air, dielectric constant of water, the Hamaker constant of Water, *etc*., are given in the simulator by default but may be changed if desired.

Flowsheet Simulation Package

Flowsheet simulation is a crucial step in plant design and circuit optimization. If it is done right, it can be a very powerful tool for process engineers. In order to be able to develop complex flowsheets using a user-friendly graphical interface, the flotation model described above has been integrated into a flowsheet simulation package. The simulator was developed on Microsoft Excel using Visual Basic for Applications (VBA) programming language. Microsoft Excel was selected as the development platform as it is the most widely used spreadsheet software by engineers. Also, Microsoft Excel gives much freedom and flexibility to its users unlike many other simulation platforms.

The simulation process starts with drawing a flowsheet using Microsoft Excel's drawing tools. Then the simulation routine analyzes this flowsheet and creates separate worksheets that contain model equations for each unit. After the user inputs required information (*i.e*. size-by-size and class-by-class mineralogical compositions, particle size distribution, chemical and physical properties of the materials, cell dimensions, power input, *etc*.), the simulation routine calculates and produces recovery, grade, and other necessary output values.

RESULTS AND DISCUSSION

Contact Angle

Ideally, it would be useful to be able to predict the flotation rate constants (k) for large flotation cells from laboratory experiments. However, this is a challenging task, because k changes with scale up. As shown in Eq. [7] and associated equations, flotation rate constant (k) is a function of a large number of variables; therefore, it would be difficult to expect k to remain constant. For one thing, the energy dissipation rates of laboratory flotation machines are much higher, as much as ten-times, than those of full-size units. If dissipation rate changes, many other variables changes as well. In the present work, the values of k have been computed as particles in a flotation feed move long from one cell to another in a plant and calculated recoveries. One key variable that remains constant is the contact angle (θ) and some other intensive parameters. Once the values of θ are known for the various classes of particles in a feed stream, Eq. [7] can be also used to calculate k values and hence recovery and grade.

In the present work, we have simulated flotation to see the effects of some of the key variables such as contact angle, particle size, forth height, *etc*. Figure 1 shows the effects of increasing θ from 40 to 60°. Various other input parameters are given in the figure as legends. The results show bell-shaped recovery *vs*. particle size curves as reported by Trahar and Warren (1976). The results show

difficulties in floating coarse particles above approximately 149 μm (100 mesh) and fine particles below approximately 10 μm. The simulation results show, however, that the problems of floating both the coarse and fine particles can be overcome by increasing the contact angles of particles. Particle hydrophobicity along with bubble size and particle size may represent three of the most important parameters in flotation.

Muganda, *et al*. (2010) conducted lab-scale flotation tests on pure chalcopyrite samples of different size fractions of known advancing contact angles. The values of θ were controlled by conditioning the particles at different dosages of potassium amyl xanthate (KAX). The flotation tests were conducted at 0.3 cm/s superficial gas rate, 14.0 kW/m^3 energy dissipation rate, 1 cm froth height, 2% solids, and 20 ppm PPG-425. Figure 2 shows the size-by-size recovery *vs*. grade curves obtained at three different levels of contact angles, *i.e.*, θ = 36-40^o, 66-70^o, and 71-75^o. The solid lines represent the results of our simulations carried out using these contact angles, while the points represent the experimental results. Note here that data presented in Figure 5 are due to 'true' flotation, meaning that the authors subtracted the recoveries due to entrainment from the experimental recoveries. Since Muganda, *et al.* did not report the values of ζ-potentials, we used the values of -77 mV for minerals and -30 mV for air bubbles. The fit between the Muganda, *et al*.'s experimental and our simulation results is reasonable. The discrepancies observed at the finer and coarser particle sizes may be due to the possible errors associated in measuring contact angles using the Washburn method and the method of correcting the experimental data for the recovery due to entrainment. In general, the data presented in Figure 2 show that the higher the contact angles, the higher the recoveries, and that the optimum flotation occurs at the particle sizes in the range of 20 to 105 μm. These findings are similar to those shown in Figure 1.

ζ-Potentials

Another set of simulations were run to study the effects of particle ζ-potentials on flotation recovery. In this exercise, the ζ-potential of air bubbles was assumed to be -30 mV. As shown in Figure 3, fine particle flotation benefits from a decrease in the negative ζ-potential of particles from -15, -12, and -9 mV, which can be attributed to a decrease in energy barrier (E_1) for bubble-particle interaction. It is well known that the ζ-potentials of both air bubbles and mineral particles are negative particularly in sulfide flotation. By reducing the electrostatic repulsion between particles and bubbles, one can reduce the energy barrier for bubble-particle attachment and hence increase the flotation rate. As shown in Eq. [11], a decrease in E_1 should increase the probability of bubble-particle attachment (P_a) and hence the flotation rate. It is interesting that the beneficial effect of

controlling the particle ζ-potentials is observed with the flotation of finer particles but not with the coarse particles. However, the results can change under different operating conditions.

Mineralogical Composition

Figure 4a shows a set of size-by-size and class-by-class recovery curves reported by Sutherland (1989) from the QEM*SAM data obtained from a copper (chalcopyrite) flotation plant. As expected, the recovery curves shifted upward with increasing degree of liberation. Each curve is bell-shaped regardless of liberation indicating the importance of particle size in flotation.

Figure 4b shows the results obtained using the FlotSim package developed in the resent work. As shown in the figure legend, we assigned different contact angles for different classes of composite particles: the values of θ were varied in the range of 25 to 60^o for composite particles containing 15 to 95% chalcopyrite as measured by exposure on the surface of the polished specimens that are used for QEM*SEM mineral liberation analyzer. With these boundary conditions, we were able to simulate the results reported by Sutherland.

Flotation Kinetics

A set of flotation tests was conducted using a 9.2 L circular lab-scale flotation cell with a cross-sectional are of 0.048 m^2. It was custom designed and constructed to retain geometric similitude with full-scale mechanically-agitated flotation cells. The cell content was agitated at 1,200 RPM by a top-driven mixer equipped with a torque sensor that can be used to monitor energy dissipation rate. Air was supplied from a pressurized sourced, regulated and measured by a rotameter, and introduced to the cell through the mixing shaft and the rotor itself. Times-cut flotation products were taken to determine flotation rates.

The flotation tests were conducted on samples of glass spheres (A-Series Technical Quality, Potter Industries, with 35 μm nominal particle size) at a pulp density of 1.9% solids. Each test was used in the presence of $4x10^{-6}$ M dodecylamine hydrochloride (DAH) as collector and 10 mg/L MIBC as frother at a superficial gas rate of 2.0 cm/s and 1 cm froth height. After the completion of each flotation tests, the dried samples were homogenized and split to representative samples and analyzed for particle size (d_1) using a Honeywell MicroTrak laser size analyzer and the specific gravity by volumetric analysis. The SG of the glass beads was measured to be 2.5. The equilibrium contact angle of the particles was 48^o as measured on a glass slide that had been immersed in the flotation pulp during conditioning. The ξ-potential of the particles (3-10 μm fraction) was -42 mV as measured using a Malvern Zetasizer.

Figure 5 shows a set of recovery *vs*. time curves obtained at three different energy inputs. The fit between the experiment (points) and simulations (curves) were excellent. As expected, flotation rate increased with increasing energy dissipation rate.

Figure 6 shows another set of flotation kinetics data reported by Muganda, *et al*. (2010), with the curves representing our simulation results. The experiments were conducted on mono-sized particles of known contact angles, and the simulations were carried on the basis of the information given in the Muganda, *et al*.'s report. The fit between the experimental and simulation results is reasonable. As shown, the flotation kinetics and hence the recovery vary depending on particle size and hydrophobicity.

SUMMARY AND CONCLUSIONS

A model-based flotation simulator, called FlotSim, has been developed. The model is based on a flotation rate equation derived from first principles by considering both the hydrodynamic and surface forces involved in flotation. Thus, the FlotSim package is capable of predicting both flotation recovery and grade from various surface chemistry and hydrodynamic parameters, which include the contact angles (θ) and the ζ-potentials of the particles in a flotation feed, surface tension (or frother dosage), particle size, bubble size, energy dissipation rate (ε), cell geometry, flow rates of liquid, gas and solids, and circuit arrangements. The simulator package can predict flotation from the mineralogical compositions of a flotation feed, mineral liberation data, flotation machine characteristics, and circuit arrangement. The simulation results presented in this communication are consistent with flotation practice, and the predictions have been validated in laboratory experiments.

ACKNOWLEDGEMENTS

The authors would like to express sincere appreciation for the financial support (DE-FC26-05NT42457) from the National Energy and Technology Laboratory, DOE, and the FLSmidth Salt Lake City, Inc.

REFERENCES

Abrahamson, J, 1975. Collision rates of small particles in a vigorously turbulent fluid, Chem. Eng. Sci., 30, 1371-1379.

Ahmed, N and Jameson, G J, 1985. The effect of bubble size on the rate of flotation of fine particles, Int. J. Miner. Process., 14: 195-215.

Do, H, 2010. Development of a Turbulent Flotation Model from First Principles, PhD Dissertation, Virginia Polytechnic Institute and State University, Blacksburg, VA.

Goren, S L and O'Neill, M E, 1971. On the hydrodynamic resistance to a particle of a dilute suspension when in the neighbourhood of a large obstacle, Chem. Eng. Sci., 26: 325-338.

Hogg, R, Healy, T W, and Fuerstenau, D W, 1966. Mutual coagulation of colloidal dispersions, Transactions of Faraday Society, 62:1638-1651.

Lee, C A, and Erickson, L E, 1987. Bubble breakup and coalescence in turbulent gas-liquid, Chem. Eng. Commun., 59:65-84.

Luttrell, G H, and Yoon, R-H, 1992. A Hydrodynamic Model for Bubble-Particle Attachment, J. Colloid Interface Sci., 154:129-137.

Muganda, S, Zanin, M and Grano, S R, 2011. Influence of particle size and contact angle on the flotation of chalcopyrite in a laboratory batch flotation cell, Int. J. Miner. Process., 98(3-4):150-162.

Pan, L and Yoon, R-H, 2010. Hydrophobic Forces in Wetting Films, Faraday Discuss., 146:325-340.

Pan, L, Jung, S. and Yoon, R-H, 2011. A fundamental study on the role of collector in the kinetics of bubble–particle interaction, J. Colloid Interface Sci., 361(1):321-330.

Pan, L, Jung, S. and Yoon, R-H, 2012. Effect of Hydrophobicity on the Stability of the Wetting Films of Water Formed on Gold Surfaces, Int. J. Miner. Process., 106-109:37-41.

Pazhianur, R and Yoon, R-H, 2003. Model for the origin of hydrophobic force, Miner. Metall. Process, 20:178-184.

Rabinovich, Y and Churaev, N V, 1979. Effect of electromagnetic delay on the forces of molecular attraction, Kolloidn Zh, 41:468-474.

Schubert, H, 1999. On the turbulence-controlled microprocesses in flotation machines, Int. J. Miner. Process., 56:257-276.

Schulze, H J, 1984. Physico-chemical Elementary Processes in Flotation. (Elsevier. New York)

Sherrell, I and Yoon, R-H, 2005. Development of a Turbulent Flotation Model, in *Proceedings of the Centenary of Flotation Symposium*, pp 611.

Sutherland, K L, 1948. Kinetics of the flotation process, J. Phys. Chem., 52:394-425.

Sutherland, D N, 1989. Batch Flotation Behaviour of Composite Particles, Miner. Eng., 2:351-367.

Trahar, W J and Warren L J, 1976. The flotability of very fine particles - A review, Int. J. Miner. Process., 3(2):103-131.

Tomlison, H S and Fleming, M G, 1963. Flotation rate studies, in *Mineral Processing. Congr. of Miner. Process*., (ed: A Roberts) pp 563-579 (Pergamon Press, New York).

Yang, Y, Ma, J, Jung, S and Yoon, R-H, Dynamics of Bubble-particle Interaction, in Separation Technologies for Minerals, Coal, and Earth Resources, (ed: C A Young and G H Luttrell) pp 27-34 (Society for mining, metallurgy, and exploration, Inc., Colorado)

Xu. Z and Yoon, R H, 1989. The Role of Hydrophobic Interactions in Coagulation, J. Colloid Interface Sci., 132(2):532-541.

Yoon, R-H and Aksoy B S, 1999. Hydrophobic Forces in Thin Water Films Stabilized by Dodecylammonium Chloride, J. Colloid Interface Sci., 211:1-10.

Yoon, R-H and Mao, L, 1996. Application of Extended DLVO Theory, IV: Derivation of Flotation Rate Equation from First Principles. J. Colloid Interface Sci., 181:613-626.

Yoon, R-H and Ravishankar, S A, 1994. Application of Extended DLVO Theory: III. Effect of Octanol on the Long-Range Hydrophobic Forces between Dodecylamine-Coated Mica Surfaces, J. Colloid Interface Sci., 166(1):215-224.

Yoon, R-H, Flinn, D H and Rabinovich, Y I, 1997. Hydrophobic Interactions between Dissimilar Surfaces. J. Colloid Interface Sci., 185:363-370.

Yoon, R-H and Wang, L, 2006. Hydrophobic Forces in Foam Films, in *Colloid Stability -The Role of Surface Forces, Colloid and Interface Science Series*, (ed: T F Tadros), pp 161-186(Wiley-VCH).

FIGURE CAPTIONS

Fig 1 – Effect of contact angle on chalcopyrite recovery. Input parameters: energy dissipation rate, 1.5 kW/m^3; aeration rate, 2 cm/s; S.G. = 4.1, θ = 60° and 40°; frother, 192 mg/m^3 MIBC; ζ-potential, -15 mV; 4-cell bank; 3 min retention time per cell, 10 cm froth height, Q_{liq}= 1022 L/min, Q_{air}=1472 L/min, E_l = 0.10

Fig 2 – Effect of contact angles on the recovery of pure chalcopyrite particles of different contact angles. Experimental data are from Muganda, *et al*. (2011), and the curves are from simulation.

Fig 3– Effect of ζ-potentials on chalcopyrite recovery. Input parameters: energy dissipation rate, 1.5 kW/m^3; aeration rate, 2 cm/s; θ = 60°, 192 mg/m^3 MIBC; 4-cell bank; 3 min per cell retention time; 10 cm froth height; ζ = -15,-12, and -9 mV; Q_{liq}= 1,022 L/min, Q_{air}=1,472 L/min, E_l = 0.10.

Fig 4 - Effect of liberation on copper recovery (a) from Sutherland (1989) and (b) simulation results with FlotSim. Input parameters: θ = 25°, 33°, 40°, 60° for 15, 45, 75, 95% chalcopyrite liberation, respectively; 2.5 kW/m^3 energy dissipation rate; 2 cm/s superficial gas velocity; 9 cm froth height; 192 mg/m^3 MIBC; ζ = -8 mV; 4-cell bank with 2 min retention time per cell; Q_{liq}= 1533 L/min, Q_{air}=1472 L/min, E_l = 0.2.

Fig 5 - Results of the flotation kinetics tests conducted on mono-sized silica spheres at different energy dissipation rates. The curves show simulation results.

Fig 6 - The effects of contact angles and particle size on the kinetics of flotation. The experimental data were obtained by Muganda, *et al*. (2011) on pure chalcopyrite samples, and the curves represents the simulation results.

TABLE CAPTIONS

Table 1

Fitting Parameters for K_{131}

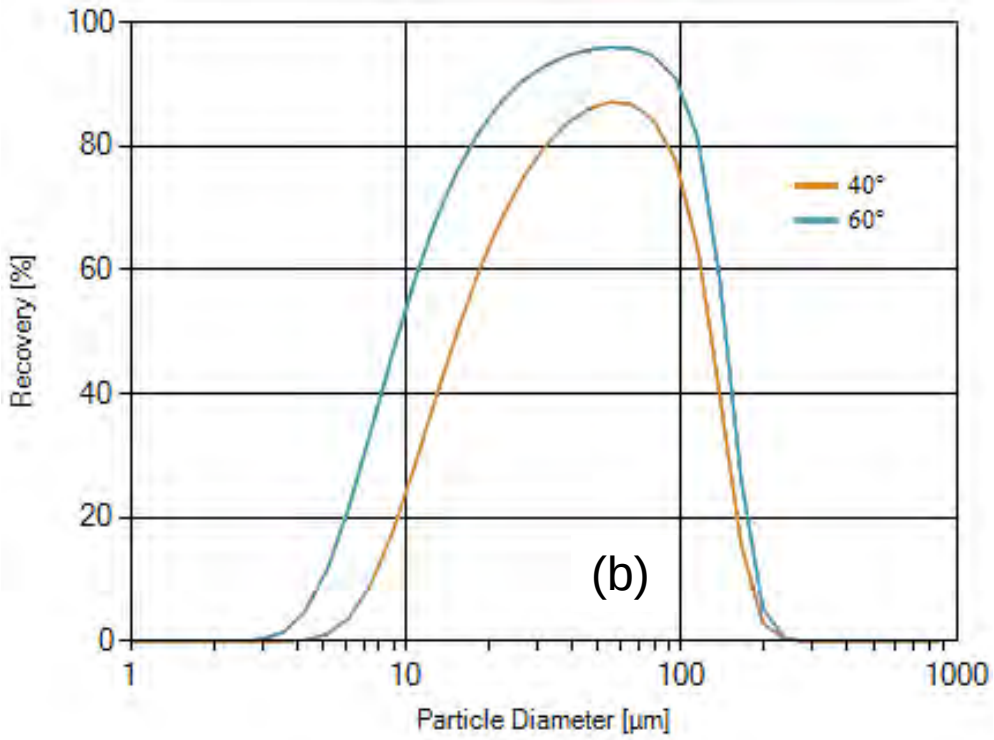

Fig 1 – Effect of contact angle on chalcopyrite recovery. Input parameters: energy dissipation rate, 1.5 kW/m^3; aeration rate, 2 cm/s; S.G. = 4.1, θ = 60° and 40°; frother, 192 mg/m^3 MIBC; ζ-potential, -15 mV; 4-cell bank; 3 min retention time per cell, 10 cm froth height, Q_{liq}= 1022 L/min, Q_{air}=1472 L/min, E_l = 0.10

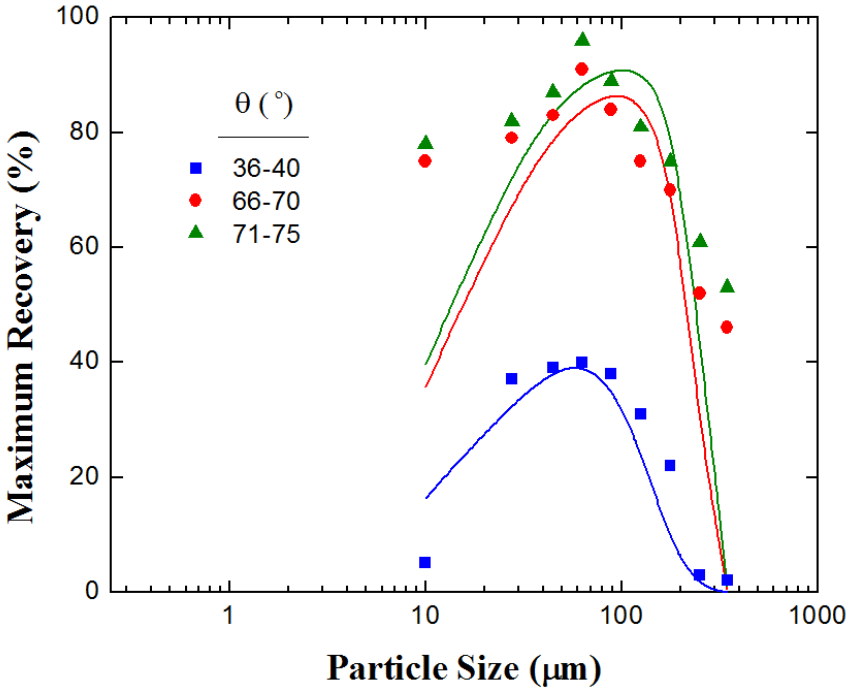

Fig 2 – Effect of contact angles on the recovery of pure chalcopyrite particles of different contact angles. Experimental data are from Muganda, *et al*. (2011), and the curves are from simulation.

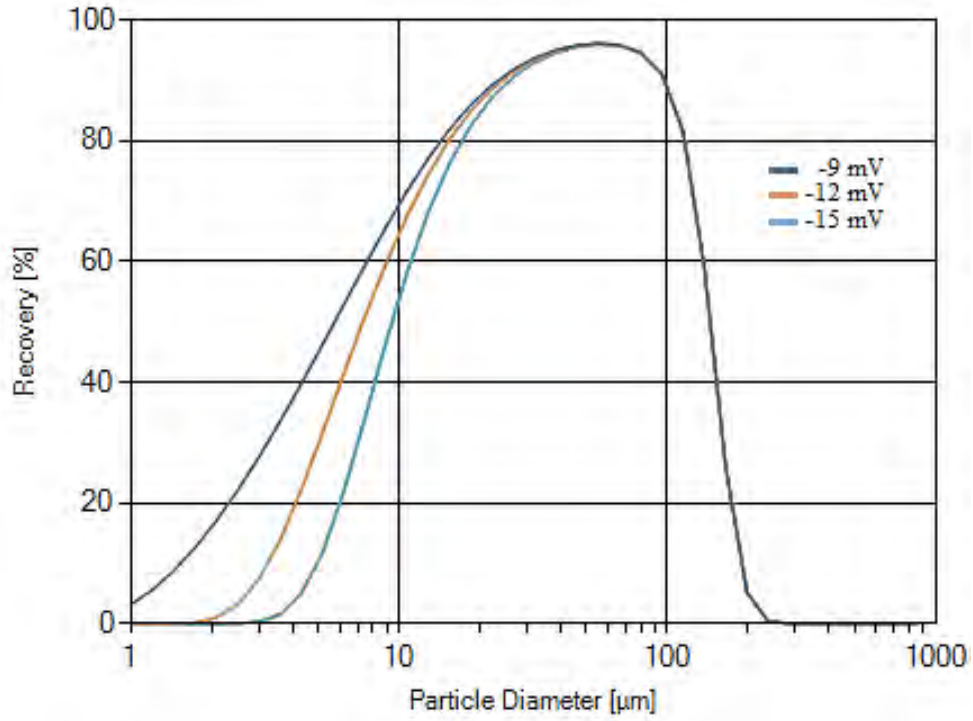

Fig 3– Effect of ζ-potentials on chalcopyrite recovery. Input parameters: energy dissipation rate, 1.5 kW/m^3; aeration rate, 2 cm/s; θ = 60°, 192 mg/m^3 MIBC; 4-cell bank; 3 min per cell retention time; 10 cm froth height; ζ = -15,-12, and -9 mV; Q_{liq}= 1,022 L/min, Q_{air}=1,472 L/min, E_l = 0.10.

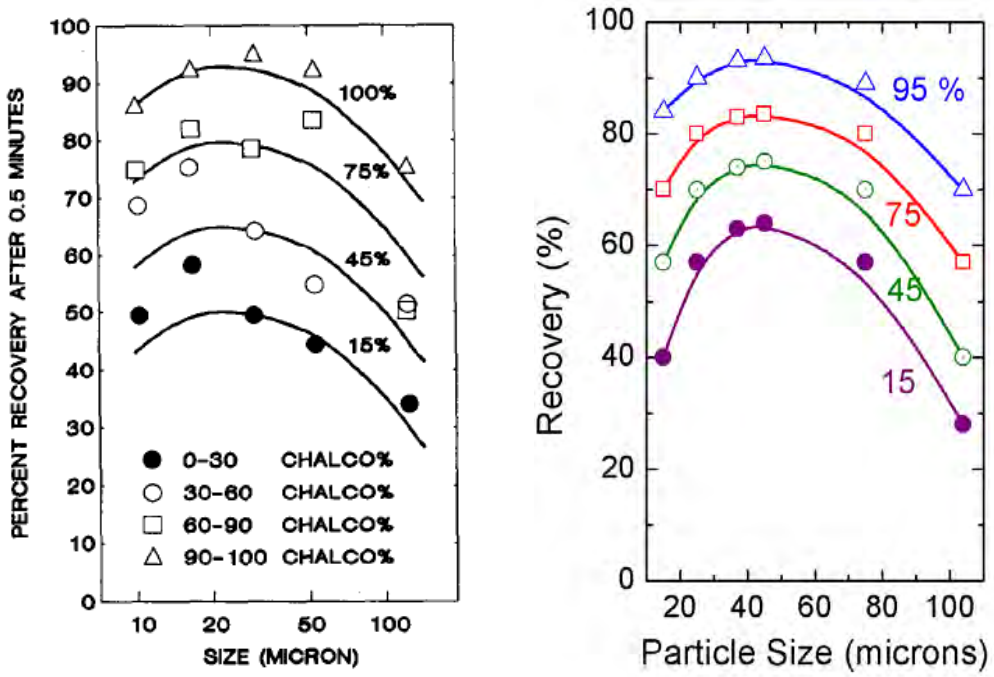

(a) (b)

Fig 4 - Effect of liberation on copper recovery (a) from Sutherland (1989) and (b) simulation results with FlotSim. Input parameters: $\theta = 25°, 33°, 40°, 60°$ for 15,45, 75, 95% chalcopyrite liberation; 2.5 kW/m^3 energy dissipation rate; 2 cm/s superficial gas velocity; 9 cm froth height; 192 mg/m^3 MIBC; ζ = -8 mV; 4-cell bank with 2 min retention time per cell; Q_{liq}= 1533 L/min, Q_{air}=1472 L/min, E_l = 0.2.

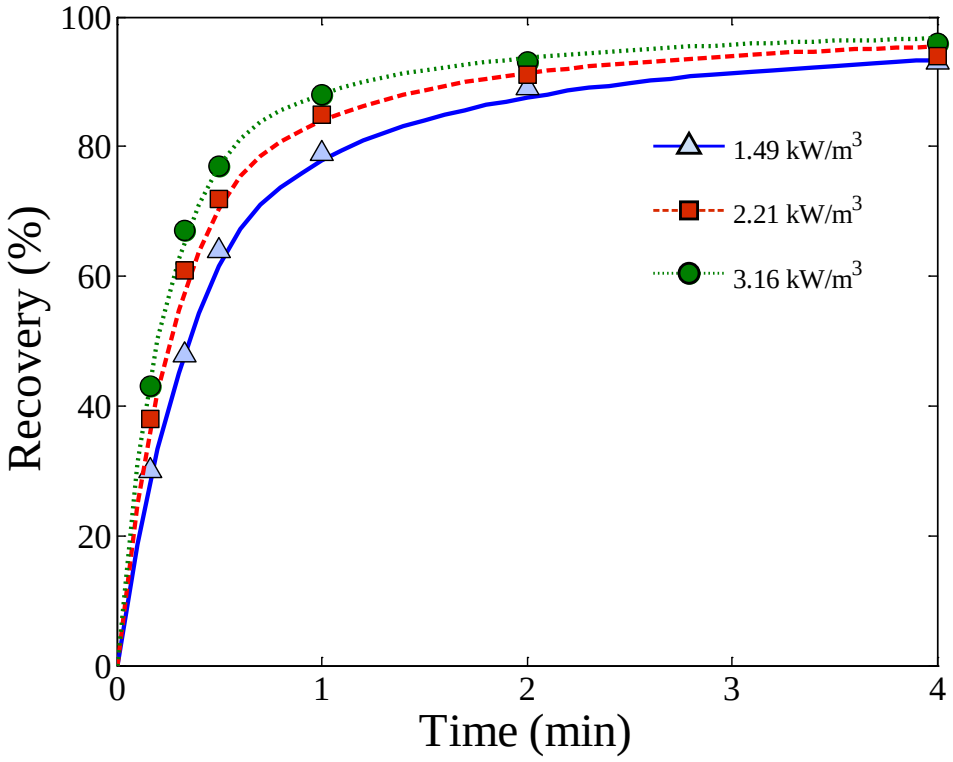

Fig 5 - Results of the flotation kinetics tests conducted on mono-sized silica spheres at different energy dissipation rates. The curves show simulation results.

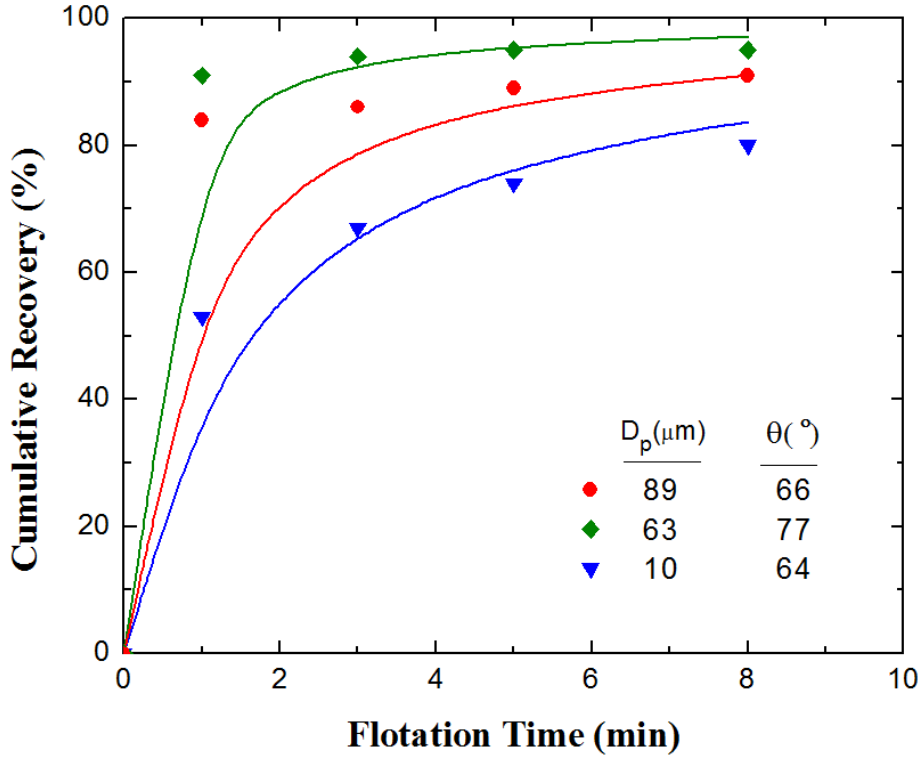

Fig 6 - The effects of contact angles and particle size on the kinetics of flotation. The experimental data were obtained by Muganda, *et al*. (2011) on pure chalcopyrite samples, and the curves represents the simulation results.

Table 1
Fitting Parameters for K_{131}

θ	a	b_k
> 92.28°	6.327×10^{-27}	0.2127
92.28° > θ > 86.89°	4.888×10^{-44}	0.6441
< 86.89°	2.732×10^{-21}	0.04136

APPENDIX 21 - Characterization, Analysis and Simulation of Fine Coal Filtration (UT011)

-

TECHNICAL REPORT

Contract Title and Number:	Period of Performance:
Continuation in Crosscutting Technology Development at CAST. (DE-FC26-05NT42457)	Starting Date: 10/1/08 Ending Date: 9/30/10

Sub-Recipient Project Title:
Characterization, Analysis and Simulation of Fine Coal Filtration

Principal Investigators:
J.D. Miller, C.L. Lin

Contact Address:
University of Utah
135 South 1460 E. Room 412
Salt Lake City UT 84112

Subcontractor Address:
No subcontracts issued

Report Information:
Type: Final
Number:
Period: 10/1/08-09/30/10
Date: 11/15/10
Code: UT011-FINAL

Contact Information:
Phone: (801) 581-5160
Fax: (801) 581-4937
E-Mail: Jan.Miller@utah.edu

Subcontractor Information:
Phone:
Fax:
E-Mail:

Disclaimer

The Disclaimer must follow the Title Page and must contain the following paragraph: "This report was prepared as an account of work sponsored by an agency of the United States Government. Neither the United States Government nor any agency thereof, nor any of their employees, make any warranty, express or implied, nor assume any legal liability or responsibility for the accuracy, completeness, or usefulness of any information, apparatus, product, or process disclosed, or represents that its use would not infringe privately owned rights. Reference herein to any specific commercial product, process, or service by trade name, trademark, manufacturer, or otherwise does not necessarily constitute or imply endorsement, recommendation, or favoring by the United States Government or any agency thereof. The views and opinions of authors expressed herein do not necessarily state or reflect those of the United States Government or agency thereof. "

Abstract

Fine coal filtration and dewatering are of great importance to the coal industry due to its significant impact in the quality, shipping and handling of the coal product. High moisture content in the coal product reduces its heating value, increases costs, and reduces the coke yield in the case of metallurgical coal. In this regard, it is of significant importance to improve our fundamental understanding of water removal from the pore network structures present in filtration cakes.

The multiphase flow and dewatering which occurs during fine coal filtration can be described by the results from Lattice-Boltzmann (LB) simulations. As is known, important factors which influence the efficiency of filtration include – particle size distribution (pore network structure is determined by X-ray micro computed tomography), pressure drop (flow rate), and wetting characteristics of the coal (water contact angle). Results from permeability experiments are used to validate preliminary simulations. Research is in progress to simulate coal filtration and identify conditions that will lead to improved water removal and minimum cake moisture content.

Table of contents

Executive Summary

This research presents the results of our exploration into the study of fluid transport phenomena in fine coal filter cake using x-ray microtomography techniques to characterize the complex three-dimensional pore geometry. The 3D porous structures captured by HRXMT analysis are coupled with the Lattice Boltzmann Method (LBM) to simulate and to establish a fundamental relationship between pore microstructure and filtration operation variables.

High resolution X-ray micro CT (HRXMT) will allow for further advances in the 3D characterization of pore network structures in filtration cakes. With a voxel resolution of less than 1 micron, particles as small as 5 microns can be distinguished and described.

In order to gain a better understanding of the complex transport phenomena that occur in a filter cake, study of the effect of 3-dimensional pore geometry on the effective transport properties of the filter cake is necessary. Transport calculations have been carried out for the actual three-dimensional porous media (in our case packed bed of coal particles) using the single phase Lattice-Boltzmann method. Permeability from single phase LB simulation has been estimated to be 9.28×10^{-8} cm^2 for minus 0.85 mm (20 mesh) coal particles.

We have been successful in implementing the 2D and 3D software capabilities of LB simulation for multiphase fluid flow in porous media. The single component multiphase flow He-Chen-Zhang LBM model has been extended to incorporate fluid-solid interaction forces and has been applied to the simulation of percolation in actual HRXMT images of pore network structures created by packed particle beds. Finally, in order to evaluate the actual potential of this mathematical model to simulate real multiphase problems a comparison between experimental data and simulation results is in progress with the intent to describe conditions that will lead to improved water removal and minimum cake moisture content. Of course this is a challenging problem because of the complexity of the physical phenomena involved and the size of the computing resources required.

Introduction

Fine coal filtration and dewatering are of great importance to the coal industry due to its significant impact in the quality, shipping and handling of the coal product. Of particular significance is the moisture of filter cake as mentioned by Gary Meenan (CONSOL Energy) at his presentation during the 2005 CAST conference,

"Half of the plant product moisture is associated with the filter cake product. This has a negative impact on plant operation and ... on the bottom line."

The significance of dewatering and moisture reduction in clean coal products was further reinforced by Van Davis (Senior Process Engineering, Alpha Natural Resources) in his presentation at the 2007 CAST Conference,

"*… Residual moisture continues to be problematic for the coal industry. Industry needs to develop a cost effective means of reducing moisture on fine coal flotation products. The potential increased value of coal recovery or operating cost reduction can be measured in millions of dollars per year per plant*."

The high moisture content in coal products reduces its heating value, increases costs, and reduces the coke yield in the case of metallurgical coal. So, what is the economic benefit of moisture reduction? Based on the discussion with Professor Luttrell at Virginia Tech, there are two ways the industry can look at this issue. The "first method" considers only the impact of moisture on the sales price ($/ton) of the clean coal product. Consider a typical bituminous coal having a heat content of 12,500 BTU/lb coal that sells for $50/ton. Based on this:

1 ton = 25 MM BTU
$50/25 MM BTU = $2.00/MM BTU
$50/12,500 BTU/lb = $0.40 per 100 Btu/lb
1% moisture = 150 BTU/lb (approx.)
1% drop = $0.60/ton premium (approx.)

A one percentage point reduction in moisture (or ash for that matter) adds about $0.60 per ton to the sales price of the coal. The increased price is a reflection of the fact that utilities buy heat content, not tons of carbon.

The "second method" is often overlooked by those working in industry, but it actually provides the greatest opportunity for justifying additional moisture removal. In this case, the company foregoes the increased sales price and instead attempts to trade moisture (with no heat value) for middlings (with some heat value). For example, the tables shown below demonstrate the large financial impact of improving fines moisture from 14% to 10% for an eastern coal plant. The plant was constrained to provide a 12,300 BTU/lb clean coal product. By lowering the fines moisture from 14 to 10%, the plant was able to raise the density cutpoint from 1.5 SG to 1.6 SG in the coarse cleaning circuit. This increased the overall plant tonnage from 637 to 659 TPH without impacting the heat content of the final product (The ash content did increase slightly from 11.8% to 12.4%, but was still under the contract limit

of 12.5% ash). This represents a tonnage gain of 22 TPH, which is worth about $6.6 MM per year (22 ton/hr x $50/ton x 6,000 hr/yr=$6.6 MM/yr). Large financial gains can often be realized when you trade moisture for middlings coal.

Existing Dewatering	Clean (tph, ar)	Moisture (%, ar)	Ash (%, ar)	Heat (Btu/lb, ar)
Coarse (1.50 SG)	552.6	5.0	12.0	12450
Fines Circuits	85.0	***14.0***	10.5	11325
Total Plant	**637.6**	**6.2**	**11.8**	**12300**

Improved Dewatering	Clean (tph, ar)	Moisture (%, ar)	Ash (%, ar)	Heat (Btu/lb, ar)
Coarse (1.50 SG)	552.6	5.0	12.0	12450
Coarse (1.5x1.6 SG)	25.8	5.0	25.0	10500
Fines Circuits	81.2	***10.0***	11.0	11852
Total Plant	**659.7**	**5.6**	**12.4**	**12300**

In this regard, it is of significant importance to improve our fundamental understanding of water removal from the pore network structures present in fine coal filtration cakes.

Filtration of fine coal involves filter cake formation and removal of surface moisture by drawing air through the porous structure. An accurate assessment of the transport properties in porous media is of major importance in the development of improved filtration processes (Leonard and Hardinge 1991; Wakeman, and Tarleton 2005; Tien 2006). Currently, there is limited understanding of the fundamental phenomena involved at the pore scale level which controls the average behavior of the filtration process.

There are several factors that affect the final moisture content of a coal filter cake, including cake thickness, pressure drop across the cake, drying time, viscosity of the liquid, surface tension of the liquid, filter media, particle size distribution, permeability of the cake, specific gravity of dry solids, inherent moisture of dry solids, type of filter and construction, and volume of air or gas pulled through the cake per unit of time per unit area, among others (Leonard and Hardinge, 1991). Understanding each factor and their relationship is necessary to define the optimal conditions for coal dewatering during the filtration process. However, such a task is complicated and overwhelming since it entails a large group of variables, including the complexity of the pore geometry, which is often tedious to determine experimentally. The approach currently used involves a series of simplified assumptions in order to obtain a mathematical relationship between a small group of variables, making the decision and design process simpler. However, there is no linear or non-linear rule for a combination of the effective physical properties from the microscopic scale that can be used to predict the macroscopic scale properties. The lack of fundamental understanding at the pore scale level during the coal filtration process limits the ability to predict and resolve common operational problems such as cake cracking and moisture retention. In this regard, it is important to introduce appropriate experimental techniques and theoretical models to

describe in detail at the pore scale level the flow occurring through a packed bed of coal particles during filtration.

Computational fluid dynamics (CFD) methods have demonstrated some success in simulating multiphase flow in porous media, but it has failed in simulations where complex pore geometries are present. Unlike the conventional CFD method, a "top-down" approach based on discretization of macroscopic continuum equations, the Lattice-Boltzmann method (LBM) is based on a "bottom-up" approach where constructed kinetic models incorporate microscopic model interactions and mesoscopic kinetic equations. The major advantage claimed for pursuing the use of LBM instead of standard computational fluid dynamics (CFD) methods resides in its ability to model complex boundaries in any arbitrary geometry, a scheme suitable for code parallelization and the ability to incorporate microscopic force interactions that control interfacial dynamics. The LBM applies numerical simulations of fluid flow in the actual porous structure which leads to the determination of the local flow conditions for single and multiphase flow in the complex pore structure.

Understanding the fundamental parameters involved in the filtration process is essential in order to improve the water removal and define the condition for minimum cake moisture content. To gain better understanding of the complex transport phenomena that occur in the porous media, a study of the effect of three-dimensional pore geometry on the effective transport properties of the filter cake is necessary. X-ray microtomography is being used for the characterization of the complex three-dimensional pore geometry by direct digitalization of the real pore network structure of the coal cake. Such a system, as show in Figure 1, is the high-resolution x-ray micro CT (HRXMT) from Xradia (2009) which employs an x-ray detector with sub-micron resolution combined with a microfocus x-ray source. In this way, with a voxel resolution of about 1 micron, the real pore network structure of the coal cake composed of coal particles with a size less than 20 mesh (0.85 mm) can be described. The use of HRXMT and emerging Lattice-Boltzmann simulation methods, present a unique opportunity to explore such matters. The simulation study relies on a combination of 3D data, obtained from HRXMT measurements, and the LBM to generate a model and describe the conditions for improved water removal during filtration.

Research Objective

In view of the foregoing, an extensive two-year research program has been designed to study fine coal filtration using XMT and LBM for fluid flow simulation in order to help identify optimum conditions of operation. This is the continuation of research developed by Professors J.D. Miller and C.L. Lin at the University of Utah using LBM in 3D problems in order to improve the understanding of the phenomena associated with fluid flow in packed particle beds. This final report presents the results of the first year of the two-year research program.

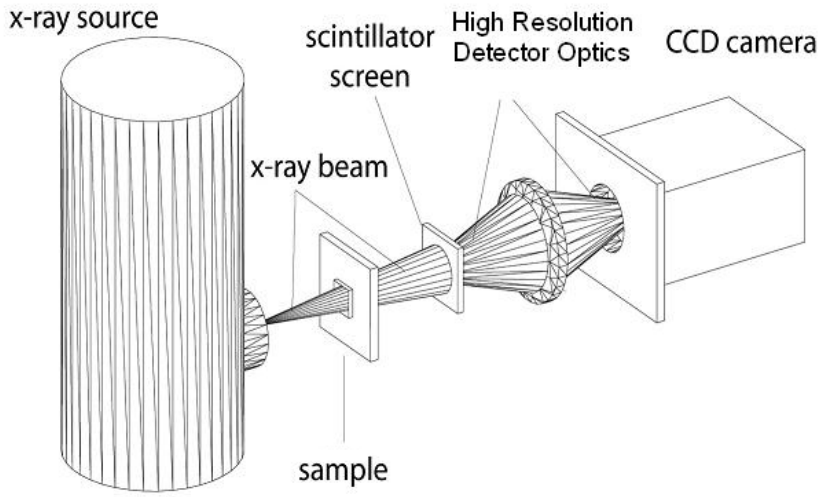

Figure 1. Xradia's High-Resolution Micro CT (HRXMT) uses a microfocus x-ray source with 150 kV accelerating voltage. The sample can be translated in x-y-z-theta directions with a high resolution stage. High resolution is achieved with a proprietary x-ray detector with an effective detector pixel size < 1 micron.

Experimental

High Resolution X-ray Micro Computed Tomography (HRXMT)

X-ray tomographic imaging is, in general terms, an X-ray-based method by which radiation of an opaque sample in different directions allows for its three dimensional (3D) reconstruction. The development of this non-invasive technique is recent but it has had a huge impact in several areas of science. In fact, the first device capable of producing true reconstructed images was developed by G. N. Hounsfield only in 1972 at EMI in England and it was based, in part, on mathematical methods developed by A. M. Cormarck a decade earlier.

The mechanics of X-ray tomography testing are relatively simple. The sample is located between the x-ray source and the detector. Then the sample is illuminated in different directions, and for each direction the projection of the attenuation coefficients is measured. Finally, a computerized reconstruction is carried out. The reconstruction of the samples is based on a mathematical formalism known as the Radon transform and its mathematical framework. After processing, the CT produces a spatial description of the object under analysis where the field of view is divided into elemental digital units known as voxels. Each voxel is characterized by the attenuation coefficient of the material of which it is composed. This spatial digital characterization of the sample under analysis allows for further digital processing of the sample.

Single Component Single Phase Lattice-Boltzmann (LB) Model

The classical approach (Tiller 1975; Dahlstrom and Silverblatt 1977; Svarosvsky 1990) for filtration analysis is based on Darcy's law, an empirical equation that describes one-dimensional fluid flow through uniform incompressible porous media. Knowledge of cake pore microstructure and its correlation to macroscopic cake properties is required to model the filtration from a fundamental point of view. Darcy's law is defined as

$$U = \frac{Q}{A} = \frac{1}{A}\frac{dV}{dt} = \frac{k\,\Delta p}{\mu\,\ell} \tag{1}$$

where U is the fluid velocity [m/s], Q is the volume flow rate [m^3/s], V is the volume of the fluid [m^3], k is the permeability [m^2], μ the dynamic viscosity of the fluid [Pa.s], A the cross sectional area [m^2] of the one dimensional sample of length (or thickness of porous media) ℓ [m] and Δp is the pressure drop [Pa].

The single component, single phase LB model has been used as a common tool to study transport phenomena through pore space (Lin and Miller 2004 and cited references; Videla, Lin and Miller 2007). In this regard, permeability was computed by modeling Stokes flow in both the simulated pore space of a packed bed and actual 3D digital pore space from HRXMT analysis using the LB method. Calculation of permeability is summarized here as follows.

For non-overlapped spheres, the permeability k (unit of length^2) is related to the drag coefficient C_d,

$$k = \frac{\upsilon}{6\pi R C_d} \tag{2}$$

where υ is the unit cell volume, and R is the sphere radius. For Darcy flow,

$$k = -\frac{U\mu}{dP/dx} \tag{3}$$

Compared with Equation 2, U is the fluid velocity average across an inlet or outlet face of the unit cell (including solids), μ is the dynamic viscosity, and dP/dx is the pressure gradient along the x-direction. Formally, the LB used in this study is a constant-pressure model, so the pressure gradient must be related to the body force. To relate the permeability to units measured in the LB simulation, a force balance was applied:

$$\text{xBody}\ \rho\ L^3 = (P_{in} - P_{out})\ L^2 = -(dP/dx)\ L^3 \tag{4}$$

or $(dP/dx) = -\ xBody\ \rho$, where L is the side of the simulation cell (in lattice units), $xBody$ is the body force, applied in the x-direction, per unit volume in the LB simulation, and ρ is the particle density per site specified in the LB simulation. Thus,

$$k = \frac{U\nu}{xBody} \tag{5}$$

where $\nu = \mu/\rho = (\tau - 1/2)/3$ is the kinematic viscosity specified in the LB simulation as shown in Equation 2. Customarily k/L^2, normalized permeability, is reported rather than k to achieve scale-independence.

Physics of Multiphase Flow in Porous Media

The flow of two immiscible fluids sharing simultaneously the complex pore space in porous medium is governed by the forces acting on the fluids, including pressure forces, viscous forces, gravity forces, inertia forces and interfacial surface forces. The relative importance of these forces is usually characterized by the Reynolds (Re), Bond (Bo), and Capillary (Ca) numbers, as well as the viscosity ratio (M) and these parameters are defined in equations 6 through 9, respectively.

$$\mathrm{Re} = \frac{u \cdot D}{\nu} \tag{6}$$

$$Bo = \frac{g\left(\rho_{nw} - \rho_{w}\right) \cdot R^2}{\gamma} \tag{7}$$

$$Ca = \frac{\nu_w \mu_w}{\gamma} \tag{8}$$

$$M = \frac{\mu_{nw}}{\mu_w} \tag{9}$$

In general, flow in porous media is dominated by the capillary forces, where inertia forces are negligible, and pressure forces and viscous forces are proportional to the rate of flow. Because the pressure forces and viscous forces depend on the flow rate, the capillary forces and gravitational forces become more important when the rate of flow is slower.

Capillary pressure

When two immiscible fluids are in contact in the porous medium a discontinuity in pressure exist across the interface. The difference in pressure is called the capillary pressure. The capillary pressure is defined as the difference between the pressures of the non-wetting fluid p_{nw} and the wetting fluid p_w as shown in equation 10.

$$p_c = p_{nw} - p_w \tag{10}$$

Figure 2 shows a curved interface between two immiscible fluids under static equilibrium. From the figure it is observed that capillary pressure depends in the curvature of the interface. In soil science, the negative of the capillary pressure is known as tension or suction head.

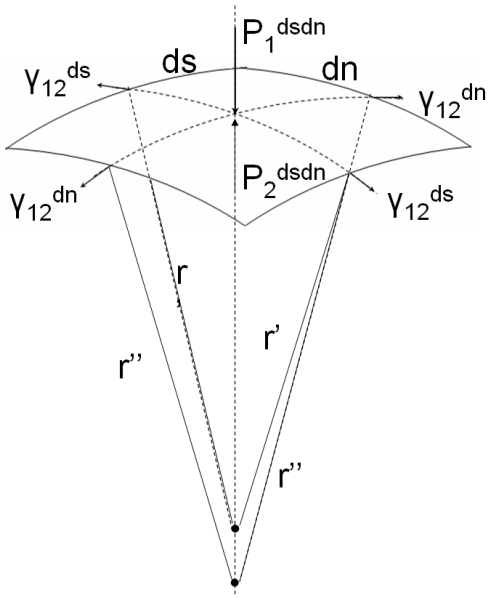

Figure 2. Forces acting on the elementary surface around a point of a curved interface between two immiscible fluids at static equilibrium.

Interfacial shapes in static and quasi-static situations are governed by the Laplace equation. By applying the condition of mechanical equilibrium of the forces acting on the interface, Laplace showed that the capillary pressure is proportional to the interfacial tension and inversely proportional to the curvature of the meniscus. Laplace's law is presented in equation 11 for a 3D pore structure and is dependent on the interfacial tension γ_{12} and the radii of curvature, r^*.

$$p_2 - p_1 = p_c = 2\frac{\gamma_{12}}{r^*} \text{ , with } \frac{1}{r^*} = \frac{1}{2}\left(\frac{1}{r'} + \frac{1}{r''}\right) \tag{11}$$

Interfacial tension and contact angle

Porous structures involve the presence of a solid phase which in a capillary system interacts with at least two fluid phases. As a result there are at least three surfaces subjected to surface tension as shown in Figure 3. The static equilibrium between the three interfacial tensions leads to the well known Young's equation as shown in equation 12.

$$\gamma_{\mathrm{lg}} \cos\theta = \gamma_{sg} - \gamma_{sl} \tag{12}$$

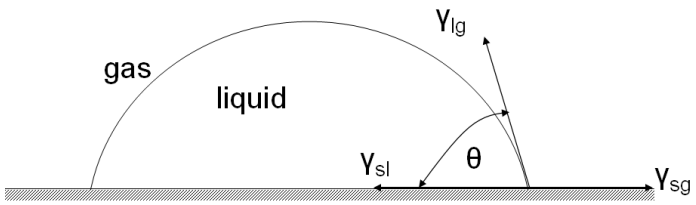

Figure 3. Static equilibrium between the three interfacial tensions at the solid surface.

The contact angle is normally used to describe the preferential characteristics of the solid surface to be wet. In some cases, no equilibrium is possible $\left(\gamma_{\mathrm{lg}} > \gamma_{sg} - \gamma_{sl}\right)$ and the liquid covers the whole surface completely, in such cases the liquid is said to wet the solid perfectly.

Capillary pressure versus saturation curves

The capillary pressure depends on the saturation, interfacial tension, wetting angle, viscosity ratio and Bond number (Marle 1981). Because the capillary pressure depends on the contact angle one may expect a hysteresis effect, meaning that different capillary pressure–saturation curves are obtained depending on the history of the fluid motion. For example, the capillary pressure–saturation curve may depend on whether a sample was initially saturated with the wetting or non-wetting fluid component. If the sample is initially saturated with the wetting fluid an increment of the capillary pressure produces the displacement of the wetting fluid for the non-wetting fluid in a process known as drainage. If the sample is initially saturated with the non-wetting fluid, a decrease in the capillary pressure produces imbibition. Figure 4 shows a typical curve which reveals the relation of capillary pressure to saturation. The entry point P* shows that if a sample is initially saturated by a wetting fluid a certain pressure must be built up before the non-wetting fluid begins to penetrate the sample, this is the so called threshold pressure or non-wetting entry value. The figure also shows that at high capillary pressure the wetting saturation reaches a minimum limit, this is the so called irreducible saturation of the wetting fluid S_{w0}. The imbibition curve shows that a maximum limiting saturation value is reached at zero capillary pressure. This point corresponds to the residual saturation S_{nw0} of non-wetting fluids that stay entrapped in the porous solid. In the case of coal filtration, S_{nw0} represents the residual moisture in the cake at break through. It is well known that pressure–saturation curves are subject to hysteresis phenomena and

therefore the capillary pressure is a function of the direction of displacement and the history of the two-phase flow in the porous sample.

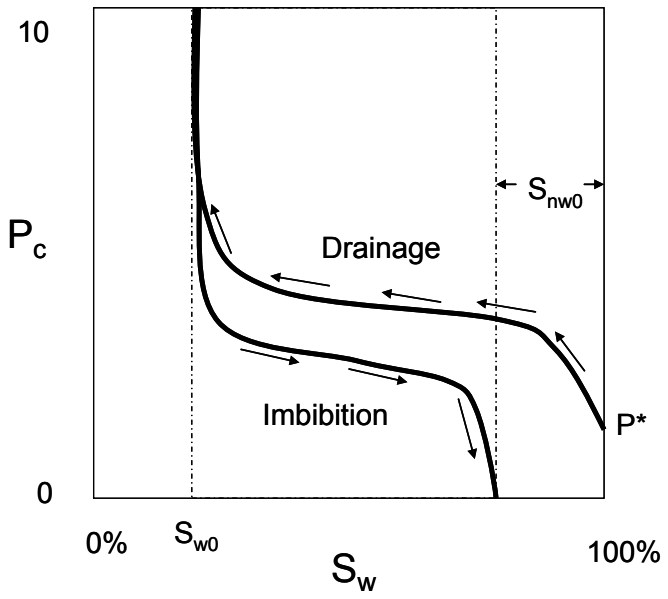

Figure 4. Typical capillary pressure curve.

Results and Discussion

Pore Network Structure of Packed Bed of Coal Particles using HRXMT Images

Figure 5 shows a packed bed of coal particles and its porous network structure as obtained by the HRXMT system at the University of Utah. The particle size is less than 850 μm, the resolution of each voxel is 5.62 μm in length and the size of the image is 400x400x800 voxels. It is possible to observe how image processing of the digital data allows for a clear separation between the solid and the air of the pore network structure due to the distinct difference in attenuation coefficients. This technique easily obtains the porous network of the packed particle bed. During simulation the fluid flows through this network structure having a specific connectivity with well defined pore dimensions not only to determine the local flow but also the overall permeability of the sample.

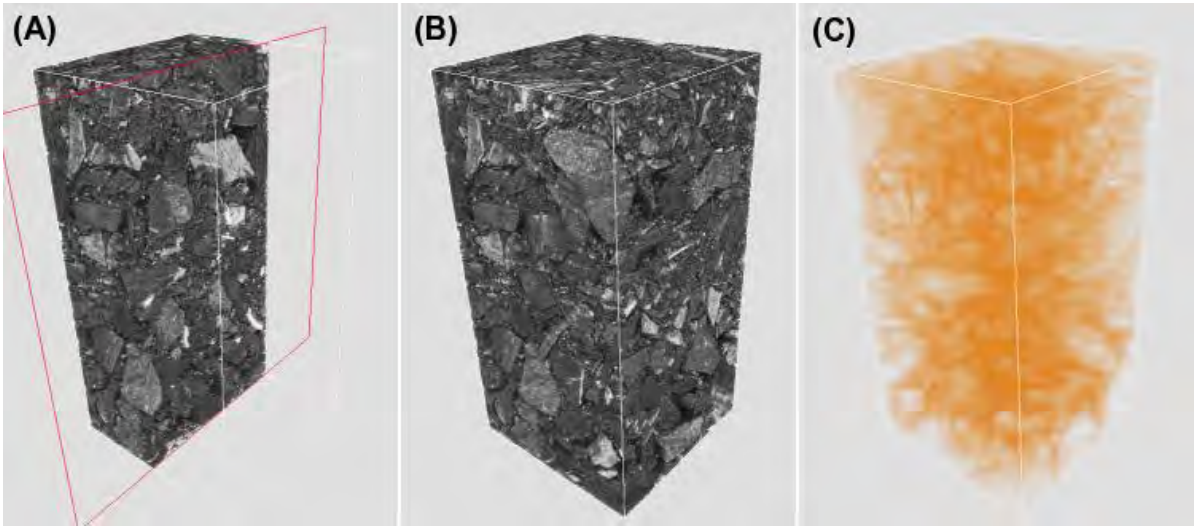

Figure 5. 3D image reconstruction of a packed bed of coal particles (< 850 μm). The voxel resolution is 5.62 μm and the image size is 400x400x800 voxels. (A) shows the cutoff view of the CT reconstructed packed particle bed, (B) shows the complete CT reconstructed packed particle bed, and (C) shows the pore network structure.

The images of the porous structures of packed particle beds reveal why the LBM method is more suitable for this kind of problem than the standard CFD mesh methods. The standard solution with a CFD solver requires the construction of a grid, the definition of the boundary conditions at the boundary nodes, and the solution of the Navier-Stokes equation at each node. The standard CFD methodology, therefore, would require an enormous amount of time for grid construction and also for computer simulation.

Single Component Single Phase Lattice-Boltzmann (LB) Model

From the 3D reconstructed HRXMT image shown in Figure 5, the pore structure for this packed bed of coal particles was determined and used for this study. The voxel size for this data set is 5.62 μm. Figure 6 illustrates the 3D view of the LB simulated flow through the pore space of the packed particle bed. Once we remove the solid particle phase, the right-hand side of Figure 6 shows the nature of the flow channels. The velocity scale is color-coded as shown by the color bar in Figure 6. Solids are white, and solution velocity ranges from black for no flow, through different grey values for the flow rates. The LB estimated permeability for this sample is 9.28×10^{-8} cm^2.

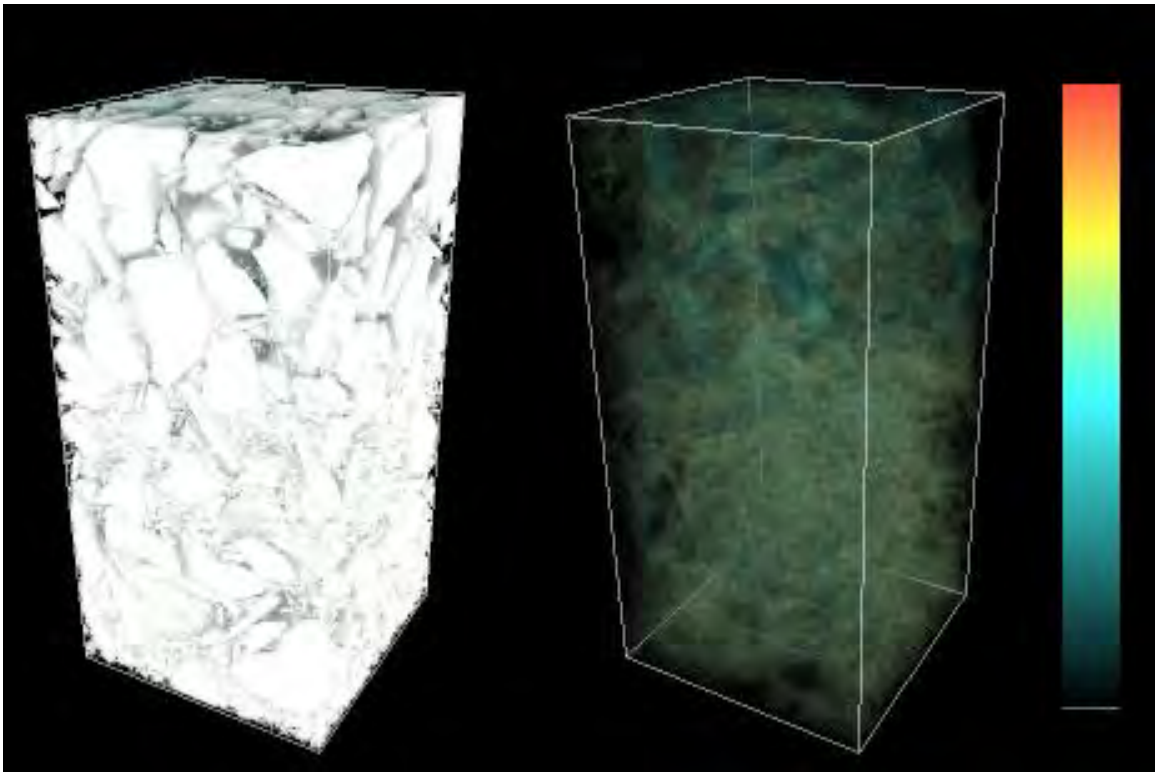

Figure 6. 3D views of LB simulated flow through a packed bed of coal particles. Left hand side with solid phase as white, and right hand side with transparent solid phase. Color bar shows that the solution velocity ranges from black for no flow, through different grey values for the flow rates.

Multiphase Lattice-Boltzmann (LB) Model and Simulation of fluid flows through Porous Media

Single component multiphase He-Chen-Zhang model

In order to improve the water removal and define the condition for minimum cake moisture content, a multiphase LB fluid flow model is required to investigate the flow through the porous media. Several Lattice-Boltzmann multiphase fluid flow models have been introduced in the past years finding applications in different areas of fluid dynamics such as phase separation (Rothman and Zaleski, 1991), and fingering phenomena in a channel (Kang et al, 2004) among others. The major advantage claimed for pursuing the use of LBM instead of standard CFD methods resides in its ability to model complex solid boundaries in any arbitrary geometry, a scheme suitable for code parallelization and ability to incorporate microscopic force interactions that control the interface dynamics.

In general, the LBMs for multiphase flow can be described as single component or multicomponent models. Single component models describe phase separation by an equation of state that under the critical temperature automatically segregates phases into two stable densities, vapor (light density) and liquid (heavy density). In this category we found the single component Shan and Chen model (1993), single component free-energy model, and the He-Shan-Doolen model to be of interest. On the other hand, multicomponent models use one particle distribution function (PDF) and one evolution equation to represent each fluid component in the system and segregation is simulated by interaction between the two independent fluids. For further discussion and comparison of these methods the reader is referred to the work done by Chen and Doolen (1998) and He and Doolen (2002).

We start with the description of the single-component multiphase flow developed by He, Chen and Zhang. In his seminal work, He et al (1999) presents a new multiphase model derived directly from discretizing the continuous kinetic equation for non-ideal fluids modified for incompressible flow. As was mentioned previously, the He-Chen-Zhang (1999) model is an extension of the He-Shan-Doolen model (1998). The model has not been used extensively and is not as popular as the Shan and Chen model. Videla (2009) has applied the model to 2D and 3D Rayleigh-Taylor instability simulations (He et al, 1999; Zhang et al, 2000) and compared the data with theoretical values and results from another CFD simulation showing good qualitative and quantitative agreement.

Unlike the traditional CFD methods that resolve the macroscopic governing equations using a free boundary surface approximation, the He-Chen-Zhang model simulates the interfacial dynamics, such as phase segregation and surface tension, from mesoscopic kinetic equations. In this model the interfacial dynamics are the result of molecular interactions where two distributions functions are used, one for tracking the pressure and velocity, and another for tracking only the density. When the molecular attraction is strong enough, the fluid automatically segregates into two different phases. One of the major advantages with respect to the Shan and Chen model is that the surface tension in the He model can be adjusted beforehand as a free parameter due to its thermodynamic consistency.

Theoretically speaking, the use of these equations of state should allow consideration of high density ratios for the single component multiphase system. The problem arising is

that as density ratios increase the spurious velocity magnitudes also increase making simulations numerically unstable. We have been able to run simulations with density ratios up to 30. Numerical instability is an area that requires more research in the whole area of LBM.

Simulation of fluid penetration and capillary phenomena in porous media

The solid-fluid interaction explained before can be extended to the analysis and simulation of two-phase flow in complex porous structures. Firstly, the behavior of the LB model in simple capillary tubes is illustrated, then the model is expanded for the simulation of filtration in an actual 3D image of a packed bed of coal particles as obtained from x-ray microtomography (XMT) analysis.

In a capillary tube, there is fluid displacement when the flow is driven by a difference in pressure strong enough to overcome the capillary pressure. Figure 7 shows LB simulated results for capillary tubes where the non-wetting fluid displaces the wetting fluid (drainage process) from left to right at the same final iteration step for several driving pressure differences. From these images it is possible to observe that the wettability of the wall as defined by the wetting film parameter D_ρ creates a wetting film at the surface which remains attached to the wall while the non-wetting fluid front advances. The width of this wetting film depends of the strength of the attraction and herein the result is about three lattice units.

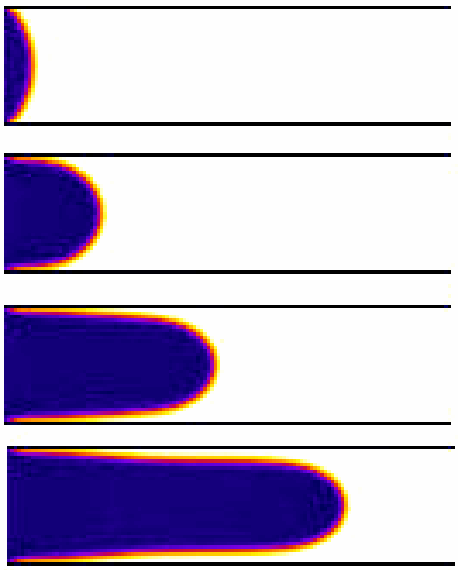

Figure 7. Simulations of fluid displacement for increasing difference in pressure controlled by the density at the outlet which has values from top to bottom: 0.2508, 0.2498, 0.2482 and 0.2466. D2Q9 lattice of size 35x130 lu^2. Parameters for simulations are k=0.1, D_ρ=0.99 and $\rho_l/\rho_g = 10$.

In LBM simulations, the difference in pressure between the inlet and outlet can be set by fixing the density of the fluids where the densities are related to the pressure by the equation of state. The entry pressure for displacement of one fluid by another in a porous capillary is a function of the radius (R) of the pore, the surface tension (γ) of the fluids, and the contact angle (θ). The entry pressure is given by equation 13.

$$P_{entry} = \frac{2\gamma \cos\theta}{R} \tag{13}$$

The capillary phenomenon of interest, similar to the network microstructure of the filter cake, is the behavior of the system when two or more capillary tubes (throats) are present. We have taken the simplest case of two-phase flow of two porous channels of different diameters under the same pressure difference. As Figure 8 shows, one of the throats is six times smaller than the other and therefore has a six times higher entry pressure. The pressure across the phases has been set in such a way that the value is higher than the entry pressure for the bigger diameter throat but smaller than the entry pressure for the smaller diameter throat. Figure 8 shows a sequence of images from left to right and top to bottom. In this sequence it is possible to observe the preferential flow that is developed by the meniscus which invades the channel with the higher throat radius having a smaller flow resistance. In conclusion, it is evident that this modified He-Chen-Zhang model has good qualitative agreement with theory for two-phase flow in porous media and in the following discussion we proceed with application to actual porous network structure such as would be found in the cake developed during fine coal filtration.

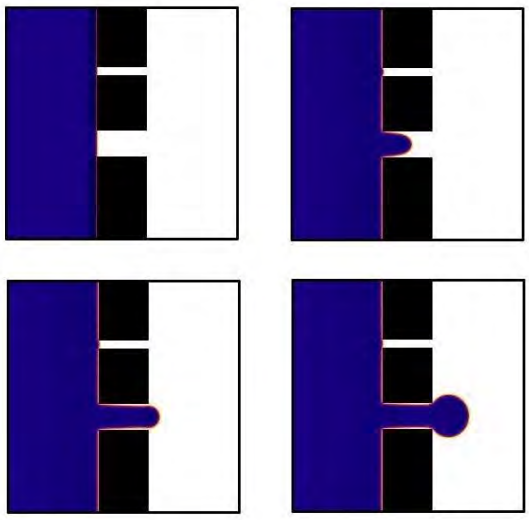

Figure 8. Simulations of fluid displacement in a capillary tube with two throats of different radius. From left to right and top to bottom image: flow after 1000, 10000, 20000 and 30000 iterations. D2Q9 lattice of size 35x130 lu^2. Parameters for simulations are $\bar{k}$=0.1, D=0.99 and $\rho_l/\rho_g = 10$.

Lenormand et al (1988) ran numerous network simulations and experiments performed in transparent etched networks to identify patterns and describe percolation of a non-wetting fluid when injected into a medium saturated with a wetting fluid. As an outcome of his research, he proposed a phase diagram for immiscible displacement characterized by the capillary number (eq. 8) and the viscosity ratio (eq. 9) as shown in Figure 9. Parameters γ, ν_w, μ_w and μ_{nw} are defined as interfacial tension, kinematic viscosity of the wetting fluid and the viscosities of the wetting and non-wetting fluids, respectively. The diagram shows the existence of three basic domains for fluid penetration: stable displacement, viscous fingering, and capillary fingering. In the stable displacement region, the major force is due to viscosity interaction of the injected fluid. The flow shows a flat front moving towards the exit with some irregularities with the dimensions of a few pore scales.

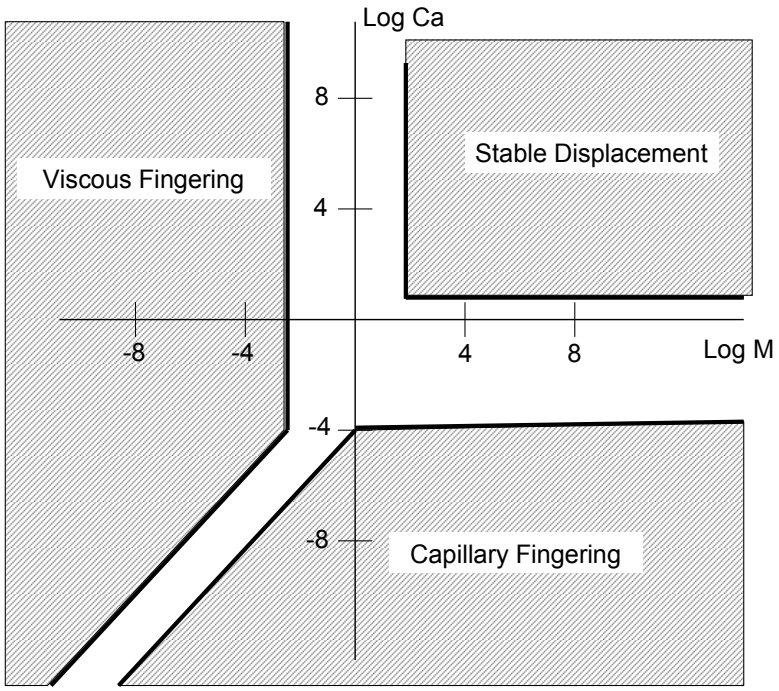

Figure 9. Lenormand Diagram. (After Lenormand et al, 1988)

In the viscous fingering region the major force is due to viscosity interaction of the displaced fluid. In this type of flow the fingers look like a tree with no loops and they spread across the porous network growing towards the exit.

In the capillary fingering region the major force is due to capillarity which also exhibits tree-like fingering but the fingers grow in all directions, even toward the entrance forming loops. These loops trap the displaced wetting fluid leading to a higher final saturation (residual moisture content in the case of coal filtration) than the viscous fingering.

Figure 10 shows 2D simulations of the interface advance by using the He-Chen-Zhang model applied to a packed bed of sand particles where the pore network structure has been captured by XMT analysis. In this simulation a two-dimensional XMT image slice has

been used and flow goes from top to bottom, induced by a fixed pressure difference. Parameters of simulation in Figure 10 are set in such a way as to obtain flow in the transition zone between capillary fingering and stable displacement as described by Lenormand. The capillary number is 6.77×10^{-2} and the density ratio of 3.

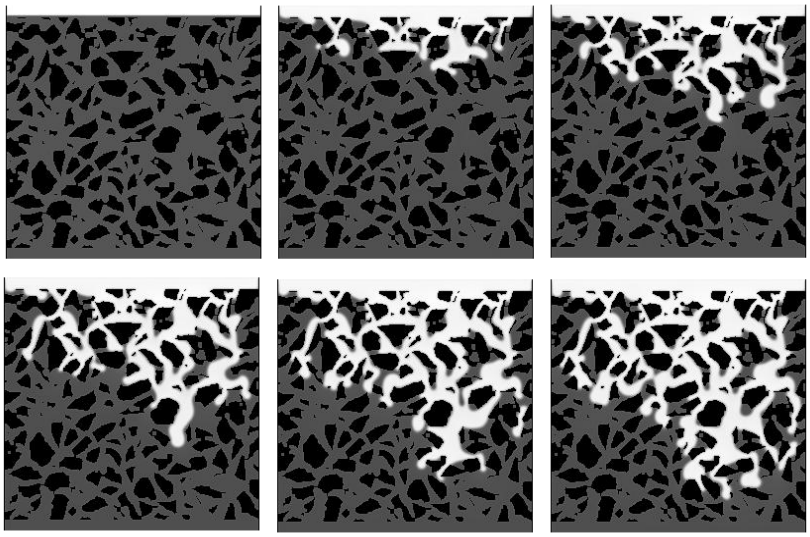

Figure 10. Sequence of simulations of two-phase flow in a packed bed of sand particles. Percolation simulations by the single component He-Chan-Zhang LBM. For a density ratio = 3.0 and Ca = 6.77×10^{-2}. Lattice size of 256x256. Images each 5000 iteration steps.

As can be seen in the sequence of images, the simulation starts from complete saturation of the wetting phase which is displaced by a non-wetting phase (white). In the course of simulation the flow goes through the less resistant paths (coarser pore diameters) leaving behind some residual wetting phase trapped in very small pore spaces which have a high flow resistant and where the non-wetting phase can not enter until the pressure increases. In agreement with the diagram proposed by Lenormand (1988), even though we are working at a pore scale level, the pattern of percolation shows a capillary fingering type of flow with relatively short fingers.

Figure 11 shows a comparison of the same structure shown in Figure 10 with a new 2D simulation condition where the surface tension is varied. Comparison at the same level of iteration shows that the percolation follows the same pattern for both multiphase flow in porous media simulations in this porous network structure, probably due to the fact that both simulations are run with the same pressure gradient and therefore the path of least resistance has not changed, however reduction of the surface tension produces longer and thinner fingers.

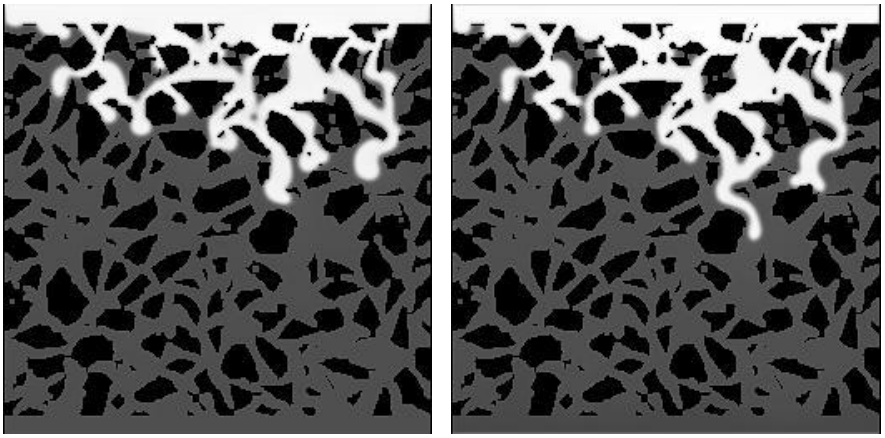

Figure 11. Two different penetration simulations for the same density ratio = 3.0 and pressure gradient but different surface tension. Left image has a high surface tension ($\bar{k}$=0.1, Ca = 6.77x10-2) and right image has a low surface tension ($\bar{k}$=10^{-5}, Ca = 230). Both images after 10000 iterations. Parameter $\bar{k}$ defines the surface tension.

Figure 12 shows a comparison again between the 2D simulations of Figure 10 (left image) with a simulation where the density ratio has being inverted (right image). In this new case, the low density fluid displaces the heavier fluid and the pattern of flow changes since the pressure field has changed. According to the Lenormand diagram (Figure 9) a stronger viscous fingering type of flow is expected to be observed with more and longer fingers being formed due to the stronger viscous interaction and interface front instability. As the comparison shows, there is a clear qualitative agreement between theory and simulations. Fingers are formed in zones of low resistance to flow and once formed they start growing rapidly towards the exit.

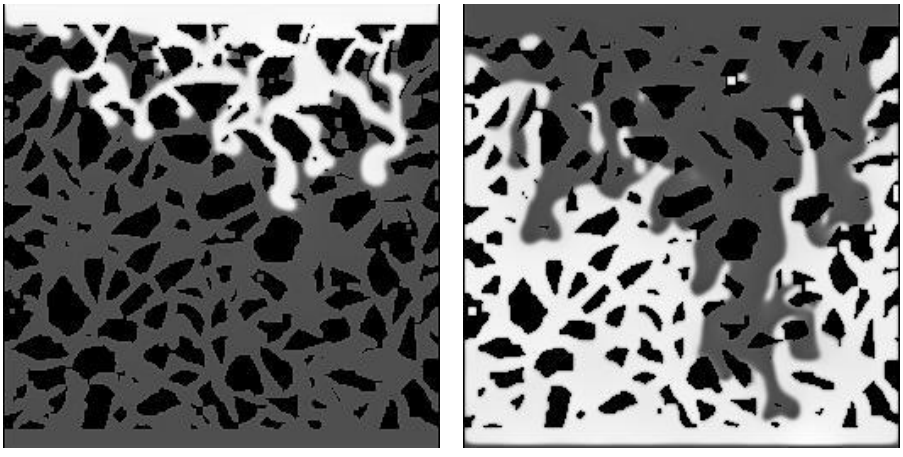

Figure 12. Two different penetration simulations for the same surface tension but inverse density ratio. Left image has a density ratio =3/1 and Ca = $6.77x10^{-2}$. Right image has a density ratio =1/3 and Ca = $1.32x10^{-1}$. Both images after 10,000 iterations.

Even though the He-Chen-Zhang model has advantages over other methods such as its thermodynamic consistency which makes the treatment of the surface tension easier because it can be set before actually running the simulation, it has on the other hand, the problem that it has not been extended to consider more than one component and therefore the two-phase flow is a mathematical artifact where both fluid phases are related by an equation of state. This characteristic imposes some restrictions, such as under certain pressure changes and flow conditions unexpected condensation and evaporation of the phases can be induced.

Although the use of an equation of state to induce phase segregation is a simple and elegant formulation for interfacial dynamics simulation, it restricts the one component simulation to industrial applications for the simulations of liquid-vapor phase systems like water/water-vapor. Nevertheless the simulations can be of great importance for a better understanding of the complex multiphase problems if we use the concept of dynamic similitude for fluid flow conditions and if the condensation/evaporation effect can be assumed to be negligible.

Application of the single component multiphase flow LBM known as the He-Chen-Zhang model coupled with XMT analysis to define the complex pore geometry allows for simulation of flow in porous media. The model is used for simulation of fluid penetration into porous samples and the analysis of capillary phenomena. At present, the LBM has been applied for 3D simulations of filtration for a packed bed of coal particles digitalized by HRXMT. Preliminary results from LBM simulations are shown in Figure 13.

Conclusion

High resolution X-ray micro CT (HRXMT) will allow for further advances in the 3D characterization of pore network structures in filtration cakes. With a voxel resolution of less than 1 micron, particles as small as 5 microns can be distinguished and described.

In order to gain a better understanding of the complex transport phenomena that occur in a filter cake, study of the effect of 3-dimensional pore geometry on the effective transport properties of the filter cake is necessary. Transport calculations have been carried out for the actual three-dimensional porous media (in our case packed bed of coal particles) using the single phase Lattice-Boltzmann method. Permeability from single phase LB simulation has been estimated to be 9.28×10^{-8} cm^2 for minus 0.85 mm (20 mesh) coal particles.

We have been successful in implementing the 2D and 3D software capabilities of LB simulation for multiphase fluid flow in porous media. The single component multiphase flow He-Chen-Zhang LBM model has been extended to incorporate fluid-solid interaction forces and has been applied to the simulation of percolation in actual HRXMT images of pore network structures created by packed particle beds. Finally, in order to evaluate the actual potential of this mathematical model to simulate real multiphase problems a comparison between experimental data and simulation results is in progress with the intent to describe conditions that will lead to improved water removal and minimum cake moisture content. Of

course this is a challenging problem because of the complexity of the physical phenomena involved and the size of the computing resources required.

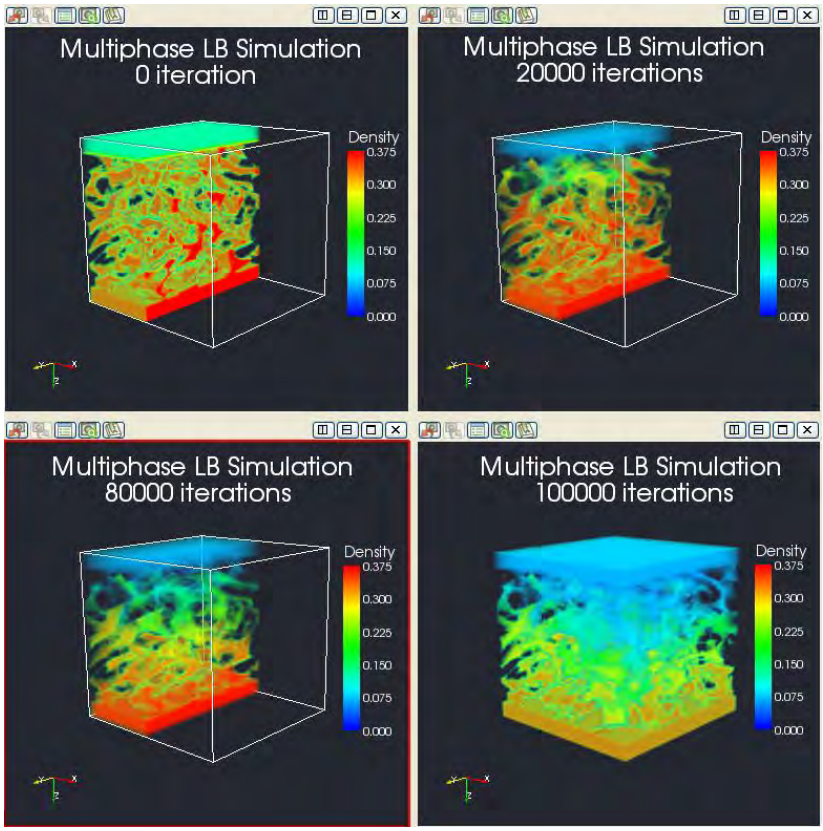

Figure 13. Preliminary results of LB simulation of multiphase flow through a packed bed of coal particles (0.850x0.589 mm).

References

Chen, S., and Doolen, G., 1998. Lattice boltzmann method for fluid flows. *Annu. Rev. Fluid Mech*. 30:329.

Dahlstrom, D.A., and Silverblatt, C.E., 1977. Continuous vacuum and pressure filtration. In *Solid Liquid Separation and Scale Up,* Edited by D.B. Purchas. Croydon: Up Lands Press.

He, X., Shan, X., and Doolen, G., 1998. Discrete boltzmann equation model for nonideal gases. *Phys. Rev. E*. 57:R13.

He, X., Chen, S., and Zhang, R., 1999. A lattice boltzmann scheme for incompressible multiphase flow and its applications in simulation of Rayleigh-Taylor instability. *J. Comput. Phys*. 152:642.

He, X., and Doolen, G., 2002. Thermodynamics foundations of kinetic theory and lattice boltzmann models for multiphase flow. *J. Stat. Phys*. 107:309.

Kang, Q., Zhang, D., and Chen, S., 2004. Immiscible displacement in a channel: simulations of fingering in two dimensions. *Advances in Water Resources*. 27:13.

Lenormand, R., Touboul, E., and Zarcone, C., 1988. Numerical methods and experiments on immiscible displacements in porous media. *J. Fluid Mech.* 189:165.

Leonard, J.W., and Hardinge, B.C., 1991. *Coal Preparation*, *5th Ed.,* Littleton, CO: Society for Mining, Metallurgy, and Exploration, Inc.

Lin, C.L., and Miller, J.D., 2004. Pore structure analysis of particle beds for fluid transport simulation during filtration. *Int. J. Miner. Process*. 73:281.

Marle, C.M., 1981. *Multiphase Flow in Porous Media*, Houston: Gulf Publishing Company.

Rothman, D.H., and Zaleski, S., 1991. Lattice-gas models of phase separation: interfaces, phase transitions, and multiphase flow. *Review of Modern Physics*. 66:1417.

Svarosvsky, L., 1990. Filtration fundamentals. In *Solid-Liquid Separation,* Edited by L. Svarosvsky. London :Butterworths.

Shan, X., and Chen, H., 1993. Lattice boltzmann model for simulating flows with multiple phases and components. *Phys. Rev. E.* 47:1815.

Shyy, W., Udaykumar, H.S., Madhukar, M.R., and Smith, R.W., 1996. *Computational Fluid Dynamics with Moving Boundaries*. Mineola, NY: Dover Publications, Inc.

Tien, C., 2006. *Introduction to Cake Filtration*. New York: Elsevier.

Tiller, F.M., 1975. *Filtration and Separation*, 12:386.

Videla, A.R., Lin, C.L., and Miller, J.D., 2007. Simulation of saturated fluid flow in packed particle beds – the lattice-boltzmann method for the calculation of permeability from XMT images. *Journal of the Chinese Institute of Chemical Engineers*. 39:117.

Videla, A.R., 2009. *Explorations in Three-Dimensional Lattice Boltzmann Simulation for Fluid Flow in Packed Particle Bed.* Ph. D. Dissertation, University of Utah.

Wakeman, R., and Tarleton, S., 2005. *Principles of Industrial Filtration*. New York: Elsevier.

Xradia, 2009. www.xradia.com.

Zhang, D.F., and Stone, H.A., 1997. Drop formation in viscous flows at a vertical capillary tube. *Phys. Fluids*. 9:2234.

Zhang, R., He, X., and Chen, H., 2000. Interface and surface tension in incompressible lattice boltzmann multiphase model. *Computer Physics Communications*. 129:121.

APPENDIX 22 - Removal of Selenium (Se) from Coal Mine Wastewater by GAC-Based Iron-Containing Adsorbents. (WV020)

FINAL TECHNICAL REPORT

Contract Title and Number:	Period of Performance:
Continuation in Crosscutting Technology Development at CAST. (DE-FC26-05NT42457)	Starting Date: 10/1/05 Ending Date: 9/30/10

Sub-Recipient Project Title:
Removal of Selenium (Se) from Coal Mine Wastewater by GAC-Based Iron-Containing Adsorbents

Principal Investigators:
Lance Lin
Dianchen Gang

Contact Address:
Department of Civil & Environmental Engineering
West Virginia University
Morgantown, WV 26506-6103

Subcontractor Address:
Daniel Dianchen Gang
Department of Civil Engineering
University of Louisiana at Lafayette
P.O. Box 42291
Lafayette, LA 70504-2291

Report Information:
Type: Final
Number:
Period: 10/1/08-9/30/10
Date: 12/16/2010
Code: WV020-FINAL

Contact Information:
Phone: (304) 293-9935
Fax: (304) 293-7109
E-Mail: lianshin.lin@mail.wvu.edu

Subcontractor Information:
Phone: (337)482-5184
Fax: (337)482-6688
E-Mail: ddg7603@louisiana.edu

DISCLAIMER

We have developed the method for the iron-coated adsorbents preparation. A series of instruments were set up and run smoothly. Task 1 and 2 were carried out according to the schedule. The preparation method was found to be effective based on the characterization results. A few batch adsorption experiments were also conducted to investigate the selenite removal efficiency and high efficiency (97.03%) was observed.

ABSTRACT

Removal of selenite from aqueous phase using iron-coated granular activated carbons (GAC) was investigated in this study. Five different types of GAC were used for iron coating by oxidizing ferrous chloride with sodium hypochlorite in adsorbent preparation. Darco 12×20 GAC coated with 0.1 M ferrous chloride was shown to be the most effective adsorbent for selenite (97.3%) among the five tested GACs. Fe-GAC (Darco 12×20) was characterized using various techniques (i.e., BET surface area analysis, point of zero charge (pH_{pzc}), scanning electron microscopy (SEM), energy-disperse spectra (EDS), X-ray photoelectron spectroscopy (XPS)). Results show that pore size and pore volume deceased with the iron coating. Lab scale experiments were both carried out for selenite and selenate to examine the adsorption efficiency of Fe-GAC in selenium removal. High removal efficiencies were both achieved for selenite (>97%) and selenate (>75%) under acidic condition (i.e., pH from 2 to 5). Effect of various factors (e.g., pH, ionic strength, initial concentration, time, temperature and competitive anions) was also investigated for selenite and selenate. Results indicated that adsorption reached equilibrium for both selenate and selenite after 48 hours. Langmuir isotherm characterized selenite adsorption well and selenate adsorption fitted the Freundlich model better at higher ionic strength. Ionic strength affected selenate adsorption significantly, which was not observed with selenite. Competitive adsorption of binary adsorbates (selenite and selenate) showed a decreasing trend of selenite adsorption capacity with decreasing ionic strength, indicating stronger competition of selenate against selenite under the low ionic strengths.

TABLE OF CONTENTS

LIST OF GRAPHICAL MATERIALS

INTRODUCTION

Background

Selenium (Se) is a natural occurring element and its release to the environment can be enhanced due to irrigation and mining activities. In particular, Se content in coals was reported to be significantly higher than that in other geologic materials in the United States (Coleman *et al.*, 1993; Vesper *et al.*, 2008). As a result, Se was found to be present in elevated concentrations in acid mine drainage which can vary from 1 to 7,000 μg/L (Kapoor *et al.*, 1995). An environmental impact study of mountain top mining and valley fills in the Appalachian region found that the concentrations of Se in streams are greater than 5 μg/L EPA criteria, in some watersheds downstream from valley fills (EPA, 2005). These elevated concentrations of Se have caused concerns for its potential impacts on aquatic ecosystems and human health.

In aquatic environments, selenite and selenate are the predominant inorganic forms of selenium. Selenite exists under moderated redox potentials and in wide pH ranges. Its chemical forms vary with pH, such as H_2SeO_3 at acidic pHs, $HSeO_3^-$ at neutral pHs and SeO_3^{2-} at alkaline pHs (Séby *et al.*, 1997). Selenate is a weakly basic group VI oxyanion and commonly present either in a fully deprotonated form (SeO_4^{2-}) or singly protonated biselenate ($HSeO_4^-$) (Shriver *et al.*, 1994). Selenite in surface and subsurface soils tends to be oxidized and transformed into selenate under low moister content and oxidation rate is increased with the temperature (Zawislanski and Zavarin, 1996). An Eh-pH diagram can be found elsewhere (Séby *et al.*, 1997). Selenite is similar to phosphate in terms of mobility in the environment and tends to be adsorbed more strongly than selenate onto adsorbents such as goethite and hematite (Neal *et al.*, 1987; Barrow and Whelan, 1989). On the other hand, selenate shows relatively low adsorption onto most adsorbents and has high mobility in aqueous systems (Davis and Leckie, 1980; Hayes *et al.*, 1988).

Control and mitigation of selenium impacts on the environment require cost-effective treatment technologies to remove selenium from the aqueous streams. A variety of treatment technologies have been reported to remove selenium from contaminated waters (Marinas and Selleck, 1992; Gallup, 1996; Frankenberger *et al.*, 2004; Mavrov *et al.*, 2006). Traditional treatment methods (e.g., coagulation, lime softening and sand filtration) are reported not effective (Kapoor *et al.*, 1995). Some advanced techniques (e.g., ion-exchange,

reverse osmosis, nanofiltration and etc.) are not economically feasible in treating large scale selenium and meeting EPA's high criteria (i.e., 5 μg/L) (Zhang *et al.*, 2005). Adsorption onto iron oxide/hydroxides is widely used and promising options in removing selenium.

Objective and Approach

This study focuses on selenite and selenate adsorption at ppm levels using iron coated granular activated carbon (Fe-GAC) Surface properties of Fe-GAC were characterized using microscopy techniques and titration experiments. Batch experiments were conducted to investigate adsorption equilibrium and kinetics and relevant factors that affect the adsorption, including pH, ionic strength and presence of oxy-anions were examined. In addition, a binary adsorbates system of selenite and selenate was also examined to investigate competitive adsorption using the Fe-GAC.

EXECUTIVE SUMMARY

During the project period, iron coated granular activated carbon adsorbents (Fe-GAC) were developed by the oxidation of ferrous and followed by ferric precipitation onto porous surface of several types of commercial GAC. The 0.1 M iron coated Darco 12X20 GAC was found most effective in removing selenite from solutions in the initial brief adsorption experiments. Hence, further characterization and adsorption studies were conducted utilizing 0.1 M iron coated Darco 12X20 GAC unless specially indicated.

Detail adsorbent characterizations were performed employing various tools and methods to obtain a sophisticated and thorough understanding of the newly developed adsorbents, as well as further assessing its application for large volume wastewater treatment. Surface morphology and chemical composition was analyzed by SEM coupled with EDS. To evaluate the changes in surface area before and after coating, BET specific surface area was measured for virgin GAC, 0.02 M iron coated GAC and 0.1 M iron coated GAC. Results show that the coating procedure is efficient in impregnating iron into porous structure without significant interfering effect on surface area. Acid-base titration experiments were carried out for three ionic strengths (i.e., 0.001, 0.01 and 0.1M) and showed point of zero charge (pH_{pzc}) at pH 7.8 for the tested Fe-GAC (0.1 M iron coated Darco 12X20 GAC). The results are consistent with previous studies for iron mineral adsorbents (e.g., goethite and hametite) which present the similar adsorbent behavior with Fe-GAC used in this study. Iron contents on Fe-GAC surface was quantitative and qualitative examined. Percentages of 2.8% (total iron) and 1.2% (amorphous iron) were obtained for 0.1 M iron coated GAC . Additionally, to confirm the success of ferrous oxidation, XPS analysis for iron chemical states was performed for Fe-GAC adsorbents after suspended in electrolytes solutions (0.1 M, NaCl) at the pH of 5. Both Fe2p and O1s spectrum were collected for the dry adsorbent samples. According to the spectrum interpretation, it is found that ferrous was successfully oxidized into ferric. A mixture composition for ferric including ferric oxide, ferric oxyhydroxide and ferric hydroxide is suggested as the predominant species.

Adsorption behavior for both selenite and selenate were investigated using 0.1 M iron coated Darco 12×20 GAC. Kinetics for these two anions was found to fit pseudo-second-order

model and equilibrium was observed within 48 hours. Results showed adsorption capacity of selenite was higher than that of selenate. Langmuir model was applied to characterize selenite adsorption, and Freundlich model was used to describe selenate adsorption. Ionic strength was a significant factor that affected the selenate removal efficiency but not the selenite removal. These results implicated the different adsorption mechanisms between selenite and selenate. Four types of anions were tested for competitive adsorption with selenite and selenate also. Competitive adsorption of binary adsorbates (selenite and selenate) was modeled by SRS multi-adsorbate competitive adsorption isotherms. Selenate was found to compete against selenite more strongly under low ionic strengths. Only slight decreases in the selenite and selenate adsorption capacities in binary system were observed as they were compared to their respective single-adsorbate systems.

EXPERIMENTAL

Adsorbent Preparation

The adsorbents were prepared by oxidizing ferrous using sodium hypochlorite to form ferric precipitation on the outside surface and inner porous structures of GAC. The detailed synthesis procedure was described elsewhere (Gu *et al.*, 2005; Zhang *et al.*, 2008). Figure 5 illustrates the ferrous oxidation process in a beaker incorporated with NaClO titration.

Fe-GAC Performance Testing

Five types of GACs were coated individually with 0.02 and 0.1 M ferrous chloride to test their effectiveness for selenite removal. Selenite working solution (25 mL) was diluted in flasks to obtain an initial selenium concentration of 2 mg/L. Ionic strength was controlled and pH was adjusted to 5 ± 0.3 by using a HCl solution (0.1 M). An acetic buffer solution (0.1 M) was used to stabilize the pH during the batch adsorption experiments. Adsorption was carried out for 24 hours and temperature was kept at 25 °C.

Adsorbents Characterizations

Adsorbents Morphology and Properties

The Fe-GAC samples were examined by a scanning electron microscope (SEM, Hitachi S4700) for surface morphology with the working distance of 12 mm and an accelerating voltage of 20 KeV. The SEM was equipped with an energy dispersion spectrometer (EDS) and it was used to perform the analysis of chemical constituents of the adsorbents. BET surface area and mesoporous size distribution were measured by nitrogen adsorption and desorption analysis (Micrometritics, ASAP 2020).

Acid Base Titration

Point of zero charge (pH_{pzc}) of the Fe-GAC under two ionic strengths (0.01 and 0.1 M NaCl) was determined using an acid-base titration method. For each ionic strength, two suspension samples (50 mL) each containing de-ionized water with a predetermined amount of NaCl,

and Fe-GAC (0.1 g to obtain adsorbent loading 2 g/L) were prepared in flasks. The suspension samples were mixed for 12 hours to equilibrate. Thereafter, one of the two suspension samples was filtered through a 0.45 μm membrane to remove the solids. The remaining suspension sample and the filtrate were then adjusted to pH 3 with a HCl solution (0.1 N) as the initial titration point. Prior to the titration, nitrogen gas was bubbled into the samples to removal CO_2. The solutions were then titrated to pH 10 with a NaOH solution (0.02 N). Titration was performed by a 50 mL Digitrate Pro™**,** digital burette (Jencons, UK), during which pH was monitored by a pH meter (Accumet Basic AB15 Plus, Fisher Scientific, NY). During the titration, the aqueous solution along with burette and pH electrode was sealed with parafilm to prevent CO_2 exchange between the atmosphere and the aqueous solution. Equilibrium for each data point was assumed if there was no change of 0.2 units for pH observed within 30 seconds and it ranged from a few seconds to 10 minutes to reach equilibrium. A net titration curve was obtained by subtracting the total added acid/base concentration for titrating the filtrate to pH 10 from the added acid/base concentration for every titration data point of the suspension sample. The concentration of acid/base on the net titration curve can be calculated using the equation reported by Wen *et al.* (1998). The concentrations of added acid (-) or base (+) were plotted as a function pH, and pH_{pzc} was determined by the intersection of the two net titration curves for two ionic strengths (Huang, 1981; Schulthess and Sparks, 1986; Reed and Matsumoto, 1991).

Iron Contents Analysis

To investigate the efficiency of coating procedure, total iron percentage and amorphous iron oxide percentage coated onto Fe-GAC were analyzed using iron extraction methods followed by ICP-MS measurement. Total iron was extracted off from GAC surface followed by acid digestion procedures (Lu, 1995; Gu *et al.*, 2005). Amount of 0.1 g adsorbents was suspended into 30 mL HCl (1:1). Then, shake it for 2 hours and followed by heating in a water bath at 90 °C for 20 minutes. Liquid phase was separated by filtration from solids. Remaining solids were washed by de-ionized water for several times. Collect all the supernant for further iron concentration analysis. For the analysis of active or amorphous iron oxide contents, first ground the Fe-GAC adsorbents (approximate 1 g), so that the particles are fine enough to pass through a 100 mesh in^{-1} (0.15 mm nominal pore size) sieve. Thereafter, transfer the particles into a 50-mL light proof tube. Amount of 30 mL of ammonium oxalate solution (pH = 3) was added into the tube, and then tube was immediately caped following by a two hour shaking. After that, filter out the suspension, particles were washed several times by de-ionized water. All the supernants were collected for further iron analysis.

Iron Chemical State Analysis

Iron coating procedure involves the oxidation of Fe (II) and precipitation of Fe (III). To better understanding the coating reaction mechanisms, it is necessary to investigate the chemical states of iron on adsorbents surface. X-ray photoelectron spectroscopy (XPS, Physical Electronics PHI 5000 Versa Probe Scanning ESCA Microprob) was applied to perform this task. To prepare the samples for XPS analysis, a few amount of Fe-GAC adsorbents were suspended in electrolyte solutions (NaCl, 0.1 M) for 24 hours. pH was adjusted to 5 using HCl (0.1 N) or NaOH (0.02 N) and monitored every 6 hours. Thereafter,

the surpernate was removed and solid was ready for XPS analysis after dried. Prior to analysis, all the samples were put into chamber for vacuum purpose. Monochromatic Al X-rays (1486.6 eV) were used for both low resolution survey and high resolution scans. The analysis passing energy of 117.4 eV and step size of 0.5 were used for survey scans, passing energy of 23.5 eV and step size of 0.025 eV were used for high resolution scans. Spectrum was analyzed using PHI Multipak Software (ULVAC-PHI, Inc., MN). All the spectra were charge corrected using C1s line at 284.8 eV.

Adsorption Batch Experiments

Isotherms and Kinetics

Selenium concentrations were monitored for 48 hours during the adsorption process to study adsorption kinetics. Adsorption for both selenite and selenate was conducted under the same conditions (i.e., 1 mg/L initial selenium concentration, 25 °C and pH 5 ± 0.3) except ionic strength (0.1 M for selenite and 0.05 M for selenate) and adsorbent loading rate (1.5 g/L for selenite and 3.5 g/L for selenate). Pseudo-second-order kinetic model was used to characterize the adsorption kinetics. Adsorption isotherms were developed for both chemical forms at 0.05 M ionic strength and initial selenium concentration of 1 mg/L.

Effect of pH

A range of pH (2 – 11) was used to study pH effects on selenite and selenate adsorption. For each batch experiment, pH was monitored every 6 hours and maintained within ± 0.2 of each pH value by adding 0.1 N HCl or 0.02 N NaOH to the mixture. After 24-hour adsorption, samples were collected and processed for analysis.

Effect of Competitive Oxy-anions

Co-existing anions (e.g., SiO_3^{2-}, SO_4^{2-}, PO_4^{3-} and CO_3^{2-}) were used to study their effects on selenite and selenate adsorption. Tests were conducted for initial Se concentration of 1 mg/L with different concentrations (0 to 5 mM) of the four anions under ionic strength of 0.05 M. Temperature and pH were fixed at 25 °C and 5, respectively. Adsorption lasted for 24 hours before samples were analyzed.

Selenite and Selenate Biadsorbates System

Both the selenite and selenate working solutions were added to a series of flasks to obtain initial Se concentration of 1 mg/L for both anions. NaCl (1 M) and acetate (0.01 M) solutions were used to control ionic strength and stabilize pH at 5. Adsorbent loading rate was varied from 0.5 to 3.5 g/L to obtain an isotherm for each chemical form. After 48-hour adsorption, two 10 mL sub-samples were collected from each flask with one sample used for selenite measurement and the other for total selenium measurement. Selenate concentration was calculated by subtracting the selenite concentration from the total Se concentration. Freundlich-type multi-adsorbate adsorption isotherm model developed by Sheindorf *et al.* (1981) was used to characterize the competitive adsorption between selenite and selenate.

The general Sheindorf-Rebuhn-Sheintuch (SRS) model equation for adsorbate *i* in an *N*-component system is given as:

$$q_{e,i} = K_{F,i} c_{e,i} (\sum_{j=1}^{N} a_{ij} c_{e,j})^{n_i - 1}$$

where $q_{e,i}$ (mg-Se/g-adsorbent) is the adsorption capacity for adsorbate *i*; $c_{e,i}$ and $c_{e,j}$ (mg/L) are equilibrium concentrations in the solution for adsorbate *i* and *j*, respectively. The pre-exponential coefficient $K_{F,i}$ and exponent n_i are Freundlich parameters that determined from its single-adsorbate system. The competition coefficient a_{ij} (unitless) describes the inhibition on the adsorption of adsorbate *i* caused by adsorbate *j*. The SRS equation assumes that (i) each adsorbate individually follows the Freundlich isotherm; (ii) there exists an exponential distribution of site adsorption energies for each component in a multi-component adsorbate adsorption system; and (iii) the coverage by each adsorbate molecule at each energy level is governed by multi-adsorbate Langmuir isotherm equation (Sheindorf *et al.*, 1981).
The competition coefficient a_{ij} in the competitive model was estimated using the competitive adsorption data of selenite and selenate by minimizing the Marquardt's percent standard deviation (MPSD), which is described as below:

$$MPSD = 100 \sqrt{\frac{1}{n_m - n_p} \sum_{i=1}^{n} \sum_{j=1}^{N} (\frac{q_{e,i,\exp} - q_{e,i,cal}}{q_{e,i,\exp}})^2} \quad \%$$

where n_m is the number of measurements and n_p is the number of parameters in the model. In this study, n_m and n_p equal to 7 and 3, respectively. *N* is the number of experimental data points and *n* is the number of adsorbates in the system. The subscripts "*exp*" and "*cal*" represent the solid phase concentrations determined from the competitive adsorption experiments and model predictions, respectively. Sheindorf *et al.* (1982) suggested that values for a_{ij} typically are larger than zero and normally smaller than 10. In this study, an iterative algorithm was implemented in MS EXCEL to estimate the values of a_{ij} that minimizes the MPSD. In the algorithm, an initial guess value was assigned to a_{12} (inhibition on selenite adsorption caused by selenate) and a_{21} which was equal to $1/a_{12}$ by default for binary systems was calculated. The MPSD value was then calculated. The value of a_{12} was then adjusted iteratively until a minimal MPSD was obtained.

Selenium Measurement

Selenite Analysis

A colorimetric method was used to measure selenium (III) concentration (USEPA standard methods 3500C, 1998). The method relied on a reaction of selenite ion with DAN that produced a brightly colored and strongly fluorescent piazselenol compound, which was extracted in cyclohexane and measured colorimetrically. The DAN solution was prepared by dissolving 200 mg DAN in 200 mL HCl (0.1 N), and then extracted three times using 25 mL cyclohexane, followed by filtration into an opaque container. An HA-EDTA solution prepared by adding 2.25 g Na_2EDTA and 6.25 g hydroxylamine hydrochloride (NH_2OHHCl) into 250 mL de-ionized water was used to eliminate negative interference from Fe^{2+}. For the colometric measurements, 2 mL of the HA-EDTA solution was added to a 50 mL test tube containing 10 mL water sample. The mixture solution pH was adjusted to 1.5 ± 0.3 using a 0.1 N HCl solution. The sample solution was then added with 5 mL of the DAN solution and

put into a covered water bath at 45 ºC for one and half hours to allow color formation. The sample solution was allowed to cool down and added with 2 mL cyclohexane. The sample test tube was capped securely and shaken vigorously for 5 minutes, followed by 5-minute without mixing to separate the organic layer from the aqueous solution. The aqueous phase was removed using a disposable pipet attached to a vacuum line. Organic layer was analyzed by a UV/Visible spectrophotometer (Varian, Cary 50) for selenium concentration.

Selenate Analysis

Selenate in the aqueous samples was first reduced to selenite using an acid digestion method (Blaylock and James, 1993) and the selenite concentration was then quantified using a colorimetric method with a detection limit of approximately 0.01 mg/L (Standard Methods 3500 C, USEPA, 1998). For samples containing both selenite and selenate, total selenium was measured as selenite after the reduction of selenate. It has been shown in previous studies that the recovery of selenate varied under different reaction conditions and several chemical digesters could be used for the selenate reduction (Bye, 1983). Among those, concentrated HCl was reported to be the most effective and reliable reductant. In this study, 8 mL of a concentrated HCl (12.1 N) was added to 10 mL selenate sample in a 50 mL tube. The tube was then loosely capped and put into a 90 °C water bath for an hour, followed by sample cooling to room temperature with the cap tightly closed. Excess HCl was neutralized by a NaOH solution (5 N) before final adjustment of pH to 1.5 ± 0.1 for selenite measurement.

RESTULS AND DISCUSSION

Fe-GAC Performance Testing

Figure 1 shows the removal efficiency of five GAC coated with various ferrous chloride concentrations after 24-hour adsorption. The results show that Darco 12x20 Fe-GAC was the most effective for removing selenite. Selenite removal efficiencies of 95.8%, and 97.1% were achieved with the GAC coated with 0.02 M and 0.1 M FeCl2, respectively. The later research experiments in this study were conducted using the Darco 12x20 Fe-GAC coated with 0.1 M ferrous chloride.

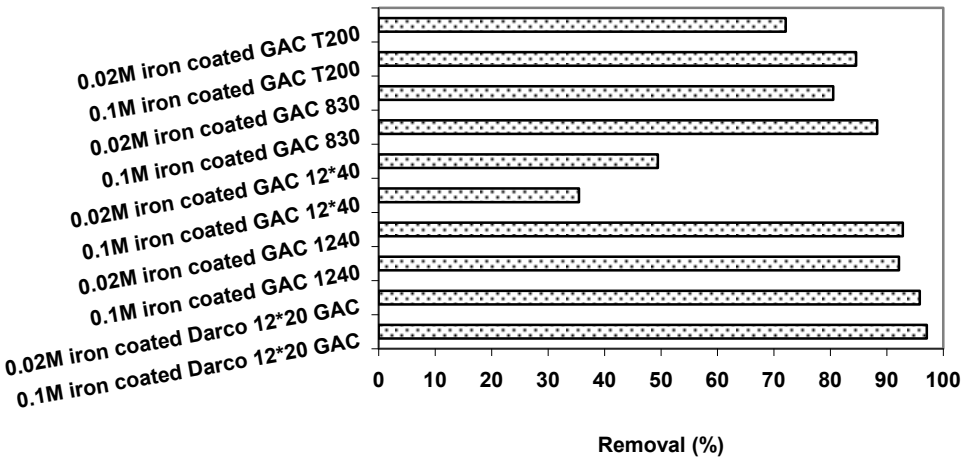

Figure 1. Adsorptive removal percentages of Fe-GAC adsorbents for selenite with an initial concentration of 1 mg/L.

Physical Properties Measurement

Table 1 lists the BET specific surface area, total pore volume, and pore size of Darco 12x20 GAC and its iron-coated products. The surface area was decreased from 592.6 m^2/g to 518.6 m^2/g by the 0.02 M $FeCl_2$ treatment, and further reduced to 434.1 m^2/g by the 0.1 M $FeCl_2$ treatment. The results were consistent with the data reported in a similar study (Gu *et al.*, 2005). Pore volume and average pore size also showed a decrease. These trends were attributed to blockage of pores and corresponding surface area by ferric precipitation after the oxidation of ferrous ions by sodium hypochlorite.

Table 1. **Surface and pore measurements for Darco 12x20 GAC.**

Adsorbent	BET specific surface area m^2/g	Pore volume m^3/g	Ave. pore size nm
Virgin GAC	592.6	0.63	4.3
0.02 M Fe-GAC	518.6	0.53	4.1
0.10 M Fe-GAC	436.1	0.44	4.1

Surface Morphology Analysis

The SEM micrograghs in Figure 1a-c show that there were considerable small cavities and attached fine particles over the virgin Darco 12x20 surface, forming a system of complicated pore networks. The iron coating on the carbon surface reduced the number of small cavities. These micrographs clearly show a reduction in pore space and surface area available for adsorption as a result of iron coating. Figure 1d shows the EDS spectra of the adsorbent samples. The intensities of the peaks at 6.38 KeV for iron indicate that higher $FeCl_2$ concentration resulted in a larger amount of iron coating on the GACs.

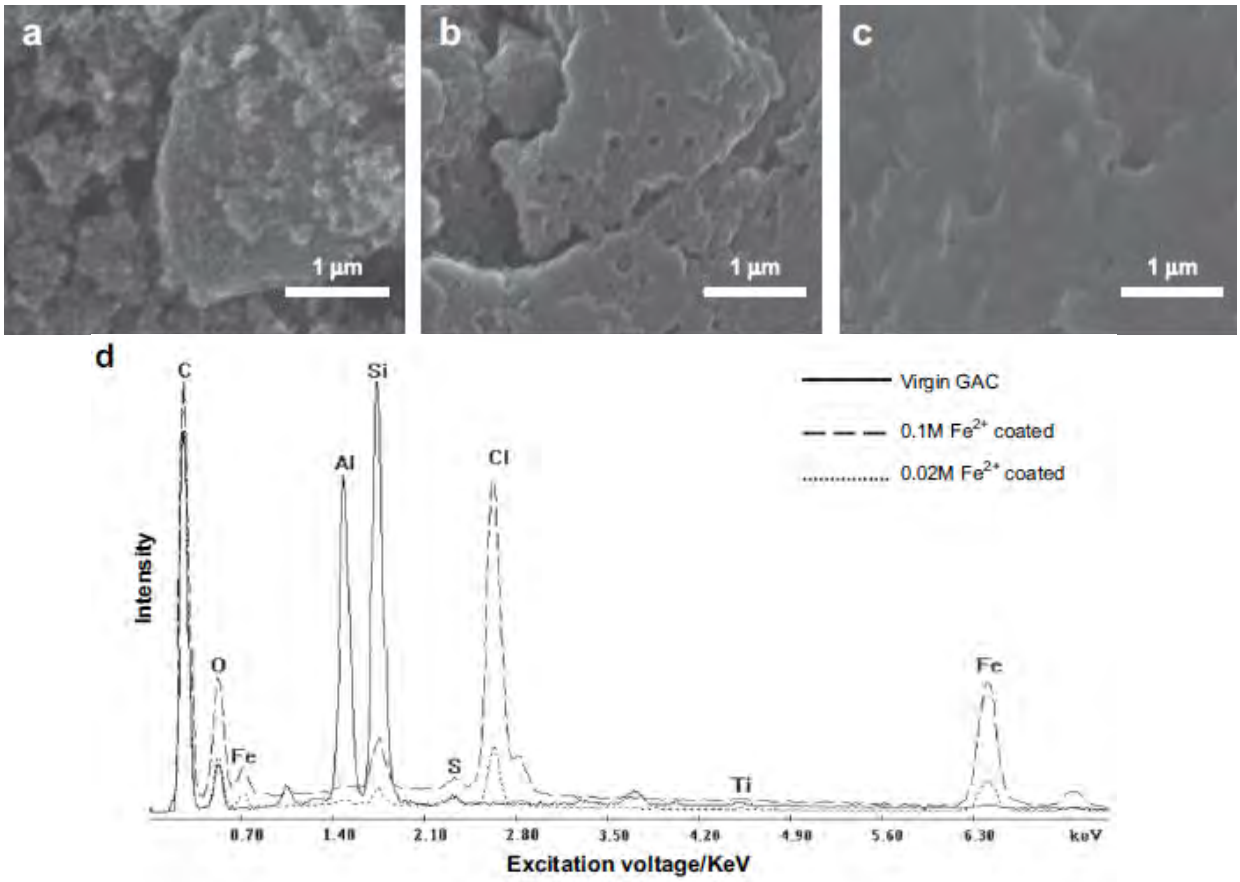

Figure 2. **SEM micrographs with a magnification of 1:30,000 for Darco 12x20 GAC samples: (a) virgin GAC, (b) coated with 0.02 M $FeCl_2$, (c) coated with 0.1 M $FeCl_2$, and (d) energy-disperse spectra of the virgin and iron-coated Darco 12x20 GAC.**

Point of Zero Charge

Point of zero charge (pH_{pzc}) of the Fe-GAC under two ionic strengths (0.01 and 0.1 M NaCl) was determined using an acid-base titration method. Detailed description of experimental procedure can be found elsewhere (Schulthess and Sparks, 1986; Reed and Matsumoto, 1991). The concentrations of added acid (-) or base (+) were plotted as a function pH, and pH_{pzc} was determined by the intersection of the two net titration curves for two ionic strengths (Huang, 1981; Schulthess and Sparks, 1986; Reed and Matsumoto, 1991). Figure 2 shows the titration results for determining point of zero charge of the Fe-GAC. The titration curves gave an estimate of pH_{pzc} at 7.5. The result is consistent with the conclusion drawn by Vaughan and Reed (2005) for iron impregnated GAC (using virgin GAC1240), which was reported to be pH 7.5.

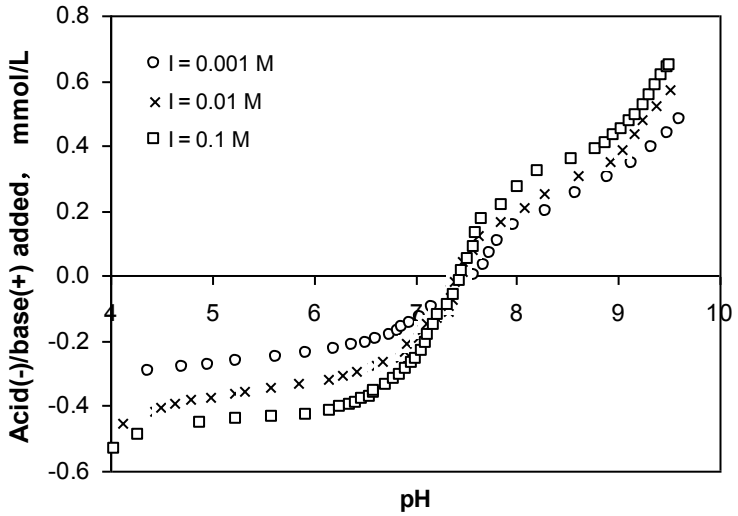

Figure 3. Acid base titration curves for the Fe-GAC (loading rate = 2 g/L) for two different ionic strengths.

Contents of Coated Iron

Percentages of coated total iron and amorphous iron in Fe-GAC (Darco 12×20) are listed in Table 2. The data shows that amorphous iron is approximately the half of the total iron. Also, the coated iron percentage increase from 0.18% to 2.8% with the increase of ferrous concentration employed in coating process. Srivastava *et al.* (2002) suggested an advantage for amorphous iron over the well defined crystalline iron in catalysts, sorption and other applications. Gu *et al.* (2005) reported a total amount of 3.32% iron coated onto Darco 12×20 GAC treated with 0.1 M Fe (II). They further revealed that the Darco GAC samples produced by steam activation of lignite may result in structures and reactive moieties with high abilities for Fe impregnation.

Table 2. Contents of iron on the surface of GAC after impregnation.

Ferrous Concentration Used in Coating Process	0 M	0.01 M	0.05 M	0.1 M
Coated Total Iron (%)	0.06	0.18	2.10	2.80
Coated Amorphous Iron (%)	0.00	0.10	1.00	1.20

Chemical State of Coated Iron

Figure 4 shows the XPS spectrum for Fe2p (a) and O1s (b) for Fe-GAC adsorbents suspended in NaCl solution at pH 5. Peaks for $Fe2p_{3/2}$ and $Fe2P_{1/2}$ are observed at 710.8 and 724.5 eV. The binding energy difference between two peaks is 13.7 eV. A shakeup satellite is also observed between $2p_{3/2}$ and $2P_{1/2}$ levels. According to the Handbook of XPS, the 2p peaks for Fe element are shown at 707 and 720 eV for $2p_{3/2}$ and $2P_{1/2}$, respectively. Both the chemical shifts to higher banding energy region and the increasing of binding energy difference between peaks indicate the oxidized state of iron. Comparing with the binding energy (709.1 - 709.6 eV) of peak position for Fe(II) in ferrous oxide (FeO), slight shift of

$2p_{3/2}$ level for Fe in Fe-GAC adsorbent indicates the presence of Fe(III) rather than Fe(II). Additionally, the shakeup satellite is clearly found to locate close to higher energy region, comparing with the satellite for Fe(II) rising from $2p_{3/2}$ peak and causing the peak width increasing which was observed by Watts and Wolstenholme (2003).

In Figure 4b, multiplet peaks for O1s are observed for O on Fe-GAC surface. The multiplets can be assigned to O1s (529.8 eV) and hydroxide (531.3 eV). Barr (1994) suggested that the lower binding energy multiplet indicates the formation of ionic bonds with metal elements (i.e., Fe). Furthermore, the intensity ratio of the multiplet peaks (OH:O) is relatively higher than 1, it indicates hydroxide content is higher than that of oxygen. These facts implicate the iron on Fe-GAC surface exists in multi compositions, which may include ferrous oxide (Fe_2O_3), ferrous oxyhydroxide (FeOOH) and ferrous hydroxide precipitant ($Fe(OH)_3$).

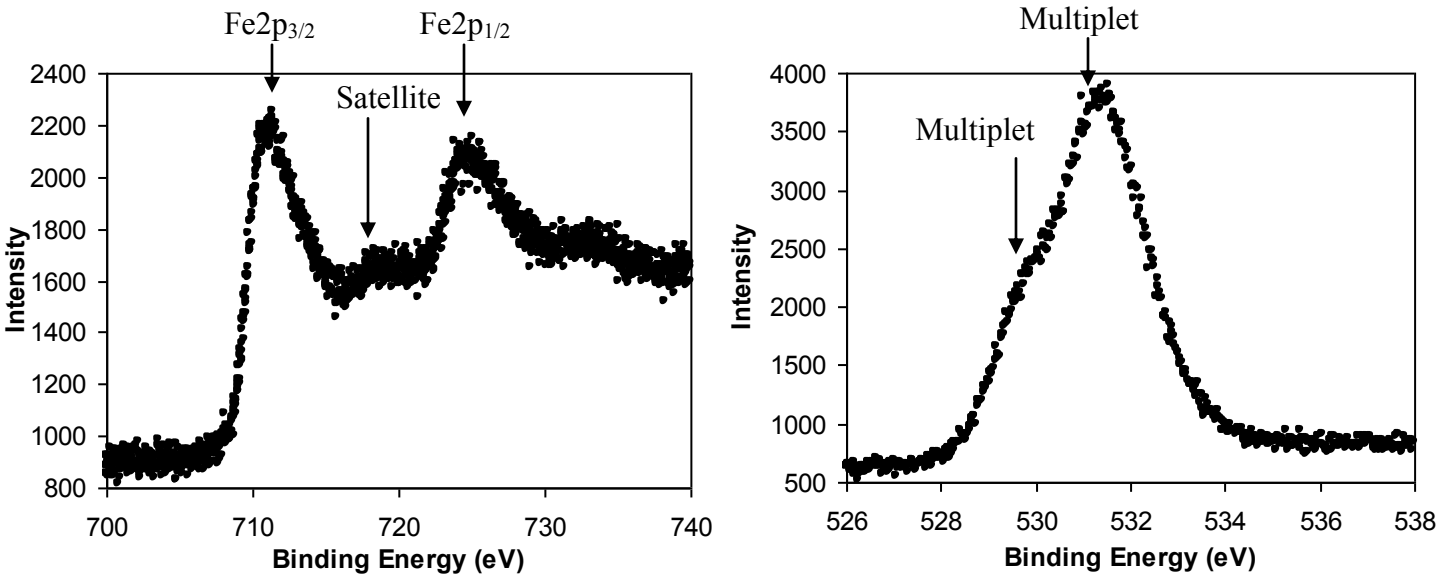

Figure 4. XPS spectrum of Fe2p (a) and O1s (b) for Fe-GAC after suspended in NaCl (0.1 M) solution at pH 5 for 24 hours.

pH Effect on Se Adsorption

Effects of pH on selenite and selenate removal efficiency are shown in Figure 5. Overall, the Fe-GAC absorbent exhibited higher removal of selenite than selenate. In both cases, the adsorbent had higher affinity for the adsorbates at low pHs, with decrease in selenate adsorption for pHs above 5 and selenite for pHs above 8. The pH-dependent adsorption behaviors of the two anions can be attributed to the release of OH^- upon adsorption of the anions or weak acids onto (hydr)oxides, which favors anion (e.g., SeO_3^{2-} and SeO_4^{2-}) adsorption at lower pHs (Stumm and Morgan, 1995). Selenate is believed to form weak bond with adsorbent surface sites, which is easier to be broken than selenite at alkaline pHs.

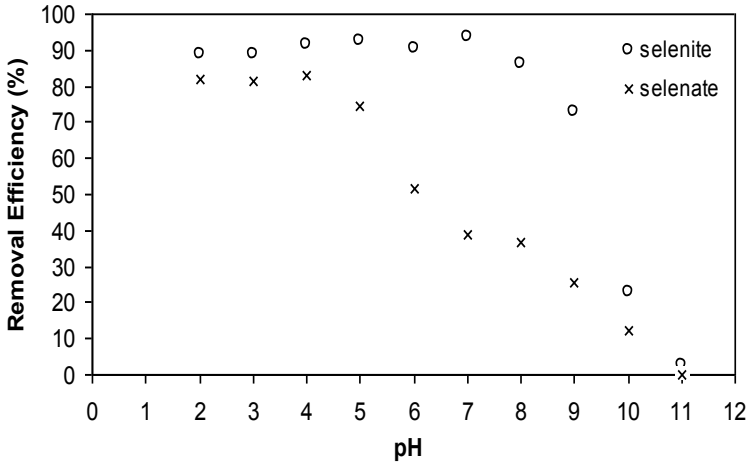

Figure 5. **Effect of pH on selenate adsorption for initial selenium concentration of 1 mg/L with 0.05 M ionic strength at pH 5 and 25 °C.**

Adsorption Kinetics

Adsorption kinetics was investigated for initial selenium concentration of 1 mg/L for both selenite and selenate. Ionic strength was controlled at 0.1 M for selenite and 0.05 M for selenate adsorption with adsorbent loading rate of 1.5 and 3.5 g/L, respetively. Figure 4 shows adsorption kinetics of the Fe-GAC for selenite and selenate. The results indicate that equilibrium was obtained within 48 hours for both selenite and selenate, with 95% and 80% removal at equilibrium, respectively. A pseudo-second-order kinetic model was applied for both anions ($R^2 > 0.99$). Adsorption rate constant for selenate (0.073 g/(mg·min)) was higher than that for selenite (0.018 g/(mg·min)). The adsorption capacity at equilibrium was estimated as 0.66 mg-Se/g-adsorbent for selenite and 0.23 mg-Se/g-adsorbent for selenate.

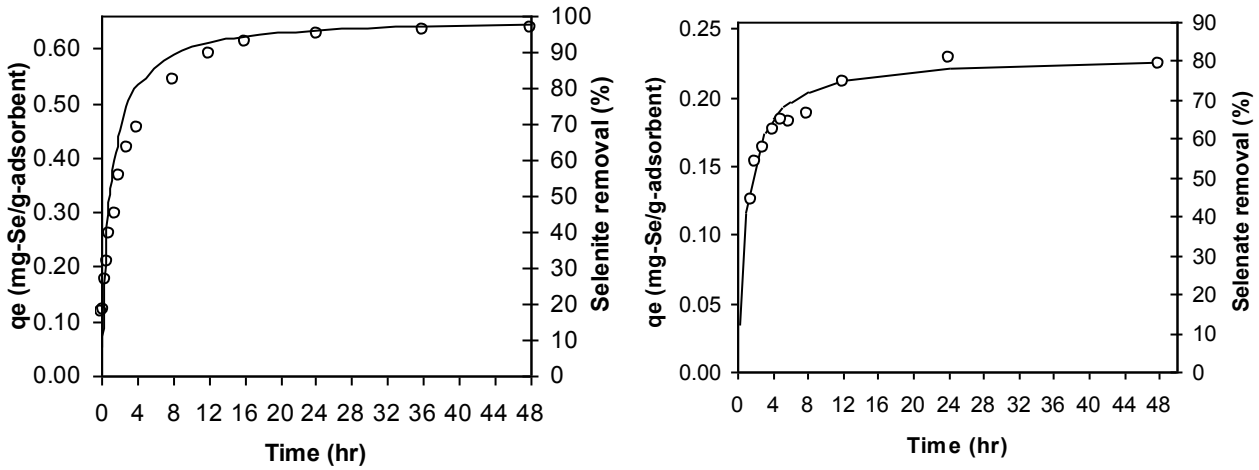

Figure 6. Adsorption kinetics and pseudo-second-order kinetic models for (a) selenite with initial selenium concentration of 1 mg/L at 0.1 M ionic strength level; (b) selenate with initial selenium concentration of 1 mg/L at 0.05 M ionic strength level at pH 5 and 25 °C.

Adsorption Isotherms

Figure 7 illustrates single-adsorbate adsorption isotherms and corresponding isotherm model prediction for selenite (Langmuir) and selenate (Freundlich) under various ionic strengths. The isotherm data of both anions fitted the Langmuir and Freundlich model well ($R^2 > 0.97$). Adsorbent loading rates ranging from 0.2 to 7 g/L were used in the isotherm experiments. There were no plateaus observed for selenate isotherms due to the low initial Se concentration used in this study. The results for selenite adsorption did not exhibit any apparent difference and the maximum adsorption capacity was found to range approximately from 2.50 to 2.60 mg-Se/g-adsorbent under the studied ionic strengths. The results for selenate adsorption show that adsorption capacity increased significantly as ionic strength decreased, which was not observed for selenite adsorption. Goh and Lim (2004) also reported similar effect for ionic strength on selenite and selenate adsorption onto tropical soil.

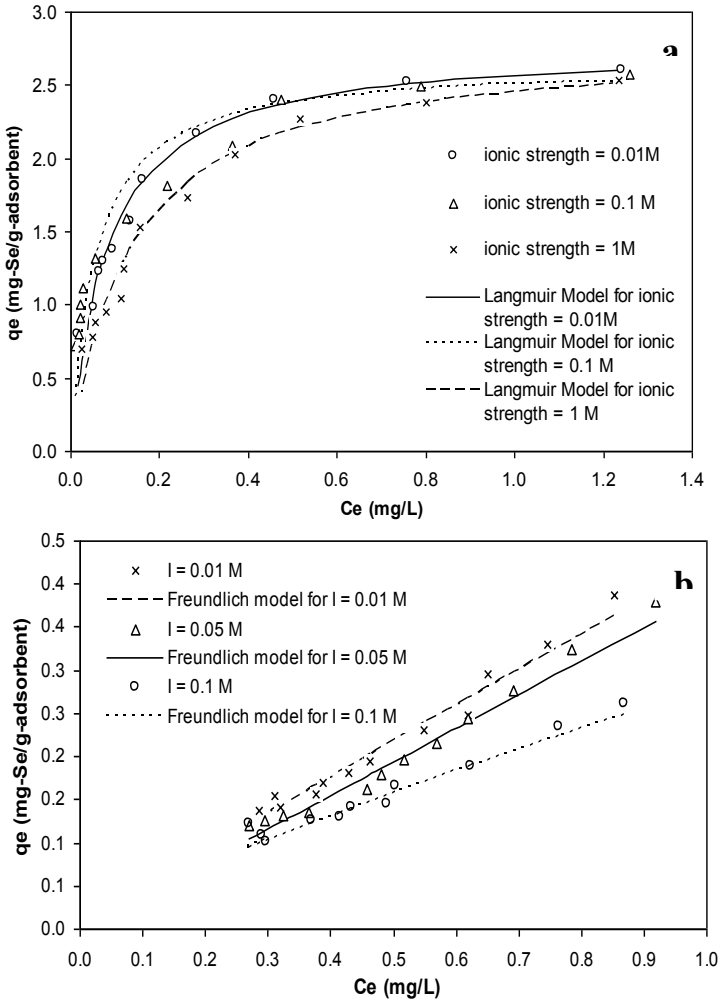

Figure 7. Adsorption isotherms and models at pH 5 and 25 °C under various ionic strengths for (a) selenite with initial selenium concentration of 2 mg/L; (b) selenate with initial selenium concentration of 1 mg/L. The adsorption isotherm models are indicated by the curves.

Coexisting Anions Competitive Adsorption

Figure 8 shows the results for selenite competitive adsorption. The presence of SO_4^{2-} did not cause significant impact on the selenite adsorption. In the presence of SiO_3^{2-}, PO_4^{3-} and CO_3^{2-}, the removal of selenite decreased to various degrees. The results can be explained using the triple layer model (Stumm and Morgan, 1995). Anions such as sulfate and selenate often are weakly bound with surface sites of metal hydroxides forming outer-sphere (b-plane) surface complexes (Hayes et al., 1988). Adsorption of this sort is significantly affected by ionic strength. On the contrary, anions such as selenite and phosphate are bound relatively strongly with the surface sites. The complexes formation often takes place on inner-sphere (o-plane) and is barely affected by ionic strength. As for selenate competitive adsorption, all four types of anions were found to compete with it to various degrees within the studied concentration range (0, 0.1, 1 and 5 mM). Similar with selenite, PO_4^{3-} was observed as the most competitive anion, which reduced the selenate remove efficiency from 70% to 0. Goh and Lim (2004) reported great impact on selenate adsorption caused by PO_4^{3-}. Unlike selenite, SO_4^{2-} was also found to compete with selenate significantly. Selenate removal decreased to 11% with the presence of 5 mM SO_4^{2-}. At high concentration of SiO_3^{2-} and CO_3^{2-} (i.e. 5 mM), only 14% and 9% selenate removals were achieved, respectively.

Selenite and Selenate Bi-adsorbate System

Figure 9 shows the results for selenite competitive adsorption. The presence of SO_4^{2-} did not cause significant impact on the selenite adsorption. In the presence of SiO_3^{2-}, PO_4^{3-} and CO_3^{2-}, the removal of selenite decreased to various degrees. The results can be explained using the triple layer model (Stumm and Morgan, 1995). Anions such as sulfate and selenate often are weakly bound with surface sites of metal hydroxides forming outer-sphere (b-plane) surface complexes (Hayes et al., 1988). Adsorption of this sort is significantly affected by ionic strength. On the contrary, anions such as selenite and phosphate are bound relatively strongly with the surface sites. The complexes formation often takes place on inner-sphere (o-plane) and is barely affected by ionic strength. As for selenate competitive adsorption, all four types of anions were found to compete with it to various degrees within the studied concentration range (0, 0.1, 1 and 5 mM). Similar with selenite, PO_4^{3-} was observed as the most competitive anion, which reduced the selenate remove efficiency from 70% to 0. Goh and Lim (2004) reported great impact on selenate adsorption caused by PO_4^{3-}. Unlike selenite, SO_4^{2-} was also found to compete with selenate significantly. Selenate removal decreased to 11% with the presence of 5 mM SO_4^{2-}. At high concentration of SiO_3^{2-} and CO_3^{2-} (i.e. 5 mM), only 14% and 9% selenate removals were achieved, respectively.

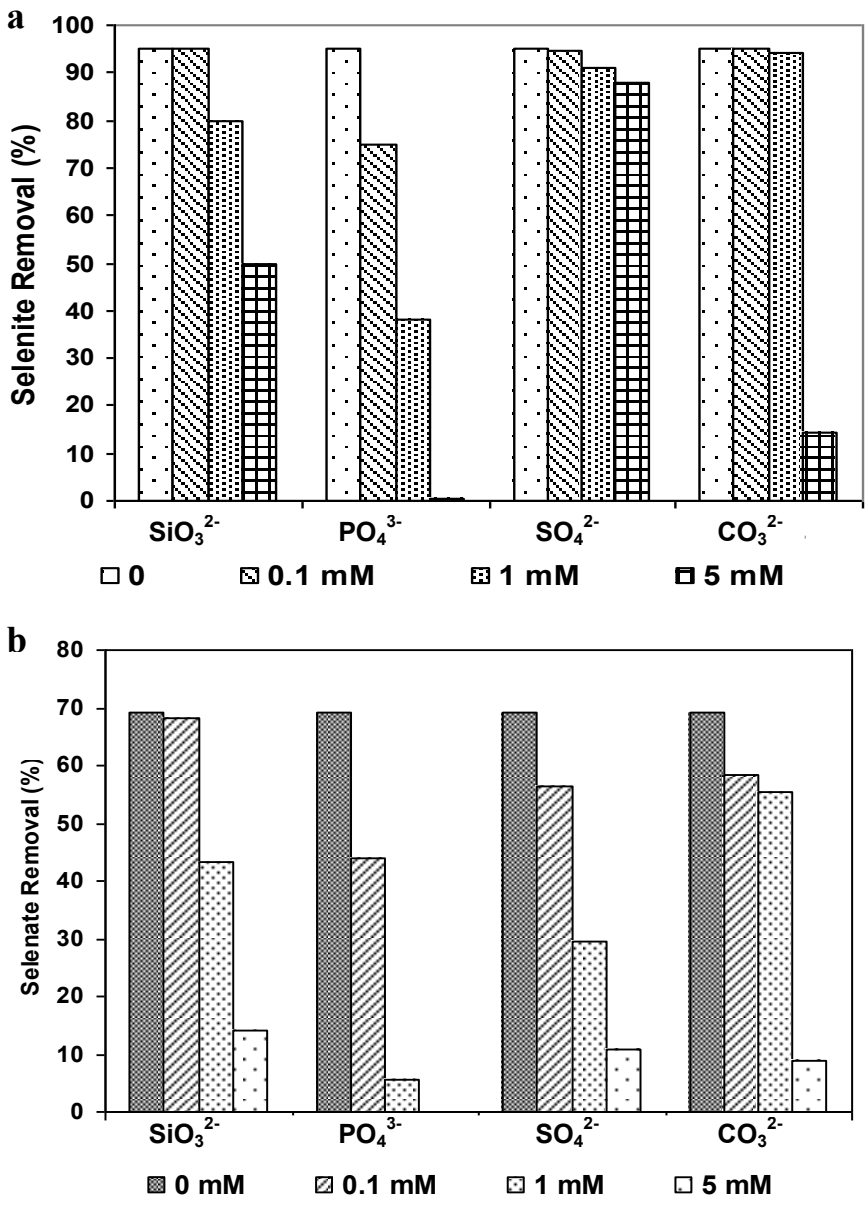

Figure 8. Anion competitive effect on (a) selenite and (b) selenate adsorption after 24 hours for initial selenium concentration of 1 mg/L with ionic strength of 0.1 and 0.05 M, respectively at pH 5 and 25 °C.

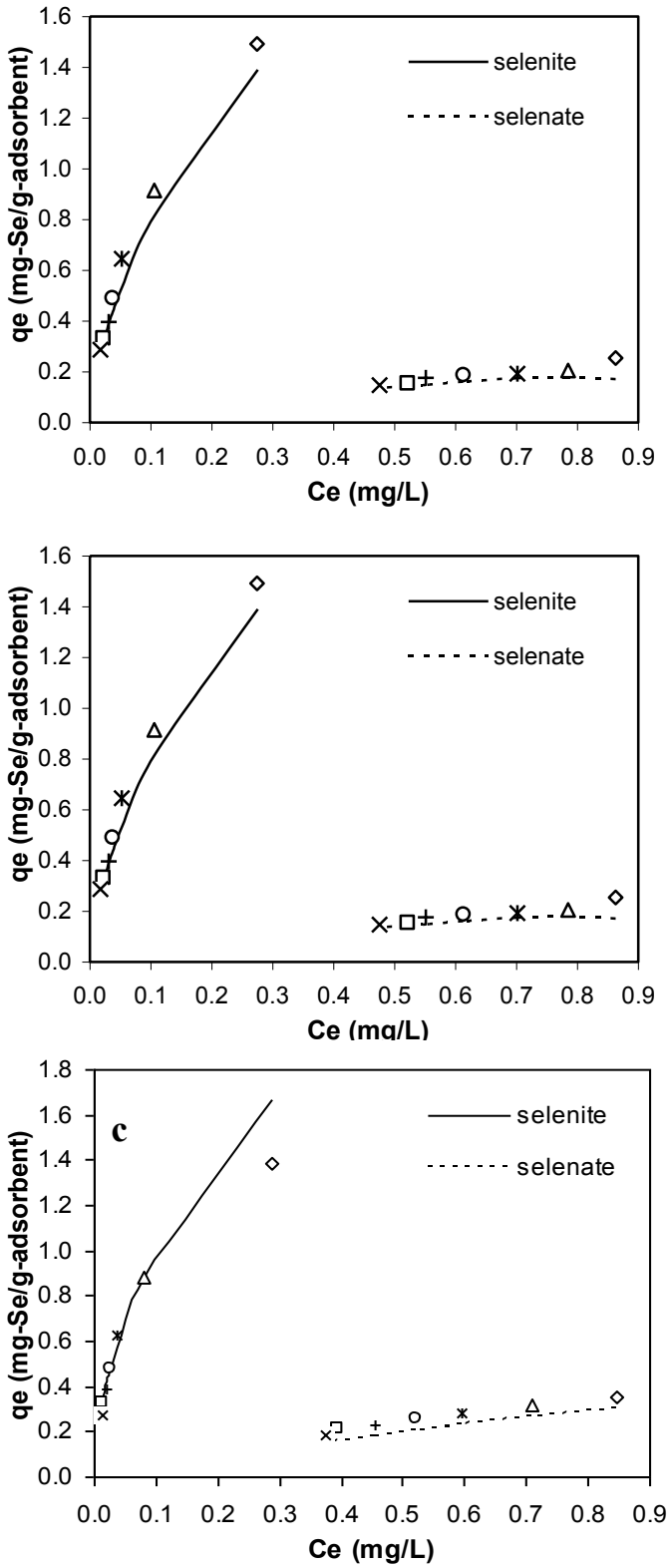

Figure 9. Competitive adsorption isotherms of the Fe-GAC for selenite and selenate (initial Se concentration 1 mg/L for each) under ionic strength (a) 0.1 M, (b) 0.05 M, and (c) 0.01 M, pH 5 and 25 °C. Pairs of the same symbols represent selenate/selenite

concentrations in the same batch reactor. ×: 0.5 g/L; □: 1.0 g/L; +: 1.5 g/L; ○: 2.0 g/L; *: 2.5 g/L; Δ: 3.0 g/L and ◊: 3.5 g/L.

CONCLUSION

Based on the findings obtained during the project period, we conclude that the method of coating iron onto GAC surface is simple and successful. Newly developed Fe-GAC adsorbents demonstrate promising properties for selenite and selenate removal from aqueous phase at low concentration level. It was also found Fe-GAC can work efficiently under a wide condition, i.e., pH range from 2 – 7, ionic strength as high as 1 M. The adsorbents also maintain the relatively high removal efficiencies in the presence of various co-existing anions. Additionally, only slight decreases in the selenite and selenate adsorption capacities in binary system were observed as they were compared to their respective single-adsorbate systems. This suggests the feasibility of removing selenite and selenate simultaneously.

REFERENCES

Barrow, J. J. and Whelan, B. R. (1989) Testing a mechanistic model VII. The effects of pH and of electrolyte on the reaction of selenite and selenate with asoil. *Soil Science Society of America Journal*, 40, 17-28.

Barr, T. L. (1994) *Modern ESCA: the principles and practice of X-ray photoelectron spectroscopy*, CRC Press, Inc., Boca Raton, FL.

Coleman, L., Bragg, L.J., Finkelman, R.B., (1993) Distribution and mode of occurrence of selenium in US coals. *Environmental Geochemistry and Health*, 15 (4), 215–227.

Davis, J. A., Leckie, J. O. (1980) Surface ionization and complexation at the oxide/water interface. 3. Adsorption of ions, *Journal of Colloid and Interface Science*, 74, 32-43.

Frankenberger, W. T. J., Engberg, R. A. (1998) Environmental Chemistry of selenium, Marcel Dekker, Inc., New York, 713.

Goh, K. and Lim, T. (2004) Geochemistry of inorganic arsenic and selenium in a tropical soil: effect of reaction time, pH, and dompetitive anions on arsenic and selenium adsorption, *Chemosphere*, 55, 849-859.

Gallup, D. L. (1996) *In Proceedings of the 69th Water Environment Federation Conference*, Dallas, TX; Water Environment Federation: Alexandria, VA, 447-453.

Hall, K., Eagleton, L., Aerivos, A., Vermeulen, T. (1996) Pore and solid diffusion kinetics fixed bed adsorption under constant pattern conditions. *Industrial and Engineering chemistry Fundamentals* 5, 212–213.

Hayes, K. and Leckie, J. (1987) Modeling ionic strength effects on cation adsorption at hydrous oxide/solution interfaces, *Journal of Colloid and Interface Science*, 115, 564-572.

Hayes, K., Papelis, C., Leckie, J. (1988) Modeling ionic strength effects of anion adsorption at hydrous oxide/solution interfaces. *Journal of Colloid and Interface Science* 125, 717–726.

Kapoor, A., Tanjore, S. and Viraraghavan, T. (1995) Removal of selenium from water and wastewater, *International Journal of Environmental Studies*, 49, 137-147.

Machala, L.; Zboril, R. and Gedanken, A. (2007) Amorphous iron (III) oxide - A review, *Journal of Physical Chemistry B*, 111, 4003 - 4018.

Marin□as, B. J. and Selleck, R. E. (1992) Reverse osmosis treatment of multicomponent electrolyte solutions, *Journal of Membrane Science*, 72, 211–229.

Moreira, R.F.P.M., Peruch, M.G., Kuhnen, N.C. (1998) Adsorption of textile dyes on alumina equilibrium studies and contact time effects. *Brazilian Journal of Chemical Engineering* 15 (1), 21–28.

Neal, R. H., Sposito, G. Holtzclaw, K. M. and Traina, S. J. (1987a) Selenite adsorption on alluvial soils: I. Soil composition and pH effects, *Soil Science Society of American Journal,* 51, 1165-1169.

Parfitt, R.L. (1978) Anion adsorption by soils and soil materials. *Advances in Agronomy* 30, 1–50.

Peak, D., Sparks, D.L. (2002) Mechanisms of selenate adsorption on iron oxides and hydroxides. *Environmental Science and Technology* 36, 1460–1466.

Reed, B. E. and Matsumoto, M. R. (1991) Modeling surface acidity of two powered activated carbons: comparison of diprotic and monoprotic surface representations, *Carbon*, 29, 1191-1201.

Rovira, M., Gimenéz, J., Martínez, M. Martínez-Lladó, X., Pablo, J. Martí, V. and Duro, L. (2008) Sorption of selenium (IV) and selenium (VI) onto natural iron oxides : Goethite and hematite, *Journal of Hazardous Materials*, 150, 279-284.

Séby, F.; Potin-Gautier, M.; Lespes, G. and Astruc, M. (1997) Selenium speciation in soils after alkaline extraction, *Science of the Total Environment*, 207, 81-90.

Shriver, D. F., Arkins, P. A., Langford, C. H. (1994) *Inorganic Chemistry*, W. H. Freeman and Company: New York.

Shulthess, C. P. and Sparks, D. L. (1986) Backtitration techniques for proton isotherm modeling of oxide surface, *Soil Science Society of America Journal*, 50, 1406-1411.

Srivastava, D. N.; Perkas, N.; Gedanken, A. and Felner, I. (2002) *Journal of Physical Chemistry B*, Sonochemical synthesis of mesoporous iron oxide and accounts of its magnetic and catalytic properties, 106, 1878-1883.

Stumm, W. and Morgan, J.J., (1995) *Aquatic Chemistry*, John Wiley and Sons, New York.

Su, C. and Suarez, D. L. (2000) Selenatte and selenite sorption on iron oxides: an infrared and electrophoretic study, *Soil Science Society of American Journal*, 64, 101-111.

Swaine, D. J. (1990) Trace elements in coal. Butterworths, London, 278.

USEPA (2005) Mountaintop mining/valley fills in Appalachia, *Final Programmatic Environmental Impact Statement* (http://www.epa.gov/region3/mtntop/eis.htm) (Accessed Nov., 2006)

Vesper, D. J., Roy, M. and Rhoads, C. J. (2008) Selenium distribution and mode of occurrence in the Kanawha formation, southern West Virginia, U.S.A., *International Journal of Coal Geology*, 73, 237-249.

Weber, T.W., Chakravorti, R.K. (1974) Pore and solid diffusionmodels for fixed-bed adsorbers. *AIChE Journal* 20, 228–237.

Watts, J. F. and Wolstenholme, J. (2003) *An introduction to surface analysis by XPS and AES*, John Wiley and Sons, New York.

Zhang, Y.; Wang, J.; Amrhein, C; and Frankenberger, W. T. Jr. (2005) Removal of selenate from water by zerovalent iron, *Journal of Environmental Quality*, 34, 487-495.

LIST OF ACRONYMS AND ABBREVIATIONS

1. **BET** - Brunauer-Emmett-Teller
2. **EDS** - Energy Dispersion Spectrometer
3. **EPA** - Environmental Protection Agency
4. **DAN** - 2, 3-Diaminonaphthalene
5. **GAC** - Granular Activated Carbon
6. **XPS** - X-Ray Photoelectron Spectroscopy
7. **SEM** - Scanning Electron Microscopy

APPENDIX 23- Mercury Removal from Clean Coal Processing Air Stream (MT007)

FINAL TECHNICAL REPORT

Contract Title and Number:	Period of Performance:
Crosscutting Technology Development at the Center for Advanced Separation Technologies (DE-FC26-05NT42457)	Starting Date: 10/01/05 Ending Date: 3/31/12

Sub-Recipient Project Title:
Mercury Removal from
Clean Coal Processing Air Stream

Principal Investigators:
Dr. Kumar Ganesan
Professor and Head
Department of Environmental Engineering
Montana Tech of the University of Montana Tech

Contact Address:	Contact Information:
Department of Environmental Engineering Montana Tech of The University of Montana 1300 West Park Street Butte, Montana 59701	Phone: 406-496-4239 Fax: 406-496-4650 E-Mail: kganesan@mtech.edu
Subcontractor Address: Insert address of subcontractor. If none awarded, insert "No subcontracts issued."	Subcontractor Information: Phone: Fax: E-Mail:

DISCLAIMER

ABSTRACT

Mercury is a high-priority regulatory concern because of its persistence and bioaccumulation in the environment and its neurological health impacts. The focus of this research is to develop cost effective filters to control mercury from clean coal processing flue gas. The main objective of this research is to use metallic nano particle (MNP) filters to remove mercury from air stream. The MNP filter is a new innovation and expected to sustain efficiency and integrity for longer filtration life. During this project period, six different filters were prepared and tested to assess the potential in removing mercury. To increase the mercury removal efficiency, the filter was then modified with a polymer addition in the fabrication. This ceramic MNP filter with polymer coat was successfully tested for mercury removal efficiency as well as regeneration potential. Experiments were conducted to determine the optimal temperature at which spent filters can be efficiently regenerated. The new filter was tested at a higher flow rate to simulate the field condition. Large scale filters were fabricated for future lab as well as field tests. And also mercury removal efficiency test was successfully performed with an additional filter. The results reinforced the performance of the filter to remove mercury at 90% efficiency for a longer period than the previous filters tested in the lab. In conclusion the ceramic based MNP filter with polymer coating is a viable filtration system to remove mercury from gas stream including clean coal processing air stream.

TABLE OF CONTENTS

LIST OF FIGURES

EXECUTIVE SUMMARY

Mercury is a pollutant of concern because of its persistence and bioaccumulation in the environment and its neurological health impacts. The focus of this research is to develop cost effective filters to control mercury from clean coal processing flue gas. The main objective of this research is to develop the metallic nano particle (MNP) filters to remove mercury from air stream. Nanotechnology concepts were introduced to make a colloidal solution and the ceramic substrates were doped with MNP, to achieve high efficient mercury filters. The use of MNP and the porous ceramic substrate, combines several advantages such as: use of much smaller amounts of the special metal; the substrate will have low flow resistance, chemically stable, highly porous providing tremendous contact surface area; sustain stability under thermal desorption cycles to recover mercury; and easy to pack as a filter and effective in holding the nano metallic particle in place. The MNP filter is a new innovation and expected to sustain efficiency and integrity for longer filtration life.

The filters were assembled by dispersing MNP in solution and depositing on to the substrate using a technique developed by Montana Tech's mercury research laboratory. To achieve maximum deposition and to reduce the overall cost of the filtration system, different techniques were experimented. This proprietary technique was repeated several times to optimize the amount of MNP coverage on the substrate. To evaluate mercury removal efficiency of the filter, mercury-contaminated air was passed through it and the inlet and outlet mercury concentrations were measured throughout the test period. The goal of the laboratory testing was to achieve mercury removal efficiencies above 90%. Therefore all testing results were evaluated based on how well this 90% efficiency goal was met. The thermal desorption process consisted of heating the saturated MNP filter to volatilize the captured mercury. Thermal desorption of mercury from the spent filters offers several benefits including reusability of the filters back into the system and recovery of mercury. To perform thermal desorption in the lab, a tube furnace was used. The thermal desorption process was continued until the mercury concentration in air leaving the metallic filter was below 0.5$\mu g/m^3$. The experiments were performed under a fume hood for added safety.

During this project period six different MNP filters were prepared and tested for mercury removal efficiency. To increase the mercury removal efficiency, the filter was modified with a polymer addition during the fabrication. This MNP filter with polymer coat was successfully tested for mercury removal efficiency as well as regeneration potential. Experiments were conducted to determine the optimal temperature at which spent filters can be efficiently regenerated. Large scale filters were assembled for future lab as well as field tests. And also mercury removal efficiency test was successfully performed with an additional new filter. The new filter was tested at a higher flow rate to simulate the field condition. The results reinforced the performance of the filter in removing mercury at 90% efficiency for a longer period than the previous filters tested in the lab.

The performance of the polymer coated ceramic MNP is a breakthrough in our research. Of all the mercury filters developed and tested, in the past several years, this polymer coated MNP filter showed the best performance. Based on this result, the polymer coating was incorporated in the filter fabrication process.

In conclusion the result of this research clearly indicates that the polymer coated ceramic MNP filters has very high potential as a mercury control device.

1.0 INTRODUCTION

Mercury is a high-priority regulatory concern for EPA because of its persistence, bioaccumulation, cycling ability in the environment, and its neurological health effects. Mercury is present in three forms in a coal fired flue gas: elemental mercury, divalent mercury (II), and particulate bound mercury. Elemental mercury is the mercury vapor released during combustion, mercury (II) results from the oxidation of elemental mercury by various elements in the flue gas, and particulate mercury forms when elemental mercury or mercury (II) attaches to solid particles such as fly ash in the flue gas. Currently, there is no effective control technology that removes all three forms of mercury, especially the elemental form, from coal-fired flue gas. Montana Tech has successfully developed, tested, and patented metallic mercury filter that can remove elemental form of mercury at or above 90 % efficiency. However, these metallic filters are expensive because of the high cost of metals that is used to fabricate the filters. To increase the cost effectiveness of the filters, the PI continuously explored novel materials to use in the filtering system. Based on the funding from CAST and the Montana MBRCT programs, the PI has successfully completed some preliminary tests on a new metallic nano particle filter to make it cost effective.

In general, low rank coals like the Powder River Basin sub-bituminous coals have high moisture content and low Btu values. Therefore, the cost of transporting and burning high moisture and low Btu coal is economically not attractive compared to low moisture and high Btu bituminous coal. The clean coal technologies are aimed to reduce the initial moisture content by 30-40% and increase the Btu values of sub-bituminous coal by 30-40%. There are abundant low-rank coal deposits in the United States and throughout the world that will be utilized in energy production for decades to come. Clean coal technology seeks to reduce environmental effects by using multiple technologies to clean coal and contain its emissions. A significant co-benefit of clean coal process is that contaminants are eliminated before its combustion. The clean coal technologies that use thermal treatment processes claim mercury removal up to 70 % in addition to the co-benefits of lower sulfur and nitrogen oxide emissions. This elimination of the contaminants at the source, “source reduction” is the best pollution prevention approach that any industry and community would like to accomplish. In addition, the back-end capital costs and maintenance costs of large control equipment involved in reducing mercury emissions is minimized if not completely avoided.

1.1 Technical Background

The US DOE has been intensely involved in developing technologies to control mercury and other emissions from coal combustion. Most of the technologies under consideration for mercury control are post-combustion processes where the flue gas is treated to control mercury emissions. It is reported that most of the (~90%) mercury from the combustion of western coal is released in vapor form mainly due to lower chloride content in coal. While the coal containing higher chloride content tends to release mercury in ionic form(40-80%) and elemental form(60%-20%). Most of the ionic form of mercury could be captured readily in a conventional flue gas desulphurization system while particulate bound mercury can be effectively captured by existing particulate control devices such as bag houses or electrostatic

precipitators. Mercury present in the elemental form is the hardest one to remove in the existing air pollution control devices. Montana Tech has successfully developed and tested metallic mercury filters that can remove elemental form of mercury at or above 90 % efficiency.

Most of the technologies currently under review for commercialization are focused on oxidizing the vapor form of mercury in a more readily soluble ionic form. These technologies merely convert mercury from one form to another and distribute the transformed mercury into water and solid waste streams including the fly ash. This can potentially cause serious problems in the future due to mercury being released into the environment through byproducts containing the transformed mercury. In addition, because of its relatively high solubility, the oxidized form of mercury eventually may release mercury from the waste stream into the environment, causing environmental concern and potential future liability. Therefore, long term solution for mercury must be focused on eliminating the mercury rather than transforming and transferring the mercury into byproducts and waste streams. This will make more economic and environmental sense on a long range basis.

The traditional control devices like electrostatic precipitator, bag house, and flue gas desulphurization(FGD) systems are capable of removing mercury from the coal fired flue gas in varying amounts ranging from 20-90% however only 15% of the plants have FGD systems, and 16% have bag houses. The best control device that helps to oxidize mercury to ionic mercury form is the SCR systems that are used for NOx control in power plants. Again only less than 40-80% of the plants in US have such systems. In a pre-combustion process, mercury is released into a smaller volume of air with higher mercury concentration than in a post-combustion system. This reduces the capital as well as maintenance cost. Above all mercury reduction at the source is environmentally beneficial compared to the “end of pipe treatment” method.

There are several pre-combustion coal processing methods available. One of such pre-combustion techniques is the Western Research Institute’s patented thermal treatment process where moisture and mercury are separated at two different temperature zones. When the coal is heated to 200-280^{o}F, the water vapor is released, where as mercury is released only at about 450-550F in the Hg-free water removal zone. The focus of the CAST III research was to remove mercury from the air stream using MNP filters. The mercury removal from this waste stream is an important step towards mercury emission control because it eliminates mercury before the combustion of coal. The air stream from clean coal sweep gas will have higher concentration of mercury than the power plant gas stream and the presence of other contaminants might pose a challenge. In this CAST III research the filtration system was modified to work in a higher mercury concentration levels than the power plant stack gas for which the filters were originally intended.

Montana Tech has been intensely involved in developing technologies to reduce mercury emissions from coal fired flue gas streams. This project is aimed at a sustainable solution to eliminate mercury from entering the environment especially from a clean coal treatment process. During this project period a new filter system was developed to remove mercury from clean coal off gas. Nanotechnology concepts were introduced to make a colloidal

solution and the ceramic substrates were doped with MNP, to achieve highly efficient mercury filters. The use of MNP and the porous ceramic substrate, combines several advantages such as: use of much smaller amounts of the special metal; the substrate will have low flow resistance (low pressure drop) and chemically stable; the high porosity substrate will yield tremendous contact surface area; sustain stability under thermal desorption cycles to recover mercury; and easy to pack as a filter and effective in holding the nano metallic particle in place.

1.2 Objective and Approach

The main objective of this research is to use metallic nano particle (MNP) filters to remove mercury from pre-combustion low-rank clean coal processing air stream. CAST project in 2008, allowed the PI to develop a new MNP filter using ceramic substrates aiming to reduce the overall cost of the filtration system. In CAST 2008, the main performance parameters considered were the base metals or materials characteristics, the physical characteristics, filter stability, maximum surface area per volume of filter, and air flow characteristics. The CAST 2008 experiments and study results are included in the Appendix A and B. The objectives of this CAST III research are: to assemble filters with maximum MNP; to optimize thermal desorption; to generate synthetic gas to simulate the sweep gas stream of clean coal process and to assemble large scale filtration system to test in the lab as well as in the field.

During this project period (2009 to 2011) the following tasks were completed at the Montana Tech Mercury Laboratory. To assess the potential of the MNP filters, six different filters were prepared and tested by using varied MNP volume in solution as well as concentrations. To increase the mercury removal efficiency, the filter was modified with a polymer addition during the fabrication. This polymer coated MNP filter was successfully tested for mercury removal efficiency as well as regeneration potential. Experiments were conducted to determine the optimal temperature at which spent filters can be efficiently regenerated. We were unable to proceed with generating synthetic gas to simulate the sweep gas stream of the clean coal process because of high temperature and safety reasons associated in building one. Large scale filters were fabricated for future lab as well as field tests. And also mercury removal efficiency test was successfully performed with an additional filter. A new filter was tested at a higher flow rate to simulate the field condition. The results reconfirmed that the filters are capable of mercury removal at or higher than 90% for relatively longer periods than previous filters. The performance of this filter is very promising to build the mercury control system.

2.0 EXPERIMENTAL PROCEDURES

The laboratory experiments were conducted at Montana Tech of the University of Montana Mercury Laboratory. The experimental procedures consisted of MNP filter fabrication, mercury removal efficiency testing, and thermal desorption setup. The entire experimental setup was under the fume hood. The outlet air was sent through a carbon filter before released into the atmosphere.

2.1 MNP Filter Fabrication

MNP filters were assembled using ceramic substrates (figure 1) aiming to reduce the overall cost of the filtration system. To achieve maximum deposition of the MNP on the substrate, different techniques were experimented. MNP was dispersed in solution and deposited on the porous substrate using a technique developed by Montana Tech's mercury research laboratory. This proprietary technique was repeated several times to achieve maximum amount of MNP coverage on the pores of the substrate.

Figure 1 MNP Filter Preparation

2.2 Mercury Removal Efficiency Testing

Mercury-contaminated air was passed through the MNP filter at a flow rate of 2.5 L/min. A mercury vaporizing system that produces a constant concentration of elemental mercury was used as the mercury source. Figure 2 shows the experimental setup. The inlet and outlet mercury concentrations of the filters were measured throughout the test period. Based on the results the mercury removal efficiency of the filter was evaluated. Mercury concentrations were measured using a portable mercury analyzer, Mercury Tracker, which has a sensitivity of 0.01 $\mu g/m^3$. Once the mercury removal efficiency of the MNP filter dropped below 50%, the test was terminated. Since the goal of the laboratory testing was to achieve mercury removal efficiencies above 90%, and all testing results were evaluated based on how well this 90% efficiency goal was met.

Figure 2: Mercury Removal Efficiency Testing Setup

2.3 Thermal Desorption Setup

The thermal desorption process consisted of heating the saturated/spent MNP filter to volatilize the captured mercury vapor. This thermal desorption was performed using a tube furnace (Figure 3). The thermal desorption process was continued until the mercury concentration in the gas stream leaving the MNP filter was below 0.5μg/m^3.

Figure 3: Thermal Desorption Setup

3.0 RESULTS AND DISCUSSION

Initially six different filters were tested for mercury removal efficiency. Figure 4 and 5 show the results. Thermal desorption experiments were conducted to determine the optimum temperature at which the spent filters can be desorbed and the results are in Figure 6 and 7. Following these testing to achieve maximum MNP deposition to increase the mercury removal efficiency of the filters, a polymer coating was tried and Figure 8 shows the results.

Thermal desorption testing on this spent filter was performed (Figure 9) to verify the reusability of this polymer coated filter. The thermally desorbed polymer coated filter was tested again for mercury removal efficiency (Figure 10). An additional MNP filter was tested to reinforce the results using higher flow rate. Synthetic gas generation was attempted and high flow rate testing was performed with a new filter.

3.1 Mercury Removal Testing of the First Six Filters

Initially three different filters were prepared using 75 ml, 150 ml and 182 ml of the 0.2 g/L MNP colloidal solution on 92 grams of BioMax substrate for each set. Each filter was evaluated for mercury removal efficiency. The filters #1, #2 and #3 were exposed to an average mercury concentrations of 44, 43, and 45 µg/m^3 respectively. Figure 4 shows the test results.

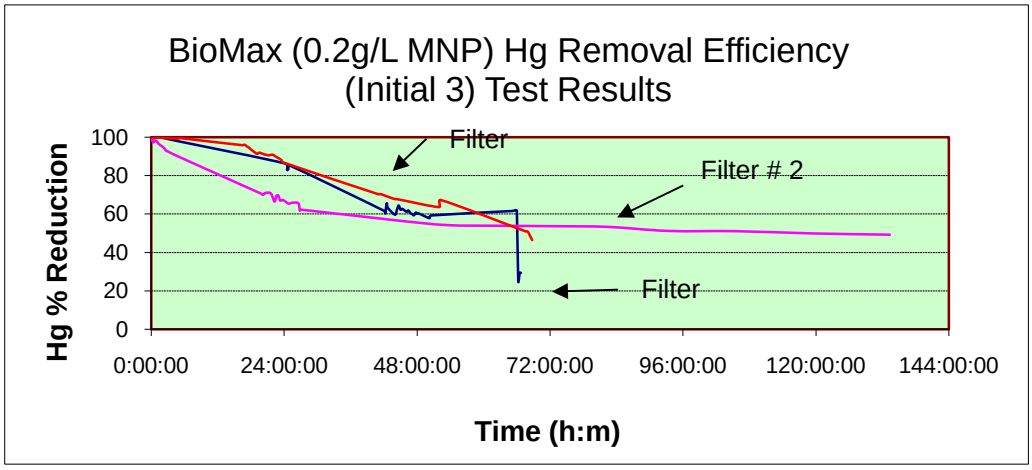

Figure 4: Mercury Removal Efficiency Test Results of Initial Three MNP Filters

The test results of the initial three filters indicate that filter #3 is the best, showing above 90% efficiency lasting more than 22 hours whereas, filter number #1 and #2 indicated above 90% efficiency lasting about 15 and 6 hours respectively. However, for the 50% efficiency filter #2 performed the best lasting 130 hours where as filter # 1 and 3 lasted 66 and 68 hours respectively. As our goal is to achieve 90% or above mercury removal efficiency, among these three, filter # 3 was considered as the best.

A second set of three filters were prepared by increasing the MNP concentrations to 1.5 times and also varying the solution (Filter #4: 76 ml, Filter #5: 114 ml, Filter # 6: 152 ml). The filters #4, #5 and #6 were exposed to an average mercury concentrations of 51, 53, and 38 µg/m^3; respectively for the entire testing period. As for the previous testing the flow rate was kept at 2.5 L/min. The results are given in Figure 5.

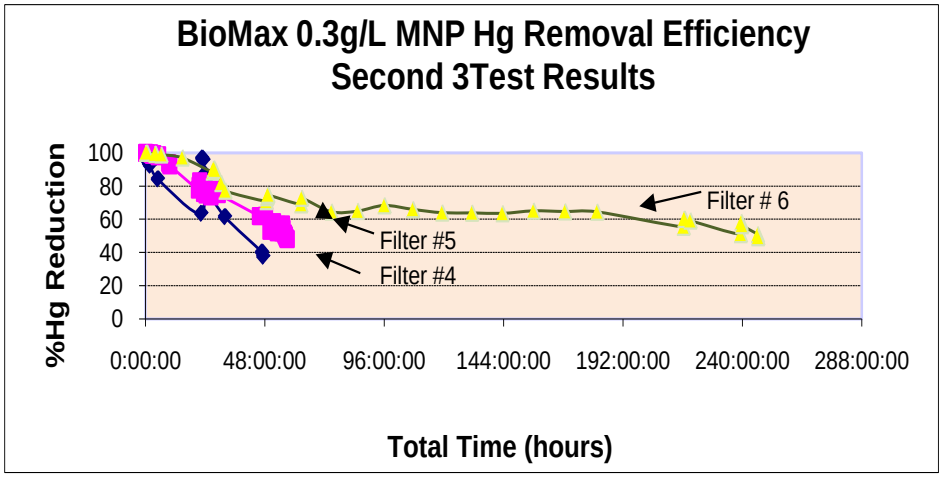

Figure 5: Mercury Removal Efficiency Test Results of Second Three MNP Filters

From the test results filter #4 shows above 90% mercury removal efficiency lasting more than 23 hours and the 50% efficiency lasting more than 40 hours. However, two readings showed decline in efficiency and the reason is unknown at this point. Filter number 5 shows 10 hours of 90% efficieny and the 50% efficiency lasted only 56 hours. Of all the filters tested this far, filter number 6 showed the best results. The 90% efficiency lasted 28 hours and the 50% mercury removal efficiency lasted for a total of 246 hours (more than 10 days).

The mercury concentration from the mercury generator was observed to be varying between 35-56 µ/m3 during these tests. The mercury concentration variation has an effect on the mercury removal efficiency of the filters tested. However, the general indication is that the filter #6 has outperformed other filters.

3.2 Thermal Desorption Tests to Identify Optimal Temperature

Thermal desorption of mercury from the MNP filters offers several benefits including reusability of the spent filters back into the system and mercury can be condensed to recover mercury. Experiments were conducted to determine the optimal temperature at which spent filters can be efficiently regenerated. Figure 3 shows the thermal desorption setup. About 150 g of MNP filters were made and tested for mercury removal efficiency till the efficiency lasted 50%. These mercury saturated MNP filters were divided into 5 different samples. A tube furnace (Figure 3) was used for this thermal desorption proceedure, the flow rate of the clean air was kept at 5L/min, and the five samples were desorbed at five different 300, 350, 400, 450, and 500 °F temperatures. Mercury released from the filters was measured at various time intervals.

Experimental Results

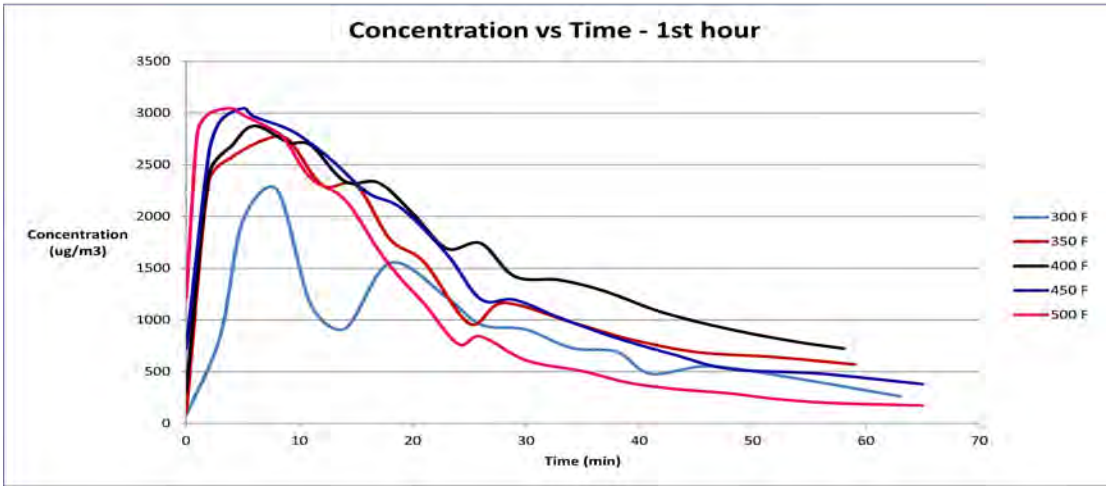

Figure 6: Thermal Desorption Results for the First Hour

The results of the thermal desorption of this five different sample at the first hour indicated that most of the mercury is being released within the first 30 minutes regardless of the temperature.

Experimental Results

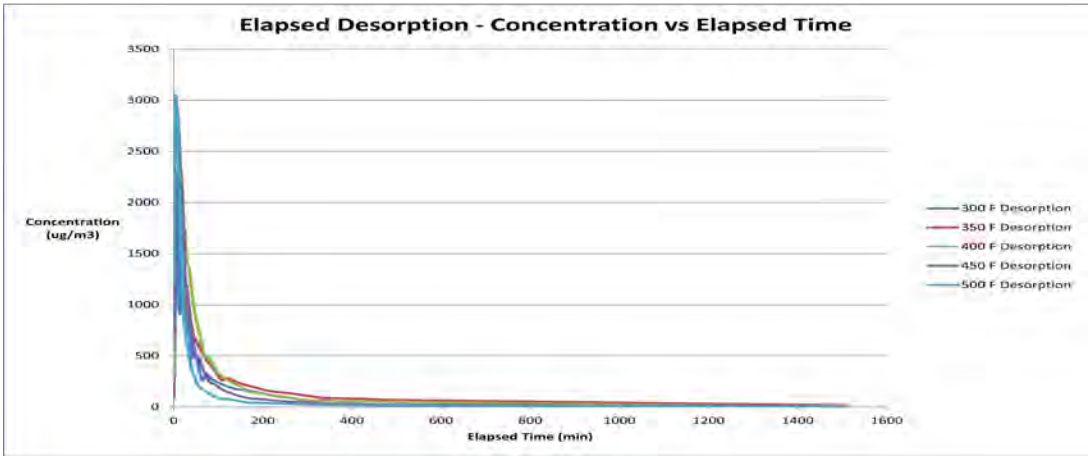

Figure 7: Thermal Desorption Results for Longer Period (24 hours)

However the thermal desorption results indicated that the regeneration of the filter was effective at 450 F in terms of temperature and time it took to release the captured mercury.

3.3 Polymer Coated MNP Filter Testing

The performance of this polymer coated ceramic MNP is a breakthrough in our research on developing a mercury control device. Of all the mercury filters developed and tested, this filter showed the best performance relative to previous filters.

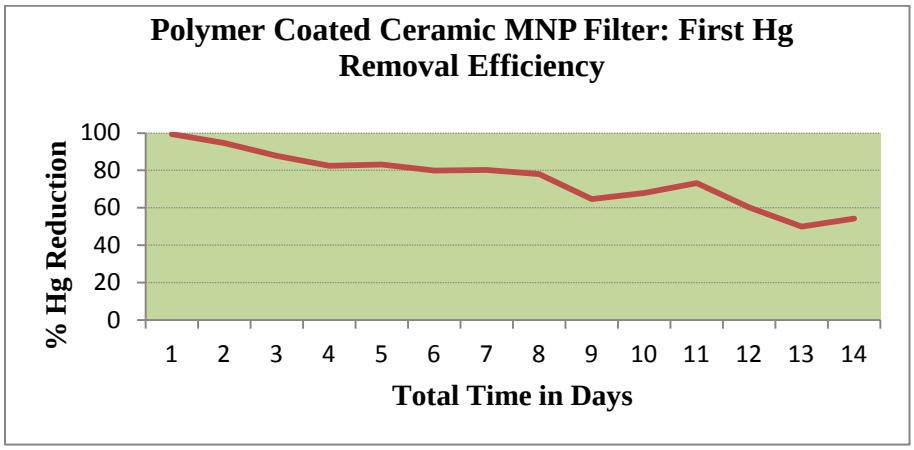

Figure 8: Polymer Coated MNP Filter Mercury Removal Efficiency Test

The mercury removal efficiency was above 90% for more than two days (Figure 8). The 50% mercury removal efficiency lasted 14 days.

To assess the reusability of this filter, the spent mercury filter was thermally desorbed. Because of the polymer addition the initial temperature was kept at 200^{o}F as a precautious measure.

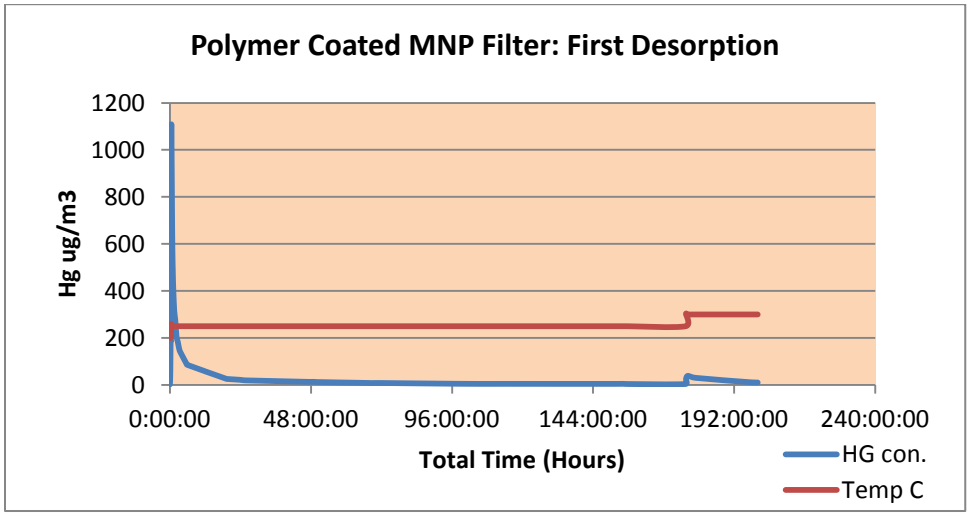

Figure 9: Polymer Coated Ceramic MNP Filter: First Thermal Desorption Test

Figure 9 shows the results of the thermal desorption. Most of the mercury was released within the first 30 minutes with temperatures raised to 250F. The mercury was released at the rate of above 1000 µg/m^3 for about 5minutes with an air flow of 5L/min. During the final 25 hours, the temperature was again increased to 300^{o}F and data was collected until the concentration in the air stream reached less than 0.5µg/m^3.

The thermally regenerated filter was tested for mercury removal efficiency following the same procedures. Figure 10 shows the test results. The 90% efficiency lasted more than a day and the 50% mercury removal efficiency lasted for a total of 8 days. The results indicated that the thermal desorption can be performed safely at 300^{o}F without damaging the polymer. This is a remarkable preformance and this MNP with ploymer filter has great potential in developing into a mercury control system.

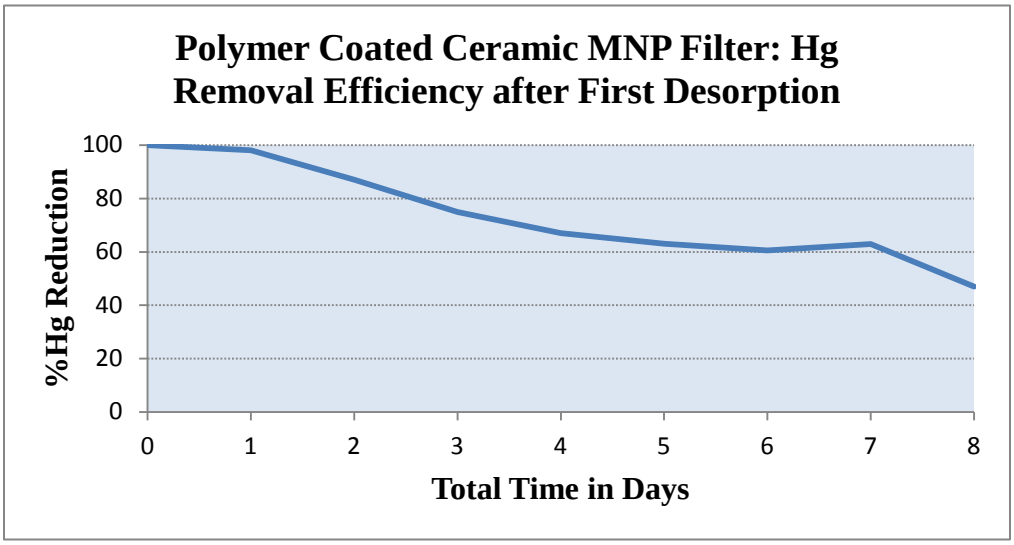

.

Figure 10: Polymer Coated MNP Regenerated Filter: Mercury Removal Efficiency Test Results After First Thermal Desorption

3.4 Additional Filter Testing

At the mercury laboratory, additional mercury removal efficiency tests were performed with another bench scale filter (Filter #8) to verify the performance of the filter for commercialization purposes. The filter was exposed to an average mercury concentration of 19µg/m^3. The test results are in figure 11.

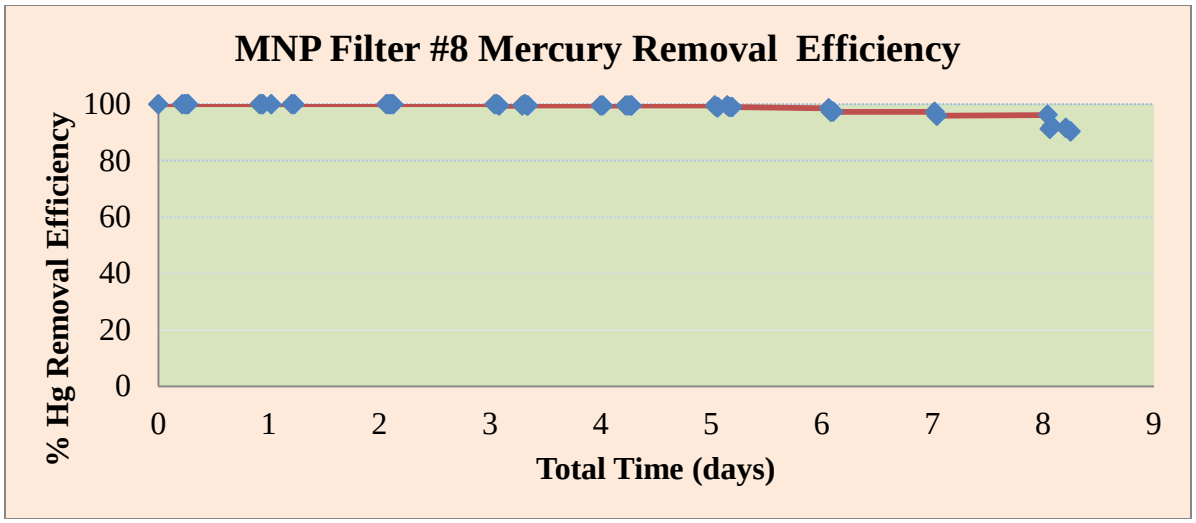

Figure 11: Filter #8 Mercury Removal Efficiency Test Results

Of all the filters tested in the lab previously this filter #8 showed better performances. The 90% and above mercury removal efficiency of this filter lasted over 8 days. Since our focus is to achieve 90% mercury removal efficiency the testing was terminated once the removal efficiency declined below 90%. The weight of this filter was less than 30 grams and for this size the test results are excellent and increasing the quantity of the filter for the field is expected to give better results.

3.5 Synthetic Gas Generation Attempt

In order to simulate the sweep gas stream of the clean coal process we need SOx concentration between 50and100 ppm and NOx concentration between 300 and 350 ppm. After exploring several options, we attempted to generate the SOx and NOx gas streams using commercially available permeation tubes. The Dynacalibrator, the mercury generator used in the laboratory, uses permeation tubes as the trace gas source. By adjusting the permeation chamber temperature and the carrier gas flow, different concentrations of mercury is produced. The focus was to use the same mercury generator to produce SOx and NOx. However there are no permeation tubes available for SOx and NOx at the concentration levels needed for our testing and that left us to consider cylinder gases.

Mixing SOx and NOx cylinder gas opened new issue of safety. Our mercury lab is not equipped with the facility to mix cylinder gases and also it is not equipped with SOx and NOx gas concentration measuring devices.

3.6 High Flow Rate Testing

A laboratory test system at a higher flow rate of 20 lpm was successfully established. The filter system was packed with larger volume of filter material and exposed to 28 $\mu g/m^3$ of average mercury concentration. Mercury removal efficiency test was conducted at 20 lpm flow rate. Figure 12 shows the results. The high flow rate test was successful.

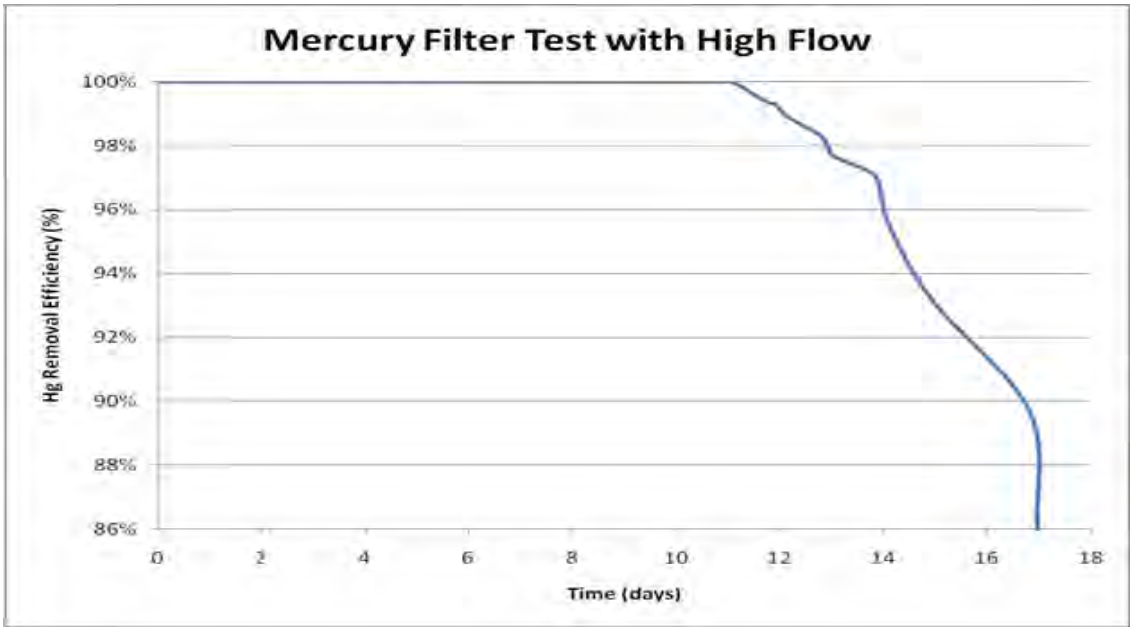

Figure 12: Mercury Removal Efficiency at High Flow Rate Test Results

The results indicated that the filter lasted for almost seventeen days at or above 90% efficiency. It also indicated that one could design a filter system to last any length of time by increasing the filter volume.

4.0 CONCLUSION

The nano metallic filter is a new innovation. Testing and improving the filter further for applications in other gas streams such as a clean coal process air streams will significantly expand the marketability of these filters. In conclusion, this project focused on developing a new filter using metallic nano particle with polymer coating on ceramic substrates to capture mercury from clean coal process air streams. The indication is that, it is possible to improve the efficiency of the filter by simple techniques like polymer coating. Thermal desorption to regenerate the filter was very promising. The reusability of the filter back into the mercury removal system is successful. The results of this research helped to determine the potential of the proposed technology and its viability to use in reducing mercury emissions from clean coal processing air stream. Improving the filter further with additional tests will provide the needed design data for pilot scale system design especially for a clean coal combustion process.

REFERENCES/LITERATURE CITED

Ah, C. S., Han, H. S., Kim, K., & Jang, D. (2000). Phototransformation of alkanethiol-derivatized noble metal nanoparticles. *Pure and Applied Chemistry, 72*, 91.

An Assessment of Mercury Emissions from U.S. Coal-Fired Power Plants; EPRI Report No. 1000608; EPRI: Palo Alto, CA 2000. "EM for AWMA Environmental Managers", February, 2003.

Bland et al. " Beneficial Options for the Pre-Combustion Thermally Treated Subbituminous Coal: Initial Findings," 22nd Annual International Pittsburg Coal Conference, September 12-15,2005

Brockman, J. M., Frutos, A. G., & Corn, R. M. (1999). A multistep chemical modification procedure to create DNA arrays on gold surfaces for the study of protein-DNA interactions with surface plasmon resonance imaging. *Journal of the American Chemical Society, 121*(35), 8044-8051.

"Coal Chlorine Content Influences Mercury Removal", PRECIP Newsletter. January 2002, No. 312. www.mcilvainecompany.com/newsletters/precipn1312/Coal%20Chlorine%20

EPRI. (2003). *An assessment of mercury emissions from U.S. coal-fired power plants* No. 1000608.

EPRI. (2003). *Impacts of NO, controls on mercury controllability* No. 1004000.
Fleming, M. S., & Walt, D. R. (2001). Stability and exchange studies of alkanethiol monolayers on gold-nanoparticle-coated silica microspheres. *Langmuir, 17*(16), 4836-4843.

Gorishi, B.; Gullet, B.K., "Sorption of Mercury Species by Activated Carbon and Calcium Based Sorbents: Effect of Temperature, Mercury Concentration and Acid Gases", Waste Management & Research, 1998, 6, 582-593.

Granite, E.J.; H.W., Hargis, R.A. "Carbon-Based Sorbents For the Removal of Mercury From Flue Gas", U.S. Department of Energy.

Guijarro, M. I., Mendioroz, S., & Munoz, V. (1998). "Effect of morphology of sulfurized materials in the retention of mercury from gas streams". *Industrial & Engineering Chemistry Research, 37*(3), 1088-1094.

Hwang, J.Y., Huang, X., Tieder, R.E., Liu, X. "Control of Mercury Emissions from Coal Fired Power Plants Using Fly-Ash-Derived Carbon", Michigan Technological University, EPA Grant Number R825370C028, www.es.epa.gov/ncer_abstracts/centers/cencitt/year3/material/hwang.html.

Ihle, J., “Mercury Emissions and Fuel Switching: What’s in Your Coal?”, October 2002. www.coalage.com/ar/coal_mercury_emissions_feul/.

Impacts of NO, Controls on Mercury Controllability; EPRI Report No. 1004000; EPRI; Palo Alto, CA, 2000. “EM for AWMA Environmental Managers”, February, 2003.

Karatza, D.; Lancia, A.; Musmarra, D., “Fly Ash Capture of Mercuric Chloride Vapors From Exhaust Combustion Gas”, Environ.Sci.Technol.1998, 32, pg.3999-4004.

Keating, M. H. (1996). *Mercury study report to congress. volume 7. an evaluation of mercury control technologies and costs. sab review draft* No. PB--96-184684/XAB; EPA--452/R-96/001G)

Kosuge, K., Murakami, T., Kikukawa, N., & Takemori, M. (2003). Direct synthesis of porous pure and thiol-functional silica spheres through the S+X-I+ assembly pathway. *Chemistry of Materials, 15*(16), 3184-3189.

Lee, J.,Shick., & Park, J.,Koo. (2001). Preparation of porous ceramic pellet by pseudo double-emulsion method from 4-phase foamed slurry. *Chemistry and Materials Science, 20*(3), 205-207.

Love, J. C., Estroff, L. A., Kriebel, J. K., Nuzzo, R. G., & Whitesides, G. M. (2005). Self-assembled monolayers of thiolates on metals as a form of nanotechnology. *Chemical Reviews, 105*(4), 1103-1169.

Meij, R. “Distribution of Trace Species in Power Plant Streams: A European Perspective”, American Power Conference, Chicago, 1994.

Mendioroz, S; Guijarro, M.I.; Bermejo, P.J.; Munoz, V., “Mercury Retrieval from Flue Gas by Monolithic Absorbents Based on Sulfurized Sepriolite”, Environ.Sci.Technol. 1999, 33, pg.1697-1702.

Mercury Study Report to Congress, EPA-452/R-96-001g, 1996.

Mercury Study Report to Congress: Volume I: Executive Summary; U.S. Environmental Protection Agency, Office of Air Quality Planning and Standards and Office of Research and Development: Research Triangle Park, NC, 1997. “EM for AWMA Environmental Managers”, February, 2003.

Morency, J.R., Panagiotou, T., Senior, C.L. “Laboratory Duct Injection of a Elite-Based Mercury Sorbent”, Physical Sciences Inc.

Nordin, A.; Schager, P,; Hall, B., “ Mercury Speciation in Flue Gases: A Comparison of Results from Equilibrium Calculations with Results from Laboratory Experiments”, Swedish Fame Days, Turkoo, Finland, 1990.

Pavlish, J. H., Sondreal, E. A., Mann, M. D., Olson, E. S., Galbreath, K. C., Laudal, D. L., et al. (2003). Status review of mercury control options for coal-fired power plants. *Fuel Processing Technology, 82*(2-3), 89-165.

Posthumus, W., Magusin, P. C. M. M., Brokken-Zijp, J. C. M., Tinnemans, A. H. A., & van der Linde, R. (2004). Surface modification of oxidic nanoparticles using 3-methacryloxypropyltrimethoxysilane. *Journal of Colloid and Interface Science, 269*(1), 109-116.

PRECIP. (2002, January). Coal chlorine content influences mercury removal. *PRECIP Newsletter,*

Study of Hazardous Air Pollutant Emissions from Electric Utility Steam Generating Units Final Report to Congress: Executive Summary; US Environmental Protection Agency, Office of Air Quality Planning and Standards and Office of Research and Development; Research Triangle Park, NC, 1998. "EM for AWMA Environmental Managers", February, 2003.

Tang, E., Liu, H., Sun, L., Zheng, E., & Cheng, G. (2007). Fabrication of zinc oxide/poly(styrene) grafted nanocomposite latex and its dispersion. *European Polymer Journal, 43*(10), 4210-4218.

Tumati, P.R.; DeVito, M.S., "Partitioning Behavior of Mercury During Coal Combustion", Joint ASME/IEEE Power Conference, Kansas City, KS, 1993.

U.S. EPA (2005), "EPA Proposed Options for Significantly Reducing Mercury Emissions from Electric Utilities". *http://www.epa.gov/mercury*.

Westcott, S. L., Oldenburg, S. J., Lee, T. R., & Halas, N. J. (1998). Formation and adsorption of clusters of gold nanoparticles onto functionalized silica nanoparticle surfaces. *Langmuir, 14*(19), 5396-5401.

Wilson, K. S., & Antonucci, J. M. (2006). Interphase structure–property relationships in thermoset dimethacrylate nanocomposites. *Dental Materials, 22*(11), 995-1001.

Wong, E. M., Hoertz, P. G., Liang, C. J., Shi, B. -., Meyer, G. J., & Searson, P. C. (2001). Influence of organic capping ligands on the growth kinetics of ZnO nanoparticles. *Langmuir, 17*(26), 8362-8367.

Young, B.C.; Miller, S.J.; Laudal, D.L., "Carbon Sorption of Trace Mercury Species", Proceedings of the 11th Annual Pittsburg Coal Conference, 1994, pg. 575-580.

APPENDIX A

TECHNICAL PROGRESS REPORT

Contract Title and Number:	Period of Performance:
Continuation in Crosscutting Technology Development at CAST. (DE-FC26-05NT42457)	Starting Date: 7/1/08 Ending Date: 8/31/09

Sub-Recipient Project Title:
Mercury Removal from
Clean Coal Processing Air Stream

Principal Investigators:
Dr. Kumar Ganesan

Contact Address:
Department of Environmental Engineering
Montana Tech of The University of Montana
1300 West Park Street
Butte, Montana 59701

Subcontractor Address:
"No subcontracts issued."

Report Information:
Type: Semi Annual
Number: 1
Period: 9/01/08-12/9/08
Date: 12/12/08
Code: MT 008-R01

Contact Information:
Phone: 406-496-4239
Fax: 406-496-4650
E-Mail: kganesan@mtech.edu

Subcontractor Information:

Mercury Removal from Clean Coal Processing Air Stream

ABSTRACT

This project is developing a new metallic filter that sustains integrity for longer filtration life to remove mercury from clean coal off gas. A new nano-technology based filter material was formulated and prepared in the laboratory. The new filter is also aimed to reduce the over all cost of filtration system.

INTRODUCTION

Mercury is at the top of the EPA's list among the air toxic metals to be controlled. Mercury is a high-priority regulatory concern because of its persistence and bioaccumulation in the environment and its neurological health impacts. The focus of this research is to develop a suitable filter media which will remove mercury cost effectively from the clean coal

processing air stream and also be applicable for removing mercury from coal-fired power plant flue gas.

Background

The US DOE has been intensely involved in developing technologies to reduce mercury emissions from coal fired power plants. One of the ways to reduce mercury emissions at the source is to reduce mercury content in the fuel itself. In coal mercury is bound in forms that could be released during a coal cleaning process. In general, mercury is present in elemental, ionic and particulate bound forms in a coal fired flue gas. The technologies currently under review for commercialization are focused on oxidizing the elemental mercury in a more readily soluble ionic form. These technologies merely convert mercury from one form to another form and redistribute the transformed mercury in water and solid waste streams including in fly ash byproducts. This can potentially cause serious problems in the future due to mercury being released into the environment through byproducts and waste streams containing the transformed mercury. Therefore, long term solution for mercury must be focused on eliminating mercury from entering the environment rather than transforming and transferring it into waste streams and byproducts. The focus of this project is to remove mercury from a pre-combustion thermal treatment clean coal process using metallic filters.

Objective and Approach

The clean coal technologies are aimed to reduce the initial moisture content by 30-40% and increase the Btu values of sub-bituminous coal by 30-40%. There are abundant low-rank coal deposits in the United States and through out the world that will be utilized in energy production for decades to come. A significant co-benefit of clean coal process is that contaminants are eliminated before its combustion. The goal of this research is to develop cost effective filters to control mercury from coal fired flue gas and similar air streams. Montana Tech has successfully developed and tested metallic mercury filters that can remove elemental form of mercury at or above 90 % efficiency. To increase the cost effectiveness of the filters, the following tasks are planned:

- To assemble a special filtering material using nano technology. Metallic nano particles and ceramic substrates are used. This new filter is aimed to reduce the over all cost of the filtration system.
- To analyze the efficiency of the filter by using a mercury generator that produces known concentration of mercury in gas streams.
- A Mercury Tracker instrument will be used to measure the mercury removal efficiency.
- To evaluate, the filter performance, testing will be continued till 50% efficiency is reached.
- To capture the mercury absorbed by the filters by thermal desorption process, a tube furnace will be used.

PROJECT TASKS

Task 1: Preparation of filters:

Commercially available ceramic macro cylinders (BioMax, Biological filter media) were used as substrates. The macro cylinders have high surface area and it is porous. The cylinders are about 2 cm long and 3.5 cm in diameter. These ceramic substrates were pre-washed and cleaned using acetone. The cleaned cylinders were then submerged in an alkanethiol (3-mercaptopropyl trimethoxysilane) (MPTMS) solution of 15% (v/v) in acetone to form a self assembled monolayers. The oxygen chain is expected to attach to the rings leaving the thiol ligand free for adsorption of metallic nano-particles. The cylinders were submerged into MPTMS in acetone solution for three hours at constant room temperature with low stirring. Then the ceramic cylinders were washed twice with acetone to inhibit the MPTMS reaction. The metallic nano-particles were assembled on the ceramic substrates by submerging the thiol functionalized cylinders in a metallic colloidal solution. These metallic nano-particle-filled porous ceramic cylinders have significant amounts of surface area for the mercury to be captured. These cylinders are also expected to have low pressure drop and can be regenerated by thermal desorption. The ceramic substrates were functionalized and deposited with nano metallic particles and then were analyzed by SEM to confirm the deposition. It appears that about 10-13% by mass of substrate consisted of nano-metallic particles deposited on the top 5 um surface of the ceramic cylinders. The result from SEM analysis is given in the Appendix.

SUMMARY

In summary during this reporting period, this project focused on developing a new cost effective filter to capture mercury from clean coal process streams using nano technology to functionalize ceramic substrates.

FUTURE WORK

Metallic filters using nano technology will be prepared and tested in the laboratory to evaluate their performance. Once the performance parameters are satisfied the filters will be made in sufficient numbers for use in the mercury filtration system. The main performance parameters considered are the base metals or materials characteristics, the physical characteristics, filter stability, maximum surface area per volume of filter, and air flow characteristics.

Next task in this project will focus on synthetic gas generation with known mercury concentration to test the filter efficiency in removing mercury. After that the filters will be tested exposing to six different mercury concentrations.

REFERENCES

Ah, C. S., Han, H. S., Kim, K., & Jang, D. (2000). Phototransformation of alkanethiol-derivatized noble metal nanoparticles. *Pure and Applied Chemistry, 72*, 91.

EPRI. (2003). *Impacts of NO, controls on mercury controllability* No. 1004000.
Fleming, M. S., & Walt, D. R. (2001). Stability and exchange studies of alkanethiol monolayers on gold-nanoparticle-coated silica microspheres. *Langmuir, 17*(16), 4836-4843.

Guijarro, M. I., Mendioroz, S., & Munoz, V. (1998). Effect of morphology of sulfurized materials in the retention of mercury from gas streams. *Industrial & Engineering Chemistry Research, 37*(3), 1088-1094.

Lee, J.,Shick., & Park, J.,Koo. (2001). Preparation of porous ceramic pellet by pseudo double-emulsion method from 4-phase foamed slurry. *Chemistry and Materials Science, 20*(3), 205-207.

Pavlish, J. H., Sondreal, E. A., Mann, M. D., Olson, E. S., Galbreath, K. C., Laudal, D. L., et al. (2003). Status review of mercury control options for coal-fired power plants. *Fuel Processing Technology, 82*(2-3), 89-165.

Westcott, S. L., Oldenburg, S. J., Lee, T. R., & Halas, N. J. (1998). Formation and adsorption of clusters of gold nanoparticles onto functionalized silica nanoparticle surfaces. *Langmuir, 14*(19), 5396-5401.

PUBLICATIONS/PRESENTATIONS

None

APPENDICES

The initial results of the nano metallic particle deposited on the functionalized ceramic substrate from SEM are given in the Appendix.

Appendix

Functionalization experiments on porous substrates with nanoparticles: Results from SEM: secondary (SE) and back-scattered electron (BSE) mode

Substrate

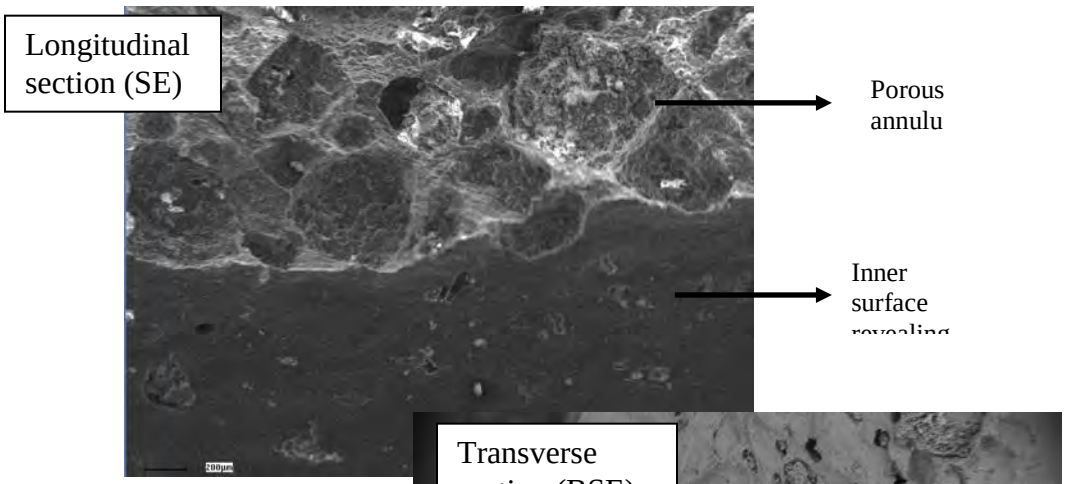

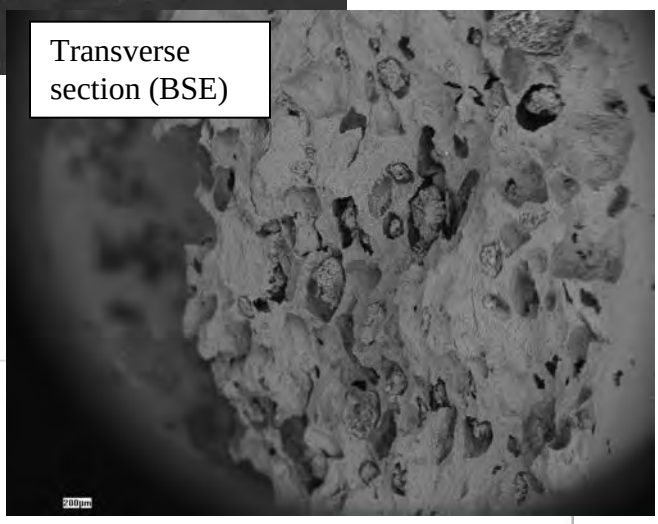

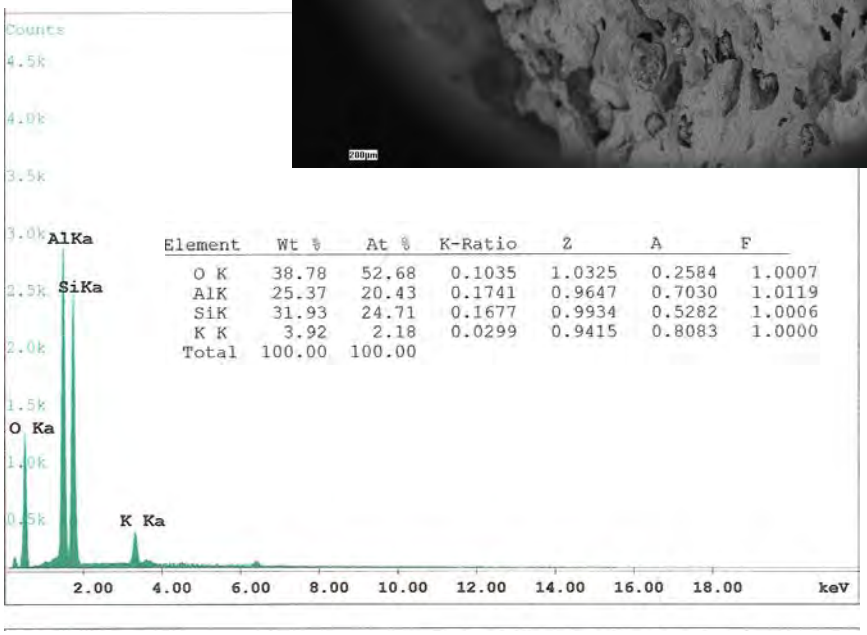

Element	Wt %	At %	K-Ratio	Z	A	F
O K	38.78	52.68	0.1035	1.0325	0.2584	1.0007
AlK	25.37	20.43	0.1741	0.9647	0.7030	1.0119
SiK	31.93	24.71	0.1677	0.9934	0.5282	1.0006
K K	3.92	2.18	0.0299	0.9415	0.8083	1.0000
Total	100.00	100.00				

After functionalization (BSE mode) – bright regions indicate locations where nano metallic particles have been deposited (substrates were functionalized with alkane-thiols)

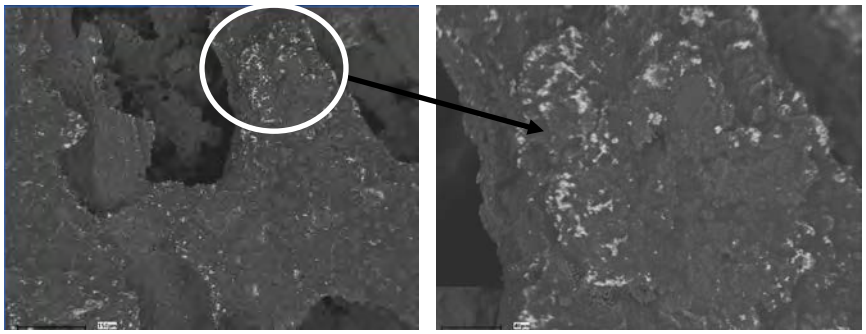

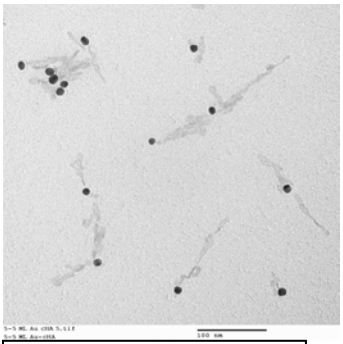

TEM of Metallic NPs ~ 10 nm and

EDX analysis revealed that the substrate contained about 13 wt % on the surface. Given the size of the nano particles this would be approximate about 13 % of the surface covered with the nano particles.

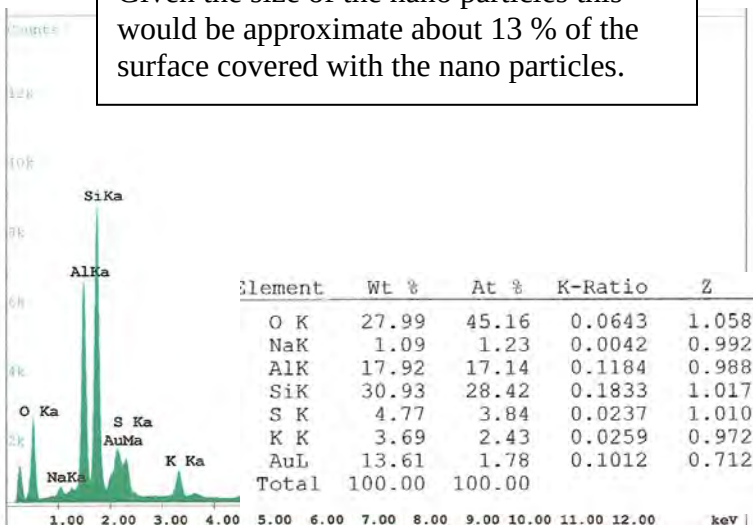

Element	Wt %	At %	K-Ratio	Z	A	F
O K	27.99	45.16	0.0643	1.0582	0.2170	1.0005
NaK	1.09	1.23	0.0042	0.9922	0.3837	1.0062
AlK	17.92	17.14	0.1184	0.9882	0.6605	1.0124
SiK	30.93	28.42	0.1833	1.0175	0.5816	1.0016
S K	4.77	3.84	0.0237	1.0102	0.4918	1.0011
K K	3.69	2.43	0.0259	0.9722	0.7224	1.0000
AuL	13.61	1.78	0.1012	0.7129	1.0429	1.0000
Total	100.00	100.00				

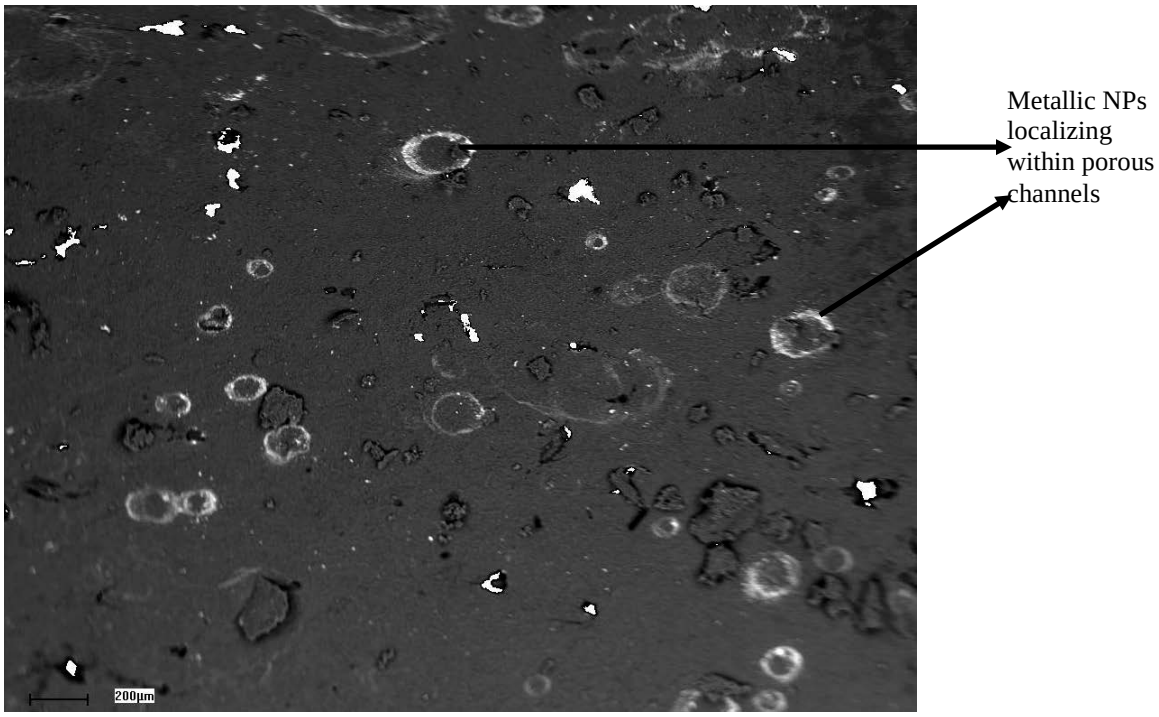

Functionalization (BSE mode) the inner surface of the substrate revealed nano metallic particle deposited in the porous channels

APPENDIX B

TECHNICAL PROGRESS REPORT

Contract Title and Number:	Period of Performance:
Continuation in Crosscutting Technology Development at CAST. (DE-FC26-05NT42457)	Starting Date: 8/1/08 Ending Date: 9/30/09

Sub-Recipient Project Title:	Report Information:
Mercury Removal from Clean Coal Processing Air Stream	Type: Annual Number: 1 Period: 8/01/08-9/30/09
Principal Investigators:	Date: 10/30/09
Dr. Kumar Ganesan	Code: MT 008-R01
Contact Address:	Contact Information:
Department of Environmental Engineering Montana Tech of The University of Montana 1300 West Park Street Butte, Montana 59701	Phone: 406-496-4239 Fax: 406-496-4650 E-Mail: kganesan@mtech.edu
Subcontractor Address:	Subcontractor Information:
"No subcontracts issued."	

Mercury Removal from Clean Coal Processing Air Stream

ABSTRACT

During this reporting period, lab experiments focused on developing commercially available BioMax ceramic rings as filter material to use in the mercury removal system. Nanotechnology concepts were introduced to make metallic colloidal solution and the BioMax ceramic substrates were doped with metallic nano particles (MNP) to achieve highly efficient mercury filters. The use of metallic nano-particles and the use of porous ceramic substrate as base filtering material, combines several advantages such as: 1. use of much smaller amounts of the special metal, 2. the substrate will have low flow resistance (low pressure drop), 3. the substrate has high porosity that will yield tremendous contact surface area, and 4. can be thermally regenerated to recover mercury. The performance of the MNP filters is evaluated based on the mercury removal efficiency and the length of time it takes for mercury saturation. The second sequence of tests are performed to evaluate its thermal desorption potential, to assess reusability characters of the MNP filters.

INTRODUCTION

Mercury is a high-priority regulatory concern because of its persistence and bioaccumulation in the environment and its neurological health impacts. The focus of this research is to

develop a suitable filter media which will remove mercury cost effectively from the clean coal processing air stream.

Background: Montana Tech has been intensely involved in developing technologies to reduce mercury emissions from coal fired flue gas streams. The focus of this project is to remove mercury from a pre-combustion thermal treatment clean coal process using metallic filters and finding long term solution to eliminate mercury from entering the environment. This project is developing a new metallic filter that sustains integrity for longer filtration life to remove mercury from clean coal off gas. A new nano-technology based filter material was formulated and prepared in the laboratory.

Objective and Approach: The goal of this research is to develop cost effective filters to control mercury from coal fired flue gas. To increase the cost effectiveness of the filters, the following tasks are performed: Metallic nano particle (MNP) filters were assembled using ceramic substrates aiming to reduce the over all cost of the filtration system; analyzed the efficiency of the filter by using a mercury generator and a Mercury Tracker. The filter performance was evaluated by testing the time it takes 50% efficiency. A tube furnace was used in the thermal desorption process to release the mercury absorbed by the filters.

PROJECT TASKS

Task 1: Preparation of filters: Commercially available ceramic BioMax cylinders that are about 2 cm long and 1.5 cm in diameter were used as substrates. Pre-washed and cleaned substrates were submerged in an alkanethiol (3-mercaptopropyl trimethoxysilane) (MPTMS) solution of 15% (v/v) in acetone for three hours at constant room temperature with low stirring to form a self assembled monolayers. The oxygen chain is expected to attach to the rings leaving the thiol ligand free for adsorption of metallic nano-particles. After washing twice with acetone to inhibit the MPTMS reaction, the metallic nano-particles were assembled on the ceramic substrates by submerging the thiol functionalized cylinders in a metallic colloidal solution. Filters were prepared using double the amount of thiol. Additionally two more varieties of filters were prepared by directly soaking it in the MNP solution without functionalizing with thiol. Single coat filter was soaked for a day and removed from the solution to air dry. Then two coat filter was soaked two times in the same solution for two days and dried. These filters were made in sufficient quantity to test for mercury removal efficiency. While preparing the BioMax filter material one trial focused on directly dripping the MNP solution (instead of soaking) on the ceramic substrate. Observation indicated that the solution seems to coat well and get absorbed by dripping than by soaking. Sufficient quantity was made and tested for mercury removal efficiency. The results are promising.

Task 2: Synthetic gas generation with known mercury concentration: At Montana Tech's mercury research laboratory VICI Metronics Dynacalibrator is used as mercury generator. A passivated glass-coated permeation chamber with temperature control, houses the mercury permeation device, with inert carrier gas sweeping the mercury vapor from the chamber. The desired mercury concentration is established by simply varying the carrier flow and adjusting the temperature.

Task# 3: Laboratory testing of the filters: To perform the bench scale testing, each nano metallic filter set was placed in a stainless steel tube, and mercury-contaminated air passed

through the filter at a flow rate of 2.5 L/min. The filter's inlet and outlet mercury concentrations were measured with a portable mercury analyzer, Mercury Tracker throughout the test period and used to calculate the mercury removal efficiency of the filter. Initial mercury removal efficiency tests were conducted on these three (MNP double thiol, MNP with single coat and MNP with double coat) filters. Test results are given in figure 1.

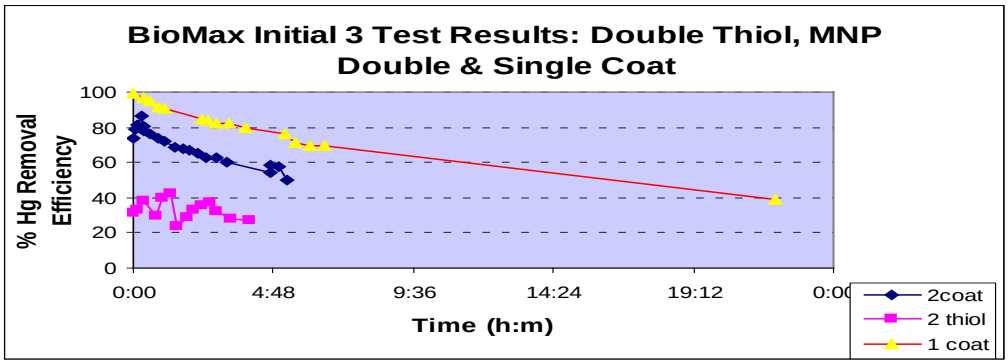

Figure: 1.BioMax filters with MNP double thiol, double coat MNP and single coat MNP test results

These results indicated that MNP filters can remove mercury from gas stream. Of all the three filters the single coat MNP filters showed longer efficiency time than the other two. The single coat MNP filter was selected and it went through a thermal desorption process to release the captured mercury. For this experiment a tube furnace was used, the flow rate of the clean air was kept at 5L/min, and the temperature was set at 500º C. Again after the first thermal desorption, this spent (single coat MNP) filter was tested for mercury removal efficiency following the same procedures. When this filter was saturated with mercury, it went through another cycle of thermal desorption for the second time. These 2 thermal desorption test results are given in figure 2.

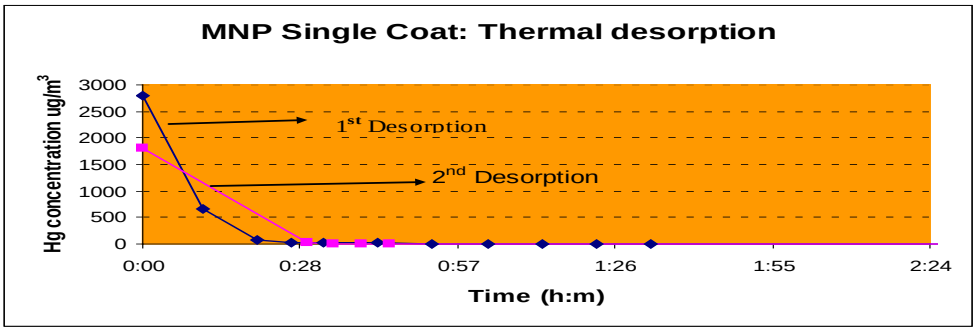

Figure: 2.Two cycles of thermal desorption test results of the single coat MNP filter.
The results show that at 500º C the thermal desorption process occur immediately and within the initial 15minutes most of the mercury was released and in less than two hours the entire mercury vapor was released (Figure: 2).

Once again for the third time the filter was tested for mercury removal efficiency. The three mercury removal efficiency test results are given in figure 3.

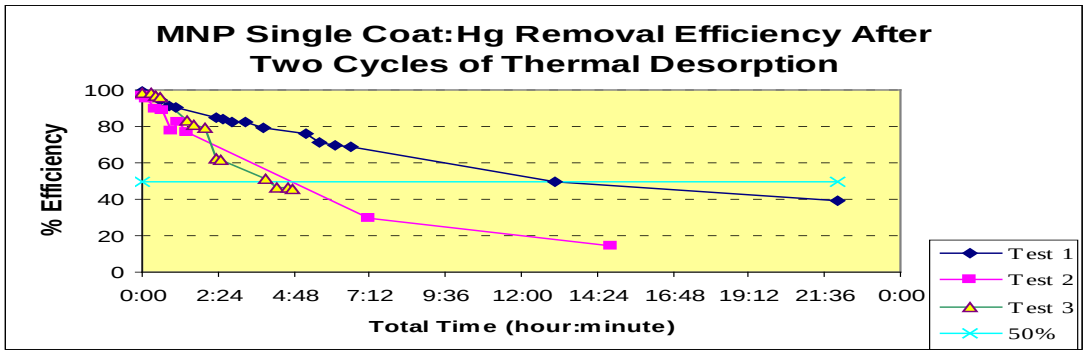

Figure 3: MNP single coat filter's mercury removal efficiency test results. Test 1: is the initial mercury removal efficiency test; Test 2: after first thermal desorption; Test 3: after second thermal desorption.

Thus the MNP filters have high potential to be used in the mercury control system. After thermal desorption, there is a decrease in the time the mercury removal efficiency of the MNP filters to reach 50% efficiency, but it shows reusability potential of the filter.

A batch of MNP filters using direct drip method was tested and the results are in figure 4.

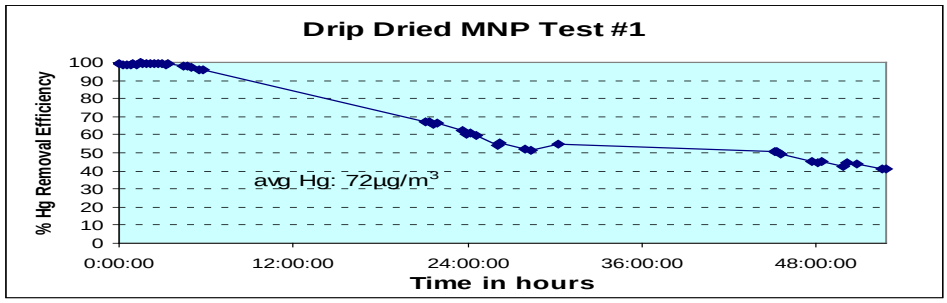

Figure 4: Directly dripped MNP test results.

This is the best performed filter so far and the above 90% efficiency lasted more than 8 hours and the 50% efficiency lasted about 40 hours. The spent filter was thermally desorbed as before. Figure 5 gives the results.

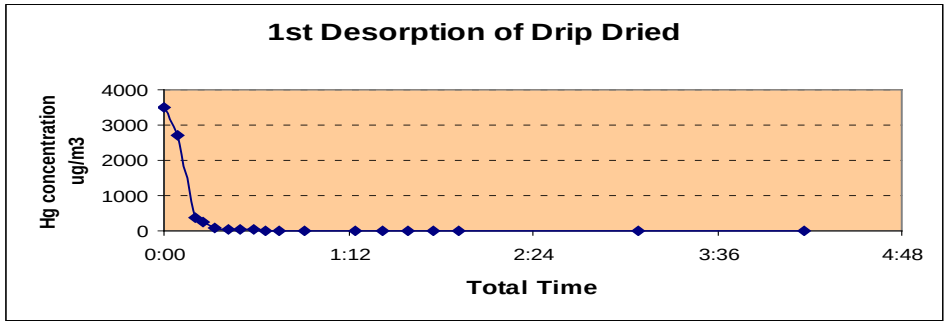

Figure: 5. First thermal desorption of the directly dripped filters

In less than 20 minutes almost all the mercury was removed from the filter. Then the filter was tested again for mercury removal efficiency just like the previous testing. Test results are given in figure 6.

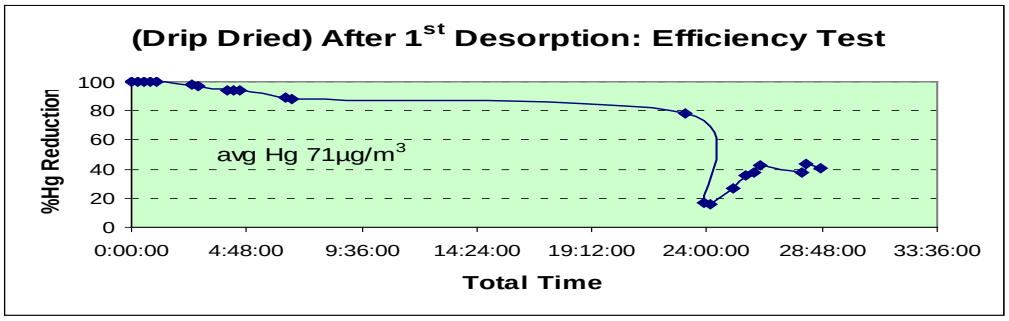

Figure: 6. Mercury Removal Efficiency Test Results After First Thermal Desorption

Even after the thermal desorption the 90% mercury removal efficiency lasted more than 5 hours and the 50% efficiency lasted more than 24 hours. Thus, it is promising that it is possible to improve the efficiency of the filter by simple techniques like drip method.

SUMMARY

The initial laboratory testing shows that the MNP filters have great potential to remove mercury from the coal-fired flue gas. Thermal desorption does cause a slight decrease in the time period the filter's efficiency above 50%, but the reusability of filter back into the mercury removal system is promising.

FUTURE WORK

Future work will focus on: assembling filters with maximum MNP; to quantify the deposition; to examine the surface characteristics of the MNP filters before and after thermal desorption to determine what changes occur on the MNP filter's surface; and to generate mercury concentration between 5µg/m^3 and 60µg/m^3; to further evaluate the performance of the filters and to assemble large scale filtration system to test in the lab as well as in the field.

REFERENCES

Ah, C. S., Han, H. S., Kim, K., & Jang, D. (2000). Phototransformation of alkanethiol-derivatized noble metal nanoparticles. *Pure and Applied Chemistry, 72*, 91.

EPRI. (2003). *Impacts of NO, controls on mercury controllability* No. 1004000.

Fleming, M. S., & Walt, D. R. (2001). Stability and exchange studies of alkanethiol monolayers on gold-nanoparticle-coated silica microspheres. *Langmuir, 17*(16), 4836-4843.

Guijarro, M. I., Mendioroz, S., & Munoz, V. (1998). Effect of morphology of sulfurized materials in the retention of mercury from gas streams. *Industrial & Engineering Chemistry Research, 37*(3), 1088-1094.

Lee, J.,Shick., & Park, J.,Koo. (2001). Preparation of porous ceramic pellet by pseudo double-emulsion method from 4-phase foamed slurry. *Chemistry and Materials Science, 20*(3), 205-207.

Pavlish, J. H., Sondreal, E. A., Mann, M. D., Olson, E. S., Galbreath, K. C., Laudal, D. L., et al. (2003). Status review of mercury control options for coal-fired power plants. *Fuel Processing Technology, 82*(2-3), 89-165.

Westcott, S. L., Oldenburg, S. J., Lee, T. R., & Halas, N. J. (1998). Formation and adsorption of clusters of gold nanoparticles onto functionalized silica nanoparticle surfaces. *Langmuir, 14*(19), 5396-5401.

APPENDIX 24 - Determination of Factors Affecting the Separation of Potentially Hazardous Trace Elements and their Behavior in Coal Tailings Impoundments (KY005)

TECHNICAL REPORT

Contract Title and Number:	Period of Performance:
Continuation in Crosscutting Technology Development at CAST. (DE-FC26-05NT42457)	Starting Date: 10/01/2005 Ending Date: 09/30/2008

Sub-Recipient Project Title:
Determination of Factors Affecting the Separation of Potentially Hazardous Trace Elements and their Behavior in Coal Tailings Impoundments

Principal Investigators:
Huggins, Shah, Huffman

Contact Address:
University of Kentucky
533 S. Limestone Street
Lexington KY 40506

Contact Information:
Phone: (859) 257-4045
Fax: (859) 257-7215
E-Mail: fhuggins@engr.uky.edu

Subcontractor Address:
No subcontracts issued.

Subcontractor Information:
Phone:
Fax:
E-Mail:

Report Information:
Type: Final
Number: Final
Period: 10/1/06-9/30/08
Date: 9/30/07
Code: KY005-Final

ABSTRACT

Conventional coal cleaning methods effectively reduce the concentrations of many trace elements in cleaned coals that are burnt in power plants. However, as a result, trace element concentrations in tailings from coal washing operations are enhanced and their behavior in tailings disposal may then become an environmental issue. Data on elemental concentrations alone do not provide sufficient insight to understand completely the behavior of trace elements during coal cleaning or in tailings disposal scenarios. In this project, modes of occurrence of trace elements in an Illinois #6 coal, the resulting clean coal and tailings fractions, and leached tailings fractions were determined by XAFS spectroscopy to complement data obtained from conventional elemental (XRF, ICP-MS, etc.) and mineralogical (XRD) analyses. Two long-term leaching tests (~150 days) were investigated because the 18-hour TCLP test was negative for all elements of interest. In one method, the tailings were stored continuously under water, while in the second (a variant of ASTM D-5744) the tailings were cycled through dry and wet (submerged) periods on a weekly basis. Most elements of interest were found to be associated with either pyrite (As, Se, Hg) or with illite (Cr, V, Ni?), which largely dictated the behavior of these elements in the physical separation processes and in the leaching tests. Only Ge and to a lesser extent Hg and Se were noted to have significant affinity with the coal macerals and did not separate efficiently. The rapid mobilization of Na and alkaline earth elements (Mg, Ca, Sr) was important in effectively buffering the pH during the alteration of pyrite and preventing or delaying the mobilization of arsenic. The formation of insoluble natrojarosite during the alteration of pyrite was also instrumental in sequestering arsenic.

TABLE OF CONTENTS

List of Figures

List of Tables

EXECUTIVE SUMMARY

One of the perceived problems associated with contamination of local streams and rivers by waters from breached or failed impoundment dams is the possible introduction of potentially hazardous trace elements into surface waters and groundwater that might be used for public water supplies. Such elements are introduced into impoundment waters as a result of the aqueous leaching and alteration of pyrite and other minerals in coal tailings that can mobilize trace elements associated with them. How and in what quantity such elements are released depends on a number of factors, including not only how much of the element is present in the tailings but also how it occurs in the tailings. Whereas there have been many studies of the concentrations of trace elements in coals and coal tailings, there have been virtually no investigations of the modes of occurrence of trace elements in coal tailings and their significance in providing answers to questions relating to the mobility of trace elements in coal impoundments and similar disposal situations. In this project, we attempt to fill this knowledge gap by first determining the modes of occurrence of various key elements (S, Fe, Cr, V, Mn, Zn, As, Se) in clean coal and tailings fractions obtained from an Illinois #6 coal by gravity separation methods employed at a commercial coal-cleaning plant in Southern Illinois. With this information on elements in the coal fractions, we then examine the leaching of arsenic and other trace metals from the tailings fractions in experiments that simulate disposal of tailings under water in coal impoundments. Such experiments included the 18-hour Toxicity Characteristic Leaching Procedure (TCLP), and two much longer term (up to 150 days) experiments. One of these tests, termed the baseline or static test, consisted of passively storing the tailings under water for the full length of the test; the other test, termed the cyclic test, was based on ASTM Standard Method D-5744 and was a much more aggressive test. This test was designed to accelerate the oxidation of pyrite and the mobilization of associated trace elements. It consisted of weekly cycles of submerging the tailings under water for 1 day, followed by 3 days' exposure to first dry air and then 3 days' exposure to humid air. These cycles were repeated for 22 weeks and the leachate obtained after each weekly submersion was collected for analysis.

Detailed information on trace elements in the Illinois #6 coal and related fractions, as well as in the residues from the leaching tests, was obtained from (i) conventional coal analyses, (ii) multi-element analysis methods such as X-ray fluorescence (XRF) for major elements and ICP-MS for trace elements, (iii) X-ray diffraction to quantify the mineralogy of the coal fractions, and (iv) Mössbauer and X-ray absorption fine structure (XAFS) spectroscopic methods that provided direct information on elemental occurrences. A synthesis of the results from these analyses led to the following conclusions regarding the occurrence of key elements in this Illinois #6 coal:

- Arsenic: 100% associated with pyrite in all fractions; increasing oxidation of arsenical pyrite to arsenate noted over time during sample storage.
- Chromium: Largely present in association with illite with remainder in organic association; >98% Cr in tailings fractions is associated with illite
- Germanium: Highly organically associated
- Iron >90% associated with pyrite, ~5% associated with illite and ~3% with jarosite; slow conversion of pyritic iron to sulfate over time
- Manganese: Complex – appears to be at least 3 significant distinct species

- Mercury: Some apparent association with pyrite; some with coal macerals
- Nickel: Similar to Cr and V?
- Selenium: Associated with pyrite, but some organic Se as well
- Vanadium: Similar to chromium, but with more of the element in organic association; >95% V in tailings fractions is associated with illite
- Zinc: Complex – three distinct major species: sphalerite (ZnS); Zn assoc. w/ illite; and $Zn_3(PO_4)_2.xH_2O$ (tentative).

Armed with this information on elemental modes of occurrence in the Illinois #6 coal fractions, similar examination was undertaken of the leachates and residues obtained in the experiments designed to simulate leaching during tailings impoundments. The 18-hour TCLP test gave negative results for all RCRA elements indicating that these tailings were not an environmental hazard. Consequently, this test was not informative regarding trace element mobilities. In the longer term baseline and cyclic tests, it was observed that the pH of the leachates remained close to neutral until the very end of the test when more acidic values were encountered. The elements that were most mobile in these tests were sodium and the alkaline earth elements, Mg, Ca, and Sr. Sulfate also showed significant mobility and exhibited a marked correlation ($r^2 > 0.99$, 16 observations) with conductivity. However, neither iron nor arsenic showed any mobility although Mossbauer spectroscopy did indicate that a minor amount of iron as pyrite was oxidized to iron as jarosite and arsenic XAFS indicated that a considerable fraction of the arsenic was oxidized to arsenate (AsO_4^{3-}) over the course of the leaching treatments. Elements primarily associated with illite, such as K, Cr and V, exhibited no significant mobility. Trace elements that did exhibit some mobility during these tests included Mn, Co, Ni, and, to a lesser extent, Zn.

To account for these observations, it is hypothesized that the rapid dissolution of Na, followed by the slower dissolution of alkaline earth elements effectively buffers the pH of the leachates thereby minimizing the formation of acid [H^+] that would accelerate the dissolution of pyrite and the release of arsenic and other associated elements. In addition, the presence of sodium at near-neutral pH values also promotes the formation of insoluble natrojarosite ($Na(Fe)_3(SO_4)_2(OH)_6$) from any alteration of the pyrite that does occur. This sulfate mineral can also act as a sink for the arsenate anions as a result of their substitution for the sulfate anions thereby preventing the mobilization of As as arsenate. The following chemical equation effectively accounts for all of these observations:

$$3FeS_2 + 3H_2O + 13.5O_2 + [Na^+]_{sol'n} \rightarrow NaFe_3(SO_4)_2(OH)_6 + 4[SO_4^{2-}]_{sol'n}$$

Not only does formation of insoluble jarosite by this reaction prevent the release of arsenic, but it also does not result in the formation of significant acid [H^+] formation, while allowing for release of some [SO_4^{2-}] anions, consistent with observation. It is clear that in these coal tailings, sodium plays an important role in preventing or delaying the dissolution of pyrite and the release of associated trace elements. These findings may have significant application to preventing and minimizing acid formation associated with disposal of coal tailings.

INTRODUCTION

The major goal of separation technology is to increase the yield of valuable product by separating it from undesirable waste components. In the coal separation industry that serves the electrical power generation industry, the specific goal is to separate the incombustible mineral matter from the combustible macerals in order to develop a clean-coal product that has a higher calorific value and generates less combustion wastes and emissions. Such coal cleaning is especially valuable for coals from the bituminous coal regions of the eastern United States, since the mineralogy of the coals from these regions is generally dominated by quartz, clays and pyrite, which are minerals in coal that can be separated efficiently by conventional and/or advanced coal-cleaning methods. Such cleaning also removes certain trace elements designated as hazardous air pollutants (HAPs) by the 1990 Clean Air Act Amendments (CAAA). However, such HAP elements are then often concentrated in coal tailings and may become of concern to the 1976 Resource Conservation and Recovery Act (RCRA) during disposal of the mineral-rich tailings. The partitioning of a trace element between clean product and tailings is determined by the mineral phase in which the element occurs, its valence and magnetic states, and association with major inorganic or carbonaceous components of the coal. These mode-of-occurrence factors have only rarely been determined with respect to trace elements in coal cleaning operations and, as far as we can tell, never with respect to their behavior in coal tailings disposal options.

The first objective of this investigation was to determine why some hazardous air pollutant (HAP) elements separate well and others poorly during various coal cleaning processes. A second objective was then to investigate and interpret the behavior of the HAP elements in laboratory simulations of the disposal of tailings in ponds. To address these issues, basic information regarding the occurrence of trace elements and minerals in coal and their behavior in coal cleaning processes and tailings disposal scenarios has been obtained using a variety of techniques that enable us to determine the mineralogy of the coal and mode of occurrence of specific elements. Such techniques, supplemented by more conventional analysis methods, included X-ray diffraction (XRD) to determine the mineralogy and X-ray absorption fine structure (XAFS) spectroscopy to obtain direct data on the speciation of trace elements of interest in both clean and tailings fractions and in residues after leaching tests on the tailings fractions.

EXPERIMENTAL

Collection and preparation of coal and tailings samples

Approximately 800 lbs each of raw coal, the cleaned coal, and two tailings fractions were collected from a commercial preparation plant in Southern Illinois. Samples were collected incrementally over 30-minute intervals. The preparation plant treats feed from a single mine on the Illinois #6 seam at a capacity of 1,000 tph. The overall separation scheme is shown in Figure 1. Reject from the plant is normally sent to a tailings impoundment.

The raw coal to the plant was screened after initial crushing in a rotary breaker. The coarse fraction of the raw coal screen, 2½" × 1 mm, was fed to heavy media (HM) cyclones. The clean coal overflow from the HM cyclone separates from mineral-rich tailings due to the differences in density between coal, the mineral matter, and the magnetite heavy media. The minus 1 mm fine fraction of the raw coal screen was sent to classifying cyclones which in turn fed a spiral circuit. The spiral circuit also separates clean coal and mineral matter based on density differences. The combined clean product of the coarse and fine cleaning circuits has a size range of 2½" × 0.

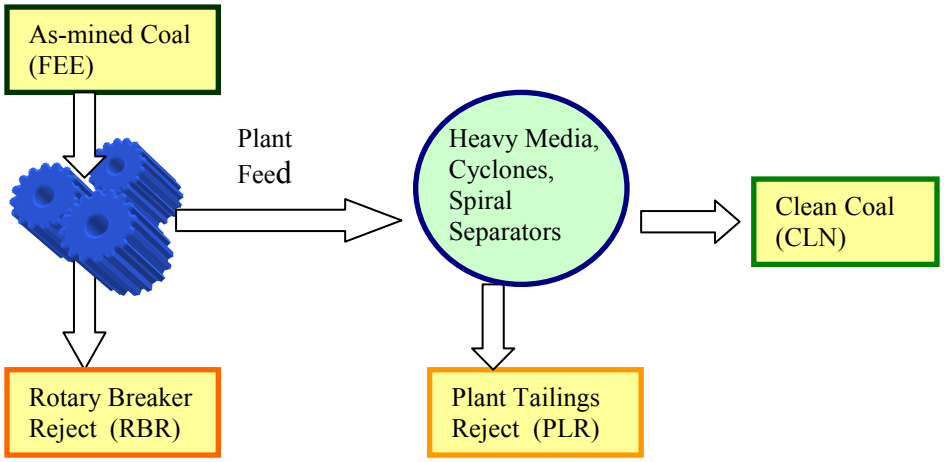

FIGURE 1: Diagram showing coal fractions generated at the preparation plant.

Samples of the raw feed, rotary breaker (RB) reject, the plant reject, and the clean coal were dried, crushed to 100% passing ¼" mesh, and riffle split to obtain representative samples. Final samples for the analyses were further crushed to 100 mesh top size and split into various fractions, according to the mass needed for each type of analysis.

Analysis methods

The following conventional analyses were carried out on each major coal fraction:

- Ultimate, proximate, forms of sulfur, heating value;
- X-ray fluorescence (XRF) of major elements in 500^{o}C ash from each fraction;
- Trace element analyses by ICP-MS and individual analyses for Hg by mercury analyzer;

- Mineral matter by X-ray diffraction (XRD) using Rietveld method.

Mode of occurrence analyses consisted of:

- Fe speciation and oxidation state determinations by Mössbauer spectroscopy;
- Speciation of sulfur and key trace elements by X-ray absorption fine structure (XAFS) spectroscopy.

Leaching experiments

To investigate the behavior and mobility of elements in simulated tailings disposal scenarios, the two tailings fractions have been subjected to three different leaching experiments. The first method attempted was the Toxicity Characteristic Leaching Procedure (TCLP). Samples were sent to a commercial laboratory for testing. All RCRA elements in both tailings fractions were found to be negligibly leached by the 18-hour TCLP test. Hence, two tests of longer duration were devised and constructed.

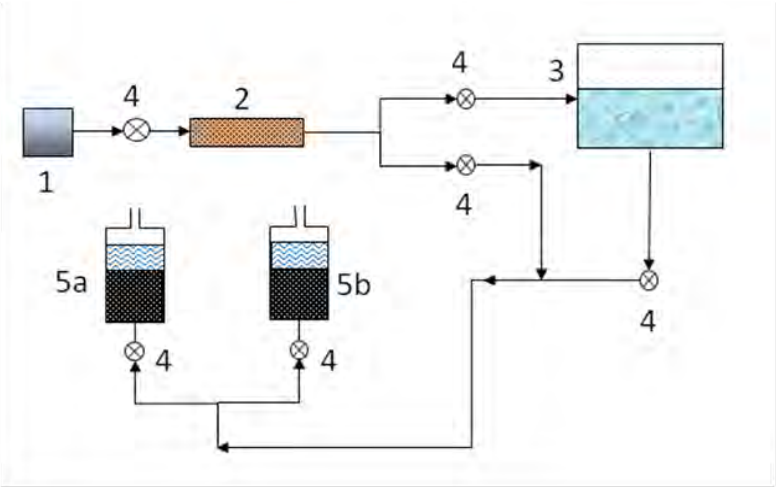

- 1. Compressed Air 2. Desiccant 3. Humidifier 4. Valve 5. Leach Vessel (a) RBR (b) PLR
- Cyclic leaching consists of 1 day water submersion, 3 days' dry air and 3 days' moist air, repeated weekly

FIGURE 2: Schematic diagram for the cyclic leaching test of Illinois #6 coal tailings fractions constructed for this project. The arrows indicate air flow paths.

One method, termed the baseline static test, consisted simply of storing 200 g of each tailings fraction under 200 ml of de-ionized water and using pH to indicate any significant leaching activity. The second method, termed the cyclic test and shown schematically in Figure 2, was based on ASTM Method D-5744 (ASTM, 1996). This test operated on a 7-day cycle in which 200 g of tailings were soaked in 200 ml of de-ionized water for one day, exposed to dry air for three days and then moist air for three days. For each cycle, the leachate was collected and a new cycle was started with fresh de-ionized water. The leachates were combined, as needed, to generate a multi-week sample, which was then sent for a battery of analyses consisting of measurements of pH, Eh, and sulfate, and ICP-MS for elemental analysis. Analyses were conducted after 0, 1, 3, 6, 7, 12, 15, 20 and 22 weeks. Small

amounts of the solids were sampled after 7 and 22 weeks for Mössbauer and XAFS spectroscopy determinations. Both the static and cyclic tests were on-going for more than 150 days.

RESULTS AND DISCUSSION

Conventional coal analyses

Data on the coal feed to the rotary breaker (FEE), the clean coal (CLN), and the tailings fractions generated by the rotary breaker (RBR) and gravity separation at the plant (PLR) are summarized in Table 1. Proximate analyses of the coal fractions are also shown in Table 1.

TABLE 1: Heating Value (HV) and Proximate Analyses for Four Fractions of Illinois #6 Coal

Stream	*Wt% Stream**	*HV Btu/lb*	*Moisture wt%*	*Volatile Matter*	*Ash wt%*	*Fixed Carbon***	*VM daf basis*
RB Feed (FEE)	100	10,278	4.91	29.71	27.11	38.27	43.7
RB Reject (RBR)	1.5	1,869	5.70	10.83	76.83	6.65	--
Clean Coal (CLN)	65	13,132	4.53	36.80	9.14	49.54	42.6
Plant Reject (PLR)	33.5	2,644	3.01	13.90	73.55	9.54	--

*based on plant historical data; ** by difference; daf – dry, ash-free

Ultimate analyses and forms of sulphur analyses, including estimates of pyritic sulphur from Mössbauer spectroscopy, are summarized in Tables 2 and 3, respectively.

TABLE 2: Ultimate Analyses of Different Streams at the Preparation Plant

Stream	*%Ash*	*%Moisture*	*%C*	*%H*	*%N*	*%O*	*%S*
RB Feed (FEE)	27.66	5.15	52.52	4.10	0.98	10.65	4.09
RB Reject (RBR)	76.47	5.53	10.78	1.58	0.25	7.38	3.54
Clean Coal (CLN)	9.16	4.64	67.54	5.14	1.25	13.61	3.30
Plant Reject (PLR)	73.16	3.21	13.85	1.50	0.34	6.01	5.14

TABLE 3: Forms of Sulfur Analyses (wt %) of Different Streams at the Preparation Plant

Stream	*Pyritic*	*Sulfate*	*Organic*	*Pyr Mossb.**
RB Feed (FEE)	1.98	0.11	2.00	2.20
RB Reject (RBR)	2.88	0.10	0.56	3.59
Clean Coal (CLN)	0.86	0.11	2.33	1.05
Plant Reject (PLR)	4.67	0.19	0.28	4.46

*estimated from Mössbauer spectroscopy

Partitioning of elements among coal fractions

Major elements and trace elements were determined in the different fractions using XRF on ash prepared at 500^{o}C (Table 4) and ICP-MS on digested coal (Table 5), respectively. Hg was determined independently by CVAAS. The mineralogy of the different fractions was

determined by X-ray diffraction using Rietveld analysis, supplemented by data from Mössbauer and chemical analyses (Table 6).

TABLE 4: Major Element Analyses of 500^{O}C Ash Prepared from Illinois #6 Coal and Derived Fractions (wt%)

*Oxide**	*CLN*	*FEE*	*RBR*	*PLR*
SiO_2	52.62	56.49	63.17	57.81
TiO_2	1.02	0.85	0.85	0.83
Al_2O_3	20.68	18.02	16.89	17.58
Fe_2O_3	15.52	13.55	8.20	12.58
MgO	0.97	1.34	1.60	1.48
CaO	3.94	3.71	2.86	3.27
SrO	0.02	0.02	0.02	0.02
BaO	0.03	0.04	0.04	0.05
Na_2O	1.14	0.97	1.07	0.89
K_2O	2.17	2.57	2.71	2.87
SO_3	1.60	1.81	1.97	1.84
P_2O_5	0.15	0.50	0.48	0.63
Total	99.86	99.87	99.86	99.85

*by X-ray fluorescence (XRF)

TABLE 5: Trace Element Analyses of Illinois #6 Coal and Derived Fractions (ppm)

*Element**	*CLN*	*FEE*	*RBR*	*PLR*
^{9}Be	1	1	2	1.8
^{31}P	<lod	445	1900	1410
^{45}Sc	<lod	5.5	12.5	12
^{47}Ti	552	1510	3900	3670
^{51}V	29	55	116	154
^{52}Cr	23	68	161	230
^{55}Mn	24	81	180	170
^{59}Co	2.5	5.5	16	12
^{60}Ni	10	31	83	98
^{63}Cu	7	20	44	54
^{64}Zn, ^{66}Zn	20	52	165	300
^{72}Ge	2.6	2.2	1.8	0.7
^{75}As	1.2	4.2	8.7	11
^{85}Rb	11	11	30	22
^{88}Sr	21	51	113	73
^{118}Sn	0.55	1.3	2.8	2.7
^{121}Sb	0.6	1.2	1.75	2.3
^{133}Cs	1	2	3.5	3.4
^{137}Ba, ^{138}Ba	31	96	180	200
Hg	0.06	0.08	0.09	0.18
^{208}Pb	4	10	43	31

*by ICP-MS on digested samples, except Hg; <lod – below level of detection

TABLE 6: Major Mineral Data (wt% of coal) for Illinois Coal and Derived Fractions

Mineral	*Method*	*CLN*	*FEE*	*RBR*	*PLR*
Quartz	XRD	2.7	9.2	31.9	22.4
Kaolinite	XRD	1.3	3.7	9.1	5.3
Illite	XRD	2.6	9.7	26.5	35.0
Pyrite	Mössbauer	2.0	4.1	6.7	8.4
Calcite	Ca in coal	0.6	1.1	2.4	2.1
Organic	100 – wt% Ash	90.8	72.3	23.5	26.8

The partitioning of various elements between the clean coal and tailings fractions is summarized in Figure 3. This plot shows the concentrations of the elements of interest in different gravity-separated fractions as a bar: the ends of the bars indicate the concentration of the element in the CLN and PLR fractions, while the concentration of the FEE coal is the intermediate value. The relative length of the bar is therefore a measure of the efficiency of the separation for that element. For this particular sample of the Illinois #6 coal, most elements are separated with about the same efficiency as the overall ash, although some elements, notably Zn, are more efficiently segregated. The major exceptions are Hg and Ge; the relatively short length of the bar for Hg indicates that it has mixed inorganic and organic association, whereas the inverted nature of the bar for Ge indicates that it has an extremely strong organic association.

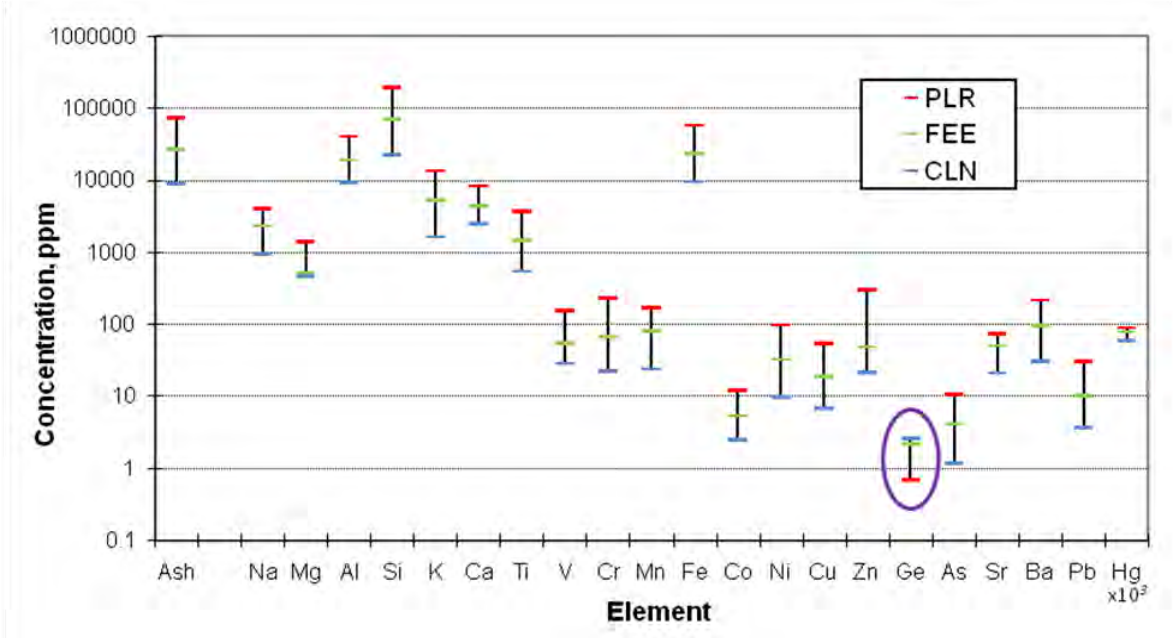

FIGURE 3: Bar diagram summarizing the efficiency of separation of various elements between the CLN and PLR fractions during gravity cleaning methods applied to the feed (FEE) coal. Note the inverted nature of the bar for Ge (circled) and the short bar for Hg.

Based on the data in Tables 4 and 6, the first separation by the rotary breaker clearly removed mineral bands enriched in quartz and kaolinite, but was less effective at removing pyrite. As

can be seen from Table 6, illite and pyrite, which are the two major trace-element containing minerals in coal, exhibited relatively monotonic increases with ash across the four fractions. However, whereas pyrite as a relative fraction of the mineral matter decreased from ~20% of the mineral matter in the CLN fraction to ~8% in the RBR fraction, illite increased from ~25% in CLN to almost 45% in PLR. Similar related variations can be seen in the wt% Fe_2O_3 and K_2O trends in Table 4. The similarities in trend for these two minerals with ash limited the usefulness of correlating trace element concentrations with mineral abundances in the different fractions for inference of trace element association with specific minerals, but at the same time, increase the value of independent, direct determinations of elemental modes of occurrence that can be obtained from techniques like XAFS and Mössbauer spectroscopies. Two examples of using XAFS spectroscopy for determining trace element modes of occurrence are now presented, one for chalcophile (As, Zn) elements, the other for lithophile elements (V, Cr, Ni), while a summary of the modes of occurrence for all key trace elements, based on both spectroscopic and chemical data, is presented in Table 7.

Example 1: chalcophile elements, arsenic and zinc

Arsenic and zinc are both thought to have a strong association with sulphide minerals in Illinois coals (Swaine, 1990; Finkelman, 1994). Arsenic XAFS spectra (Figure 4) of the Illinois coal fractions confirm that the principal occurrence of arsenic in this coal is its association with pyrite, based on their similarity to spectra in previous studies (Huggins et al., 1993; Kolker et al, 2000). Figure 5 shows the relationship between the concentrations of As and Zn and the abundance of pyrite for the four coal fractions. A highly correlated linear relationship ($R^2 > 0.99$) is revealed between As and pyrite and indicates that the pyrite in this Illinois #6 coal contains on average approximately 154 ppm As. This amount is remarkably similar to that of 144 ppm recently determined by microprobe for As in pyrite in a sampling of the Springfield (Illinois #5) coal (Kolker and Huggins, 2007).

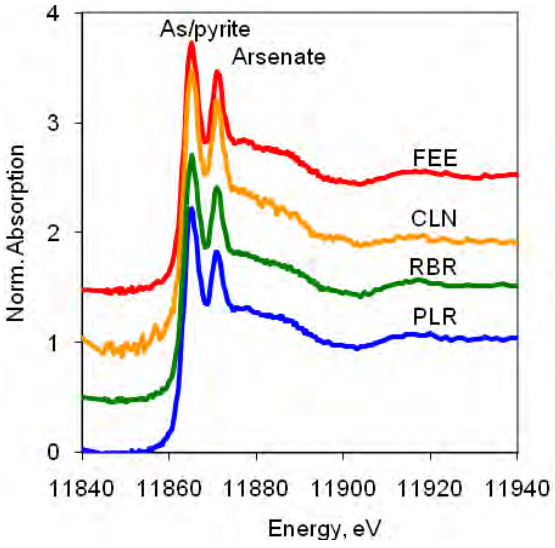

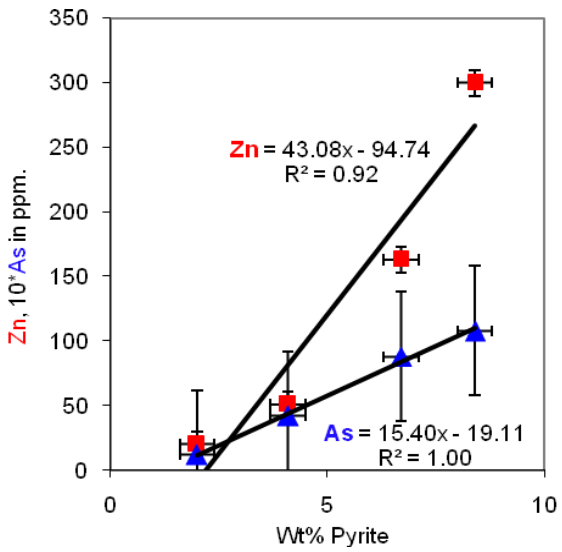

FIGURE 4 (left). Arsenic XANES spectra of the four Illinois coal fractions. Distinct peaks due to As in pyrite and As as arsenate are indicated.
FIGURE 5 (right). Correlations between As and Zn concentrations and pyrite abundance in the four Illinois coal fractions. Note that the As contents are multiplied by a factor of 10.

In contrast with arsenic, zinc does not exhibit nearly as strong a linear correlation with pyrite content. Further, zinc XAFS spectra (not shown) indicate that the zinc speciation is dominated by ZnS; however, the presence of other Zn forms (Zn/illite; Zn phosphate?) is also indicated. Consequently, it would appear that zinc in this coal is not associated strongly, if at all, with pyrite, but rather is present in independent forms.

Example 2: lithophile elements, vanadium, chromium and nickel

Figure 6 shows the correlations found between V, Cr, and Ni concentrations and the abundance of illite in the different coal fractions. For all three elements, the correlations with illite are highly significant ($R^2 > 0.99$). Evidence from previous XAFS investigations into the mode of occurrence of V and Cr in various Illinois basin coals indicates that both of these elements are likely to be distributed between illite and macerals (Maylotte et al., 1981; Huggins et al., 1997, 2000; Huggins and Huffman, 2004); however, less is established regarding the mode of occurrence of Ni and other mineral occurrences are certainly possible (Swaine, 1990; Finkelman, 1994). Based on the assumption that these three elements are distributed only between illite and the macerals in this coal, the average contents of these elements in illite are 400 ppm V, 625 ppm Cr, and 280 ppm Ni, while their contents in the macerals would average 21 ppm, 7 ppm, and 6 ppm, respectively. From these figures, the maximum percentages of V, Cr, and Ni that can be removed from this particular coal by physical separation methods are estimated to be around 67%, 92%, and 86%, respectively.

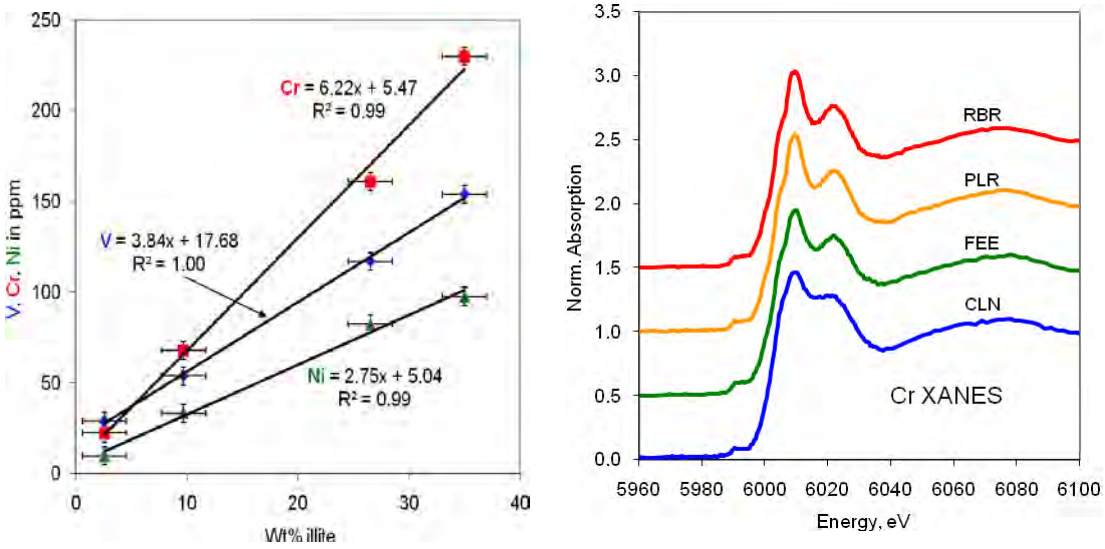

FIGURE 6 (left). Correlations between V, Cr and Ni concentrations and illite abundance in the four Illinois #6 coal fractions.
FIGURE 7 (right). Chromium XANES spectra of the four Illinois #6 coal fractions.

Direct evidence regarding the modes of occurrence of Cr and V was obtained by XAFS spectroscopy. Figure 7 shows Cr XAFS spectra obtained for the four fractions generated at the preparation plant. The corresponding V XAFS spectra were quite similar. The spectra exhibited by the tailings fractions, RBR and PLR, are clearly characteristic of the occurrence of Cr and V in illite, based on comparison with spectra presented for these elements in illite

in previous studies (Maylotte, et al., 1981; Huggins, et al., 2000). The major difference between the Cr and V XANES spectra is the height of the pre-edge peak which is much larger for V than for Cr, especially for the maceral-rich CLN fraction. Vanadium associated with the organic component in coal is mostly present in the V^{4+} oxidation state (Maylotte, et al., 1981), which results in a stronger pre-edge peak than that observed for V^{3+} or for Cr^{3+} in illite. From the height of the pre-edge peak and applying the correlation between peak-height and V valence state developed by Sutton et al. (2005), the average valence of V in illite is estimated to be about 3.3 ± 0.2, whereas it is 3.8 ± 0.2 in the form associated with the macerals. Based on the estimated Cr and V contents of the illite and the macerals, Cr and V in illite are calculated to represent more than 98% and 95%, respectively, of the total Cr and V in these fractions. Corresponding estimates for the clean coal fraction suggest that about 60 - 70% of these elements in this fraction are also present as illite; however, the XANES spectra would appear to indicate a significantly smaller contribution from these elements in illite, no more than 25%, indicating that the assumption of a constant content of these elements in illite may be an oversimplification and that the content of Cr and V in the macerals is underestimated by the intercept on the Cr trend in Figure 6. XAFS spectra for Ni have not been obtained.

Summary of elemental modes of occurrence.

The modes of occurrence, determined by a combination of both elemental and spectroscopic methods, of a number of important trace elements in the sample of Illinois #6 coal, are summarized in Table 7. Additionally, iron Mössbauer spectroscopy revealed that iron in this coal was largely in the form of pyrite with relatively minor fractions (2 – 10%) present as Fe^{2+} in clays and as iron sulfates (jarosite) (Figure 8). A minor fraction of magnetite was picked up in the CLN faction during the heavy media cleaning.

TABLE 7: Summary of modes of occurrence for key trace elements in this sample of Illinois #6 coal

Element	Comments on Mode of Occurrence in Illinois #6 Coal (this sample)
Arsenic	Entirely associated with pyrite; increasing oxidation of arsenical pyrite to arsenate noted over time during sample storage
Chromium	Largely present in association with illite with remainder in organic association; >98% Cr in tailings fractions is associated with illite
Germanium	Highly organically associated
Manganese	Complex – appears to be at least 3 significant distinct species
Mercury	Some association with pyrite; some with macerals
Nickel	Similar to Cr and V?
Selenium	Also associated with pyrite, but some organic Se as well
Vanadium	Similar to chromium, but with more of the element in organic association; >95% V in tailings fractions is associated with illite
Zinc	Complex – three distinct major species: sphalerite (ZnS); Zn assoc. w/ illite; and $Zn_3(PO_4)_2.xH_2O$ (tentative)

Measurements of the coal fractions taken about 4 months apart by As XAFS spectroscopy (Figure 9) revealed that oxidation of As in pyrite had occurred in all fractions resulting in the increased formation of arsenic as arsenate. Over this period, the percentage of arsenic as arsenate increased by between 2% for the tailings fractions and 5% for the CLN fraction. This oxidized form of As is likely associated with the oxidation product of pyrite, *viz.* jarosite ($K(Fe,Al)_3(SO_4)_2(OH)_6$), in which AsO_4^{3-} substitutes for SO_4^{2-}.

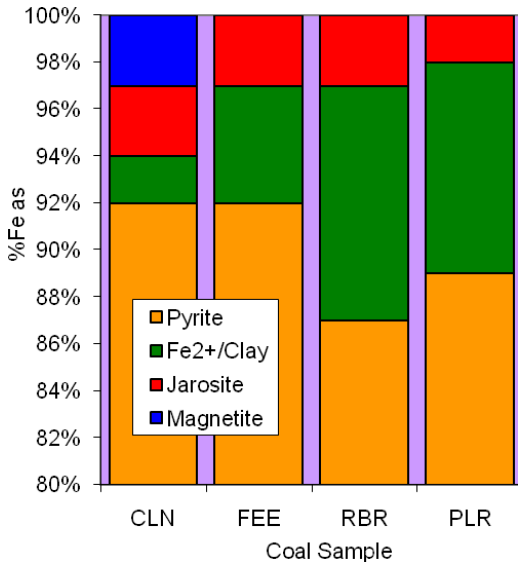

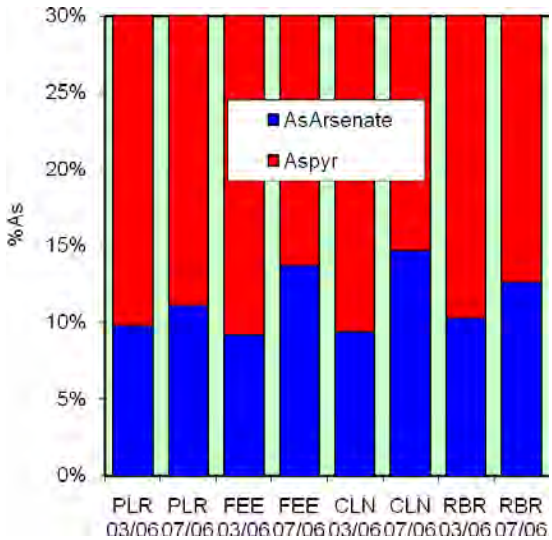

FIGURE 8 (left): Summary of the distribution of iron among different minerals in the four coal fractions as determined by Mössbauer spectroscopy. The balance of the iron is present as pyrite, FeS_2.

FIGURE 9 (right): Summary of the distribution of arsenic between pyrite and arsenate minerals in the four coal fractions measured about four months apart as determined by As XANES spectroscopy. The differences for each fraction indicate slow oxidation of arsenic associated with pyrite during sample storage. The balance of the arsenic is present as arsenic in pyrite.

Trace element mobility in leaching scenarios

With the modes of occurrence of key elements determined for the four coal fractions, the next stage of the research was to investigate their mobility in simulations of disposal of the tailings fractions in aqueous environments, such as tailings impoundments. The traditional way to do this is to subject the fractions to the Toxicity Characteristic Leaching Procedure (TCLP). However, according to the commercial testing laboratory that conducted the TCLP tests on the Illinois #6 coal fractions, no RCRA element was leached to any significant extent. Although this result is good news for environmental risk assessments, it tells the scientist little or nothing about trace element mobility from these coal fractions.

The negative result from the TCLP test was also indicated by iron Mössbauer and arsenic XANES spectra (Figure 10) of fractions before and after the TCLP test. Each before and after pair of spectra were essentially identical, indicating that any dissolution of pyrite and release of any associated pyrite during the TCLP test was negligible. Hence, it was

concluded that the duration and/or conditions of the TCLP test were not adequate to promote significant leaching of arsenic and other trace elements from the tailings fractions and therefore the TCLP test would not be informative for investigating trace element mobility. As a result, two longer-term methods of promoting trace element mobility from the tailings were constructed for such testing.

The baseline static test consisted of storing 200 g of tailings fraction under 200 ml of deionized water for 20 weeks. It was designed to be the benchmark test for the more aggressive cyclic test based on ASTM D-5744 (ASTM, 1996) that involved a cycle of submerging 200 g of each tailings for 24 hours in 200 ml of deionized water, draining off the water, followed by exposure of the tailings to first three days of dry air and then by three days of moist air. After a number of weekly cycles, the collected leachant waters were combined and submitted for determination of pH, Eh, conductivity, sulphate concentration, and major and trace elements by ICP-MS. This cyclic testing was continued for 22 weeks. For the final week of the test, week 23, the 200 ml of deionized water was replaced by an equivalent amount of dilute (0.1 N) HNO_3 in order to make the final stage more acidic and aggressive.

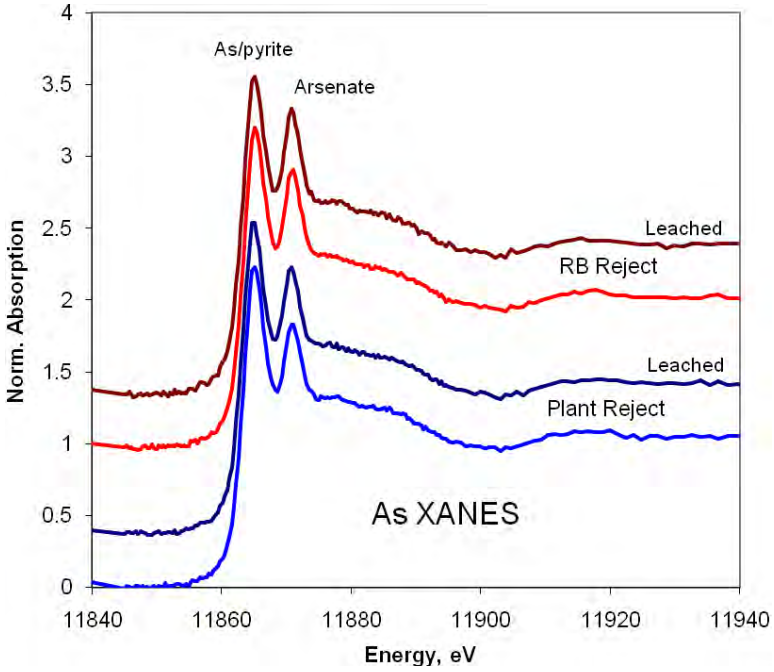

FIGURE 10: Arsenic XANES spectra for the RBR and PLR tailings fractions before and after (leached) the TCLP test. Note the unchanged nature of the spectra before and after the test, indicating that there was no significant change in arsenic speciation as a result of the test, consistent with the lack of any As leached during the test.

Data on the variation with time of conductivity, Eh, pH, and sulfate concentration are presented in Table 8 for the leachates from the rotary breaker reject (RBR) and plant reject (PLR) tailings fractions in the cyclic and baseline leaching tests. As documented in Figure 11, there is a very strong correlation between sulfate concentration and conductivity. This relationship implies that sulfate anions are the only significant anions being generated as a

result of the leaching conditions. As can also be seen from Table 8, the variation in pH is relatively small and it remains approximately neutral even after 22 weeks' leaching, except possibly for the last week for the PLR sample, when the pH dropped below 5. As would be expected, leaching with 0.1 N HNO_3 lowers the pH and increases conductivity significantly.

TABLE 8: Variation of conductivity, sulfate concentration, pH, and Eh of leachate samples taken at different times during the cyclic and baseline leaching tests on the Illinois #6 tailings fractions

Week	RB Reject				Plant Reject			
	Conductivity $\mu\Omega^{-1}.cm^{-1}$	Sulfate mg/L	pH	Eh	Conductivity $\mu\Omega^{-1}.cm^{-1}$	Sulfate mg/L	pH	Eh
Cyclic 0	8644	1609	8.0	192.4	8377	1469	8.1	172.2
1	6794	1268	7.3	164.4	5750	955	7.7	138.1
2-3	3958	684	7.5	207	3086	501	7.6	215
4-6	1688	292	7.3	175	1717	312	7.2	193
7	1513	278	6.8	204	1158	195	6.8	194
8-12	1887	337	7.0	191	2441	487	6.8	192
13-15	1314	230	7.1	160.6	1718	344	6.8	245.9
16-20	1475	289	7.0	220	1785	387	6.2	32
21-22	832	145	6.6	156	1302	255	4.9	233
23 (acid)	>2000	222	4.1	230	>2000	477	2.4	354
Baseline 20	>2000	7610		154	>2000	6410		155

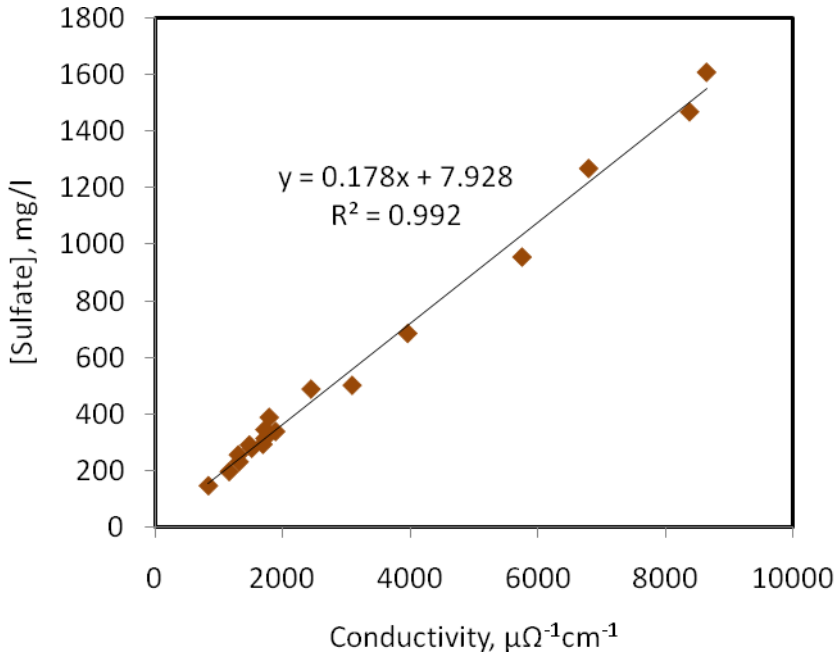

FIGURE 11: Correlation between conductivity and sulfate anion concentration determined for the aqueous leachates generated in the cyclic test. Leachates for the two tailings fractions, PLR and RBR, are not differentiated in this plot.

TABLE 9: ICP-MS Data for Leachates from Cyclic Testing on RBR Coal Tailings Fraction

Element	Week										Units	MDL
	0	1	2-3	4-6	7	8-12	13-15	16-20	21-22	23		
Aluminum	<MDL	<MDL	<MDL	<MDL	<MDL	0.23	<MDL	<MDL	<MDL	4.51	mg/L	0.061
Antimony	<MDL	<MDL	<MDL	<MDL	<MDL	<MDL	<MDL	<MDL	<MDL	<MDL	mg/L	0.012
Arsenic	<MDL	<MDL	<MDL	<MDL	<MDL	<MDL	<MDL	<MDL	<MDL	<MDL	mg/L	0.014
Barium	0.02	0.03	0.015	0.03	0.03	0.02	0.04	0.05	0.04	0.12	mg/L	0.003
Beryllium	<MDL	<MDL	<MDL	<MDL	<MDL	<MDL	<MDL	<MDL	<MDL	0.005	mg/L	0.001
Boron	1.07	0.74	0.52	0.33	0.22	0.36	0.23	0.39	0.12	1.32	mg/L	0.008
Cadmium	<MDL	<MDL	<MDL	<MDL	<MDL	<MDL	<MDL	<MDL	<MDL	0.05	mg/L	0.001
Calcium	315	325	279	231	277	386	257	321	172	1615	mg/L	0.002
Chromium	<MDL	<MDL	<MDL	<MDL	0.029	0.029	<MDL	0.05	0.05	<MDL	mg/L	0.024
Cobalt	0.15	0.005	<MDL	0.004	0.004	0.01	<MDL	0.02	0.01	0.63	mg/L	0.001
Copper	<MDL	<MDL	<MDL	<MDL	0.007	0.009	<MDL	0.005	<MDL	0.03	mg/L	0.005
Gold	<MDL	<MDL	<MDL	<MDL	<MDL	<MDL	<MDL	<MDL	<MDL	<MDL	mg/L	0.034
Iron	0.02	<MDL	<MDL	0.09	0.006	0.01	<MDL	0.02	0.03	6.02	mg/L	0.002
Lead	<MDL	<MDL	<MDL	<MDL	<MDL	<MDL	<MDL	<MDL	<MDL	<MDL	mg/L	0.01
Lithium	0.77	0.52	0.29	0.08	0.05	0.08	0.03	0.04	0.01	0.18	mg/L	0.001
Magnesium	59.7	48.8	34.5	21.2	23.3	30.6	17.3	20.8	8.97	86.3	mg/L	0.001
Manganese	1.46	1.61	0.82	0.43	0.49	0.77	0.46	0.88	0.41	8.76	mg/L	0.001
Nickel	0.79	0.07	0.03	0.01	<MDL	<MDL	<MDL	0.04	0.03	3.83	mg/L	0.002
Phosphorus	<MDL	<MDL	<MDL	<MDL	<MDL	<MDL	<MDL	<MDL	<MDL	39.3	mg/L	0.009
Potassium	23.9	28.7	23.9	18.8	18.8	25.3	14.4	19	9.55	59.7	mg/L	0.191
Selenium	0.45	0.24	0.05	<MDL	0.03	0.02	<MDL	0.04	0.014	0.09	mg/L	0.011
Silicon	1.86	2.01	2.17	1.65	1.58	2.57	1.55	3.38	1.4	73.9	mg/L	0.009
Silver	<MDL	<MDL	<MDL	<MDL	<MDL	<MDL	<MDL	<MDL	<MDL	<MDL	mg/L	0.003
Sodium	1600	1220	581	116	35.1	34.5	10.9	5.64	1.81	8.86	mg/L	0.058
Strontium	5.33	4.27	3.27	2.05	2.41	3.12	1.87	2.18	1.04	16.1	mg/L	0.01
Sulfur	1530	1310	742	284	277	368	232	290	152	216	mg/L	0.014
Thalium	<MDL	<MDL	<MDL	<MDL	<MDL	<MDL	<MDL	<MDL	<MDL	<MDL	mg/L	0.041
Tin	<MDL	<MDL	<MDL	<MDL	<MDL	<MDL	<MDL	<MDL	<MDL	<MDL	mg/L	0.012
Vanadium	<MDL	<MDL	<MDL	<MDL	<MDL	<MDL	<MDL	<MDL	<MDL	<MDL	mg/L	0.008
Zinc	<MDL	0.006	<MDL	0.11	<MDL	<MDL	<MDL	0.27	0.14	2.54	mg/L	0.002

TABLE 10: ICP-MS Data for Leachates from Cyclic Testing on PLR Coal Tailings Fraction

Element	Week										Units	MDL
	0	1	2-3	4-6	7	8-12	13-15	16-20	21-22	23		
Aluminum	<MDL	<MDL	<MDL	<MDL	0.1	0.2	<MDL	0.17	1.07	58.1	mg/L	0.061
Antimony	<MDL	<MDL	<MDL	<MDL	<MDL	<MDL	<MDL	<MDL	<MDL	0.04	mg/L	0.012
Arsenic	<MDL	<MDL	<MDL	<MDL	<MDL	<MDL	<MDL	<MDL	<MDL	<MDL	mg/L	0.014
Barium	0.02	0.02	0.02	0.03	0.04	0.02	0.02	0.02	0.02	0.1	mg/L	0.003
Beryllium	<MDL	<MDL	<MDL	<MDL	<MDL	<MDL	<MDL	<MDL	0.001	<MDL	mg/L	0.001
Boron	1.64	1.18	0.77	0.41	0.27	0.37	0.27	0.43	0.15	0.5	mg/L	0.008
Cadmium	<MDL	<MDL	<MDL	<MDL	<MDL	<MDL	0.002	0.02	0.03	0.18	mg/L	0.001
Calcium	288	297	299	297	214	561	351	415	277	1579	mg/L	0.002
Chromium	<MDL	<MDL	0.025	0.025	<MDL	0.028	<MDL	0.06	0.05	<MDL	mg/L	0.024
Cobalt	0.1	0.01	0.02	0.027	0.004	0.03	0.03	0.22	0.18	1.13	mg/L	0.001
Copper	<MDL	<MDL	<MDL	0.007	0.01	0.009	<MDL	<MDL	<MDL	1.29	mg/L	0.005
Gold	<MDL	<MDL	<MDL	<MDL	<MDL	<MDL	<MDL	<MDL	<MDL	<MDL	mg/L	0.034
Iron	0.01	<MDL	<MDL	<MDL	0.007	0.07	0.008	1.44	11.1	95	mg/L	0.002
Lead	<MDL	<MDL	<MDL	<MDL	<MDL	<MDL	<MDL	<MDL	<MDL	<MDL	mg/L	0.01
Lithium	0.68	0.43	0.18	0.06	0.03	0.07	0.03	0.05	0.03	0.19	mg/L	0.001
Magnesium	53.5	44	36.9	28.9	19.7	44.3	21.1	25	11.5	63.9	mg/L	0.001
Manganese	1.53	1.53	1.64	1.65	1.44	2.82	2.06	4.4	2.92	14.4	mg/L	0.001
Nickel	0.43	0.14	0.15	0.09	<MDL	0.01	0.11	1.1	1.05	6.75	mg/L	0.002
Phosphorus	<MDL	<MDL	<MDL	<MDL	<MDL	<MDL	<MDL	<MDL	<MDL	20.1	mg/L	0.009
Potassium	27.1	29.7	23.2	16.9	13.1	23.3	14.8	17.3	10.8	55.1	mg/L	0.191
Selenium	0.45	0.36	0.2	0.1	0.1	0.07	0.02	0.21	0.12	0.25	mg/L	0.011
Silicon	3.23	2.8	2.85	2.21	2.13	2.58	2.12	5.35	4.46	53.6	mg/L	0.009
Silver	<MDL	<MDL	<MDL	<MDL	<MDL	<MDL	<MDL	<MDL	<MDL	<MDL	mg/L	0.003
Sodium	1510	978	348	57.2	16.7	26.2	9.56	5.92	2.22	7.7	mg/L	0.058
Strontium	5.11	3.71	2.94	2.05	1.38	2.94	1.66	1.73	1.05	10.2	mg/L	0.01
Sulfur	1400	1080	571	308	208	505	329	379	260	450	mg/L	0.014
Thalium	<MDL	<MDL	<MDL	<MDL	<MDL	<MDL	<MDL	<MDL	<MDL	<MDL	mg/L	0.041
Tin	<MDL	<MDL	<MDL	<MDL	<MDL	<MDL	<MDL	<MDL	<MDL	0.31	mg/L	0.012
Vanadium	<MDL	<MDL	<MDL	<MDL	<MDL	<MDL	<MDL	<MDL	<MDL	0.03	mg/L	0.008
Zinc	<MDL	<MDL	<MDL	0.1	0.002	<MDL	0.06	0.67	0.93	7.15	mg/L	0.002

Major and trace element concentrations for all leachates from the cyclic testing of the two tailings fractions are summarized in Tables 9 and 10. The corresponding data set for the baseline testing after 20 weeks is shown in Table 11. Data for all elements sought in the ICP-MS analyses are listed in these tables, even if their concentrations were below the minimum detection limit (MDL) in all samples.

TABLE 11: ICP-MS Data for Leachates from Baseline Testing (Week 20) on Coal Tailings

Element	RBR	PLR	Units	MDL
Aluminum	0	0.17	mg/L	0.061
Antimony	0	0.04	mg/L	0.012
Arsenic	<MDL	<MDL	mg/L	0.014
Barium	0.01	0.01	mg/L	0.003
Beryllium	<MDL	<MDL	mg/L	0.001
Boron	0.44	0.78	mg/L	0.008
Cadmium	0.003	0.003	mg/L	0.001
Calcium	384	401	mg/L	0.002
Chromium	0.029	0	mg/L	0.024
Cobalt	<MDL	<MDL	mg/L	0.001
Copper	0.01	0.006	mg/L	0.005
Gold	<MDL	<MDL	mg/L	0.034
Iron	0.09	0.23	mg/L	0.002
Lead	<MDL	<MDL	mg/L	0.01
Lithium	0.99	0.9	mg/L	0.001
Magnesium	77.5	69.4	mg/L	0.001
Manganese	1.41	1.62	mg/L	0.001
Nickel	0.09	0.11	mg/L	0.002
Phosphorus	<MDL	<MDL	mg/L	0.009
Potassium	30.5	37.6	mg/L	0.191
Selenium	<MDL	<MDL	mg/L	0.011
Silicon	1.59	2.38	mg/L	0.009
Silver	<MDL	<MDL	mg/L	0.003
Sodium	1785	1606	mg/L	0.058
Strontium	6.58	6.72	mg/L	0.01
Sulfur	1912	1750	mg/L	0.014
Thalium	<MDL	<MDL	mg/L	0.041
Tin	<MDL	<MDL	mg/L	0.012
Vanadium	<MDL	<MDL	mg/L	0.008
Zinc	<MDL	<MDL	mg/L	0.002

A comparison of the cumulative leached amounts for the cyclic testing after weeks 22 and 23 with the baseline data after week 20, as a percentage of the total amount of an element originally present in the tailings, is shown in Figure 12. These data confirm that the cyclic test was more aggressive than the baseline static test with respect to removal of elements from the tailings. In addition, these data show (Figure 13) that the elements most readily leached from the tailings were the alkali and alkaline earth metals (Na, Mg, Ca, and Sr). Larger elements in these groups (K, Ba) were much more resistant to leaching. Among the trace elements, only Mn, Co, Ni, Zn,

and Se were leached to any significant extent in these tests. Other key elements such as Al, Si, V, Cr, Fe, and As were not significantly leached. It is clear from the lack of significant leaching of K, Al, and Si, as well of Cr and V, that illite is unaffected by the leaching treatments. It was found that more than 10% of the sulfur in the tailings is removed by leaching in the form of sulfate. However, there does not appear to be a corresponding fraction of iron leached to indicate significant alteration of pyrite. So where does the sulfur come from? The answer to this question was provided by spectroscopic examination of the tailings after leaching.

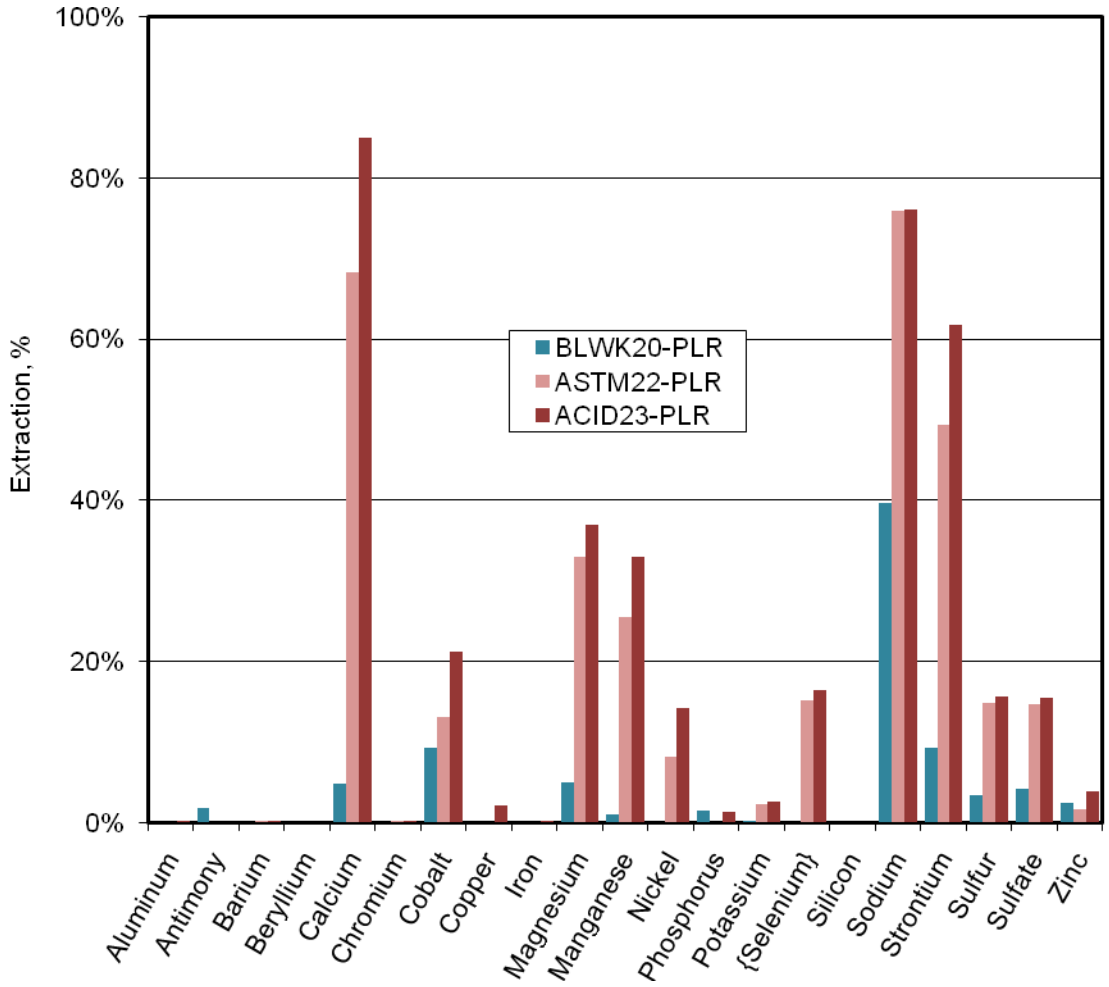

FIGURE 12: Comparison of the cumulative amounts of leached elements from PLR tailings after weeks 22 and 23 of the cyclic testing and after week 20 of the baseline test. The data are presented as a percentage of the total amount of an element originally present in the tailings. Elements not shown were negligibly leached in all tests. Data for the RBR tailings were similar.

After weeks 7 and 22 of the cyclic leaching treatment, small samples of both tailings fractions were separated and used for Fe Mössbauer and As XAFS speciation determinations. Both iron and arsenic showed significant increases in oxidized forms; specifically, about 8-10% of the iron in pyrite has been converted to iron as jarosite and a larger percentage of arsenic has been converted to arsenate forms (Figure 14). However, these oxidized forms clearly resist leaching since neither iron nor arsenic is detected to any significant extent in the leachates (q.v. Figure 12).

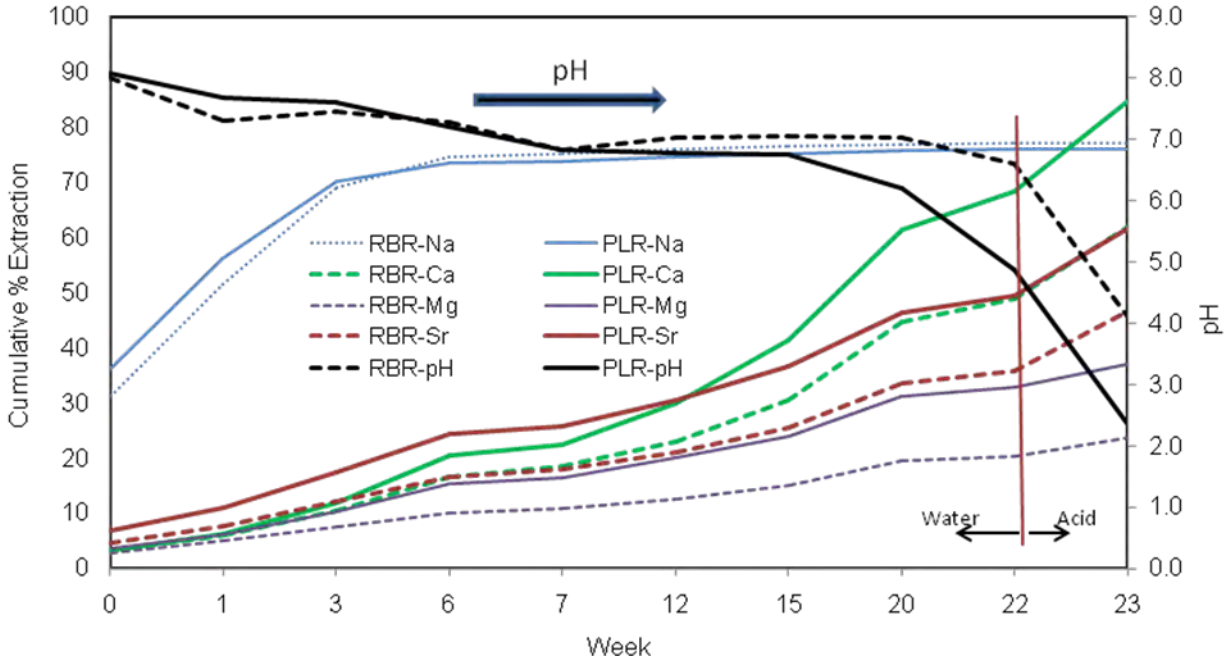

FIGURE 13: Cumulative % extraction of alkali (Na) and alkaline earth (Ca, Mg, Sr) elements from RBR (dashed lines) and PLR (solid lines) tailings fractions with length of time in the cyclic leaching test. Also shown is the variation of pH for the leachates.

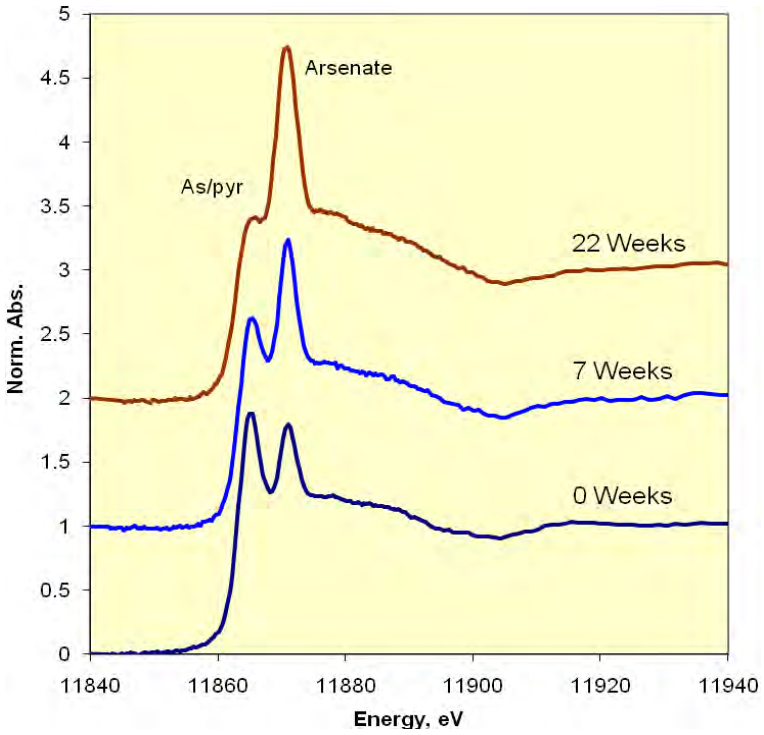

FIGURE 14: Arsenic XANES spectra from samplings of the coal tailings fractions taken after 7 and 22 weeks into the cyclic test. Note the increasing intensity of the peak due to arsenate relative to that for As/pyrite.

The following scenario appears to account for the leaching behavior exhibited by these samples of tailings from coal from the Illinois #6 seam. The first elements leached from the tailings in quantity are alkali and alkaline earth elements, including Na, Mg, Ca, and Sr. Sodium in particular is easily and rapidly leached from these tailings. It is followed by the slower release of Ca, Mg, and Sr. The dissolution of these basic elements effectively buffers the pH of the leachate and delays it from becoming highly acidic, as would be anticipated for a coal so rich in pyrite. As long as the pH of the extract remains close to neutral, oxidation of pyrite, the associated release of arsenic, and, more importantly, the formation of acid, $[H^+]_{sol'n}$, is minimal. Even though the pyrite and associated arsenic do show signs of significant oxidation, as demonstrated by the formation of jarosite and the large increase in arsenate relative to As associated with pyrite, these oxidized forms of these elements remain immobile. The following equation, which results in the formation of insoluble jarosite, is consistent with the observations made to date:

$$3FeS_2 + 3H_2O + 13.5O_2 + [Na^+]_{sol'n} \rightarrow NaFe_3(SO_4)_2(OH)_6 + 4[SO_4^{2-}]_{sol'n}$$

This reaction explains not only the release of some sulfate but also the lack of mobilization of iron and the lack of formation of acid ($[H^+]_{sol'n}$]). Arsenic must remain predominantly with the jarosite, presumably as a result of the substitution of AsO_4^{3-} for SO_4^{2-} (Paktunc and Dutrizac, 2003). As long as insoluble jarosite formation is maintained and the acidity is buffered to near neutral pH, mobilization of trace metals in pyrite such as arsenic can be avoided. The role of readily solublized Na^+, which appears to act as an effective buffer to acid formation and is necessary for formation of jarosite, is clearly important and may lead to effective strategies to retard trace element mobilization from coal tailings.

CONCLUSIONS

The combination of multi-elemental analysis methods and techniques such as Mossbauer and XAFS spectroscopies, supplemented by conventional coal analyses, has been used to obtain detailed information regarding the modes of occurrence of sulphur, iron, and a number of key trace elements in an as-mined Illinois #6 coal and in various clean coal and tailings fractions separated from the coal at a commercial preparation plant. For this coal, it was established that As is entirely associated with pyrite. Se and Hg are also associated with pyrite but to lesser extents. Conversely, Cr, V, and possibly Ni are principally associated with illite, while Zn exhibits a sulphide (as ZnS) occurrence as well as a clay occurrence and possibly also a phosphate occurrence. The occurrence of Mn is also complex. Germanium was shown to be strongly associated with macerals and Hg also exhibited a significant organic association as well. By and large, the associations of trace elements with pyrite and illite determined to a large extent their separation efficiency in the coal cleaning processes.

With this framework established, the mobility of trace elements from leaching tests simulating tailings impoundments was then examined. Three different leaching tests were examined including the standard 18-hour TCLP test, which proved to be quite uninformative regarding trace element behaviour during leaching. Two longer-term (>150 days) tests were then carried out, one of which was a variation of the cyclic test method, ASTM Standard Method D-5744, while the other was a baseline method involving storage of the tailings under water for the length

of time of the test. Elements such as Cr and V, which are associated (>95%) with illite, exhibited no mobility whatsoever over the duration of the tests, no doubt reflecting the resistance of clay minerals to aqueous leaching at near-neutral pH. Elements associated with pyrite, such as Fe and As, also showed little mobility. Elements that were mobilized included Na, Mg, Ca, and Sr. The solubilisation of these alkali and alkaline earth elements effectively buffered the pH of the leachate solutions and prevented significant alteration of pyrite and the release of elements associated with it. What alteration of pyrite did occur was limited to minor formation of jarosite, which remained insoluble throughout the leaching tests and acted as a sink for arsenate anions formed during the alteration. The role of sodium in buffering the pH of the leachates and the formation of insoluble natrojarosite is clearly important for preventing release of potentially harmful trace elements from pyrite.

ACKNOWLEDGEMENTS

The experimental work described in this Report was largely carried out by Laal B. A. Seidu, a M. Sc. Candidate in the Department of Mining Engineering at the University of Kentucky. He also had the responsibility for the compilation and management of the analytical data. The cyclic leaching test was constructed by Mr. Seidu, with assistance from Nick Cprek.

Important advice on coal selection and the collection and preparation of samples for analysis was provided by Prof. Rick Honaker of the Department of Mining Engineering at the University of Kentucky.

The Principal Investigators acknowledge the following persons for their analytical skills and contributions to this study: G. Thomas, Center for Applied Energy Research, University of Kentucky, for proximate and ultimate analyses and Hg analyses of the Illinois coal fractions; H. Francis and J. Backus, Kentucky Geological Survey, for X-ray fluorescence analyses of the ash and ICP-MS, pH, Eh, and sulfate analyses of the leachates from the cyclic and static leaching tests; J. Kyger, B. L. Higgins, and J. D. Robertson, University of Missouri at Columbia, for ICP-MS determinations of trace metals in the coal fractions; and S. Pal, and M. Seehra, West Virginia University for Rietveld X-ray diffraction analyses of the mineralogy of the coal fractions.

This research was supported by a grant from the U.S. Department of Energy through the Center for Advanced Separation Technologies at Virginia Polytechnic Institute and State University, Blacksburg, VA. The Principal Investigators also acknowledge the U.S. Department of Energy for its support of the synchrotron facilities for XAFS spectroscopy at the National Synchrotron Light Source, Brookhaven National Laboratory, NY, and at the Stanford Synchrotron Radiation Laboratory, Stanford University, CA.

REFERENCES

ASTM. (1996). Standard Method D-5744-96. Standard test method for accelerated weathering of solid waste materials using a modified humidity cell. American Society for Testing and Materials, Philadelphia, PA.

Finkelman, R. B. (1994). Mode of occurrence of potentially hazardous elements in coal: levels of confidence. *Fuel Process. Technol.* 39, 21– 34.

Huggins, F. E. and Huffman, G. P. (2004). How do lithophile elements occur in organic association in bituminous coals? *Int. J. Coal Geol*., 58, [3], 193-204.

Huggins, F. E., Shah, N., Zhao, J., Lu, F. and Huffman, G. P. (1993). Nondestructive determination of trace element speciation in coal and ash by XAFS spectroscopy. *Energy Fuels* 7, 482– 489.

Huggins, F. E., Srikantapura, S., Parekh, B. K., Blanchard, L. and Robertson, J. D. (1997). XANES spectroscopic characterization of selected elements in deep-cleaned fractions of Kentucky #9 coal. *Energy Fuels* 11, 691– 701.

Huggins, F. E., Shah, N., Huffman, G. P., Kolker, A., Crowley, S., Palmer, C. A. and Finkelman, R. B. (2000). Mode of occurrence of chromium in four U.S. Coals. *Fuel Process. Technol*. 63, 79– 92.

Kolker, A. and Huggins, F. E. (2007). Progressive oxidation of pyrite in five bituminous coal samples: An As XANES and ^{57}Fe Mössbauer spectroscopic study. *Applied Geochemistry*, 22, [4], 778-787.

Kolker, A., Crowley, S., Palmer, C. A., Finkelman, R. B., Huggins, F. E., Shah, N. and Huffman, G. P., (2000). Mode of occurrence of arsenic in four U.S. coals. *Fuel Process. Technol.* 63, 167–178.

Maylotte, D. H., Wong, J., St. Peters, R. L., Lytle, F. W. and Greegor, R. B. (1981). X-ray absorption spectroscopic investigation of trace vanadium sites in coal. *Science* 214, 554–556.

Paktunc, D. and Dutrizac, J. E. (2003). Characterization of arsenate-for-sulfate substitution in synthetic jarosite using X-ray diffraction and X-ray absorption spectroscopy. *Canad. Mineral.* 41, 905-919.

S.R. Sutton, J. Karner, J. Papike, J.S. Delaney, C. Shearer, M. Newville, P. Eng, M. Rivers, and M.D. Dyar, (2005). A new microscale oxybarometer for solar system basaltic glasses based on vanadium K edge XANES. *Geochim. Cosmochim. Acta* 69(9), 2333-2348.

Swaine, D. J. (1990). *Trace Elements in Coal.* Butterworths, Chichester, U.K.

U.S. Congress. (1976). Public Law 94-580, October 21st, 1976.

U.S. Congress. (1990). Amendments to the 1990 Clean Air Act, *Federal Register*.

BIBLIOGRAPHY

F. E. Huggins, L. B. A. Seidu, N. Shah, G. P. Huffman, and R. Q. Honaker, Behavior of arsenic and other trace elements during cleaning of an Illinois coal and simulated leaching of its tailings. *Program and Full Papers, 2007 International Conference on Coal Science and Technology (Nottingham, U.K.)*, Paper 10D3, CD-ROM, 10 pp., (2007).

LIST OF ACRONYMS AND ABBREVIATIONS

ASTM	American Standards for Testing and Materials
CAAA	Clean Air Act Amendments
CLN	Clean (Coal)
FEE	Feed (Coal)
HAP	Hazardous Air Pollutant (Element)
ICP-MS	Inductively Coupled Plasma- Mass Spectroscopy
MDL	Minimum Detection Limit
PLR	Plant Reject (Tailings)
ppm	parts per million
RBR	Rotary Breaker Reject (Tailings)
RCRA	Resource Conservation and Recovery Act
TCLP	Toxicity Characteristic Leaching Procedure
tph	tons per hour
XAFS	X-ray Absorption Fine Structure (Spectroscopy)
XANES	X-ray Absorption Near-Edge Structure (Spectroscopy)
XRD	X-ray Diffraction
XRF	X-ray Fluorescence

APPENDIX 25 - Selenium Removal from Mine Influenced Water (MIW) Using Nano-Magnetite (WV022)

TECHNICAL PROGRESS REPORT

Contract Title and Number:	Period of Performance:
Continuation in Crosscutting Technology Development at CAST. (DE-FC26-05NT42457)	Starting Date: 10/1/05 Ending Date: 9/30/10

Sub-Recipient Project Title: Selenium Removal from Mine Influenced Water (MIW) Using Nano-Magnetite	Report Information: Type: Final Number: Period: 10/01/07-9/30/10 Date: 10/29/10 Code: WV022-FINAL
Principal Investigators: Xinchao Wei and Benoit Van Aken	
Contact Address: Dept. of Civil and Environmental Engineering West Virginia University PO Box 6103 Morgantown, WV 26506	Contact Information: Phone: (304)293-9954 Fax: (304)293-7109 E-Mail: xinchao.wei@mail.wvu.edu
Subcontractor Address: No subcontracts issued	Subcontractor Information: Phone: Fax: E-Mail:

DISCLAIMER

ABSTRACT

Mining operations and the subsequent processing and utilization of coal and minerals result in the release of selenium into mine influenced waters (MIWs). Management of selenium in MIWs is becoming a great challenge for the mining industry in response to increasing public concerns, more stringent environmental regulations, and the difficulty in removing selenium to levels that meet current discharge criteria. Consequently, there is an urgent need to develop cost-effective selenium removal processes. Samples were taken from streams impacted by mining in Northern, Central, and Southern WV to characterize the MIWs. Synthesized nano-magnetite was used as an adsorbent to evaluate its effectiveness in removing Se from aqueous solutions. In order to facilitate the use of nano-magnetite in continuous column adsorption, nano-magnetite was employed to modify the surfaces of diatomaceous earth (DE), taking advantage of the functionality of magnetite and DE‟s unique properties. The adsorption performance of nano-magnetite impregnated DE was evaluated in batch and column tests. The Se adsorption demonstrated nano-magnetite could be a very promising nano-sorbent in removing Se from water or wastewater. Column studies showed that adsorption columns could be used to remove both selenite and selenite continuously and nano-magnetite impregnated DE can be a practical solution to selenium-impaired waters. The adsorption capacities obtained in the column adsorption tests were ~ 845µg-Se/g and ~ 600µg-Se/g for selenite and selenate, respectively.

TABLE OF CONTENTS

LIST OF GRAPHICAL MATERIALS

EXECUTIVE SUMMARY

Mining operations and the subsequent processing and utilization of coal and minerals result in the release of selenium into mine influenced waters (MIWs). Management of selenium in MIWs is becoming a great challenge for the mining industry in response to increasing public concerns, more stringent environmental regulations, and the difficulty in removing selenium to levels that meet current discharge criteria. Consequently, there is an urgent need to develop cost-effective selenium removal processes.

Samples were taken from streams impacted by current or past mining activities in Northern, Central, and Southern WV to characterize the MIWs. Water samples collected from Central WV indicated the streams in Beaver Creek watershed were not impaired by Se. Results of water quality analysis for the 11 streams in Southern WV and 1 stream in Northern WV confirmed the presence of selenium in each stream sampled with concentrations ranging from 0.54 to 16.26 μg/L, indicating all streams were impaired by Se.

Synthesized nano-magnetite was used as an adsorbent to evaluate its effectiveness in removing Se from aqueous solutions. A series of batch adsorption experiments were conducted to study adsorption kinetics, isotherms, and adsorptive thermodynamics in conjunction with studies on the effects of pH, temperature, concentration, contact time, and presence of competing anions on Se removal efficiency. As opposed to either natural magnetite (<5μm) or nano-iron (~10 nm), nano-magnetite (10-20 nm) was found to be a better adsorbent for selenite, while nano-iron showed better adsorption performance for selenate. The results indicated that a final effluent concentration of less than 5 μg-Se/L could be achieved in removing selenite from Se laden solutions with initial concentrations of 100 μg-Se/L or lower, comparable to those commonly found in mine water or mining impacted streams. The high selenite removal efficiency in low pH range (<4) was an advantage for nano-magnetite to be used in treating low pH waters such as acidic mine water or mine drainage. Adsorption of selenite onto nano-magnetite was a spontaneous, endothermic process, indicating high temperatures favored Se removal. The selenite adsorption followed the Freundlich isotherm model and the adsorption was heterogeneous at the surfaces of nano-magnetite. Presence of common anions did not significantly affect the adsorption capacity of nano-magnetite for selenite. The selective Se adsorption demonstrated nano-magnetite could be a very promising nano-sorbent in removing Se from water or wastewater.

In order to facilitate the use of nano-magnetite in continuous column adsorption, nano-magnetite was employed to modify the surfaces of diatomaceous earth (DE), taking advantage of the functionality of magnetite and DE‟s unique properties. The adsorption performance of nano-magnetite impregnated DE was evaluated in batch tests. This binary oxide system was successfully applied to remove selenium oxyanions from water. The nano-magnetite impregnated DE showed the potential for achieving drinking water maximum contaminant levels (MCLs) as required by the USEPA. Moreover, the regeneration of this adsorbent could be achieved by increasing the pH to a basic range. The data showed that the maximum removal of selenite and selenate was achieved under acidic conditions (2 – 3.5), indicating the adsorption process was suitable for treating selenium-impaired acid mine drainage. The adsorption of selenate was more strongly dependent on pH than that of selenite. The adsorption of selenite and selenate onto nano-magnetite impregnated DE fitted well the Freundlich model and low temperatures favored Se

adsorption. The competition adsorption of sulfate with respect to selenite and selenate was more evident than that of nitrate and chloride.

The adsorption performance of nano-magnetite impregnated DE was also evaluated in continuous column tests. Column studies showed that adsorption columns could be used to remove both selenite and selenite continuously and nano-magnetite impregnated DE can be a practical solution to selenium-impaired waters. The adsorption capacities obtained in the column adsorption tests were ~ 845µg-Se/g and ~ 600µg-Se/g for selenite and selenate, respectively. From the column studies it was also observed that competing anions such as sulfate and chloride, commonly present in natural waters, reduced the uptake of selenate by the nano-magnetite impregnated DE.

1 INTRODUCTION

Selenium (Se), an emerging contaminant for many regions globally, is widely but unevenly distributed in rocks, soils, coals and other fossil fuels (Lemly, 2004). It is an essential micronutrient for humans and animals, but considered toxic when ingested in amounts higher than those needed for optimum nutrition. Regulations on Se vary from country to country. For drinking water, most countries adopt the 10 µg-Se/L limit of World Health Organization guideline (WHO, 2003). In the US, 50 µg-Se/L is still the current Environmental Protection Agency (EPA) limit for both the maximum contaminant level (MCL) and the MCL goal (MCLG), although a new limit of 5 µg-Se/L is being proposed. The US Clean Water Act (CWA) lists Se as a priority toxic pollutant and adopts freshwater acute and chronic criteria of 20 µg-Se/L and 5 µg-Se/L, respectively. Se levels exceeding the freshwater criteria can pose a serious risk to aquatic life and humans due to the likelihood of bioaccumulation through the food chain.

In addition to its natural occurrence in the environment, Se can be released as a result of anthropogenic processes such as mining of minerals, combustion of coal, metal smelting, oil refining and utilization, and agricultural irrigation (Lemly, 2004). In particular, mining operations and subsequent processing and utilization of coal and minerals can result in the release of Se as oxyanions into wastewater and mine drainage (Adams and Pennington, 2005; Renner, 2005). Se concentration in streams impacted by surface coal mining in the central Appalachian basin was higher (median 12 µg-Se/L) than streams draining the undisturbed areas (median 1.5 µg-Se/L) (Neuzil et al., 2007). In aquatic environments, Se can be present in four different oxidation states viz. selenide (Se^{2-}), elemental selenium (Se^{0}), selenite (SeO_3^{2-}), and selenate (SeO_4^{2-}) (Parida et al., 1997), of which selenite and selenate are more soluble and mobile (Sharmasarkar and Vance, 2002; Benjamin, 1983).

Technologies in removing Se from aqueous solutions include: 1) Conventional water treatment practices such as lime neutralization, softening and ferric coagulation. The drawbacks of these technologies are the high residual Se and large volumes of Se-containing sludge. 2) Ion exchange and membrane processes such as reverse osmosis, nanofiltration, and emulsion liquid membranes. Ion exchange was reported to be more effective for selenite rather than selenate and total dissolved solids and other anions interfered greatly with the Se removal (Twidwell, 2005). Reverse osmosis and nanofiltration techniques are rather uncommon because pre-treatment for both these methods is complicated. Emulsion liquid membrane is preferential in removing sulfate instead of selenate and is pH dependent (Mavrov et al., 2006; Gleason et al., 1996). 3) Se reduction. Selenate can be reduced to selenite or elemental Se to facilitate its removal. However generation of large volumes of sludge, high cost of reagents and interferences by dissolved oxygen and other anions are factors that affect the wide application of this technique (Mavrov et al., 2006). 4) Biological processes. Removing Se biologically has received great attention in recent years (Hunter and Manter, 2009; Takada et al., 2008) and the operating time and size of bioreactors are the obvious challenges. 5) Adsorption processes using such adsorbents as alumina, activated carbon, manganese nodule leached residues sulphuric acid-treated peanut shell and various iron oxides/hydroxides (El-Shafey, 2007; Dash and Parida, 2007). Adsorption is by far the most researched and most promising method in treating Se laden waters. The iron-based adsorbents include amorphous iron oxyhydroxide (Parida et al., 1997; Balistrieri and Chao, 1990; Benjamin, 1983), goethite (Zhang and Sparks, 1990), ferrihydrite (Parida et al., 1997), „waste" iron (III) hydroxide (Namasivayam

and Prathap, 2006), hematite and magnetite (Martinez et al., 2006), goethite and hematite (Rovira et al., 2008), and iron-coated granular activated carbon (Zhang et al., 2008). The major drawbacks involved in using those adsorbents are the preferential adsorption for either SeO_3^{2-}or SeO_4^{2-} and interferences by anions such as phosphates.

Nanotechnology is a cross-discipline field with a great potential in pollution prevention, treatment, and remediation. While the applications of nanoparticles are promising, the associated high costs and the potential consequences of nanoparticles on public health are the limiting factors. Consequently, low-cost, environmentally friendly nano-materials are the focus of many recent research efforts in environmental treatment or remediation. Among them, nano-magnetite has received significant attention because it is relatively inexpensive to make, safe to handle, and friendly to the environment. The objective of this study was to develop an adsorption process to remove Se from water and wastewater using nano-magnetite.

2 EXPERIMENTAL

2.1 Mine Influenced Water (MIW) Sampling and Characterization

MIW samples were collected from: 1) 9 sites in the *Beaver Creek* watershed in Central WV, near Davis, Tucker County (Fig. 1); and 2) 11 streams in Southern WV and 1 stream in Northern WV (Fig. 2**).** Field measurements included pH and specific conductance. Lab analyses included: alkalinity, acidity, sulfate (SO_4), total iron (Fe), total manganese (Mn), total calcium (Ca), total magnesium (Mg), total aluminum (Al), and total selenium (Se). Grab samples were collected, preserved, and analyzed in accordance with the methods presented in Standard Methods for the Examination of Water and Wastewater (APHA, 1999). The measured analytes, analytical methods employed, and associated method detection limits (MDLs) are presented in Table 1. Selenium was analyzed using a *Varian SpectrAA* 210 Zeeman graphite furnace atomic absorption spectrometer (GFAAS) with a detection limit of 1 ug/L.

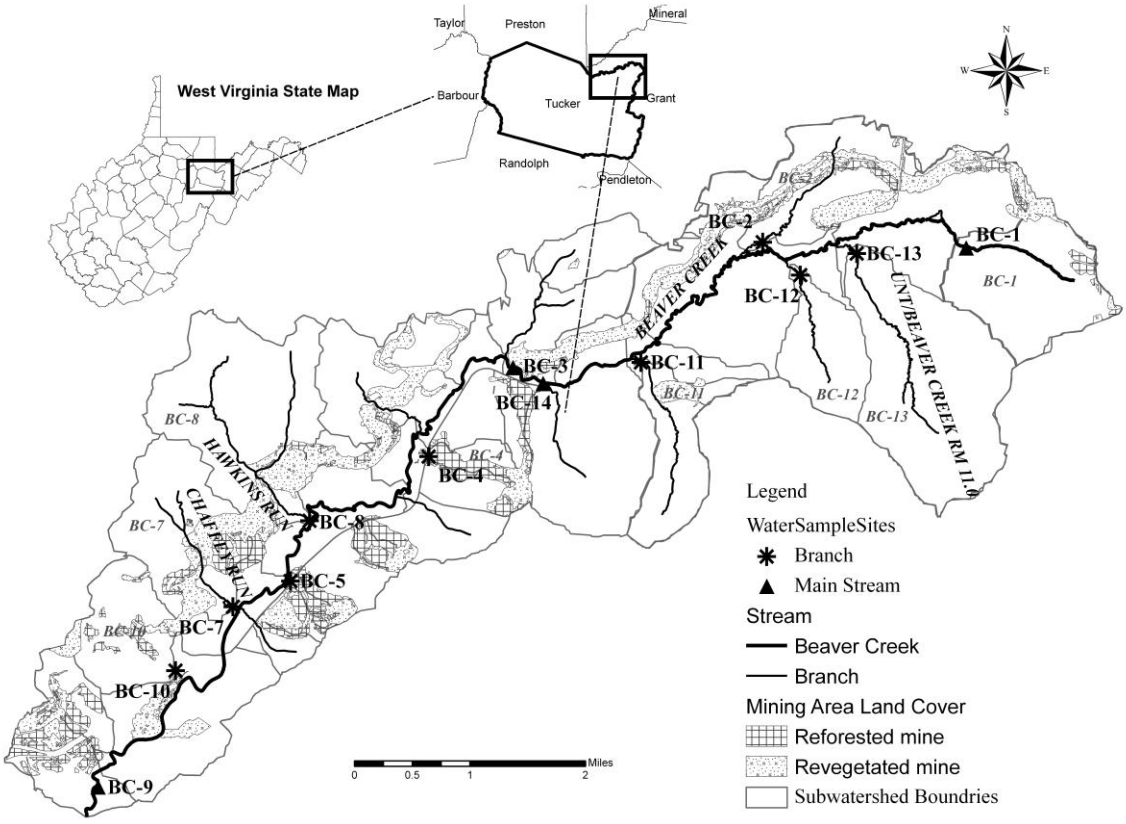

Figure 1. Sampling sites in *Beaver Creek* watershed in Central WV

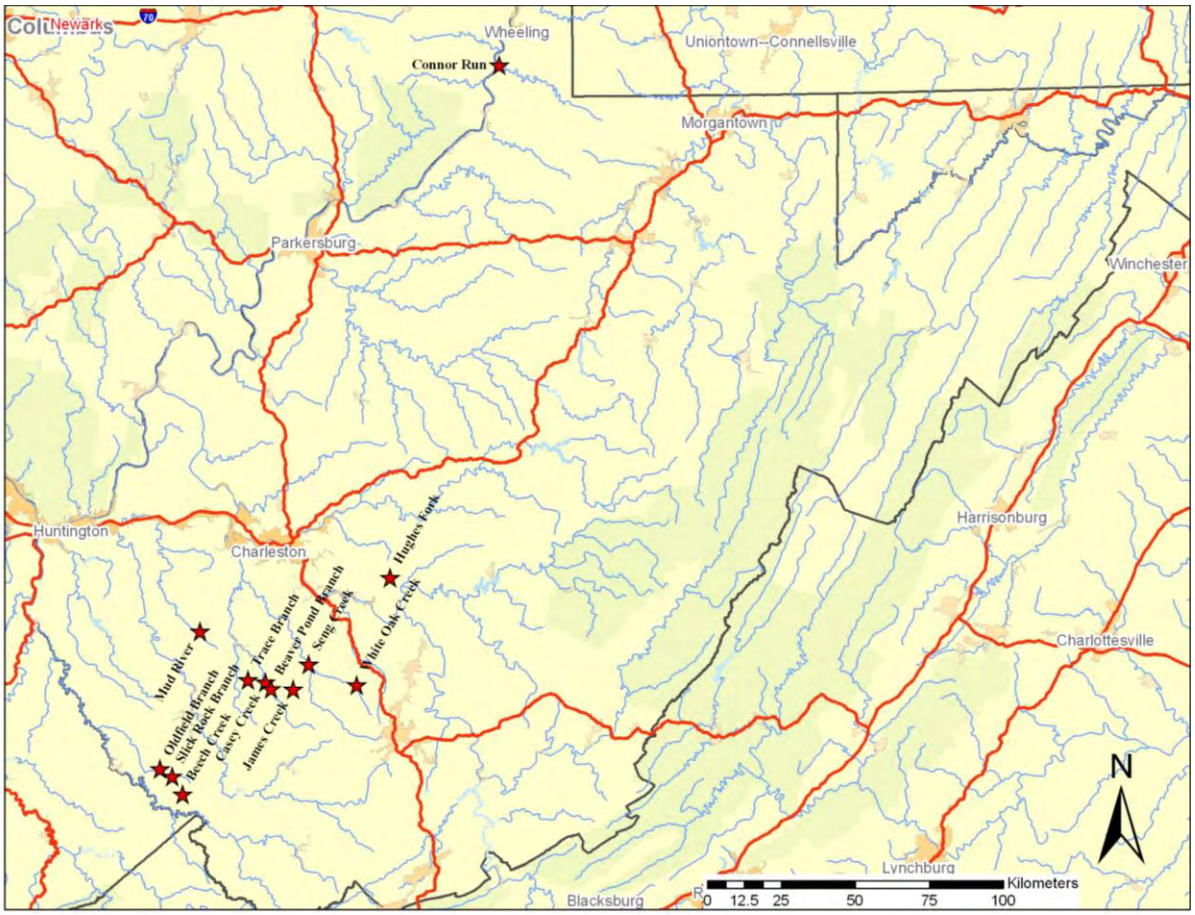

Figure 2. Sampling sites in mining impacted watersheds in Northern and Southern WV

Table 1. Water quality method and detection limits.

Analytical Test	Method	Detection Limit
pH	4500 H+ - B	0.1 pH units
Specific Conductance	2510 B	10.0 µS/cm
Alkalinity	2320 B	0.75 mg/L as CaCO3
Acidity	2310 B (4d)	0.75 mg/L as CaCO3
Sulfate	4500 - SO4 - E	7.0 mg/L
Iron, Total	3120 B	0.1 mg/L
Calcium	3120 B	0.1 mg/L as CaCO3
Magnesium	3120 B	0.1 mg/L
Manganese	3120 B	0.01 mg/L
Aluminum	3120 B	0.1 mg/L

2.2 Evaluation of Selenium Removal Using Nano-Magnetite in Batch Adsorption Tests

2.2.1 Materials

Analytical grade chemicals of iron (III) sulfate ($Fe_2(SO_4)_3$), ammonium hydroxide (NH_4OH), sodium hydroxide (NaOH) and sulfuric acid (H_2SO_4) were purchased from Fisher Scientific, Inc. (Rochester, NY). Iron (II) sulfate ($FeSO_4 \cdot 7H_2O$) and sodium selenate (Na_2SeO_4) were obtained from ACROS Organics (NJ, USA). Sodium selenite (Na_2SeO_3) was purchased from MP Biomedicals (Solon, OH). All chemical solutions were prepared using Millipore de-ionized water. A stock solution of 100 mg-Se/L was prepared with de-ionized water using the aforementioned Se salts, and working solutions (50, 100, 250, 500 and 1000 µg-Se/L) for the adsorption experiments were prepared from the stock solution. Natural magnetite (<5 microns, Fe_3O_4) was acquired from Cerac Inc. (Milwaukee, WI) and zero-valent nano-iron (~10 nm, element Fe) was obtained from Quantum Sphere (Santa Ana, CA).

2.2.2 Nano-magnetite preparation

Synthesis of nano-magnetite was performed under room temperature using a coprecipitation method developed by Wei and Viadero (2007). Briefly, a solution of $[Fe^{3+}]:[Fe^{2+}]= 2:1$ was prepared with de-ionized water that was de-aerated by $N_{2(g)}$ bubbling prior to use. A 25% ammonium hydroxide solution was gradually added to the solution to form black precipitates. Precipitation was allowed to continue at 25°C for 30 min, with mechanical stirring and continuous $N_{2(g)}$ bubbling. The synthesized nano-magnetite particles were then separated from the solution using a magnet. After that, the magnetite particles were washed 3-4 times by re-suspending the particles in de-ionized water followed by centrifugation at 4000 rpm for 10 min (Sorvall RC 5C+ centrifuge). The nano-magnetite was then vacuum-dried and pulverized. Particle sizes were analyzed by a transmission electron microscope (TEM) and estimated to range from 10 to 20 nm. In addition, natural magnetite (<5µm) or nano-iron (~10 nm) were also evaluated as adsorbents for the purpose of comparison. The amounts of adsorbents applied in the experiments were reported in grams of dry weight.

2.2.3 Batch adsorption studies

Batch adsorption experiments were performed by mixing 100 ml of Se (selenite or selenate) solutions of different concentrations with predetermined amounts of the three adsorbents (0.1, 0.5, 1.0, 2.0 and 5.0 g/L) in a temperature-controlled shaker (200 rpm) at 25ºC for 24 h. Each mixture was then subject to a magnet to separate nano-magnetite from the solution and the supernatant was subsequently filtered through a 0.45 µm membrane filter. Se concentration was measured using a graphite furnace atomic absorption spectrometer (GFAAS, Varian SpectrAA 210 Zeeman). Adsorption kinetics was studied by allowing adsorption to take place for different periods of time ranging from 5 to 1440 min with two initial Se concentrations (100 or 250 µg-Se/L) at pH 4 and at 25ºC. The effect of pH was evaluated for the range of 2 – 9 with increment interval of 1. The solution pH was adjusted by adding diluted H_2SO_4 and NaOH and adsorption was allowed to last for 24 hrs to ensure the adsorption equilibrium. Temperature effects were evaluated for the range of 25 – 45°C for three initial Se concentrations (100, 250 and 500 µg-Se /L). Adsorption capacities wee

characterized by developing isotherms (e.g. Freundlich) for equilibrium conditions (24 hrs) at two different levels of initial pHs (4 and 6). All the adsorption tests were carried out in triplicates and the mean values were reported.

2.2.4 Effect of interfering anions

Three competitive anions (chloride, sulfate and nitrate) that may co-exist with Se oxyanions in water or wastewater were also studied for their effect on Se adsorption. The experiments were conducted at 25ºC, pH 4.0 ± 0.1 and adsorbent dose of 0.1 g/L for a contact time of 24 h. The concentrations of the various anionic species were controlled at 0.05 M. The effect of sulfate anions was further investigated by varying its concentrations (0.01, 0.03, 0.05 and 0.1 M) with all other experimental conditions remaining unchanged.

2.3 Impregnation of Diatomaceous Earth (DE) with Nano-Magnetite and Batch Adsoprption Test

2.3.1Materials

The analytical grade chemicals used were iron (III) sulfate ($Fe_2(SO_4)_3$), ammonium hydroxide (NH_4OH), sodium hydroxide (NaOH), nitric acid (HNO_3), sodium nitrate ($NaNO_3$), sodium chloride (NaCl), Sodium Sulfate (Na_2SO_4), oleic acid ($C_{18}H_{34}O_2$), and ethanol (anhydrous) purchased from Fisher Scientific, Inc.(Rochester, NY). Iron (II) sulfate ($FeSO_4.7H_2O$) and sodium selenate (Na_2SeO_4) were obtained from ACROS Organics (NJ, USA). Sodium selenite (Na_2SeO_3) was purchased from MP Biomedicals (Solon, OH). Celite 545 (flux calcinated diatomaceous earth) was acquired from World Minerals (CA, USA). All the chemical solutions utilized were prepared using Millipore deionized water. A stock solution of 100 mg/L of selenium was prepared with de-ionized water using the aforementioned selenium salts, and the working solutions (100, 250, and 500 μg/L) for the adsorption experiments were prepared from the stock solution.

2.3.2 Impregnation of DE with nano-magnetite and characterization

In order to obtain a uniform coating, the surface of the diatomaceous earth (DE) was modified using oleic acid. 10 g DE and 50 ml of de-ionized water were mixed in a beaker for 10 min. with a magnetic stirrer, followed by the addition of 1ml of oleic acid and continued stirring for 60 min. Then, 6ml of ammonia solution was added and mixed for a period of 8 hr. The resulting mixture was centrifuged for 5 min at 4000 rpm, rinsed with 1:1 ethanol/water solution 3-4 times and dried overnight at room temperature. The DE impregnation was achieved through coprecipitation at room temperature, in the presence of both ferric and ferrous iron. In order to avoid the presence of dissolved oxygen in the liquid phase, N_2 bubbling was maintained throughout the process. First, a solution containing 210.35 ml of de-ionized water and 48.3 ml of Fe^{3+} solution [10g/L] was stirred for 10 min, followed by the addition of 241.35 ml of Fe^{2+} solution [1g/L] and 10g of oleic acid-modified DE. After 30 min, 70 ml ammonia was gradually added and a black precipitated was observed. The precipitation process was allowed to occur for additional 30 min with mechanical stirring and continuous $N_{2(g)}$ bubbling. After that, the synthesized particles were

separated from the solution by vacuum filtration using 0.45 μm membrane. The dark precipitate was then resuspended and washed 3-4 times by adding de-ionized water followed by filtration. The final sample was dried overnight at room temperature. By this way, a sample of 10% nano-magnetite impregnated diatomaceous earth (w/w) was obtained.

The morphology of synthesized particles on the DE surface was examined using a Hitachi S-4700 field emission scanning electron microscope (FE-SEM). The mineralogical composition of the sample was determined by X Ray Diffraction. XRD patterns were recorded at a scanning rate of 4º/min on a X'Pert Pro X-ray diffractometer (XRD) by Panalytical Inc equipped with a Cu Kα radiation course under target voltage 40kV and current 30mA. For comparison purposes, XRD patterns of raw DE and pure nano-magnetite (prepared following the same procedure previously described but without adding DE particles) were also recorded. Reference data for the different mineral phases were taken from the RRUFF online database.

2.3.3 Determination of the point of zero charge

Acid/base titrations were performed in order to determine the point of zero charge (PZC) of the new material following the technique described by Schulthess and Sparks (1986). Further, in order to compare the PZC of the nano-magnetite impregnated DE with that of the plain DE and the pure nano-magnetite, acid/base titrations were also carried out for these substrates. The concentration of the acid (HCl) and the base (NaOH) employed for the titrations was 0.02 N. Titration was carried out in three different ionic strength conditions: 0.001 M, 0.01 M and 0.1 M. The point of zero charge (PZC) is indicated by the pH value at which an intersection of three titration curves occurs.

2.3.4 Batch adsorption studies

Batch adsorption studies were performed to examine adsorption of selenite onto nano-magnetite impregnated DE by agitating 100 ml of solution containing selenium ions of desired concentration with predetermined amounts of adsorbent using a temperature controlled incubator shaker at 25ºC for 24 h at 200 rpm (Fig. 3). The resulting mixture was filtered through a 0.45 μm membrane filter and the selenium concentration was measured using a Varian SpectrAA 210 Zeeman graphite furnace atomic absorption spectrometer (GFAAS). The amount of adsorbent applied during each test is reported in grams based on its dry weight. To test the effect of contact time, a series of conical flasks with selenite/selenate solutions (250 μg-Se/L) and 0.5 g/L of adsorbent were shaken for periods of time ranging from 5 min to 24 h at pH 3 and at 25ºC. The effect of pH on selenite removal was studied using a series of 100 ml solutions of selenite (250 and 500 μg-Se/L) and selenate (100 and 250 μg-Se/L) with 0.5 g/L adsorbent at 25ºC. The pH of the solutions was adjusted in the range pH 2-9 by adding dilute solutions of HNO_3 and NaOH and shaken for 24 hrs to ensure the adsorption equilibrium. To examine the effect of temperature on selenium adsorption, a dose of 0.5 g/L nano-magnetite impregnated DE was added to batches of 100 mL solutions of selenite (250 and 500 μg-Se/L) and selenate (100 and 250 μg-Se/L). Then the solutions were shaken for 24 h at five different levels of temperature: 25, 30, 35, 45 and 60°C. The effect of competing anions such as chloride, sulfate and nitrate that may coexist

with selenium oxyanions in water or wastewater was studied. The experiments were conducted at 25ºC, pH 3.0 ± 0.1 and adsorbent dose of 0.5 g/L for a contact time of 24 h with an initial concentration of 250 µg-Se/L. Sodium nitrate ($NaNO_3$), sodium chloride (NaCl), and sodium sulfate (Na_2SO_4) were used as source for the various anionic species and the ionic strength was controlled at four different levels: 0.1, 1.0, 5.0 and 10 mM.

The desorption of selenite and selenate was evaluated in order to determine if the adsorbent can be regenerated after Se adsorption for reuse. Initially, a series of conical flasks with 100 ml selenite/selenate solutions (250 µg-Se/L) and 0.5 g/L of adsorbent were shaken for 24 h at pH 3 and at 25ºC. Then, samples were taken to measure selenium concentrations in the aqueous phase to determine the amount of selenium adsorption. After that, the pH of the solutions was adjusted in the range pH 4 – 10 using a solution of NaOH and the flasks were shaken for another 24 h. Finally, selenium concentrations in the aqueous phase were measured again to determine the selenium desorption at different pHs.

2.4 Column Adsorption Studies with Nano-magnetite Impregnated DE

Column adsorption tests were carried out by using columns of 1.1 cm diameter and 50 cm length. The columns were packed with ~5.5 g (11.4 cm^3) of the nano-magnetite impregnated DE and the depth was ~12 cm. Thin layers of glass wool (~3cm) and sand (~1cm) were also used at the bottom to provide a base layer of support for the media bed and facilitate the drainage. Columns filled with raw diatomaceous earth (DE) were used as "blank" controls for the experiment.

Feed solutions containing 500 µg-Se/L (selenite or selenate) were continuously supplied to the columns by a squibb pear-shaped funnel. A constant hydraulic head in the column was maintained by making the inflow and outflow rates equal. The pH value of the solutions was fixed at pH 4.0 for selenite adsorption and at pH 3.0 for selenate adsorption. The flow rate was kept at ~0.45ml/min, which corresponded to a space velocity of ~2.2 bed-volumes/h. In order to evaluate the applicability of the adsorption process in treating actual selenium-containing waters (such as mining impacted waters), column adsorption tests were also carried out using water from Monongahela River, near Morgantown, WV, which is heavy impacted by mining drainage. The river water sample was spiked with selenite or selenate solutions at 500 µg-Se/L and the pH was adjusted using concentrated nitric acid. The effluent was collected periodically in 3 mL fractions and subjected to GFAAS analysis in order to determine the concentration of selenium.

3. RESULTS AND DISCUSSION

3.1 Mine Influenced Water (MIW) Sampling and Characterization

Results of water quality analysis for the 9 sampling sites in Beaver Creek, near Davis, Central WV are presented in Table 2. The low pH and elevated metals were typical for mining impacted streams. However, the selenium concentrations in all samples were below detection limit (BDL), indicating streams in this watershed were not impaired by Se.

Table 2. Physicochemical characteristics of water samples in Beaver Creek watershed.

Site ID	pH	Sp. Cond.* uS/cm	Alkalinity mg/L as $CaCO_3$	Acidity mg/L as $CaCO_3$	SO_4 mg/L	Fe mg/L	Mn mg/L	Al mg/L	Ca mg/L	Mg mg/L	Se** µg/L
BC-1	5.3	57.4	14.2	9.1	9.4	0.4	0.0	0.7	5.3	0.5	BDL
BC-4	4.4	294.6	10.4	47.8	107.	2.6	1.9	2.8	18.	8.1	BDL
BC-5	2.9	710.0	0.4	126.4	164.	8.9	5.3	5.8	13.	18.	BDL
BC-9	5.9	143.1	14.5	6.8	50.6	0.7	0.6	0.6	13.	3.8	BDL
BC-10	3.7	231.6	5.2	38.8	65.3	1.7	0.9	2.6	4.7	3.8	BDL
BC-11	4.8	20.0	10.5	6.3	7.2	0.3	0.1	0.2	0.8	0.4	BDL
BC-12	4.5	19.4	10.1	6.4	4.1	0.3	0.1	0.2	0.5	0.4	BDL
BC-13	4.3	22.5	10.1	9.0	5.4	0.5	0.1	0.3	0.5	0.3	BDL
BC-14	5.9	102.9	13.8	8.1	32.5	0.6	0.3	0.4	6.3	1.8	BDL

*Sp. Cond.: specific conductance; BDL: below detection limit.

Results of water quality analysis for the 11 streams in Southern WV and 1 stream in Northern WV are presented in Table 3. Selenium was identified in each stream sampled with concentrations ranging from 0.54 to 16.26 µg/L, indicating all streams in this watershed were impaired by Se. It should be noted that the data in Table 2 were the results of one sampling trip and the Se concentration variations in these streams were unknown.

Table 3. Physicochemical characteristics of water samples in mining impacted streams.

Site ID	pH	Sp. Cond.* uS/cm	Alkalinity mg/L as $CaCO_3$	Acidity mg/L as $CaCO_3$	SO_4 mg/L	Fe mg/L	Mn mg/L	Al mg/L	Ca mg/L	Mg mg/L	**Se µg/L**
MR	7.2	1064	235.4	27.1	711	0.00	0.01	0.14	98.8	102.6	**2.89**
OF	8.2	448	115.0	8.0	156	0.01	0.00	0.04	47.7	28.20	**4.73**
SR	8.2	831	192.3	13.6	445	0.00	0.01	0.06	62.5	92.10	**1.71**
BC	8.0	481	150.6	11.3	200	0.00	0.01	0.00	56.4	33.00	**2.66**
BP	8.3	1129	382.0	12.0	584	0.00	0.01	0.07	69.3	136.5	**5.52**
CC	8.4	738	222.8	5.0	290	0.00	0.01	0.00	51.7	69.15	**4.01**
TB	7.9	461	72.4	7.6	309	0.00	0.00	0.08	50.7	44.55	**1.30**
JC	8.0	1083	300.1	18.9	412	0.02	0.00	0.01	91.0	86.40	**9.69**
SC	8.3	834	183.8	5.2	429	0.00	0.01	0.18	66.6	75.00	**5.31**
WO	8.3	429	89.2	5.5	174	0.00	0.01	0.24	41.7	24.75	**0.54**
HF	8.1	570	130.9	6.7	220	0.00	0.01	0.02	51.0	49.35	**2.51**
CR	8.5	2023	110.5	1.2	720	0.00	0.01	0.28	87.9	13.65	**16.2**

3.2 Batch Adsorption with Nano-magnetite

3.2.1 Effect of contact time

Rapid adsorption was observed in the first 30 min with almost 50% removal of selenite, thereafter the adsorption slowed down and gradually reached equilibrium. Consequently, 24 h mixing was used as the contact time in all further adsorption tests since no significant adsorption was observed after that time period. A similar behavior was observed for Se adsorption on a tropical soil in which the adsorption rate was reported to have been rapid in the first hour, plateaued after 8 h and approached equilibrium at about 24 h (Goh and Lim, 2004). A few other studies in the literature using iron oxide as adsorbents reported comparatively shorter time required for adsorption, such as 2 h reported for adsorption of selenite on different forms of iron oxyhydroxides and ferrihydrite (Parida et al., 1997).

3.2.2 Comparison of nano-magnetite with natural magnetite and nano-iron: selenite (SeO_3^{2-}) and selenate (SeO_4^{2-}) adsorption

Presented in Fig. 3(a) is the effect of adsorbent doses on the selenite removal for the three adsorbents. With an initial selenite concentration of 100 µg-Se/L (comparable to the Se level commonly found in mine water or mining impacted streams), the Se concentration decreased with increasing doses for all adsorbents. The nano-magnetite synthesized for this study clearly demonstrated a superior adsorption performance in removing selenite compared to the nano-iron and natural magnetite. For nano-magnetite, a final concentration of less than 5 µg-Se/L was achieved at a dose of 0.1 g/L with an adsorption capacity of ~ 1 mg-Se per gram of adsorbent. The greater surface area offered by the nano-magnetite in comparison to the natural magnetite (<5 µm) might be the reason for better selenite adsorption. The poor performance of nano-iron could be due to the surface oxidation and severe agglomeration during storage.

Further study was conducted to investigate if the nano-magnetite was equally efficient in removing selenate oxyanion since both selenite and selenate are commonly present in Se laden waters. The effect of adsorbent doses on the final selenate concentration for the three adsorbents is presented in Fig. 3(b). Clearly, natural magnetite was ineffective in removing selenate from aqueous solutions. Nano-iron showed best adsorption for selenate among the three adsorbents, which might be contributed to its stronger reducing power which can convert selenate to selenite, a species considered an easier target for adsorption (Mavrov et al., 2006). Compared with Fig. 3(a), nano-iron demonstrated similar adsorption performance for both selenite and selenate, while nano-magnetite showed lower adsorption for selenate than for selenite. The lower adsorption of magnetite for selenate is not in agreement with a previous study by Martinez et al. (2006), who found that magnetite had similar or greater adsorption for selenate as compared to selenite.

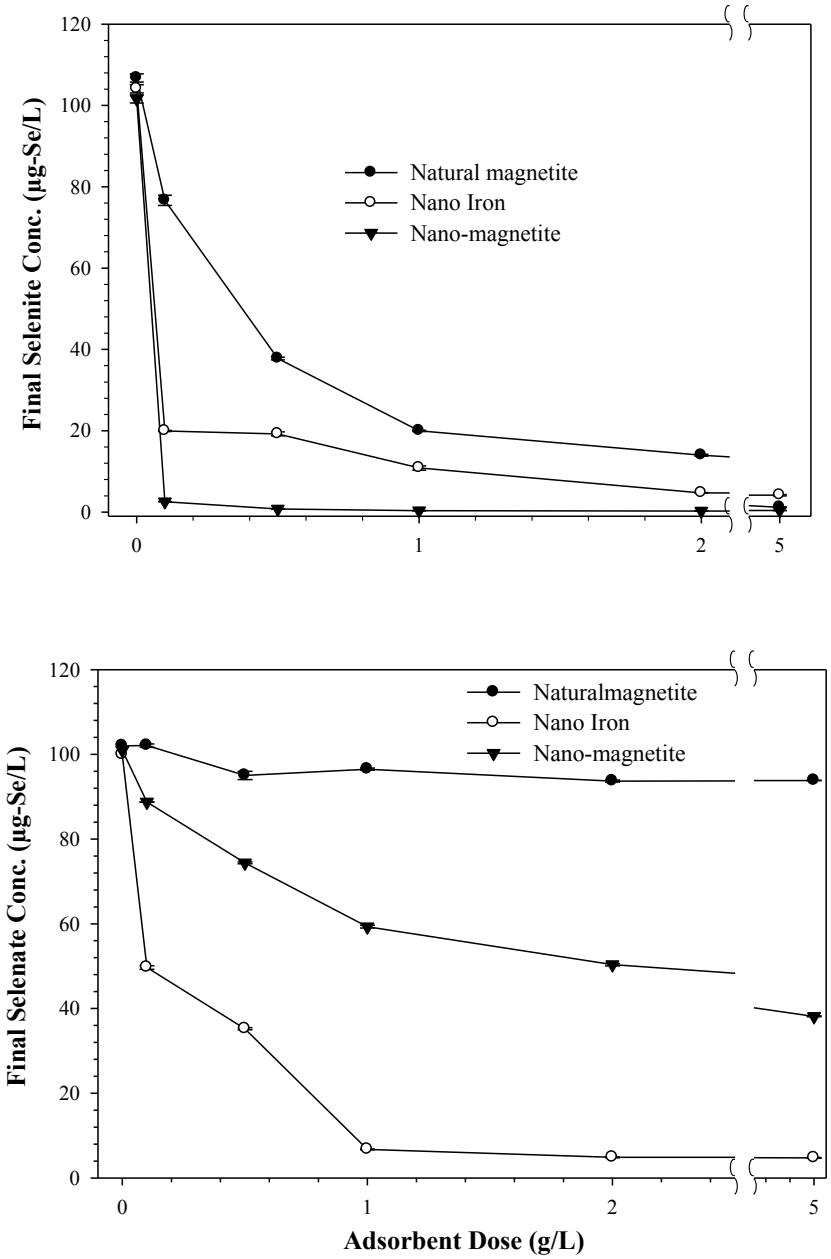

(b)

Figure 3. Selenite (a) and selenate (b) removal by three adsorbents at varying doses (mixing time 24 h; 25°C; pH 4.0±0.1; initial concentration 100 µg-Se/L).

3.2.3 Effect of pH

The effect of pH on final selenite concentration is presented in Fig. 4. The final Se concentration increased as pH increased from 4.0 to 9.0, indicating that lower pH favored Se adsorption. When pH was lower than 4.0, the selenite adsorption onto nano-magnetite was relatively independent of pH. The better Se removal at low pH could be an advantage for nano-magnetite to be used in treating mine water, which is typically low in pH (Wei et al., 2005). The trend followed similar behavior irrespective of initial concentrations of 100 µg-

Se/L and 500 µg-Se/L, showing a significant decrease in selenite adsorption at pH ≥8.0. This behavior could be attributed to two theories, namely surface charge and speciation of Se in aqueous solution. The greater adsorption achieved at pH < 8.0 might be due to the attraction between anionic selenite ions and positively charged adsorbent surfaces because surface charge of nano-magnetite is positive below pH 8.0 and negative above pH 9.0 (Cornell and Schwertmann, 2003). In addition, the biselenite ion ($HSeO_3^-$) being the predominant ion in aqueous solution at a pH range between 3.5 and 8.0 might be responsible for maximum adsorption at the low pH (Rovira et al., 2008; El-Shafey, 2007; Linkson, 1990). Similar trends were previously observed in case of selenite adsorption onto iron oxyhydroxides and ferihydrite and were attributed to characteristic anionic behavior of selenite species (Parida et al., 1997). The similarity repeated with selenite adsorption studies using goethite and hematite where the sorption edge for selenite was reported to coincide with the predominance of $HSeO_3^-$

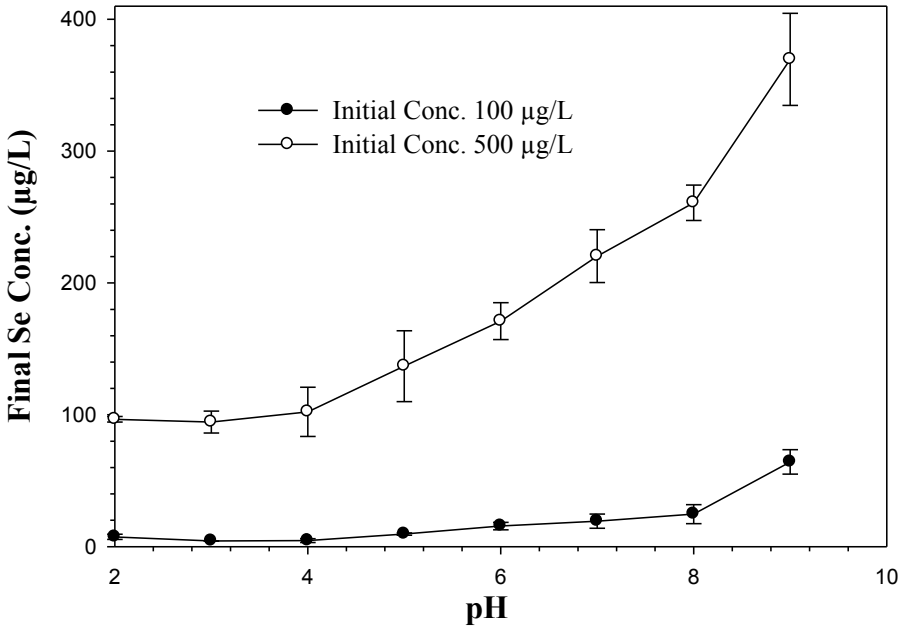

Figure 4. Effect of pH on final selenite concentration (adsorbent dose 0.1g/L; pH 4.0 ± 0.1; mixing time 24h; 20°C; initial concentration 100µg/L and 500µg/L).

3.2.4 Effect of temperature and adsorption thermodynamics

The effect of temperature on final selenite concentration is presented in Fig. 5. It was observed that the final selenite concentration decreased as temperature increased from 25ºC to 45ºC, at which point, the removal efficiency for selenite was above 90%. The trend was independent of the initial Se concentrations, indicating high temperatures favored selenite adsorption onto the surfaces of nano-magnetite. The results were in an agreement with previous studies, in which selenite removal was achieved using iron-coated granular activated carbon (GAC) (Zhang et al., 2008). Selenite adsorption onto untreated Fe(III)/Cr(III) hydroxide solid waste increased as temperature increased from 32 to 60 ºC (Namasivayam and Prathap, 2006). A similar phenomenon was also observed for selenite adsorption using manganese nodule leached residues between 25 to 55 ºC (Dash and Parida,

2007) and selenite sorption onto sulfuric acid-treated peanut shell between 25ºC to 45ºC (El-Shafey, 2(

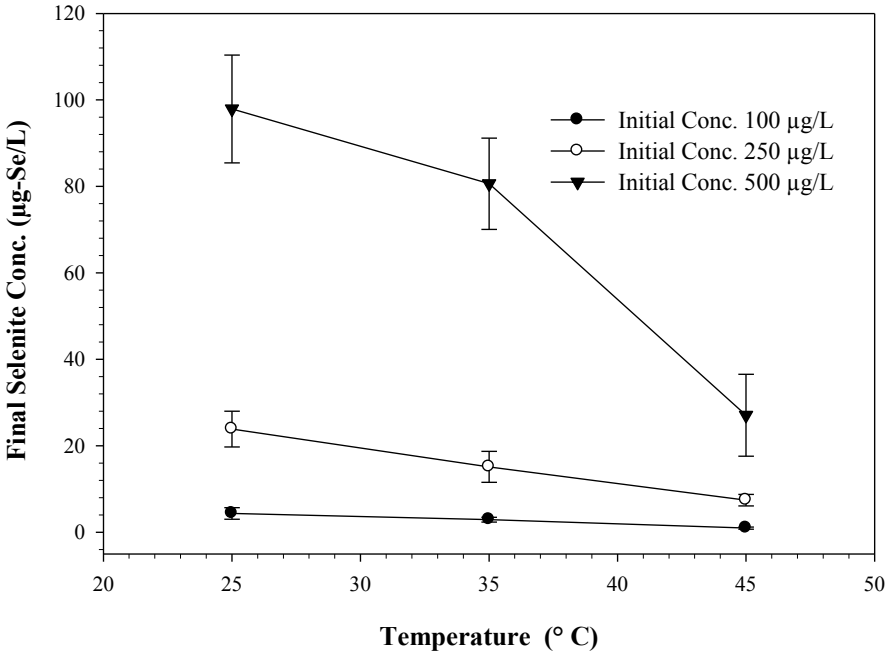

Figure 5. Effect of temperature on final selenite concentration (adsorbent dose 0.1 g/L; pH 4.0 ± 0.1; mixing time 24 h; initial concentrations 100, 250 and 500 µg-Se/L).

The thermodynamic parameters of adsorption, viz. free energy (ΔG^o), enthalpy (ΔH^o_{ads}), and entropy (ΔS^o), were calculated in order to explain the thermodynamic nature involved in the adsorption process. The calculated thermodynamic parameters are presented in the Table 4. The negative values of ΔG^o indicated the spontaneity of the adsorption process. The positive value of ΔH^o_{ads} indicated endothermic adsorption, which explains why the elevated temperature led to enhanced selenite adsorption onto the surfaces of nano-magnetite (Fig. 4(a)). Higher temperature might also have increased the kinetic energy of selenite ions so that they could be transported easily to adsorption sites. The finding was consistent with selenite adsorption onto untreated Fe(III)/Cr(III) hydroxide solid waste and manganese nodule leached residues (Dash and Parida, 2007; Namasivayam and Prathap, 2006). The positive value of entropy change (ΔS^o) revealed an increase in randomness at the solid/solution interface due to the adsorption of selenite onto nano-magnetite.

3.2.5 Adsorption isotherms

Adsorption isotherms can predict adsorption processes at equilibrium conditions and thereby are the best means of assessing the performance of a system (Basha and Jha, 2008). The relationship between equilibrium selenite concentration and adsorption capacity is illustrated in Fig. 6. The adsorption capacity at pH 4.0 was approximately 470 µg-Se/g with a final selenite concentration of 0.80 µg-Se/L and increased to 7,500 µg-Se/g with a final selenite concentration of 347 µg-Se/L. The adsorption capacity was lower at pH 6.0 with 400 µg-Se/g at a final selenite concentration of 3.11 µg-Se/L and 7000 µg-Se/g at 370 µg-Se/L.

The linear relationship on a log-log scale in Fig. 6 indicated adsorption of selenite onto the surface of nano-magentite followed the Freundlich isotherm, expressed by Eq. 1:

$$q_e = KC_e^{1/n} \qquad (1)$$

where C_e and q_e are equilibrium selenite concentration in solution (µg-Se/L) and the corresponding adsorption capacity on nano-magnetite (µg-Se/g-adsorbent), and *K* and *1/n* are empirical constants determined through regression analysis. The *n* values of 2.19 (pH 4.0) and 1.80 (pH 6.0) fell in the range from 1 to 10, indicating favorable adsorption (Basha and Jha, 2008; Hamdaoui and Naffrechoux, 2007). In addition, the applicability of the Freundilch isotherm model revealed that selenite adsorption took place heterogeneously due to the diversity of sorption sites offered by the nano-magnetite.

Table 4. Thermodynamic parameters for the adsorption of selenite on nano-magnetite at different temperatures.

Initial Conc. (µg-Se/L)	Temperature (°C)	K_c	ΔG^0 (kJ/mol)	ΔH^0_{ads} (kJ/mol)	ΔS^0 (kJ/mol/K)
100	25	22.9	-7.7	7.32	0.028
	35	33.3	-9.0		
	45	103.5	-12.2		
250	25	3.2	-2.9	6.43	0.023
	35	5.5	-4.4		
	45	12.5	-6.7		
500	25	0.02	9.5	22.9	0.073
	35	0.2	3.7		
	45	2.7	-2.6		

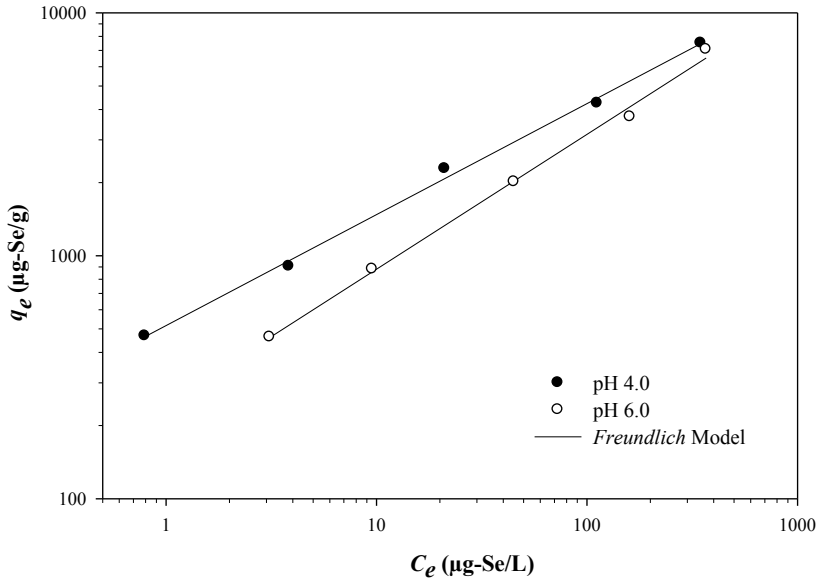

Figure 6. Relationship between equilibrium selenite concentration and adsorption capacity of nano-magnetite (adsorbent dose 0.1 g/L; mixing time 24 h; 25°C).

3.3 Batch Adsorption with Nano-magnetite Impregnated DE

3.3.1 Characterization of nano-magnetite impregnated DE

SEM images of plain DE and nano-magnetite impregnated DE are presented in Fig. 7. The smooth surfaces of plain DE (Fig. 7(a)) were coated with a layer of magnetite nanoparticles (Fig. 7(b)) and the coverage was relatively uniform (Fig 7 (b, c, d). It was also found that the porous structure of DE was partially filled by magnetite (Fig. 7(d)).

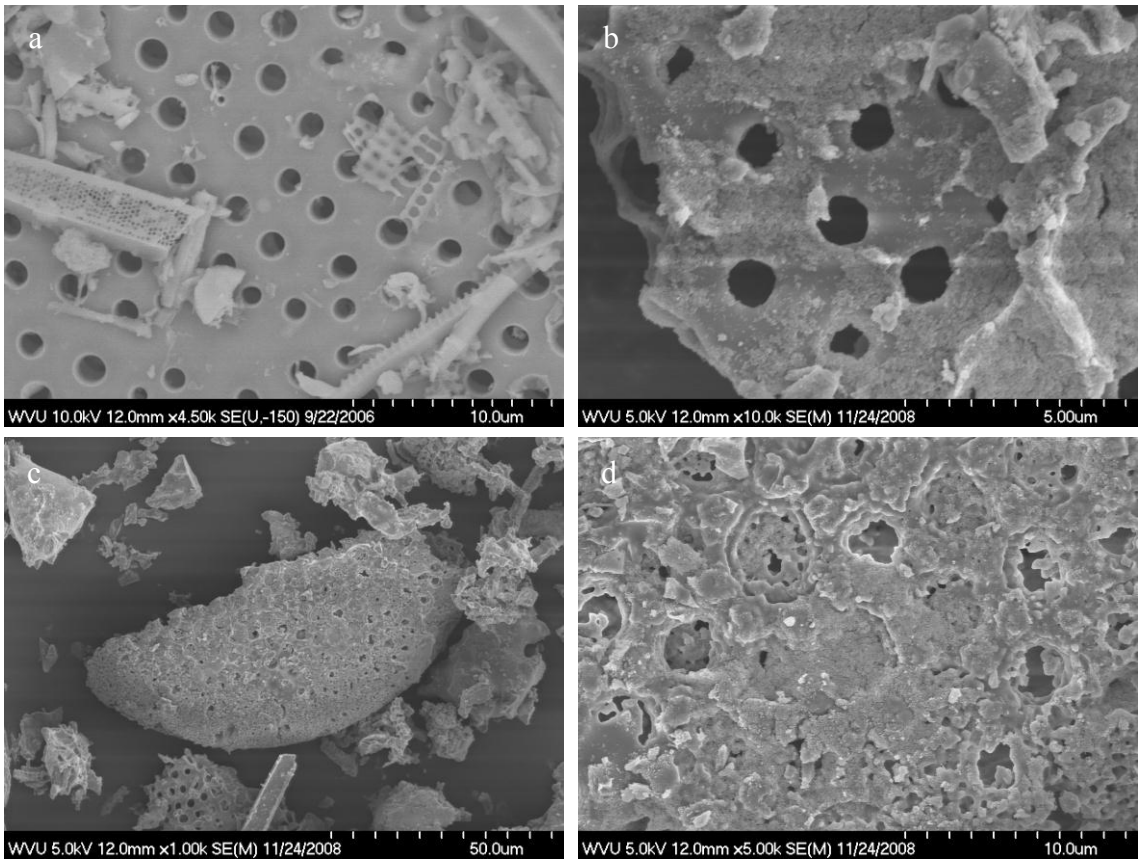

Figure 7. SEM images of (a) pure diatomaceous earth, (b), (c), and (d) nano-magnetite impregnated DE showing a uniform coating.

3.3.2 Point of zero charge (PZC) for adsorbents

The titration curves of raw DE, pure nano-magnetite, and nano-magnetite impregnated DE indicated that the PZC of the raw DE was at pH 2.4, which is in a good agreement with the values reported in the literature for silica (pH ~ 2 – 3) (Persello, 2000) and diatomaceous earth particles (pH 2.0) (Gao et al., 2005). The PZC obtained for pure nano-magnetite particles was 6.5, which coincides with the reported values of 6.0 – 7.0 (Cornell and Schwertmann, 2003). The PZC of nano-magnetite impregnated DE was at pH 6.8. Therefore, the PZC of DE particles moved from pH 2.4 before modification to pH 6.8 after

the impregnation with nano-magnetite, which was almost the same as the PZC of pure magnetite (6.5). The change of DE surface property indicated a good coverage of the magnetite nanoparticles on the surface of DE particles, which is consistent with the results from the SEM images (Fig. 7).

A change in the PZC as a result of modification process has already been reported for other systems of mixed oxides. After the modification of silica particles using aluminum hydroxide ($Al(OH)_3$), it was observed that the resulting zeta potential of the mixed oxide coincided with the PZC of pure $Al(OH)_3$ (pH 9.1) (Meng and Letterman, 1993). In contrast to the $Al(OH)_3/SiO_2$ system, pHpzc measurements for the $Fe(OH)_3/SiO_2$ system showed that the pZC of the mixed oxide was much lower than that of pure $Fe(OH)_3$ (Chan et al., 2009). This difference was considered as the overall results contributed by negatively charged silica and positively charged ferric hydroxide. Furthermore, the $Fe(OH)_3$ coating on the surface of the silica particles was not as uniform as that observed when $Al(OH)_3$ was employed.

3.3.3 Effect of contact time

The effect of contact time on final selenium concentration for selenite is presented in Fig. 8. Rapid adsorption was observed in the first 30 – 60 min with almost 95% removal of selenite. Thereafter, the adsorption slowed down and quickly reached equilibrium (Fig. 8).A similar behavior was observed for selenium adsorption on binary oxide systems such as Al^{3+}/SiO_2 and Fe^{3+}/SiO_2, (Chan et al., 2009) and on different forms of iron oxyhydroxides and ferihydrite (Parida et al., 1997) where the adsorption rate was rapid in the first minutes and approached equilibrium at about 2 h. In the same way, selenite adsorption on magnetite nanoparticles reached equilibrium in approximately 30 min (Lopez de Arroyabe et al., 2008). Longer times to reach equilibrium have also been reported for selenium adsorption: about 30 h for selenium adsorption onto natural magnetite (Martinez et al., 2006), or 50 h for selenium adsorption onto goethite and hematite (Rovira et al., 2008).

The effect of contact time on final selenium concentration for selenate is presented in Fig. 9. For selenate adsorption, it can be seen that as time increases, part of the selenium already adsorbed by the nano-magnetite impregnated DE was released back to the solution (Fig. 9). This phenomenon occurred independently of the initial concentration of selenium (100 µg-Se/L and 250 µg-Se/L) and could be related to the stabilization of the pH in the system during the adsorption test period. Even though an initial pH of 3.0 was set for all the samples tested, after mixing for 24 h the pH values recorded fell in the range 3.2 – 3.5, indicating a consumption of protons from the solution during the sorption process. El-Shafey et al. (2007) reported an increase in the final pH value for a sorption process of selenite using modified rice husk and concluded that the consumption of protons indicated a reduction of selenite.

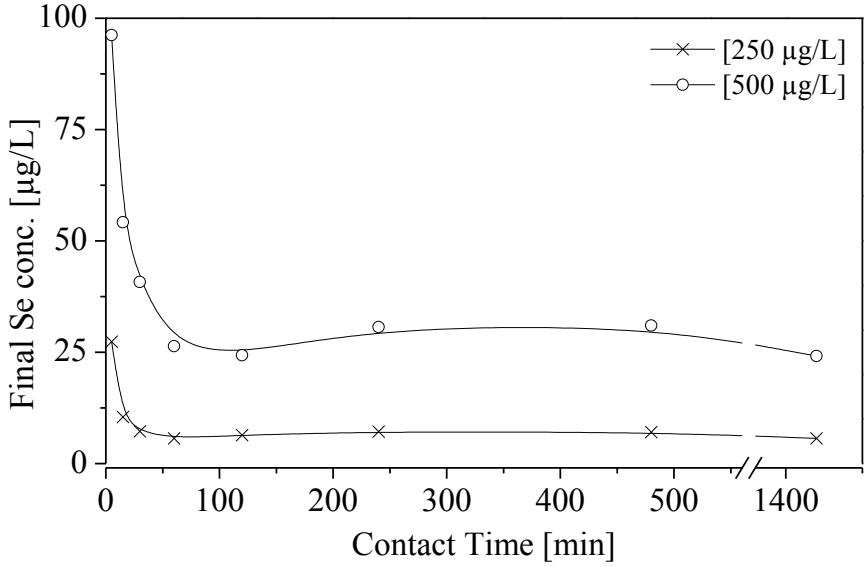

Figure 8. Effect of contact time on final selenite concentration (adsorbent dose 0.5g/ L; pH 3.0 ± 0.1; 25°C; 24 h mixing time; initial concentrations 250 µg/L and 500 µg/L).

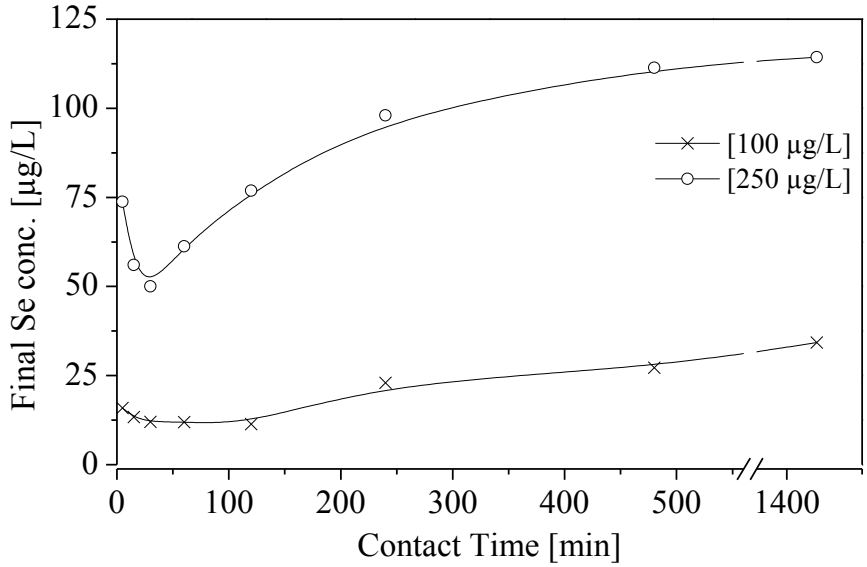

Figure 9. Effect of contact time on final selenate concentration (adsorbent dose 0.5g/ L; pH 3.0 ± 0.1; 25°C; 24 h mixing time; initial concentrations 100 µg/L and 250 µg/L).

The fact that this phenomenon was noticeable for selenite adsorption (Fig. 8, especially at the highest concentration evaluated: 500 µg-Se/L) and evident for selenate adsorption (Fig. 9) could be attributed to a weaker dependence of selenite adsorption on pH in comparison to selenate (as shown in Section 3.3). Previous studies on selenium adsorption onto activated alumina (Ghosh et al., 1994) and Fe^{3+}-coated silica (Chan et al., 2009) concluded that the adsorption of selenate (Se(VI)) was more strongly dependent on pH than that of selenite (Se(IV)). The theory of a partial dissolution of the adsorbent was also considered, although the solubility of magnetite at pH 3.0 was very low. It was reported that at pH 2.0 and a

concentration of 2g/L, less than 1.2% of the magnetite was dissolved after one month (Missana et al., 2009). The small particle size and large surface area might have facilitated the dissolution of magnetite. Our exploratory tests indicated that the dissolved iron in solution was around 0.06 mg/L after 24 h contact time at pH 3.0, corresponding to 0.17% of the iron contained in the nano-magnetite. Since the dissolution of magnetite was almost negligible, the stabilization of pH over time could be the principal factor affecting selenate adsorption.

In order to adequately ensure adsorption equilibriums were reached, mixing time of 24 h was used in all further adsorption tests since no significant changes in adsorption were observed after that time period.

3.3.4 Effect of pH

The effect of pH on selenite and selenate adsorption is shown in Figs. 10 and 11, respectively. In general, it was observed that the sorption of both selenite and selenate oxyanions decreased as pH was increased, indicating that lower pH favored selenium adsorption. In the case of selenite, it was possible to differentiate three stages or levels of adsorption (Fig. 10), irrespective of the initial concentration (250 and 500 µg/L): (1) First, selenite adsorption was relatively independent of pH at low pH (2.0 – 3.5) with very high percent adsorption. (2) Then, the adsorption dropped sharply to 47 – 55% in the range of pH 4.0 – 7.0. (3) Finally, very low or no adsorption occurred at pH values > 7.0. In the case of selenate adsorption, maximum removal (80 – 94%) was obtained at pH < 2.5. Thereafter, a significant decrease in selenate adsorption occurred as pH was increased, and no adsorption was observed at pH > 4.0 (Fig. 11).

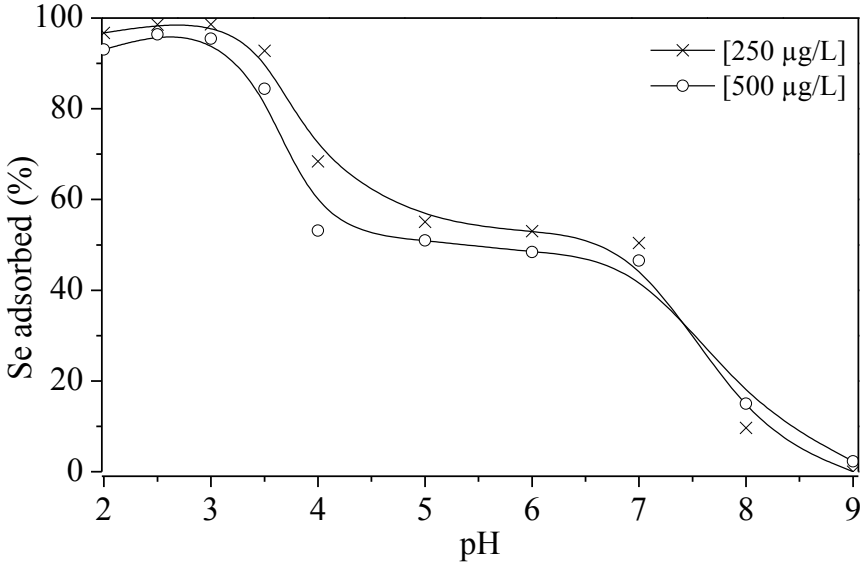

Figure 10. Effect of pH on final selenite concentration (adsorbent dose 0.5g/L; mixing time 24h; 25°C; initial concentrations 250µg/L and 500µg/L).

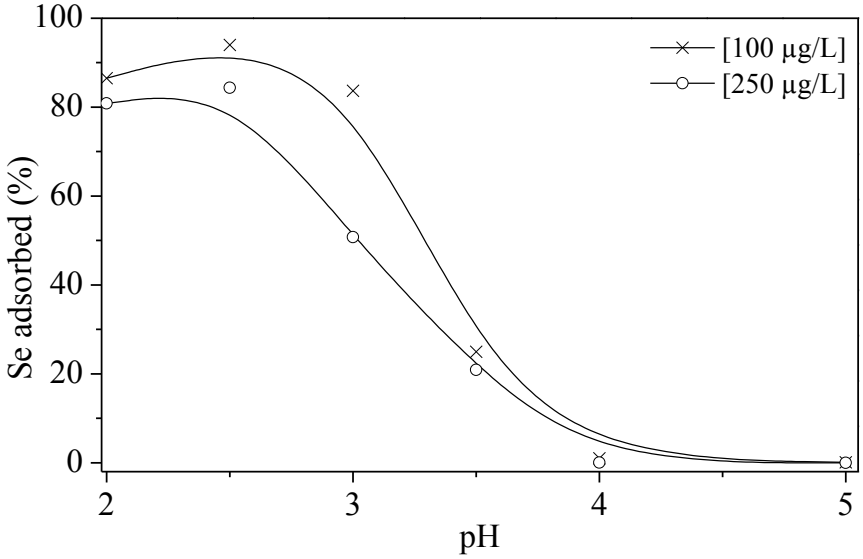

Figure 11. Effect of pH on final selenate concentration (adsorbent dose 0.5g/L; mixing time 24h; 25°C; initial concentration 100µg/L and 250µg/L).

As a result, the effective pH range for adsorption of both selenium species onto the surfaces of nano-magnetite impregnated DE was pH 2 to 3.5. Considering most mine drainages are acidic and some have very low pH, utilization of nano-magnetite impregnated DE for selenium-impaired mine water can be advantageous. In addition, within pH 2 to 3.5, selenate adsorption was more pH dependent and selenite adsorption was relatively pH independent (Figs. 10 and 11), which helped explain the increase of selenate concentration (Fig. 9) because there was a slight pH increase during the course of adsorption tests.

The dependence of selenite/selenate adsorption on the pH can be attributed to two theories, namely surface charge and speciation of selenium in aqueous solution. The PZC of nano-magnetite impregnated DE was at pH 6.8, indicating the surfaces of nano-magnetite were negatively charged at pH>6.8. At pH 7.0 or above as illustrated in Fig. 10, there was a sharp decrease in selenite adsorption by nano-magnetite impregnated DE. There were low selenite adsorption for pH>7 (Fig. 10) and negligible selenate adsorption at pH>4 (Fig. 11). Consequently, the effect of pH on surface charges of nano-magnetite impregnated DE played a significant role in selenium adsorption

On the other hand, the biselenite ion ($HSeO_3^-$) being the predominant form of selenite in aqueous solution at a pH range 2.6 - 8.5 might be responsible for maximum adsorption at low pH, whereas above pH 8.0 selenite (SeO_3^{2-}) species dominates in solution (Plant et al., 2007; Rovira et al., 2008). Similar trends were previously observed in the case of selenite adsorption onto iron oxyhydroxides and ferihydrite and were attributed to characteristic anionic behavior of selenite species (Parida et al., 1997; Goh and Lim, 2004; Rovira et al., 2008;). Likewise for selenate (Se(VI)), the sorption decreased as pH increased due to a reduced fraction of aqueous species $HSeO_4^-$ in solution as well as surface charge variation with pH.

From Figs. 10 and 11, it could be seen that the highest removal efficiency of both selenite and selenate species was achieved at pH 2.5. Besides, the adsorption of selenate was more strongly dependent on pH than that of selenite. At pH > 4.0 the nano-magnetite impregnated DE was not able to adsorb selenate from solution (Fig. 11) but it was still able to adsorb 50% of the selenite oxyanions (Fig. 10). Selenite typically has a significantly greater propensity to adsorb (attach) onto other molecules than selenate due to its level of protonation. Since the pK_{a1} for selenate (pK_{a1} = 1.7) is lower than that of selenite (pK_{a1} = 2.6), under most naturally occurring conditions the protonation of selenate is diminished which reduces weak bonding with other metal hydroxides. This result is in agreement with previous studies, where it was found that at any given pH value, the binary oxide systems have higher affinities for selenite than selenate, and the selenium oxyanion removal capacity of the binary oxide systems is strongly influenced by the surface charge and the environmental pH (Chan et al., 2009).

3.3.5 Effect of temperature

The effect of temperature on final selenium concentration is presented in Figs. 12 and 13. It was observed that the final selenite concentration increased with a temperature rise from 25ºC to 60ºC, at which point, the removal efficiency was about 60% for selenite anions (Fig. 12) and 10-15% for selenate anions (Fig. 13). The trend was independent of the initial selenium concentration and the selenium speciation (selenite or selenate), indicating high temperatures disfavor selenium adsorption onto the surfaces of nano-magnetite impregnated DE.

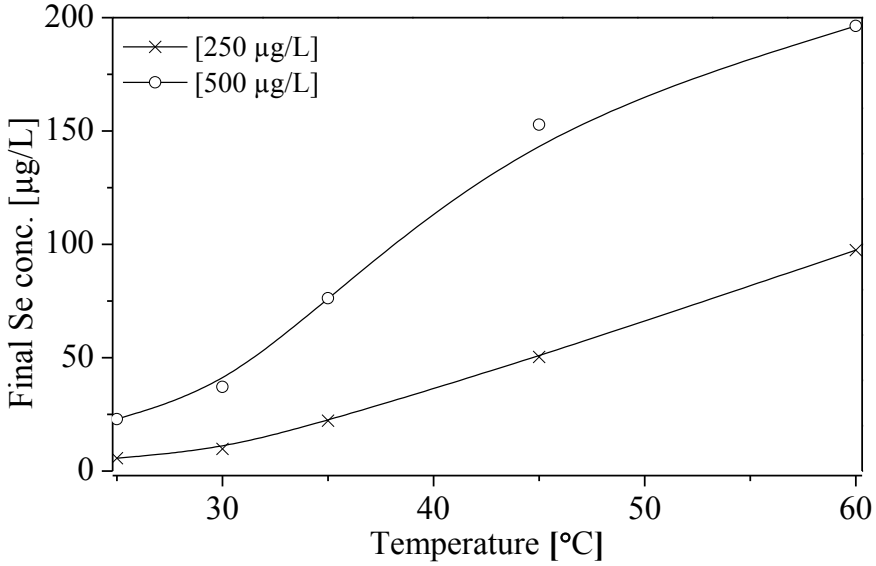

Figure 2. Effect of temperature on final selenite concentration (adsorbent dose 0.5g/L; pH 3.0 ± 0.1; mixing time 24h; initial concentrations 250 and 500 µg/L).

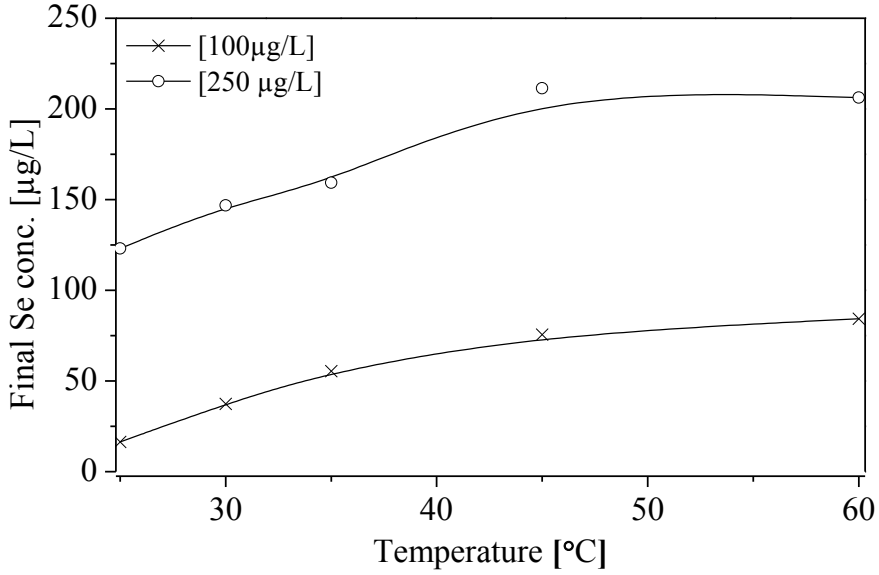

Figure 3. Effect of temperature on final selenate concentration (adsorbent dose 0.5g/L; pH 3.0 ± 0.1; mixing time 24h; initial concentrations 100 and 250 µg/L).

3.3.6 Adsorption Isotherms

Adsorption isotherm data confirmed the applicability of the Freundlich isotherm model indicating selenite adsorption took place heterogeneously due to the diversity of sorption sites offered by the nano-magnetite impregnated DE. In the Freundlich model, the magnitude of the exponent *n* gives an indication on the favorability of adsorption. Values of *n* in the range 2 – 10 represent good, 1 – 2 moderately difficult, and less than 1 poor adsorption characteristics (Treybal, 1981). It is observed that the adsorption of selenite was only favorable at pH 3.0 ($n = 2.13$), whereas at pH 4.0 and 5.0 the coefficients indicated poor adsorption ($n < 1$). This finding is consistent with effect of pH on selenite adsorption. On the other hand, for selenate adsorption the coefficients fell in the range 1 – 2, indicating moderately difficult adsorption at pH 2.0 and 3.0 for selenate, which might explain its poorer adsorption performance by nano-magnetite impregnated DE as opposed to selenite.

3.3.7 Effect of interfering anions

The effect of competing anions as chloride, nitrate and sulfate in the removal of selenite and selenate is shown in Figs. 14 and 15. It was observed that the presence of chloride and nitrate at different concentrations caused a minor decrease in selenite adsorption (from 97% to 93%, Fig. 14) but a significant reduction in selenate adsorption (from 46% to 8-24%, Fig. 15). On the other hand, the presence of sulfate reduced the uptake of both selenite and selenite species significantly (Fig. 14 and 15). At even very small concentration of sulfate (0.1mM), the removal was reduced in almost 10% for both species and at the highest concentration evaluated (10 mM), the removal decreased in 15% and 40% for selenite and selenate anions, respectively.

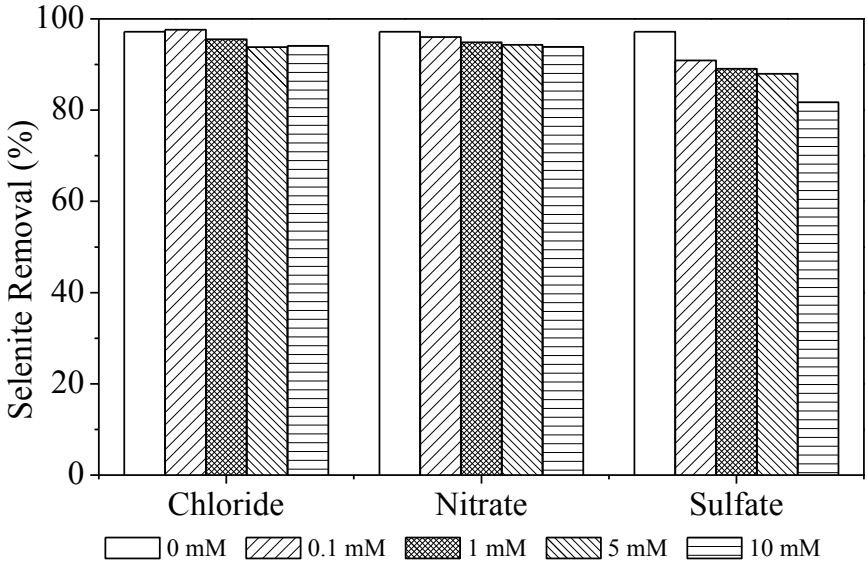

Figure 14. Effect of anions on selenite removal by nano-magnetite impregnated DE (mixing time 24h; 25°C; pH 3.0±0.1; initial concentration 250µg/L; adsorbent dose 0.5g/L).

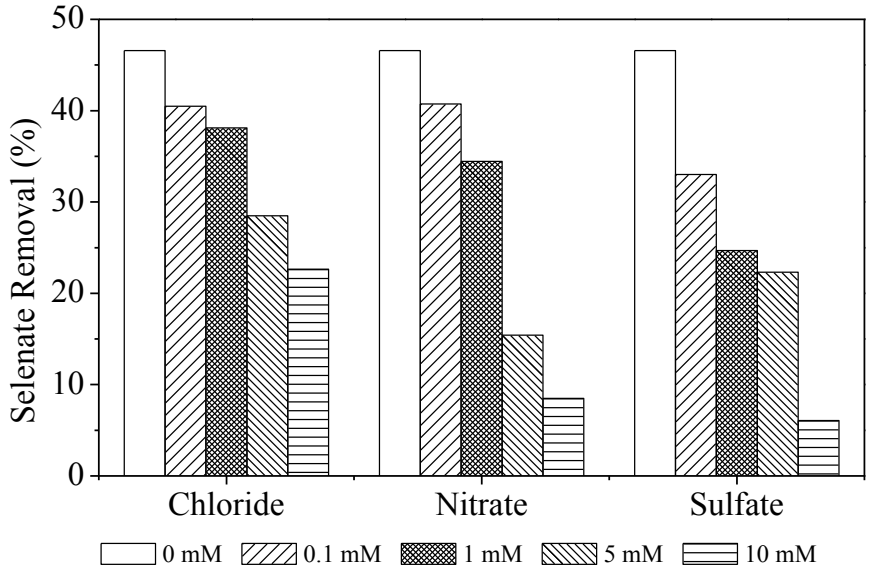

Figure 15. Effect of anions on selenate removal by nano-magnetite impregnated DE (mixing time 24h; 25°C; pH 3.0±0.1; initial concentration 250µg/L; adsorbent dose 0.5g/L).

These observations suggested that sulfate could compete with selenite and selenate oxyanions for adsorption sites. Nonetheless, the adsorption behavior of selenite was less affected by the changes of SO_4^{2-} ionic strength, which is in agreement with previous studies for selenite and selenate adsorption using a tropical soil (Goh and Lim, 2004) and goethite (Hayes et al., 1988) as adsorbents. The relative sorption independence of ionic strength in the case of selenite could be macroscopic evidence for strong specific binding mechanism

(inner-sphere complex) between selenite and the iron oxide (Hayes et al., 1988; Missana et al., 2009). Conversely, adsorbed selenate anions were more easily displaced by sulfate because both of them might only form weak bonds (outer-sphere complex) with the adsorbent (Goh and Lim, 2004).

3.3.8 Desorption tests

The results for selenite and selenate desorption from the nano-magnetite impregnated DE as a function of pH are shown in Fig. 16. Selenate desorption occurred at lower pH values than selenite desorption. It was observed than a rise in the pH by one unit (pH 3.0 to pH 4.0) produced almost 72% desorption of selenate anions but only 4% of selenite anions. Furthermore, at pH values higher than 5.0 almost all the sorbed selenate anions were desorbed from the nano-magnetite impregnated DE, indicating that the adsorption process was reversible and the nano-magnetite impregnated DE could be regenerated.

In the case of selenite, as pH was raised from 5.0 to 9.0 the percentage of desorbed anions increased gradually from 10% to 90%, and a further increase in the pH did not produce any additional desorption of selenium. A less exhaustive desorption of selenite anions in comparison to that of selenate indicated that the former was strongly bonded to the adsorbent surface, which is in agreement with previous studies for selenium adsorption/desorption on different oxides as aluminum-oxide-coated sand (Kuan et al., 1998) and goethite (Su et al., 2000). Overall, the desorption results demonstrated nano-magnetite impregnated DE could be easily regenerated and reused after adsorption.

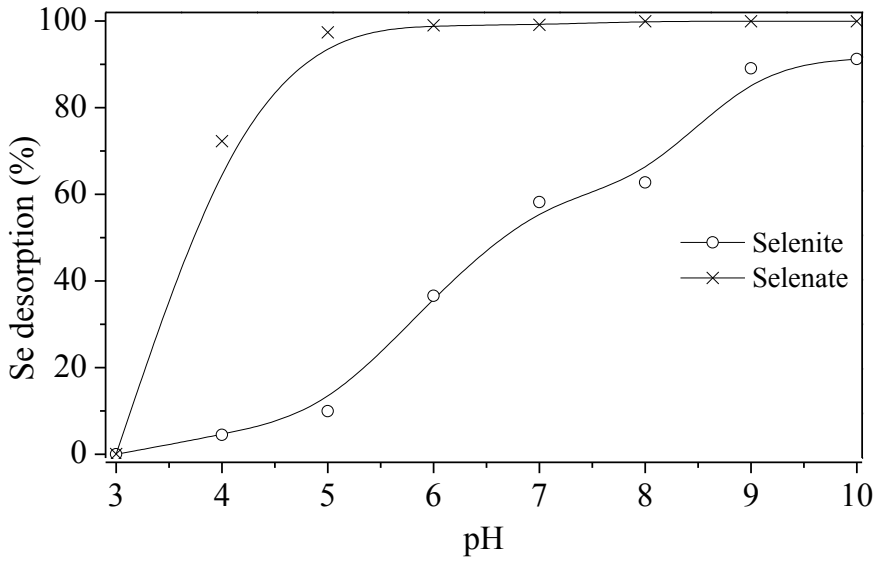

Figure 16. Desorption of selenite and selenate from nano-magnetite impregnated DE as a function of pH for an adsorption process at pH = 3.0±0.1(mixing time 24h; 25°C; initial concentration 250µg/L; adsorbent dose 0.5g/L).

3.4 Column Adsorption Study

Presented in Fig. 17 are the breakthrough curves for the column adsorption of selenite and selenate onto nano-magnetite impregnated DE and plain DE. The selenium concentrations in the effluents are shown in terms of bed volumes (BV) of selenite/selenate solution. The breakthrough point for the curves was identified at the point where there was a rapid increase of selenium concentration in the effluent. From Fig. 17, it was observed that DE itself (control tests) could not remove either selenite or selenate anions from solution, indicating that the selenium adsorption using nano-magnetite impregnated DE can be attributed to nano-magnetite.

When nano-magnetite impregnated DE was used as adsorbent, the column reached saturation earlier for selenate adsorption compared to selenite adsorption, which is consistent with the batch study results. The effluent concentration at the breakthrough point for selenite was 35µg-Se/L, corresponding to 773 bed volumes of solution treated. In the case of selenate, 550 bed volumes passed through the column to the breakthrough point and the effluent concentration was 12 µg-Se/L. The adsorption capacity of the columns at the breakthrough point was ~ 845 µg-Se/g and ~ 600 µg-Se/g for selenite and selenate, respectively.

When Monongahela River water was used instead of deionized water used in preparing the feeding solution, the breakthrough point was achieved earlier for selenite adsorption (Fig. 18). About 540 BV of selenite solution were treated to the breakthrough point, corresponding to a concentration of 50 µg-Se/L. However, in the case of selenate the adsorption was almost negligible and no breakthrough point can be identified in the curve. This phenomenon could be attributed to the presence of competing ions such as chloride and sulfate in the natural water sample, as it can be seen from the chemical analyses presented in Table 4.

Anion competition affected the removal of selenite from Monongahela River water by reducing the volume of water that can be treated in the column to the breakthrough point from 773 to 540 bed volumes (BV). In the case of selenate, the effect produced by the presence of sulfate and chlorides in the water was more dramatic since the lowest concentration in the effluent was 377 µg-Se/L and it quickly increased to 500 µg-Se/L after 40 VB passed through the column. These results are in agreement with the anion competition tests (Figs. 14 and 15), where it was observed that low concentrations of sulfate, chloride, and nitrate had a greater impact on the adsorption of selenate than that of selenite.

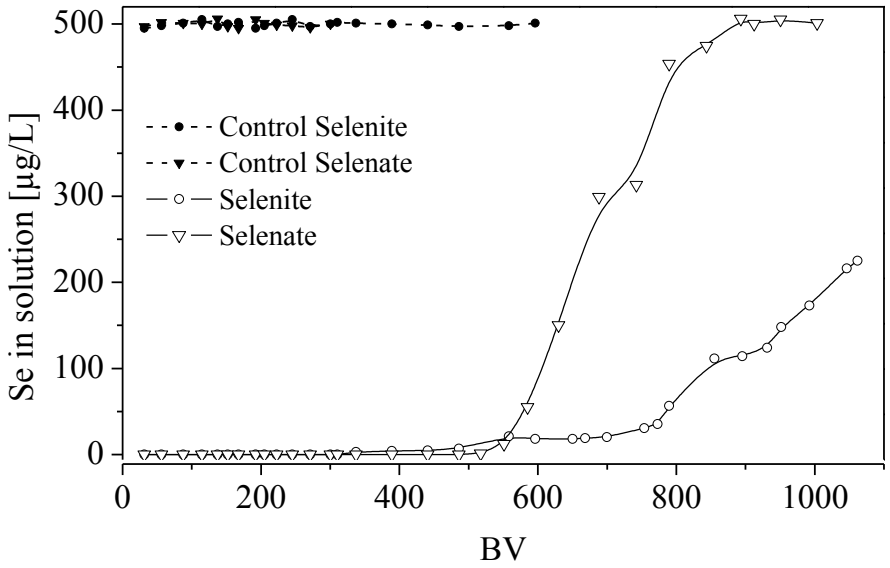

Figure 17. Breakthrough curves for selenite and selenate adsorption by nano-magnetite impregnated DE and plain DE (control tests). Initial concentration 500µg-Se/L; pH = 3.0 for selenate adsorption, pH = 4.0 for selenite adsorption; 1BV ~ 12 cm^3.

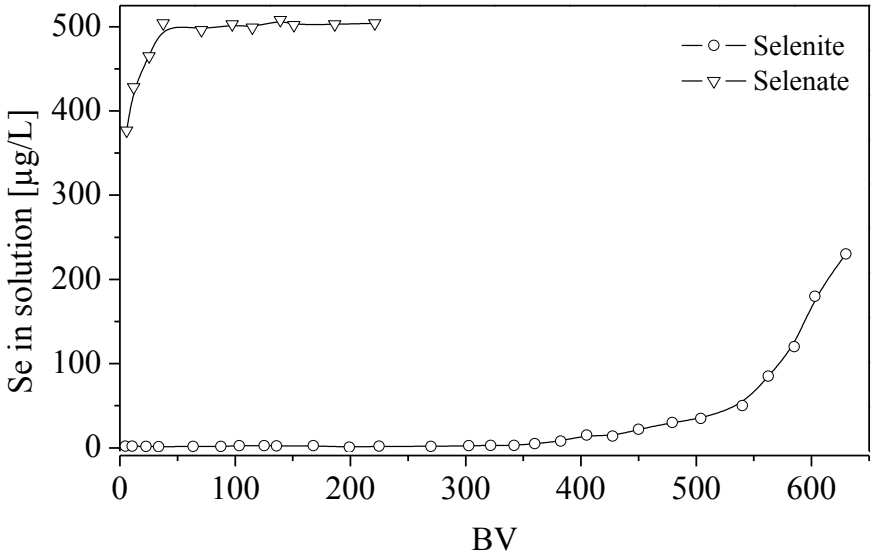

Figure 18. Breakthrough curves for selenite and selenate adsorption when Monongahela River water was used as feeding solution. Initial concentration 500 µg-Se/L; pH = 3.0 for selenate adsorption, pH = 4.0 for selenite adsorption; 1BV ~ 12 cm^3

Table 4. Water chemistry of the Monongahela River sample used for column adsorption studies

Parameter	*Value*
pH	7.94
Total suspended solids (TSS)	1.87 mg/L
Alkalinity	76.06 mg/L as $CaCO_3$
Acidity	10.63 mg/L as $CaCO_3$
Chlorides	19.4 mg/L
Sulfates	203 mg/L
Fe	0 mg/L
Ca	51.1 mg/L
Mg	11.2 mg/L
Mn	0 mg/L

4. CONCLUSION

Water samples collected from a mining impacted watershed in Central WV indicated streams in this watershed were not impaired by Se. Results of water quality analysis for the 11 streams in Southern WV and 1 stream in Northern WV confirmed the presence of selenium in each stream sampled with concentrations ranging from 0.54 to 16.26 μg/L, indicating all streams in this watershed were impaired by Se.

Synthesized nano-magnetite was used as adsorbents to investigate the Se removal from aqueous solutions. As opposed to either natural magnetite (<5μm) or nano-iron (~10 nm), nano-magnetite (10-20 nm) was found to be a better adsorbent for selenite, while nano-iron showed better adsorption performance for selenate. The results indicated that a final effluent concentration of less than 5 μg-Se/L could be achieved in removing selenite from Se laden solutions with initial concentrations of 100 μg-Se/L or lower, comparable to those commonly found in mine water or mining impacted streams. The high selenite removal efficiency in low pH range (<4) was an advantage for nano-magnetite to be used in treating low pH water such as acidic mine water or mine drainage. Adsorption of selenite onto nano-magnetite was a spontaneous, endothermic process, indicating high temperatures favored Se removal. The selenite adsorption followed the Freundlich isotherm model and the adsorption was heterogeneous at the surfaces of nano-magnetite. Presence of common anions did not significantly affect the adsorption capacity of nano-magnetite for selenite. The selective Se adsorption demonstrated nano-magnetite could be a very promising nano-sorbent in removing Se from water or wastewater.

Nano-magnetite was employed to modify the DE surfaces, taking advantage of the functionality of magnetite and DE‟s unique properties, such as high surface area, high porous structure, chemical and thermo-stability, and low cost. This binary oxide system was successfully applied to remove selenium oxyanions from water. The nano-magnetite-impregnated DE showed the potential for achieving drinking water maximum contaminant levels (MCLs) as required by the USEPA. Moreover, the regeneration of this adsorbent could be achieved by increasing the pH to a basic range without affecting the modification process of the diatomaceous earth. The data showed that the maximum removal of selenite and selenate was achieved under acidic conditions (2 – 3.5), indicating the adsorption process was suitable for treating selenium-impaired acid mine drainage. The adsorption of selenate was more strongly dependent on pH than that of selenite. The adsorption of selenite and selenate onto nano-magnetite impregnated DE fitted well the Freundlich model and low temperatures favored Se adsorption. The competition adsorption of sulfate with respect to selenite and selenate was more evident than that of nitrate and chloride.

Column studies showed that adsorption columns could be used to remove both selenite and selenite continuously and nano-magnetite impregnated DE can be a practical solution to selenium-impaired waters. The adsorption capacities obtained in the column adsorption tests were ~ 845μg-Se/g and ~ 600μg-Se/g for selenite and selenate, respectively. From the column studies it was also observed that competing anions such as sulfate and chloride, commonly present in natural waters, reduced the uptake of selenate by the nano-magnetite impregnated DE.

REFERENCES

Adams, D.J., Pennington, P., 2005. Selenium and arsenic removal from mining wastewaters. In 2005 SME Annual Meeting Preprints, Littleton, CO; p. 385-388.

APHA, 1998. Standard methods for the examination of water and wastewater. 20th Ed. Washington, DC: American Public Health Association.

Balistrieri, S.L., Chao, T.T., 1990. Adsorption of selenium by amorphous iron oxyhydroxide and manganese dioxide. Geochimica et Cosmochimica Acta 54(3), 739-751.

Basha, S., Jha, B., 2008. Estimation of isotherm parameters of biosorption of Cd(II) and Pb(II) onto brown seaweed, Lobophora Variegata. Journal of Chemical & Engineering Data 53, 449-455.

Benjamin, M.M., 1983. Adsorption and surface precipitation of metals on amorphous iron oxyhydroxide. Environmental Science and Technology, 17(11): 686 – 692.

Chan, Y.T., Kuan, W.H., Chen, T.Y., Wang, M.K., 2009. Adsorption mechanism of selenate and selenite on the binary oxide systems. Water Research, 43: 4412 – 4420.

Cornell, R.M., Schwertan, U., 2003. The iron oxides: structure, properties, reactions, occurrences, and uses. Wiley-VCH GmbH&Co. KGaA, Weinheim, Germany.

Dash, S.S, Parida, K.M., 2007. Studies on selenite adsorption using manganese nodule leached residues. Journal of Colloid and Interface Science, 307, 333 – 339.

El-Shafey, E.I., 2007a. Removal of se(iv) from aqueous solution using sulphuric acid treated peanut shell. Journal of Environmental Management, 84: 620 – 627.

El-Shafey, E.I., 2007b. Sorption of cd(ii) and se(iv) from aqueous solution using modified rice husk. Journal of Hazardous Materials, 147(1-2): 546 – 555.

Ghosh, M.M., Cox, C.D., Yuan-Pan, J.R., 1994. Adsorption of selenium on hydrous alumina. Environmental Progress, 13: 79 – 88.

Gleason, K.J., Yu, J., Bunge, A.L., Wright, J.D., 1996. Removal of selenium from contaminated waters using emulsion liquid membranes. In: Chemical separations with liquid membranes. American Chemical Society, Washington DC; p. 342–360

Gao, B., Jiang, P., An F., Zhao, S., Ge, Z., 2005. Studies on the surface modification of diatomite with polyethyleneimine and trapping effect of the modified diatomite for phenol. Applied Surface Sci., 250: 273-279.

Goh, K.H., Lim, T.T., 2004. Geochemistry of inorganic arsenic and selenium in a tropical soil: effect of reaction time, pH, and competitive anions on arsenic and selenium adsorption. Chemosphere 55(6), 849-859.

Hamdaoui, O., Naffrechoux, E., 2007. Modeling of sorption isotherms of phenol and chlorophenols onto granular activated carbon. Part I. Two-parameter models and equations allowing determination of thermodynamic parameters. Journal of Hazardous Materials 147 (1-2), 381–394.

Hayes, K.F., Papelis, L. and Leckie, J.O., 1988. Modeling ionic strength effects on anion adsorption at hydrous oxide/solution interfaces. Journal of Colloid Interface Science, 125: 717 – 726.

Hunter, W.J., Manter, D.K., 2009. Reduction of selenite to elemental red selenium by Pseudomonas sp. Strain CA5. Current Microbiology 58(5):493–498.

Kuan, W.H., Lo, S.L., Wang, M.K., 1998. Removal of Se(IV) and Se(VI) fro Water by Aluminum-oxide-coated Sand. Water Research, 32(3): 915 – 923.

Lemly, D.A., 2004. Aquatic selenium pollution is a global environmental safety issue. Ecotoxicology and Environmental Safety 59(1), 44-56.

Linkson, P.B., 1990. The stability of selenium in aqueous system. In: Chemeca 90 The Eighteenth Australasian Chemical Engineering Conference. Auckland, New Zealand; p. 161-168.

Lopez de Arroyave, R., Nikitenko, S.I., Scheinost, A.C., Simonoff, M., 2008. Immobilization of selenite on Fe_3O_4 and Fe/Fe_3C ultrasmall particles. Environmental Science and Technology, 42: 2451 – 2456.

Martinez, M., Gimenez, J., de Pablo, J., Rovira, M., Duro, L., 2006. Sorption of selenium(IV) and selenium(VI) onto magnetite. Applied Surface Science, 252: 3767 – 3773.

Mavrov, V., Stamenov, S., Todorova, E., Chmiel, H., Erwe, T., 2006. New hybrid electrocoagulation membrane process for removing selenium from industrial wastewater. Desalination 201(1-3), 290-296.

Meng, X., Letterman, R., 1993. Effect of component oxide interaction in the adsorption properties of mixed oxides. Environmental Science and Technology, 27: 970 – 975.

Missana, T., Alonso, U., Scheinost, A.C., Granizo, N., García-Gutiérrez, 2009. Selenite retention by nanocrystalline magnetite: role of adsorption, reduction and dissolution/co-precipitation processes. Geochimica et Cosmochimica Acta, 73(20): 6205 – 6217.

Namasivayam, C., Prathap, K., 2006. Removal of selenite using „waste" Fe (III)/Cr (III) hydroxide: adsorption kinetics and isotherms. Toxicological and Environmental Chemistry 88 (1), 85–89.

Neuzil, S.G., Dulay, F.T., Cecil, C.B., Fedorko, N., Renton, J.J., Bhumbla, D.K., 2007. Selenium concentrations in Middle Pennsylvanian coal bearing strata in the Central Appalachian basin. Open-File Report 2007-1090, U.S. Geological Survey, Washington, DC.

Parida, K.M., Gorai, B., Das, N.N., Rao, S.B., 1997. Studies on ferric oxide hydroxides. III. Adsorption of selenite (SeO_3^{2-}) on different forms of iron oxyhydroxides. Journal of Colloid and Interface Science 185(2), 355-362.

Persello, J., 2000. Surface and Interface Structure of Silicas. In Adsorption on Silica Surfaces; Papirer, E., Ed.; Marcel Dekker: New York.

Plant, J.A., Kinniburgh, D.G., Smedley, P.L., Fordyce, F.M., Klinck, B.A., 2007. Arsenic and Selenium. Treatise on Geochemistry, Chapter 9.02, Pages 17 – 66.

Renner, R., 2005. Proposed selenium standard under attack. Environmental Science and Technology 39(6), 125A-126A.

Rovira, M., Gimenez, J., Martinez, M., Martinez-Llado, X., de Pablo, J., Marti, V., Duro, L., 2008. Sorption of selenium (IV) and selenium (VI) onto natural iron oxides: Goethite and hematite. Journal of Hazardous Materials 150(2), 279-284.

Schulthess, C.P., Sparks, D.L., 1986. Backtitration technique for proton isotherm modeling of oxide surfaces. Soil Science Society of America, 50: 1406 – 1411.

Sharmasarkar, S., Vance F.G., 2002. Selenite-selenate sorption in surface coal mine environment. Advances in Environmental Research, 7: 87 – 95.

Su, T., Guan, X., Gu, G., Wang, J., 2008. Adsorption characteristics of As(V), Se(IV), and V(V) onto activated alumina: Effects of pH, surface loading, and ionic Strength. Journal of Colloid and Interface Science, 326: 347 – 353.

Takada, T., Hirata, M., Kokubu, S., Toorisaka, E. Ozaki, M., Hano, T., 2008. Kinetic study on biological reduction of selenium compounds. Process Biochemistry 43(11), 1304-1307

Treybal, R.E., 1981. Mass-Transfer Operations, 3rd ed., McGraw-Hill.

Twidwell, L.G., McCloskey, J., Miranda, P, Gale, M., 2000. Technologies and potential technologies for removing selenium from process and mine wastewaters. Proceedings Minor Elements, SME, Salt Lake City, UT., pp 53-66.

Wei, X., Viadero, R.C., 2007. Synthesis of magnetite nanoparticles with ferric iron recovered from acid mine drainage: Implications for environmental engineering. Colloid Surface A: Physiochemical and Engineering Aspects 294(1-3), 280-286.

Wei, X., Viadero, R.C., Buzby, K.M., 2005. Recovery of iron and aluminum from acid mine drainage by selective precipitation. Environmental Engineering Science 22(6), 745-55.

WHO, 2003. Selenium in drinking-water. In: Background document for preparation of WHO Guidelines for drinking-water quality. Geneva, World Health Organization. (WHO/SDE/WSH/03.04/13).

Zhang, N., Lin, L.S., Gang, D., 2008. Adsorptive selenite removal from water using iron-coated GAC adsorbents. Water Research 42(14), 3809-3816.

Zhang, P., Sparks, D.L., 1990. Kinetics of selenate and selenite adsorption/desorption at the goethite/water interface. Environmental Science and Technology 24(12), 1848-1856.

APPENDIX 26- Development of Biochemical Techniques for Extraction of Mercury from Coal Impoundments (WV023)

FINAL TECHNICAL REPORT

Contract Title and Number:	Period of Performance:
Crosscutting Technology Development at the Center for Advanced Separation Technologies (DE-FC26-05NT42457)	Starting Date: 10/1/05 Ending Date: 9/30/10

Sub-Recipient Project Title:
Development of Biochemical Techniques for the Extraction of Mercury from Coal Impoundment Water

Principal Investigators:
Jay M. Wiedemann, Richard Squire, and Milson Luce

Contact Address:
West Virginia University
405 Fayette Pike, Orndorff Hal
Montgomery WV 25136

Subcontractor Address:
No subcontracts issued.

Report Information:
Type: Final
Number: 1
Period: 8/17/07 to 9/30/10
Date: 05/08/09
Code: WV010-FINAL

Contact Information:
Phone: (304) 442-3135
Fax: (304) 442-1046
E-Mail: jmwiedemann@mail.wvu.edu

Subcontractor Information:
Phone:
Fax:
E-Mail:

DISCLAIMER

ABSTRACT

Our efforts focus on the biological aspects of mercury (Hg) extraction from waste streams. Specifically, we are studying the application of bacteria inherently resistant to mercury to the bioremediation of mercury-contaminated waste streams. As shown by us and others over the past decade or so, some bacteria inherent to waste streams are capable of thriving in the presence of mercury levels that are otherwise toxic. The bacteria achieve this by binding mercury in the surrounding environment, transporting Hg^{2+} into the cell and subsequently reducing it to Hg^{0}, a less toxic, volatile form of mercury that diffuses out of the cell. Such mercury-resistant bacteria bear a set of genes (the "*mer*" genes) which encode the highly-specific protein transporters, mercury binding proteins, and reductase enzymes involved in this metabolic pathway.

Our research group has formulated four main objectives using a biological approach in order to achieve this goal. These objectives will ultimately allow us to define a spectrum of bacterial species and/or genetic combinations optimum for removing mercury from mercury contaminated sites.

1) Isolate and Identify mercury-resistant bacteria native to WV coal impoundment waste sites in order to incorporate these native bacteria into mercury bioremediation schemes.
2) Genetically characterized these bacteria with respect to the *mer* genes. Because these genes have been shown, in general, to be highly diverse, we likely to encounter different versions of these genes in each of the bacteria we have identified.
3) The mer genes isolated from the mercury resistant bacteria will be used to produce partially purified bacterial mercury resistance proteins with emphasis on the Mer proteins, i.e. MerP and MerA.
4) Our group continued to emphasize the use of a series of naturally occurring, "exclusively binding mercury" Mer ligands, the so- named Mer proteins, a class of bio-organic ligands called "metallothioenes" which are used to regulate metal ions in living organisms. Our focus was three-fold:
    A. Thoroughly understand the structure of this molecule**.**
    B. Understand the nature of the specific bonding
    C. Devise a process where we could use the ligand numerous times.
    Items (A) and (B) provide considerable insight into the functioning of the MerP protein.

TABLE OF CONTENTS

INTRODUCTION

Both elemental (Hg^0) and ionic (Hg^{2+}) mercury are distributed widely in the environment: Hg^0 mainly in air, and Hg^{2+} predominantly in water and soil. Both occur as a result of natural processes, namely volcanic activity and the leaching of ores, but also as a result of human activities, including the burning of fossil fuels, the incineration of waste, and the use of mercury in industrial processes. Both forms are subject to conversion by biological processes into methylmercury and other organomercury salts. The amount of Hg released into the biosphere by human activities has increased since the advent of the industrial age and today accounts for approximately 75% of the environmental input (Mason and Fitzgerald 1996). Globally, this figure may be as large as 70,000 tons per year (Robinson and Tuovinen 1984). A typical soil sample may contain between 20 and 150 parts per billion (ppb) Hg (Von Burg and Greenwood 1991). Appalachian coal typically contains between 150 and 240 ppb. Coal from Northern Appalachia has the highest natural Hg content of all sources of coal in the USA (Telwart et al. 2005). In extreme cases, human activity has discharged enough Hg into the environment to cause large numbers of deaths and birth defects, most notably at Minamata Bay, Japan (Takeuchi et al. 1962).

Most chemical forms of mercury (including Hg^{2+}) are highly toxic. This toxicity is due to the affinity of Hg for the sulfhydryl group present on the amino acid cysteine. By attacking this sulfhydryl group, Hg is capable of rendering a cell's enzymes non-functional. Methylmercury and related organic mercury compounds present an even greater danger, in part because they accumulate in food chains. Despite this potent toxicity, however, some bacteria are capable not only of surviving, but of thriving in the presence of high levels of Hg. This remarkable capability has been studied extensively over the past thirty years (Barkay et al. 2003; Nascimento and Chartone-Souza 2003; Osborn et al.1997). It is achieved by the protein products of the *mer* operon. The seven Mer proteins encoded by this operon work collectively to confer bacterial resistance to multiple forms of Hg. In the case of Hg^{2+}, the Mer proteins transport Hg^{2+} across the plasma membrane and into the cytoplasm, where a mercury reductase (MerA) carries out the critical step of reducing Hg^{2+} to the relatively inert elemental form, Hg^0. Each of these steps is accomplished with exquisite sensitivity for Hg^{2+}. Hg^0, due to its high vapor pressure and low solubility in water, diffuses passively out of the cell and, eventually, into the air.

The *mer* operon is among the most diverse and ubiquitous in bacteria, having been identified in a broad range of species isolated from both environmental and clinical settings. *Mer* operons have been identified on plasmids (Clark et al. 1977; Griffin et al. 1987; Summers and Silver 1972), on transposons (Misra et al. 1984; Huang et al. 1999), and in genomic DNA (Inoue et al. 1991; Wang et al. 1987). As with resistance to antibiotics and other heavy metals, resistance to Hg can be disseminated through populations of bacteria by natural processes (Bogdanova et al. 1998). For the present study, we analyzed the Hg content of a waste sample collected from a West Virginia coal surface mining facility. In addition, we isolated and cultured *in vitro* from this sample several native species of bacteria and examined the susceptibility of these cultures to high levels of Hg.

EXPERIMENTAL

Isolation of Mer A Protein

Samples were collected with sterile containers in 2004 from the Kanawha River near Montgomery, WV and from an impoundment pond at a coal surface mining facility in Cabin Creek, WV. Portions of four independent samples taken from each location were analyzed in triplicate for elemental content using a ThermoFisher Scientific S Series Atomic Absorption Spectrometer (AA) equipped with a vapor generation system, graphite furnace, or flame. Procedures for each element analyzed were based on standard protocols provided ThermoFisher. Total mercury concentration (Hg^{2+}, Hg^{1+}, Hg^{o}, and organic mercury) was measured by cold-vapor atomic absorption spectroscopy. Reagents and standards for atomic absorption were obtained from Acros Organics. Remaining portions of each environmental sample were used to inoculate liquid cultures. Five types of media were inoculated: nutrient broth (NB, Fluka), half-strength NB, Luria broth (LB, Fisher), tryptic soy broth (TSB, Sigma), and litmus milk (LM, Carolina). Cultures were grown at either 25°C or 30°C for 24-48 hours with agitation. These cultures were subsequently streaked onto agar plates containing the same medium and grown at the same temperature for an additional 24-48 hours. At that point, individual colonies were isolated and expanded. Three such pure cultures were identified according to the taxonomic scheme of *Bergey's Manual of Determinative Bacteriology* (Buchanan and Gibbons 1974). Each of these three isolates was then grown in a liquid culture supplemented with $HgCl_2$. Mercury levels in these cultures were increased incrementally over a period of three months from zero up to 27,000 ppb. Reduction of Hg^{2+} by these cultures was demonstrated by elemental analysis. Chromosomal DNA was prepared from bacterial cultures using a GenElute Bacterial Genomic DNA isolation kit (Sigma) according to the manufacturer's protocol. DNA concentrations were determined using a DU 530 Spectrophotometer (Beckman). PCR analyses were performed using Maxime PCR PreMix tubes (Intron Biotechnology) containing 2.5 U of *i-Taq* DNA polymerase, 2.5 mM each dNTP, and 1x reaction buffer. To this premix was added 50 ng of template DNA, 200 ng of each forward and reverse primer, and distilled water to a total volume of 20 µl. The forward (5'-TCCGCAAGTNGCVACBGTNGG-3') and reverse (5'-ACCATCGTCAGRTARGGRAAVA-3') primers used for this study are degenerate primers developed originally by Ní Chadhain et al. (Ní Chadhain et al. 2006) and designed to amplify a 285 bp highly conserved region of the *merA* gene. PCR was carried out in a Techgene thermalcycler (Techne) with the following amplification parameters: an initial denaturation at 94°C for 5 minutes followed by 40 cycles of 94°C for 30 seconds, 56°C for 30 seconds, and 72°C for 30 seconds with a final extension at 72° for 5 minutes. PCR results were analyzed by electrophoresis on 2.0% agarose tris-borate-EDTA (TBE) gels alongside HyperLadder II (Bioline) size standards, stained with ethidium bromide (Sigma), and documented using a FOTO/Analyst Investigator Electronic Documentation and Analysis System (Fotodyne).

Bioreactor for the Removal Mercury from Coal Wastewater

The second focus consists of making a bench top bioreactor by attaching mercury resistant bacteria to a support column. We packed a 500 ml column with a cellulose, medium fiber, pH = 6.5, equilibrated with LB media containing 100 ppm Hg^{2+}. We inoculated the bioreactor with the mercury-resistant bacteria obtained from the coal impoundment pond wastewater.

RESULTS AND DISCUSSION

Isolation of Mer A Protein

We isolated on a variety of growth media a total of 26 bacterial clones: 10 from a sample of water taken from the Kanawha River and 16 from a sample of coal waste taken from an impoundment pond at a West Virginia surface mining facility. Three of these 26 clones we identified using standard morphological and biochemical assays (Buchanan and Gibbons 1974): *Citrobacter freundii* from the Kanawha River and *Enterobacter asburiae* and *Klebsiella pneumoniae* from the coal waste. We analyzed heavy metal content, including that of Hg, in samples taken from the same two environmental sources using standard atomic absorption spectrometric techniques (Table 1). These analyses indicated that the Hg concentration was significantly higher in the impoundment wastewater than in the Kanawha River, West Virginia. The elements Mn, Ni, Fe, and Pb were detected in both the impoundment wastewater and the Kanawha River. The elements Cu, Zn, Se, and Sb were not detected in either source. Levels of Hg, Mn, Ni, Fe, and Pb were significantly higher in the fine coal particles than in either the impoundment wastewater or the Kanawha River. Each of the three bacterial isolates we identified was grown *in vitro*.

Table 1: Elemental Analysis of Coal Impoundment Wastewater and Kanawha River Water

Element	Impoundment Wastewater (ppb)	Kanawha River, WVU Tech Marina (ppb)
Hg**	11.5 $\pm$ 0.3	0***
Mn*	111.2 $\pm$ 0.2	77.5 $\pm$ 21.4
Ni*	229.7 $\pm$ 0.4	20.3 $\pm$ 2.3
Fe*	181 $\pm$ 51	131.0 $\pm$ 9.1
Pb*	28 $\pm$ 5	31 $\pm$ 14

Note: For the elemental analysis on a given element the AA was equipped with a * graphite furnace or ** vapor generation system. ***Below detection limits. The metals *Zn, *Cu, *Se, and *Sb were also below detection limits. All are means $\pm$ S.E.M, where $n = 4$ and for statistical analysis $p < 0.05$ (F test).

Mercury levels in these cultures were increased incrementally over a period of three months by the addition of $HgCl_2$. All three species thrived in the presence of up to 27,000 ppb Hg. In contrast, 8,000 ppb Hg was sufficient to kill a laboratory strain of *Escherichia coli* (MM294). In the cultures of mercury-resistant bacteria, Hg^{+2} was

reduced to Hg^0, as demonstrated by atomic absorption spectrometry using a gas generation system. We subsequently extracted genomic DNA from each of these bacterial cultures, including *E. coli*, and analyzed this DNA for the presence of the *merA* reductase gene. This was accomplished using a PCR assay with primers designed to amplify a highly conserved region of *merA* gene. The products of these PCR reactions were resolved by electrophoresis and are shown in Figure 1.

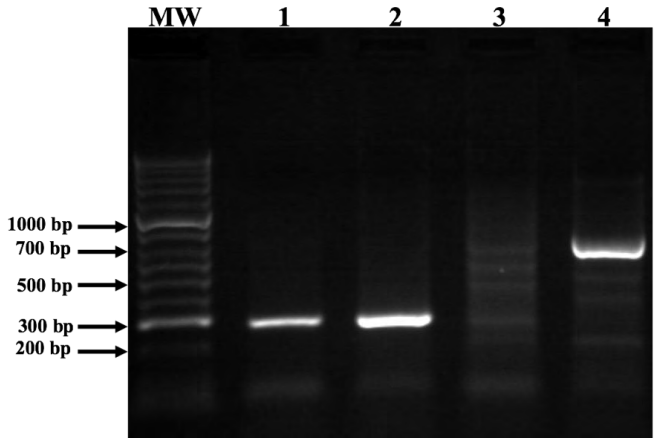

Figure One. Results of PCR analysis of the *merA* gene in chromosomal DNA extracted from bacteria. MW: molecular weight marker with size standards indicated in base pairs (bp); lane 1: DNA from *Enterobacter asburiae* isolated from coal waste; lane 2: DNA from *Klebsiella pneumoniae* isolated from coal waste; lane 3: DNA from the control *Citrobacter freundii* isolated from the Kanawha River; lane 4: DNA from control *Escherichia coli*, laboratory strain MM294. Primers used for the assay were expected to amplify a 285 bp product from a highly conserved region of the *merA* gene.

Our data indicate that native strains of mercury-resistant bacteria may be widespread in West Virginia. As demonstrated by the strain of *C. freundii* we isolated from the Kanawha River, their presence is not necessarily indicative of environmental Hg contamination, but rather of how ubiquitous the *mer* genes are among bacteria. Such bacteria are capable of thriving in the presence of high levels of Hg by employing the product of the *merA* gene, mercury reductase, to convert toxic ionic mercury (Hg^{2+}) to a less toxic volatile form (Hg^0). This raises the possibility of using such bacteria for the bioremediation of mercury-contaminated environments, assuming the volatile Hg^0 can be safely trapped (Chen and Wilson 1997; Von Canstein et al. 1999; Von Canstein et al. 2002; Nascimento and Chartone-Souza 2003). Indeed, the lower than expected levels of Hg detected in the coal particles recovered from the same containment pond from which we isolated the mercury-resistant strains of *E. asburiae* and *K. pneumoniae* suggests a significant environmental role for such bacteria in volatilizing Hg^{2+}. Further genetic and biochemical characterization of such bacteria will facilitate any attempts at bioremediation.

Bioreactor for the Removal Mercury from Coal Wastewater

In the experiments we ran 41 to 61 ppm Hg^{2+} in LB media through the bioreactor for up to 24 hrs. The flow rate was between 1 to 12 ml per min of LB media containing various concentrations of water soluble mercury. After 24 hrs the ending concentration of Hg^{+2} in the LB media from the bioreactor was not detectable by A.A. to 2.1 ppb Hg^{2+} remaining. This corresponded to a 94.8% to 100 % Hg^{2+} reduction after LB media containing Hg^{2+} ran through the bioreactor. Theoretically the elemental mercury is trapped on the bioreactor.

Molecular Modeling of Mer P

We have written a computer program that can identify the backbone by searching for elements in the molecule N-C-C=O that are linked in a series. This program is made of several subroutines. The first lists all carbon-carbon bonds, the second isolates the N-C-C links, and the third identifies all N-C-C=O links. Other subroutines isolate all N-C-C=O links that are connected in series and order them, and saves the backbone data. This step is important since it is possible to locate all components of the molecule using the backbone structure. Then, we can align two different MerP molecules by minimizing the sum of the squares of distances between corresponding atoms of backbones of the two molecules. Figures Two and Three show backbones of two different MerP molecules before alignment from two different points of views.

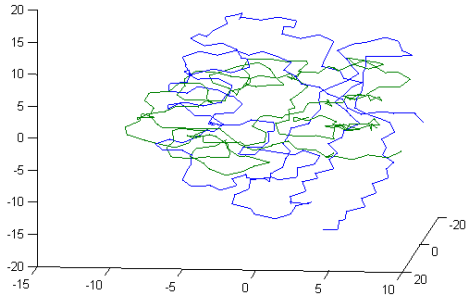

Figure Two

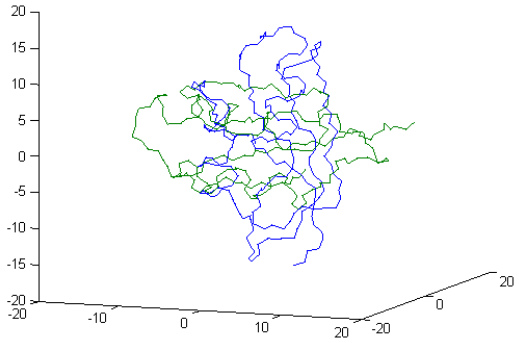

Figure Three

Figures Four and Five show the backbones of the same MerP molecules after alignment from two different points of views.

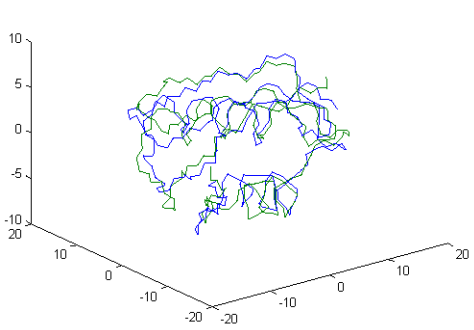

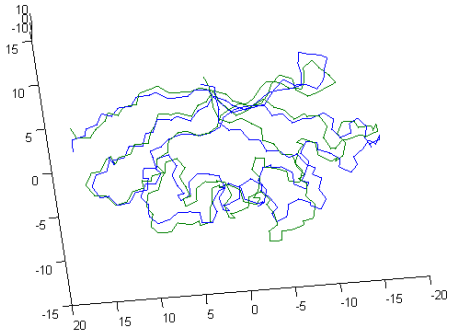

Figure Four Figure Five

By analyzing movements in the MerP molecule before and after bonding with Mercury shows that not only atoms in and near the coordination site move, but also amino acids 39 and 40 as shown in Figure Six.

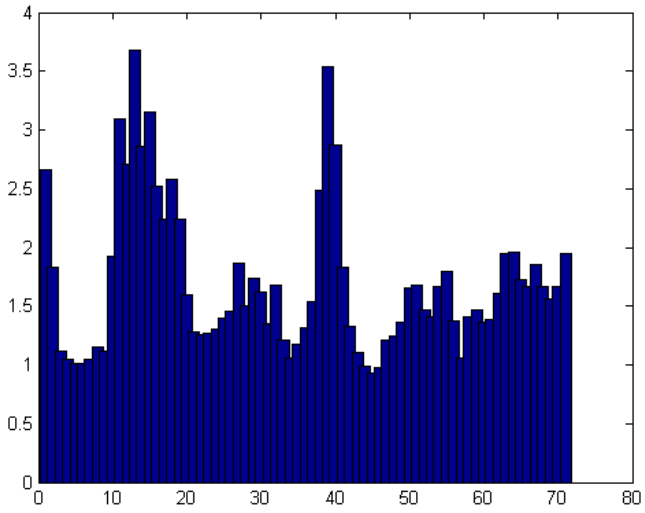

Figure Six

Distribution of the movements of all amino acids has a mean of 1.69 angstroms and the standard deviation is 0.63 angstroms. The Table Two lists the ten amino acids that move the most.

Amino Acid Number	Movement in angstroms	Movement in Standard deviations
13	3.67	3.1
39	3.53	2.9
15	3.15	2.3
11	3.09	2.2
40	2.87	1.9
14	2.86	1.9
12	2.71	1.6
1	2.66	1.5
18	2.58	1.4
16	2.53	1.3

Based on this early, but incomplete, work, one can conjecture that the movement of A.A's around site 40 indicates a crude cooperative effect. Of course the effect is much more subtle than the actual binding by cysteines; Opella, 2002, has synthesized three

MerP Jr. 18 A.A. residues with binding sites CAAC, CACA, and CCAA and they all bind mercury with CCAA being exclusive for $Hg^{2+)}$. Only estimates of various dissociation constants for the MerP Jr. segments are available, but using these Jr. segments, and calculating the actual binding by cysteines in the various conformations and the binding by MerP provides a baseline for measuring enhancements (or the reverse). We can suggest from these results that the phenyl ring (A.A. 38) interacts with the coordinated Hg^{2+} cysteines complex which cannot happen in MerP Jr., hence the modified binding constant vs. MerP Jr. NMR data in solution of mercury bound MerP Jr.'s indicate no preferred conformation. Possibly one reason MerP is CAAC is to take advantage of cooperative effects as opposed to exclusively bind mercury? Undaunted by certain ambiguity in MerP, we examine MerA and immediately see two-fold symmetry, essentially a dimer. In addition there are two pathways, one a "bulk pathway for Hg^{2+} with large ligands, and a small pathway for mercury complexed with, say, two cysteines. The reduction of Hg^{2+} in a complex occurs through inner cysteines (there are a total of 5 per monomer). NAPDH coordinates with a monomer and donates two electrons. The active site is a highly conserved XXCXXC, a common metal ion transport coordination site. Two helpful features for our study of MerA for motions cooperative for rate enhancement are the 40 percent nonconserved regions and the 70 A.A. sequence homologous to MerP which is highly conserved. All of this information Barkay, T., S.M. Miller, and A.O. Summers (2003) is conducive to our aims of finding cooperative effects because we have segments where we know what to look for and can presumable simplify into a tractable model.

The model we will initial follow in our study is that of Schwartz, 2002, modified as described. Our plan for MerA is to reduce an active site and nearby to establish a "neighborhood" for study. This will include a Schwartz (2002), Truhlar, (2006) or other analysis of rate-promoting vibrations in the condensed phase. The second phase will focus on low energy vibrations and their analysis to see if there are coupling parameters. By completing an analysis of MerA similar to the one above and finding the collective motions, we are speculating that these motions can be resolved into harmonic and anharmonic terms of low energy, be they weak vibration, librations, etc. Based on a statistical mechanical analysis of the model we create (as yet undefined), we would anticipate a tractable model to evaluate in a self-consistent manner using a custom fit into DOE'S Oak Ridge's QM/MM model system. Once again the conjecture that part of this is based on follows our work on superconductors where we have analyzed coupled order parameters which provide a very subtle and unusual, almost resonance-like behavior. If we can directly couple this type of collective mode to the rate, we can then establish an enhancement (or de-) factor, and possibly some general trends for other analysis. Our likelihood of success is medium, which is actually much higher than is typical because considerable work has been done on MerA, a large part of it is non-conserved, another large part is similar to MerP, and we have a successful experience with superconductors, but there we had outstanding STM information to guide the work. We have also spent considerable time analysis vibrational interactions in condensed matter systems and view this as an opportunity to provide possible insight into the question as to why proteins are so large; an answer is that they have anharmonic "collective" that reduces the transition state energy in a statistical manner.

CONCLUSION

Our data indicate that native strains of mercury-resistant bacteria may be widespread in WV. As demonstrated by the strain of *C. freundii* we isolated from the Kanawha River, WV, their presence is not necessarily indicative of environmental Hg contamination, but rather of how ubiquitous the *mer* genes are among bacteria. Such bacteria are capable of thriving in the presence of high levels of Hg by employing the product of the *merA* gene, mercury reductase, to convert toxic ionic mercury (Hg^{2+}) to a less toxic volatile form (Hg^0). This raises the possibility of using such bacteria for the bioremediation of mercury-contaminated environments, assuming the volatile Hg^0 can be safely trapped (Chen and Wilson 1997; Von Canstein et al. 1999; Von Canstein et al. 2002; Nascimento and Chartone-Souza 2003). Indeed, the lower than expected levels of Hg detected in the coal particles recovered from the same containment pond from which we isolated the mercury-resistant strains of *E. asburiae* and *K. pneumoniae* suggests a significant environmental role for such bacteria in volatilizing Hg^{2+}. Further genetic and biochemical characterization of such bacteria will facilitate any attempts at bioremediation.

We have used the population of mercury-resistant bacteria native to WV coal impondment ponds to construct continuous flow bioreactors. Initial results indicate that 94.8% to 99.9 % Hg^{2+} is removed from mercury containing wastewaters. A patent is pending on this technology.

We modeled each of the various conformations of the full Mer P protein (72 amino acids) established by x-ray diffraction and NMR techniques. Our modeling using advanced quantum and classical computer molecular modeling tools to try and establish why the binding to Mer P is so strong and selective. A comparison 12 amino acid sequence ("Mer P Jr.") also binds only mercury but is two orders of magnitude weaker. After considerable effort to arrive at the lowest energy conformation, it became apparent that subtle changes in the other 60 amino acids produce the additional binding strength in a small but additive manner, i.e. 2 +/- 1 kcal here, 1 +/-0.75 kcal there almost exclusively by means of hydrogen bond shifts. It is also believed that the slight conformational change that accompanies this binding signals the Mer P operon that mercury is present.

REFERENCES

Barkay, T., S.M. Miller, and A.O. Summers. 2003. *Bacterial mercury resistance from atoms to ecosystems*. FEMS Microbiol. Rev. **27**(*2-3*): 355-384.

Bogdanova, E.S., I.A. Bass, L.S. Minakhin, M.A. Petrova, S.Z. Mindlin, A.A. Volodin, E.S. Kalyaeva, J.M. Tiedje, J.L. Hobman, N.L. Brown, and V.G. Nikiforov. 1998. *Horizontal spread of mer operons among Gram-positive bacteria in natural environments.* Microbiol. **144**(*3*): 609-620.

Buchanan, R.E. and N.E. Gibbons. 1974. *Bergey's Manual of Determinative Bacteriology, Eight Edition.* Waverly Press. Baltimore. 1,246 pp.

Chen S. and D.B. Wilson. 1997. *Construction and characterization of Escherichia coli genetically engineered for bioremediation of Hg^{2+}-contaminated environments.* Appl. Env. Microbiol. **63**(*6*): 2442-2445.

Clark, D.L., A.A. Weiss, and S. Silver.1977. *Mercury and organomercurial resistances determined by plasmids in Pseudomonas*. J. Bacteriol. **132**(*1*): 186-196.

Griffin, H.G., T.J. Foster, S. Silver, and T.K. Misra. 1987. *Cloning and DNA sequence of the mercuric – and organomercurial-resistance determinants of plasmid pDU1358.* Proc. Natl. Acad. Sci. USA. **84**(*10*): 3112-3116.

Huang, C.-C., M. Narita, T. Yamagata, and G. Endo. 1999. *Identification of three merB genes and characterization of a broad-spectrum mercury resistance module encoded by a class II transposon of Bacillus megaterium strain MB1.* Gene **239**(*2*): 361-366.

Inoue, C., K. Sugawara, and T. Kusano. 1991. *The merR regulatory gene in Thiobacillus ferrooxidans is spaced apart from the mer structural genes*. Mol. Microbiol. **5**(*11*): 2707-2718.

Mason, R. and W. Fitzgerald. 1996. *Global and regional mercury cycles: sources, fluxes and mass balances*. Kluwer Academic. Dordecht. 588 pp.

Misra, T.K., N.L. Brown, D.C. Fritzinger, R.D. Pridemore, W.M. Barnes, L. Haberstroh, and S. Silver. 1984. *The mercuric-ion reistance operons of plasmid R100 and transposon Tn501: the beginning of the operon including the regulatory region and the first two structural genes.* Proc. Natl. Acad. Sci. USA **81**(*19*): 5975-5979.

Nascimento, A.M.A. and E. Chartone-Souza. 2003. *Operon mer: bacterial resistance to mercury and potential for bioremediation of contaminated environments*. Genet. Mol. Res. **2**(*1*): 92-101.

Ní Chadhain, S. N., J.K. Schaefer, S. Crane, G.J. Zylstra, and T. Barkay. 2006. *Analysis of mercuric reductase (merA) gene diversity in an anaerobic mercury-contaminated sediment enrichment.* Environ. Microbiol. **8**(*10*): 1746-1752.

Opella, Veglia, G., Porcelli, F., Prantner, A. M., DeSilva, T. M., S. J. Biopolymers (2002) **64**, 189.

Osborn, A.M., K.D. Bruce, P. Strike, and D.A. Ritchie. 1997. *Distribution, diversity and evolution of the bacterial mercury resistance (mer) operon.* FEMS Microbiol. Rev. **19**(*4*): 239-262.

Robinson, J.B. and O.H. Tuovinen. 1984. *Mechanisms of microbial resistance and detoxification of mercury and organomercury compounds: physiological, biochemical, and genetic analyses.* Microbiol. Rev. **48**(*2*): 95-124.

Schwartz, S. D. et al Chem. Rev (2006) **106**, 3170.
Summers, A.O. and S. Silver 1972. *Mercury resistance in a plasmid-bearing strain of Escherichia coli.* J. Bacteriol. **112**(*3*): 1228-1236.
Takeuchi, T., N. Morikawa, H. Matsumoto, and Y. Shiraishi. 1962. *A pathological study of Minamata disease in Japan*. Acta Neuropathol. **2**(*1*): 40-57.
Telwart, S.J., L.J. Bragg, and R.B. Finkelman. 2005. *Mercury in U.S. coal─ abundance, distribution, and modes of occurrence*. United States Geological Survey Fact Sheet 095-01.
Torsvik, V., J. Goksoyr, and F.L. Daae. 1990. *High diversity in DNA of soil bacteria*. Appl. Environ. Microbiol. **56**(*3*): 782-787.
Truhlar, D. in "Isotope Effects in Chemistry and Biology" A. Kohen, A. Limbach, Eds. Taylor and Francis (2006)
Von Burg, R. and M.R. Greenwood. 1991. *Metals and their compounds in the environment: ocurrence, analysis and biological relevance.* VCH. Weinheim. 1438 pp.
Von Canstein, H., Y. Li, K.N. Timmis, W.-D. Deckwer, and I.Wagner-Döbler. 1999. *Removal of mercury from chloralkali electrolysis wastewater by a mercury-resistant Pseudomonas putida strain*. Appl. Env. Microbiol. **65**(*12*): 5279-5284.
Von Canstein, H., S. Kelly, Y. Li, and I. Wagner-Döbler. 2002. *Species diversity improves the efficiency of mercury-reducing biofilms under changing environmental conditions*. **68**(*6*): 2829-2837.
Wang, Y., I. Mahler, H.S. Levinson, and H.O. Halvorson. 1987. *Cloning and expression in Escherichia coli of chromosomal mercury resistance genes from a Bacillus sp*. J. Bacteriol. **169**(*10*): 4848-4851.

BIBLIOGRAPHY

Jay Wiedemann

EDUCATION

1994-2000 Ph.D.- with Dr. Robert C. Nordlie (05/2000) in Biochemistry, Department of Biochemistry and Molecular Biology, University of North Dakota School of Medicine and Health Sciences, Grand Forks, North Dakota.

1991-1994 M.S.- with Dr. Paul M. Anderson in Chemistry, Department of Chemistry University of Minnesota Duluth, Duluth MN.

1986-1991 B.S.- Chemistry and a B.S. in Biology with a minor in Environmental Sciences, Department of Chemistry, University of Wisconsin-Green Bay.

PROFESSIONAL EXPERIENCE

2003-Present Assistant Professor- WVU Tech, Department of Chemistry, Montgomery, WV.

2002-2003 Assistant Professor- Minnesota State University Moorhead, Department of Chemistry, Moorhead, MN.

2000-2002 Assistant Professor- Concordia College, Department of Chemistry, Moorhead, MN.

Patents

1) "Process for removing selenium from air or water", by R. Squire, **J. Wiedemann** and R. Schoening, Invention Disclosure 403, March 20, 2008.

2) "Mercury Removal Protein" by R. Squire, R. Munasinghe, M. Luce and **J. M. Wiedemann.** Application number 60,833,332), July 26, 2007.

PUBLICATIONS

1. **Wiedemann, J.M**., Foster, J.D., and R.C. Nordlie, (2007) "Modifications by Ehrlich Ascites Tumors, *in vivo*, of the Mouse Hepatic Glucose-6-Phosphatase System" *Arch. Biochem. Biophys.* In preparation.
2. Foster, J.D., **Wiedemann, J.M**., PAN, C.J., Chou, J.Y., and R.C. Nordlie (2001) "Discriminant Responses of the Catalytic Unit and Glucose-6-Phosphate TransporterComponents of the Hepatic Glucose-6-Phosphatase System in Ehrlich Ascites-Tumor-Bearing Mice." *Arch. Biochem. Biophys.* Sept 1; 393 (1):117-22.

ABSTRACTS

1. Bricker, A., Broschinski, A. E., Craft, J., Luce, M., Munasinghe, R., Naylor,

M. A., Robinson, C. L., Squire, R. H., and **J. Wiedemann**, "Suggested Structural Changes When the Mer P Protein Selectively Binds Mercury", Presented at the Quantum Theory Project's 47th Sanibel Symposium On Atomic, Molecular, Biophysical and Condensed Matter Theory, University of Florida, Fl, Feb. 22-27, 2007.

2. Broschinski, A. E., Robinson, C. L., **Wiedemann, J. M**., and R. Squire, "Biochemical Approach for Removing Mercury from Coal Impoundment Ponds", Undergraduate Research Day at the Capitol in Feb. 2006.
3. Craft, J.E., C.L Robinson, D.M. Bailey, M.J. Luce, and **J.M. Wiedemann**, "A Biochemical Approach for extracting Mercury from Coal", Undergraduate Research Day at the Capitol in Feb. 2006.
4. Craft, J.E., C.L Robinson, A.E. Bricker, S.M. Holt, M.A. Naylor, M.R. Brackman, M.J. Luce, and **J.M. Wiedemann**, "A Biochemical Approach for Extracting Mercury from Coal", Presented at the Center for Advanced Separation Technologies Annual Workshop, Virginia Tech, Blacksburg, VA, July 26-28, 2005.
5. Broschinski, A. E., Naylor, M. A., Holt, S. M., Robinson, C. L., Bricker, A. E., Craft, J. E., Luce, M. J., **Wiedemann, J. M**., and R. Squire. "Molecular Modeling Approach to Removing Mercury from Coal", Presented at the Center for Advanced Separation Technologies Annual Workshop, Virginia Tech, Blacksburg, VA, July 26-28, 2005.

Richard H. Squire

Curriculum Vitae

Professional Preparation

Northwestern University	Chemistry	B.S.	1967
Wake Forest University	Chemistry	M.S.	1969
University of Cincinnati	Chemistry	Ph.D.	1973

Employment / Appointments

2004 – present: Assistant Professor, WVU Tech, Department of Chemistry – teaching general, organic, analytical and physical chemistry.

2001 – 2004: Training instructor for first responders and military personnel to respond to a chemical and/or WMD incident.

1974 – 2001: Technical supervisor, E. I. Dupont Company, various locations

Patents:

1) "Process for removing selenium from air or water", by **R. Squire**, J. Wiedemann and R. Schoening, Invention Disclosure 403, March 20, 2008.

2) "Mercury Removal Protein" by R. **Squire, R.** Munasinghe, M. Luce and J. Wiedemann. Application number 60,833,332), July 26, 2007.

3) “Methyl Methacrylate Production” (removal of color-formers) by **R. H. Squire**, Canada, 1,281,035, granted 3/5/91.

Publications (selection covering education and integration of chemistry and engineering plus pure research):

1) **R. H. Squire**, H. H. Jaffe, "A Photochemical Reaction with a Preequilibrium Step. The Acid-catalyzed Photochemical Wallach Rearrangement", J. Am. Chem. Soc., 95, 188-89 (1973).

2) **R. H. Squire**, "Ammonia Storage Tank Study", Ammonia Plant Safety, 30, 89, (1990), published by the American Institute of Chemical Engineers

3) J. R. Tilton, R. H. **Squire, C. S**. Saffle, and C. R. Atkins, "Ammonia Storage Tank Study, Part II", Ammonia Plant Safety, 32, 63, (1992), published by the American Institute of Chemical Engineers

4) **R. H. Squire**, "Zero Period Process – A Description of a Process to Zero Injuries, Progress Safety Progress, Vol. 20, No. 1, 1 (2001)

5) **R. H. Squire**, N. H. March, "Does the Crossover from BCS to BEC contain a Feshbach Resonance?" Intern. J. Quant. Chem., **107**, 3013 (2007).

6) K. Morawetz, N. H. March, **R. H. Squire**, "The Chemical Potential for BCS-BEC Crossover in Terms of its Kinetic and Potential Parts with Special Consideration of the Surface Potential Step", Phys Lett. A, 72, 1 (2007),

7) **R. H. Squire**, N. H. March, "Wave Function for a Pre-formed Cooper Pair," accepted for publication, Intern. J. Quant. Chem. (2008)

Milson J. Luce
Curriculum Vitae

Education

1986-1990. B.S., Biological Sciences, (Honors), University of New Orleans, New Orleans, LA. Senior Honors Thesis: immunohistochemical characterization of mouse pancreatic cell types in culture.

1991-1998. Ph.D., Microbiology, University of Alabama at Birmingham, Birmingham, AL. Dissertation: identification and characterization of novel genes involved in human B cell differentiation.

Professional Experience

1998-1999. Postdoctoral Fellow, Yale University School of Medicine, New Haven, CT. Research: transcriptional regulation of the human CD8 genes.

2000-2003. Postdoctoral Fellow, Louisiana State University Health Sciences Center, New Orleans, LA. Research: construction and evaluation of inducible lentiviral vectors for gene therapy.

2003-present. Assistant Professor, West Virginia University Institute of Technology, Montgomery, West Virginia. Teaching: General Biology, Genetics, Cell Biology, Biotechnology.

Publications and Abstracts

1. Sun., L., M.J. Luce, K. Ren, H. Ha, and P.D. Burrows. 1995. Identification of polymorphisms in the constant region of IgG3: the missing mouse allotype. Int. Immunol. 7:337-341.
2. Luce, M.J. and P.D. Burrows. 1998. Minimizing false positives in differential display. Biotechniques 24:766-768.
3. Luce, M.J. and P.D. Burrows. 1999. The neuronal EGF-related genes NELL1 and NELL2 are expressed in hemopoietic cells and developmentally regulated in the B lineage. Gene 231: 121-126.
4. Marino, M.P., M.J. Luce, and J. Reiser. Small to high scale production of lentivirus vectors. In: *Lentivirus Gene Engineering Protocols,* M. Federico, ed. Humana Press Inc., Totowa, NJ, 2002.
5. Pluta, K., M.J. Luce, L. Bao, S. Agha-Mohammadi, and J. Reiser. 2005. Tight control of transgene expression by lentivirus vectors containing second-generation tetracycline-responsive promoters. Journal of Gene Medicine 7: 803-817.
6. Ruan, S., E. Young, M.J. Luce, J. Reiser, J.K. Kolls, and J.E. Shellito. 2006. Conditional expression of interferon-gamma to enhance host responses to pulmonary bacterial infection. Pulm. Pharmacol. Ther. 19:251-7.
7. *Abstract (poster)*: A Biochemical Approach for Extracting Mercury from

Coal, J.E. Craft, C.L. Robinson, A.E. Bricker, S.M. Holt, M.A. Naylor, M.R. Brackman, M.J. Luce, and J.M. Wiedemann. Center for Advanced Separation Technologies (C.A.S.T.) Annual Workshop, July 26-July 28, 2005, Blacksburg, VA.

8. *Abstract (poster)*: A Biochemical Approach for Extracting Mercury from Coal, J.E. Craft, C.L. Robinson, D.M. Bailey; M.J. Luce, and J.M Wiedemann. Third Annual West Virginia Undergraduate Research Day at the Capitol, February 1, 2006, Charleston, WV.

Ranjith A. Munasinghe

Education

B.S. in Electrical and Electronic Engineering, University of Peradeniya, Sri Lanka,1982
M.S. in Mathematics, University of Wyoming ,1987
Ph.D. in Mathematics, University of Wyoming, 1992

Professional Experience

1992-Present: Assistant Professor/Associate Professor/Professor of Mathematics West Virginia University Institute of Technology.
Teaching: Taught more than twenty different undergraduate level mathematics courses and two graduate level courses.
Research Areas: Machine vision, Image processing, Theory of continua.
Current Projects: Object Recognition for Autonomous Systems, Modeling of MerP Molecule.
Supervised three MS thesis and several undergraduate research projects.

1985-1992: Graduate Teaching Assistant, University of Wyoming
1983-1985: Engineer, Riyadh Satellite Earth Station, Ministry of PTT, Saudi Arabia
1982-1983: Engineer, Padukka Satellite Earth Station, Dept. of Telecommunications, Sri Lanka

Publications

1. **R. Munasinghe** and Asad Davari, Elementary Methods for Improving Edge Detector Performance, Proceedings of the the 41st IEEE Southeastern Symposium on System Theory, March 2009
2. **R. Munasinghe**, An Interesting Inverse Limit Space, Topology Proceedings, Vol. 32, pp. 37-46, 2008
3. **R. Munasinghe**, Multidisciplinary Research Projects for Engineering Students Part II, Proceedings of the 40th IEEE Southeastern Symposium on System Theory, March 2008
4. R. Koshy, **R. Munasinghe**, and A. Davari, Design of a Composite Eye for Computer Vision, Proccedings of the 40th IEEE Southeastern Symposium on System Theory, March 2008
5. S. Polmottawegedara, **R. Munasinghe**, and A. Davari, Tracking Moving Targets, Proceedings of the 38th IEEE Southeastern Symposium on System Theory, 2006
6. **R. Munasinghe**, Multidisciplinary Research Projects for Engineering Students, Proceedings of the Annual conference of ASEE, 2005
7. J. Chittooru, **R. Munasinghe**, and A. Davari, Edge Detection and Segmentation for Machine Vision, Proceedings of the 37th IEEE Southeastern Symposium on System Theory, 2005

8**. R. Munasinghe**, Panoramic Vision and Target Tracking, Project Report, WVU Institute of Technology, Montgomery, WV 25136, 2005
9. C. Fernando, **R. Munasinghe**, and J. Chittooru, Catadioptric Vision Systems: Survey, Proceedings of the 37th IEEE Southeastern Symposium on System Theory, 2005
10. **R. Munasinghe** and Chris Fernando, Use of surface reconstruction for machine vision, Proceedings of the Thirty-Sixth Southeastern Symposium on System Theory, IEEE, 2004
11. Chris Fernando and **R. Munasinghe,** Hybrid AI system for geometric pattern recognition, Proceedings of the Thirty-Sixth Southeastern Symposium on System Theory, IEEE, 20047.
12. **R. Munasinghe,** Using Differential Equations to Describe Conic Sections, The College Mathematics Journal, Volume 33, No. 2, March 2002
13. **R. Munasinghe,** Some Linear Differential Equations Forget that They have Variable Coefficients, The College Mathematics Journal, Volume 35, No. 1, January 2004
14. **R. Munasinghe,** Unstable Sets of Inverse Limit Spaces on the Closed Interval with One Bonding Map, Houston Journal of Mathematics, Volume 21, No.1, 1995

APPENDIX 27- Development of Techniques for Online Monitoring of Individual Gas Constituents in Coal-Derived Synthesis Gas and Flue Gas (NM006)

TECHNICAL REPORT

Contract Title and Number:	Period of Performance:
Establishment of the Center for Advanced Separation Technologies (DE-FC26-01NT41091)	Starting Date: 10/01/2008 Ending Date: 09/30/2010

Sub-Recipient Project Title:
The development of technique for on-line monitoring of individual gas constituents in coal-derived synthetic gas and flue gas

Principal Investigators:
Ning Liu, Peng Zhang

Report Information:
Type: Final
Number:
Period: 10/01/08-09/30/10
Date: 11/15/10
Code: NM006-FINAL

Contact Address:
PRRC, New Mexico Tech
801 Leroy Place
Socorro, NM, 87801

Contact Information:
Phone:
5758355739
Fax:
E-Mail:
ningliu@nmt.edu

Subcontractor Address:
Insert address of subcontractor. If none awarded, insert ―No subcontracts issued.”

Subcontractor Information:
Phone:
Fax:
E-Mail:

DISCLAIMER

ABSTRACT

The objective of this project is to develop a gas mass spectrometer-based (MS) technique to rapidly detect and continuously monitor gas constituents in synthesis gas (syngas) and flue gas. A gas detection system with controllable gas pressure and flow rate has been set up for the detection of up to four individual gas constituents under lab conditions. With this gas detection system we have evaluated the sensitivity, detection limit, selectivity and response time of the individual constituent or dual, triple and quadruple gas mixture from N_2, CO_2, H_2, He, CH_4 and CO in flow rate range of 0 – 20 ml/min of each gas constituent. Depending on different gases, the average errors between the tested partial pressure ratio and actual partial pressure ratio (e.g., flow rate ratio) are 1-10%. The magnitude of errors depends on the relative sensitivity of gas constituent. In tested mixtures H_2 shows the highest MS sensitivity and the largest average error. The response time for all gas constituents is less than 0.5 second. The detection limit and response time of each gas constituent are not influenced by its flow rate or other co-existing gas constituents under the present multi-constituent conditions. The designed gas detection system is expected to be applicable for rapidly and continuously monitoring of actual flue gas or syngas.

TABLE OF CONTENTS

INTRODUCTION

The United States has a vast resource of coal reserves. With the steadily-increasing energy demand and the escalation of oil and natural gas prices, it is forecast that coal-based power plants will continue to play a dominant role as an energy source for the U.S. in the foreseeable future. Sustainable development and environmental regulation require near-zero emission from coal utilization. Focus has been placed on creating the most advanced collection of clean, efficient, competitively priced coal-derived products and low-cost, environmentally compliant energy systems. One way to do this is to gasify coal to create synthetic gas (syngas), which consists primarily of carbon monoxide, hydrogen, and some hydrocarbons. This syngas can be used directly to drive gas turbines in integrated gasification combined-cycle (IGCC) power plants, or to separate pure hydrogen - a source of clean energy - for use in fuel cells.

The major challenges of a gas turbine include its combustion efficiency, stability, and emission. In order to increase the efficiency and reduce the emission of nitrogen oxides - a major source of smog and acid rain - modern gas turbines are designed to operate at a premixed mode, where gas fuels are premixed with air before entering the combustors. However, premixing may potentially induce auto-ignition or flame flashback upstream, which can damage the parts not designed for heat. It is also prone to instable combustion, resulting in large amplitude of acoustic oscillation, which can significantly reduce part life. Optimizing such premixing designs requires a delicate balancing of several performance demands, including lower emissions, higher power, high turndown, high efficiency, and low pulsation levels. Unfortunately, several of these demands are in conflict operationally, leaving only a very tight allowable operation space. Under such circumstances, the composition variation of the injecting fuel gas, either syngas, natural gas, biogas, or their mixtures, needs to be monitored continuously and fed back to the control system for instantaneous adjustments of other operational parameters. Depending on the sources of coals and the techniques used in gasification, composition of syngas can vary remarkably, especially for its major combustible components, hydrogen (16-34 mol %) and carbon monoxide (6-63%). The situation becomes even worse when different gas streams from different sources may mix together.

Produced syngas from the gasification unit in an IGCC power plant system has a very high temperature (600–700°C). Several sensing techniques are potentially applicable for online monitoring of gas composition at this high temperature harsh environment, among which the solid-state sensors have shown more promising. For example, a Pt-SiO_2-SiC Schottky diode sensor can be used as hydrogen (H_2) or hydrocarbon (CxHy) sensor at temperatures higher than 600°C. Nanocrystalline SnO2 with appropriate doping can be either NOx- or CO-sensitive with optimal operating range at 350–400°C. A solid electrochemical cell containing ZrO_2 is sensitive to oxygen by conducting oxygen ions at high temperatures, while an electrochemical cell using NASICON (sodium super ionic conductor) is sensitive to CO_2. These sensors—resistor, diode, and electrochemical cell—operate on different principles and each sensor has very different responses to the individual gases. For a mixture of gases like syngas, a sensor array, or electronic nose, is necessary, though interferences among different sensors need to be carefully handled. However, the response time for these solid-state gas sensors (>10 seconds) is usually slower than what would be expected for optimally operating an IGCC gas turbine (< 1 second). Besides, different gas sensors have

different optimal operating temperatures, which may not fit to the produced syngas environment, and their sensing characteristics may drift with temperature and time.

A simpler yet very practical way to monitor and quantify syngas is to bypass a small fraction of the syngas from the main stream and analyze its composition at a relatively lower temperature. In this case it is possible to use some online analytical techniques with high accuracy and fast response time rather than the sophisticated solid-state sensors. Mass spectrometry which relies on measuring the masses of ions and their abundances play a major role in a wide range of applications, such as aging research,[1] plant systems biology,[2] and pharmacological and toxicological research.[3] A QMS200 mass spectrometer system can continuously sample gas molecules, with molecular weight up to 200amu, at low flow rates of several milliliters per minute, and with inlet capable of sampling at pressures from 1 bar to 10 mbar. It has a fast response time of less than 0.5 seconds, with individual masses being measured at rates up to 25 points per second.[4] Therefore, by bypassing a small fraction of the syngas from the main stream, the mass spectrometer can be a good candidate for online syngas analysis at a relatively lower temperature.

On another front, the U.S. DOE is committed to tackling environmental challenges, including carbon capture and sequestration. The Southwest Regional Partnership on Carbon Sequestration (SWP), of which New Mexico Tech is the lead organization, has a keen interest in the development of new approaches that can monitor the exhausted flue gas from power plants, from which CO_2 generated from combustion must be captured for sequestration. Since the gas constituents in a flue gas are similar in type of molecules (though not in composition) to those in a synthesis gas, we envision that the technique we develop through the research work proposed here can be readily applied to monitor the composition of flue gas to improve the carbon capture efficiency.

EXECUTIVE SUMMARY

The objective of this project is to develop a gas mass spectrometer-based (MS) technique to rapidly detect and continuously monitor gas constituents in synthesis gas (syngas) and flue gas. The relevant technique issues include identification of a suitable mass spectrometer for the detection of individual gas constituents in syngas and in flue gas, characterization of these gas species in their pure forms using MS, development of a gas flow setup for mixing that allows control of individual gases as well as characterization of the system accuracy, and response time to the mixture of the various gases related to syngas or flue gas.

First, we identify and purchase a mass spectrometer (QMS200) from Standford Research Systems, Inc. (Sunnyvale, CA). The QMS200 system can continuously sample gas molecules, with molecular weight up to 200amu, at low flow rates of several milliliters per minute, and with inlet capable of sampling at pressures from 1 atm to 0.01 atm. It has a fast response time of less than 0.5 seconds, with individual masses being measured at rates up to 25 points per second. All these performance characteristics could fulfill our application of online monitoring of the constituents in syngas or flue gas. Then a gas flow simulation system with controllable gas pressure and flow rate has been set up for the detection of up to four individual gas constituents under lab conditions. In this system, cylinder gas pressure is adjusted via selected regulator to a value suitable for mass flow controller (MFC). The flow rate of individual gas constituent is accurately controlled by MFC.

With above gas detection system we have evaluated the sensitivity, detection limit, selectivity and response time of the individual constituent or dual, triple and tetradic gas mixture from N_2, CO_2, H_2, He, CH_4 and CO in flow rate range of 0 – 20 ml/min of each gas constituent under inlet gas pressure of 1 atm. The selected gas species are relevant to syngas or flue gas.

For individual gas constituent test, each gas constituent shows a stable pressure value that does not change with flow rate of gas after about one hour of running. The tested pressure values are $1.95*10^{-6}$, $1.90*10^{-6}$, $1.56*10^{-4}$, $2.28*10^{-6}$, $3.91*10^{-6}$ and $2.71*10^{-6}$ torr (*133.3Pa) for N_2, CO_2, H_2, CO, He and CH_4, respectively. It is evident that H_2 has much higher sensitivity than other gases that have a relatively close sensitivity. Moreover, the response time of all gases is less than 0.5 second.

For multi-constituent gas environment, the calculation for the tested partial pressure percentage ratio of each gas must be calibrated when its MS spectrum is contributed by other co-existing gas constituents. After calibration, the tested partial pressure percentage ratio of each gas is well close to its flow rate ratio for each tested point under multi-constituent environment. Considering that flow rate ratio of gas equals to its actual partial pressure ratio, the tested partial pressure percentage ratio is well agreed with its actual partial pressure ratio for each tested gas constituent in the different mixture systems. Depending on different gases, the average errors between the tested partial pressure ratio and actual partial pressure ratio are below 10%. Generally, the errors depend on the relative sensitivities of monitored gases. Large difference in term of the relative sensitivities of monitored gas components generally result in high errors between the tested partial pressure ratio and actual partial pressure ratio. For example, 1 – 5% of errors can be found for the mixtures with N_2, and CO_2 since these two gases have close gas sensitivity. However, the error of up to 10% for H_2 are demonstrated when H_2 and other gas components are mixed. This is the reason that H_2 shows much higher sensitivity than other gas constituents. These errors will be further reduced

when a certified standard gas mixture is used for test gas source. All gases can be detected at the response time of less than 0.5 second in the flow rate range of 0 – 20 ml/min. It is clear that the detection limit, and response time of each gas constituent are not influenced by its flow rate or other co-existing gas constituents under present multi-constituent environment. However, the sensitivity and selectivity of gas may be influenced due to the fragment contribution of other co-existing gas constituents.

Based on above experiment results, it is demonstrated that the designed gas detection system is very good for evaluating the sensitivity, detection limit, response time and selectivity of gas mixture with main gas constituents of syngas or flue gas under laboratory conditions. The designed gas detection system is expected to apply for rapidly detecting and continuously monitoring of actual syngas or flue gas from coal-fired power plant.

EXPERIMENTAL

A gas detection system is set up. Figure 1 is a schematic diagram for the detection of up to four individual gas constituents and their mixture under lab conditions. Cylinder gas pressure is adjusted via selected gas regulator to a value suitable for mass flow controller (MFC). The flow rate of individual gas constituent is controlled by MFC (Aalborg Inc.).

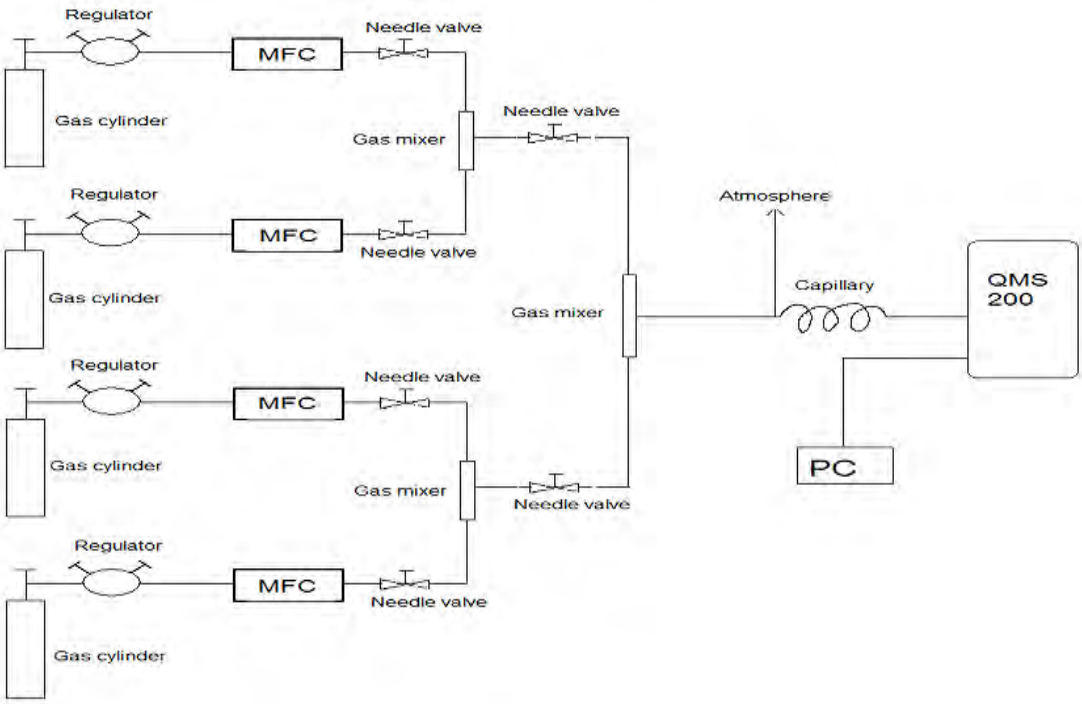

Figure 1. Schematic diagram of gas detection system

Six kinds of pure gases, e.g. N_2, CO_2, H_2, CO, He and CH_4, which are relevant to syngas or flue gas, as well as their mixture are selected for evaluating the accuracy of the mass spectrometer-based technique development. Before each test, the pipeline route system is purged by an individual gas or multi-constituent gas mixture with fixed flow rate for at least 30 min. The gas flow rate of each gas is adjusted by mass flow controller in the range of 0 – 20 ml/min. All gases are in the grade of ultra high purity (UHP). The detected mass-to-charger ratios (M/Q) are 28, 44, 2, 28, 4 and 15 for N_2, CO_2, H_2, CO, He and CH_4, respectively. Then the pressure of individual gas constituent or the partial pressures of different gases in mixture are tested by a QMS200 mass spectrometer (Stanford Research Systems, Inc.) with data recorded by a computer. The QMS200 mass spectrometer is attached a capillary that is able to sample under atmosphere pressure condition. A data collection model of pressure via time (P vs T) is used for a continuous on-line monitoring of various gas constituents.

RESULTS AND DISCUSSION

Individual gas constituent

With above gas detection system we have evaluated the sensitivity, detection limit, selectivity and response time of N_2, CO_2, H_2, He, CH_4 and CO in flow rate range of 0 – 20 ml/min under inlet gas pressure of 1 atm, respectively. The selected gas species are relevant to syngas or flue gas.

After mass spectrometer on-line runs about one hour, each gas constituent shows a stable pressure value that does not change with flow rate of gas. The tested pressure values are $1.95*10^{-6}$, $1.90*10^{-6}$, $1.56*10^{-4}$, $2.28*10^{-6}$, $3.91*10^{-6}$ and $2.71*10^{-6}$ torr (133.3 Pa) for N_2, CO_2, H_2, CO, He and CH_4, respectively. The tested pressure values are also listed in Table 1. N_2, CO_2 and CO show close pressure values. He and CH_4 show slightly higher pressure values as compared to that of N_2, CO_2 and CO. However, it is very evident that H_2 has the highest pressure value among all gases. Its mass spectrum sensitivity is about one hundred time that of other gases. Moreover, the response time of all gases is less than 0.5 second.

Table 1: The tested pressure values of nitrogen, carbon dioxide and hydrogen

Gas	Pressure values (*133.3Pa)	Flow rate (ml/min)
Nitrogen (N_2)	$1.95*10^{-6}$	$0 < r \leq 20$
Carbon dioxide (CO_2)	$1.90*10^{-6}$	$0 < r \leq 20$
Hydrogen (H_2)	$1.56*10^{-4}$	$0 < r \leq 20$
Carbon monoxide (CO)	$2.07*10^{-6}$	$0 < r \leq 20$
Helium (He)	$3.91*10^{-6}$	$0 < r \leq 20$
Methane (CH_4)	$2.71*10^{-6}$	$0 < r \leq 20$

Multi-constituent gas mixture

We have further evaluated the sensitivity, detection limit, selectivity and response time of the dual, triple and quadruple gas mixtures from N_2, CO_2, H_2, He, CH_4 and CO in flow rate range of 0 – 20 ml/min of each gas constituent under inlet gas pressure of 1 atm.

Figure 2 shows the tested partial pressure percentage ratio (P_{CO2}/P_0) of CO_2 as a function of its flow rate ratio (r_{CO2}/r_0) in N_2/CO_2 mixture. As shown in Figure 2, value of P_{CO2}/P_0 is well agreed to that of r_{CO2}/r_0 for each tested point. Considering that the flow rate ratio of gas equals to its actual partial pressure ratio, the tested partial pressure percentage ratio of CO_2 is well agreed with its actual partial pressure ratio in the N_2/CO_2 mixture. The errors between the tested partial pressure ratio and actual partial pressure ratio for CO_2 are about 1 – 5%. In turn, a similar result is obtained for N_2 in the N_2/CO_2 mixture since this mixture has only two constituents. Similarly, the errors between tested values and actual values are below 6% for any dual gas mixture from N_2, CO_2, He, CH_4 and CO.

A series gas mixtures containing H_2, e.g., H_2/CO_2, H_2/N_2, $H_2/CO_2/CH_4$ and $H_2/CO_2/CH_4$/He, have been further evaluated for the effects of the interaction between different gases since H_2 shows much higher sensitivity than other gas constituents. As an example, Figure 3 shows the tested partial pressure percentage ratio (P_{H2}/P_0) of H_2 as a function of its flow rate ratio (r_{H2}/r_0) in H_2/CO_2 mixture. Basically, the tested partial pressure

ratio is well proportional to its actual flow rate ratio, e.g., actual partial pressure ratio. In these mixtures the average errors between the tested partial pressure ratio and actual partial pressure ratio for H_2 are about 6 – 9% (Table 2). The errors are higher than that in the above dual mixtures without H_2. For other gas constituents in these mixtures with H_2, their average errors are generally no more than 6% (Table 2). It is obvious that the average error of H_2 is always higher than that of other gas constituents in each mixture. The main reason could be that H_2 has a much higher sensitivity than other tested gases.

Table 2: The average error of each gas under multi-constituent environment

Gas mixture	Average error (H_2)	Average error (CO_2)	Average error (N_2)	Average error (CH_4)	Average error (He)	Average error (CO)	Flow rate of each gas (ml/min)
H_2/CO_2	8%	4%					$0 < r_i \leq 20$
H_2/N_2	6%		4%				$0 < r_i \leq 20$
$H_2/CO_2/CH_4$	8%	5%	6%				$0 < r_i \leq 20$
$H_2/CO_2/CH_4$/He	9%	4%	4%		5%		$0 < r_i \leq 20$
$H_2/CO_2/CH_4$/CO	10%	6%		4%		7%	$0 < r_i \leq 20$

Figures 4, 5, 6 and 7 show the tested partial pressure percentage ratio as a function of flow rate ratio for H_2, CO, CO_2 and CH_4 in a $H_2/CO_2/CH_4$/CO mixture, respectively. Here it should be pointed out that, when the tested partial pressure percentage ratio of CO is calculated, the mass spectrum of CO must be calibrated by removing the contribution from CO_2 since it can produce about 8.63% mass spectrum at mass-to-charge of 28.[5,6] All gas constituents show a positive proportion relationship between the pressure ratio and flow rate ratio. It is listed in the Table 2 that the average errors between the partial pressure percentage ratio and the actual flow rate ratio are 10, 7, 6 and 4 for H_2, CO, CO_2 and CH_4, respectively. This implies that the errors depend on the relative sensitivities of monitored gases under multi-constituent environment. Large difference in term of the relative sensitivities of monitored gas components generally result in high average errors. H_2 has a much higher sensitivity than other gas constituents. As a result, H_2 show the largest test error among all tested gases. Moreover, various gases are mixed in an in-situ way in present experiments. This also brings about test error in some extent for all gases. Therefore these errors could be further reduced when a certified standard gas mixture is used for test gas source. Finally, all gases can be detected at the response time of less than 0.5 second in the flow rate range of 0 – 20 ml/min. Based on what stated above, the detection limit, and response time of each gas constituent are not influenced by its flow rate or other co-existing gas constituents under present multi-constituent environment, but the sensitivity and selectivity of gas may be influenced due to the fragment contribution of other co-existing gas constituents.

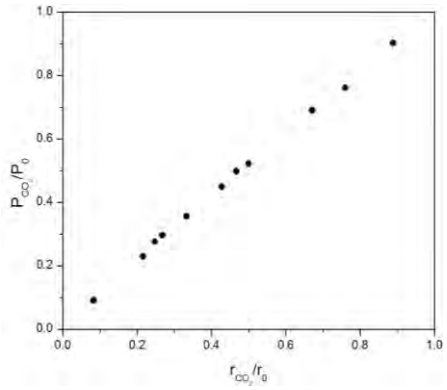

Figure 2 The tested partial pressure ratio of CO_2 as a function of its flow rate ratio in the N_2/CO_2 mixture.

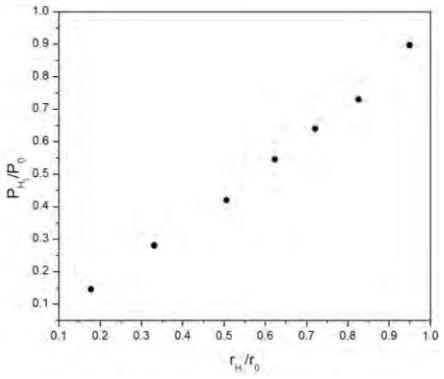

Figure 3 The tested partial pressure ratio of H_2 as a function of its flow rate ratio in the H_2/CO_2 mixture.

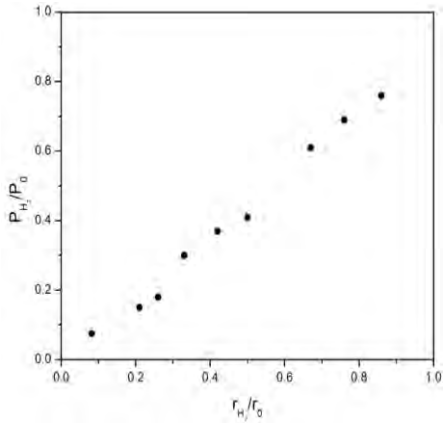

Figure 4 The tested partial pressure ratio of H_2 as a function of its flow rate ratio in the $H_2/CO_2/CH_4/CO$ mixture.

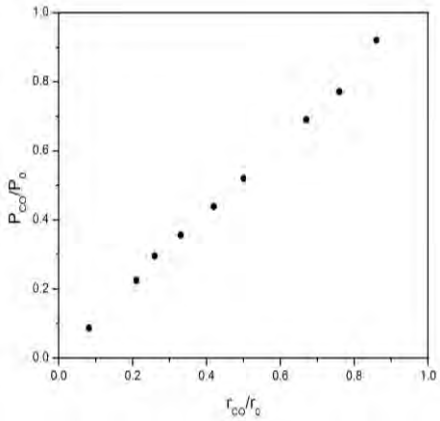

Figure 5 The tested partial pressure ratio of CO as a function of its flow rate ratio in the $H_2/CO_2/CH_4/CO$ mixture.

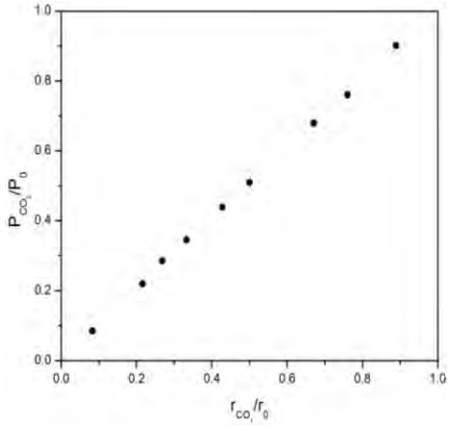

Figure 4 The tested partial pressure ratio of CO_2 as a function of its flow rate ratio in the $H_2/CO_2/CH_4/CO$ mixture.

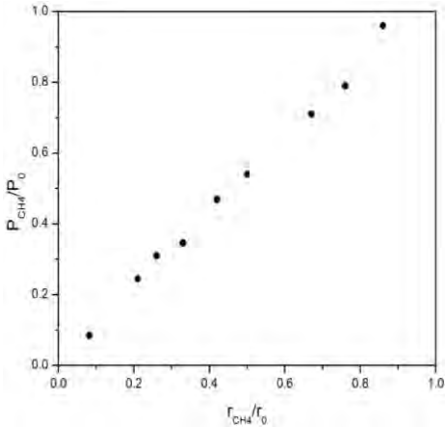

Figure 5 The tested partial pressure ratio of CH_4 as a function of its flow rate ratio in the $H_2/CO_2/CH_4/CO$ mixture.

CONCLUSION

A gas detection system with controllable gas pressure and flow rate has been set up for the detection of up to four individual gas constituents under lab conditions. With this gas detection system the sensitivity, detection limit, selectivity and response time of the individual constituent or dual, triple and quadruple gas mixture from N_2, CO_2, H_2, He, CH_4 and CO have evaluated in flow rate range of 0 – 20 ml/min of each gas constituent. The average errors between the tested partial pressure ratio and actual partial pressure ratio are below 10% for H_2 and below 7% for other tested gas constituents. The response time of all gases is less than 0.5 second. The detection limit and response time of each gas constituent are not influenced by its flow rate or other co-existing gas constituents under present multi-constituent environment. The designed gas detection system is very good for evaluating the sensitivity, detection limit, response time and selectivity of gas mixture under laboratory conditions. The designed gas detection system is expected to apply for rapidly detecting and continuously monitoring of actual flue gas or syngas.

REFERENCES

1. C. Schoneich, Mass spectrometry in aging research. Mass Spectrometry Reviews, 2005, 24, 701– 718.M. Glinski, W. Weckwerth, The role of mass spectrometry in plant systems biology. Mass Spectrometry Reviews, 2006, 25, 173– 214.
2. K. Brown, W. M. Tompkins, and I. N. H. White, Applications of accelerator mass spectrometry for pharmacological and toxicological research. Mass Spectrometry Reviews, 2006, 25, 127– 145.
3. R.G. cooks, Z. Ouyang, Z. Takats, J. M. Wiseman, Ambient mass spectrometry. Science, 2006, 311, 1566 – 1570.
4. http://www.thinksrs.com
5. Bley, ―Quantitative measurements with quadrupole mass spectrometer: important specifications for reliable measurements", Vacuum, 38(1988)103-109.
6. Cowen, et al., ―Nonlinearities in sensitivity of quadrupole partial pressure analyzers operating at higher pressures", J. Vac. Sci. Technol. A 12(1), Jan/Feb 1994.

APPENDIX 28– Gas-Gas Separation by Selective Hydrate Formation (VA022)

FINAL TECHNICAL REPORT

Contract Title and Number:	Period of Performance:
Continuation in Crosscutting Technology Development at CAST. (DE-FC26-05NT42457)	Starting Date: 07/18/08 Ending Date: 9/30/11

Sub-Recipient Project Title: Gas-Gas Separation by Selective Hydrate Formation	Report Information: Type: Final Number: Period: Date:
Principal Investigators: Yoon, Roe-Hoan and Wang, Jialin	Code: VA018-FINAL
Contact Address: 146 Holden Hall Blacksburg, VA 24060	Contact Information: Phone: 540 231 4508 Fax: 540 231 3948 E-Mail: ryoon@vt.edu
Subcontractor Address: "No subcontracts issued.	Subcontractor Information: Phone: Fax: E-Mail:

ABSTRACT

It is well known that the kinetics of gas hydrate formation is slow, involving long induction time, which is the main barrier for the practical application of gas hydrate technologies, such as gas-gas separation by selective hydrate formation, displacement of methane hydrate with CO_2, *etc*. Many investigators showed, however, that the induction times can be substantially reduced in the presence of thermodynamic or kinetic promoters such as tetrahydrofuran (THF) and long-chain surfactants. It has been found in the present work that the kinetics of hydrate formation can be greatly increased in the presence of hydrophobic particles. The test results obtained with water-in-CO_2 (or CO_2-N_2 mixture) emulsions stabilized by Teflon particles (1 μm) and CO_2-in-water emulsions stabilized by hydrophobic silica nanoparticles showed substantial improvements in the kinetics of hydrate formations of CO_2 and CO_2-N_2 mixture.

Two possible explanations may be given. One is the increased mass transfer of gas into water due to the large interfacial area between gas and water. The other is the formation of partial clathrates in the vicinity of hydrophobic surfaces. In AFM force measurements conducted in the previous reporting period, we suggested the formation of the partial clathrates as the origin of the long-range hydrophobic forces measured between hydrophobic surfaces. The partial clathrates may serve as precursors for hydrate formation.

Thermodynamically, formation of the partial clathrates should be favored at a lower temperature and a higher pressure.

INTRODUCTION

Background

In the proposed work, the possibility of separating different gases (*i.e.*, CO_2/N_2, CH_4/CO_2) by selective hydrate formation will be explored. It involves making one type of gas into hydrate (a solid) and keeping the other in gaseous form, thereby allowing the two to be separated. An advantage of the selective gas hydrate formation over the current separation method, *e.g.*, membrane, pressure swing adsorption (PSA), should include high throughput and simplicity, which can be the bases for developing a cost-effective process. One technological barrier, however, for commercial deployment may be the slow kinetics and high pressure requirement for the gas hydrate formation.

Objective and Approach

It is generally accepted that gas hydrate formation is due to "hydrophobic hydration".[1] It is also well known that water molecules form "iceberg" structures around hydrocarbon chains.[2] Both of these processes entail decrease in entropy. We found in our surface force measurements that the hydrophobic force between macroscopic surfaces also entails entropy decrease[3], which lead us to conclude that water molecules form partial or full clathrates in the vicinity of hydrophobic surfaces. This finding can be exploited to promote the formation of hydrates by using hydrophobic substrates (*e.g.*, hydrophobic silica nanoparticles, Teflon particles) or surfactants to increase the kinetics and decrease the pressure requirement.

PROJECT TASKS

1. Equipment Setup for Gas Hydrate Experiments

In addition to a large pressure reactor (15L) constructed in the previous reporting period, in the current reporting period, a mini reactor (100 ml, model 4566C, Parr Instrument Company) was purchased for the purpose of forming gas hydrates and determining the rates of their formation and dissociation. The reactor provides a means of creating a high pressure, low temperature environment where hydrate growth can occur on a gas / water interface. As shown in Figure 1, pressure is measured by a transducer that converts the deflection of a piezoelectric diaphragm into an analog current signal. Temperature is measured *via* a resistance temperature detector (RTD) probe, which correlates a voltage drop to a temperature. Analog signals are converted to digital data and saved on a computer *via* a reactor controller (model 4848).

The reactor has a maximum working pressure of 2900 psi (200 bars) and a temperature control range of -20 to 225 °C. Temperature control is achieved *via* a refrigerated/heating circulator which pumps heat transfer fluid into a bath surrounding the

Figure 1. Experimental setup for studying kinetics of gas hydrate formations. Left: 100 ml mini bench top reactor equipped with a RTD probe and a pressure transducer. Right (upper): The temperature is controlled by putting the mini reactor into a refrigerated coolant bath. Right (lower): The temperature and pressure inside the reactor are monitored by a reactor controller and recorded by a computer.

reactor (Figure 1). Pressure is controlled by adjusting a pressure regulator attached to a gas cylinder. Two safety measures are included to prevent over pressurization of the reactor: a pressure relief valve and rupture disc. The relief valve can be adjusted to release gas at a point below maximum working pressure whereas the rupture disc has been engineered to fail at the maximum working pressure (rated 3000 psi).

Hydrate formation is detected by measuring the pressure drop and the temperature increase associated with hydrate formation. In order to increase the reaction rate, a magnetically coupled mixer can be controlled to actively agitate the gas / water interface to both increase gas dissolution and break up thin hydrate layers that would otherwise impede aggregation of hydrates. Agitation is controlled by varying the motor speed through the reactor controller, as shown in Figure 1.

2. Gas Hydrate Formation in Hydrophobic Porous Medium

Using the reactor constructed in Task 1, various hydrates were formed under different conditions. The main purpose of this task is to increase the kinetics and reduce the pressure requirement for hydrate formation. According to the hydrophobic force measurements conducted previously, partial or full clathrates are formed in the vicinity of hydrophobic

Figure 2. Free-flowing dry water powder prepared by aerating 10.59 g Teflon particle (1 μm) and 60 g ultrapure water at 14100 rpm in a blender for 180 s.

surfaces. These species can serve as precursors for the hydrates containing desired guest molecules (*e.g.*, CO_2, N_2, and CH_4) in clathrates. Therefore, in the present study, we explored the possibility of improving the kinetics of CO_2 hydrate formation by using water-in-CO_2 emulsions (dry water) stabilized by small Teflon particles (1 μm) and CO_2-in-water emulsions (foam) stabilized by hydrophobic silica nanoparticles (16 nm, R972, Degussa) as emulsifiers. The dry water was prepared by vigorously mixing water and CO_2 in the presence of hydrophobic Teflon particles. Figure 2 shows the picture of dry water prepared by aerating 10.59 g Teflon particle and 60 g ultrapure water at 14100 rpm for in a blender 180 s. A 35 g emulsion was placed in a 100 ml hydrate reactor (Figure 1) at constant temperature (1.1 °C) and at a pressure well above the equilibrium pressure initially. The reactions were conducted at constant volume and constant temperature conditions, and the changes in pressure were recorded as a function of time by means of a computer. The emulsion was left to stand for 10 hours without agitation. Figure 3 shows the formation of CO_2 hydrate in the presence of Teflon dry water. The beginning of gas hydrate formation is evidenced by the abrupt decrease in pressure and at the same time increase in temperature. With the dry water, CO_2 hydrate began to form after 18 minutes, while no reaction occurred in the absence of the

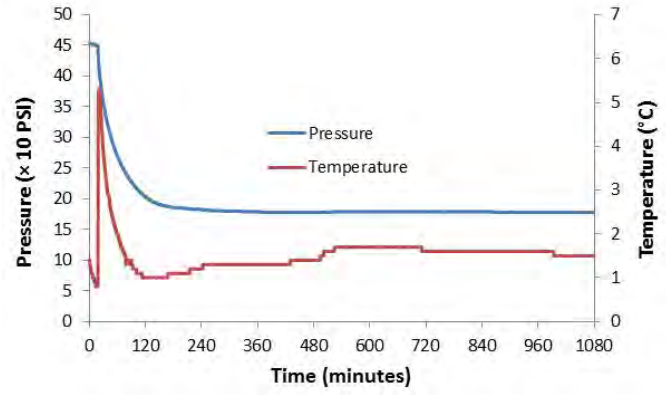

Figure 3. Experiment on the formation of gas hydrate. The beginning of gas hydrate formation is evidenced by the abrupt decrease in pressure and increase in temperature.

hydrophobic particles, as shown in Figure 4.

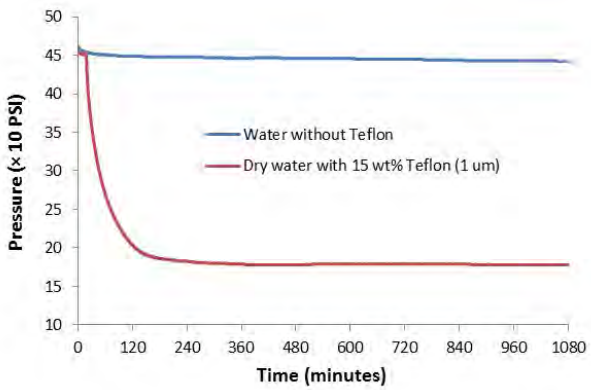

Figure 4. P-t kinetic plots for CO_2 hydrate formations in pure water and in Teflon-stabilized dry water at 1.1 °C.

It has been reported that the rates of CH_4[4] and CO_2[5] uptakes in hydrates were greatly increased by forming the hydrates in preformed dry water powders stabilized by hydrophobic silica nanoparticles. In the current reporting period, the CO_2 gas hydrate formation experiment was also conducted in the presence of silica (7 nm, R812s, Degussa)-stabilized dry water at 1.1 °C, and the result was compared with those obtained using Teflon. All of the tests were carried out at the same initial conditions, *i.e.*, 1.1 °C, 450 psi and 30 g of pure water. The dry waters were used under the non-agitated condition. The experiments were conducted over a period of less than 20 hours. The result is represented in Figure 5. It is seen that with the hydrophobic silica, CO_2 hydrate formation started instantaneously, while it took 18 minutes for CO_2 hydrate formation to get started in the presence of Teflon. This is probably due to the formation of smaller water droplets by using hydrophobic silica nanoparticles, and the increased interfacial area per unit volume may result in shorter induction time.

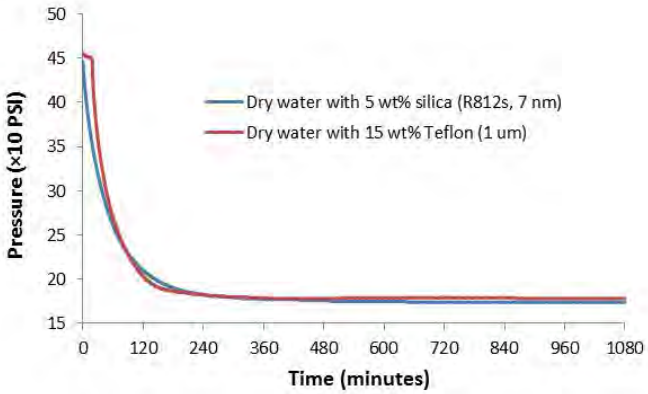

Figure 5. Comparison between silica- and Teflon-stabilized dry waters in the kinetics of CO_2 hydrate formations at 1.1 °C.

Figure 6 shows the pressure *vs*. time curves for Teflon dry water and bulk water tested for the formation of gas hydrate of CO_2-N_2 mixture. It shows that Teflon dry water had

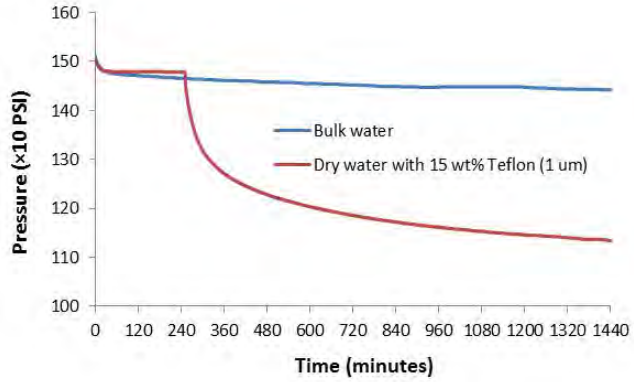

Figure 6. P-t kinetic plots for CO_2-N_2 mixture (19.87% CO_2) gas hydrate formations in pure water and in Teflon stabilized dry water at -2 °C.

shorter induction time, and the reaction took place after 240 minutes, as evidenced by the rapid pressure drop. While for bulk water, the reaction did not occur for a period of 24 hours. Therefore, it is possible that Teflon dry water can be used as promoter for the gas-gas separation by selective hydrate formation.

Figure 7. Foam was prepared by aerating 0.5 g of hydrophobic silica nanoparticle (R972, 16 nm) and 50 g of ultrapure water at 14100 rpm in a blender for 180 s.

The CO_2-in-water emulsions (foam) were prepared by agitating a mixture of CO_2 gas, hydrophobic silica (16 nm, R972, Degussa), and water in a hydrate reactor. Figure 7 shows the picture of foam prepared by aerating 0.5 g of hydrophobic silica nanoparticle and 50 g of ultrapure water at 14100 rpm for in a blender 180 s. The pressure *vs*. time curve (Figure 8) obtained by adding CO_2 gas as an emulsion shows much faster kinetics than the case of adding CO_2 directly in the absence of hydrophobic particles. In the former, the pressure dropped from 450 to 188 psi in 60 minutes, indicating hydrate formation. In the latter, there were no indications for hydrate formation for a period of 1200 minutes. The pressure drop from 450 to 340 psi was due to CO_2 dissolution in water.

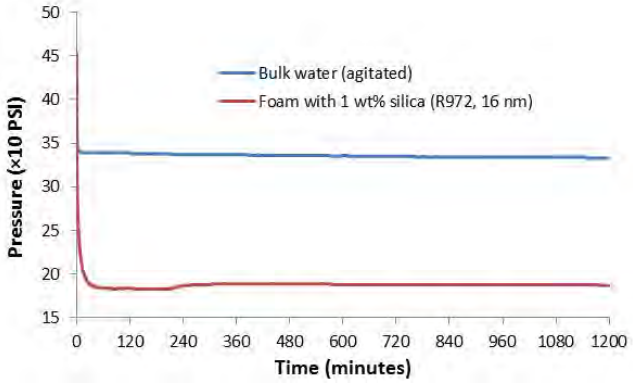

Figure 8. P-t kinetic plots for CO_2 hydrate formations in pure water and in silica-stabilized foam at 1.1 °C.

Effect of Using Surfactants on Gas Hydrate Formation

It is well known that certain types of surfactants can be used as kinetic promoters for gas hydrate formation. Some scientists speculate that these surfactants can increase the solubility of hydrophobic solutes such as methane in water, and hence promote its mass transfer and hydrate formation. Another possibility may be that the hydrocarbon chains, particularly micelles, can form partial clathrates (or "icebergs") around the hydrocarbon chains, which can serve as precursors for gas hydrate formation. In this task, we have tested various ionic and non-ionic surfactants. Figure 9 shows the effect of adding glutaric acid on the kinetics of CO_2 hydrate formation. The gas hydrate formation experiments were conducted under the agitated condition. As shown, with glutaric acid, the reaction took place after 100 minutes, while no reaction occurred in pure water. It can be concluded that glutaric acid can serve as gas hydrate promoter. The mechanism associated with the increased gas hydrate formation kinetics in the presence of glutaric acid will be the subject of further investigation.

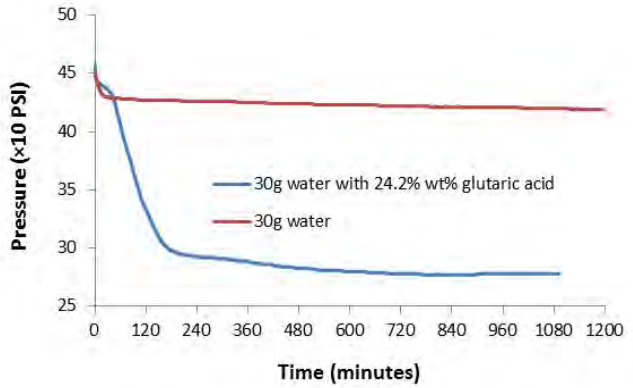

Figure 9. P-t kinetic plots for CO_2 hydrate formations in pure water and in glutaric acid water solution at 1.1 °C.

SUMMARY

In the current reporting period, we explored the possibility of improving the kinetics of CO_2 hydrate formation. Our approach was to use the water-in-CO_2 emulsions (dry water) or CO_2-in-water emulsions (foam) stabilized by using Teflon particles (1 μ) and hydrophobic silica nanoparticles (16 nm), respectively, as emulsifiers. We discovered that the kinetics of gas hydrate formation can be dramatically improved in the presence of hydrophobic particles. With foam emulsions stabilized by hydrophobic silica particles, the formation of CO_2 hydrate took place immediately. With Teflon-stabilized dry water, the reaction occurred after only 18 minutes.

REFERENCES

1. Lipkowski, J., *J. Therm. Anal.* **2006,** *83* (3), 525-531.
2. Tanford, C., *The Hydrophobic Effect*. 2 ed.; Wiley: New York, 1980.
3. Wang, J. AFM Surface Force Measurements between Hydrophobized Gold Surfaces. Virginia Tech, Blacksburg, 2008.
4. Weixing Wang, C. L. B., Dave J. Adams, Andrew I. Cooper, *J. AM. Chem. Soc* **2008,** *130* (35), 11608-11609.
5. Benjamin O. Carter, W. W., Dave J. Adams, Andrew I. Cooper, *Langmuir* **2010,** *26* (5), 3186-3193.

PUBLICATIONS/PRESENTATIONS

Two abstracts entitled “Effect of Hydrophobic Surfaces on the Kinetics of Hydrate Formation” and “The Role of Acid-Base Interaction in the Formation of CO_2 Hydrate” were submitted to 7^{th} International Conference on Gas Hydrates, 17^{th}-21^{st}, July 2011, Edinburgh, Scotland.

APPENDICES

No appendices are included in this report.